DISSERTATION

in

PHYSICS

for the degree

DOCTOR RERUM NATURALIUM

THE CASCADE ^{10}B THERMAL NEUTRON DETECTOR

AND

SOIL MOISTURE SENSING BY COSMIC-RAY NEUTRONS

ON THE PHASE FRONT OF NEUTRON DETECTION

by

DIPL. PHYS.

MARKUS OTTO KÖHLI

Supervisor

PROF. DR. ULRICH SCHMIDT

Nuclear and Neutron Physics Divison
Precision Experiments in Nuclear and Particle Physics
Physikalisches Institut
Department of Physics and Astronomy

ALMA MATER

UNIVERSITAS RUPERTO-CAROLA HEIDELBERGENSIS

Reviewers:
Prof. Dr. Ulrich Schmidt (Physikalisches Institut, Heidelberg University)
Prof. Dr. Ulrich Uwer (Physikalisches Institut, Heidelberg University)
Thesis Commitee:
Prof. Dr. Matthias Bartelmann (Institute of Theoretical Astrophysics, Heidelberg University)
Prof. Dr. Ulrich Glasmacher (Institute of Earth Sciences, Heidelberg University)

Physikalisches Institut
Fakultät für Physik und Astronomie
Ruprecht-Karls-Universität
Heidelberg
Germany

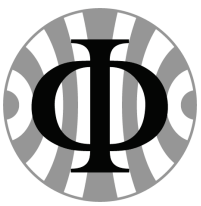

Submission: March 25th, 2019
Defense: June 5th, 2019

DISSERTATION
submitted to the
Combined Faculties for the Natural Sciences and for Mathematics
of the Ruperto-Carola University of Heidelberg, Germany
for the degree of
Doctor of Natural Sciences

Put forward by
Dipl.-Phys. Markus Otto Köhli
Born in Emmendingen

Oral examination: 05.06.2019

The CASCADE ^{10}B thermal neutron detector and soil moisture sensing by cosmic-ray neutrons

Referees: Prof. Dr. Ulrich Schmidt
Prof. Dr. Ulrich Uwer

Abstract

This work connects the three domains of experimental nuclear physics, computational physics and environmental physics centered around the neutron. The CASCADE thermal neutron detector is based on a combination of solid ^{10}B coatings in several layers, GEMs as gas amplification stages, a microstructured readout, multichannel ASICs and FPGA hardware triggered data acquisition. The detailed analysis to improve the system in terms of time-of-flight resolution for Neutron Resonance Spin Echo Spectroscopy required for a simulation model of the detector. The limitations of existing codes led to the development of the Monte Carlo transport code URANOS, which fully integrates the detector components and features a voxel-based geometry definition. The simulation could then successfully be applied to precisely understand neutron transport within the frame of Cosmic-Ray Neutron Sensing. This novel and interdisciplinary method offers the possibility to non-invasively measure soil moisture on the hectare scale using neutrons of the environmental radiation. The endeavor of this work led to the development of the footprint weighting function, which describes the neutron density change by different hydrogen pools in the air-ground interface. Significant influences of the near-field topology around the sensor were predicted by this work, experimentally verified and correction methods were successfully tested.

Zusammenfassung

Die vorliegende Arbeit befasst sich mit den drei Disziplinen der experimentellen Kernphysik, der computergestützten Physik und der Umweltphysik mit dem Neutron als Pivotelement. Der zur Messung von thermischen Neutronen entwickelte CASCADE Detektor besteht aus einer Kombination aus mehreren Ebenen von ^{10}B Schichten, GEMs zur Gasverstärkung, eine mikrostrukturierte Auslese, Vielkanal-ASICs und einer FPGA-gestützten digitalen Datenverarbeitung. Die detaillierte Analyse um das System hinsichtlich seiner Flugzeitauflösung zur Anwendung in der Neutronen-Resonanz-Spin-Echo-Spektroskopie zu verbessern, erforderte ein Simulationsmodell des Detektors. Die Limitationen bestehender Softwarelösungen führten zur Entwicklung des Monte-Carlo Neutronentransportprogramms URANOS, welches alle wesentlichen Komponenten des Detektors abbildet und über eine voxelbasierte Geometrie-Engine verfügt. Die Simulation konnte erfolgreich angewendet werden um den Neutronentransport im Rahmen des Cosmic-Ray Neutron Sensings präzise zu verstehen. Diese neuartige und interdisziplinäre Methode bietet die Möglichkeit der nichtinvasiven Bodenfeuchtebestimmung auf der Hektarskala mit Hilfe von Neutronen aus der kosmischen Höhenstrahlung. Das Bestreben dieser Arbeit führte zu der Ausarbeitung der Flächengewichtungsfunktion, welche die Neutronendichteänderung hinsichtlich verschiedener Wasserstoffpools an der Luft-Boden-Schnittstelle beschreibt. Der maßgebliche Einfluss der Topologie des unmittelbaren Nahbereichs um den Sensor herum wurde in dieser Arbeit vorhergesagt, experimentell bestätigt und Korrekturmethoden wurden untersucht.

An den Mistral

CONTENTS

PREFACE

The world of neutron detection is changing.
Much of what once was established technology has been discarded. For them now alternative ones have been presented. It began with production of tritium and peaked at the crisis of helium-3. Part of that was given to sciences for basic or applied research. Part for the industry, explorating oil deep in the rocks. And the largest part was given to homeland security, which above all demanded for it for the protection against hazards. After the stockpile was nearly exhausted, alerts on the future supply, which are especially critical to perspectives of the European Spallation Source led to developments of replacement technologies, most of them adapted from particle physics. The CASCADE thermal neutron detector is such a new generation system, which was designed specifically for the purposes of Neutron Spin Echo (NSE) spectroscopy. This method and its successors, Neutron Resonance Spin Echo (NRSE) and MIEZE (Modulation of IntEnsity by Zero Effort), demanded a highly granular and time-resolved detector to be operated efficiently at high rates. Contrary to triple-axis spectrometry or standard time-of-flight measurements, NRSE methods can achieve a high energy resolution using wavelength distributions of up to 20 % width. In a research field, where beam intensity in general is scarce due to limitations in the upscaling of the source, this technology offers in combination with a high-end detector the benefits which are looked for.
The CASCADE design is based on a combination of solid ^{10}B coatings in several layers, GEMs as gas amplification stages, a microstructured readout, multichannel ASICs and FPGA hardware triggered data acquisition. The developments of this work successfully brought the CASCADE detector into operation at the Forschungs-Neutronenquelle Heinz Maier-Leibnitz at the instruments RESEDA and MIRA.

The world of neutron simulations is changing.
What once was the most demanding domain for high performance computing infrastructures can meanwhile be realized on a modern personal computer. Along with this loss of exclusivity the heritage of those system architectures can be abandoned: Fortran-based ASCII interfaces, which aim for criticality calculations. And set back the scope to focus on the neutron as a probe to the otherwise invisible and impenetrable. What makes neutrons to messengers for hidden orders in matter, makes them likewise hard to control and hard to describe. They are produced randomly, their momentum and their interaction appear to be stochastic. While being less abundant than photons or electrons but far from few-body systems in terms of numbers, the Monte Carlo simulation is the most suitable tool bridging the gap between thermodynamic flux models and analytical calculations. Neutrons also interact with volumes rather than with surfaces. Hence, the essential unit to comprehend and implement a geometry model is the voxel, a threedimensional pixel.
The URANOS Monte Carlo simulation has been created based on this computational philosophy and has been realized in a collaboration with environmental physics as a valuable community tool.

The world of neutron applications is changing.
What began with the fission of uranium as source of energy and peaked with the development of a thermonuclear arsenal has been discarded. Large-scale research centers with most recently the European Spallation Source being built are shaping the research infrastructure to consequently stretch out the scope of fundamental research to other

science domains. Sources like the FRM II, ILL, SNS or ISIS are equipped with dozens of different experiments to investigate structures on the nanoscale from complex crystals to polymers or biomolecules, to image the magnetic ordering of superconductors or skyrmion lattices, to provide direct insights into storage cells or artifacts of cultural heritage and also to support the production of radio-isotopes and the medical treatment of cancer.
Since the recent initiative of Desilets and Zreda the method of Cosmic-Ray Neutron Sensing is gaining momentum. It allows to determine soil moisture on the hectare scale by the density of neutrons created in the atmosphere and reflected from the ground. It represents a technology to quantify non-invasively the most essential resource in food production: water. The effect that soil moisture influences the above-ground neutron flux had been known at least since the 1960s. Several attempts, however, failed to comprehensively understand the signal dependencies due to the lack of resources and interest to address the complexity of the transport problem. With the development of URANOS using computationally efficient the nowadays available off-the-shelf hardware, the model dependencies within the environmental system have been tracked down in extensive simulations. This work manages to unfold the intricacy of the cosmic-ray neutron transport, discovering the solution of a 50-year old problem and enabling CRNS to become an established hydrological method.

The world of neutrons is changing.

This is the phase front.

INTRODUCTION

THE CASCADE DETECTOR - THE CHALLENGE

The CASCADE detector is designed for thermal neutron scattering measurements at high intensities. The active detection volume is comprised of solid enriched ^{10}B converter layers in a gas detector. Gas Electron multiplier foils (GEMs) are stacked ontop of each other acting as a gas amplification stage and at the same time as a substrate for the converter. The limited efficiency of a single boron-10 layer of around 5 % can be improved by projecting the conversion ion tracks onto a common readout without significantly losing spatial resolution.
At the beginning of this work, a CASCADE detector with six layers in two half-spheres had already been successfully employed in twodimensional measurements. For the application in time-resolved Neutron Resonance Spin Echo Spectroscopy it was necessary to additionally identify the layer in which the conversion took place. This seemed to be feasible by measuring the charge signal of electrons traversing the stack, however, the correct identification turned out to be far more complicated than assumed. With the whole detector already in place it was also not possible toe easily disentangle different parts to reduce the complexity. Additionally, this detector was neither characterized nor simulated, therefore the focus of this work was first set to close the knowledge gap and understand the detector in its technical and physical details. It turned out, that crosstalk and misidentification were more dominant than the signal itself and therefore a rework of a manifold of functional parts of the detector was necessary in order to achieve a stable operation. The electrical design had to be optimized for increasing the signal-to-noise ratio for the already weak signals. The introduction of metal meshes in between the GEM layers improved the capacitive decoupling, the boron coatings were partly too thick and the firmware had to be adapted to the event topology from raw data as it was based rather on assumptions about the data structure than on the actual signals.

COSMIC-RAY NEUTRON SENSING - THE CHALLENGE

From 2008 on the method of Cosmic-Ray Neutron Sensing rapidly developed. Its intriguing aspects are the possibility to measure soil moisture non-invasively at so-called intermediate scales, which cannot be accessed by other technologies, but especially match typical soil water correlation lengths. The method relies on the fact, that in collisions with hydrogen neutrons are stopped much more efficiently than with any other element due to the high cross section and the equal masses of the projectiles.
High energetic cascades in the upper atmosphere generate neutrons, which finally tend to be reflected by dry soil or get moderated under wet conditions. A significant amount of data could be collected by deploying a network of standardized Cosmic-Ray Probes. Such are detectors sensitive to epithermal neutrons and similar in the buildup to Bonner Spheres with a one inch moderator around a proportional counter filled with a converter gas. However, it became clear that the data sets could not be fully understood and several attempts of analyzing the soil response using the Monte Carlo tool MCNPX failed. In 2013, the pioneers of the method, Desilets and Zreda, published a paper, in which they stated the footprint of the method would be approximately 30 ha and not significantly depend on the soil moisture content. As the data not at all showed

evidence for such a relation, the interest rose for an accurate understanding of the system. The already existing code URANOS could be tailored to address the neutron transport problem in the air-ground interface, yet requiring some modifications on the scattering and scoring kernel and the implementation of additional processes like inelastic scattering. Initial calculations showed already promising results as the simulation could reproduce experimental data already better than the results presented by the authors of the mentioned paper. However, it turned out, that whereas some parts of the problem like the above-ground neutron intensity follow rather simple laws, others like the radial distribution revealed complex dependencies on different hydrogen pools. The sophisticated neutron transport problem, which indeed has remained unexplained for nearly 50 years, along with the possible fundamental impact of the method paved the ground for the necessity of a plain and conclusive analysis of the CRNS signal formation in this work.

Part I

THE PHYSICS OF NEUTRONS AND CHARGED PARTICLES

1

THE PHYSICS OF NEUTRONS

1.1 | ABOUT THE NEUTRON

1.1.1 | FUNDAMENTALS

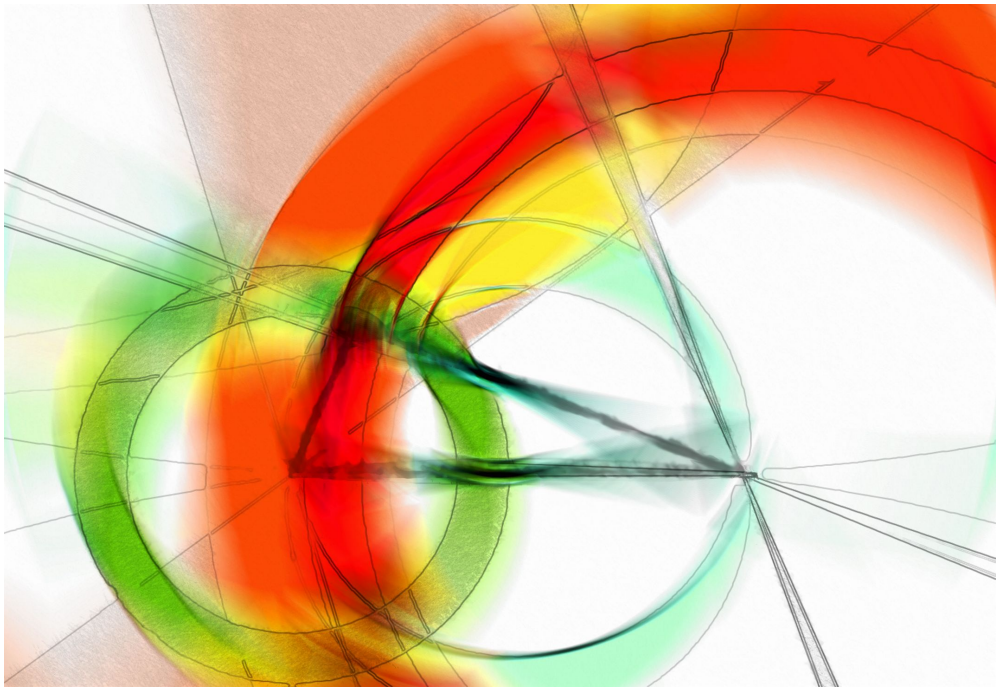

Figure 1: Artistic adaptation of measurement constraints on the CKM matrix [1, 2], inspired by results from [3]. The element V_{ud} [4], which is located in the lower left corner of the unitarity triangle, represents the transition probability for up and down type quarks. It is, among others [5], linked to nuclear beta decay and can be derived from neutron lifetime measurements.

Mass	m = 1.0086649159(5) u
	m = 939.565413(6) MeV
Spin	$s = 1/2\ h/(2\pi)$
Lifetime	τ = 880.2(1.0) s
Mean-square charge radius	$< r_N^2 >$= -0.1161(22) fm^2
Charge	q = -0.2(8) 10^{-21} e
Magnetic moment	μ = -1.9130427(5) μ_N
Electric dipole moment	$d_N < 0.30\ 10^{-25}\ e$cm (90 % CL)

Table 1: Basic physical properties of the neutron [1].

The neutron has a net charge of zero and a spin of $1/2\ h/(2\pi)$. Its dipole moment is expected to be $d_N \approx (10^{-37}–10^{-40})$ ecm according to the standard model and measurements with nuclear bound states and sensitivities up to 10^{-32} ecm so far confirm this value [6]. Yet, they have a magnetic moment caused by small loop currents [7]. Its rest mass is slightly higher than the one of the proton, therefore it can decay weakly [4] into an electron and an electron antineutrino by

$$\mathrm{n} \rightarrow \mathrm{p} + \mathrm{e} + \nu_\mathrm{e}$$

with a maximum kinetic energy transfer of 781.32 keV and a lifetime of approximately 15 min [8]. Thus there are nearly no free neutrons in the universe as the only stable condition available is the bound state in a nucleus.

1.1.2 | HISTORICAL OVERVIEW

The term 'Neutron' describing an electrically neutral entity of matter appeared as early as the end of the 20th century [9]. It was mainly discussed as an assumed bound state of the electron and its counterpart, which could for example make up the ether[a] and explain the results of experiments with cathode rays [10]. Though Rutherford[b] empirically discovered in 1911 [11] and theoretically described the nuclei of atoms, the neutron was proposed to be a particle comprised of a proton and an electron [12][c]. Albeit in the late 1920s the newly developed quantum mechanics raised serious questions about such a model of nuclear electrons regarding the incorrectly predicted spin of this compound and the escape probability of the electron due to its large wavelength, the fundamental questions about nuclei stayed unanswered.
Experiments in 1930 by Bothe[d] [14] showed evidence of an at that time unknown type of reaction. In a test series of exposing light elements to alpha particles, beryllium showed the production of hard gamma rays, which originated as they supposed from nuclear excitations, producing furthermore a new type of neutral radiation. It could knock off protons with kinetic energies of several MeV from a hydrogen-rich material through several centimeters of lead. In 1932, based on the experiments of Curie[e] and Joliot[f] [15], it was quickly understood by kinetic considerations that this radiation is made of particles as heavy as the proton - in terms of comments reported first of Majorana[g] [16], then of Chadwick[h] [17]. Iwanenko[i], who had theoretically worked on the problems of spin statistics before, realized that the neutron could also be a constituent of the nucleus [18], which was then confirmed [19] and celebrated as the birth of the neutron. This discovery was the key to understand the structure of atoms as composed of a shell and a small nucleus which itself is made up of protons and neutrons [20].
It is notable that in the first series of experimental trials boron has its first mention as a neutron absorber [21] and furthermore that the cosmic radiation soon after its discovery has been proposed to be partially made up of neutrons [22].

[a] to be noted: there was neither a common conception of the ether nor a consistent framework of theories. However, as in the case of the invention of the special relativity theory, this heritage can be considered an important foundation.
[b] Ernest RUTHERFORD, *1871-†1937, New Zealand, United Kingdom of Great Britain.
[c] Rutherford himself, however, had already mentioned in 1904 in a sidenote of his book 'Radio-activity' [13] a proper description of the neutron appearing as a form of radiation.
[d] Walther Wilhelm Georg BOTHE, *1891-†1957, German Empire.
[e] Iréne JOLIOT-CURIE, *1897-†1956, France.
[f] Frédéric JOLIOT-CURIE, *1900-†1958, France.
[g] Ettore MAJORANA, *1906-?1938, Kingdom of Italy.
[h] Sir James CHADWICK, *1891-†1974, United Kingdom of Great Britain.
[i] Дмитрий Дмитриевич Иваненко., *1904-†1994, Russian Empire.

Neutron interactions are mainly governed by the nuclear force. Due to the small extension of nucleon potentials in the order of femtometers, the de Broglie[j] wavelength of the (slow) neutron instead defines the range for the interaction. Typical cross sections can be related to the geometric size of the nucleus and therefore path lengths in matter can easily be in the order of centimeters[k]. In this work the kinetic energy is limited to 1 GeV and neutrons are treated as a single particle, which means that they are neither subject to Coulomb[l] forces due to a net charge of zero nor to strong forces acting on the parton level in deep inelastic scattering and beyond. It is of importance, that, besides the participation of (strong) nuclear forces, interactions with nuclei are dominated by the probability of a neutron joining and forming a compound. For the production of such a state energy and momentum, including spin, relations have to be conserved. Furthermore, nuclear resonance widths are small compared to their separation, especially for low energies and light elements, and the transition probabilities depending on the small overlap integrals appear to be small.
Absorption and scattering are described in a similar interaction picture, except for the final state. For an absorption reaction the compound is produced as real state by requiring that its excitation energy is of the same magnitude as the binding energy of the neutron. Therefore, the nucleus also decays predominantly by emitting a neutron again - or by a photon in case that process is suppressed if the potential difference slightly exceeds the binding energy like for the capture of slow neutrons. This gives rise to the fact that typically the cross section for elastic scattering is the most dominant. Inelastic scattering leaves the target in an excited state and so differs from elastic scattering only by the recoil to the neutron minus the excitation energy. In the case of fission a heavy nucleus decays by deformation into fragments due to the energy gained from the additional neutron. The declaration scheme is the following (see also Fig. 2):

$$
\begin{aligned}
\mathrm{n} + (\mathrm{A,Z}) &\rightarrow (\mathrm{A+1,Z}) \rightarrow (\mathrm{A,Z}) + \mathrm{n} && (\mathrm{n,\ n}) \\
&\rightarrow (\mathrm{A,Z})^{*} + \mathrm{n'} && (\mathrm{n,n'}) \\
&\rightarrow (\mathrm{A+1,Z}) + \gamma && (\mathrm{n,}\ \gamma) \\
&\rightarrow (\mathrm{A_1,Z_1}) + (\mathrm{A_2,Z_2}) + \mathrm{xn} && (\mathrm{n,\ f}),
\end{aligned}
$$

where (n,n) denotes elastic and (n,n') inelastic scattering off a nucleus with mass number A and atomic number Z.

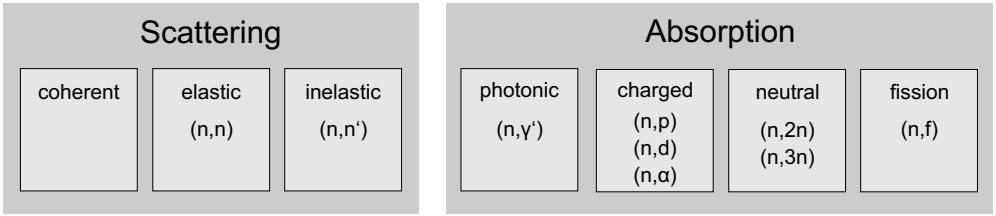

Figure 2: Types of neutron interactions and their classification.

Typical interactions neutrons undergo can be classified as either with one neutron in the initial and final state:

- Coherent Scattering describes the interference of incoming neutrons in terms of wave mechanics, therefore leading to distinct spatial distributions like in the

[j] Louis Victor Pierre Raymond, 7e duc DE BROGLIE, *1892-†1987, France.
[k] Neutrons, when treated as a form of radiation, are often compared to x-rays in common literature. This is understood from an engineering point of view in terms of the mean free path in materials. Such a number can be derived for both types of interactions, but it cannot be compared in its quality as neither the interaction partners are the same nor the action principle. The only valid direct link can be shown for the case of diffraction.
[l] Charles-Augustin de COULOMB, *1736-†1806, France.

case of Laue[m] diffraction. Originally coming from crystallography there is a distinction between elastic scattering, which refers to the prior mentioned process, and inelastic scattering, which refers to the additional excitation of phonons in the sample. This definition is ambiguous in its terminology[n] taking into account the further mentioned interaction types. Furthermore, quasi-elastic scattering applies to the case of (thermal) motion of the atoms giving rise to a significant contribution blurring the observed line shape.

- Elastic Scattering is the predominant mechanism of losing energy and can be understood as an elastic collision with energy and momentum conservation in the center-of-mass frame.
- Inelastic Scattering is an inelastic collision with the nucleus leaving it in an excited state. The allowed energy transfer is determined by the available nuclear excitation levels and therefore this process is mostly suppressed for kinetic energies below 1 MeV.

or such altering the target nucleus:

- Radiative Capture brings the nucleus into a A+1-state, which de-excites by emission of a photon.
- Charged Capture means that after absorbing a neutron the nucleus will decay by emitting either electrons, protons or larger compounds like helium ions, which in the case of light elements can be considered as fragments of the nucleus.
- Neutral Capture appears as an inelastic collision with similar initial and final states. Due to the absorption process and the following decay time constants and kinematics are different.
- Fission can occur for heavy elements absorbing a slow neutron if the final state energy budget is in favor of several fragments. Besides those, typically an energy dependent number of neutrons is emitted which are not any more needed to stabilize the smaller nuclei.
- Spallation is not limited incoming neutron. Any high energetic projectile with energies larger than approximately 100 MeV can induce the total breakup of a nucleus, which is described as a hadron shower.

1.3 | Units and definitions

1.3.1 | Kinematics

The possible reactions heavily depend on the energy of the neutron, which therefore is classified by its energy domain. The kinetic energy E of a neutron can be described in the non-relativistic limit by its wavelength λ derived from the de Broglie relationship

$$\lambda = \frac{h}{m_n v} \qquad \rightarrow \qquad E = \frac{1}{2} m_n v^2 = \frac{h^2}{2 m_n \lambda^2}, \tag{1}$$

where h is the Planck[o] constant, v and m_n velocity and mass of the neutron. The neutron's energy regimes are described as follows.

[m] Max Theodor Felix von Laue, *1879-†1960, German Confederation.
[n] This work will not refer to lattice structure analysis in particular and therefore will not make use of this naming scheme.
[o] Max Karl Ernst Ludwig Planck, *1858-†1947, German Empire.

	kinetic energy [eV]	wavelength [Å]	velocity [m/s]
ultra cold	$< 3 \cdot 10^{-7}$	< 520	< 7.5
very cold	$3 \cdot 10^{-7} - 5 \cdot 10^{-5}$	$520 - 40$	$7.5 - 100$
cold	$5 \cdot 10^{-5} - 5 \cdot 10^{-3}$	$40 - 4$	$100 - 1000$
thermal	$5 \cdot 10^{-3} - 5 \cdot 10^{-1}$	$4 - 0.4$	$1000 - 10000$
thermal peak	$25.3 \cdot 10^{-3}$	1.8	2200
epithermal	$5 \cdot 10^{-1} - 10^{3}$	$0.4 - 0.01$	$10^{3} - 4.4 \cdot 10^{5}$
intermediate	$10^{3} - 10^{5}$	$0.01 - 0.001$	$4.4 \cdot 10^{5} - 4.4 \cdot 10^{6}$
fast	$10^{5} - 2 \cdot 10^{7}$	$0.001 - 6 \cdot 10^{-5}$	$4.4 \cdot 10^{6} - 6.2 \cdot 10^{7}$
high energy	$> 2 \cdot 10^{7}$	$< 6 \cdot 10^{-5}$	$> 6.2 \cdot 10^{7}$

Table 2: Classification of neutrons by kinetic energy and corresponding interaction distances.

The most widely used definitions of the energy range, especially the thermal regime with the standard wavelength of 1.8 Å, are derived from the temperature T of the medium the neutrons are interacting with. According to the kinetic theory of ideal gases the velocities v of the particles in the system can be described by a Maxwell[p]-Boltzmann[q] distribution[r]

$$f_M(v) = \sqrt{\left(\frac{m}{2\pi k_B T}\right)^3} 4\pi v^2 \exp\left(-\frac{mv^2}{2k_B T}\right), \tag{2}$$

where m is the particle's mass and k_B the Boltzmann constant. The typical speed of particles v_p at the maximum of this probability distribution can be related to the temperature by

$$\frac{\mathrm{d}f_M(v)}{\mathrm{d}v} = 0 \qquad \rightarrow v_p = \sqrt{\frac{2k_B T}{m}} \quad \text{and} \quad T = \frac{mv_p^2}{2k_B} \tag{3}$$

and therefore, assuming the energy of neutrons can be described as $k_B T$ in a statistical thermodynamical interpretation, temperature models are applied.

1.3.2 | Neutron flux

Let $n(\vec{r}, \Omega, E)$ be the neutron density as a function of space $\vec{r}$, direction Ω[s] and energy E. Then $n(\vec{r}, \Omega, E)\,\mathrm{d}V\,\mathrm{d}\Omega\,\mathrm{d}E$ is called the differential density of neutrons in a volume V. The total number density of neutrons at point $\vec{r}$ is obtained by integration over all energies and angles *neutrons/cm³*

$$n(\vec{r})\,\mathrm{d}V = \int_{4\pi} \int_{0}^{\infty} n(\vec{r}, \Omega, E)\,\mathrm{d}V\,\mathrm{d}\Omega\,\mathrm{d}E. \tag{4}$$

The differential neutron flux, defined by $F(\vec{r}, \Omega, E)\,\mathrm{d}\Omega\,\mathrm{d}E = n(\vec{r}, \Omega, E)v\,\mathrm{d}\Omega\,\mathrm{d}E$, leads to the number of neutrons per second by taking into account the individual velocities v *neutrons/cm²/s*

[p] James Clerk Maxwell, *1831-†1879, Scotland.

[q] Ludwig Eduard Boltzmann, *1844-†1906, Austrian Empire.

[r] Nota bene: for a single direction, say v_z, the distribution is $f_M^{(1)}(v_z) = \sqrt{\frac{m}{2\pi k_B T}} \exp\left(-\frac{mv_z^2}{2k_B T}\right)$, as by integrating over all directions the spherical volume element given by $\mathrm{d}V = v^2 \sin\vartheta\,\mathrm{d}\vartheta\,\mathrm{d}\phi\,\mathrm{d}v$ is needed.

[s] Often the unit vector Ω is expressed in spherical coordinates, especially for scattering interactions. Then it is composed of the mean direction angle ϑ at the mean azimuthal angle ϕ. For many special cases a canonical axis of the neutron beam direction is used.

and therefore represents the total path length covered by all neutrons. The quantity

$$\Phi(\vec{r}) = \int_{4\pi} F(\vec{r}, \Omega)\, \mathrm{d}\Omega = n(\vec{r})\overline{v} \tag{5}$$

is called the total neutron flux and

$$\varphi(\vec{r}) = \int \Phi(\vec{r})\, \mathrm{d}t. \tag{6}$$

neutrons/cm² defines the neutron fluence. The terms fluence rate and flux are often used equivalently.

The integral neutron flux takes the whole ensemble of energies into account, as it assumes an equilibrium (thermalized) state of the system. Therefore, it is necessary to
neutrons/cm²/s/MeV introduce the energy dependent flux quantity

$$\widetilde{\phi}(\vec{r}, E) = \frac{\mathrm{d}\Phi(\vec{r}, E)}{\mathrm{d}E}, \tag{7}$$

which is called the neutron spectrum. However, most interaction processes lead to a partial energy transfer proportional to the initial energy. Therefore, the number of particles per logarithmic energy decrement ratio is a constant and the neutron spectrum
neutrons/cm²/s can be depicted as an energy weighted spectrum

$$\phi(\vec{r}, E) = E\frac{\mathrm{d}\Phi(\vec{r}, E)}{\mathrm{d}E}. \tag{8}$$

Nota bene:

- In general the term 'flux' describes a directionality in the particle transport by an underlying vector field. In the field of neutron sciences it is a scalar quantity. However, the corresponding vector quantity, which is obtained by the gradient of the flux, is called a current J[t]. This misalignment in terminology is of historic origin and has to be kept in mind.
- Additionally, as a consequence there is also a subtle difference between flux and fluence rate. As the latter is the time derivative of an integral quantity there is no information about directionality, contrary to the flux, which in the picture of neutron motion with gain and loss effects, still has a directional dependence.
- In the following the term 'neutron spectrum' will not specifically refer to (7), but rather be used as a synonym to the energy weighted neutron spectrum, which will be the standard representation.

[t] This quantity is not used in this work.

Neutron transport theory describes the flux through a medium by a Boltzmann equation in order to model the neutron field by conserving the total number of particles. This balance is kept by the four terms

- leakage out of the volume ①,
- loss due to absorption and scattering out of the volume or energy range ②,
- in-scattering from outside the volume and/or a different energy ③,
- gain by a source inside the volume ④.

$$\begin{aligned}\frac{\delta n(r,\Omega,E)}{\delta t} =& -v\Omega\nabla n(r,\Omega,E) && ①\\ &-(\Sigma_a(E)+\Sigma_s(E))vn(r,\Omega,E) && ②\\ &+\int_{4\pi}\int_{0}^{\infty}\Sigma_s(\Omega'\to\Omega,E'\to E)vn(r,\Omega',E')\,\mathrm{d}\Omega'\,\mathrm{d}E' && ③\\ &S(r,\Omega,E). && ④ \end{aligned} \tag{9}$$

with the macroscopic cross sections, which are also called linear attenuation coefficients, for absorption Σ_a and scattering Σ_s. Both are combined to the total macroscopic cross section *1/cm*

$$\Sigma_t = \Sigma_a + \Sigma_s\ (+\ldots). \tag{10}$$

The macroscopic cross section Σ can be derived from the microscopic cross section[u] σ, which defines the probability of interaction in a mass element divided by the product of interaction centers and the fluence: *cm^2*

$$\Sigma = \rho N_A \frac{\sigma}{M}, \tag{11}$$

where ρ denotes the density of a material with atoms of molar mass M and N_A the Avogadro[v] or also called Loschmidt[w] constant. On a microscopic level vice versa the microscopic cross section is described as

$$\sigma = \frac{1}{nl}. \tag{12}$$

It has the dimension of an area and is defined as the inverse of the product number density $n = \rho N_A/M$ and the mean free path l, which by themselves describe the interaction opacity of the material[x]. The typical unit is the barn: $1\,\mathrm{b} = 10^{-28}\,\mathrm{m}^2$.
As reactions can depend on parameters like the incoming energy or the (emission) angle, one introduces the differential cross section $\frac{\mathrm{d}\sigma}{\mathrm{d}\Omega}$.
The cross section can be composed like the attenuation coefficient of a sum energy dependent absorption σ_a and scattering σ_s contributions

$$\sigma(E) = \sigma_a(E) + \sigma_s(E)\ (+\ldots). \tag{13}$$

[u] In this work the term cross section will always refer to σ. For the macroscopic cross section the term attenuation coefficient is preferred.
[v] Lorenzo Romano Amedeo Carlo AVOGADRO, Conte di Quaregna e Cerreto, *1776-†1856, Italian Empire.
[w] Johann Josef LOSCHMIDT, *1821-†1895, Austrian Empire.
[x] To be noted: Macroscopic cross sections have the dimension of a reciprocal length, microscopic cross sections the dimension of an area.

In case of a compound with weight fractions w_i of n elements the weighted sum of cross sections is evaluated:

$$\Sigma_t = \rho N_A \sum_{i=1}^{n} w_i \frac{\sigma_i}{M_i}. \tag{14}$$

Therefore, the occurrence probability of an interaction type at an element can be calculated by the relative fraction of the cross sections σ_i/σ and is called reaction rate.

In a homogeneous medium the mean free path[y] between two interactions is

$$l(E) = \frac{1}{\Sigma_t(E)}. \tag{15}$$

Therefore, in case of dominant absorption, the abundance of neutrons follows the Beer[z]-Lambert[aa] attenuation law.

The probability distribution function can be denoted as

$$p(l, E)\,\mathrm{d}l = \Sigma_t(E) \exp\left(-\Sigma_t(E) l\right) \mathrm{d}l. \tag{16}$$

Integrating over a finite length leads to the number of neutrons N in a distance L

$$\frac{N(L,E)}{N_0} = \int_0^L p(l, E)\,\mathrm{d}l = \int_0^L \Sigma_t(E) \exp\left(-\Sigma_t(E) l\right) \mathrm{d}l = 1 - \exp\left(-\Sigma_t(E) L\right). \tag{17}$$

Therefore, the percentage of neutrons traversing a thin layer of thickness d without interaction is $\exp\left(-\Sigma_t(E) d\right)$.

1.4.1 | Slowing down

Neutrons of typical energies up to 200 MeV can be treated non-relativistically for collisions by energy and momentum conservation. As for elastic interactions only the relative rather than the absolute masses are required, the neutron can be considered of mass 1 and a nucleus of mass A. It is furthermore convenient to transform the collision

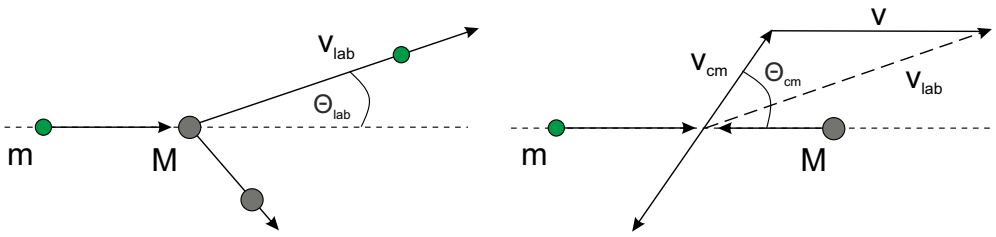

Figure 3: Kinematics of an elastic collision in the laboratory (left) and center-of-mass frame (right).

from the laboratory (lab) into the center-of-mass (cm) frame as in such the angular distribution is isotropic. The velocity of the cm system with velocities of the neutron v and the nucleus V can be calculated as follows

$$v_{\mathrm{cm}} = \frac{1}{1+A}\left(v_{\mathrm{l}} + A V_{\mathrm{l}}\right) = \frac{v_{\mathrm{l}}}{1+A} \tag{18}$$

[y] also called the distance to the next collision.
[z] August Beer, *1825-†1863, German Empire.
[aa] Johann Heinrich Lambert, *1728-†1777, France.

and within the cm system the velocities of the particles are

$$v_c = v_l - v_{cm} = \frac{A}{A+1} v_l \tag{19}$$

$$V_c = -v_{cm} = -\frac{1}{A+1} v_l \tag{20}$$

The energy of the neutron in the cm system E_c can be derived as well according to

$$E_c = \frac{1}{2} v_{c^2} + \frac{1}{2} A V_c^2 = \frac{A}{A+1} \frac{1}{2} v_l^2 = \frac{A}{A+1} E_l. \tag{21}$$

In the cm frame the absolute values of velocities of the particles do not change, so $v_c' = v_c$. The angles can be calculated as

$$\tan \vartheta_l = \frac{v_c' \sin \vartheta_c}{v_{cm} + v_c' \cos \vartheta_c} = \frac{\sin \vartheta_c}{\frac{1}{A} + \cos \vartheta_c} \tag{22}$$

or by trigonometric transformation

$$\cos(\pi - \vartheta_c) = \frac{(v_c')^2 + (v_{cm})^2 - (v_l')^2}{(A+1)^2}. \tag{23}$$

Using (18) the kinetic energy after scattering can be derived as

$$\frac{\frac{1}{2}(v_l')^2}{\frac{1}{2}(v_l)^2} = \frac{E_l'}{E_l} = \frac{A^2 + 1 + 2A \cos \vartheta_c}{(A+1)^2} = \frac{(1+\alpha) + (1-\alpha) \cos \vartheta_c}{2} \tag{24}$$

with

$$\alpha = \left(\frac{A-1}{A+1} \right)^2. \tag{25}$$

From (24) it can be derived that the angle in the cm system, and therefore also in the lab frame, is correlated to the energy loss. This is maximized for

- $\vartheta_c = \pi$, a central 'head-on' collision, and
- $A = 1$, a hydrogen nucleus consisting only of a proton of equal mass.

Under these conditions the kinetic energy of a neutron can be transferred to the target nucleus in one single collision. Typically the energy loss depends on the impact parameter, which can be assumed as randomly distributed, so following the standard representation for elastic scattering the probability for a neutron to scatter[ab] into a cone of $2\pi \sin \vartheta_c \, \mathrm{d}\vartheta_c$ around ϑ_c from energy E to a range of energies $\mathrm{d}E'$ around E' is

$$\sigma_s(E) P(E \to E') \, \mathrm{d}E' = -\sigma_{cm}(E, \vartheta_c) 2\pi \sin \vartheta_c \, \mathrm{d}\vartheta_c. \tag{26}$$

Using (24) yields

$$P(E \to E') = \frac{4\pi - \sigma_{cm}(E, \vartheta_c)}{(1-\alpha) E \sigma_s(E)} \qquad \text{for } \alpha E \le E' \le E \tag{27}$$

or zero otherwise. The scattering can mostly be considered isotropic (except for high energies, see also sec. 6.4.3.1) in angle, so $\sigma_{cm}(E, \vartheta_c) = \sigma_s(E)/4\pi$ leading to

$$\sigma_s(E \to E') = \sigma_s(E) P(E \to E') = \frac{\sigma_s(E)}{(1-\alpha)E} \qquad \text{for } \alpha E \le E' \le E. \tag{28}$$

[ab] an increase in the scattering angle means a larger energy loss.

With the probability for each angle and consecutively for the corresponding energy transfer, the average energy loss can be calculated as

$$\overline{\Delta E} = E - \int_{\alpha E}^{E} \mathrm{d}E' E' P(E \to E') = \frac{1}{2}(1-\alpha)E \tag{29}$$

and the important quantity of the average logarithmic energy loss as

$$\xi = \int_{\alpha E}^{E} \mathrm{d}E' \ln\left(\frac{E}{E'}\right) P(E \to E') \tag{30}$$

$$= 1 + \frac{\alpha}{1-\alpha}\ln\alpha = 1 - \frac{(A-1)^2}{2A}\ln\left(\frac{A+1}{A-1}\right). \tag{31}$$

The logarithm represents the fact, that by elastic collisions not an absolute quantity but always a fraction of the kinetic energy is lost. Therefore, the moderation power of a material is defined as the average number of collisions from an initial energy, say $E_0 = 10\,\mathrm{MeV}$, until entering the thermal regime at 1 eV

$$n_{\mathrm{col}} = \frac{u}{\xi} = \frac{\ln(E_0/E)}{\xi}, \tag{32}$$

where the lethargy u is defined as

$$u = \ln\left(\frac{E_0}{E}\right). \tag{33}$$

So ξ represents the average change in lethargy per collision. According to (31) this property of a material decreases with nuclide mass and the slowing down requires more collisions.

1.4.2 | Thermal neutrons

In the previous chapter 1.4.1 it has been assumed that the target nucleus is at rest. Yet, as soon as the kinetic energy of the neutron is

- comparable to the mean kinetic energy of atoms in a gas phase or
- in the order of the binding energy or excitation of modes of additional degrees of freedom in molecules

the process has to be extended. As thermal neutron transport has been worked out elaborately by many authors, this chapter summarized the key ideas. For further reading and derivation chapter 10 of [23] is recommended. In the case of gases the velocity distribution of the particles is known - it is assumed that atoms follow a Maxwell-Boltzmann distribution (2), which allows for a straightforward treatment of the interaction. This effect of thermal motion on the scattering process is discussed in detail in sec. 5.1.3.
For a relative velocity between target and neutron before the collision of $v_r = \|\vec{v} - \vec{V}\| = \sqrt{v^2 + V^2 - 2vV\cos\vartheta}$, the velocity in the laboratory system after the collision will be

$$v' = \sqrt{v_{\mathrm{cm}}^2 + \left(\frac{A}{A+1}\right)^2 v_r^2 + 2v_{\mathrm{cm}}\frac{A}{A+1}v_r\cos\vartheta} \tag{34}$$

and the largest and smallest velocities are

$$v_{\max} = v_{\mathrm{cm}} + \frac{A}{A+1} v_r \qquad \text{and} \qquad v_{\min} = v_{\mathrm{cm}} - \frac{A}{A+1} v_r. \tag{35}$$

The total cross section as to the third term of (9) is obtained by integrating the microscopic cross section

$$\mathrm{d}\sigma\left(v', V, \cos\vartheta\right) = \frac{1}{2}\,\frac{v_r}{v'}\,\sigma_s^{\mathrm{free}}\,p(V)\,\mathrm{d}V\,\mathrm{d}\cos\vartheta, \tag{36}$$

which relates the free elastic scattering cross section σ_s^{free} to the probability of interacting with a target nucleus having a velocity distribution $p(V)$. So the probability of a velocity change of the neutron $v \to v'$ is represented by the modified cross section

$$\sigma\left(v \to v'\right)\mathrm{d}v = \frac{1}{2}\,\frac{1}{v'}\int_0^{\infty} \mathrm{d}V \int_{-1}^{1} v_r\,\mathrm{d}\cos\vartheta\,\sigma_s^{\mathrm{free}}\,p(V)\,g(v' \to v)\,\mathrm{d}v \tag{37}$$

with

$$g(v' \to v) = \begin{cases} 0, & v < v_{\min} \text{ or } v > v_{\max} \\ \frac{2v}{v_{\max}^2 - v_{\min}^2}, & v_{\min} < v < v_{\max}. \end{cases} \tag{38}$$

By integrating (36) over V and $\cos\vartheta$ and substituting velocities by energy the total cross section can be obtained[ac]:

$$\sigma_s(E') = \sigma_s^{\mathrm{free}}\,\frac{1}{\beta^2\sqrt{\pi}}\,\Psi\left(\beta\right), \tag{39}$$

where $\beta^2 = AE'/k_BT$ and

$$\Psi\left(\beta\right) = \beta\exp\left(-\beta^2\right) + \left(2\beta^2+1\right)\frac{\sqrt{\pi}}{2}\,\mathrm{erf}(\beta). \tag{40}$$

The $\Psi\left(\beta\right)$ function is originating from kinetic gas theory, therefore using β as a variable. For $\beta < 1$ the cross section can roughly be approximated by $\sigma_s(E') \sim \sigma_s^{\mathrm{free}}/\sqrt{E'} \sim \sigma_s^{\mathrm{free}}/v$.

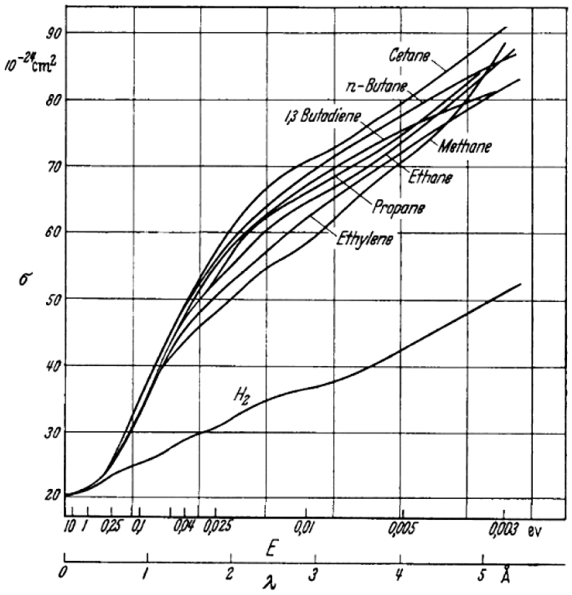

Figure 4: Cross section of protons bound in various hydrocarbons (C_XH_Y) and in hydrogen gas H_2, modified from [24]. For H_2 the deviation from the unbound cross section is small. H_2O scales nearly as the presented curve for cetane ($C_{16}H_{34}$). In complex molecules the interaction probability around thermal energies and below strongly depends on the binding type and the associated degrees of freedom.

[ac] As $\sigma_s(E') = \int_0^{\infty} \sigma_s(E' \to E)\,\mathrm{d}E$.

2

THE PHYSICS OF ELECTROMAGNETIC INTERACTIONS

All charged particles dissipate energy while crossing a medium. Depending on the particle species and the material, different processes play a role. The most important processes are in ascending order of the energy range: Electron excitation of atoms, ionization, Bremsstrahlung, pair production, nuclear excitation and following the relativistic processes like Čherenkov and transition radiation, which are not relevant here.

2.1 | ENERGY LOSS IN THE MEDIUM

2.1.1 | ENERGY LOSS BY IONIZATION

The Bethe[a]-Bloch[b] equation describes the energy loss dE per length dx in a medium:

$$-\frac{\mathrm{d}E}{\mathrm{d}x} = 2\pi N_A r_e^2 m_e c^2 \rho \frac{Z}{A}\frac{z^2}{\beta^2}\left(\ln\left(\frac{2m_e\gamma^2 c^2\beta^2 W_{\max}}{I^2}\right) - 2\beta^2 - \delta - 2\frac{C}{Z}\right). \tag{41}$$

r_e	classical electron radius	ρ	weight density
m_e	electron mass	z	projectile charge
N_A	Avogadro number	β	$= v/c$ projectile velocity
I	mean excitation potential	γ	$= (1-\beta^2)^{-1/2}$
Z	charge number	δ	density correction
A	atomic weight	C	shell correction

The scaling constants are often combined to

$$\kappa = 2\pi N_A r_e^2 m_e c^2 \frac{Z}{A}\frac{1}{\beta^2}. \tag{42}$$

The maximum energy transfer $W_{\max}$ possible in a single head-on collision for an incident projectile of mass m_A can be calculated as follows:

$$W_{\max} = \frac{2m_e c^2\beta^2\gamma^2}{1 + 2\frac{m_e}{m_A}\sqrt{1+\beta^2\gamma^2} + \frac{m_e^2}{m_A}}. \tag{43}$$

For $m_A \gg m_e$ the energy transfer can be approximated as

$$W_{\max} \approx 2m_e c^2\beta^2\gamma^2. \tag{44}$$

The density factor is a correction for projectiles of high energies and describes the polarization of the atoms in the medium along the path, whereas the shell correction accounts for projectiles which have a velocity in the order of or smaller than those of

[a] Hans Albrecht BETHE, *1906-†2005, German Empire.
[b] Felix BLOCH, *1905-†1983, Switzerland.

the electrons orbiting the target atoms. These empirical constants are mainly important for relativistic particles. The mean excitation potential can be approximated by

$$I \approx 16\,\mathrm{eV} \cdot Z^{0.9}. \tag{45}$$

Fig. 5 shows exemplarily the energy deposition for the counting gas argon and the neutron converter boron.

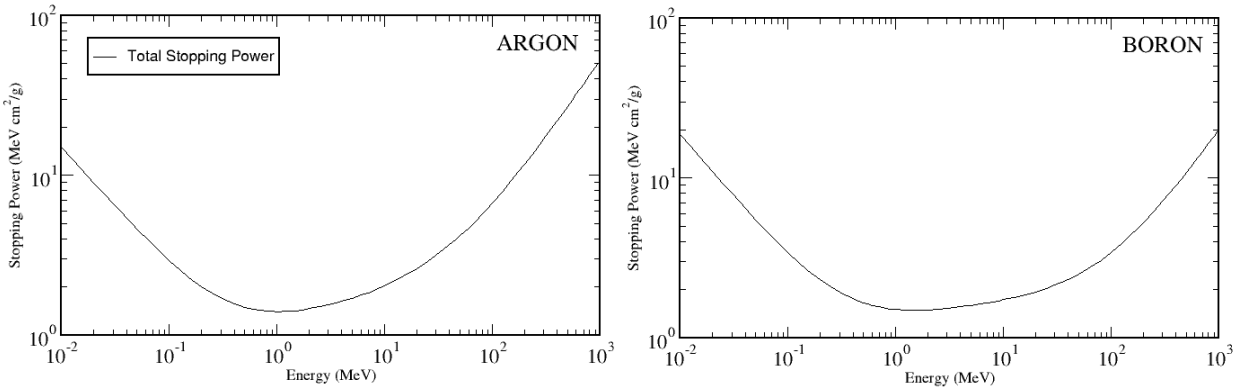

Figure 5: Energy loss dE per unit length dx for electrons in argon (NTP) and boron, modified from [25].

The process of energy loss is of statistical nature and (41) describes the mean energy deposition. Its energy dependent function, as shown in Fig. 5, is specific to the particle species and the medium. Yet, the Bethe-Bloch equation has a minimum for all particles which satisfy $\beta\gamma \approx 3$. Such are called **m**inimum **i**onizing **p**articles (MIP). The ionization density increases towards small momenta, which is equivalent to a projectile losing a large fraction of the kinetic energy on a close range at the end of its trajectory. This is called the Bragg[c] peak.
The Bethe-Bloch-equation provides a good approximation for heavy particles, e.g. ions. For light particles like electrons Bremsstrahlung has to be taken into account as well.

2.1.2 | BREMSSTRAHLUNG

Particles in a medium are deflected by the Coulomb potential of the host atoms. Accelerated particles radiate photons, therefore this effect has to be considered in addition to ionization. For (light) particles with large kinetic energy this effect is called Bremsstrahlung, see also the Feynman[d] graph of Fig 6 and for electrons one can derive for the mean energy loss

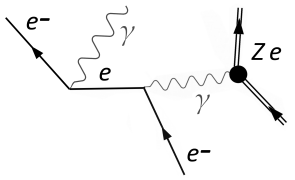

Figure 6: First order Feynman graph for Bremsstrahlung.

$$-\frac{\mathrm{d}E}{\mathrm{d}x} \approx 4\alpha N_A r_e^2 z^2 E \frac{Z^2}{A} \ln\left(\frac{183}{Z^{1/3}}\right). \tag{46}$$

The coupling constant $\alpha = e^2/(2ch\epsilon_0)$ with the electric charge e and the electric field constant ϵ_0, represents the strength of the Coulomb interaction. Compared to ionization (41) there is an explicit energy dependence in (46), which makes this effect not only dependent on the surrounding medium, but also the momentum of the particle.

[c] William Lawrence BRAGG, *1890-†1971, Australia.
[d] Richard Phillips FEYNMAN, *1918-†1988, USA.

Therefore one can summarize all constants of (46) under the term radiation length X_0 and write

$$-\frac{\mathrm{d}E}{\mathrm{d}x} = \frac{E}{X_0}. \tag{47}$$

As the differential equation (47) can be solved by an exponential function of the form $\exp(-x/X_0)$, the radiation length defines the distance in which the energy of the particle drops to $1/e$ of its original value.

2.1.3 | Multiple scattering

Multiple Scattering describes a manifold of Coulomb deflections. Such are mostly weak, which means that the trajectory of a particle keeps its general direction. A simplified model [26] of this statistical process leads to a particle of momentum p after a distance x to a gaussian[e] distribution of the scattering angles around the original axis of the trajectory $\vartheta = 0$ with a width of

$$\sigma_\vartheta = \frac{13.6\,\mathrm{MeV}}{\beta c p}\sqrt{\frac{x}{X_0}}. \tag{48}$$

2.2 | Processes in gaseous media

Particles can be detected via their ionization track in a gas. In the case of neutrons a so-called converter captures the uncharged particle by nuclear absorption and then either fragments or releases excitation or binding energy in form of radiation. This chapter summarizes the relevant physics starting from the ionization track to the transport and gas gain, which is necessary to detect the electron cloud.

2.2.1 | Ionization

In a small finite volume the Landau[f] distribution [27] describes the possible energy transfer to a host atom. The Landau distribution approximates the energy loss for thin absorbers, which do not significantly reduce the overall momentum of the propagating particle. Due to the large amount of collisions with small momentum transfer, the Landau distribution has a maximum at low values and has a positive skew towards higher values, which model the unlikely hard collisions with large energy transfers. It takes the following form

$$f(\Lambda) = \frac{1}{\sqrt{2\pi}} e^{-\frac{1}{2}\left(\Lambda + e^{-\Lambda}\right)}, \tag{49}$$

whereas for a length element x of an absorber of a density ρ the quantity $\Lambda = (\Delta E - \Delta E_p)/(\kappa\rho x)$ describes the deviation of a possible energy loss ΔE from its most probable value ΔE_p, which is the maximum of the Landau distribution. It can be calculated by [26]

$$E_p = \kappa\rho x \left[\ln\left(\frac{2m_e c^2\beta^2}{I(1-\beta^2)}\right) + \ln\left(\frac{\kappa\rho x}{I}\right) + 0,2 - \beta^2 - \delta\left(\frac{\beta}{1-\beta^2}\right)\right]. \tag{50}$$

[e] Johann Carl Friedrich Gauss, *1777-†1855, Holy Roman Empire.
[f] Лев Давидовицч Ландау, *1908-†1968, Russian Empire.

2.2.2 | Energy resolution

The energy deposition for the primary ionization along the trajectory of a charged particle can be described by a Poisson[g] distribution. However in case the full energy is transferred, there is no variance and hence there is a correlation between the single processes of energy deposition. Then, the usage of Poisson statistics is inadequate. Instead of a variance of $\sigma^2 = N$ for N ionization processes, a material- and energy-dependent correction term F, with $F \leq 1$, is introduced, which is called Fano[h] factor [28]:

$$\sigma^2 = FN. \tag{51}$$

Due to the variance reduction the resolution is improved by a factor of $\sqrt{F}$. As an example for an electron with a kinetic energy $O(1\,\mathrm{keV})$ in argon a Fano factor of $F = 0.16$ can be calculated [29].

The factual mean energy W for creating an electron-ion pair indeed is higher than the minimum ionization potential I as additional energy is transferred to vibration modes or kinematics. For gases the approximation $W \approx$ (2-3) I [27] can be assumed.
Using W allows to calculate the number of free charge carriers n_t released by a process of energy ΔE by $n_t = \Delta E/W$. For a gas mixture of different fractions c_i one has

$$n_t = \Delta E \sum_i \frac{c_i}{W_i}. \tag{52}$$

This is the total number of primary electrons due to primary and secondary ionization for a given energy deposition ΔE.

2.2.3 | Drift and diffusion

Charged particles in a gas can be accelerated under the influence of electromagnetic fields. Yet, decelerating effects like scattering off atoms in the medium lead to a balance in the forces and so to an on average constant propagation. This is called drifting. The non-deterministic and omnidirectional transport by interaction with other particles at rather thermal energies is called diffusion.

Under the influence of an electric $\vec{E}$ and a magnetic field $\vec{B}$ the trajectory of a charged particle is described by the Langevin[i] equation. The solution for constant drift velocities $\vec{v}_D$ can be denoted as

$$\vec{v}_D = e\,\frac{\tau}{m}\,\frac{1}{1+\omega^2\tau^2}\left[\vec{E} + \omega\tau\,\frac{\vec{E}\times\vec{B}}{\left|\vec{B}\right|} + \omega^2\tau^2\,\frac{\left(\vec{E}\cdot\vec{B}\right)}{\left|\vec{B}\right|^2}\cdot\vec{B}\right]. \tag{53}$$

ω denotes the cyclotron frequency with $\omega = (e/m)|\vec{B}|$. τ represents the mean time between two collisions with atoms of the medium.
For electrons in the absence of a magnetic field (53) can be simplified to

$$\vec{v}_D = \frac{e}{m}\,\tau\vec{E}. \tag{54}$$

[g] Siméon Denis Poisson, *1781-†1840, France.
[h] Ugo Fano, *1912-†2001, Italian Empire.
[i] Paul Langevin, *1872-†1946, France.

For ions a different parametrization of the motion of the particles is used, as for such the ratio of the actual pressure p to standard pressure p_0 has a strong influence on the kinetics. Therefore one uses

$$\vec{v}_D = \mu \vec{E} \frac{p_0}{p}. \tag{55}$$

Due to their higher mass, the drifting of ions is typically three order of magnitude lower than the drift velocity of electrons and therefore is characterized by the mobility μ.

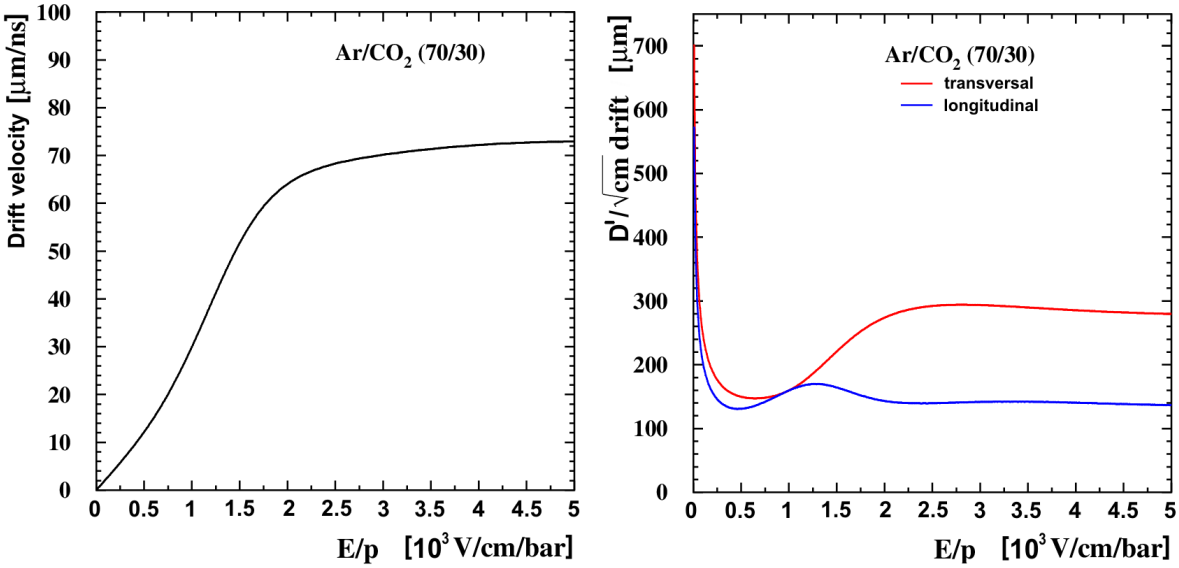

Figure 7: Drift velocity for electrons in argon:CO_2 as a function of electric field strength and pressure (left) and (right) simulations of the diffusion constant D' for the same functional dependencies and gas mixture, modified from [30].

Without fields or gradients, charged particles like neutrons are carrying out a random-walk propagation by collision with other atoms. This diffusion leads to a gaussian-shaped spatial particle density of the form

$$\rho(r,t) = \left(\frac{1}{\sqrt{4\pi D t}}\right)^3 \exp\left(-\frac{r^2}{4Dt}\right). \tag{56}$$

Its width $\sigma_D = \sqrt{2Dt}$ increases over time t. D denotes a diffusion constant and depends on the medium, but also on the electric field strength. Therefore, charge diffusion is typically modeled using a longitudinal and a transverse component with respect to the field. If the transverse axis with the diffusion constant D_T is denoted by the spatial coordinates x and y and the longitudinal axis coordinate with D_L is described by z, one writes

$$\rho(r,t) = \left(\frac{1}{\sqrt{4\pi D_T t}}\right)^2 \left(\frac{1}{\sqrt{4\pi D_L t}}\right) \exp\left(-\frac{x^2+y^2}{4D_T t} - \frac{(z-v_D t)^2}{4D_L t}\right). \tag{57}$$

The diffusion constant can be defined as a function of drift velocity $D' = \sqrt{2D/v_D}$, yielding

$$\sigma_{D'} = D'\sqrt{x}. \tag{58}$$

2.2.4 | GAS GAIN

Typically the primary ionization is often not sufficient to generate a signal large enough for detection. A gaseous medium allows for applying the principle of charge multiplication. If electrons, e.g. the primary charge carriers, can be accelerated to energies, which are high enough to ionize other atoms of the medium, an avalanche effect occurs, which can increase the number of electrons by a factor of 10^4 to 10^6. The so created additional electron-ion pairs $\mathrm{d}N$ for an actual number of electrons N satisfies the differential equation

$$\mathrm{d}N = \alpha(r)N(r)\mathrm{d}r, \tag{59}$$

whereas α denotes the Townsend[j] coefficient, which depends on the track length coordinate r as far as the electric field strength changes. The solution for an initial number of final charge carriers N_{total} for an initial number of charge carriers N_0 takes the following form

$$N_{\mathrm{total}} = N_0 \exp\left(\int_{r1}^{r2} \alpha(r)\mathrm{d}r\right). \tag{60}$$

The ratio $G = N_{\mathrm{total}}/N_0$ is called gas gain.

[j] Sir John Sealy Edward TOWNSEND, *1868-†1957, Ireland.

Part II

NEUTRON SOURCES

3

NATURAL SOURCES: COSMIC NEUTRONS

Due to the limited lifetime of approximately 15 minutes, all free neutrons, naturally abundant or from laboratory sources, originate from an ongoing production mechanism - either the interaction of cosmic radiation with the atmosphere and the soil or natural radioactivity, which can sometimes even scale up to so-called „natural reactors“ [31]. The following section presents a short overview about how cosmic neutrons are created. A good summary can also be found in [32].

3.1 FROM SUPERNOVAE TO SEA LEVEL

Cosmic rays consist mostly of ionized atomic nuclei with protons being the most abundant species with a contribution of 90 % of the total measured particle number, followed by helium ions. The fraction of electrons, positrons, antiprotons, gamma rays and neutrinos can be considered negligible. The net charge of the cosmic radiation is highly positive with protons being overrepresented with a ratio of 10:1 [33]. While in general sources, also on galactic scales [34], are charge conserving, the reason for this asymmetry is inverse Compton scattering [35]. This effect leads to especially light charged particles like electrons losing energy by interactions with photons of the cosmic microwave background and therefore being slowed down more efficiently than their hadronic partners.
The cosmic ray spectrum, see Fig. 8, extends from the MeV regime up to ZeV energies with meanwhile more than a dozen candidates of extremely high energies of $\sim 10^{20}$ eV, observed by the Fly's Eye detector [36].

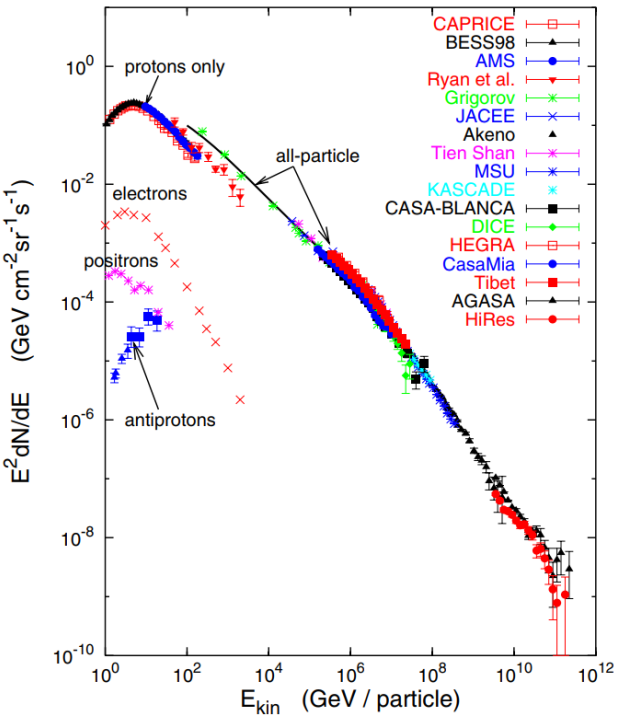

Figure 8: Energies and rates of the primary cosmic ray particles before entering the atmosphere from various experiments [37].

The lowest part of the spectrum is result of the solar wind, $\sim 10^{36}$ particles per second released from the plasma of the Sun's corona and especially from solar flares [38]. Particles in the range of 1 GeV to ~100 TeV mostly come from supernova remnants. Therefore, the cosmic ray flux has one component of extragalactic origin overlayed by the charge emission from the Sun with a separation of low energy and high energy contributions. Theoretical considerations of the diffusive shock acceleration[a] needed to achieve such energies [39] as well as observations from the Crab nebula[1] can heavily support these generators, see also the overview in [40]. For higher energies the production and transport mechanisms change around the points, which in the log-log plot

[1] *NGC 1952*

[a] thermal cosmic rays passing a dense matter distribution in which the strong magnetic gradient leads to an acceleration by turning several times around the 'shock' region.

are called 'knee' and 'ankle'. Below the knee at around $3{\cdot}10^{17}$ eV the spectrum follows approximately an $E^{-2.7}$ power law and beyond $\sim E^{-3.1}$. Between these two points the typical composition changes towards more massive particles. Yet, for the identified sources, like a reacceleration in the galactic wind termination shock [41] or neutron stars [42], the theoretical understanding has not condensed to an accepted answer. For Ultra High Energy Cosmic Rays the discussion around the proposed sources is even broader, see also the overview in [43]. The direct observation of such phenomena is suppressed by the diffusive motion of particles on the galactic scale in the interstellar medium. This leads to an almost isotropic and time-independent flux of cosmic radiation - which is then influenced by the solar activity.

As the former experiences an energy decrement from the outward gradient of the Sun's particle flux this leads to an inverse proportional relation between solar activity and cosmic ray flux. There are several mechanisms influencing the measured particle density with the most prominent being the 11-year intensity modulation cycle, which is due to the underlying solar magnetic field activity of the 22-year Hale[b] cycle, see also Fig. 9. Yet, modulations with larger period lengths can also be identified [44] as well as shorter cycles like 27 days caused by the Sun's rotation around its own axis [45]. Due to their low energy these particles have a minor direct influence on the Earth except in case of large plasma releases, called coronal mass ejections. These can cause a sudden increase in the cosmic ray intensity, which are measured in the form of ground level enhancements [46]. However, these events can also lead to an increase in the activity of the Sun and consequently a drop in cosmic ray intensity, called Forbush[c] decrease [47].

The cosmic ray intensity measured on Earth varies on average around 20 %, occasionally reaching 30 %. During periods of high solar activity, coronal mass ejections can appear several times per day and in periods of low solar activity once in a few days. Since the beginning of the global recordings by neutron monitors, see sec. 8.2.2, around 70 ground level enhancements and 40 Forbush decreases have been observed.

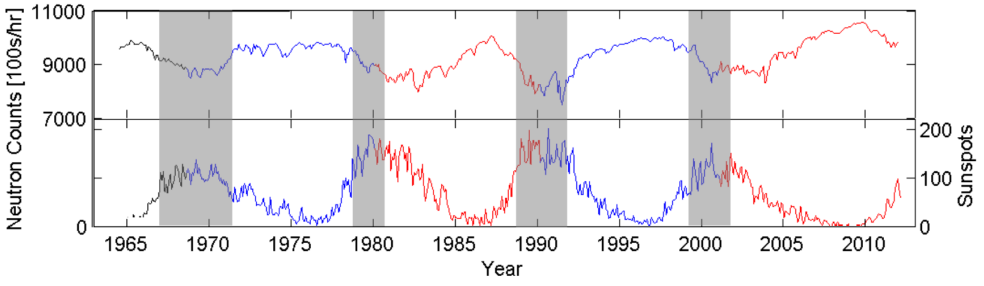

Figure 9: Time series of the cosmic ray flux (top) measured by the neutron monitor McMurdo, Antarctica, and the number of sun spots (below). Colors indicate the heliospheric magnetic field in near-Earth space and gray boxes the polarity change thereof, modified from [48].

The magnetic field of the Earth exhibits in the first order a dipole structure tilted by 11 degrees with respect to the rotation axis. It deflects and reflects charged particles entering from the outside, especially the low energetic part from the solar wind. The Lorentz[d] force leads to an equation of motion for a particle with charge q, mass m and velocity $\vec{v}$ in the presence of a magnetic field $\vec{B}(r)$

$$\frac{\mathrm{d}\vec{v}}{\mathrm{d}t} = \frac{q}{\gamma m}\,\vec{v}\times\vec{B}(r), \tag{61}$$

[b] George Ellery HALE, *1868-†1938, USA
[c] Scott Ellsworth FORBUSH, *1904-†1984, USA
[d] Hendrik Antoon LORENTZ, *1853-†1928, Netherlands

where $\gamma = 1/\sqrt{1 - v^2/c^2}$ is the Lorentz factor. Depending on the inclination angle to the field a particle spirals around the field lines with a radius r

$$q\vec{v} \times \vec{B}(r) = \gamma m \frac{\vec{v}^2}{r}, \tag{62}$$

which can be written in scalar form as

$$Br = \frac{\gamma m v}{q} = \frac{p}{q} \tag{63}$$

using the momentum p of the particle. The quantity Br is called magnetic rigidity and can be expressed in units of GV[e], momentum per unit charge. Depending on incoming direction and destination location there is an energy threshold for which the particle flux due to magnetic shielding on the ground becomes zero. This parameter, the cutoff rigidity r_c, characterizes the local deflection capability of a magnetic field. On the Earth the cutoff rigidity ranges from a few hundred MV at the poles, where particles are barely deflected due to being orthogonally incident with respect to the field, to nearly 18 GV around the equator, where the Lorentz force is maximized. The cutoff rigidity

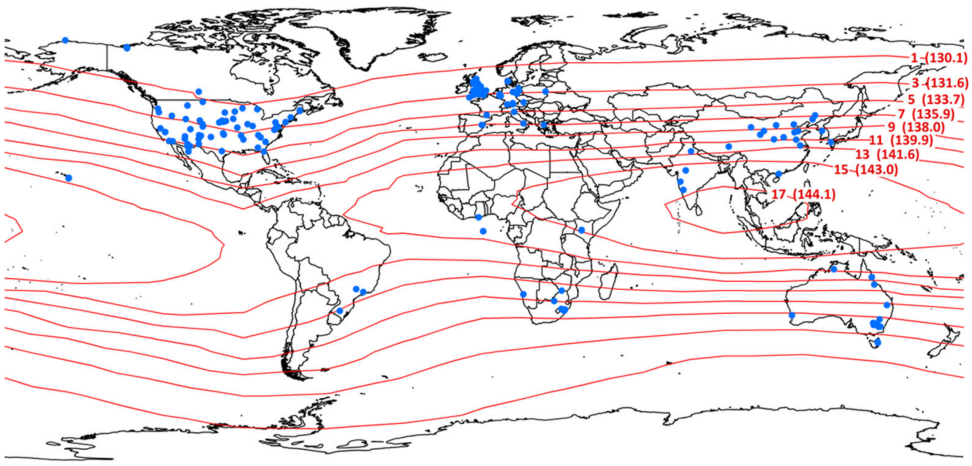

Figure 10: Vertical cutoff rigidity contours of the International Geomagnetic Reference Field calculated for the year 2010 (red countour lines with rigidities in GV and atmospheric attenuation lengths) based on the work of [49], and locations of all cosmic ray stations (blue) listed in 2017. The slow changes of the magnetic field of the Earth also alters the cutoff rigidity regions. [50]

can be used to estimate [51] the particle flux N entering the atmosphere by

$$N(r_c) = N_0 \left(1 - \exp\left(-\alpha r_c^{-k}\right)\right), \tag{64}$$

with the parameters $\alpha \approx 9.02$ and $k \approx 1.05\,\mathrm{GV}^{-1}$.
Those highly energetic particles then create air showers of elementary particles by interacting with molecules of the atmosphere, that can be regarded as a large calorimeter[f] [53]. Such showers consist partly or entirely of an electromagnetic and an hadronic cascade, which both feature a different phenomenology, see also Fig. 11. Electromagnetic showers, governed by the Coulomb interaction, consist of leptons and photons with electron and muon bremsstrahlung together with pair production being the dominant processes. This leads to the cascade being dependent mainly on the charge number Z - for example the electromagnetic radiation length X_0 can roughly be estimated [54] by

$$X_0 \approx \frac{710\,\mathrm{MeV}}{Z + 0.92}, \tag{65}$$

[e] conveniently leaving the $1/c$ factor.
[f] the term refers to an energy measurement - as the principles compare well to detectors for calorimetry in nuclear and particle physics, see also [52]. Yet, although its integral, height dependent, properties can be well estimated, its variation in time is a large uncertainty.

which leads to $X_0^{\text{air}} \approx 86\,\text{MeV} \approx 37\,\text{g/cm}^2 \approx 310\,\text{m}$ for dry air [55]. One can compare this value to the total scale height of the atmosphere $h_0 \approx 8400\,\text{m}$, known from the barometric pressure formula. Therefore, a substantial part of a shower will be absorbed in the atmosphere. Hadronic showers are mainly created in collisions of protons with other nuclei. They can also be comprised of an electromagnetic component[g] but mainly consist of particles, which interact by the strong force, like pions. Unlike cascades governed by Coulomb force, hadronic interactions at high energies are much more complicated in their event topology and less well understood on the level of perturbative quantum chromo dynamics. However, a number of phenomenological models have been developed. For energies in the lower GeV range soft multiparticle production with small transverse momenta are the dominant feature [56]. At higher energies of the projectile additionally hard scattering of partons carrying only a small fraction of the momentum of the hadron can take place, which leads to smaller sub-cascades [57]. For much higher energies gluon interactions finally start to compete with quark-quark interactions.

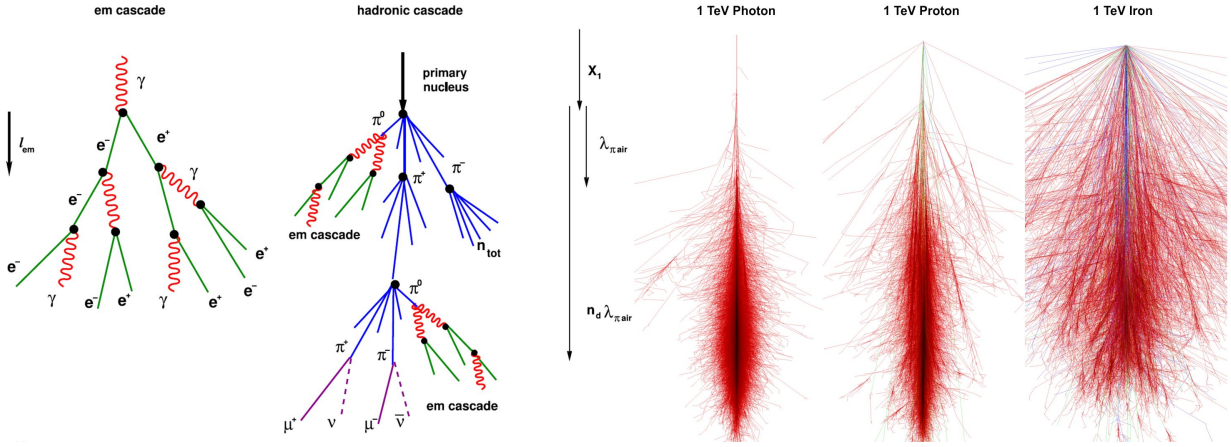

Figure 11: Air showers: (left) Feynman graph representation of electromagnetic and hadronic cascades with the typical interaction lengths [58] and (right) simulation of leptons, hadrons and heavy nuclei in the atmosphere (same scale) [59].

The hadronic interaction length λ_{had} therefore mainly depends on the atomic number A and their corresponding cross section.

$$\lambda_{\text{had}} \sim \frac{1}{n\sigma_0 A^{2/3}}, \tag{66}$$

whereas the mean cross section σ_0 being specific for the particle species. For example the interaction length for GeV pions in air amounts to $\lambda_{\text{had}}^{\pi} \approx 120\,\text{g/cm}^2$ [55]. This leads to hadronic showers in general developing faster due to the multiplicity and lasting longer as the hadronic cross section is smaller than in the electromagnetic case.
One of the by-products in these cascades are neutrons. Although neither being present in cosmic radiation nor being the dominant production channel neutrons make up a large part of the particles at ground level as their interaction probability is smaller compared to charged particles and their lifetime is long enough to traverse the atmosphere, see also Fig. 12. The neutron density increases until a height of around 20 km or (50-100) g/cm^2, the so-called Pfotzer[h] maximum [60], by spallation reactions in the upper atmosphere, and beyond it follows a simple exponential law as a function of atmospheric depth. As seen in Fig. 12, the initial flux decreases by several orders of magnitude with only marginal deviations of the base spectrum until reaching the ground level.

[g] Muons are for example primarily produced by pion decay, which is mediated by the weak force.
[h] Georg PFOTZER, *1909-†1981, German Empire

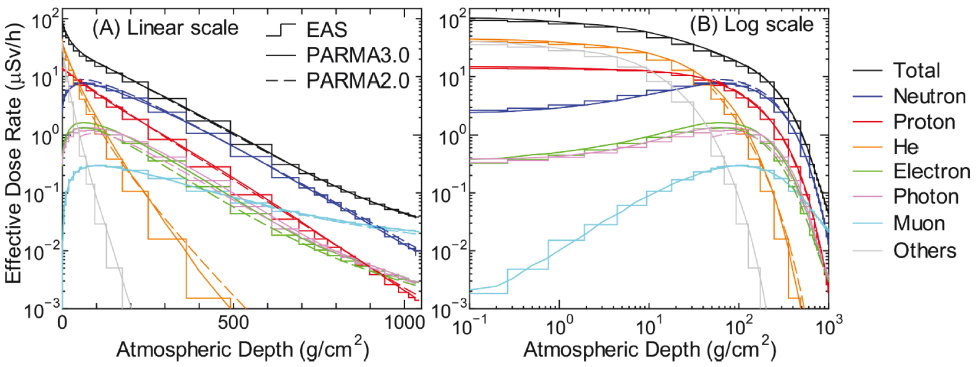

Figure 12: Atmospheric depth dependencies of effective dose rates at r_c = 0 GV for solar minimum conditions in log-linear (left) and log-log representation (right), calculations carried out using PARMA [61].

The spectrum of cosmic-ray induced neutrons, see Fig. 13, offers some distinct features with three prominent peaks, which originate from the physics involved from the process of creation until absorption, see here sec. 1.4. Highly energetic neutrons at ≈ 100 MeV are produced as secondary particles by intra-nuclear cascades and pre-equilibrium processes [62]. When high-energy neutrons or protons interact with atoms of the atmosphere, the excited nuclei evaporate neutrons at a lower energy. This process manifests itself at the peak at ≈ 1 MeV and shows additional absorption fine structure due to distinct resonances of non-hydrogen atoms, especially oxygen, compare also the cross sections in Fig. 31. Neutron interactions in the sub-MeV region are entirely dominated by elastic collisions, in which the energy loss is correlated to the mass of the target nucleus. Due to the mass of hydrogen being nearly equal to the one of the neutron, this energy band is most sensitive to water and organic molecules and thus most relevant for the method of cosmic ray neutron sensing. Below ≈ 1 eV the kinetic energy of the target, which is usually in thermal equilibrium at $k_B T \approx 25$ meV, significantly contributes to the neutron's energy during a collision. As a consequence, neutrons finally become thermalized at ≈ 25 meV. Since neutrons cannot leave the thermal equilibrium they perform a random walk until they are absorbed[i].

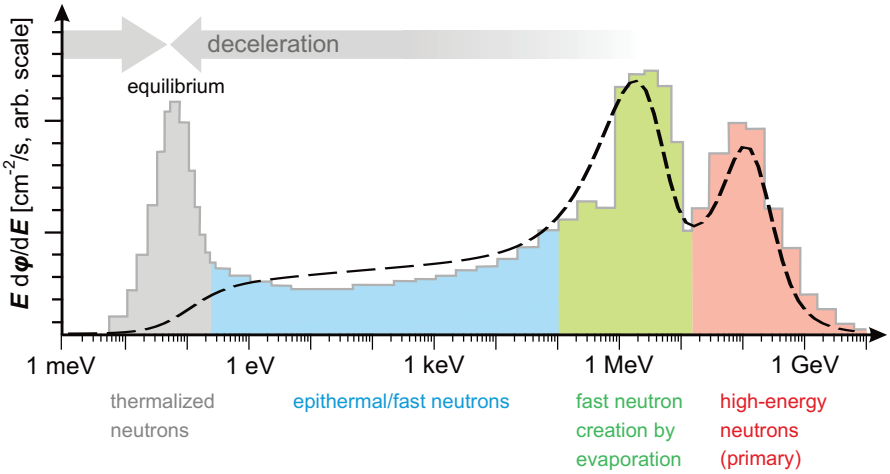

Figure 13: The cosmic ray neutron spectrum with its different domains. Data (histogrammed) from [65] and analytical description (dashed line) by [66].

[i] The dominant channel [63] is absorption by nitrogen, $^{14}\mathrm{N} + n \rightarrow ^{14}\mathrm{C}$, being the main source of atmospheric carbon-14 used in radiocarbon dating for inferring the chronometric age for materials recovered from archeological contexts [64].

Cosmic ray propagation in the atmosphere has been modeled extensively by Sato et al. [66] using PARMA [67], which is based on PHITS [68], see also sec. 5.2.1. They provide an energy spectrum of cosmic ray neutrons for a variety of altitudes, cutoff-rigidities, solar modulation potentials and surface conditions. These simulations have been validated with various independent measurements, i.e. [65] and [69], at different altitudes and locations on Earth. Moreover, the analytical formulations of the spectra turned out to be effective in use for subsequent calculations. The presented energy-dependent flux $\phi(E)$ is described by a mean basic spectrum ϕ_{B}, a function for neutrons below 15 MeV ϕ_{L}, an extension for thermal neutrons ϕ_{th}, and a modifier f_{G} for the geometry of the interface, which is defined by the ratio in comparison to a hypothetical spectrum of a semi-infinite atmosphere:

$$\phi\left(s, r_c, d, E, w\right) = \phi_{\mathrm{B}}\left(s, r_c, d, E\right) \cdot \left(f_{\mathrm{G}}(E, w) + \phi_{\mathrm{th}}(E, w)\right) \cdot \phi_{\mathrm{L}}\left(s, r_c, d\right). \tag{67}$$

The individual terms are

$$\begin{aligned}\phi_{\mathrm{B}}\left(s, r_c, d, E\right) = \\ & 0.229\left(\frac{E}{2.31}\right)^{0.721}\exp\left(-\frac{E}{2.31}\right) + c_4(d)\exp\left(-\frac{\left(\log(E)-\log(126)\right)^2}{2\left(\log(2.17)\right)^2}\right) \\ & + 0.00108\log\left(\frac{E}{3.33}10^{12}\right) \\ & \cdot\left(1+\tanh\left(1.62\log\left(\frac{E}{9.59}10^{8}\right)\right)\right)\left(1-\tanh\left(1.48\log\left(\frac{E}{c_{12}}\right)\right)\right),\end{aligned} \tag{68}$$

$$\log\left(f_{\mathrm{G}}(E, w)\right) = -0.0235 - 0.0129\left(\log(E) - g_3(w)\right)\left(1-\tanh\left(0.969\log\left(\frac{E}{g_5(w)}\right)\right)\right), \tag{69}$$

$$\phi_{\mathrm{L}}\left(s, r_c, d\right) = a_1(r_c)\left(\exp\left(-a_2(r_c)d\right) - a_3(r_c)\exp\left(-a_4(r_c)d\right)\right), \tag{70}$$

and

$$\phi_{\mathrm{T}}(E_T, w) = \frac{0.118 + 0.144\exp\left(-3.87w\right)}{1. + 0.653\exp(-42.8w)}\left(\frac{E}{E_T}\right)^2\exp\left(\frac{-E}{E_T}\right), \tag{71}$$

denoting the solar modulation potential s, cutoff rigidity r_c, the weight fraction of water w and atmospheric depth d. $E_T = k_B T$ represents the thermal energy. The calculation of the individual parameters is described in appendix B.2.4 by (192). For some parameters the solar modulation potential can be set to a minimum and a maximum condition, whereas here the latter has been chosen allowing to already expand many numerical values.

4

ARTIFICIAL HIGH FLUX SOURCES

4.1 | OVERVIEW OF FACILITIES

The earliest research with neutron sources, see sec. 1.1.2, was based on natural α emitters interacting with targets like beryllium. Nuclear fission quickly became the standard source yielding a high flux of up to 10^{15}n/cm^{2}s. Meanwhile, in the 21st century, pulsed sources based on accelerator, apart from the design exception of the IBR-II in Dubna, started to outperform the existing reactors.

In 1968, Brugger [70] reviewed the progress in flux intensity as a function of time. In this plot, see also Fig. 14, which has been updated over decades [71, 72], two phenomena can be observed: that every baseline technology levels off, sooner or later, and that there is belief, that, although recent trends indicate stagnation, upcoming projects would succeed to achieve tremendous steps forward.

In neutron physics up to now only three (Radioisotopes with α particles, fission and spallation) out of five (fusion and photofission) main production methods are used efficiently as sources for large-scale research centers. Technological trends and limitations, the leveling-off, can for example be observed in the history of particle accelerators. In this related field, having a larger variety of acceleration mechanisms, the beam energy of charged particle experiments saturated very quickly and so in most facilities one can find them as boosters chained one after the other. Yet, as a consequence of reviewing only a limited time frame, this engineering principle has been disregarded in particle physics, when extrapolating the „energy frontier“ exponentially like Moore's[a] law[b] [73]. Although the original publication showed the contrary, see Fig. 16, this expected trend is often displayed as a Livingston[c] plot. The conclusion, which can be drawn instead, is, that rather a new technology can introduce a boost to outperform existing systems instead of the upscaling of already established methods.

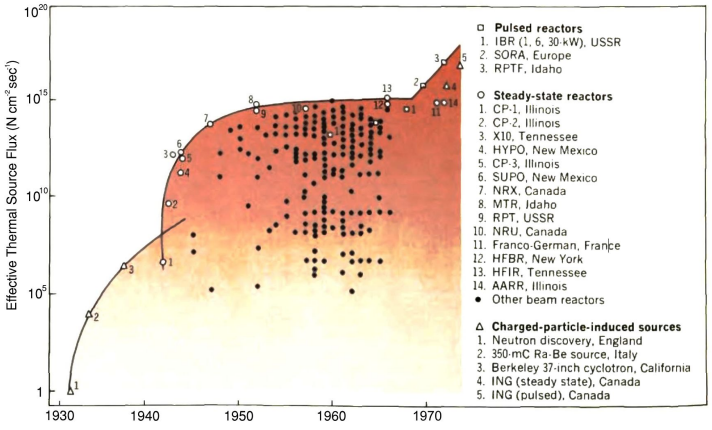

Figure 14: Neutron sources with their thermal neutron flux plotted by the initial year of operation (Note: the axis is not scaled correctly). The optimistic extrapolation presented by Brugger [70] in 1968 calls for a next generation of sources based on novel technologies.

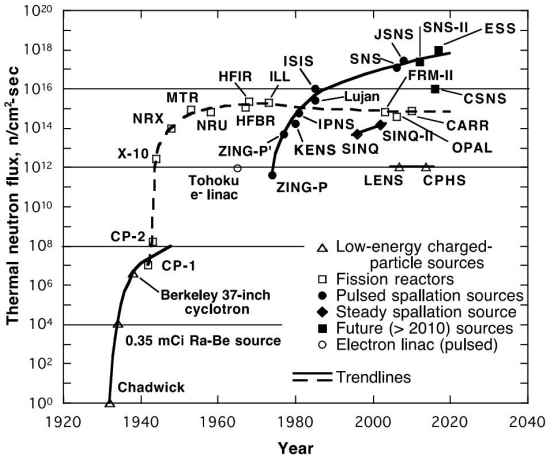

Figure 15: Highest flux sources as a function of initial year of operation and grouped by production method. The initial plot by Carpenter [71] has been updated in 2009.

[a] Gordon Earle MOORE, *1929, USA
[b] The paradigm of the semiconductor industry that since the 1970s the packing density of integrated circuits doubles in a period often referred to as 18 months.
[c] Milton Stanley LIVINGSTON, *1905-†1986, USA

To understand the limitations of actual neutron sources in their intensity, the characteristics of the production mechanisms are summarized in the following. Spallation and fission differ in their released neutron energy spectrum, which is significantly harder for spallation. Both also contrast in their production mechanism. The overall number of neutrons released per fission event is on average 2.4 for ^{235}U, which is less than the incoming beam energy dependent 10-20 neutrons for spallation. Furthermore, in fission one neutron is required to sustain the chain reaction and in typical fuel elements nearly half of the remaining fraction of ^{239}U ends in the production of plutonium. For fission around 180 MeV is deposited as heat, for spallation in tungsten it is around 32 MeV. In a fission process the average gamma energy deposited is 12 MeV, whereas for spallation it is 2 MeV per neutron. Yet, for spallation the kinetic energy of the incident ion beam, which is dumped in the target, has to be added to the heat budget. Finally the limitation for the overall intensity is a trade-off between the source geometry, which focuses on maximizing the neutron flux in the surrounding moderator by minimizing self-absorption, and the cooling capabilities for a compact source or target. This effectively limits the thermal design power to ≈100 MW[d] and the total neutron flux to ≈ 10^{15} n/(cm^2·s). Spallation sources can operate in a pulsed mode and therefore achieve a much higher peak flux within the duty cycle.

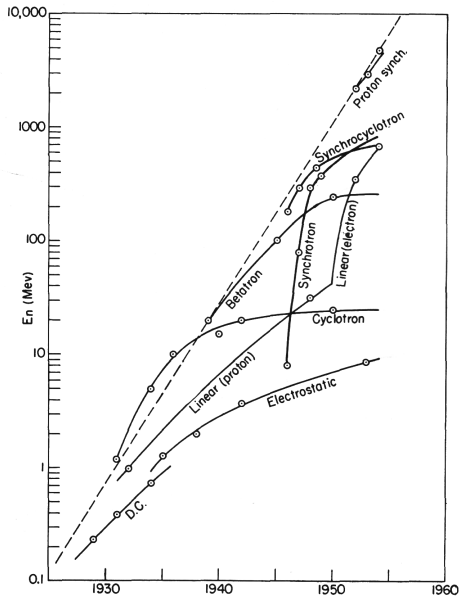

Figure 16: The original Livingston plot [74] shows the collision energy of of different charged particle accelerators. The non-proton labeled entities denote electron machines.

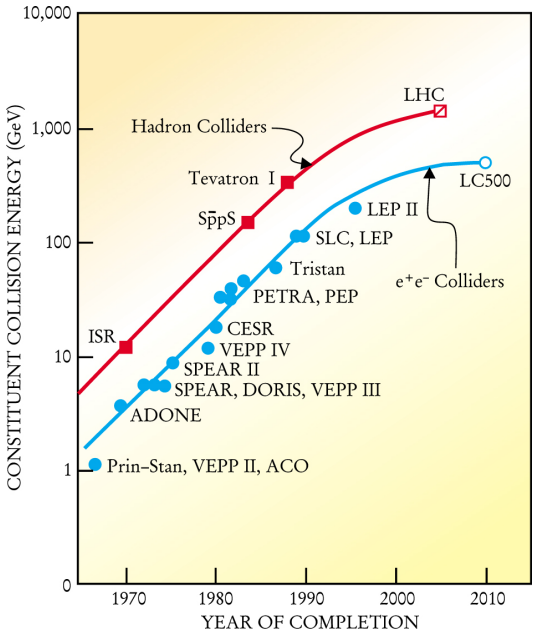

Figure 17: One of the rare graphs showing that hadron and lepton synchrotrons and storage rings are reaching their technological limits in the 21st century [75].

[d] compared to 1500 MW per block for conventional nuclear power plants.

The following neutron research centers in Europe directed towards scattering methods are currently operating a research reactor, see the map presented in Fig. 18.
A detailed overview is given in tab. 3. Spin-Echo instruments are available at FRM II,

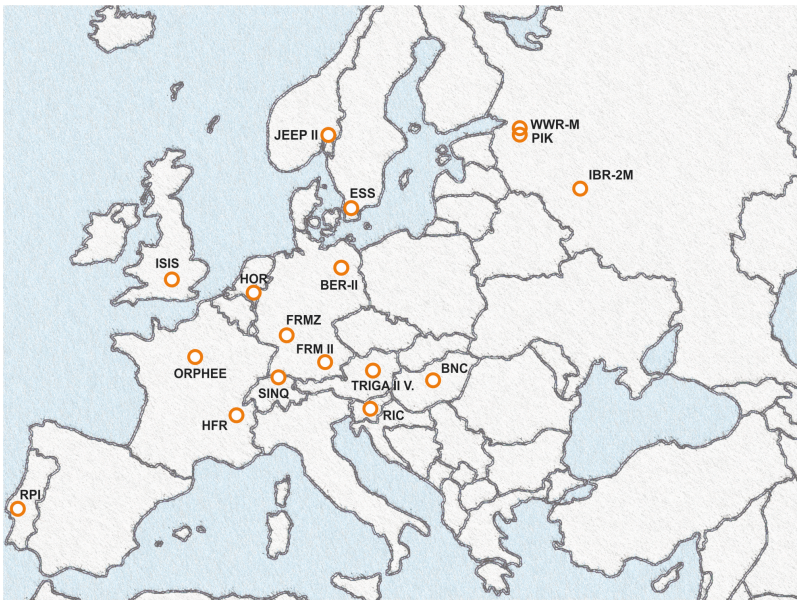

Figure 18: Overview: Sites of neutron sources of scattering facilities in Europe organized in the ENSA association, collected in [76].

ILL, LLB, ISIS and formerly at BER II and BNC.

Facility	Organization	Country	Type	Year
ESS	ERIC Consortium	Sweden	Spallation	2025
ISIS	Rutherford Appleton Laboratory	England	Spallation	1985
SINQ	Paul Scherrer Institute	Switzerland	Spallation	1996
PIK	Petersburg Nuclear Physics Institute	Russia	100 MW	2018
ILL	Institute Laue-Langevin	France	58 MW	1971
FRM II	Heinz Maier-Leibnitz Zentrum	Germany	20 MW	2004
WWR-M	Petersburg Nuclear Physics Institute	Russia	18 MW	1960
LLB	CEA/CNRS	France	14 MW	1980
BNC	Budapest Research Centre	Hungary	10 MW	1992
BER-II	Helmholtz-Zentrums Berlin	Germany	10 MW	1973
JEEP-II	Institute for Energy Technology	Norway	2 MW	1967
RID	Delft University of Technology	Netherlands	2 MW	1963
IBR-2	Frank Laboratory of Neutron Physics	Russia	2 MW	1982
RPI	Instituto Superior Técnico	Portugal	1 MW	1960
RIC	Jožef Stefan Institute	Slowenia	250 kW	1966
TRIGA II V	Atominstitut Wien	Austria	250 kW	1962
FRMZ	Johannes Gutenberg University Mainz	Germany	100 kW	1967

Table 3: Neutron research facilities in Europe with their operational period ordered by type and thermal design power as a rough estimator for the total neutron flux [76][77][78].

The total amount of research facilities and training reactors in Europe is 48, this also includes the n_TOF facility at CERN. In addition the Russian Federation keeps currently another 63 reactors in operation [78].

4.3 | THE FRM II SOURCE

The Forschungs-Neutronenquelle Heinz Maier-Leibnitz[e], FRM II, is a research reactor cooled by light water with a heavy water moderator. The compact fuel element [79], see Fig. 19 (left), has specifically been developed in order to achieve the highest thermal neutron flux [80] for its nominal power of 20 MW. The active core, see Fig. 19 (right), consists of 113 curved $AlMg_3$ embedded U_3Si_2 fuel elements between a cylinder 6.75 cm (for the control rod) and 11.2 cm with an active region of 70 cm. The uranium is enriched to 93 % of ^{235}U. A maximum of unperturbated thermal neutron flux of $8{\cdot}10^{14}$ n/cm^2/s can be achieved, whereas typically a fuel element can be operated non-stop for 60 days until the power density cannot be held any more, which means that the control rod is at its maximum position. Neutrons are extracted by guides which are directed towards the region of highest flux but perpendicular to the line of sight to the reactor core. This tangential arrangement significantly reduces the background of gamma radiation and fast neutrons. Several dedicated moderators tailor the neutron energy to the needs of specific instruments. Besides the room temperature (~320 K) of the deuterium moderator there is a hot and a cold source, see below and Fig. 20. The hot source consists of a cylindrical graphite block of 14 kg heated to 2300 K and the cold source of a spherical containment for 12 l of liquid deuterium at 18 K. A fission neutron converter can in turn again produce MeV-neutrons for the fast neutron tomography station [81]. Most of the eleven beam tubes (SR) supply experiments in the Experimental Hall, which require the highest flux, and some are fanned out into the Neutron Guide Hall (SR-1 split into six guides NL-1 to NL-6). The Spin Echo instruments RESEDA [82] and MIRA [83] are located at the end of NL-5 and NL-6, respectively. The HEiDi [84] single crystal diffractometer aims at the hot source.

The spectrum of a moderator can be described in a first order approximation by a Maxwell-Boltzmann distribution (99), see also sec. 1.3.1. Fig. 20 shows the results of simulations of the neutron flux density at the beginning of the respective beam tubes. The D_2O thermal neutron source can be well approximated by a distribution with a temperature of 318 K - as the heavy water moderator is sufficiently large to achieve a thermally equilibrated flux. For the description of the hot and cold source the fit has to be carried out by a sum of Maxwell-Boltzmann functions. As for technical reasons both vessels are limited in size the results are undermoderated spectra, which do not correspond to the temperature of the moderators but can be described by a thermal spectrum with shifts towards a cold or a hot thermal bath. Experiments then limit the phase space by wavelength selectors like choppers or monochromators.

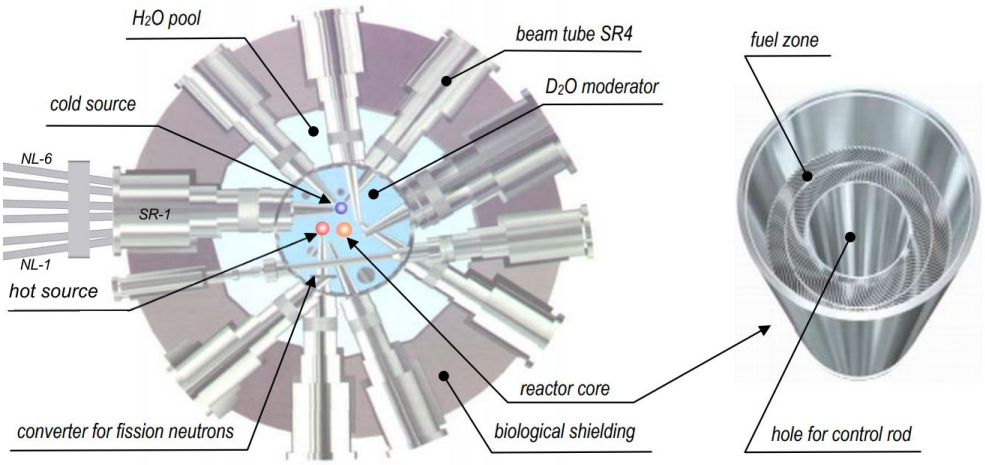

Figure 19: Horizontal section through the reactor core with its different moderators and beam tubes (left). The cylindrical fuel element (right) is specifically designed to maximize the flux per thermal power, modified from [85].

[e] Heinz MAIER-LEIBNITZ, *1911-†2000, Germany

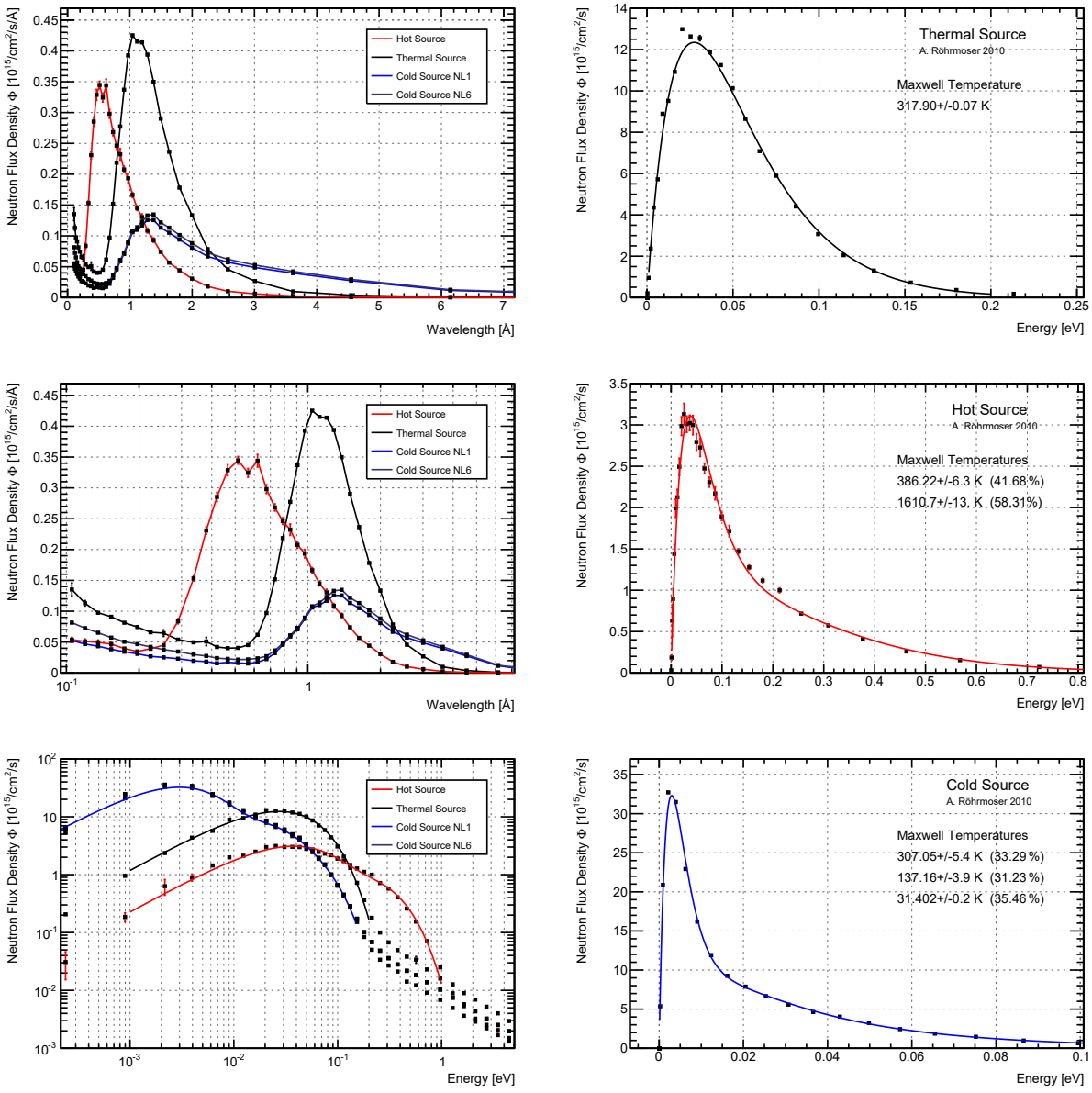

Figure 20: Monte Carlo simulations of the neutron flux at the FRM-II for different moderators relevant in this work. The left column shows from top to bottom the results for all sources as a function of wavelength, logarithmic wavelength and logarithmic energy. The right column shows each flux distribution as a function of energy fitted by one or more Maxwell-Boltzmann functions (99) in order to describe the spectrum. These fits are also shown in the same color in the left column.

Part III

URANOS MONTE CARLO TRANSPORT CODE

5

MODELING AND MONTE CARLO APPROACH

The Monte Carlo [86] method is a brute-force calculation technique, which is used for complicated problems consisting of well-defined or independent sub-tasks. The method retains a close relation to the problem it is trying to solve by repeated random sampling from a set of initial conditions. Although especially in high-energy physics the modeling of complicated particle interactions and transport problems by means of such simulations have even become an own discipline, it has to be noted, that the first realization of this method in physics was carried out by the initiative of Fermi[a] in order to solve problems of neutron transport. His FERMIAC [87], an analog computer, consisted of an adjustable trolley, which was able to ray-trace neutron paths on a two dimensional technical drawing. In the same year, 1947, von Neumann[b] then set up similar programs [88] on the first entirely digital computer, the ENIAC [89], in order to calculate thermonuclear reactions in spherical symmetric geometry [90].

5.1 | SAMPLING

The Monte Carlo approach is a stochastic method, in which a randomly chosen subset of a system is used as an estimator for specific parameters, observables of the system. The requirements are

- the sample space S is defined,
- the values associated with the sample space need to be accessible, either by a known probability distribution function $f(x)$ or
  an invertible cumulative probability distribution $F(x) = \int_{-\infty}^{x} f(t)\,\mathrm{d}t$,
- a method for the generation of random numbers.

After one or more random numbers ξ_i have been chosen there are two methods for evaluation. The sampling by rejection accepts a random number if

sampling by rejection

$$f(\xi_1) < \xi_2, \tag{72}$$

whereas for real $\xi \in [0, 1]$ the support and the codomain of the function should be normalized accordingly, i.e. $\|f\|_{\max} \leq 1$. Then the result will be $x = \xi$.
The sampling by the inverse cumulative distribution function calculates the resulting number by

sampling by the inverse cumulative function

$$x = F^{-1}(\xi). \tag{73}$$

5.1.1 | RANDOM NUMBER GENERATION

The pseudo-random number generator `TRandom3` uses the Mersenne[c]-Twister algorithm MT 19937 [91] based on the Mersenne prime number 19937. It has the following features:

[a] Enrico FERMI, *1901-†1954, Kingdom of Italy.
[b] John VON NEUMANN, *1903-†1957, Austro-Hungarian Empire.
[c] Marin MERSENNE, *1588-†1648, France.

- a very long period of $p = 2^{19937} - 1 \approx 4.3 \cdot 10^{6001}$[d],
- low correlation between subsequent numbers (k-distributed for the output sequence),
- relatively fast, as it generates the output sequence of 624 32bit integers at once.

The random generator is seeded at the initialization of the program by the system time in milliseconds. This is taken as the first integer of the seed sequence, the remaining 623 numbers[e] are generated by the multipliers from [92].

5.1.2 | Sampling free path length

According to the definition of the macroscopic cross section Σ_t, which in general is energy dependent, see sec. 1.4, the probability p of an interaction on a distance $\mathrm{d}x$ in a homogeneous material can be stated as

$$\mathrm{d}p = \Sigma_t \, \mathrm{d}x. \tag{74}$$

Solutions of this type of differential equation are exponential functions. For the non-interaction probability one therefore can write

$$p(x) = \exp\left(-x\Sigma_t\right). \tag{75}$$

The probability distribution function for the distance to the next collision (75) assuming conditional probabilities transforms to

$$p(x)\,\mathrm{d}x = \Sigma_t \exp\left(-x\Sigma_t\right)\mathrm{d}x. \tag{76}$$

The free path length l is obtained by the cumulative probability distribution function of (76)

$$\int_0^l p(x)\,\mathrm{d}x = \int_0^l \Sigma_t \exp\left(-x\Sigma_t\right)\mathrm{d}x = 1 - \exp\left(-\Sigma_t l\right) = P(l). \tag{77}$$

Now, in order to retrieve a path length, (77) can be sampled using the inversion method (73). This means, that the normalized cumulative function is set equal to a random number ξ on a unit interval:

$$l = -\frac{\ln(1-\xi)}{\Sigma_t} = -\frac{\ln(\xi)}{\Sigma_t}. \tag{78}$$

As ξ is uniformly distributed in $[0, 1)$ the same holds true for $1 - \xi$, justifying the latter transformation.

It is assumed in (78) that the material is homogeneous and the cross section and therefore the energy stay constant. In case of an inhomogeneous material it is possible that the integral cannot be resolved in a closed form. The solution is to split the domain into entities of homogeneous materials and only evaluate the path to the respective border. This procedure is equal to the prerequisite already stated in (76), that the probability at any point x does not depend on the individual path history.

[d] A typical URANOS run can easily require more than 2^{32} random numbers. `TRandom3` takes approximately 10 ns for each random number on a modern architecture, e.g. the one presented in sec. 6.6.4.

[e] If too many zeros are in the initial seed tuple it can take up to 10^5 calls until the output vector is equidistributed.

5.1.3 | Sampling thermal velocity distributions

In order to describe scattering processes with thermal neutrons an algorithm has to be applied which preserves the thermally-averaged reaction rate. Such has been introduced by [93], whereas this modified version follows the implementation by [94] and [95]. Besides sampling a Maxwell-Boltzmann distribution, see also (2), for the velocity of the target nuclide it has to be taken into account, that velocities that lead to relative velocities which correspond to a high cross section will have a larger effect on the reaction rate. Therefore, by using the effect of thermal motion on the interaction probability

$$v\overline{\sigma}(v,T) = \int v_r \sigma(v_r) f_M^{(1)}(V) \mathrm{d}\vec{V}, \tag{79}$$

one has to conserve the reaction rate (integrand of (79))

$$R(V) = \|\vec{v} - \vec{V}\| \sigma\left(\|\vec{v} - \vec{V}\|\right) f_M^{(1)}(V), \tag{80}$$

whereas $f_M^{(1)}(V)$ denotes the speed distribution as in (2) for target nuclei of temperature T, velocity $\vec{V}$ and magnitude of velocity V. The CM system of the collision of a neutron with velocity $\vec{v}$ moves at $v_r = \|\vec{v}_r\| = \|\vec{v} - \vec{V}\| = \sqrt{v^2 + V^2 - 2vV\cos\vartheta}$. Such a probability function can be constructed by

$$p(V)\mathrm{d}V = \frac{R(V)\mathrm{d}V}{\int R(V)\mathrm{d}V}. \tag{81}$$

Defining the denominator of (81) as the normalization factor C and

$$\beta = \sqrt{\frac{m}{2k_B T}} \tag{82}$$

as well as $\mu = \cos\vartheta$ one obtains

$$p(V,\mu)\,\mathrm{d}V\,\mathrm{d}\mu = \frac{4\sigma(v_r)}{\sqrt{\pi}C'}\sqrt{v^2 + V^2 - 2vV\mu}\,\beta^3 V^2 \exp\left(-\beta^2 V^2\right)\mathrm{d}V\,\mathrm{d}\mu. \tag{83}$$

In order to obtain a sampling scheme one can divide (83) into two parts such that

$$\begin{aligned} p(V,\mu) &= g_1(V,\mu)\, g_2(V) \\ g_1(V,\mu) &= \frac{4\sigma(v_r)}{\sqrt{\pi}C'}\,\frac{\sqrt{v^2 + V^2 - 2vV\mu}}{v+V} \\ g_2(V) &= (v+V)\beta^3 V^2 \exp\left(-\beta^2 V^2\right). \end{aligned} \tag{84}$$

Here the reason for dividing and multiplying (83) by $v + V$ is that g_1 is bounded. As $\|\vec{v} - \vec{V}\|$ can take on arbitrarily large values, dividing by the sum of the speeds as the maximum value ensures it to be bounded. In general a probability distribution function $q(x) = g_1(x)g_2(x)$ can sampled by sampling x' from a normalized distribution $q(x)$

$$q(x)\,\mathrm{d}x = \frac{g_2(x)}{\int g_2(x)} \tag{85}$$

and accepting it with a probability of

$$p_{\text{accept}} = \frac{g_1(x')}{\max[g_1(x)]}, \tag{86}$$

with $g_1(x)$ bounded. In order to determine $q(V)$ it is necessary to integrate g_2 into (84)

$$\int_0^\infty \mathrm{d}V(v+V)\beta^3V^2\exp\left(-\beta^2V^2\right) = \frac{1}{4\beta}\left(\sqrt{\pi}\beta v+2\right), \tag{87}$$

leading to sampling the probability distribution function

$$q(V)\,\mathrm{d}V = \left(\frac{4\beta^2vV^2}{\sqrt{\pi}\beta v+2}+\frac{4\beta^4V^3}{\sqrt{\pi}\beta v+2}\right)\exp\left(-\beta^2V^2\right). \tag{88}$$

By substituting $x=\beta V$, likewise $\mathrm{d}x=\beta\,\mathrm{d}V$, and $y=\beta v$ leads finally to

$$q(x)\,\mathrm{d}x = \left[\left(\frac{\sqrt{\pi}y}{\sqrt{\pi}y+2}\right)\ \frac{4}{\sqrt{\pi}}x^2\exp\left(-x^2\right)+\left(\frac{2}{\sqrt{\pi}y+2}\right)\ 2x^3\exp\left(-x^2\right)\right]\mathrm{d}x. \tag{89}$$

The terms outside the parentheses are normalized probability distribution functions which allow to be sampled directly and the expressions inside the parentheses are always <1.
The **thermal neutron scattering sampling scheme** therefore is the following:
A random number ξ_1 is sampled from $[0,1)$ and if

$$\xi_1 < \frac{2}{\sqrt{\pi}y+2}, \tag{90}$$

the function $2x^3\exp\left(-x^2\right)$ is sampled using method (72), otherwise $4/\sqrt{\pi}x^2\exp\left(-x^2\right)$. The retrieved x gives the value for V by dividing by β.
For this velocity it has to be decided to accept it based on (86). The cosine of the angle can be sampled by another random number ξ_2 in $[0,1]$ by

$$\mu = 2\xi_2 - 1 \tag{91}$$

and as the maximum of g_1 is $4\sigma(v_r)/\sqrt{\pi}C'$ another sampling random number ξ_3 can be used to accept speed and angle by

$$\xi_3 < \frac{\sqrt{v^2+V^2-2vV\mu}}{v+V}. \tag{92}$$

If this condition is not met speed and cosine of the angle have to be resampled.

5.1.4 | Evaluated Nuclear Data Files

Experimental and theoretical results on neutron-nuclear interactions and their subsequent products are collected in libraries. The main data base is the Experimental Nuclear Reaction Data Library (EXFOR) [96], which stores most of the accepted published results in a scheme of general observables. Such measurements are often not comprehensive or contradictory, therefore so called evaluated data bases exist, which assess the literature especially regarding the intercomparison of different results and compress them to standardized and consistent values. The maintained data bases, which are used for this work are the United States Evaluated Nuclear Data File (ENDF/B) [97] and the Japanese Evaluated Nuclear Data Library (JENDL) [98].

5.1.4.1 DATA FORMATS

The standard reference data is provided in the ENDF-6 format [99], which for reasons of downward compatibility uses 80-character records and variables in FORTRAN form. A typical file could look like the following example

```
#LIBRARY     JENDL-4.0
#REACTION    H-1(N,EL)H-1-L0,SIG
#NUCLEUS     H-1
#MF          3
#MT          2
#EN-MIN      1e-05
#EN-MAX      2e+07
#E,eV        Sig,b                Interpolation
1E-05        1156.94              Lin-Lin
1.1024E-05   1101.91              Lin-Lin
...          ...                  ...
```

Table 4: Example for an ENDF card: the elastic scattering cross section of hydrogen.

The header describes the data according to the parameters: Energies are given in eV,

Library	Collection (JENDL) and version (4.0)
Reaction	Element (H), Isotope (H-1), Projectile (Neutron),
	Reaction type (elastic scattering) and data type (cross section)
MT	Type of the reaction (elastic scattering)
MF	Subdivision of MT into data types (cross section)
Range	Minimum and maximum of the energy

angles in dimensionless cosines of angles, cross sections in barns and temperatures in Kelvin. For the data types the important numbers are MF=3, which is the reaction cross section, and MF=4, which is the angular distribution of the emitted particles. The MT numbers necessary for this work are given in table 5.

MT	Description
1	Neutron total cross section
2	Elastic Scattering
3	Sum of non-elastic processes
4	Sum of inelastic cross sections
5	Sum of processes without any MT number
16-21	Neutron final state reactions (incl. fission)
22-26	Neutron and charged particle final state
$50+i$	Inelastic scattering to the ith excited state
102	Radiative capture
103-117	Neutron capture with charged particle emission
208-210	Pion (π^+, π^-, π^0) production
211,212	Myon (μ^+, μ^-) production

Table 5: Selection of relevant MT numbers and designated purpose [99].

5.1.4.2 INTERPOLATION LAWS

Cross sections are treated by the following rules given in table 6. As seen, the extrapolation rules take into account the typical logarithmic behavior of the cross section. Nevertheless there is no hyperbolic law supposed to be applied, which would take into account especially the $1/v$ behavior in the thermal regime; instead, the values are tabulated in very short intervals.

Table 6: Interpolation rules for tabulated cross sections.

law	Description	law	Description
const	σ is constant (a histogram)		
lin-lin	σ is linear in x	lin-log	σ is linear in $\ln x$
log-log	$\ln \sigma$ is linear in $\ln x$	log-lin	$\ln \sigma$ is linear in x

Angular distributions are described by normalized probability distributions. That means a process describing an incident particle of energy E into an interval $\mathrm{d}\mu$ around the angular cosine $\mu = \cos\vartheta$ by a probability function $f(\mu, E)$ with

$$\int_{-1}^{1} f(\mu, E)\,\mathrm{d}\mu = 1.$$

Due to the azimuthal symmetry of the distribution, they are represented by Legendre[f] polynomial series[g]

$$f(\mu, E) = \frac{2\pi}{\sigma_s(E)}\sigma(\mu, E) = \sum_{l=0}^{N} \frac{2l+1}{2} a_l(E) P_l(\mu), \tag{93}$$

where the number l denotes the order of a Legendre polynomial with coefficient a_l. The zero order factor $a_0 = 1$ is implicitly assumed. So the cross section is obtained by

$$\sigma(\mu, E) = \frac{\sigma_s(E)}{2\pi} \sum_{l=0}^{N} \frac{2l+1}{2} a_l(E) P_l(\mu). \tag{94}$$

5.1.4.3 INTERPOLATION ALGORITHM

Data in structures defined by the ENDF cards are stored by points and corresponding interpolation laws, see chapter 5.1.4.2. Therefore, in order to calculate a cross section as a function of energy, the upper and lower tabulated values have to be selected from the arrays they are stored in. These are found by an interpolation search algorithm [100]. The performance is $O(n)$ in a general case, but $O(\log\log n)$ on linear data set. As some cross sections are stored in files with a mixed metric, consisting of a point matrix of fluctuating density regarding a linear energy scale, if the interval limits during the algorithm are not changed fast enough, the algorithm changes to logarithmic interval search. This improves the performance in case the cross section does not change between 20 MeV and 1 GeV.

Interpolation search defines upper and lower limits of the interval L and R, starting at the minimum and maximum of the data set, and compares the value at $(L+R)/2$ to the search value x. Then the L or R limit is set to $(L+R)/2$, dependent on in which of interval x is located. If $L+1 = R$, the search is stopped and result provided is determined either by a linear or a logarithmic interpolation of the values at L and R according to their relative position compared to x.

[f] Adrien-Marie LEGENDRE, *1752-†1833, France.
[g] with up to 20 coefficients.

5.2 | Neutron Monte Carlo codes

Among the existing Monte Carlo tools, most codes do have a long history and strong aim towards nuclear fuel calculations. Besides dedicated programs, the most widely used in neutron physics is MCNP, especially for purposes of the ESS, GEANT4 can be considered the most important.

5.2.1 | General purpose packages

MCNP (**M**onte **C**arlo **N-P**article) was developed in Los Alamos as a general purpose software to treat neutrons, photons, electrons[h] and the coupled transport thereof. Versions until MCNP4 [101] were capable of simulating neutrons up to 20 MeV, which is the maximum of most of the cross sections available in the evaluated data bases, and were written in FORTRAN 77 [102], which was until the mid-90s considered the standard in scientific computing. With version 5 [103] the development was forked to the MCNPX [104](MCNP e**X**tendend) branch, which converted the code to Fortran 90 [105] and included the LAHET [106] framework. This especially introduced the extension of the energy range for many isotopes up to 150 MeV and some to GeV by using the continuously improved Cascade-Exciton Model (CEM) [62] and ontop the Los Alamos Quark-Gluon String Model (LAQGSM) [107]. It also can treat (heavy) ion transport for charged particles with energies larger than 1 MeV/nucleon by tabulated ranges. The actual version 6 [108] re-merged the X-branch into the main development branch. Since it also provides an optional cosmic-ray source [109] it has gotten large attention for the calculation of the cosmic neutron spectrum as seen in [110]. *USA*

A more recent general purpose tool is PHITS [68] (**P**article and **H**eavy **I**on **T**ransport code **S**ystem), as extension of the high energy particle transport code NMTC/JAM [111], which, besides the features mentioned above, also supports charged particles in magnetic fields, dE/dx calculations in the **C**ontinuous-**S**lowing-**D**own **A**pproximation [112] (CSDA) and intra-nuclear cascade (JAM) [113] (**J**et **A**A **M**icroscopic Transport) models up to 1 TeV. PHITS is also typically linked against the JENDL-4/HE(High Energy) data base, consisting of files evaluated by CCONE [114], which is a more sophisticated model compared to INCL [115] and JAM. However, it comes along with many adjustable parameters for each nucleus, which often leads to a better accuracy compared to other physics models. PHITS also features a rudimentary graphical user interface. Like MCNP and the following codes it is also written in Fortran. One of the recent follow-up developments is PARMA [67] (**P**HITS-based **A**nalytical **R**adiation **M**odel in the **A**tmosphere). It calculates the spectra of leptons and hadrons providing effective models for fluxes of particles of different species, especially with the aim of dose estimations. *Japan*

The FLUKA [116](**FLU**ktuierende **KA**skade) code is mostly oriented towards charged hadronic transport and nuclear and particle physics experiments. For neutron calculations, the full spectrum is divided into 260 energy groups, which are not directly linked to an evaluated data base, but operate on their own set of reprocessed and simplified mean values. Especially for neutrons and geometrical representations, it contains reimplementations from the MORSE [117] neutron and gamma ray transport code. *CERN*

GEANT4 [118] (**GE**ometry **AN**d **T**racking) can be regarded as FLUKA's successor, based on multithreaded C++ and OpenGL visualizations. It is designed specifically for the needs of high energy and accelerator physics. GEANT4 especially excels in describing a complex geometry of the setup. Since 2011, also driven by requests from the European Spallation Source, an increasing number of low energy neutron calculation capabilities *CERN*

[h] MCNP does not handle magnetic fields for charged particles.

were introduced. Meanwhile the software has advanced to a level where there is a good agreement with other codes like MCNP for fast neutrons [119] as well as slow neutrons [120].

5.2.2 | Specific neutron interaction codes

USA VIM [121] is a continuous energy neutron and photon transport code written mainly in Fortran 90. It is developed by Argonne National Laboratory for reactor physics and shielding. The geometry is limited to hexagonal or rectangular lattices of combinatorial unit cells and especially focuses on the description of critical states.

France TRIPOLI [122] is a neutron, photon and electron transport code written in FORTRAN 77 and C by the Commissariat à l'énergie atomique, Saclay. It uses, unlike VIM, not only the ENDF data bases but is able to extract cross sections from several libraries by a specific interface allowing for example neutron energies up to 150 MeV.

USA Similar to both mentioned programs there are a number of codes with approximately the same scope allowing photon and neutron transport. Among them are TART [123] with 700 energy groups up to 1 GeV, but neutron calculations only up to 20 MeV. Whereas earlier versions were written in LRLTRAN, a language unique to the Lawrence Livermore National Laboratory to run on their Cray supercomputers[i], the releases after 1995 were ported to Fortran. It's successor, MERCURY [124], then was rewritten in C with improvements in geometry definitions by XML steering files. Furthermore,

Russia *USA* *Finland* with dedicated scope on reactor analysis there are PRIZMA [125] and Shift [126], which partly includes also deterministic codes, Serpent [127], which does not only use the average interaction length calculations, but also the Woodcock delta-tracking method [128] that continues across geometrical borders by pseudo fictitious steps in

China *France* *UK* the subsequent material. This feature is also included in RMC [129] (Reactor Monte Carlo) and MORET [130]. These codes were developed at governmental institutions and mostly for the research program pursued. For the MONK [131] code there also have been made the approach to commercialize such a tool. The only German contribu-

Germany tion to be mentioned in the field of reactor analysis is KAMCCO [132], a pseudo Monte Carlo transport code, which was developed in Karlsruhe for the fast breeder reactor in the 1970s [133].

USA The most recent development is the publicly available MIT OpenMC [94]. Although mostly written in Fortran 90, it features a Python [134] API and XML geometry definition files as well as Jupyter [135] notebook parsers.

[i] Still holding the claim that TART would be the fastest Monte Carlo available.

6

URANOS

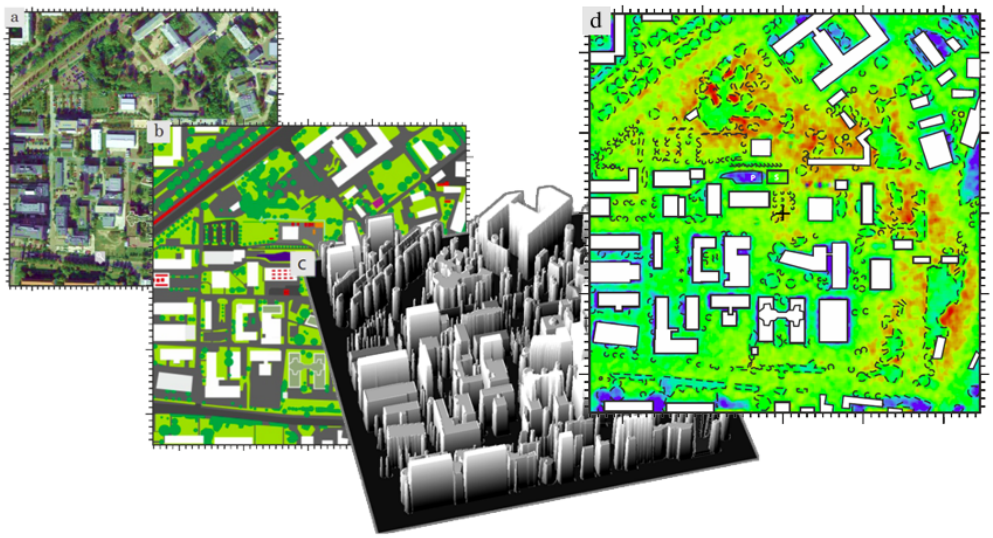

Figure 21: URANOS modeling process, exemplarily for a neutron density in an urban environment: a) Choice of a simulation context, b) Transfer to a (layered) pixelated image, c) Extrusion of a voxel model by the geometry unit and d) Export of the result - here: the above-ground neutron density in a chosen energy interval.

The acronym URANOS stands for **U**ltra **Ra**pid **N**eutron-**O**nly **S**imulation. The program is designed as a Monte Carlo tool which simulates exclusively contributions in a detection environment from neutron interactions. The standard calculation routine features a ray casting algorithm for single neutron propagation and a voxel engine. The physics model follows the implementation declared by the ENDF database standard and was described by OpenMC [94]. It features the treatment of elastic collisions in the thermal and epithermal regime, as well as inelastic collisions, absorption and emission processes such as evaporation. Cross sections, energy distributions and angular distributions were taken from the databases ENDF/B-VII.1 [97] and JENDL/HE-2007 [98]. The entire software is developed in C++ [136], linked against CERN's analysis toolbox ROOT [137], whereas the GUI uses the QT cross-platform framework [138]. This section focuses on the computational and physical description, the user interface is explained and displayed in appendix B.4.
The choice for creating an own independently operating Monte Carlo based program apart from the software mentioned in section 5.2 was based on evaluating the specific demands of understanding the physics of neutron detectors. The key ideas are:

- Most of the existing codes are not publicly available and fall under the export control law for nuclear related technology - whereas the underlying data bases are free of access. High precision detector development is not a use case which is envisaged by the authorities.
- Most of the existing codes were developed in the 1970s or 1980s. Written in the procedural programming language Fortran, which has been proven useful in the ages of limited execution orders and memory, but nowadays suffers the drawback of requiring sophisticated and time consuming code tuning, these tools in the best case received wrappers in C, rarely in C++. Today, facing multithreading, distributed network topologies and distributed memory in abundance, the changes of computing technology also have a strong impact on the code design and coding strategies.

- Meanwhile even more complex mathematical operations are readily available from standard packages like the GSL [139] (**G**NU **S**cientific **L**ibrary) and frameworks such as Root [137].
- The majority of codes focuses on the evaluation of radiation sources, including gamma emissions. Signal generation in a boron based hybrid detector requires two additional steps of charged particle transport mechanisms - within the conversion layer itself and subsequently in the gas. In the most cases it is not possible to integrate such a calculation path directly, but it would have to be added on top of the simulation. Furthermore, typical codes expect for the geometry objects of roughly equal size - boron layers having an aspect ratio of 10^5 due to the low thickness cannot be described.
- All available codes propagate a take-off amount of neutrons in time due to the fact that in typical applications concerning criticality calculations the neutrons themselves change the state of the environment, for example by generating a significant amount of heat. Therefore, the whole ensemble has to be propagated, especially until an equilibrium state is reached. Due to limited computing resources this also required the multigroup method, see also the following key point.
- The multigroup method is a technique, which allows significant improvement of the calculation speed by not treating every neutron track individually but assigning an effective weight to propagating particle. This weight gets increased for (n,xn) processes and reduced, if a neutron is absorbed or loses enough energy to drop out of a specific interval. The method is derived from solving Fermi age diffusion equations [140] and is applied in many codes. However, it requires many interactions to generate enough randomness and thus it leads to a significant bias whether or not a neutron will undergo most probably only one collision. Yet, for the study of background contributions in detectors or albedo neutrons, such a systematic error should be avoided.

The only software package which does not suffer from the mentioned drawbacks was GEANT4. But at the beginning of this work the code did not at all feature any accurate low energy neutron calculation. Materials in GEANT4 are usually described under a free gas assumption with unbound cross sections with no information about interatomic chemical bindings, this especially comes into account when treating hydrogen collisions[a]. Therefore, the main part of the relevant physics would still have to be integrated. In conclusion it has been decided to focus on a design from scratch in modular, object oriented language.

6.1 | URANOS CONCEPTS

The buildup of the software can be motivated based on the following general aspects:

- The geometry is represented in a 3-dimensional coordinate space.
- In typical situations the number of neutrons can easily reach 10^9, whereas the relevant neutrons contributing to an observable might scale down this initial amount by more than 10^6.
- Neutrons are neither as abundant nor as simple to describe as necessary to apply means of ensemble statistics.

[a] GEANT4 though can be coupled to the constantly developed models for evaluating the JEFF-3.X [b] ACE formatted thermal scattering law files. For scattering in crystal structures meanwhile the NXSG4 extension [141] has been released.

- Neither energy nor particle number is conserved, moreover both are linked to each other depending on the medium, which implies complex transport equations, that often can only be solved numerically.
- In general interactions are not deterministic but of statistical nature.
- Important parameters like cross sections cannot be derived but are to be extracted from data bases.
- Whereas possible physical interactions are numerous, the relevant ones within a specific energy interval are predominately not more than two different types.
- Secondary particles, except conversion ions, are typically not contributing.

One specific feature of URANOS is its layer geometry, which takes advantage of the symmetry of the envisaged problem. The concept is presented in Fig. 22. In one case a neutron detector has to be simulated which consists of several mostly identical layers of a boron coated substrate. Whereas along the horizontal and vertical axes the geometric scales vary significantly, the mean free path lengths are comparable. For example the absorption probability for a neutron in a 500 nm film of boron might be around 3 %, the scattering probability in a polymer foil of 100 times the thickness is approximately the same number and in the air gap of 100 times the thickness of the plastic it may be 0.3%. This also means that the spatial definitions in such a simulation should not be build on concepts requiring objects of roughly equal size. The solution of URANOS is using layers. This allows to easily build up a geometry of homogenous materials with the main parameter being position and height of such a layer. Each layer furthermore can be sub-structured by twodimensional matrices into voxels.

URANOS uses ray casting [142], a technique, which refers to conducting a series of

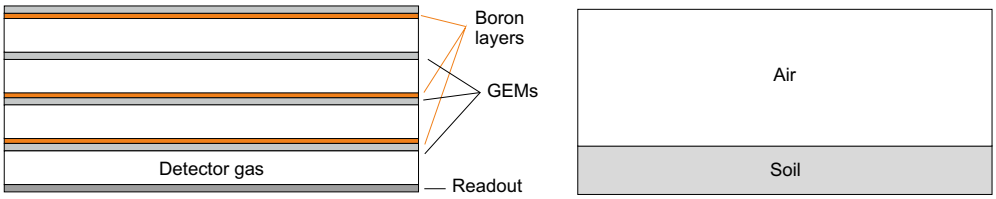

Figure 22: Idea of the URANOS layer geometry representing two problems: (left) simulation of a neutron detector consisting of a stack of substrates coated with a converter and (right) evaluating the propagation of albedo neutrons.

ray-surface intersection tests in order to determine the first object crossed by tracks from a source. These intersections are either defined by analytical surfaces, like the layer structure, or computed from extruded voxels, which do not at all consist of surfaces. Similar types of geometry definitions with mixed volume and surface data were for example used in early computer games when no powerful hardware acceleration was available[c] and nowadays for X-ray tomography image reconstruction in material research [143], geociences [144] and especially medical imaging [145]. The method of ray casting also allows to only record and store the variables necessary for each run. The neutron is physically propagated forward in time through the domain and flags are used as boolean operators for each possible output. If for example the recording observable is defined as the density above the surface not the whole track but only the tracklet within the layer above the ground is kept in the memory.

[c] Notable examples are the Voxel Space engine by NovaLogic or the GAIA/Paradise-Engine by Appeal.

6.2 | COMPUTATIONAL STRUCTURE

The basic concept of URANOS relies on looping over a set of neutrons, which features initial conditions, predefined or randomized, and for each neutron a loop tracking its path through the geometry. Both entities are referred to as 'stacks'. In each step the geometrical boundaries are determined and handed over to the physics computation unit. For specific cases actual variables of the neutron or its track history are recorded emulating a real or a virtual detector. This process is called 'Scoring' and can be invoked when passing a layer or an absorption in a converter takes place. A track is defined as the shortest path between two points of interaction. It can, as will be seen later, be cut by layer or material boundaries, which dissects it into tracklets. The pseudo flow chart of Fig. 23 illustrates the entire simulation process, which will be described in the following.

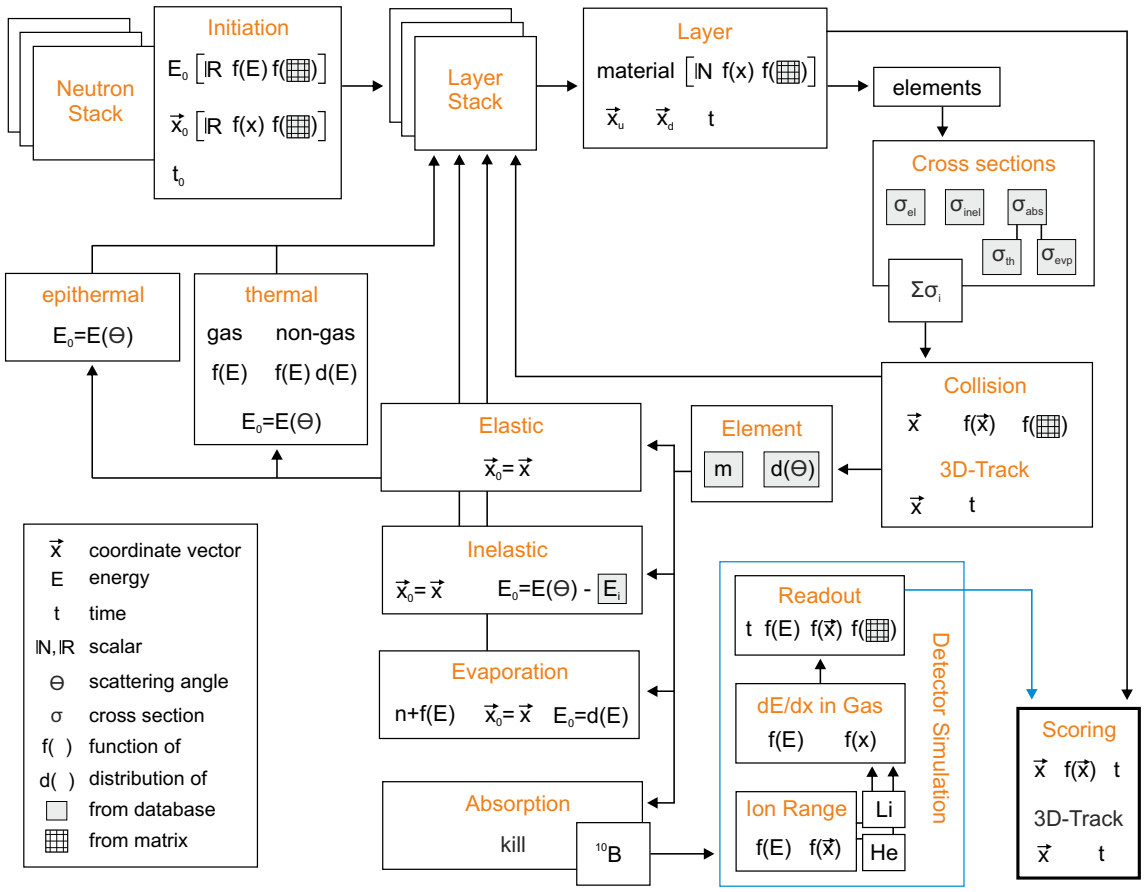

Figure 23: Pseudo flow chart of the internal buildup of URANOS. Each calculation step is represented by a block describing the structural function in orange and the corresponding physics variables.

6.2.1 | STARTUP

Before the main calculation routine shown in Fig. 23 three steps are performed:

- Assigning memory to objects, which will be used throughout the calculation, by creating empty containers. These are at least 50 one and two dimensional root histograms.
- Reading the configuration files, creating the geometry and, if available, reading the voxel extrusion matrices.
- Reading the necessary tables from the ENDF library [99], see also sec. 5.1.4.1.

The configuration is split into two files, one containing the basic settings for URANOS, like the number of neutrons to calculate and furthermore import and export folders for the data, and one containing information how to geometrically structure the layers, see here also the next sec. 6.2.2.
Cross sections and angular distributions are read from tabulated ENDF files, exemplarily shown in Fig. 24, grouped into absorption, elastic and inelastic scattering. Exemplarily for ^{1}H, ^{10}B and ^{16}O the selected cross sections to be loaded are shown in tab. 7, whereas the full list of available isotopes can be found in appendix B.2.2. For the selection only

Isotope	Elastic	Inelastic	Absorption
^{1}H	MT=2 (MF=3, 4)	n/A	MT=5, 102, 208-210
^{10}B	MT=2 (MF=3, 4)	MT=51-54	MT=107
^{16}O	MT=2 (MF=3, 4)	MT=51-70	MT=5, 102, 103, 107, 208-210

Table 7: Example cross sections according to [99] and chapter 5.1.4.1.

MT numbers with significant contributions are taken into account, which translates to omitting processes with overall less than 10^{-2} % of the total cross section. Furthermore, the cross section tables are compressed before loaded into the program. Except for hydrogen, the algorithm skips every new value with a relative difference of less than 1 % to its non-skipped predecessor, removing 0 % (rare elements) to 98 % (iron) of data, which saves a significant amount of iteration steps in the process of the cross section lookup, see sec. 5.1.4.3. The smallest error listed on cross sections can be found for elastic scattering of hydrogen with 0.3 %, other isotopes exhibit standard deviations of 1 % and larger, which justifies the compression method. For calculating the total

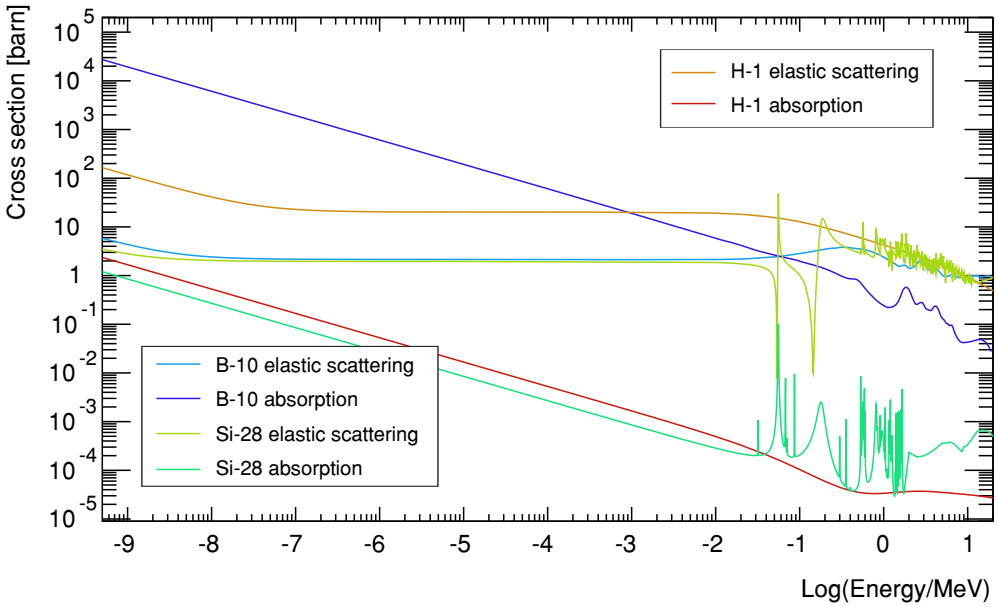

Figure 24: Examples of cross sections for the light isotopes hydrogen (efficient moderator), boron (efficient absorber) and silicon (transparent) from the ENDF library [97] from thermal energies in the meV domain to the MeV range.

macroscopic cross section the individual contributions of elastic Σ_{el} and inelastic Σ_{in} scattering as well as absorption Σ_a are summed up

$$\Sigma_t = \Sigma_a + \Sigma_{\mathrm{el}} + \Sigma_{\mathrm{in}}, \tag{95}$$

whereas for 'inelastic' cross sections the integrally mainly contributing ones are summed up, see table 26, and 'absorption' itself is understood as a sum of MT numbers stated in table 7, which can either lead to capture without consecutive particles or the creation of new neutrons by for example evaporation or charged particle ejection by converters.

6.2.2 | GEOMETRY

URANOS uses analytical definitions and voxel geometry as introduced in sec. 6.1. The following top-down structure is applied for describing the simulation environment:

$$\text{geometry} \rightarrow \text{layer} \rightarrow \text{voxel mesh} \rightarrow \text{material} \rightarrow \text{isotope}$$

Fig. 25 illustrates the buildup of such a structure of three layers. A thick and a thin solid layer are combined with a voxel geometry creating an arbitrary arrangement of materials of different density and air. Each layer of the stack is either entirely composed

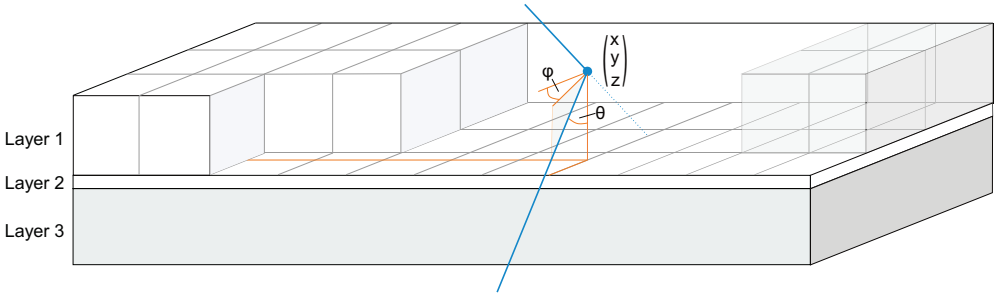

Figure 25: Schematic of the URANOS geometry definition for layers of different height (black) and tracks (blue). Layer 1 is defined by a voxel mesh, Layer 2 and 3 contain a uniformly defined material.

of a solid or subdivided into several sections using a twodimensional matrix from which voxels are extruded. The solids are filled with predefined materials. A material is a specific atomic composition of isotopes with their atomic weight and density. Table 8 provides an example of such a definition, whereas all available materials can be found in appendix B.2.3. Most compounds are taken from [146]. The voxel mesh is auto-

Material	Density	Composition
Air	1.2 kg/m^3 NTP	78 % $^{14}N_2$, 21 % $^{16}O_2$, 1 % ^{40}Ar
Boron	2.46 g/cm^3	80.1 % ^{11}B, 19.9 % ^{10}B

Table 8: Example composition of the material 'dry air' and a neutron converter.

matically loaded if a file with a name corresponding to a layer number is found. It can be either a tab separated ASCII [147] matrix of equal row and column rank or a quadratic portable network graphics (PNG) [148] image. The integer values w or grayscale values denote the material numbers which primarily override the global layer definition. Typically solids are directly extruded from these values, yet there are three further declaration modes:

- the material is soil and w defines the amount of water in volume percent,
- the material is defined globally by the layer and w scales the density,
- the material is defined globally by the layer, w scales the height of this material and the remaining volume extended to the full layer height is filled with air.

The layers can be stacked on top of each other with individual definitions to realize complex geometries. Fig. 26 provides examples to illustrate the scope of applications (not discussed here) and the scales which can be targeted. The images of one single layer act hereby as sectional view. Especially landscapes can be modeled using the third declaration mode, an example is provided in Fig. 27. The geometry of each layer is simply defined by an array of 8 elements:

$$\begin{aligned} g = [&x \text{ lower bound}, x \text{ upper bound}, y \text{ lower bound}, y \text{ upper bound}, \\ &\text{upper } z \text{ position}, \text{height}, \text{material}, \text{layer number}], \end{aligned} \tag{96}$$

whereas the lateral lower and upper bounds are defined globally and the layer number acts as an additional identifier to create subgroups within the stack. Furthermore,

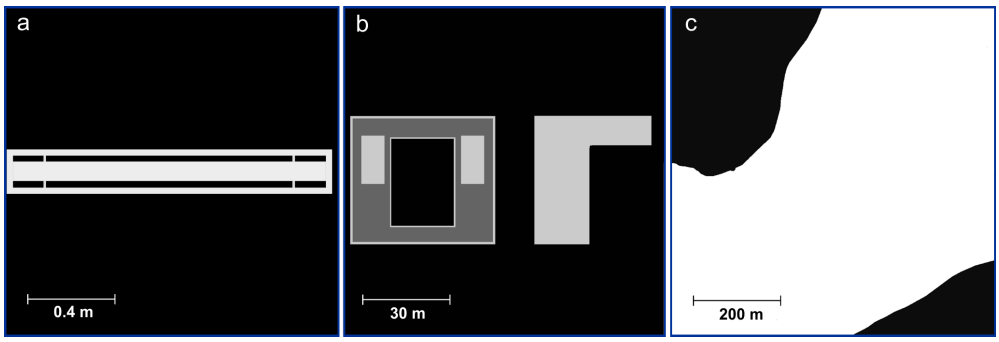

Figure 26: Examples of layers for voxel geometry definitions (all in top view): a) a moderated 2 inch proportional counter, b) the rooftop of the Physikalisches Institut in Heidelberg, c) a part of a lake where a buoy has been deployed. Grayscale values define preconfigured materials.

the forward and backward propagation direction are defined according to if the layer number along the path increases or decreases, respectively.

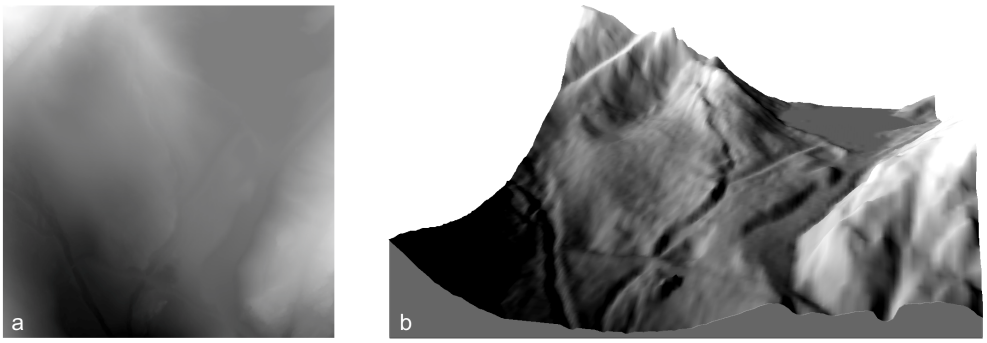

Figure 27: Example of a complex layer structure in voxel geometry for a digital environmental model (Kaunertal Glacier at N46° 52.2 E10° 42.6). (a) Grayscale image with 500 × 500 pixels at a lateral resolution of 1 m and 0.5 m in height by the 8 bit gray card. (b) Shaded illustration of the resulting layered voxel structure of soil/air.

Neutron tracks $\vec{S}$ are described by a mixed geometry definition of support vectors $\vec{x}$ in Cartesian[d] coordinates and spherical direction vectors $\vec{r}$:

$$\vec{x} = \begin{pmatrix} x \\ y \\ z \end{pmatrix} \quad \text{and} \quad \vec{r} = \begin{pmatrix} r \\ \vartheta \\ \phi \end{pmatrix}, \tag{97}$$

denoting the three spatial coordinates x, y, z and the angles ϑ, ϕ with the range r. The choice for this system is due to the fact that this characterization provides direct access to the necessary observables. Examples are point sources which are randomly distributed in both angles or detector planes for which the beam inclination is an important parameter considering sensitivity. Hence new coordinates $\vec{x}'$ are calculated by

$$\vec{x}' = \begin{pmatrix} x \\ y \\ z \end{pmatrix} + \begin{pmatrix} r\cos(\phi)\sin(\vartheta) \\ r\sin(\phi)\sin(\vartheta) \\ r\cos(\vartheta) \end{pmatrix}$$

and for determining the position on a layer at elevation z_L

$$\vec{x_L} = \begin{pmatrix} x \\ y \\ z \end{pmatrix} + (z - z_L) \begin{pmatrix} r\cos(\phi)\tan(\vartheta) \\ r\sin(\phi)\tan(\vartheta) \\ 1 \end{pmatrix}.$$

[d] René DESCARTES, *1596-†1650, France.

Time is an indirect quantity. It is derived from the geometrical position of the neutron calculated from energy and initial conditions.

In URANOS three layers can be assigned specific functions. These are source layer, detector layer and ground layer. The **source layer** defines the origin for all neutron histories. Especially all height values for starting positions, see also sec. 6.3, are restricted to be initiated here. This layer may neither be the upper- nor lowermost as otherwise neutrons would escape the computational domain. The **ground layer** is used in cosmic neutron simulations to record the spectra at the air/ground interface. In the **detector layer**, which can be superimposed to another layer, either single real or virtual detectors can be placed, or the layer itself acts as a virtual detector and records every neutron passing, see also sec. 6.5.

6.3 | Sources and energy

URANOS provides a variety of sources. A source is defined by a spatial distribution and an energy spectrum from which random values are sampled. They are either defined as

- point sources with all neutrons starting from the same coordinate vector,
- a plane source with all neutrons sharing the same z coordinate within lateral boundaries,
- a volume source, which randomly distributes neutrons in the source layer within lateral boundaries, and alternatively extends the volume source downwards to the ground layer with exponentially distributed height values[e].

As explained in sec. 6.2.2 the source has to be placed in the source layer, which defines its z-position. For the coordinates $(x, y) \in A$ in the source area A in case of plane or volume sources the options are:

- rectangular boundaries with either equal aspect ratio (square) or any other, sampling the origins uniformly from possible positions in (x, y), and
- circular boundaries, sampling the origins either uniformly in radius r from the center or in (x, y).

Furthermore, the starting angle ϑ can be set to:

- full or half sphere, sampling ϑ in $[0 \dots \pi]$ or $[0 \dots \pi/2]$, or
- unidirectional beam, which allows to set theta to a specific inclination. Additionally a divergence s_ϑ can be chosen. Then, the angles are sampled from a gaussian function centered around ϑ with a width of s_ϑ.

The starting energy for the neutrons are derived from normalized distributions, which are described in the following sections. The method of sampling by rejection is applied according to (72) in sec. 5.1. For source definitions on a linear support in $[a, b]$, like in sec. 6.3.2, the random variable $\xi \in [0, 1]$ is scaled to the abscissa test quantity

$$\xi_t = a + (b - a)\xi.$$

For source definitions on a logarithmic support in $[10^a, 10^b]$, like in sec. 6.3.1, ξ is scaled to

$$\xi_t = 10^{a+(b-a)\xi}.$$

[e] This option is called artificial cosmic source and accounts for neutrons which are generated by physical processes URANOS is not capable of simulating like high energy protons, myons or induced cascades thereof.

6.3.1 | THE COSMIC NEUTRON SOURCE

The cosmic neutron source definition is specifically designed for the problem of soil moisture dependent neutron transport in the vicinity of the atmosphere-soil interface. Instead of propagating primary particles through several kilometers of atmosphere, a source definition near the ground level is chosen. Recent works, especially from Sato et al. [66], have provided analytical functions modeling cosmic-ray spectra for various conditions. As such spectra are always integrated over all trajectory angles, based on these models, which are covered in sec. 3.2, a net incoming spectrum has been reconstructed. The procedure and a detailed description can be found in sec. 14.1.1 and the result is used as the generalized cosmic neutron incoming spectrum. Further explanation about the composition and features con be found in sec. 3.1.
Fig. 28 shows the URANOS cosmic-ray neutron spectrum (cyan) and exemplarily the total spectrum above ground for dry conditions. The energy of neutrons can range over more than 12 orders of magnitude. The plot here as well as the following will be presented logarithmically in units of lethargy, see (33) in sec. 1.4.1. The intensity I or flux density per logarithmic unit of energy is given in units of

$$I = \mathrm{d}\Phi/\mathrm{d}(\log(E)) = E\,\mathrm{d}\Phi/\mathrm{d}E. \tag{98}$$

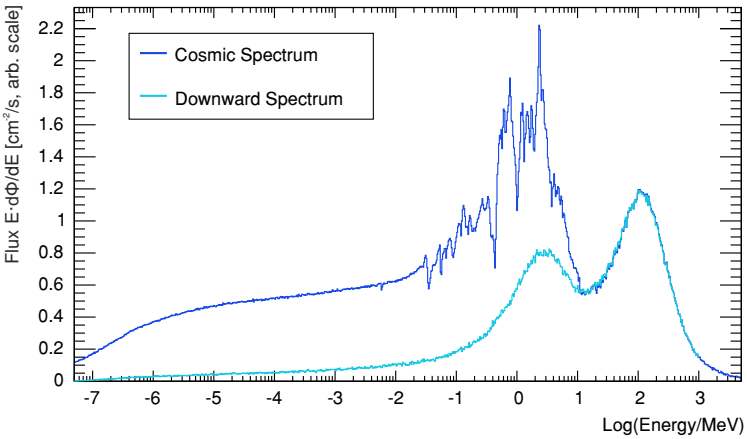

Figure 28: The URANOS Cosmic Neutron Source Spectrum: Total angular integrated flux after interaction with the soil (blue) and only incoming flux (cyan).

6.3.2 | GENERAL SOURCES

Besides the cosmic neutron source definition in sec. 6.3.1, which expands over several decades of energy, energy distributions for specific sources have been implemented. These available source configurations allow sampling from thermal as well as fission spectra. Exemplarily some are shown in Fig. 29.

- **Monoenergetic**: neutrons of energy E or wavelength λ,
- **Thermal**: neutrons at a temperature T described by a Maxwellian distribution

$$N(E) = \frac{E}{(k_B T)^2} \exp\left(-\frac{E}{k_B T}\right). \tag{99}$$

- **Predefined**: americium-beryllium spectrum from [149],
- **Evaporation**: assuming the nucleus to form a degenerate Fermi gas [150] one can derive various forms of density distributions

$$N(E) \propto E \exp\left(-\frac{E}{k_B T}\right), \tag{100}$$

which are simply described by a temperature parameter [151]. Therefore, the energy distribution of the neutrons released by fission are commonly represented either by a Maxwellian distribution or the following Watt spectrum [152].

- **Fission**: A semi-empirical description is the Watt spectrum [153], especially used for ^{235}U, which can be selected as a source although the isotope itself is not implemented,

$$N(E) = 0.4865 \sinh\left(\sqrt{2E}\right) \exp(-E), \tag{101}$$

and for ^{252}Cf [154]

$$N(E) = \sinh\left(\sqrt{2E}\right) \exp(-0.88E), \tag{102}$$

which are both specific cases of the more general form of a Maxwellian distribution[f], which allows a more accurate modeling by introducing the Watt parameters a and b taking into account the mean neutron kinetic energy of and those of the fission fragments:

$$N(E) = 2 \frac{\exp\left(-\frac{ab}{4}\right)}{\sqrt{\pi a^3 b}} \sinh\left(\sqrt{bE}\right) \exp\left(-\frac{E}{a}\right). \tag{103}$$

The parameters a, b are typically tabulated as a function of energy, element and isotope.

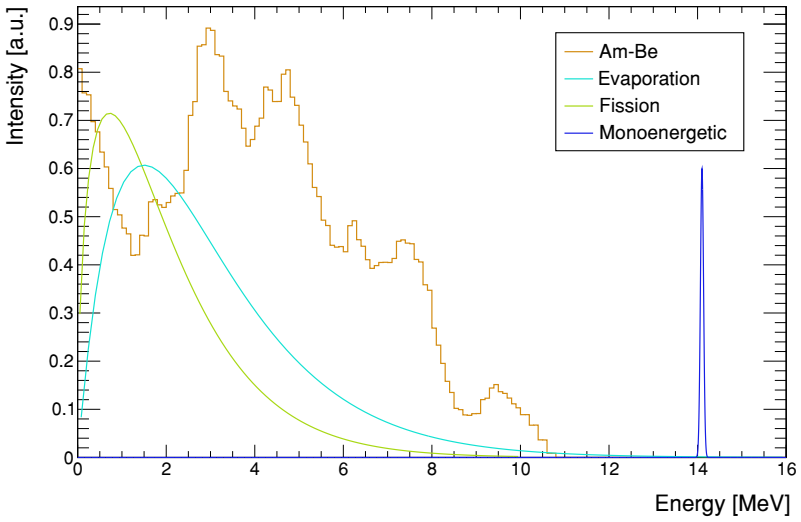

Figure 29: Different preconfigured source distribution functions in URANOS in the MeV range covering different use cases: laboratory test sources like americium-beryllium (yellow) with a variety of resonances, spontaneous fission (green), evaporation (cyan) from de-excitation and fusion (blue)

6.4 | Calculation Scheme

6.4.1 | Loop Nodes

URANOS runs in the main calculation routine on two loops, these are

$$\text{Neutron Stack} \rightarrow \text{Layer Stack}$$

whereas both are used differently - each onset neutron is a placeholder and only initialized at runtime. Furthermore, the particle number is not conserved due to physical

[f] Although several earlier reports before [153] mention this formula, none of them states the origin.

processes generating neutrons, which are lined up in the stack. The layer stack is created at startup and consists of a fixed amount of elements which are traversed by an iterator either forwards or backwards, depending on the direction vector. The possible initial conditions for neutrons are

- energy: available source definitions from sec. 6.3, which can be either real values, normalized functions to be sampled from or lookup tables.
- geometry: definition from sec. 6.2.2, which can be either a fixed vector from a source, a distribution function to be sampled from or lookup tables, which are normalized at startup.
- time: either a real value or a function[g] to be sampled from.

Using these initial conditions the loop over the layer stack commences. Each layer, which is geometrically described in sec. 6.2.2, can either consist of a homogeneous material defined by its isotope composition, a material defined by an analytical function or an input matrix from which voxels are extruded. A comprehensive material list is provided in appendix B.2.3. The neutron iterates to the following layer if it geometrically leaves the boundaries and no change of materials can be found in the collision detection. Otherwise the layer iterator keeps its value and if the neutron has not been absorbed, the calculation procedure is repeated with an updated history.

6.4.2 | Tracking in finite geometry regions

For each layer the material setup is loaded according to the actual spatial position of the neutron. The definition either accounts integrally for the whole layer or for regions, which can be described by analytic functions or voxelwise. For the selected material the total macroscopic cross section Σ_t is composed isotope by isotope. The amount and type of reactions (MT identifiers), loaded according to sec. 5.1.4.2, depends on the element, see also the description in sec. 6.2.1 or the isotope list in appendix B.2.2. Elemental hydrogen for example cannot undergo inelastic scattering and ^{10}B exhibits a negligible radiative capture, so only charged reaction paths are relevant. The selection criteria in detail are

- elastic and absorption cross sections are always calculated if available.
- inelastic cross sections are loaded for energies 750 keV $< E <$ 50 MeV.

Using the macroscopic cross section Σ_t defined by (14) the free path length l is sampled from a random number ξ as described in sec. 5.1.2 from (78):

$$l = -\frac{\ln(\xi)}{\Sigma_t}. \tag{104}$$

In case the material definition contains a density multiplication factor, it is applied to Σ_t before evaluating (104). The distance to the border l_{trj} is calculated by the z-coordinate of the last interaction of the neutron z_0 and the layer z-position z_l and height d_l

$$l_{\mathrm{trj}} = \begin{cases} \left|\frac{z_l + d_l - z_0}{\cos(\vartheta)}\right|, & \text{if already scattered within the layer and forward,} \\ \left|\frac{z_0 - z_l}{\cos(\vartheta)}\right|, & \text{if already scattered within the layer and backward,} \\ \left|\frac{d_l}{\cos(\vartheta)}\right|, & \text{otherwise (crossing).} \end{cases} \tag{105}$$

[g] such a function would for example be a phase for the polarization vector in NRSE.

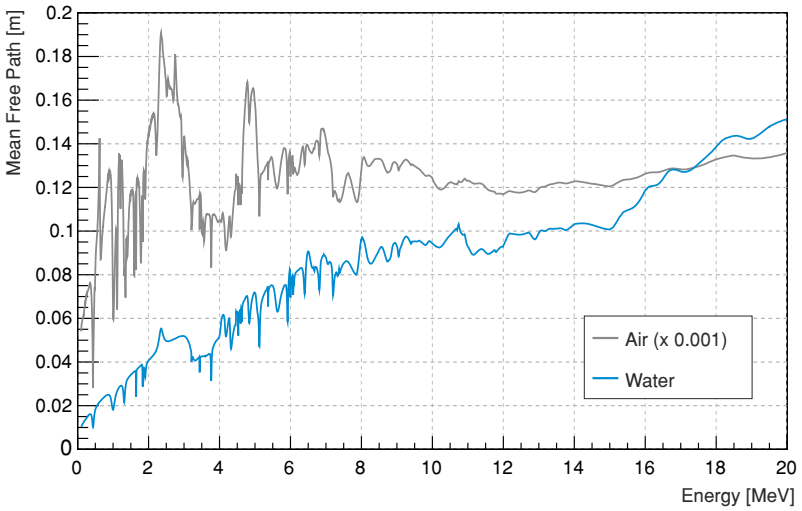

Figure 30: Mean free path $1/\Sigma_t$ for neutrons in the MeV range. The dominant peaks originate from the contribution of the elastic scattering cross section, in dry air (NTP) mainly by nitrogen, in water by oxygen, see also Fig. 31.

In case the material is defined by voxels, additionally a procedure is applied, which samples the trajectory according to the underlying pixel matrix:

- determination of the z-projected length z_m of one lateral unit pixel s_p for the actual direction vector by $z_m = s_p/\tan(\vartheta)$. The unit pixel size is determined by the spatial extension of the domain divided by the number of pixels.
- If the material of the voxel at $\vec{x}'$ for $z_0 \pm z_m$ is different from the actual, stop and repeat the range calculation for the actual composition and geometry. If the material does not change iterate $\pm z_m$ until the end of the layer. The propagation direction, forward or backward, determines $\mathrm{sgn}(z_m)$.

If $l_{\mathrm{trj}} > l$ no interaction takes place and the neutron can proceed to the following layer. If $l_{\mathrm{trj}} < l$ the spatial coordinates of the interaction $\vec{x}_i$ are calculated by

$$\vec{x}_i = \begin{pmatrix} x_0 \\ y_0 \\ z_i \end{pmatrix} + \begin{pmatrix} \cos(\phi)|\tan(\vartheta)(z_i - z0)| \\ \sin(\phi)|\tan(\vartheta)(z_i - z0)| \\ 0 \end{pmatrix}, \tag{106}$$

whereas the new z coordinate is given by

$$z_{\mathrm{i}} = \begin{cases} z_l + \left|\cos(\vartheta) l_{\mathrm{trj}}\right|, & \text{if not scattered within the layer and forward,} \\ z_l + d_l - \left|\cos(\vartheta) l_{\mathrm{trj}}\right|, & \text{if not scattered within the layer and backward,} \\ z_0 + \left|\cos(\vartheta) l_{\mathrm{trj}}\right|, & \text{if scattered within the layer and forward,} \\ z_0 - \left|\cos(\vartheta) l_{\mathrm{trj}}\right|, & \text{if scattered within the layer and backward.} \end{cases} \tag{107}$$

Consecutively the type of reaction is determined by another random number ξ by intervals of the relative fraction of the constituents of the macroscopic cross section:

$$\begin{aligned} \xi &< \frac{\sigma_{\mathrm{el}}}{\sigma} \rightarrow && \text{scattered elastically,} \\ \frac{\sigma_{\mathrm{el}}}{\sigma} < \xi &< \frac{\sigma_{\mathrm{el}} + \sigma_a}{\sigma} \rightarrow && \text{absorbed,} \\ \xi &> \frac{\sigma_{\mathrm{el}} + \sigma_a}{\sigma} \rightarrow && \text{scattered inelastically,} \end{aligned} \tag{108}$$

as the probability of selecting a reaction i from all possible reaction channels is

$$p_i = \frac{\Sigma_i}{\sum_{j=0}^{n} \Sigma_j} = \frac{\Sigma_i}{\Sigma_t}.$$

The target interaction element is determined by a randomly choosing from a proportional lookup table. Each reaction type is accompanied by two `vectors` - one `<double>` represents the cumulative probability distribution v_s and one `<int>` a list of corresponding elements v_e[h]:

$$v_s[n] = \left\{ i \middle| \sum_{j=0}^{i} \Sigma_j \right\}, \tag{109}$$

$$v_e[n] = \{ i | \text{ isotope of } i \}. \tag{110}$$

For inelastic scattering additionally the excited state of the target isotope has to be determined. One vector `vector` of `<double>` like in (110) contains the cumulative cross section distribution and two support `vectors` contain the q-values representing the energy loss in MeV in a `<float>` list and the inelastic angular distributions in a `<TMatrixF>` list.
The individual contributor, which will be used to determine the reaction target, is chosen by a random number ξ. If

$$v_s[i] \leq \xi \leq v_s[i+1], \ \forall i > 0, \tag{111}$$

then the corresponding isotope is taken from $v_e[i]$[i].

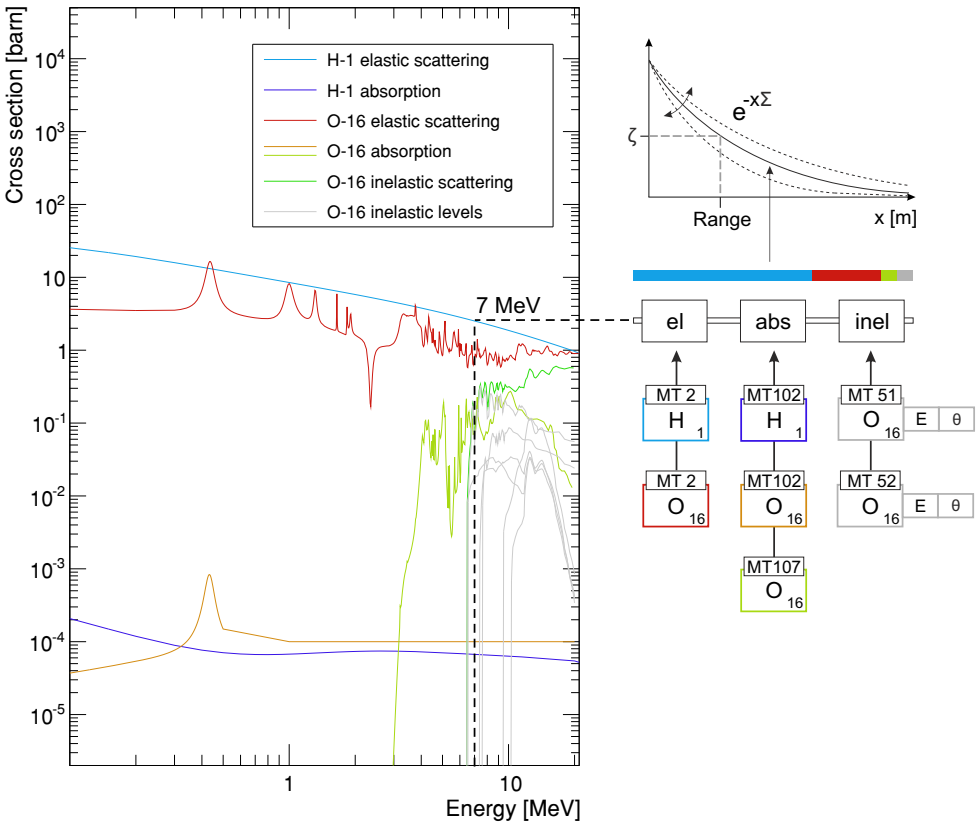

Figure 31: Range calculation in URANOS: For a given neutron energy, here in the MeV range, the cross sections from the isotope list are evaluated according to elastic, inelastic and absorption processes. Only possibly relevant ENDF [97] cards are evaluated. The left panel shows such a list of reaction probabilities for water. Inelastic levels are only displayed up to MT56 and are link additionally to energy loss and angular distribution. The cumulated cross section multiplied by the atom number density (14) yields the macroscopic cross section (10). By sampling a random number ξ as in (78), a free path length value for the range (77) is obtained.

[h] Example: Natural boron, see also tab. 8, contains ≈ 80 % ^{11}B and ≈ 20 % ^{10}B. For a reaction the cross section $\Sigma_i = \Sigma_i(^{10}\text{B}) + \Sigma_i(^{11}\text{B})$ is accompanied by a `vector` of individual contributions $[\Sigma_i(0), \Sigma_i(0) + \Sigma_i(1)]$ and a `vector` of isotopes [^{10}B,^{11}B].

[i] If $i = 0$, then $\xi \leq v_s[1]$.

6.4.3 | Interaction channels

For each interaction the following quantities are updated:

- the position vector $\vec{x}$, including time, by adding the path length l to the last position,
- the direction vector $\vec{r}$,
- energy, including velocity v and wavelength λ.

6.4.3.1 Elastic and inelastic scattering

Scattering is described by the collision of a neutron with a nucleus of mass A assuming energy and momentum conservation according to (23), (24) and (25) of sec. 1.4.1. The problem has a radial symmetry regarding the impact parameter, therefore only one angle ϑ_{CMS} has to be calculated. The second angle can be determined by a random number ξ in $[0, 1)$

$$\phi_{\mathrm{cm}} = \pi\,(2\xi - 1)\,. \tag{112}$$

For inelastic scattering the energy loss is substituted by the q-value obtained from (111) and (110), respectively. The target velocity V can be neglected for kinetic energies E of the neutron:

$$V \approx 0 \text{ if } \begin{cases} 0.11\,\mathrm{eV} < E < 1\,\mathrm{MeV} & \text{in case of hydrogen,} \\ 0.15\,\mathrm{eV} < E < 0.01\,\mathrm{MeV} & \text{otherwise.} \end{cases} \tag{113}$$

For **lower energies** the interaction result has to be calculated by laws of thermal scattering taking into account the velocity distribution of the target material. In case of amorphous material or fluids there is no analytical form to describe such, therefore only sampling from an effective thermal spectrum like (99) is carried out. For solids with a crystal lattice Bragg scattering is the dominant channel. The kinetic theory of gases allows a cohesive description of the scattering process. For such the energy and angle are sampled according to (90), (91) and (92) in sec. 5.1.3.

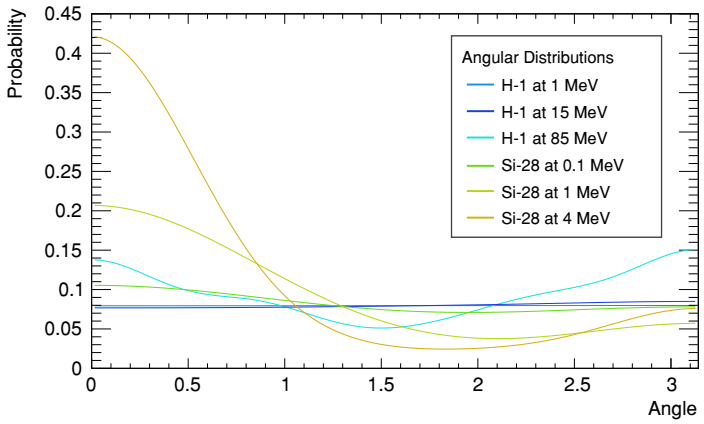

Figure 32: Energy dependent representation of angular distributions in the center of mass frame for two isotopes. Above 20 MeV for hydrogen there are 12 and below 6 Legendre coefficients. For silicon 7,9 and 13 coefficients are given for the stated energies in ascending order.

In case of **higher energies** than stated in the above limits the angular distribution in the center of mass frame can be found in ENDF cards either tabulated or described by Legendre polynomials. Depending on the energy for the interaction a set of (interpolated) factors is compiled according to (93). Exemplarily Fig. 32 shows such distributions. With increasing energy the forward direction is preferred, except for

hydrogen - here the asymmetry is much weaker than for heavy elements and only for very high energies a significant deviation from an even distribution can be observed.

For inelastic scattering with an energy transfer E^* the evaluation of the angular distributions is carried out likewise, whereas the lowest energy, for which the reaction can occur, is given by the q-value. Hence, the reaction kinematics of inelastic processes share some similarities with elastic processes of corresponding kinetic energies $E' = E - E^*$.

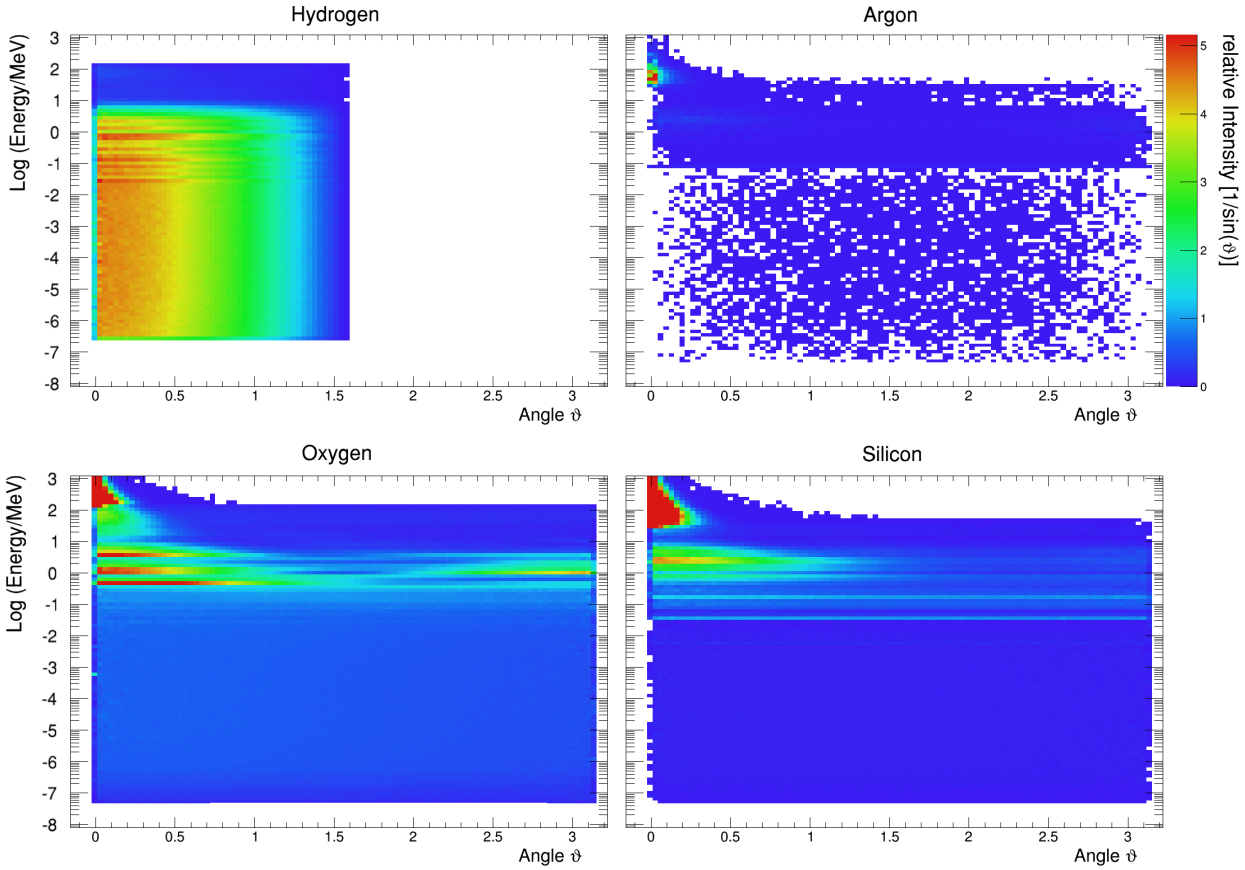

Figure 33: Relative occurrence of scattering angles in an air-ground interface for selected isotopes. The distributions in spherical coordinates are weighted by $\sin^{-1}$ of the scattering angle for the projection onto the theta axis, see also (91). Due to the neutron having approximately the same mass as the proton in collisions with hydrogen atoms (top left) backward facing angles are not allowed as far as the relative velocity of the target is not considered (thermal cutoff). As the plots show in-situ distributions the dominant features in the MeV region for hydrogen originate from the relative abundance in the corresponding energy range by collisions with other elements, see also Fig. 28 and 31. For oxygen (bottom left) the angular sampling up to 150 MeV is carried out via Legendre polynomials, see for example Fig. 32, and above via tabulated distributions. For other elements like silicon (bottom right) the Legendre representation is typically only available up to 20 MeV.

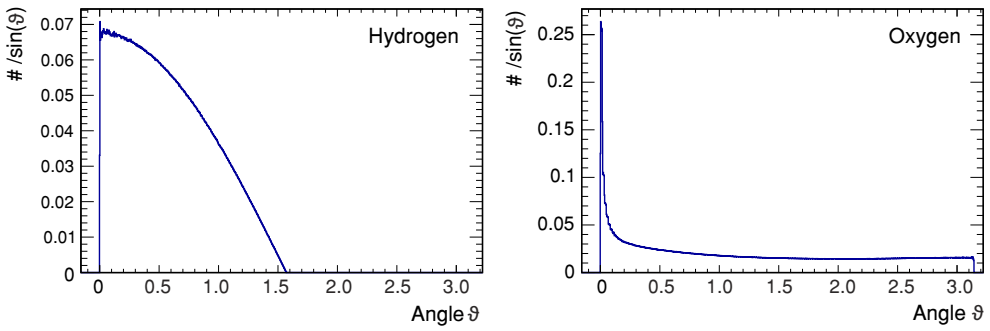

Figure 34: Projection of the weighted scattering angles of the in-situ calculations of Fig. 33 for all energies, exemplarily for H and O.

As the scattering kinematics have been calculated in the center of mass system, a transformation to the laboratory system is carried out via

$$\vartheta_\mathrm{l} = \arccos\left(\frac{1 + A\cos\left(\vartheta_\mathrm{cm}\right)}{\sqrt{A^2 + 1 + 2A\cos\left(\vartheta_\mathrm{cm}\right)}}\right), \tag{114}$$

and added to the existing direction vectors

$$\vartheta_u = \cos\left(\vartheta^\mathrm{old}\right)\cos\left(\vartheta_\mathrm{cm}\right) + \sin\left(\vartheta^\mathrm{old}\right)\sin\left(\vartheta_\mathrm{cm}\right)\cos\left(\pi + \phi_\mathrm{cm}\right), \tag{115}$$

$$\vartheta_l^\mathrm{new} = \arccos\left(\vartheta_u\right), \tag{116}$$

$$\phi^\mathrm{new} = \phi^\mathrm{old} \pm \arccos\left(\frac{\cos\left(\vartheta_\mathrm{cm}\right) - \cos\left(\vartheta^\mathrm{old}\right)\vartheta_u}{\sin\left(\vartheta^\mathrm{old}\right)\sin\left(\vartheta_\mathrm{cm}\right)}\right). \tag{117}$$

Due to the choice of the coordinate system, see also the geometry definition (97), adding direction vectors is less convenient than the otherwise direct and intuitive declaration. The method presented here equals an Euler[j] rotation in θ and ϕ around the direction axis given by the trajectory of the particle.

6.4.3.2 Evaporation

URANOS simplifies the calculation of the evaporation process as in the low-Z and intermediate energy range most otherwise for fissionable elements discussed quantities are approximately invariable. The mean number of evaporated neutrons can be considered constant $\overline{n}_\mathrm{evap} \approx 1$ for projectile energies below several hundred MeV and mass numbers of $A < 100$ [155]. Furthermore, for the emission energy a Maxwellian spectrum according to (100) with a mean neutron energy of 1.8 MeV [156] and a flat angular distribution [157] is assumed[k].

6.4.3.3 Absorption

The neutron is either absorbed by a non-radiating process and consequently the calculation is terminated or the material is a specific absorber, which leads to a scoring by the detection unit, see the following sec. 6.5.

A specific case is the High Energy Cascade: URANOS mainly carries out neutron interactions. For the generation of high energetic radiation in the atmosphere charged particles are also largely contributing to the production of the neutron component [158]. As far as for low energetic and albedo neutrons such can be neglected, in order to simulate more than 100 m of atmosphere the generation of the primary spectrum is emulated by an effective model: For any absorption occurring above 16 MeV leading to otherwise the generation of new particles the neutron is not eliminated if a random number ξ is below a specific value k_HE, receiving only a fractional energy loss and angular deviation. This value k_HE is tuned to emulate an effective atmospheric attenuation length L_prim of the primary spectrum component of 145 cm^2/g[l].

[j] Leonhard Euler, *1707-†1783, Old Swiss Confederacy.
[k] In order to provide upper limits in comparison: ^{235}U produces on average $\approx 2.4 + E/\mathrm{MeV}$ neutrons per fission.
[l] Experimental values for L_prim are in the range of (135-155) cm^2/g, depending on the site. Here, the value from [66] is taken.

6.5 | Detector configurations

Scoring options are evaluated in the detector layer. For a spatially resolved detector this is the readout structure. For CRNS there are furthermore the following possibilities:

- scoring the coordinates of a neutron passing the upper/lower boundary or the full track within the layer,
- scoring if a neutron track intersects a predefined volume entity, called a detector, and
- scoring for any voxel, which has the material definition to be a 'detector'.

6.5.1 | Scoring options for CRNS

In the most simple case a uniform detection efficiency ϵ can be chosen for a specific range of energies, which is a useful configuration for CRNS detectors

$$\epsilon = \begin{cases} 1 & \text{for } E_{\min} < E < E_{\max}, \\ 0 & \text{otherwise.} \end{cases} \tag{118}$$

In order to not model a whole cosmic-ray neutron sensing system in a large environment, the detector has been modeled independently and integrated as an effective model. Fig. 35 shows the implemented functions, which represent averaged values for the whole unit. In this work cubic spline interpolation is used for describing the absolute efficiency and the angular dependence is modeled by

$$\epsilon_\vartheta = 1.24 - 0.254 \exp\left(\frac{x}{0.92}\right). \tag{119}$$

As far as thermal neutrons are not considered, the flux in the epithermal/fast region, see also sec. 3.2, can be considered a plateau region, justifying the established choice of (118), see also sec. 13. The options above can be applied to the whole detector layer.

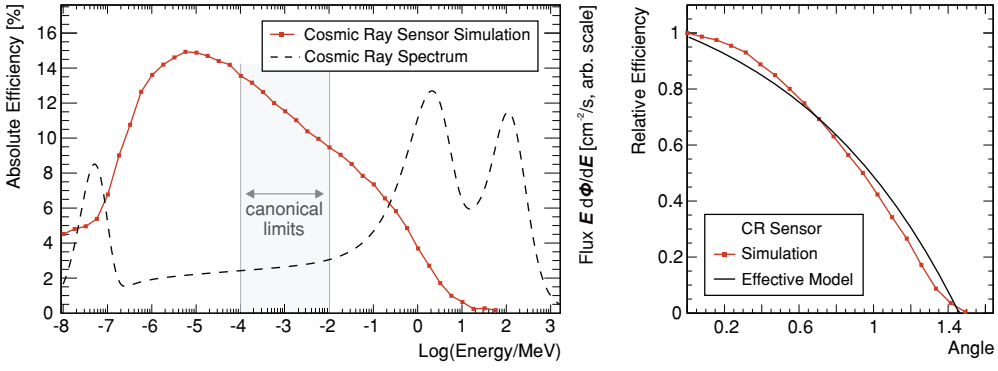

Figure 35: . Detection efficiencies for CRNS detector models. (left) Energy dependent absorption probability for perpendicular irradiation, here: simulation of a monoenergetic beam with results (red markers) averaged over the surface. (right) Energy independent, averaged, angular dependence relative to the left panel.

This allows mainly scoring the upward and downward directed flux. If for example angular resolution is required one can place two types of scoring units within the detector layer, which is either

- a plane in z-direction, a sphere or a vertical cylinder,

whereas in both cases the radius can be specified[m]. The geometrical calculation can be found in the appendix B.2.1 in (191) and (189), respectively.

[m] The cylinder height corresponds to the detector layer. If due to positioning or the choice of the radius of the sphere there is an intersection with the layer boundary only the volume inside the detector layer is taken into account.

Whereas in gaseous converters like ^{3}He regarding the detection efficiency only the macroscopic cross section has to be taken into account, as nearly all converted neutrons can be detected, for hybrid solid state detectors the entire signal generation path has to be considered. Compared to the attenuation length at $\lambda = 1.8\,\text{Å}$ of 20 µm the range within a converter layer is $< 4\,\mu\text{m}$. Even for thin layers therefore the efficiency can be significantly reduced by inactive material. The two main absorption reactions in boron-10 are:

$$\begin{aligned} {}^{10}\text{B} + \text{n} \rightarrow {}^{7}\text{Li}(0.84\,\text{MeV}) + \alpha(1.472\,\text{MeV}) + \gamma(0.48\,\text{MeV}) \quad & (93.6\,\%)[a], \\ {}^{7}\text{Li}(1.013\,\text{MeV}) + \alpha(1.776\,\text{MeV}) \quad & (6.4\,\%)[b]. \end{aligned} \tag{120}$$

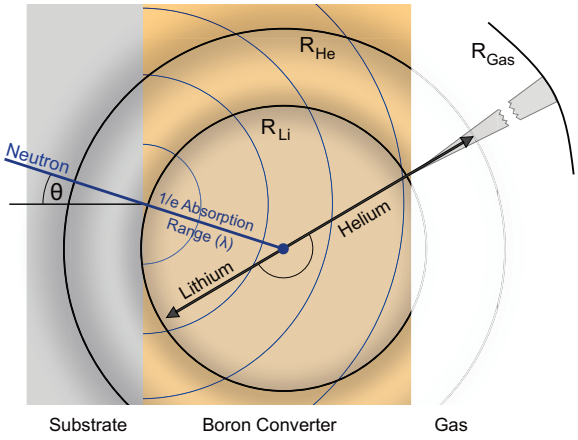

Figure 36: Physics of a hybrid boron converter layer: a neutron impinges at an angle ϑ normal to the surface. The absorption probability is wavelength dependent. By the conversion process lithium (Li) and helium (He) ions with fixed energies are created. In the medium itself they lose energy by collisions leading to a Bragg distributed range R, different for both agents. After reaching the gas an ionization track is produced with the remaining energy at the boundary. [K2016]

In the boron medium itself the particles are emitted isotropically and back to back. Two geometries are possible: (1) the front side irradiation describes the case of the active surface being oriented towards the incoming neutrons and therefore the detection medium being situated prior in beam direction. (2) Vice versa the backside irradiation refers to the inverted geometry. Therefore, as only one of both can enter the gas, a random number ξ_1 determines[n] the type of ion I and another random number ξ_2 assigns the decay branch ([a] or [b]). Two more random numbers ξ_2, ξ_4 determine the emission angles

$$\vartheta_I = 0.5\pi\xi_3, \tag{121}$$

$$\phi_I = \pi(2\xi_4 - 1). \tag{122}$$

The remaining distance to the layer border d_S can then be calculated either upwards or downwards. The fragments lose kinetic energy mainly by ionization. These energy-range-relations have been calculated by SRIM [159] and transferred to analytical models. For boron carbide the energy loss in the medium can be described as

$$\begin{aligned} \text{Li}^{+++}\text{:}\ (E_0 = 1.013\,\text{MeV})\ E_{\text{out}} &= E_0 - (-0.209 d_S^2 + 0.924 d_S), \\ (E_0 = 0.840\,\text{MeV})\ E_{\text{out}} &= E_0 - (-0.2195 d_S^2 + 0.8574 d_S), \\ \text{He}^{++}\text{:}\ (E_0 = 1.776\,\text{MeV})\ E_{\text{out}} &= E_0 - (-0.0165 d_S^3 + 0.1003 d_S^2 + 0.289 d_S), \\ (E_0 = 1.472\,\text{MeV})\ E_{\text{out}} &= E_0 - (-0.0285 d_S^3 + 0.1267 d_S^2 + 0.3354 d_S), \end{aligned} \tag{123}$$

[n] All random numbers here are assumed to cover a range within $[0, 1)$, hence the rule for the ion choice is $\xi_1 < 0.5$.

and for boron

$$\begin{aligned}
\mathrm{Li}^{+++}\colon (E_0 = 1.013\,\mathrm{MeV})\ E_{\mathrm{out}} &= E_0 - (-0.019 d_S^3 - 0.1166 d_S^2 + 0.8065 d_S), \\
(E_0 = 0.840\,\mathrm{MeV})\ E_{\mathrm{out}} &= E_0 - (-0.1863 d_S^2 + 0.7891 d_S), \\
\mathrm{He}^{++}\colon (E_0 = 1.776\,\mathrm{MeV})\ E_{\mathrm{out}} &= E_0 - (-0.0069 d_S^4 + 0.047 d_S^3 - 0.0732 d_S^2 + 0.3998 d_S), \\
(E_0 = 1.472\,\mathrm{MeV})\ E_{\mathrm{out}} &= E_0 - (-0.0115 d_S^4 + 0.0581 d_S^3 - 0.0634 d_S^2 + 0.4189 d_S).
\end{aligned} \tag{124}$$

These models are independent of the isotope ratio of ^{10}B and ^{11}B as only electromagnetic interactions contribute, the nuclear charge number and the ionization level. The average maximum ranges are from (1.69-1.90) µm for lithium to (3.27-4.05) µm for helium ions in the branches [a] and [b] of (120) with a straggling variation in the order of $\sigma \approx 5\,\%$, which are reflected by an additional relative smearing of the track length by a gaussian random number corresponding to an equal spread. Fig. 37 shows in the left panel the energy-range-relation of the conversion products, which are depicted in Fig. 36 as spheres.
The ions enter the gas volume with a broad spectrum of energies. Here, first the maximum range $d_{g,\mathrm{max}}$ in the medium has to be calculated. For Ar:CO_2 the following descriptions are used, which are also exemplarily displayed in the right panel of Fig. 37:

$$\begin{aligned}
\mathrm{Li}^{+++}\colon d_{g,\mathrm{max}} &= -6.6034 E_{\mathrm{out}}^4 + 18.215 E_{\mathrm{out}}^3 - 18.783 E_{\mathrm{out}}^2 + 11.732 E_{\mathrm{out}}, \\
\mathrm{He}^{++}\colon d_{g,\mathrm{max}} &= 4.7579 E_{\mathrm{out}}^5 - 20.64 E_{\mathrm{out}}^4 + 33.888 E_{\mathrm{out}}^3 - 25.727 E_{\mathrm{out}}^2 + 13.216 E_{\mathrm{out}},
\end{aligned} \tag{125}$$

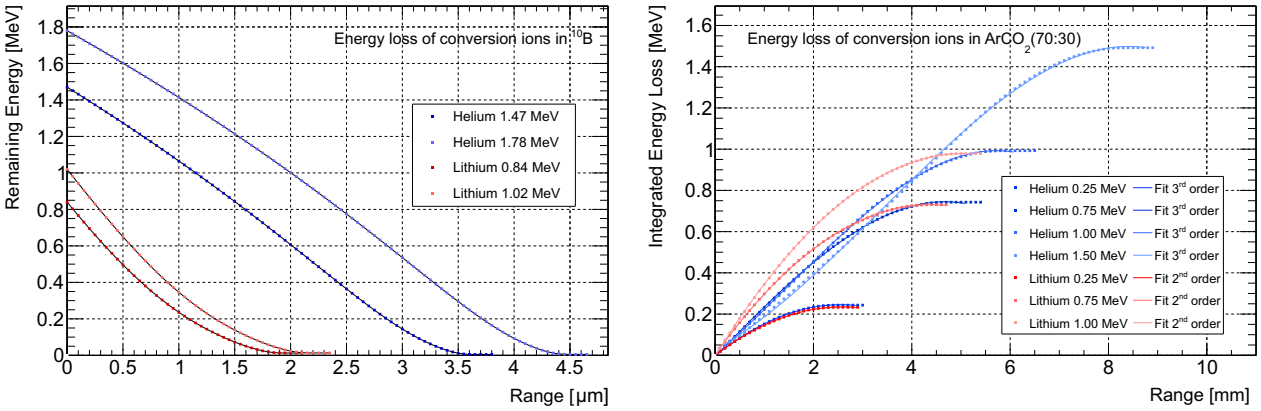

Figure 37: Calculated energy loss of helium and lithium ions from boron conversion. (Left) Energy-range relation shown for solid ^{10}B and a density of $13.05 \cdot 10^{22}$ atoms/cm^3 with 4$^{\mathrm{th}}$ order (helium) and 3$^{\mathrm{rd}}$ order (lithium) polynomial fit functions. (Right) After leaving the conversion layer the energy spectrum of the ions is continuous, an exemplary set of energy-range relations in Ar:CO_2 with 3$^{\mathrm{rd}}$ order (helium) and 2$^{\mathrm{nd}}$ order (lithium) polynomial functions are shown.

After determining the ionization track length the available distance to the next layer has to be calculated. Here it has to be taken into account that a grid of thickness h_{Grid} is inserted, which has an optical transparency $T^{[o]}$. Therefore, the track can pass the grid in case of

$$\xi < 0.5\sqrt{T}\left(1 - \frac{\tan(\vartheta_I)}{\sqrt{T}}\right). \tag{126}$$

If the ionization track length is longer than the available space, the track is cut in length and in its energy deposition, otherwise both is scored unaffectedly. The result is an

[o] In general optical transparency does not equal zero-diffusion flux transparency, yet, this is the case for typical mesh geometries (thickness ≈ 50 µm and ≈ 100 µm pitch) and reasonably high drift fields in the order of 1 kV/cm in Ar:CO_2. [160]

ionization tracklet s_I. If no spatial resolution information is necessary, the simulation stops and calculates the geometric mean x and y values from the projected track. These are handed over to the $n \times n$ readout matrix of a detector with n pixels and a pixel pitch of d_p.

For determining signals of a spatially resolved system it is necessary to not only know the geometry of track but also the ionization distribution $\mathrm{d}E/\mathrm{d}x$. Each of the nuclear fragments released by the absorption process exhibit a different behavior. Whereas helium ions entering the gas with energies of MeV and more still sit on the plateau regime of the Bethe-Bloch equation (41), lithium ions already start on the descending branch of the Bragg peak. Fig. 38 shows the ionization density in the Ar:CO_2 detector gas. In order to yield the correct energy distribution in the gas the energy loss in the boron layer has to be subtracted from the initial value, which corresponds to shifting the curves to the left. The energy loss calculated by SRIM has been fitted by polynomials

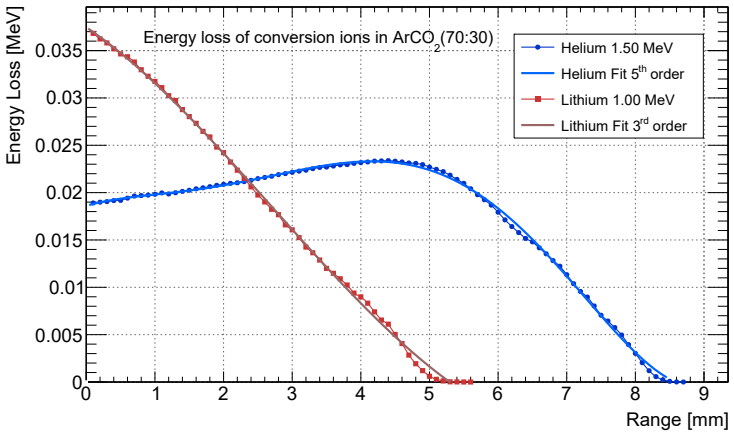

Figure 38: Energy loss per 0.1 mm in the counting gas for both conversion ions. The initial energy is chosen to be just above the maximum q value of the production channels of (120).

along the track, which is carried out as a onedimensional projection with straggling being neglected here. The following functions describe the ionization density:

$$\begin{aligned} \mathrm{Li}^{+++}\colon\ \mathrm{d}E/\mathrm{d}x &= 0.000145x^3 - 0.001185x^2 - 0.004865x + 0.037458, \\ \mathrm{He}^{++}\colon\ \mathrm{d}E/\mathrm{d}x &= 0.0000079x^5 - 0.0001455x^4 + 0.0007924x^3 \\ &\quad - 0.0015872x^2 + 0.0021239x + 0.018607. \end{aligned} \tag{127}$$

Yet, the readout of the CASCADE detector, see also sec. 9.3.2, has its own specificity. The main printed circuit board features a crossed stripes design, not independent pixels, and each pixel is comprised of an interwoven comb structure with an x- and a y-component, see also the left panel of Fig. 40. Therefore, the actual energy distribution on the individual strips for the resulting event topology has to be simulated on exactly such a structure. The same principle is used as described in sec. 6.2.2. A boolean ASCII matrix $M(x_M, y_M)^{[\mathrm{p}]}$, represented in the right panel of Fig. 40 by a monochromatic image, derived from the actual copper layer of the readout board, is used to project the track onto. The following steps are performed:

- randomizing the start coordinates of the track (x_t^S, y_t^S) within the innermost four detector pixels according to the metric (length per pixel),

$$x_t^S = (2\xi_1 - 1)d_p, \qquad y_t^S = (2\xi_2 - 1)d_p, \tag{128}$$

[p] Representing not the entire readout but only a cutout large enough to contain a single track. These are 12×12 pixels of the detector at 400×400 image pixels.

- projecting the track (s_I with ϑ_I and ϕ_I) onto the pixel matrix M by a straight line with end coordinates (x_t^E, y_t^E),

$$x_t^E = \sin(\phi_I)\sin(\vartheta_I), |s_I| \qquad y_t^E = \cos(\phi_I)\sin(\vartheta_I)|s_I|, \tag{129}$$

- determining for every pixel in the matrix the distance to the track d_t by taking the smaller value of either the orthogonal distance to the line or the distance to its end points,
- simulating transverse charge spreading (diffusion) by assigning a relative (charge) deposit value for this image pixel $p_i = (x_M, y_M)$. Each is weighted by a gaussian function $G_{p_i}(d_t, s_t)$ with an abscissa offset of d_t for the distance to the track and a width s_t representing the average track smearing width.
- Dividing the total energy deposition of the ion track in the gas by the sum of the total relative deposits on the matrix and multiplying each pixel by this factor,
- summing up all energy deposits for each strip, separately for the x- and a y-component of the readout and
- subtracting a threshold value from each strip.

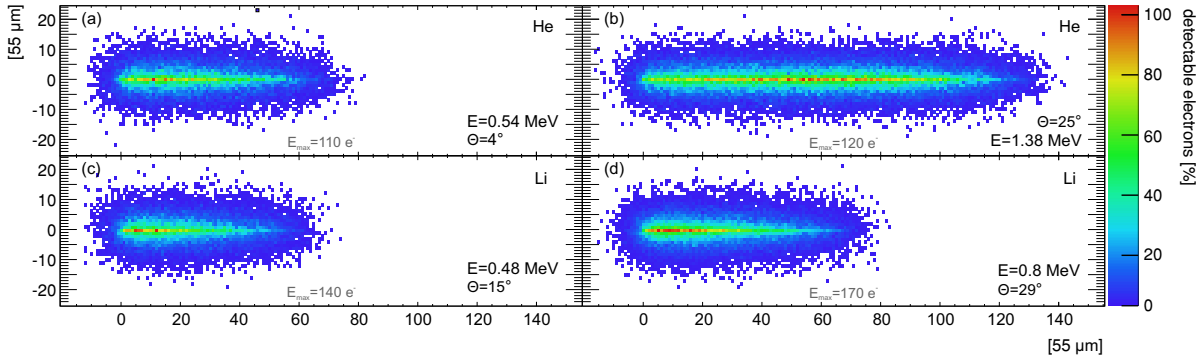

Figure 39: Simulation of four examples of helium (top) and lithium (bottom) tracks for a drift distance of 40 mm, without obstacles, a drift speed of 10 µm/ns and a longitudinal/transverse drift constant of 0.15 mm/$\sqrt{\text{cm}}$. The binning is chosen in units of the smaller TimePix [161] pixel units.

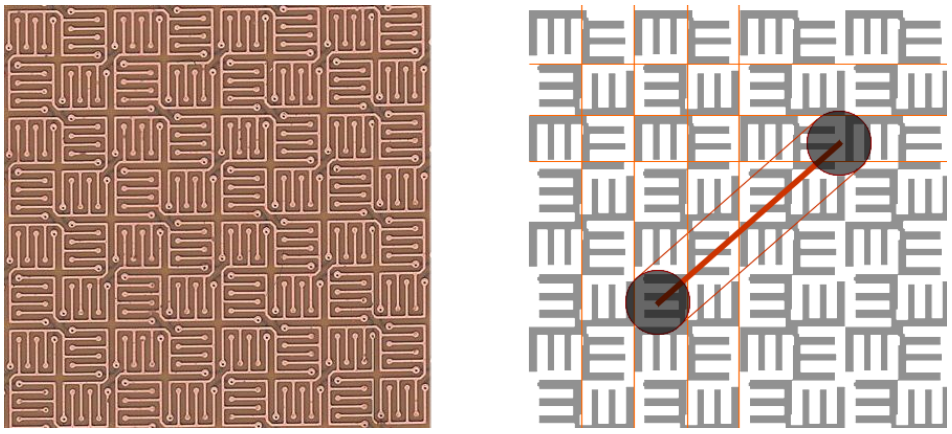

Figure 40: The readout in a cutout of 8 × 8 pixels: (Left) The actual PCB, (Right) Illustration of the track projection simulation with the monochromatic input readout matrix. Orange lines mark the pixel borders. Each pixel has an x- and a y−component in white and black, respectively. A track track with its outlines symbolizing diffusion deposits the total charge according to the pixels hit.

The relative charge deposit on each image pixel p_i represents the weighted energy density deposited on the readout, as especially for crossed strips only the integrated charge along each channel plays a role. This means that in the case of the CASCADE detector the signal display is composed of two linear spatial and one time data set. In order to visualize the charge distribution, in Fig. 39 a pixelated readout has been assumed and the electron distribution is discretized. The exemplarily chosen energies

at rather slant angles visualize the spatial spread of the charge density shown in Fig. 38 for a maximum (free) drift distance of 40 mm. At the beginning and the end of the ionization tracklet the charge is effectively distributed in two dimensions, whereas in the center the distribution can be considered as only being relevant orthogonal to the main axis.

This leads to the following effects:

- the effective width of the tracklet depends on the energy loss along its axis, therefore the tail is slightly more 'pointy'-shaped than the origin, which renders a simple geometric description impossible,
- the origin is not located at the coordinate of highest $\mathrm{d}E/\mathrm{d}x$ even if in the case of lithium the track has its highest ionization density at the beginning. The reason is that the diffusion leads to a relatively stronger smearing out at the ends of the track. Therefore, the origin is not directly correlated to the highest measured $\mathrm{d}E/\mathrm{d}x$.

In summary the schematic Fig. 41 describes the steps specific for calculating the geometry and the readout in the CASCADE detector in a unit-cell like picture. A track is generated from a neutron conversion inside the boron. Its length is calculated analytically by the energy loss in the converter and subsequently in the gas. Due to the narrow drift spaces of the layer geometry a track can be limited in its extension by the subsequent grid or GEM. Finally the track broadened by the diffusion in the gas is projected onto the readout with discrete spacing (pixel) and time (clock cycles) units.

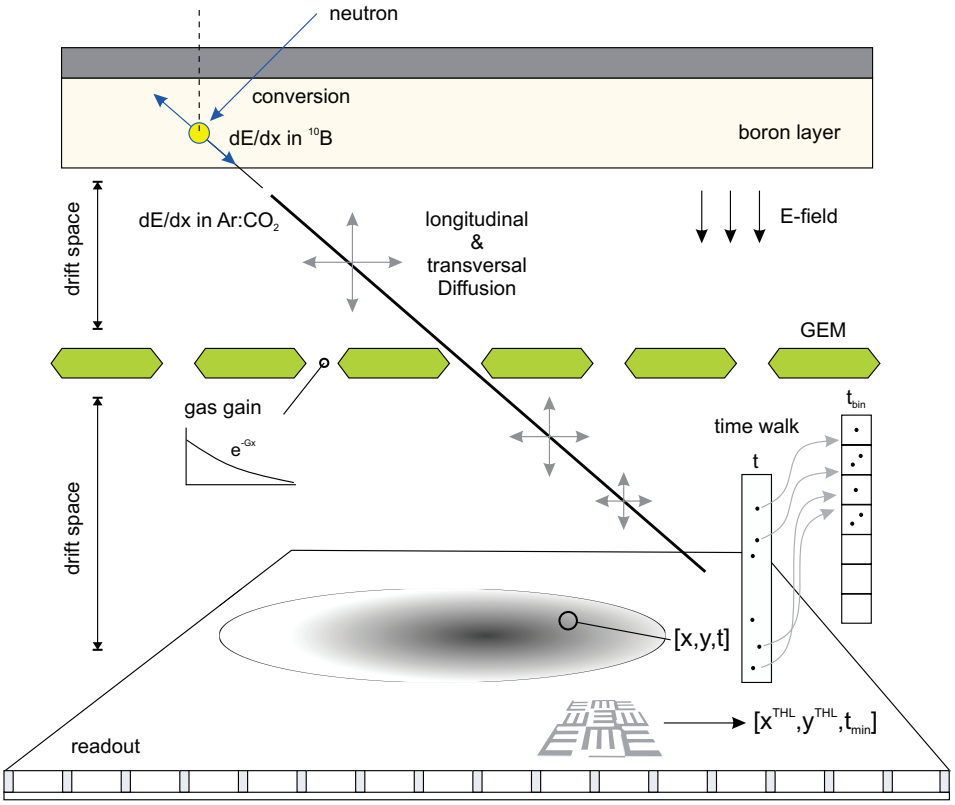

Figure 41: Elements of the CASCADE detector in URANOS from the particle simulation to the signal generation with focus on the description of the charged particle track inside the gaseous volume.

6.6 | BASIC PERFORMANCE EXAMPLES

In order to visualize the tracking capabilities of URANOS Fig. 42 shows two non-trivial neutrons paths from generation until absorption, exemplarily in air (left) and in the ground (right). It already acts as a demonstrator for the interactions at this specific interface. In air the main scattering partners are nitrogen and oxygen, which leads to a large amount of scatterings with small energy decrements. By the long path lengths in the thin medium the neutron also can acquire hundreds of meters of integrated travel distance. Inside the soil typical scattering lengths are far below one meter. For high energy neutrons, the main scattering partners can be silicon, aluminum and oxygen. However, due to the presence of water a few interactions with light nuclei can thermalize a neutron (blue lines). Then it will carry out a random walk which will be dominated by hydrogen scattering.

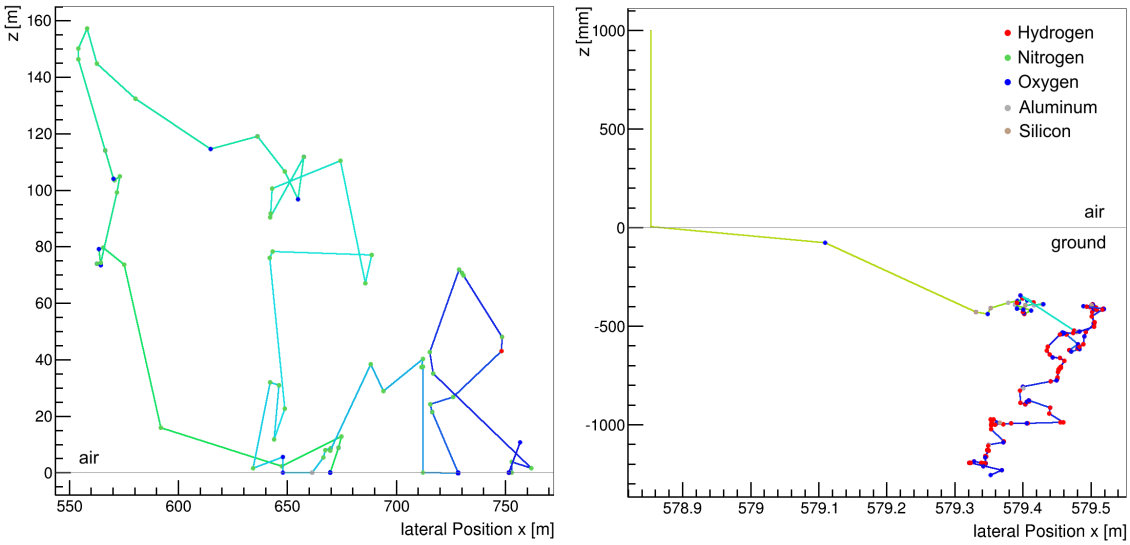

Figure 42: Projection of track calculations in an air ground interface. The simulated neutrons, which are artificially released from 1 m above the soil, are rainbow-colored according to the logarithm of the corresponding energy scaling from 10 MeV (red) to thermal (blue). Left: a neutron which mainly scatters in the air. Right: a neutron thermalizing inside the soil. To be noted: both x- and y-axes are not scaled equally.

6.6.1 | DIFFUSION LENGTH IN WATER

The attenuation of fast neutrons by efficient moderators is a basic example of neutron physics and the main source of thermal neutrons. Modeling the slowing down process properly requires the correct description of interaction lengths, energy loss and geometric transport. Therefore, it can be regarded as validation test of the Monte Carlo code. In public literature sources a few examples of well controlled and simple measurements can be found. CASWELL, GABBARD, PADGETT, and DOERING [162] describe an experiment of determining the radial distribution of neutrons in a water tank from 14.1 MeV to thermal energies and 1.46 eV. A deuterium beam is delivered by an aluminum tube onto a tritium target inducing fusion. The tank measures 2.4 m in length and 1.2 m in height, whereas the particle injector is located at a distance of 0.6 m from one wall and vertically centered. The flux is measured pointwise by indium foil activation, which provides data for the non-equilibrium state above 1 eV, and thermal neutron detectors with cadmium shielding. Although both energy regimes are supposed to exhibit similar range distributions they have to be treated by different methods of neutron transport. Until reaching the indium resonance a maximum mean energy loss by elastic collisions, including a few inelastic reactions, can be attributed to hydrogen interactions. Beyond

this limit the kinetic energy of the neutron is becoming dominated by thermal scattering leading to a constant average energy. This system can bee easily reproduced in a model setup including the generalization of an infinitely large domain. The fluxes Φ are scored at thermal (9-120) meV and indium resonance (1.3-1.6) eV energies on a sphere of radius r yielding a surface flux of $r^2\Phi$. Fig. 43 shows the measured fluxes from [162] in comparison to the simulation results. Both attenuation distributions are in good agreement. The particle density in both cases peaks at around 15 cm followed by a nearly exponential decay with similar attenuation lengths[q].

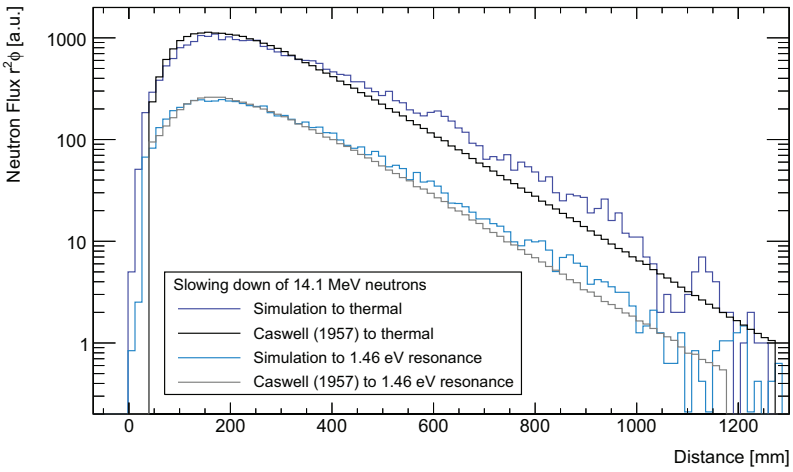

Figure 43: Comparison of the attenuation length from [162] for deuterium-tritium fusion neutrons emitted into water. The spherical surface flux for thermal and indium resonance neutrons as a function of distance from the source is compared to the simulation results from URANOS.

6.6.2 | Bonner Sphere evaluation

A case similar to the previous sec. 6.6.1 are Bonner Spheres, see also sec. 8.2.3, which are proportional counters surrounded by shells of polyethylene. As this spectrometer type of array is used to monitor environmental fluxes, various studies were carried out for the modeling of such [163–168]. Whereas the neutron range distribution in water in the previous example demonstrated geometric transport and collision treatment, the Bonner Sphere offers the possibility to focus on an energy-dependent comparison and on the interplay of moderator and absorber. Among the various existing technical realizations the helium-based version was chosen, equipped with a 3.2 cm spherical counter. For reasons of convenience, the whole model has been discretized in 17 layers, which are symmetrically arranged around the center and depicted in Fig. 44. Laterally the resolution by the pixel matrix was set to 1 mm, therefore the voxel size of a X inch sphere is 1 mm × 1 mm × $(X/17)$". For the simulation the model was irradiated by a neutron beam of the same diameter as the sphere under an angle of 0 °.

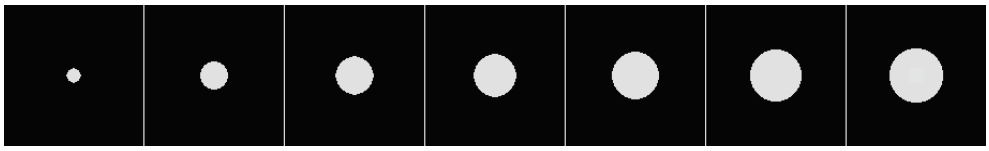

Figure 44: Discretized URANOS Input files for the upper half of a 2 inch Bonner Sphere.

Furthermore, hydrogen atoms in polyethylene have been emulated by the scattering kernel derived from the (oxygen-)bound cross section in water. This can yield exclusively for thermal energies a systematic uncertainty of around 10 %. Due to the statistical nature of neutron transport the actual geometrical shape of a body has a minor influence compared to other parameters like overall volume or thickness. Exem-

[q] Fermi age transport theory, which is not taken into comparison here, can very well reproduce the attenuation at radial distances larger than 25 cm. For fluxes more close to the source the theoretical distribution peaks much earlier.

plarily for the calculation routine some track views are shown in Fig. 45 and Fig. 46 as a central cut through the model and for the whole domain.

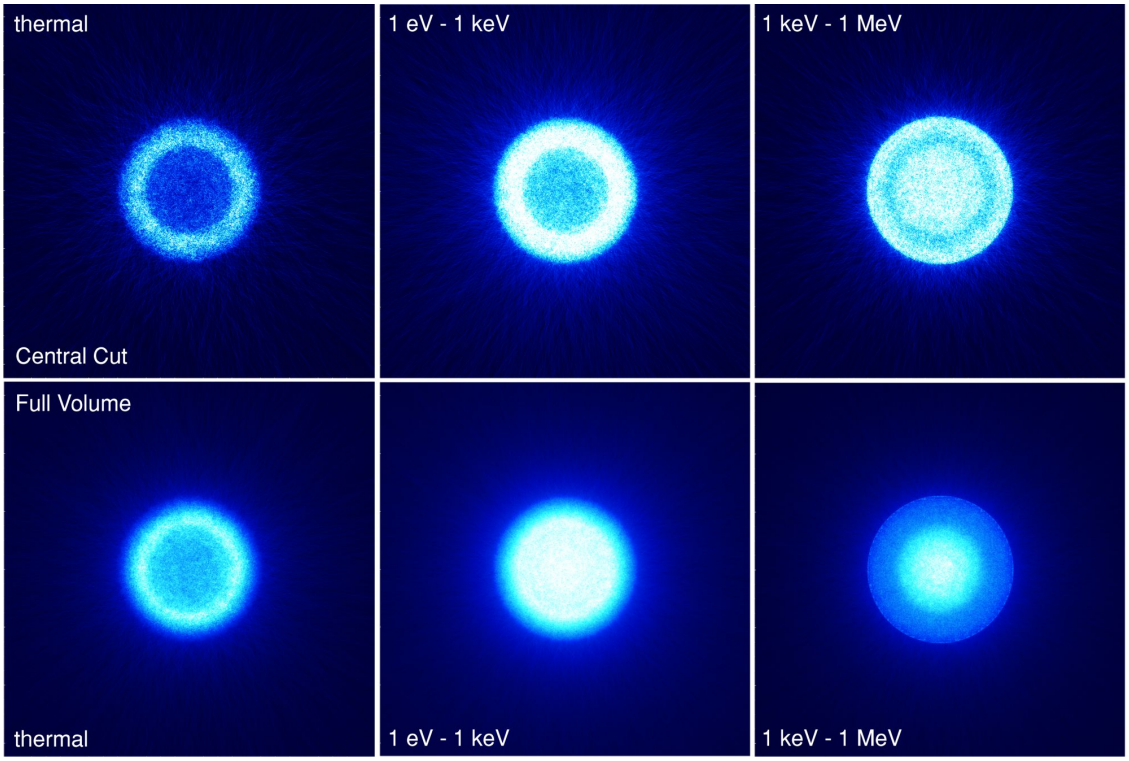

Figure 45: Flux calculation of Bonner Spheres of 2 inch diameter. The simulated neutron tracks (E_{kin} = 10 keV) of 10^6 histories are displayed in a central cross section of 3 mm height (top row) and the full domain of 13 cm × 13 cm × 5.4 cm (bottom row).

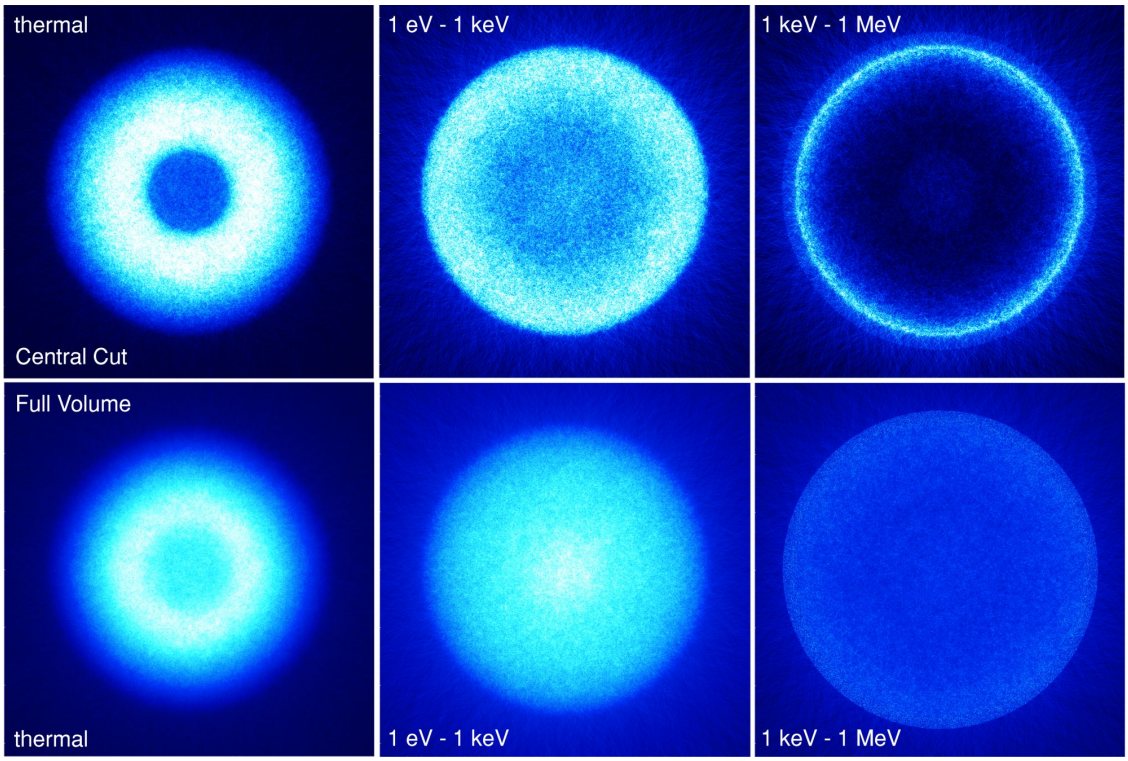

Figure 46: Flux calculation of Bonner Spheres of 4 inch diameter. The simulated neutron tracks (E_{kin} = 10 keV) of 10^6 histories are displayed in a central cross section of 6 mm height (top row) and the full domain of 13 cm × 13 cm × 11 cm (bottom row).

Comparing to calculations from [169], see Fig. 47, there is a good agreement in the energy sensitivity between response curves from literature and URANOS results. This successfully validates the simulation for basic scattering calculations.

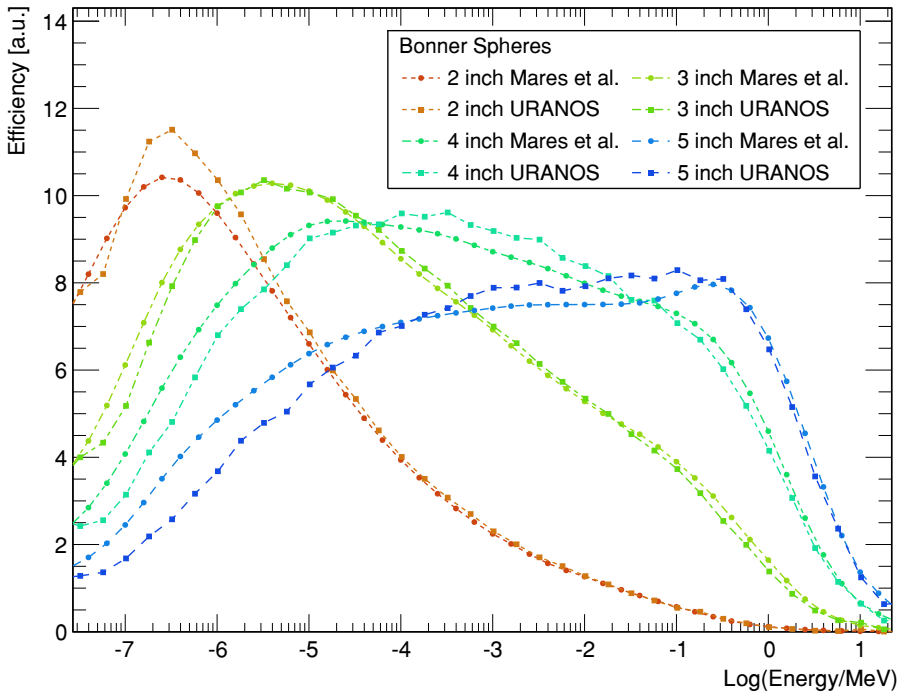

Figure 47: Comparison of simulations of the energy dependent response function of Bonner Spheres of URANOS and MCNP calculations by MARES, SCHRAUBE, and SCHRAUBE [169]. The detectors are HDPE spheres with diameters in the range of (2-5) inch, equipped with a 3.2 cm ^{3}He counter.

6.6.3 | COSMIC SPECTRUM EVALUATION

Although since more than 50 years the general shape and height-dependent scaling of the cosmic-ray neutron spectrum at ground level is known [170], there is a perpetual discussion about precise features of the intensity distribution, especially at the soil interface. The reasons are:

- high-energy neutron interaction cross sections above 20 MeV were not seriously investigated nor integrated into transport codes. Their evaluation and corresponding measurements are recent developments, mainly of the 21st century.
- The invention of the Bonner Sphere, see also sec. 8.2.3, could standardize dosimetric flux evaluations, yet, by means of this type of spectrometer the neutron spectrum is determined indirectly. The experimental findings themselves are the result of unfolding algorithms [171], which rely only on a few absolute values and energy-dependent response functions from Monte Carlo models of the detectors themselves [172], which typically do not take into account the incoming angular distribution. This means that different simulations can produce slightly different weightings for different parts of the spectrum. Sometimes such unfoldings even yield physically wrong reconstructions[r].

In the following Fig. 48 and Fig. 49 an overview of different results from the most widely used codes, see sec. 5.2, are presented along with experimental results. The main differences appear in the high energy regime, for which the usual data bases, see also sec. 5.1.4, until very recently provided only poor support. These uncertainties were partly compensated by effective nuclear interaction models, but propagate to the

[r] Seen for example in the sudden increase of flux meanwhile slowing down in the epithermal regime in [173] or [174].

lower energetic parts of the flux distribution. For now only the general shape of the spectrum has to be considered. The peak structures at around 1 MeV, which are de facto spectral lines of inelastic resonances, mostly oxygen, cannot be resolved experimentally by spectrometers and are displayed only at times. By normalizing to the intensity of the thermal peak Fig. 48 accumulates possible uncertainties and therefore maximizes the deviations between the presented evaluations. A better convergence is displayed in Fig. 49.

In order minimize this general problem URANOS uses a validated neutron spectrum near the surface as a source and releases it directly onto the ground to minimize typical uncertainties of atmospheric propagation. The implementation of the works presented by [66] and [158], which are based on [68] and [67], are discussed in sec. 6.3.1.

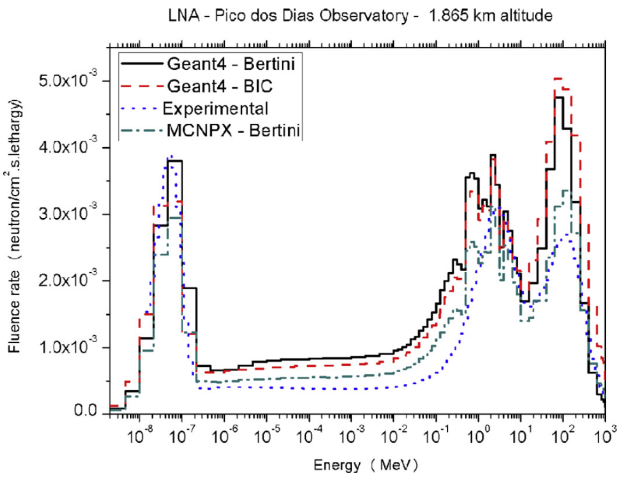

Figure 48: Energy dependent neutron flux at an altitude of 1860 m calculated by MCNPX, GEANT with the two high energy models Bertini [175, 176] and BIC [177] and determined experimentally from [178]. [179]

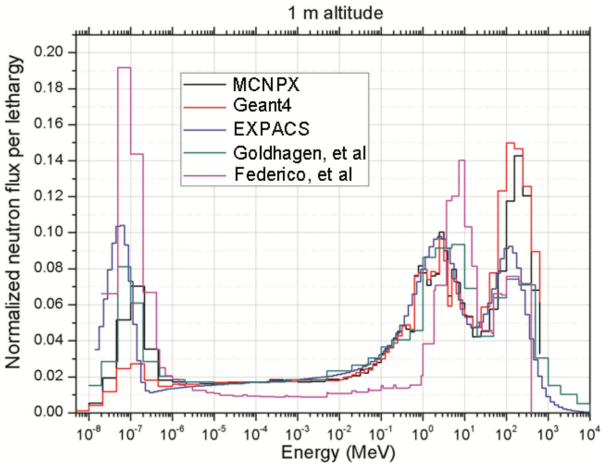

Figure 49: Energy dependent neutron flux at 1 m altitude calculated by EXPACS, MCNPX, GEANT4 and determined experimentally from [180] and from [181]. Environmental conditions are not the same. [182]

Fig. 50 presents the result from URANOS for the calculated neutron flux (black) above the surface in an infinite domain. The input is drawn in green. On the qualitative level

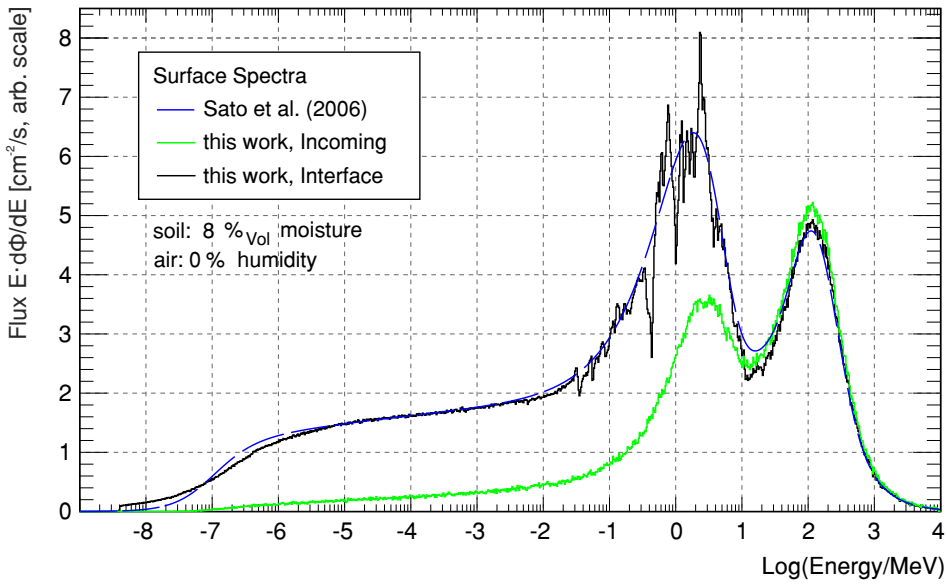

Figure 50: URANOS cosmic-ray neutron spectrum comparison. The incoming spectrum (green), which is generated from the analytical functions (68) and (69) from [66], is released onto the soil. The resulting intensity distribution, shown in black, is compared to the original spectrum for the same environmental conditions from [66] in blue.

the underlying physics model correctly calculates the response to the soil. In the high energy domain around 100 MeV the incoming flux is only reduced, no influence of backscattering can be observed. In the region around 1 MeV the evaporation peak ap-

pears correctly in width and mean energy value. The spike structure on the peak itself is result of elastic scattering on strong nuclear resonances, mainly in oxygen - for example at 435 keV[s]. As there are no significant sources in the range of 1 eV to 0.1 MeV, in a lethargy-dependent plot there is a flat plateau between neutron generation and thermalization, the latter being truncated here. This plateau can feature a slant angle in case there are significant absorption processes involved, but no other features like bumps or steps should be visible. It has to be pointed out that the resulting spectrum here requires nearly the full physics and tracking computation.
For a quantitative investigation due to the lack of a generally accepted standardized spectrum or a consensus in the literature, the evaluation of the URANOS code focuses on the capability to reproduce the above-ground cosmic neutron spectrum for typical conditions. This implies that the input spectrum released on the ground should reproduce the same densities as the input formulae (68) and (69). This test twice evaluates the computational correctness of the code - by yielding the same predictions as the Monte Carlo reference and indirectly by showing that the reverse-engineered input spectrum has been modeled correctly.

6.6.4 | Performance benchmarks

The performance of the code heavily depends on the setup, which is to be simulated. The most significant contributor is the mean lifetime of neutrons in terms of scatterings within the domain. In simple configurations like for the analysis of detectors most neutrons undergo only a few interactions before either being absorbed or leaving then domain. Atmospheric neutrons can have up to hundreds of scatterings before ending up thermalized, see also later 14.1.6. Additionally, depending on the chosen materials and energy range, only a few cross sections like for elastic scattering plus absorption are evaluated. In the MeV regime adding up all inelastic channels scales up to dozens of address requests.
In order to provide some practical estimations a standard scenery can be defined as in table 9. This domain measures 900 m × 900 m with a source dimension of 840 m × 840 m. It contains a minimum configuration of six layers for analyzing a neutron density which can be considered in spatial equilibrium in the innermost 400 m × 400 m.

Table 9: The standard setup for a layer composition in cosmic neutron sensing.

Layer	Position [m]	Height [m]	Material	Function
1	-1000	920	air	top buffer layer
2	-80	30	air	source layer
3	-50	47.5	air	-
4	-2.5	0.5	air	detector layer
5	-2	2	air	-
6	-0	3	soil	ground layer

A similar setup has also been used for simulating the so-called 'UFZ site' in the publication [SK2017b] - an urban environment with many concrete buildings, streets, green spaces, a railroad line, a lake and trees. From the twelve layers in total eight contained a pixel matrix of 1800 × 1800 voxel definitions. The composition 21 introducing the URANOS chapter shows the layer model setup as well as one of the calculation results for the above-ground neutron density.

[s] The structure of the evaporation peak can rather be compared to a transmission spectrum, as those energies are missing which correspond to resonances. There neutrons are scattered off to lower energies more likely than otherwise.

The machine, on which the URANOS v0.99ρ[t] was evaluated, is based on a 4 GHz i7 central processing unit. The technical specifications relevant for this benchmark are:

CPU: Intel Core i7-6700K, 4 cores at 4 GHz (40x multiplicator), 4×(32+32) KB L1-Cache, 4×256 KB L2-Cache, 8 MB L3-Cache,
Mainboard Chipset: Intel Z170 Skylake,
RAM: 16 GB DDR4, 1067 MHz, CL15, tRCD15, tRP15, tRAS36, CR2T,
OS: Windows 7, 64 bit (Build 7601)[u].

The following table 10 summarizes the single core performance of the code in terms of neutrons per second. The 'standard setup' and 'UFZ site' are described above and are simulated in combination with the cosmic neutron spectrum like presented in sec. 6.6.3 Fig. 50, the detector is a rover type instrument, see sec. 12.2.1, which is a setup similar to the Bonner Sphere models presented in sec. 6.6.2 and the other benchmarks are synthetic. Without additional voxel geometry descriptions by pixel matrices one instance of URANOS requires approximately 230 MB of memory, mainly for storing ENDF data.

№	n/s	name	description
1	3730	std. setup	water body, 5 g/m^3 air humidity NTP
2	1800	std. setup	like № 1, ground with 10 % soil moisture
3	1060	std. setup	like № 1, ground with 1 % soil moisture
4	2850	std. setup	like № 1, with full domain tracking enabled
5	880	std. setup	like № 3, with full domain tracking enabled
6	1030	std. setup	like № 1, with thermal transport enabled
7	600	std. setup	like № 2, with thermal transport enabled
8	510	std. setup	like № 3, with thermal transport enabled
9	470	std. setup	like № 3, with thermal transport and full domain tracking enabled
10	2000	UFZ site	with 10 % soil moisture
11	1680	UFZ site	like № 10, without voxel geometry but same layering
12	36700	detector	thermal spectrum onto a side face with $\vartheta = 0°$
13	16250	detector	like № 12, with an americium-beryllium spectrum (see sec. 6.3.2)
14	14100	detector	like № 12, with a 1 MeV monoenergetic beam
15	14200	water	thermal spectrum with $\vartheta = 0°$ from air into a water body
16	7100	water	like № 15, with an americium-beryllium spectrum
14	6300	water	like № 15, with a 1 MeV monoenergetic beam

Table 10: Single core performance of URANOS (v0.99ρ) for a number of practically relevant scenarios. The above described system with a 4 GHz i7-6700K CPU was used to evaluate the benchmarks.

[t] compiled by Qt 5.2.1 linked against ROOT 5.34.20 in Visual C++ MSVC 2010 32bit. The integration was restricted to previous versions of the library and runtime as far as no ROOT 5.34.X version provided binaries for later versions.

[u] Spectre [183] vulnerability patched.

Part IV

THE CASCADE DETECTOR

7

SPIN ECHO SPECTROSCOPY

When Spin Echo was discovered in 1949 [184] it opened the field of precision physics for stochastically distributed ensembles by making use of the nuclear spin as an individual quantum marker: A single radio frequency pulse close to the Lamor[a] frequency causes a macroscopic non-equilibrium state for the subjected particles. After a few precessions in an external field, the ensemble seems to come to thermal equilibrium, however, two successive radio frequency pulses produce a so-called spin echo. The observed loss of coherence is due to the dephasing of the sum of single particles, but an inverting pulse [185] can refocus the system and entirely retrieve the original polarization state. This principle, which found its first applications in nuclear magnetic resonance spectroscopy [186] has been applied by F. Mezei in 1972 to neutron physics [187, 188], which allowed for high energy resolution without the otherwise necessary drastic intensity losses, as spin manipulations can be precisely carried out by external magnetic fields. In **N**eutron **S**pin **E**cho (NSE), the Lamor precession phase acquired by the magnetic field integrals $\int \vec{B}\,\mathrm{d}\vec{l}$ from traversing two solenoid coils with opposite currents, can give information about a possible energy transfer since the interference pattern vanishes by interaction with a sample inside the setup. With the neutron velocities v_i and gyromagnetic ratio $\gamma_L = 183.25\,\mathrm{Mhz/T}$ the precession angle ϕ obtained is $\gamma_L \int \vec{B}\,\mathrm{d}\vec{l}/v$ and so the polarization before and after the scattering is

$$P_x = \langle \cos(\phi) \rangle = \left\langle \cos\left(\gamma_L \frac{\int \vec{B}_{\mathrm{in}} \mathrm{d}\vec{l}}{v_{\mathrm{in}}} - \gamma_L \frac{\int \vec{B}_{\mathrm{out}} \mathrm{d}\vec{l}}{v_{\mathrm{out}}} \right) \right\rangle. \tag{130}$$

ϕ is typically expressed by a time τ and a frequency ω as to $P_x = \langle \cos(\omega\tau) \rangle$. This time, which is called the Spin Echo time, has in linear approximation a cubic dependency on the de Broglie wavelength

$$\tau_{\mathrm{NSE}} = \frac{\phi}{\omega} = \frac{h}{2\pi m} \frac{\gamma_L \int \vec{B}\,\mathrm{d}\vec{l}}{\overline{v}^3} = \frac{m^2 \gamma_L \int \vec{B}\,\mathrm{d}\vec{l}}{2\pi h^2} \lambda^3. \tag{131}$$

As a consequence of having a broad velocity distribution of rather slow particles this instrument also becomes a Mach[b]-Zehnder[c] interferometer in time: Not only static energy losses lead to a loss of polarization but also the single-particle interference with translating scattering centers. This opened up the field to the study of molecular and protein dynamics [189] or polymer melts like in the case of the reptation model [190]. The specific scattering technique, which focuses on the point where sample dynamics starts to smear out the interference pattern, is called quasi-elastic scattering [191].
The important quantities which are measured by the instrument are momentum transfer $\vec{q}$ and energy transfer $\Delta E = h/(2\pi\omega)$, which is linked to the phase change and the spin echo time by

$$\Delta E = \frac{h}{2\pi\omega} = \frac{h}{2\pi} \frac{(\Delta\phi = 2\pi)}{\tau_{\mathrm{NSE}}} = \frac{h}{\tau_{\mathrm{NSE}}}. \tag{132}$$

As far as elastic and quasi-elastic scattering is considered, both can be measured independently of each other. Their combined observable is called scattering function $S(\vec{q}, \omega)$.

[a] Sir Joseph LAMOR, *1857-†1942, Ireland.
[b] Ludwig MACH, *1868-†1951, Austro-Hungarian Empire.
[c] Ludwig ZEHNDER, *1854-†1949, Swiss Confederation.

A classical example for a function of ω would be a Lorentzian with a natural line width Γ. Then, (130) translates using (131) to

$$P_x = \frac{1}{N}\int_{-\infty}^{\infty} S(\vec{q},\omega)\cos(\tau(\omega-\overline{\omega}))\,\mathrm{d}\omega \sim \int_{0}^{\infty} S(\vec{q},\omega)\cos(\tau(\omega))\,\mathrm{d}\omega = \mathcal{F}_c\left[S(\vec{q},\omega)\right]. \quad (133)$$

with the normalization $N = \int_{-\infty}^{\infty} S(\vec{q},\omega)\,\mathrm{d}\omega$. Therefore, P_x is proportional to the Fourier[d] cosine transform of $S(\vec{q},\omega)$, which is called the intermediate scattering function $F(\vec{q},\tau)$. An analyzer before the detector then projects the beam of intensity I_0 to the respective spin component as

$$I = \frac{I_0}{2}\cdot(1+P). \quad (134)$$

In 1987 Gähler and Golub [192] developed **N**eutron **R**esonance **S**pin **E**cho (NRSE) [193], where the constant field regions are replaced by a pair of compact radio-frequency spin flipper coils, which generate a combination of a constant and an oscillating field. Using this technique a µeV resolution can be achieved[e], however it does not allow for depolarizing effects. To overcome these restrictions the NRSE variant „**M**odulation of **I**nt**E**nsity with **Z**ero **E**ffort“ (MIEZE) [194, 195] uses only the first pair of coils and achieves the Spin Echo by detuning both frequencies with respect to each other. This provides the advantage, that the signal modulation is achieved before the sample. Therefore, it is insensitive to depolarizing effects and allows to study ferromagnetic samples at high or low temperatures or magnetic skyrmions[f] [196]. The change from fields perpendicular to the flight direction to longitudinal ones, called LNRSE [197, 198], improves the field correction possibilities and therefore increases the energy resolution [199]. In order to provide a balanced classification, Fig. 51 compares Spin Echo to other neutron scattering techniques and photon-based methods. See also the overviews [200] and [201].

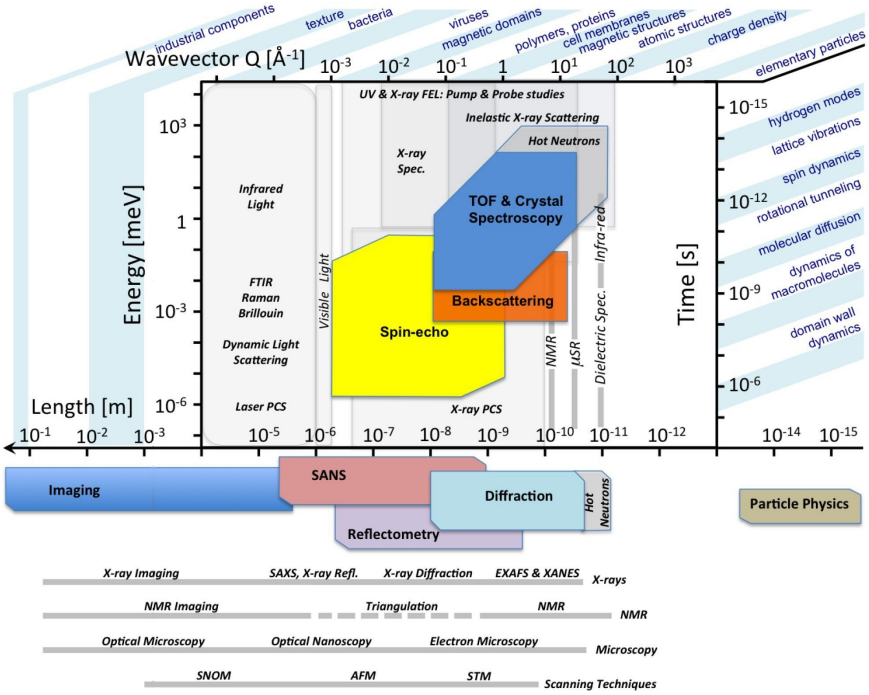

Figure 51: The neutron scattering map: Comprehensive overview of energy and time resolution resolution of a large variety of measurement techniques along with possible applications. [202]

[d] Jean Baptiste Joseph FOURIER, *1768-†1830, France.
[e] As an example, 10,000 precessions can be achieved for an effective field integral of 0.25 Tm, which means an energy change of 10^{-4} on the neutron energy times the polarization loss resolution can be measured.
[f] Tony Hilton Royle SKYRME, *1922-†1987, Great Britain.

Neutron Resonance Spin Echo relies instead of the precision a in static field on high frequency resonance coils inducing Rabi[g] oscillations around a zero-field region. It represents a time-dependent interaction, which in addition to the spin rotation comes along with an energy exchange according to the Zeeman[h] energy $E_{\uparrow\downarrow}$. In NRSE at the beginning and end of each „arm“ the precession only takes place during the short rotation in the phase-synchronous π flip coils. The principle of the flipper is to create a superposition of a static field B_0 and a rotating field B_{rf} with an RF frequency equal to the Larmor frequency. This leads to the neutrons spin precessing around the rotating B_{rf} axis. In the w.l.o.g. around the z axis rotating frame the static field vanishes and the rotating field is static

$$\vec{B}(t) = \vec{B}_0(t) + \vec{B}_{\mathrm{rf}}(t) = \begin{pmatrix} B_{\mathrm{rf}}\cos(\omega_{\mathrm{rf}}t) \\ B_{\mathrm{rf}}\sin(\omega_{\mathrm{rf}}t) \\ B_0 \end{pmatrix} \rightarrow \begin{pmatrix} B_{\mathrm{rf}} \\ 0 \\ B_0 - \omega_{\mathrm{rf}}/\gamma_L \end{pmatrix} = \begin{pmatrix} B_{\mathrm{rf}} \\ 0 \\ 0 \end{pmatrix}. \tag{135}$$

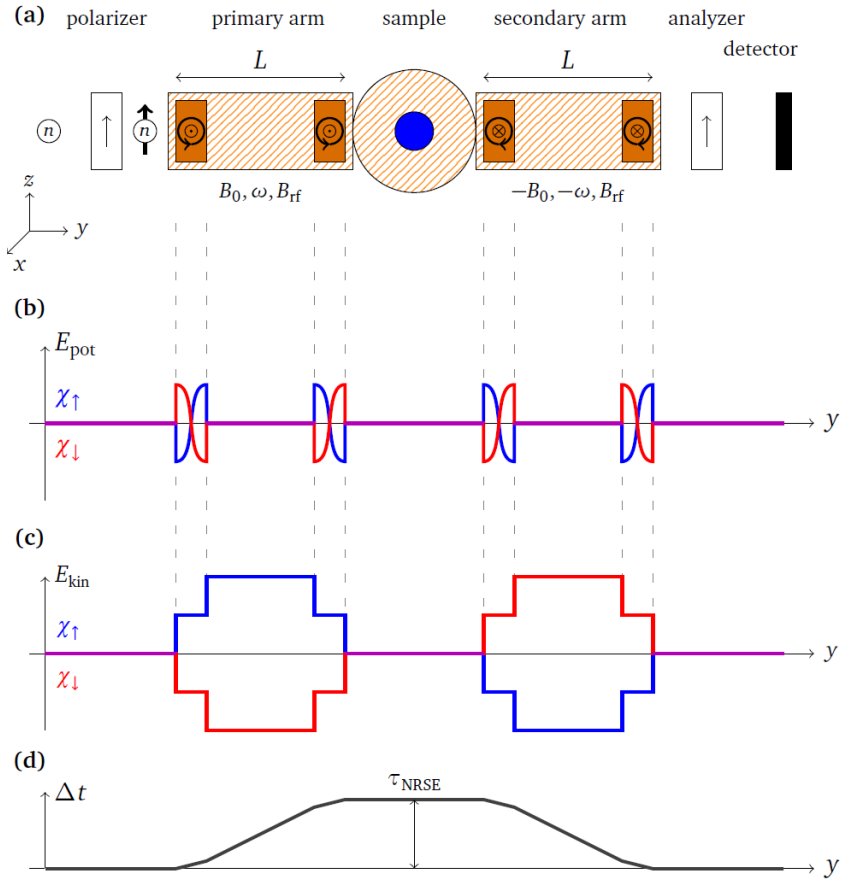

Figure 52: Schematic of an NRSE spectrometer (a). Polarized neutrons pass the precession regions, which consist of two resonance flippers at both ends, and the analyzer before entering the detector. Panel (b) and (c) depict the potential and kinetic energies corresponding to the up $\chi_\uparrow$ and down $\chi_\downarrow$ eigenstates as a function of the position along the flight path. Panel (d) shows the flight time difference of both eigenstates. The Spin Echo time τ_{NRSE} is given by the flight time difference at the sample position. [203]

[g] Isidor Isaac RABI, *1898-†1988, Austro-Hungarian Empire.
[h] Pieter ZEEMAN, *1865-†1943, Kingdom of the Netherlands.

A π flip can be achieved if the time Δt to pass the flipper equals a rotation in the rotating frame of $\pi = \omega_{\mathrm{rf}}\Delta t$. By transformation to laboratory system the angle from the rotating frame is added.
In the quantum mechanical plane wave description [204] one can express monochromatic neutrons polarized in x-direction by Dirac[i] spinors Ψ of momentum k. Entering a magnetic field in z-direction, both degenerate spin eigenstates $\uparrow$ and $\downarrow$ are energetically split by $E_{\uparrow\downarrow} = \pm\mu_B B$, with the Bohr[j] magneton μ_B.

$$\Psi_0 \rightarrow \Psi(t) = \frac{1}{\sqrt{2}} \begin{pmatrix} \exp\left(i((k+\Delta k)y - \omega t)\right) \\ \exp\left(i((k-\Delta k)y - \omega t)\right) \end{pmatrix}, \quad \text{with} \quad \Delta k = \frac{\gamma_L B}{2v}. \tag{136}$$

After leaving the magnetic field of length L, both states are again degenerate with respect to their potential energies, however, due to the different k vectors there is a phase difference between both of

$$\phi = L2\Delta k = \gamma_L B \frac{L}{v} = \omega_{\mathrm{rf}} \frac{L}{v}. \tag{137}$$

As the RF field switches additionally both states the difference in kinetic energy gains a factor of $\alpha = 2$, see also Fig. 53(b) and (c). For the setup of two coil pairs this is, besides the gain in α, equivalent to (130) and one can write the phase difference in terms of energy loss

$$\Delta\phi = \alpha\gamma_L BL\left(\frac{1}{v_{\mathrm{in}}} - \frac{1}{v_{\mathrm{in}}+\Delta v}\right) \approx \alpha\gamma_L BL\frac{\Delta v}{v_{\mathrm{in}}^2} = \underbrace{\alpha \overbrace{\gamma_L B}^{\omega_{\mathrm{rf}}} L \frac{h}{2\pi m v_{\mathrm{in}}^3}}_{\tau_{\mathrm{NRSE}}} \omega \tag{138}$$

For a spectrum of neutron energies $f(\omega_n)$ (136) becomes

$$\Psi_f(t) = \frac{1}{\sqrt{2}} \begin{pmatrix} \exp\left(i(ky - \omega t)\right) \\ \exp\left(i(ky - \omega t)\right) \end{pmatrix} \int_{-\infty}^{\infty} f(\omega_n) \exp\left(i\omega_n \frac{y}{v(\omega_n)} - t\right) \mathrm{d}\omega_n. \tag{139}$$

If one assume a triangle-shaped spectral density of width $h/(2\pi)\Delta\omega_n$ centered around ω_0 the Fourier transform of the spectrum yields a cardinal sine function

$$\widetilde{f}(y,t) = \frac{\sin^2\left(\frac{1}{2}\Delta\omega_n\left(\frac{y}{v(\omega_n)} - t\right)\right)}{\left(\Delta\omega_n\left(\frac{y}{v(\omega_n)} - t\right)\right)^2}. \tag{140}$$

For the polarization then one yields

$$P(\Delta y) = \frac{\sin^2\left(\Delta\omega_n \tau \Delta y\right)}{(\Delta\omega_n \tau \Delta y)^2} \cos\left(\frac{\omega_{\mathrm{rf}}\Delta y}{v_{\mathrm{in}}}\right), \tag{141}$$

with Δy denoting the flight path distance with respect to the Spin Echo point with its polarization maximum, which lies after traversing both magnetic fields with length L. The cosine term originates from the fact, that beyond the Spin Echo point the velocity spread leads again to a spatio-temporal dephasing by integration over all flight paths and spin directions. τ denotes as above the Spin Echo time

$$\tau_{\mathrm{NRSE}} = \frac{h\omega_{\mathrm{rf}} L}{\pi m v_{\mathrm{in}}}. \tag{142}$$

[i] Paul Adrien Maurice DIRAC, *1885-†1962, Great Britain.
[j] Niels Henrik David BOHR, *1902-†1984, Kingdom of Denmark.

As shown in sec. 7.1 and Fig. 53 the traversing of one spin flipper leads to an energy separation of the ↑ and ↓ states. Over a flight path L it translates to a flight time difference τ. In NRSE after the sample a mirrored setup reverses the process and this leads to acquiring the full interference pattern again at the end of the instrument. In MIEZE the second flipper coil of the first arm already overcompensates the energy splitting. This leads to both states continuously reducing their flight time difference until being spatially coincident at a location in a distance L_2 from the instrument. As the Spin Echo group width in NRSE is given by the envelope function from the Fourier transform of the velocity distribution its spatial extension is anyway limited. For MIEZE this principle of overlap is the same, however, both states are still energetically detuned with respect to each other. In MIEZE the Spin Echo group therefore is dynamic and the polarization itself oscillates in time, which requires a time-resolved detector.

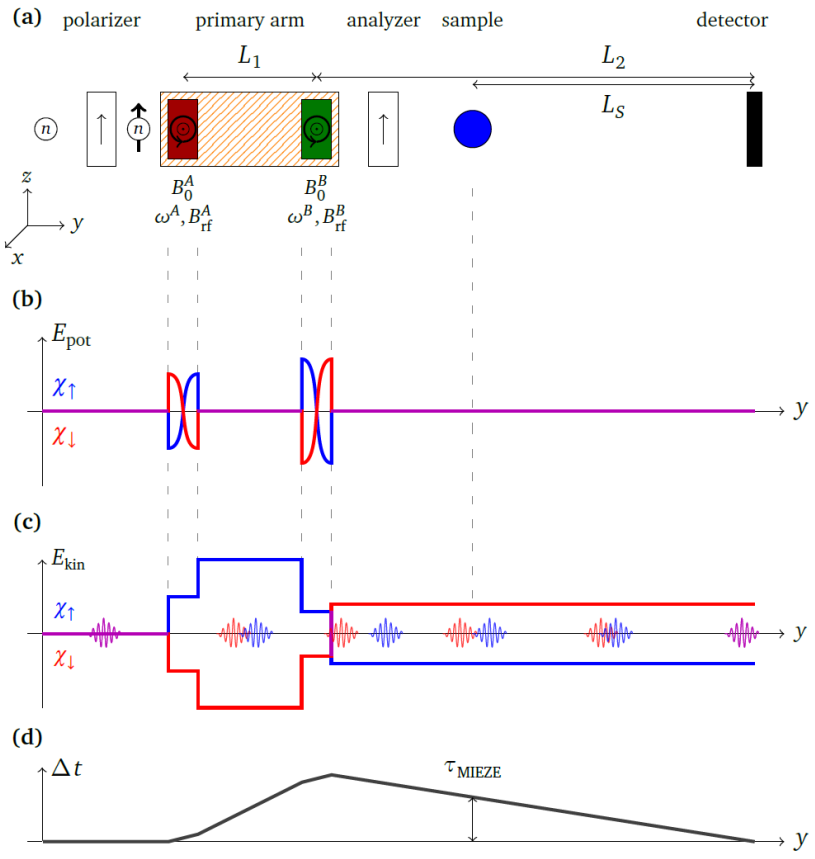

Figure 53: Schematic of a MIEZE spectrometer (a). Polarized neutrons pass the precession region, which consist of two resonance flippers at both ends with different frequencies. The analyzer can be place in front of the sample. Panel (b) and (c) depict the potential and kinetic energies corresponding to the up $\chi_\uparrow$ and down $\chi_\downarrow$ eigenstates as a function of the position along the flight path. Panel (d) shows the flight time difference of both eigenstates. The Spin Echo time τ_{MIEZE} is given by the flight time difference at the sample position. [203] and [205]

The velocity separation can be calculated by the difference after the first flipper v^{A} driven at frequency of $\omega_{\mathrm{rf}}^{\mathrm{A}}$ and the second v^{B} at $\omega_{\mathrm{rf}}^{\mathrm{B}}$ is

$$\Delta v = \Delta v^{\mathrm{B}} - \Delta v^{\mathrm{A}} = \frac{\overbrace{\gamma_L B_{\mathrm{rf}}^{\mathrm{B}}}^{\omega_{\mathrm{rf}}^{\mathrm{B}}} - \overbrace{\gamma_L B_{\mathrm{rf}}^{\mathrm{A}}}^{\omega_{\mathrm{rf}}^{\mathrm{A}}}) h}{\pi m v_{\mathrm{in}}} \tag{143}$$

The distance L_2 at which both wave packets intersect can be calculated as

$$\frac{L_1}{L_2} = \frac{\omega_{\mathrm{rf}}^{\mathrm{B}} - \omega_{\mathrm{rf}}^{\mathrm{A}}}{\omega_{\mathrm{rf}}^{\mathrm{A}}} \frac{v_{\mathrm{in}}^2 - \left(\frac{\omega_{\mathrm{rf}}^{\mathrm{A}} h}{2\pi m\, v_{\mathrm{in}}}\right)^2}{\underbrace{v_{\mathrm{in}}^2 - \left(\frac{\left(\omega_{\mathrm{rf}}^{\mathrm{B}} - \omega_{\mathrm{rf}}^{\mathrm{A}}\right) h}{2\pi m\, v_{\mathrm{in}}}\right)^2}_{\to 1}} \approx \frac{\omega_{\mathrm{rf}}^{\mathrm{B}} - \omega_{\mathrm{rf}}^{\mathrm{A}}}{\omega_{\mathrm{rf}}^{\mathrm{A}}} = \frac{\omega_{\mathrm{rf}}^{\mathrm{B}}}{\omega_{\mathrm{rf}}^{\mathrm{A}}} - 1. \tag{144}$$

This ratio is called the MIEZE condition. The spatio-temporal separation of the wave packets depends on the sample position L_{S} in front of the detector, so does the Spin Echo time

$$\tau_{\mathrm{MIEZE}} = \frac{\left(\omega_{\mathrm{rf}}^{\mathrm{B}} - \omega_{\mathrm{rf}}^{\mathrm{A}}\right) h\, L_{\mathrm{SD}}}{m\, v_{\mathrm{in}}^3} = \frac{m^2}{\pi h^2} \left(\omega_{\mathrm{rf}}^{\mathrm{B}} - \omega_{\mathrm{rf}}^{\mathrm{A}}\right) L_{\mathrm{S}} \lambda^3. \tag{145}$$

A detailed description with focus on NRSE and MIEZE is provided by the theses [206–210].

7.3 | Spin Echo spectrometry at RESEDA

The **RE**sonance **S**pin **E**cho for **D**iverse **A**pplications beamline (RESEDA) [82] is an instrument at the Forschungs-Neutronenquelle Heinz Maier-Leibnitz FRM II in Garching, operated by the Technical University Munich. Fig. 55 shows its location in the neutron guide hall and the scale of the instrument, which is also drawn in a cross section in its original setup [211]. The neutron guide NL-5S provides a cold neutron spectrum of approximately (3.5-15) Å, see also Fig. 20, which can be tuned by a velocity selector with a triangular wavelength distribution and a $\Delta\lambda/\lambda \approx 12\,\%$, see sec. 11.2.1. RESEDA originally consisted of one primary and two secondary Mu-metal shielded spectrometer arms. Fig. 54 shows the primary arm in the back of the photograph and one of the secondary arms without shielding in front. Additionally, the first Spin Echo setup [187] is depicted in comparison, which illustrates the scaling of this technology within the past 40 years.

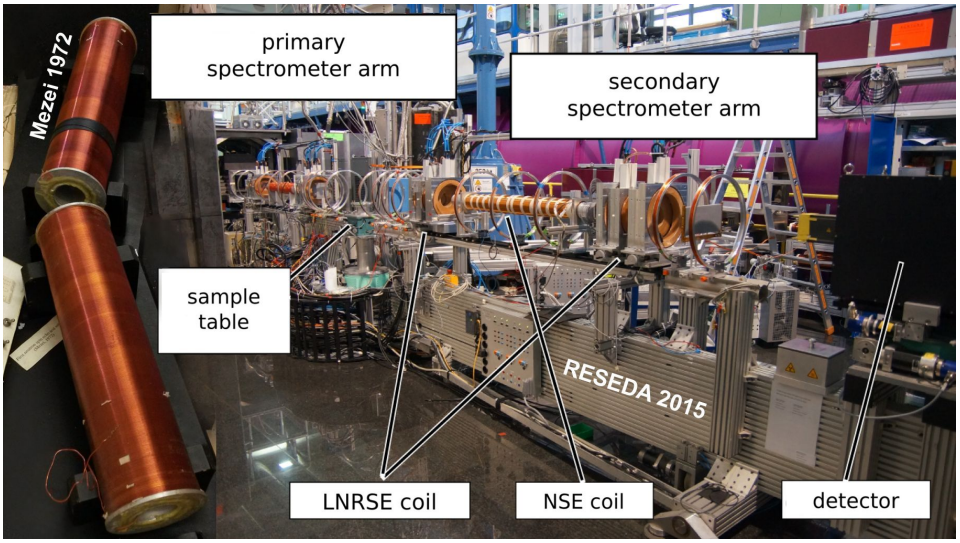

Figure 54: Spin Echo Instruments over time: The first now disassembled setup used by originally by Mezei [187] (left) and the spectrometer RESEDA, modified from [212] (right). Whereas NSE relies on static coils, NRSE uses spin flipper with a zero field in between. RESEDA can be operated in both modes, in MIEZE and additionally is equipped with longitudinal Spin Echo coils.

The secondary spectrometer can be turned around the sample allowing for scattering angles up to 40° corresponding to a maximum q value of $2.5\,\text{Å}^{-1}$. For quasielastic scattering NSE, transversal NRSE and MIEZE measurements can be carried out in a

range of Spin Echo times of (0.001-5) ns. Both NRSE coils were mounted in a distance of $L = 2.625\,\mathrm{m}$ [213], later $L = 1.925\,\mathrm{m}$. Coupling coils control the transition of the polarization of the guide field from the polarizer to the zero-field region and to the V-cavity analyzer [214]. After the measurements carried out in this work, RESEDA has been equipped [215] with a longitudinal Spin Echo setup [216].
The neutron guides [217] are evacuated glass bodies called „supermirrors“, which are coated on their inside by several layers of Ni and Ti, which are able to reflect thermal neutrons. NL5 [218] with the dimensions of $29\,\mathrm{mm} \times 170\,\mathrm{mm}$ is a polarizing $m = 2$ supermirror which translates to a critical reflection angle of

$$\vartheta_{\mathrm{crit}} = \frac{0.1^\circ}{\text{Å}} \cdot m \cdot \lambda. \tag{146}$$

For typical wavelengths the flux at the sample position is around $2{\cdot}10^6 \mathrm{n/cm^2/s}$. In order to avoid loss of intensity or decrease the signal-to-noise ratio, the flight paths inside the instrument are also evacuated. Small air gaps at the sample position or before the detector do not significantly contribute with a typical mean free path of thermal neutrons in the order of 10 m.
RESEDA is equipped with a helium-3 counter for classical Spin Echo measurements and a CASCADE detector, allowing for measurements requiring a high spatial and time resolution. Both detectors are shielded by a cube of borated polyethylene.

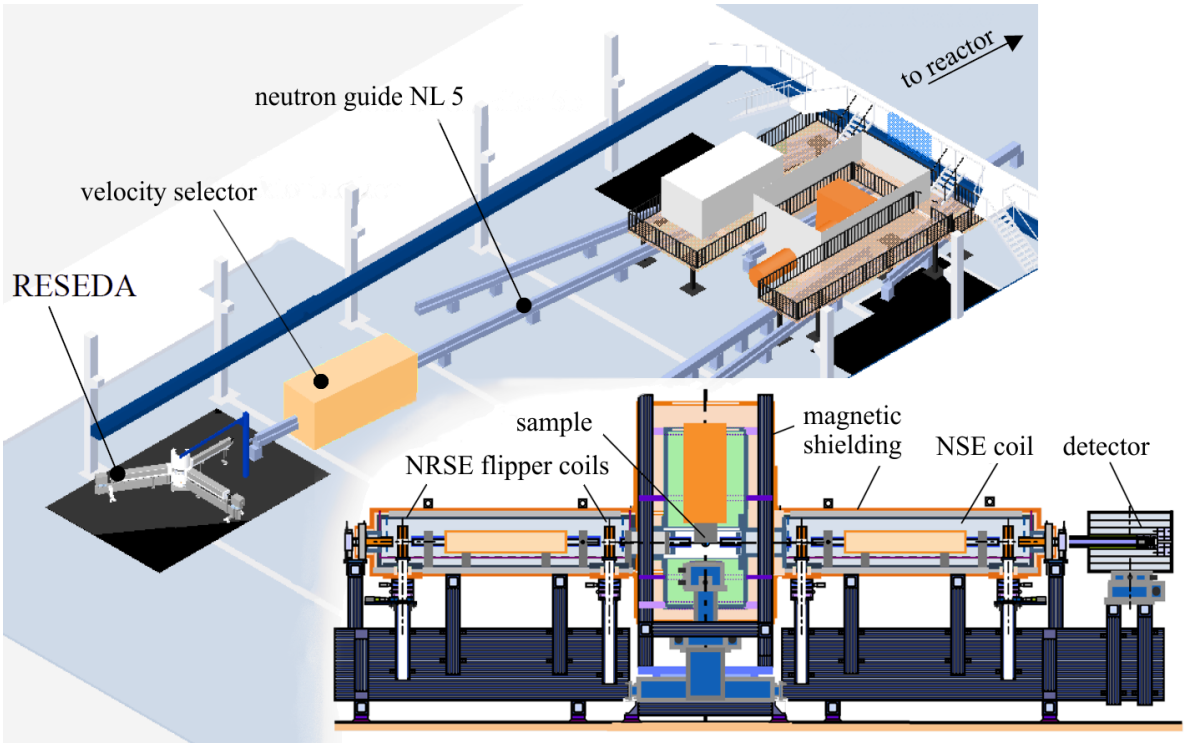

Figure 55: Illustration of the neutron guide hall of the FRM II with RESEDA located at the end of NL-5, which also leads to the other Spin Echo instrument MIRA in front (not shown). In the lower right panel a cross section of the instrument in the NRSE/NSE configuration is shown. The tower in the center hosts the cryostat for temperature dependent experiments. Modified from [211].

8

NEUTRON DETECTION SYSTEMS

The term „neutron detector“ refers to a system which detects neutrons of thermal energies (λ = 1.8 Å, E_{kin} = 25.2 meV) by absorption, followed by immediate de-exitation of the nucleus. Thermal neutrons cannot be detected directly in an efficient way as they are in equilibrium with the environment and so the change of entropy in the active medium required for a significant signal to noise ratio is too small. Converters are used to generate a strong signature by processes which are specifically sensitive to slow neutrons such as nuclear absorption followed by immediate de-excitation or fragmentation. Hereby effective energy deposition enhancements of 10^5 are needed to discriminate against other background processes. Technically a hybrid design is required, which means that the detection unit is functionally separated into three parts, the neutron absorber featuring a high cross section, the transfer medium for the conversion products and the readout. A system is called monolithic if the transfer medium and the converter are architecturally interwoven, either by function or by material.

8.1 | NEUTRON CONVERTERS

Only a few isotopes exhibit thermal absorption cross sections reasonably high compared to other processes and reaction products of charged particles unambiguous enough [219]. Besides uranium there are ^{3}He, ^{6}Li, ^{10}B[a]. Tab. 11 summarizes the common converters and their primary reaction channels.

Element	Reaction		CS at 25.2 meV
^{3}He	^{3}He+n →	^{3}H+p + 764 keV	5327 b
^{6}Li	^{6}Li+n →	^{3}H+α + 4.78 MeV	940 b
^{10}B	^{10}B+n →	^{7}Li+α + 2.79 MeV (6.4 %)	3837 b
	^{10}B+n →	^{7}Li+γ + α + 2.31 MeV (93.6 %)	
^{155}Gd	^{155}Gd+n →	^{156}Gd+γ + e^- + (30 − 180) keV	61000 b
^{157}Gd	^{157}Gd+n →	^{158}Gd+γ + e^- + (30 − 180) keV	254000 b
^{231}Th	^{231}Th+n →	^{232}Th+γ	1630 b
^{235}U	^{235}U+n →	fission fragments + 160 MeV	584 b

Table 11: Overview: neutron converters and their by-products of the main decay channels for thermal cross sections. [97]

These elements appear in different phases and compounds, therefore the characterization as a converter includes the feasibility for realizations in detection systems at standard environmental conditions. Helium-3 is strictly gaseous, others like boron-10 appear in elemental solid form, as a solid compound, or as a gaseous compound, and lithium-6 can be used as a doping agent. A high cross section at thermal energies as stated in tab. 11 is decisive for a good detection efficiency. In terms of detection precision the material absorption coefficient characterizes the conversion length and therefore the amount of active volume needed. Fig. 56 compares the absorption strength of

[a] Other elements with high cross sections are not feasible as converters like ^{135}Xe with $2{\cdot}10^6$ b or ^{149}Sm with $74.5{\cdot}10^3$ b at thermal energies, but are referred to as 'neutron poison' [220] due to the fact that their abundance or production in a nuclear reactor leads to a lower reactivity. Other methods [221], which make use of the delayed beta decay of for example silver isotopes, are also not discussed here.

different neutron converters. It displays the energy-dependent cross section, for which for thermal neutron detection the values below 1 eV are relevant. As those elements appear in different aggregation states the relative attenuation coefficients can vary by several orders of magnitude. The commonly used helium-3 for example, although having a high absorption cross section requires a large volume or a high pressure, which makes it less suited for time-of-flight applications. The variety of systems, which can be realized using such converters, will be discussed later in sec. 8.4.

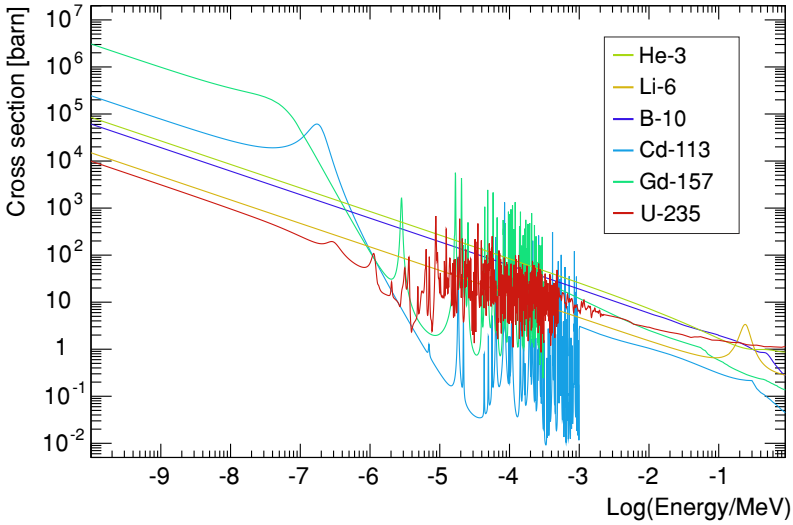

Figure 56: Neutron absorption cross sections of selected elements from tab. 11 (MT numbers 19, 102, 103, 105, 107) [98].

This work focuses on ^{10}B. Boron is a metalloid with a comparably high resistance. Although boron is a very light element, its abundance is low as against other similar elements [222] as the stable isotopes 10 and 11 are not part of the main fusion cycles[b]. Besides appearing in form of red crystals the second form of boron consists of black crystals with a metallic appearance. However, it can also occur as a brown powder with no crystalline structure and a slightly higher density. The compounds boron nitride and boron carbide are after diamond one of the hardest known materials. Boron-10 is a by-product from the production of depleted boron, necessary for example for radiation-hard semiconductors.

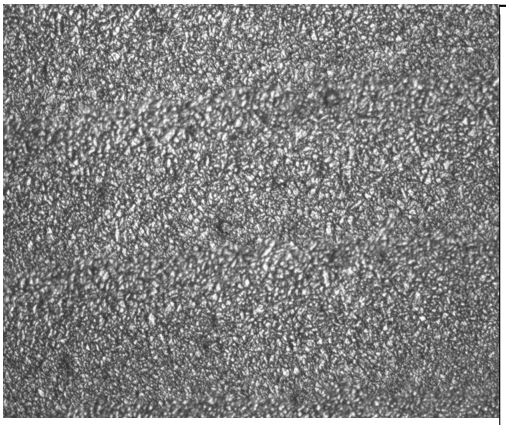

Figure 57: Microscopic image of a metal substrate coated by boron.

Physical properties of boron [224, 225]

Element category	metalloid
Phase	solid
Group, period, block	13, 2, p
Electron configuration	$2s^2 2p^1$
Atomic weight	10.811
Melting point	2348 K
Density	2.34 g/cm^3
Thermal conductivity	31.8 W/mK
Electrical resistivity	18000 Ωm
Stable isotopes	
^{10}B (19.7±0.7) %	10.0129369(4)
^{11}B (80.1±0.7) %	11.0093054(4)

[b] The so-called „boron neutrinos“ are originating from the beta decay of ^{8}B in the solar *pp*-cycle [223].

8.2 | Classical systems

8.2.1 | The counter tube

Gaseous proportional counters [226] based on the Geiger[c] tube [227] are in terms of numbers still the most used neutron detection technology. It consists of two coaxial electrodes and a gas filled volume. Negative charge carriers drift towards the anode wire by an electric field which increases by $1/r$ towards the center up to its maximum at the surface of the wire. There, the field becomes strong enough to initiate a Townsend[d] avalanche multiplication in the counting gas. Electrons are collected on the anode and the ions drift towards the cathode, whereas the change of energy in the cylindrical capacitor induces a voltage potential change during the ion drift time. This leads to the detector signal being proportional to the amount of primary ionization, to the drift time to the wire and to the anode gain, which is designed to be in the order of 10-100. Typically quench gases are added. These are organic molecules or chemical compounds like CO_2 or isobutane, which contrary to the noble gases can absorb energy into rotational or oscillation final states, i.e. kinetic modes instead of electronic excitation. This prevents from secondary discharges to happen, which can be triggered by photons released from the excited states of de-ionized drift atoms on the cathode. On the contrary even small impurities with a high electronegativity such as oxygen can lead to slowly drifting negative ions by free electrons attaching to them and effectively deteriorating the signal. Electronically the proportional counter is biased through a preamplifier followed by a shaping amplifier. The signals then are digitized by a multi-channel or peak analyzer. A more detailed description can be found in [27].
The signal generation, see also Fig. 59, in a coaxial cylinder of outer diameter b, wire

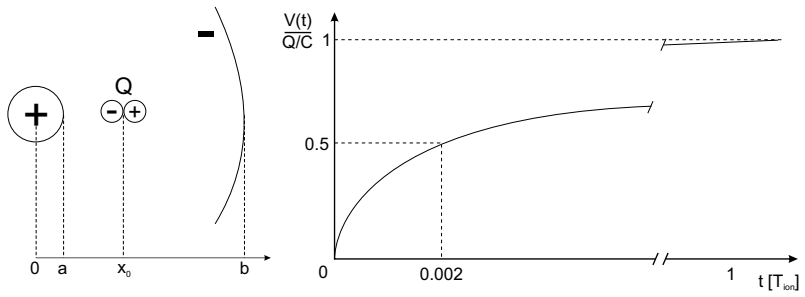

Figure 59: Schematic cross section of a proportional counter with relevant geometrical distances (left) and typical voltage pulse shape as a function of drift time (right).

diameter a, capacity C, potential difference V_s and electrical field strength [228]

$$E(x) = \frac{V_s}{\log(b/a)} \frac{1}{x} \tag{147}$$

can be, depending on radial position x_0 of a charge Q, expressed as

$$V_{\text{ion}}(t) = \frac{Q}{2C \log(b/a)} \left(\log \left(x_0^2 + \left(b^2 - x_0^2 \right) \frac{t}{T_{\text{ion}}} \right) - \log \left(x_0^2 \right) \right). \tag{148}$$

Here it is already taken into account that mainly ions contribute to the final signal and therefore their drift time T_{ion} characterizes the system response. Assuming $b \gg a$ and $x_0 = a$ leads to

$$V(t) = \frac{Q}{2C \log(b/a)} \log \left(1 + \frac{b^2}{a^2} \frac{t}{T_{\text{ion}}} \right), \tag{149}$$

[c] Johannes Wilhelm Geiger, *1882-†1945, German Empire.
[d] John Sealy Townsend, *1868-†1957, United Kingdom of Great Britain.

which describes the signal characteristics according to the required geometry and to the possible time resolution.[e]

Helium-3 has the advantage that it acts as a neutron converter as well as a counting gas. Therefore, a monolithic proportional counter can be realized. By absorbing a neutron the total reaction energy of 764 keV is distributed to both conversion products, a hydrogen (573 keV) and a triton ion (191 keV) emitted back-to-back, see also section 8.1. Low-Z elements have a small stopping power for charged particles. The ranges in helium-3 at a density of 0.125 kg/m^3 NTP [229] are 55 mm for the proton and 20 mm for the triton [159] leading to a pressure dependent total track length of 75 bar·mm. Therefore, partial signal loss by one of the reaction products colliding with the cathode is probable. This is called wall effect and can be identified in the spectrum as edges at the minimum energy possible. In order to reduce the track length a so-called buffer can be added, a higher-Z noble gas like krypton, which increases the stopping power but is transparent for neutrons [230]. Typically wall effect contributions of up to 20 % are accepted. Figure 60 shows the schematic of a helium-3 proportional counter and the pulse height reaction product spectrum shape obtained with such a device. Additionally at the lower end there is a continuum of background events by photons. It scales by the relative γ abundance and the volume to surface ratio of the device, as the main contribution are wall interactions [231]. Of relevance for low count rate applications is the contamination of the tube material by α-emitters [232], which can be, dependent on the composition, in the order of 10^{-4} cm^{-2}s^{-1} [233].

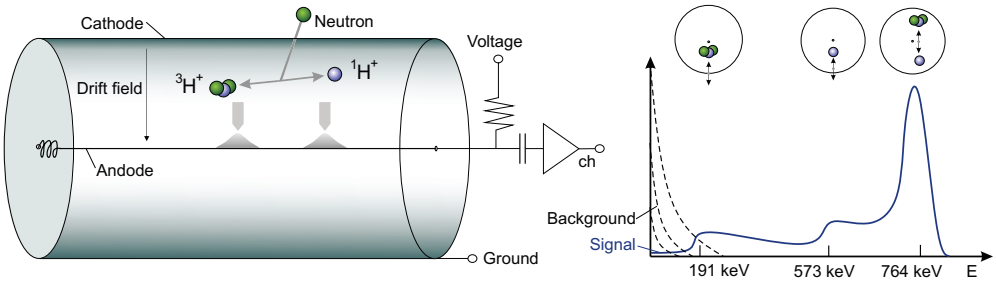

Figure 60: Schematic of a helium-3 tube (left) and pulse height spectrum (right). The neutron is converted into a hydrogen and a triton ion, which are emitted back-to-back. The primary ionization electrons drift towards the central anode with gas amplification near the wire. The pulse height spectrum is comprised of the full ionization peak and a plateau region of partial energy deposition due to wall effects.

8.2.2 | Neutron monitors

Neutron Monitors are designed to measure the hadronic component of the secondary cosmic radiation and are an example of the combination of a gas detector and a moderator. Based on the proportional neutron counter, see section 8.2.1, these systems have been developed since the 1950, whereas until the present day the standardized NM64 [234] is the most widespread unit in use[f]. Architectonically these detectors share the same components, which are depicted exemplarily in Fig. 61 for three different stages of evolution in engineering: The IGY [236] detector[g] and the

[e] For a parallel plate chamber the homogeneous field $E(x) = V_s(b-1)^{-1}$ leads to a more simplified version of 149 with only linear terms $V(t) = \frac{Q}{C}\frac{x_0-a}{b-a}\frac{b}{T_{\text{ion}}}$.

[f] Other designs possible like scintillators [235] are available but in general the term refers to the specific realization described here.

[g] abbreviation for: **I**nternational **G**eophysical **Y**ear

NM64 [234][h] detector, as well as a company-made solution [237]. The innermost component is a neutron counter tube, either filled with ^{3}He or BF_3 gas, surrounded by a low-Z moderator like paraffin, polyethylene or graphite. It is enclosed by a high-Z producer made of lead or bismuth and finally a low-Z reflector. This reflector, which can be additionally supported by a neutron absorber, prevents thermal neutrons to enter the device. High energetic particles pass this layer and generate secondary neutrons via inelastic processes in the producer. As these neutrons typically have kinetic energies in the MeV-range they have to be slowed down in the moderator before they can be detected efficiently. These systems are therefore designed the measure the fluctuations of the cosmic ray flux, see also 3.1. The main contributors to the signal can be described by simple analytical models, which holds true for the underlying physics as well as the detector characteristics. In order the address uncertainties in especially time dependencies in the model several Monte Carlo studies have been performed like [238]. A general state-of-the-art overview is provided by [239].

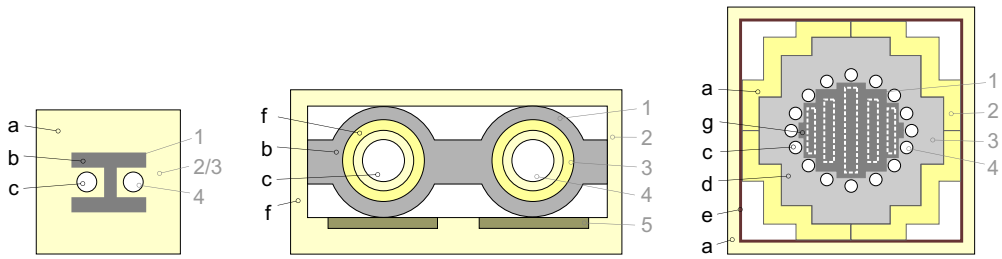

Figure 61: Schematic of three different generations of neutron monitors: The 1953 IGY [236] (left), the 1964 NM64 [234] and the 1969 Lockheed [237] Monitor. Functionally they can be separated into a producer (1), a reflector (2), a moderator (3) and a counter (4). The materials used are paraffin (a), lead (b), gas filled tubes (c), graphite (d), cadmium (e), polyethylene (f) and bismuth (g).

8.2.3 | Bonner Spheres

Bonner[i] **S**pheres (BS) are the most widely used type of neutron spectrometers. Invented in 1960 [240] the concept derives from neutron monitors by making use of the energy dependent moderation length of neutrons, see also (33). They consist of a thermal neutron sensor surrounded by spherical shells of polyethylene of different diameters. The neutron detector is typically either a ^{6}LiI(Eu) scintillating crystal or a ^{3}He proportional counter and the sphere diameters are staggered in units of 1 inch or 1/2 inch[j]. An overview is presented in Fig. 62. The arrangement covers a range of thermal energies to GeV. However, due to the statistical nature of the slowing down process, see sec. 1.4.1, each unit has a broad acceptance spectrum but peaks at a specific neutron energy according to the sphere diameter. For small diameters the number of scatterings is small as the probability of being captured, so near-thermal neutrons tend to be captured, high energetic to escape. For larger spheres the degree of moderation is high, but also the capture probability. Thermal neutrons then tend to be absorbed without reaching the counter. Consequently each sphere is assigned a response function $R_i(E)$, which can be either calculated using neutron transport theory [163], 1-dimensional transport [241] or Monte Carlo codes like GEANT4 [166] and MCNP [167].

[h] abbreviation for: **N**eutron **M**onitor.
[i] Tom Wilkerson Bonner, *1910-†1961, USA.
[j] Yet, the effective diameter of the moderator shell itself is not equal. The scintillator type sensors are much smaller, in the order of 0.5 cm, than the gaseous detectors with diameters of ~3 cm. The scaling of the polyethylene diameters in given steps can rather be regarded as a historical labeling convention.

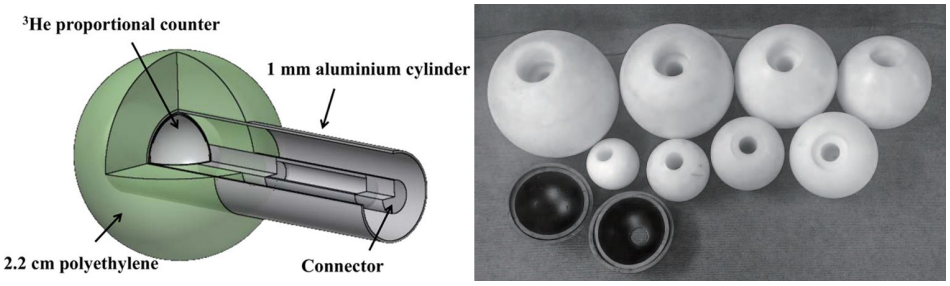

Figure 62: Buildup of a BS Detector [242] (left) and photograph of a BS spectrometer [243] (right). A single unit consists of a detector, here ^{3}He based, and spherical moderator shell. A series of such detectors with different sphere diameters, as shown here disassembled with (5-12) ", is combined to an array and additional lead producers, which can extend the range to higher energies.

If exposed to a neutron field with spectral fluence $\Phi(E)$, then the individual contribution M_i of sphere i is obtained by

$$M_i = \int R_i(E)\Phi(E)\,\mathrm{d}E, \tag{150}$$

whereas the folding operation is a Fredholm[k] integral. Typically neutron spectra are represented by discrete transport groups j, which turns (150) approximatively into a sum and the response function $R_i(E)$ into a response matrix R_{ij}

$$M_i = \sum_{j=1}^{n} R_{ij}\Phi_j \rightarrow \vec{M} = \mathrm{R}\vec{\Phi}. \tag{151}$$

In order to obtain a solution for the inverse problem, the determination of the neutron spectrum form the spectrometer it would be necessary to minimize

$$\chi^2 = \left(\vec{y} - \mathrm{R}\vec{\Phi}\right)^{\mathsf{T}} \mathrm{S}_{\vec{M}} \left(\vec{y} - \mathrm{R}\vec{\Phi}\right) \tag{152}$$

with the covariance matrix $\mathrm{S}_{\vec{M}}$. As the number of spheres m is much lower than the number of transport bins, the system is underdetermined. The unfolding [244] therefore relies on the a priori knowledge of a given neutron field, which can be motivated physically or empirically. Though neutron transport limits the amount possible solutions for (152) and procedures dedicated to the unfolding problem have been developed, the uncertainties on the full spectrum are significant [245], especially in at highest energies [246]. Especially nearly all depictions of cosmic ray neutron spectra declared as measurements are mostly a result of a Monte Carlo tuned to the measured spectrometer response.

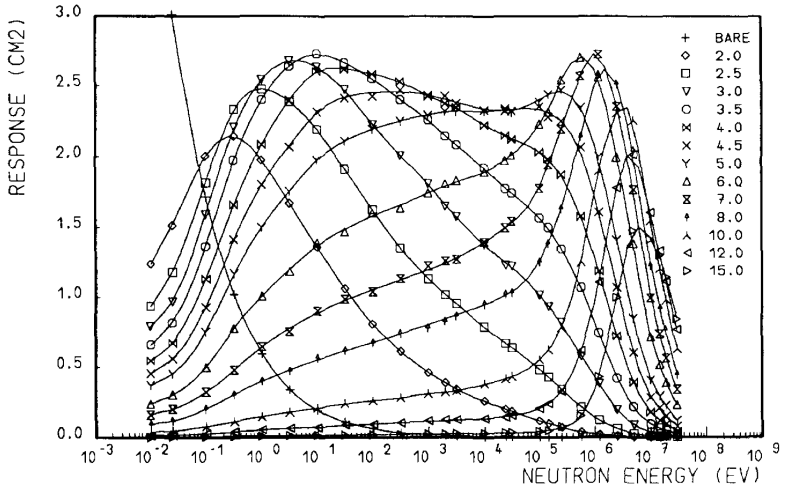

Figure 63: Energy response function of a Bonner Sphere spectrometer, equipped with a 3.2 cm ^{3}He counter, calculated with MCNP. [169]

[k] Ivar FREDHOLM, *1866-†1927, Sweden.

Until the beginning of the 2000s the community strictly relied on helium-3. Detection technologies barely evolved for their focus on wire based systems. After the so-called "Helium-3 Crisis" [247] culminated in 2010 efforts are taken in developing alternative detection systems.

Until the present day it has not become feasible to extract ^{3}He from natural resources, although the abundance in the atmosphere is about 1 ppm of the ^{4}He fraction and in some gas sources by orders of magnitude higher [249]. Virtually all helium-3 is of industrial origin, stemming from the decay of tritium, used for thermonuclear weapons as what is called a booster. Driven by the arms race in the Cold War, mainly Russia and the USA produced and stored tritium extensively, which decays by a half-life of 12.3 years to helium-3. In the beginning, due to the absence of a designated purpose, it was simply released into the environment until the potential of this resource as a neutron detector had been realized. The US government then started to accumulate it foresightfully reaching a peak amount of 235,000 liters in the late 1990s. Up to the end of the last century it has not even been considered critical that the drop out of the tritium production due to global disarmament lead consequently to a net stagnation of the contribution to the helium-3 stockpile. But caused by the terrorist threat scenario of 9/11 in 2001 [250], the US government started to install helium based radiation detectors all along their borders and in international ports to prevent radioactive material being brought into the country [251]. This demand highly exceeded the production and the US government started to release almost all helium-3 from their stockpile. In the year 2009 then a committee was set up to address the upcoming shortage leading to a policy of restricting the distribution of helium considering the leftover volume [252]. Caused by limiting the supply and the circumstance, that large companies had already requested the maximum available amount [253], the price of helium-3 raised exorbitantly from about 100 to now 2,000 dollars a liter [254][l]. This pending shortage was not clearly noticed by the majority of scientist over a quite a long period of time as research centers not least could rely on their own reserves. The J-PARC research facility itself needs for full operation approximately an amount of 100,000 liters [255], likewise for the still to be constructed European Spallation Source a similar demand was prospected [256] for its instrumented area of 130 m^2. But also the annual maintenance requests of the major research centers are more than 1,000 liters in total per year, see tab. 12, which alone is one forth of the actual yearly volume distributed to the market [257]. This suddenly raised awareness to alternative technologies to helium-3, not only to finding a replacement but also exploring new possibilities of detection. Especially concepts emerging from technologies of particle physics are asked for, as in 2013 [258] and 2015 [259] workshops in collaboration with CERN's RD51 have been held on which meanwhile a number of systems have

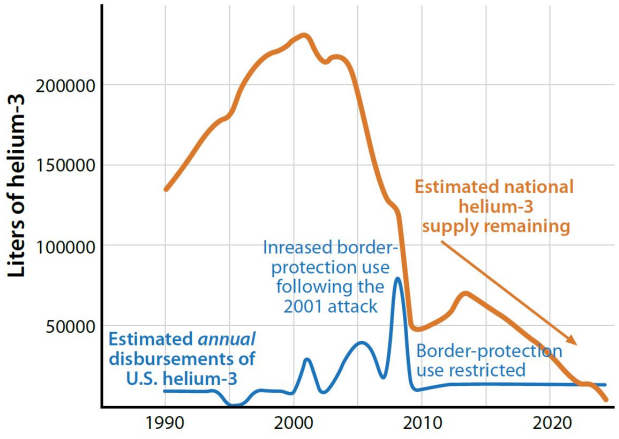

Figure 64: ^{3}He inventory in 2014: total stockpile (red) and releases (blue) [248].

[l] Yet, the real costs for industrial production would be between 11,000 and 18,000 dollars a liter. [247]

been presented.

Table 12: Projected demand of helium-3 for neutron detectors at neutron scattering facilities in the period 2009-2015 [260].

Facility	Maintenance [liter/year]	small detectors [liter]	large detectors [liter]
ORNL (SNS)	100	1,300	17,100
ORNL (HFIR)	100	1,210	1,060
Los Alamos	100	1,994	12,362
NIST	100	560	
BNL	50	180	
FRM II	100	650	4,500
HZ Berlin	100	520	7,850
ILL	100	1,000	3,000
JCNS	40	15	7,200
LLB	50	600	600
PSI	50		2,000
STFC	100	400	11,300
J-PARC	100	40	16,100
JRR-3	31	71	
BNC/KFKI	50	118	500
Sum	1,171	8,658	83,572

8.4 | State of the art

Neutrons as a new form of radiation were discovered as the methods of detection were found. The principle of generating neutrons by a beryllium emitter followed by thermalization in hydrogen containing paraffin and then conversion by lithium and boron into MeV ions has been realized as soon as 1935 [261]. This technology was sufficient for the exploration of this radiation including effects like fission. In the 1950s the interest for fast neutron detectors was the main driver in the field and one decade later the science focus shifted towards reactor physics. In the late 1960s also the turnover from boron(trifluoride) based detection systems to helium-3 tubes took place, which due to the artificially low costs of the resource, see sec. 8.3, became the standard technology. Since the 2000s the field of neutron detection had a strong boost, which led to a large variety of new systems. Fig. 65 shows the annual number of papers and citations containing the keywords „neutron“ and „detection“ indexed by the Web of Science. From the very constant baseline, which has been kept from 1970 to 2000 in the decades dominated by helium-3 detectors, a sudden steady rise in interest marks the point research on alternative systems started. This process can as well be tracked by the funding efforts for joint neutron activities in Europe in the period of the Framework Programme FP6 (2002-2006) [262], FP7(2007-2013) [263] to FP8 (2014-2020)[2] [264]. In the first period DETNI[3] [265] set the focus on the further development of the CASCADE detector and a MSGC-gadolinium based system [266] with the multichannel readout MSGCROC [267] and furthermore the n-XYTER [268] readout ASIC was designed. The parallel line of developing high pressure helium-3 detectors was discontinued[m]. The following NMI3 program [270] strongly pushed forward alternative approaches like the gas scintillation detector [271] and concepts of solid state scintillation detectors with either wavelength shifting fiber

[2] *Horizon 2020*

[3] *Detectors for Neutron Instrumentation*

[m] There is no publication available on the MILAND project (ILL) except the web presentation [269].

and silicon or standard photomultiplier readout[n]. Boron based technologies were developed for single layer converters with a Micromegas readout [274] and wire based systems with grooved cathodes [275] or modules inclined towards the beam [276]. The latter ones especially were prototypes for different boron or boron carbide coating techniques like magnetron sputtering, electron beam evaporation and plasma powder spray deposition. In the actual SINE2020 [277] program the efforts broadened to a large extent. Besides the continuation of the NMI3 projects, already abandoned technologies in new garments are proposed like zinc sulfide scintillators and helium-3 microstrip chambers, and technology transfer from particle physics is encouraged like adapting a Resistive Plate Chamber [278].

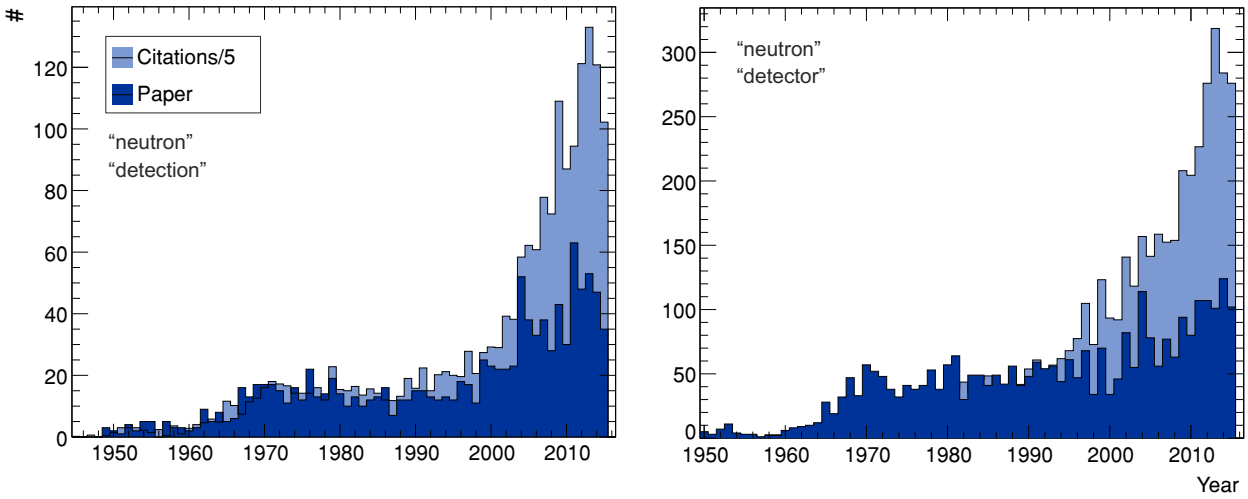

Figure 65: Annual number of papers (blue) and citations on papers (light blue) containing „neutron“ „detection“ (left) or „detector“ (right) in their title [279].

The basic characteristics of a neutron detector are:

1. spatial resolution,
2. time resolution,
3. detection efficiency,
4. gamma suppression or neutron gamma separation efficiency,
5. radiation hardness,
6. active area,
7. rate capability.

There is a manifold of systems currently under development. A summary about technological aspects regarding different applications before the 2000s can be found in [280]. The actual technologies pursued are those which are necessary for the operation of the European Spallation Source [202]. In order to sketch an overview, in the following solutions are grouped according to converter and detection medium.

[n] no publication available from JCNS or ISIS, informal report under [272]. The system is similar to the one presented in [273].

8.4.1 | Charged particle detection

8.4.1.1 Boron trifluoride

Before the widespread availability of helium-3 the majority of detectors used BF_3 as a converter and a counting gas like in [281]. Form factors and technological requirements for both fillings are identical, therefore systems are operated equally by fallback to boron trifluoride. However, its hazardous handling due to toxicity and acidity restrict the range of applications.

8.4.1.2 Boron lined

Using boron-10 or boron-10 carbide coatings requires a hybrid system with a separate gas amplification stage. In the most simple case keeping the tube form factor inside surfaces are coated like in the case of the tubelet [282] detector. By introducing a star-shaped cathode the effective amount of boron can be increased like in the case of the straw module [283]. Planar detectors can also be operated with surface-enlarging cathodes [275]. Other methods which increase the detection efficiency per unit area are the inclination of panels towards the beam direction [276] and the stacking of several similar units in a row [284]. In order to increase the spatial resolution for small active areas readouts based on highly granular devices like the Micromegas [285] chip have been tested [274]. By introducing time based track reconstruction [286] the origin of the conversion product can be located by means of a time projection chamber [287].
Another possibility to achieve a high time resolution is the resistive plate chamber [288], which can be realized by coating boron layers on thin gap separated insulators which are short circuited by the conversion ions [278].

8.4.1.3 Semiconductor electronics

Homogeneous and hybrid detectors can be realized based on semiconductor technologies which have been also employed in high energy physics experiments. Though large efforts have been done to develop radiation hard sensors typical electronics cannot withstand direct neutron beam exposure, limiting the application to a low flux or low energy environment. Systems based on diode junctions have been developed [289], which use a boron-10 doped depletion zone. In order to achieve a good charge carrier transport efficiency pillar structures, so called 3D detectors, are favored [290], which can be single or double sided [291]. Combinations of several layers of such sensors and different moderator thicknesses allow the design of a spectrometer [292].
The latest development in CMOS based particle detection are Monolithic Active Pixel Sensors (MAPS) [293], which integrate the charge collection and digital electronics in each pixel. Such sensors, fully depleted [294], can be back-thinned and backside coated to be used as a thermal or fast neutron detector [295]. Hybrid systems have been realized based on the highly granular MediPix [296] and TimePix [161] chip family, which itself is already a hybrid sensor with separated readout and semiconductor converter, that additionally can be coated by lithium or boron. Such detectors have been presented on the basis of the MediPix [297], the MediPix2 [298] and the TimePix for ultra cold neutrons with track reconstruction [299].

8.4.1.4 Various technologies

Due to its high capture cross section numerous attempts for gadolinium-157 based detectors have been carried out, which in general have to cope with gamma-ray rejection as the neutron conversion signature of low energy electrons is much weaker than ions [300]. One specific realization to overcome this problem is the use of an additional

caesium iodide converter foil [266] and a microstructured readout (MSGC) [301]. Another attempt aims at thorough event reconstruction with spatial and time resolved detectors [302], which requires that conversion electrons from the gadolinium layer are discriminated against other backgrounds due to their energy deposition and ionization track topology.
As well uranium-235 exhibits a high cross section and can at least in an reactor environment be used in form of a coating on the inside of a gaseous proportional counter [303]. Further approaches of replacing the gas in a standard counting tube are for example using a ^{10}B nanoparticle aerosol [304].
Monolithic systems have been presented using boron nitride polycrystalline grains, which are embedded in a binder [305] or lithium-borosilicate aerogel [306]. Different technologies made use of boron loaded liquid organic scintillator detector, which uses photoelectron conversion and afterwards GEM amplification stages [307]. Boron doped glass allows for an efficient detector [308] using the multi-channel-plate (MCP) technology with a TimePix readout [309].

8.4.2 | Photon detection

8.4.2.1 Scintillation plates

Scintillating materials with non-gaseous detectors are especially used in high resolution applications like neutron imaging [310], that typically combine a scintillating plate which is enriched by Gd or Li, read out by a CCD or CMOS camera. The scintillating plate can either be a homogeneous or a thin film scintillator on a wafer. The light is then optically transported by lenses to the remote camera. For such systems resolutions up to 7.6 µm have been achieved [311]. Up to now in the current systems there is no dedicated neutron optics applied, but the introduction of Wolter[o] mirrors [312] is planned.

8.4.2.2 Gaseous scintillation

A standard helium-3 tube can be equipped with a photomultiplier as by using an optimized mixture of ^3He and CF_4 a sufficient amount of scintillation light is produced [271]. Another gas scintillation detector has been realized by coating a carbon foam web by boron, which by its open area can transport photons to a side-on readout device. This technique meanwhile was also realized using GEMs as charge amplifiers while recording the scintillation light from the holes by a CCD [313].

8.4.2.3 Solid state scintillation

One of the most widespread technique is the use of lithium loaded fibres. Such a detector requires a neutron converter, a scintillator, a lightguide, optionally a wavelength shifter, and a photosensitive element. As scintillating material most often zinc sulfide is chosen. A simple detector with ZnS(Ag) and LiF is presented in [314]. An effective detector, which uses a sandwich-structure and a wavelength shifting fibre readout, can be realized as a 2D position sensitive device [273]. Recently by advances in coating techniques it has also been managed to build a ZnS(Ag) detector with boron [315].

[o] Hans Wolter, *1911-†1978, German Empire.

9

THE CASCADE DETECTOR

The CASCADE thermal neutron detector is based on thin films of 99 % enriched ^{10}B. The conversion products create a signal by ionization in the active detection volume filled with the standard counting gas Argon:CO_2 of mixtures from (70:30) to (88:12). To overcome the limited efficiency of a single film of (5-7) % at 1.8 Å a stack of several converter layers is required. The detector, see Fig. 67, is comprised of GEMs [316], which act as a substrate for the converter as well as they are charge transparent. It is further possible to detect the positive signal on the GEM surface in addition to the negative electron signal on the microstructured readout. This allows to identify the origin of the neutron conversion as the charge can be tracked while traversing through the stack. Grids are inserted in-between each stage in order to decouple the GEMs electrically and to limit the generated charge. The CASCADE detector in this work is based on 6 layers divided into two half-spaces.

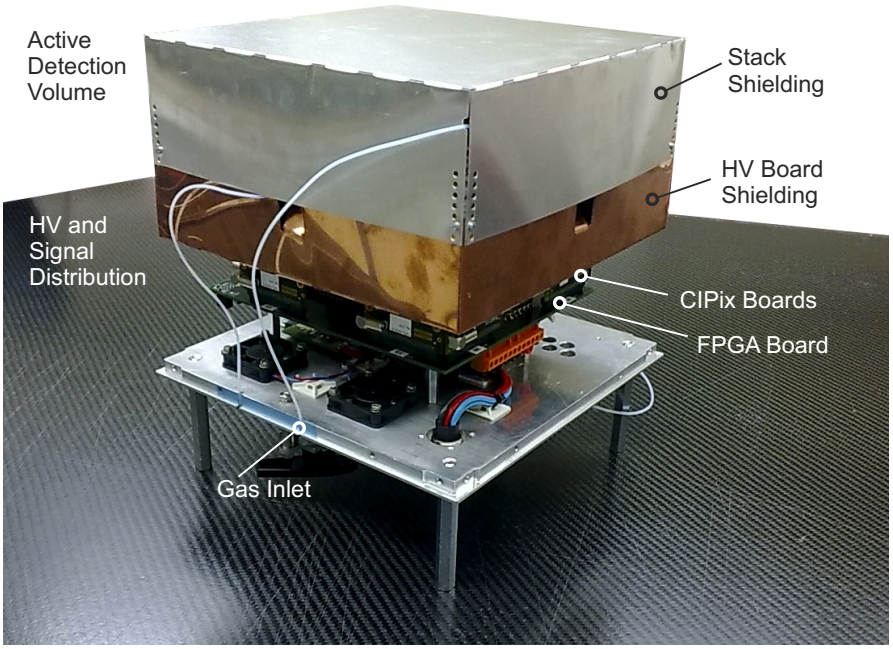

Figure 66: Overview: the Cascade Detector without housing and all subsystems completely assembled. The detector consists of the active detection volume with its two half spaces and the double sided readout, the high voltage distributor board and the readout electronics, which are a combination of the multi-channel preamplifier ASICs CIPix and an FPGA board for the data pipeline including an event identification algorithm.

9.1 | VERSION HISTORY

The CASCADE project was launched in 1999 with the goal to build the first efficient multi-layer detector, which would later be suitable for the needs of Spin Echo spectrometry. The necessary specifications for spatial and time resolution could only be met by using a solid state converter in combination with highly integrated readout electronics. The foundation of the CASCADE family was laid when it had been achieved in a first prototype [317] to coat GEMs [316] by thin layers of enriched boron-10 [318]. Different coating techniques have been tested and on the basis of the microstrip anode (MSGC) [319] according to examples already existing at the ILL [320] and a readout infrastructure has been realized. Analytical calculations have been developed which enable to determine the maximum efficiency and ion kinematics for various boron layer

configurations and beam properties. Slightly adapted, this framework was also used for describing later detectors like the Jalousie [321, 322] and MIEZE systems [323][a]. The first multilayer prototype [327] used a onedimensional 10 cm × 10 cm stripe readout and was based on the concept of achieving an effective gain of 1 between each layer of the stage but the last before the readout. This functionally separated the system into so-called transfer-GEMs and gain-GEMs. The CIPix was adapted in 2001 [328] to equip the system with highly integrated readout electronics. It was successfully tested in measuring energy spectra [329] at the PSI cold neutron source [330], for which later a dedicated VCN[b] version was developed [331]. Until 2005 the system had undergone a complete redesign [332]. The twodimensional readout in an extension of 20 cm × 20 cm was developed featuring 128 stripes on each side. The total of 256 channels were read out by 4 CIPix units, joined on a Virtex II FPGA board operated in a 10 MHz trigger&tape mode. It was furthermore possible to implement a DDR memory controller to address besides the 16 MB of SRAM another 1 GB of dynamic memory [333]. This system could be tested [334] in a setup at the RESEDA spectrometer [82] in order to determine a limit for the neutron - mirror neutron oscillation [335] time. The detector turned out to be not stable in operation for technical reasons and conception of the event reconstruction algorithm [336] and following in a ongoing series of iterations these problems were addressed individually. As the CASCADE detector was included in the DETNI FP6 framework programme [265] the development of the nXYter ASIC [268] offered the possibility to switch to a more sensitive amplifier. First tests of the chip were conducted, in particlular to additionally adapt the detector to the requirements of a MIEZE instrument [337], but as it took a total of six years to develop the chip [338] and only the resources of a larger FPGA allowed to fully implement the S3 algorithm [339], this improvement could not be realized. The nXYter development continued for other projects [340] and the chip could be finally implemented in a entirely redesigned prototype [341], which also allowed to acquire the spatial information from a segmented GEM rather than from a dedicated readout board. The first Spin Echo measurements on a single foil at RESEDA were recorded in 2009 [342]. The signal crosstalk in-between the layers had to be reduced by at least one order of magnitude to allow to reconstruct the full unambiguous event information, which could be achieved by adding metal meshes to each GEM and abandoning the transfer-and-gain concept [343].

9.2 | THE ACTIVE DETECTION UNIT

The GEMs are numbered from 1 to 6 in direction of the beam axis. The typical spacings are 2.2 mm with 1 mm for each of both metal frames of the GEM and 0.2 mm for GEM, glue and PTFE[c] spacer. The geometry of the detector with the actual spacings between the layers are listed in tab. 25 in appendix B.1.2. However, one can approximate the distances between the (boron) layers in Fig. 67 to (2.2-4.8) mm.
Functionally there is a distinction between the twodimensional imaging mode and the time-of-flight (TOF) mode with additional time information. In the latter one besides the spatial event reconstruction from the readout board a correct z-layer identification is required. Due to the high readout capacity of the whole GEM surface, the sensitivity of the z-channel is lower, therefore tracks with a small energy deposition have a significantly weaker signal strength.

[a] In parallel similar analytic or semi-analytic approaches have been reinvented in [324], in a simple version, and more developed in [325] and then later in [326].
[b] VCN stands for **v**ery **c**old **n**eutron, see also tab. 2, and requires only one layer.
[c] Polytetrafluoroethylene, also known by the trademark Teflon.

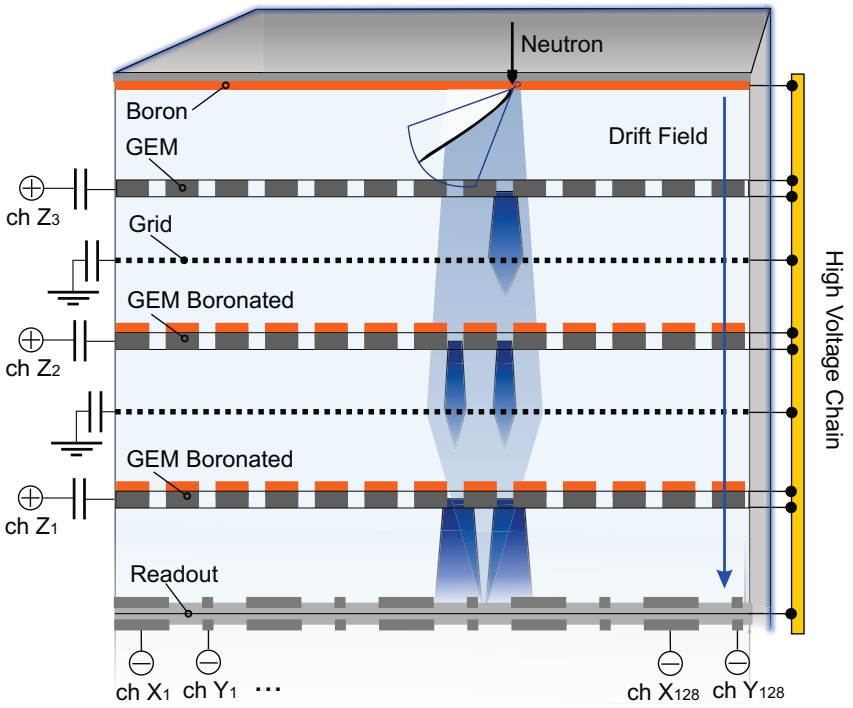

Figure 67: Schematic of the CASCADE detector of one half space: Thermal neutrons are converted in boron layers (orange), which are either coated on the aluminum casing (top) or on GEMs (below). The conversion products, lithium or helium, which leave the boron, deposit a fraction of the total kinetic energy of up to 2.7 MeV ionizing the counting gas. The semi-transparent GEMs compensate for the charge loss by gas amplification in strong electric fields in the holes. The electrons are projected towards a double sided readout with crossed stripes and additionally the signal induced on the GEMs is measured. [K2016b]

The active detection volume is shielded to the back by a strong neutron absorber (^{6}LiF-/^{10}B based mats). It suppresses the radiation intensity for the readout electronics, which is mounted directly behind, by at least 10^{6}.

9.2.1 | Boron converter

Neutrons are converted into ion fragments by boron-10 via a nuclear caption reaction with the two branches:

$$
\begin{aligned}
&^{10}\mathrm{B} + \mathrm{n} \rightarrow \\
&^{7}\mathrm{Li}(0.84\,\mathrm{MeV}) + \alpha(1.472\,\mathrm{MeV}) + \gamma(0.48\,\mathrm{MeV}) \\
&^{7}\mathrm{Li}(1.013\,\mathrm{MeV}) + \alpha(1.776\,\mathrm{MeV}).
\end{aligned}
$$

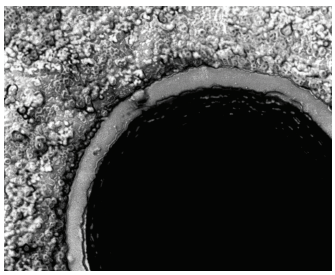

Figure 68: Microscope image with focus stacking: hole of a boron-coated GEM.

Both of the fragments are emitted back-to-back and one of both enters the gas volume. For more information see sec. 8.1, sec. 6.5.2 and later the analysis of sec. 11.1.
Whereas layer 1 and 6 are boron coated drift cathodes followed by a GEM, the in-between stages are single sided boron coated GEMs. The individual thickness of the layers according to the specifications by the manufacturing from top to bottom are: 1.5 µm, 0.8 µm, 0.99 µm, 0.95 µm, 0.8 µm and 2.0 µm. After the first measurement campaigns the original back-side drift cathode has been replaced by one with a 1 µm coating.
In the CASCADE detector the emission spectra, see Fig. 94, will be tallied approximately at 500 keV of energy deposited in the gas. The maximum track length of the conversion

products of about 10 mm in Argon:CO_2 is much higher than available from the spacing between the layers of (2-4) mm.

9.2.2 | Gas amplification stage

The potentials of the layers within the active detection volume are defined by a voltage divider of in total 31 MΩ, see also Fig. 69. Therefore, all electric fields are linked to a fixed ratio by the choice of the individual resistor values, which are provided in tab. 13. The main tuning parameter for the operation of the detector is the gas amplification, which is defined by the voltage difference between top and bottom side of the GEM and the gas mixture. As the ratio between the transfer fields above and below the GEM are scaled by the same ratio as ΔV_{GEM}, the charge collection and charge extraction efficiency are approximately constant. Grids are inserted in-between two GEMs in order to reduce the effective gas gain and to capacitively decouple the system.

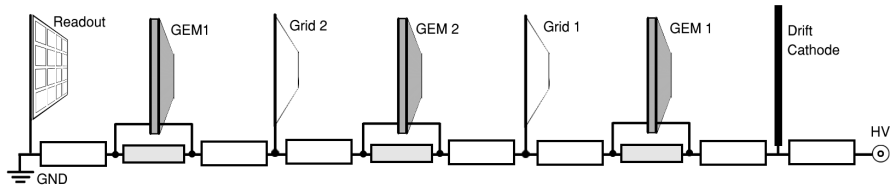

Figure 69: Simplified schematic of the voltage divider of one half space of the CASCADE detector. Resistors of in total 31 MΩ have the values 1 MΩ for the HV protection, 2 MΩ for the drift cathode, 3 MΩ for the transfer fields to the grids and 4 MΩ for the GEM potentials. The readout board is effectively at ground potential, the individual stripes have a virtual ground through the charge amplifiers. The spark protection resistors for the GEMs are not shown.

Table 13: Voltage divider configuration and effective field strength values for a low and a high amplification example in the active detection volume. The actual spacings of the detector are listed in tab. 25 in appendix B.1.2.

	HV protection	Drift Field	Transfer Field	GEM
Resistors [MΩ]	1	2	3+3	4
Distance [mm]	-	2.25	2.25	0.05
total voltage divider potential difference: 2600 V				
Potential difference ΔV [V]	-	168	252	336
E-Field [kV/cm]	-	0.75	1.12	67.1
total voltage divider potential difference: 2950 V				
ΔV [V]	-	190	286	381
E-Field [kV/cm]	-	0.85	1.27	76.1

9.2.3 | High voltage distributor board

The high voltage distributor board interfaces the active detection volume and the readout electronics, i.e. the CIPix ASICs and the FPGA board. The individual layer potentials within the GEM stack are defined by a voltage divider, which consists of a series of resistors as shown in schematic 69 in sec. 9.2.2 and corresponding decoupling capacitors. Fig. 70 shows one unit cell from the copper and decal layer of the PCB, which serves for defining potentials for a GEM and a grid. Each GEM is connected to its top and bottom side to one voltage divider pick-off by an additional resistor of 1 MΩ, which reduces the current in case of sparks. The bottom side of the GEMs

is connected by a coupling capacitor to the T-CIPix channels via a multiplexer[d]. All potentials are connected to ground by a decoupling capacitor. Footprints are rounded and all traces feature teardrops avoiding edges in the high voltage distribution line. The decoupling will be discussed in sec. 10.2. Additionally, the high voltage board acts as a feed-through for the signals from the strips to the X/Y readout ASICs. This can be seen in the full-scale view of Fig. 162 in appendix B.1.5.

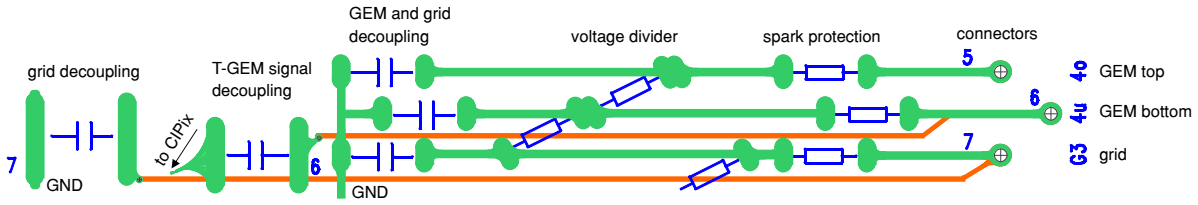

Figure 70: Unit cell of the redesigned high voltage board. The voltage divider (slanted resistors) with spark protection allows for up to five layers of GEMs and grids in two half-spaces. Each grid is decoupled by a ground capacitor and each GEM is read read out via a capacitor which is connected to the T-GEM CIPix ASIC. Top and bottom side of the board use different colors for the traces.

9.2.4 | Crossed stripes readout structure

The crossed-stripes readout printed circuit board is comprised of 128 × 128 channels for the x- and y-directions at a total area of 200 mm × 200 mm. Each direction is read out independently read out and by correlating both signals in by software or firmware the detector features $2^7 \times 2^7 = 16{,}384$ pixels with each an area of 1.56 mm × 1.56 mm. Fig. 71 shows a sketch of an elementary unit cell with each pixel being furthermore subdivided into one x-row and one y-column segment by a comb-like structure in order to achieve an equal charge deposition coverage. A macro-cell consists of 2×2 elementary cells, which are rotated against each other. The strip-to-strip capacity is approximately 30 pf, however, as the readout is arranged in units of the mentioned macro-cells the capacity of even and odd stripes is not identical, which leads to a slightly different charge sensitivities.

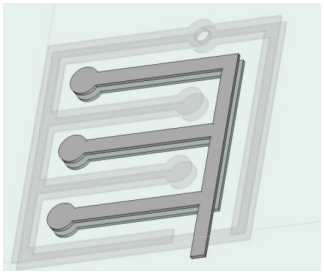

Figure 71: Unit cell of the cross stripes readout board with a spatial extension of 1.56 mm [332].

9.3 | Readout and data unit

The readout electronics of the CASCADE detector consist of two main components. Signals from the active detection volume, i.e. the crossed-stripes readout board and the GEMs, are fed into charge-sensitive multi-channel preamplifier ASICs. They are operated at a constant frequency of 40 MHz, which is scaled down by a factor of 4, leading to a time resolution of 100 ns. In total 5 CIPix boards are present in the system, whereas 4 are reserved for the (x,y) readout and one for the z coordinate. The latter one are signals from the GEMs of inverse polarity. The digital signals are handled by a Virtex II FPGA board, which can either produce a zero-suppressed raw data output or it can analyze the data patterns by firmware algorithms in the triggered event mode. This generates and stores ready-to-use histograms, for example for time-of-flight

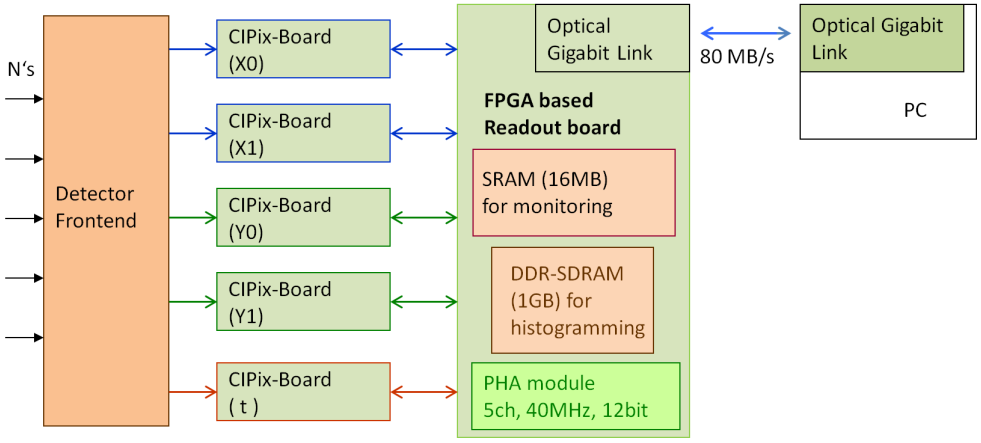

Figure 72: Block diagram of the main components of the CASCADE detector from the analog frontend to the data acquisition computer (PC). Signals as measured by the multi-channel CIPix ASICs (x/y stripes (4×) and layer-ID (1×) and transmitted to the FPGA with its event reconstruction algorithm.

measurements, or in the Spin Echo mode in combination with a phase locked loop unit (PLL) it allows to measure the polarization of the Spin Echo group.

9.3.1 | CIPix ASIC

The CIPix chip is 64-channel ASIC manufactured in the AMS[e] 0.8 µm process and designed for operation at 40 MHz. It is comprised of a low noise charge sensitive preamplifier followed by a shaper and a common threshold discriminator. The signals of each channel are digitized by an AC-coupled comparator of both polarities. Fig. 73 shows the die in a close-up.

9.3.1.1 Version history

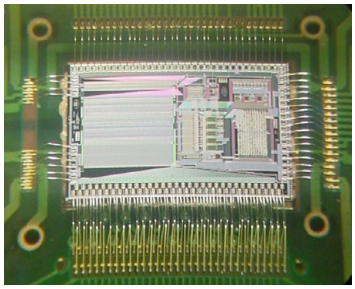

Figure 73: Bump bonded CIPix with a die size of 4.04 mm × 6.615 mm [332].

In 1991 within the RD20 collaboration at CERN a proposal [344] for high resolution silicon strip detectors at the Large Hadron Collider [345], in particular for tracking near the interaction region, has been formulated. This led until 1993 to the development of the FElix chip [346, 347], which consists of a preamplifier, shaping amplifier and of an analog delay and buffer to be operated at 67.7 MHz. Based on this architecture for the HERA-B [348] experiment at HERA [349] a new version of the chip had been developed for the silicon vertex and inner tracker microstrip detectors. After test submissions in 1995 of 32 and 128 channel versions HELIX32 and HELIX128 [350] for a trigger rate of 40 MHz, the HELIX2 chip [351] was released in 1996 and successfully in operation. An overview about the family and the submission line is given in [352]. In the following, enhanced versions [353] have been applied as radiation hard readout chips in the vertex detector upgrade of the HERMES [354] experiment (HELIX2.2) and the ZEUS [355] Microvertex Detector (HELIX3). Its successor, the Beetle chip [356], is still in operation in the readout section of the LHCb Vertex Detector [357]. The CIPix was developed [358, 359] and adapted [360, 361] at the ASIC laboratory in Heidelberg as a 64-channels-stripped-down-version of the HELIX series to equip the front end electronics of the MWPC-based central inner projection chamber (CIP) [362] of the H1 [363] experiment at HERA.

[d] For the X and Y stripes all 64 channels of a CIPix are used. For the layer identification, however, only 6 channels are necessary. Therefore, the multiplexer allows to choose between 4 different channels, especially as the amplifiers connected to the GEM-channels are prone to be damaged by high currents.

[e] austriamicrosystems AG

9.3.1.2 SPECIFICATIONS

The frontend ASIC features 64 channels with each

- a low now noise charge sensitive preamplifier for both signal polarities. The circuit is designed as a folded cascode amplifier [364], see also the schematic in Fig. 74. It can be operated at a gain of 50 mV per 10^5 electrons and a noise level of 380 e^- + 38 e^-/pF,
- a CR-RC shaper with a semi-gaussian pulse shape at a peaking time of approximately 60 ns,
- a comparator with a sampling frequency of 10 MHz and both polarities.

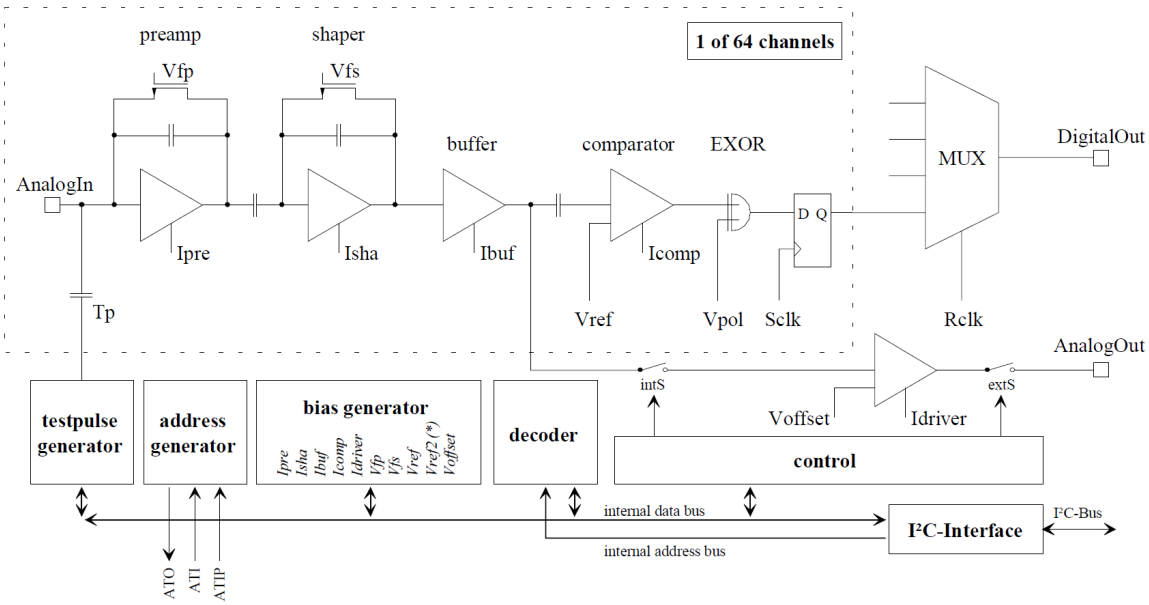

Figure 74: Block Diagram of the CIPix ASIC with focus on one channel. [358]

The CIPix 1.1 ASIC is bump bonded to the AS20B-1.1 PCB [365]. It features the slow control of the CIPix registers via I^{2}C (**I**nter-**I**ntegrated **C**ircuit) [366], 64 data channels and one analog output channel. All input channels are protected by a high speed switching diode and a 300 Ω series resistor (earlier versions 100 Ω).
Although the chip is operated at s 10 MHz system clock each channel and therefore each strip of the readout board, can accept statistical data up to a rate of approximately 330 kHz at a dead time of 10 %.

9.3.2 | THE FPGA BOARD

All data channels are fed into the FPGA board CDR 1.0. It hosts a Virtex II XC2V3000-BF957 FPGA [367] with 3,000,000 system gates, 14,336 slices, 12 DCMs, 1,728 Kb internal RAM and 720 User-I/Os [332]. The communication via an 80 MB/s optical interface (SIS1100 [368]) allows to operate the detector galvanically[f] isolated to the data acquisition computer. It furthermore connects to the IF-15 ADC card developed by the electronics workshop in Heidelberg, which allows a 4-channel parallel signal analysis for diagnostic purposes. In typical neutron applications particles are detected stochastically. Self-triggered ASICs like the nXYter [369] would allow for an inherent zero-suppression, however, the CIPix is derived from an ASIC developed for purposes

[f] Luigi Aloisio GALVANI, *1737-†1798, Papal States.

of high-energy physics with the frontend typically operated at the same frequency as the instrument event rate, e.g. the bunch crossing rate. Therefore, the ASIC delivers 64 bit of information every 100 ns, which have to be analyzed and zero-suppressed on the FPGA board by a later described algorithm. One important feature, however, is the possibility to use a **p**hase-**l**ocked **l**oop (PLL) circuit, which realizes a system trigger linked to the Spin Echo frequency. This allows to directly add up all events in-phase. The PLL generates a 17× higher frequency than its input frequency, which oversamples the sinusoidal signal by a factor of 16. The 17th time bin is later added to the first bin. This technique guarantees a jitter-free recording, which is important as the polarization, being the final Spin Echo observable, requires, that the interference pattern is commonly recorded in phase. A detailed description of the functional components is provided in [332] and [323].

9.3.3 | Firmware

The event processing follows a pipeline structure, which is shown in Fig. 75. After preprocessing of the incoming data from the ASICs the channels are mapped onto the geometry of the detector. For each 100 ns cycle a time stamp is added, which can either be a system clock counter or an external reference bin counter, which facilitates the histogramming in Spin Echo measurements. This data is stored in a FIFO (**F**irst **I**n - **F**irst **O**ut) queue. However, the firmware does not support asynchronous readout of the raw data memory. It takes around 75 ms to transfer the 4096 elements, which would correspond to a zero-suppressed[g] event rate of 5 kHz at a duty cycle of 50 %. Therefore, there is an onboard real-time histogramming and reconstruction algorithm. This „event builder“ analyzes the incoming data according to the correlation patterns, which will be described later. This unit has been especially redesigned in the course of this work in order to allow a correct GEM identification. More information can also be found in [370].

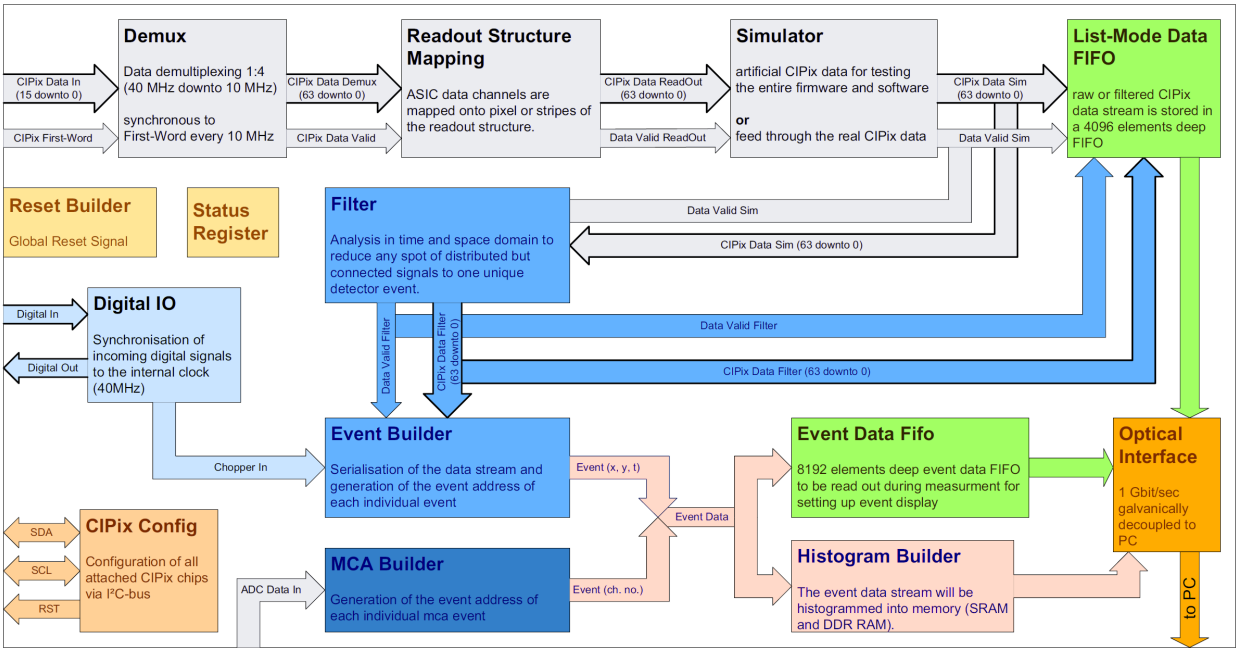

Figure 75: Block Diagram of the pipline structure for the functional units of the CASCADE FPGA firmware. [323]

[g] Zero suppressing in case of the CASCADE firmware means that time slices with no channel information are omitted.

Most of the analysis in this work has been carried out on the CASCADE raw data. The detector itself features 256 channels for the x and y coordinates and 6 channels for the layer identification, the so-called T-GEM. Each channel information is binary (hit/ no hit). Including the 12 bit counter in total 39 Byte are stored in units of 100 ns time stamps. Tab. 14 shows the data flow as it is provided by the firmware.

0x0000	0x000003db	0x00000000	0x00000000	0x00000000	0x00000000	0x00000000	0x00000000	0x00000000	0x00000000	**0x20**
0x0000	0x000003dc	0x00000000	0x00000000	0x38000000	0x00000000	0x00000000	0x000001e0	0x00000000	0x00000000	**0x30**
0x0000	0x000003dd	0x00000000	0x00000000	0x18000000	0x00000000	0x00000000	0x000001e0	0x00000000	0x00000000	**0x30**
0x0000	0x000003de	0x00000000	0x00000000	0x10000000	0x00000000	0x00000000	0x00000020	0x00000000	0x00000000	**0x36**
0x0000	0x000003df	0x00000000	0x00000000	0x00f80000	0x00000000	0x00000000	0x0000000e	0x00000000	0x00000000	**0x37**
0x0000	0x000003e0	0x00000000	0x00000000	0x00f80000	0x00000000	0x00000000	0x00000004	0x00000000	0x00000000	**0x17**
0x0000	0x000003e1	0x00000000	0x00000000	0x00000000	0x00000000	0x00000000	0x00000004	0x00000000	0x00000000	**0x17**
0x0000	0x000003e2	0x00000000	0x00000000	0x00000000	0x00000000	0x00000000	0x00000000	0x00000000	0x00000000	**0x17**
0x0000	0x000003e3	0x00000000	0x00000000	0x00000000	0x00000000	0x00000000	0x00000000	0x00000000	0x00000000	**0x13**
0x0000	0x000003e4	0x00000000	0x00000000	0x00000000	0x00000000	0x00000000	0x00000000	0x00000000	0x00000000	**0x01**
0x0000	0x000003e5	0x00000000	0x00000000	0x00000000	0x00000000	0x00000000	0x00000000	0x00000000	0x00000000	**0x01**
0x0000	0x000003e6	0x00000000	0x00000000	0x00000000	0x00000000	0x00000000	0x00000000	0x00000000	0x00000000	**0x01**
0x0000	0x000003e7	0x00000000	0x00000000	0x00000000	0x00000000	0x00000000	0x00000000	0x00000000	0x00000000	**0x01**
0x0000	0x000003e8	0x00000000	0x00000000	0x00000000	0x00000000	0x00000000	0x00000000	0x00000000	0x00000000	**0x01**

Table 14: Example for the hexadecimal raw data output with the first two column representing the clock cycle counter, the following eight columns the 128 x- and 128 y-stripes and the last the T-GEM. Early firmware from 2012 and GEM stack at 2675 V.

The relevant information without the time counter are extracted in the following cutout, which shows on the left side the actual data and on the right side the translation into binary patterns in ascending order, whereas the arrows for the GEM information indicate the direction of the charge projection from both half spaces.

X stripes	Y stripes	T-GEM	X stripes	Y stripes	top→	←bottom
0x00000000	0x00000000	**0x20**	□□□□□	□□□□□□□	□■□	□□□
0x38000000	0x000001e0	**0x30**	□□■■■	□□□■■■■	□■■	□□□
0x18000000	0x000001e0	**0x30**	□□□■■	□□□■■■■	□■■	□□□
0x0000000	0x00000020	**0x36**	□□□□□	□□■□□□□	□■■	□■■
0xf8000000	0x000000e0	**0x27**	■■■■■	■■■□□□□	□■■	■■■
0xf8000000	0x00000040	**0x17**	■■■■■	□■□□□□□	□□■	■■■
0x00000000	0x00000040	**0x17**	□□□□□	□■□□□□□	□□■	■■■
0x00000000	0x00000000	**0x17**	□□□□□	□□□□□□□	□□■	■■■
0x00000000	0x00000000	**0x13**	□□□□□	□□□□□□□	□□■	■■□
0x00000000	0x00000000	**0x01**	□□□□□	□□□□□□□	□□□	■□□

In the example one identifies two hits following each other. With four hit stripes those are larger than average. One originates from the second GEM in the top half space and the following one starts from the drift cathode in the bottom half space. In this example one cam identify some features of the data topology of the conversion tracks:

- GEM channels can provide event information 100 ns before the x/y readout,
- the time over threshold for the crossed stripes is limited to a few clock cycles, whereas the GEM signals are much longer present,
- charge signals are much longer detectable on GEMs close to the readout.

10

THE CASCADE DETECTOR REWORKED

10.1 | THE LAYER IDENTIFICATION CHALLENGE

At the beginning of this work first tests had been carried out with the CASCADE detector, but the system had not yet been characterized. As far as the earlier developed crossed-stripes readout showed an expected response, the GEM layer identification was working largely erroneous. The measured intensities did not correspond to what could be anticipated by the boron coating thicknesses. Yet, it was not a simple threshold effect, as the layer assignment seemed to be not conclusive. This could be seen in [342], where in a Spin Echo measurement each layer delivered signals, which seemed to not correspond to the same Spin Echo curve[a]. The reasons are misidentification and misassignment in an otherwise already challenging system. Without a clean layer separation for the conversion events a Spin Echo measurement is not possible. The decisive problem is, that a false negative assignment in the detector can easily lead to a type I error. Then, the signal of a sine function in one layer is added ontop of another sine function corresponding to a different phase space. This leads to a phase shift and a decrease of the amplitude in the reconstructed interference pattern, which depends on the Spin Echo frequency and neutron wavelength. As in measurements of sample dynamics for example, i.e. quasi-elastic scattering, the loss of polarization is measured as a function of Spin Echo frequency, the results would be highly inaccurate.

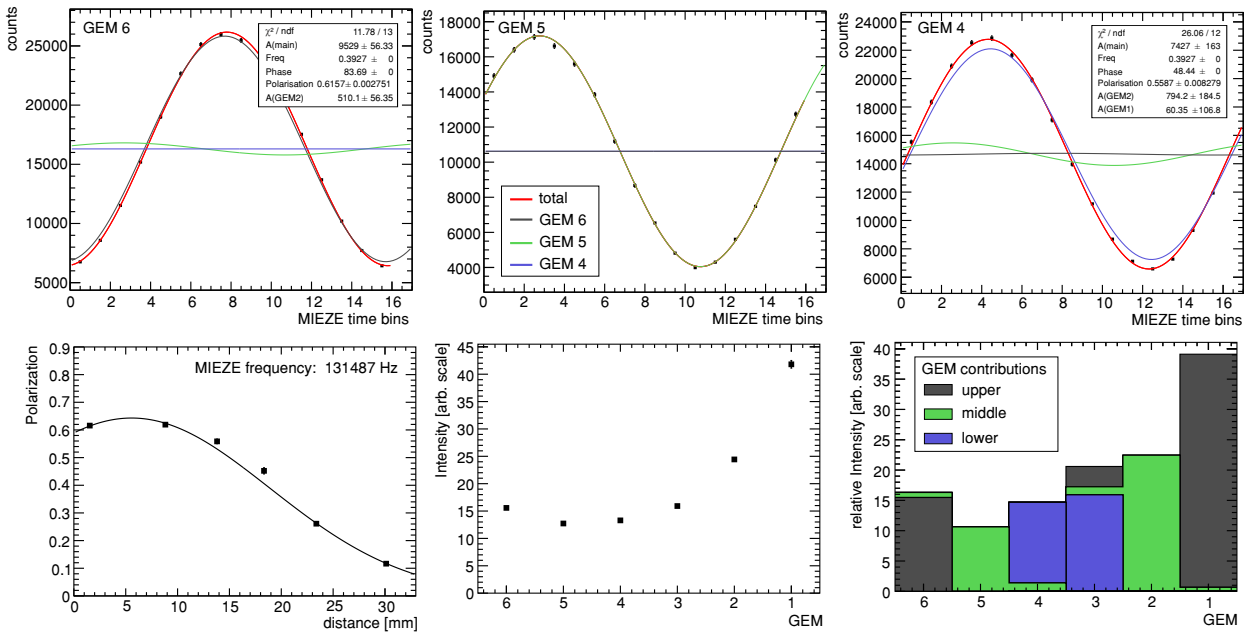

Figure 76: Spin Echo analysis for the crosstalk between layers. The signals from each GEM (top row for one half space of the detector) are fitted by sine functions which correspond to different space-time coordinates of the same Spin Echo group. For phases fixed by the geometry of the detector, a congruent description, especially for the polarization (lower left panel) is possible by allowing contributions of other layers (lower right panel). Measurements taken already with the improved capacitive decoupling described in sec. 10.2.

[a] As it will be seen later in sec. 11.2.1 the interference pattern can be probed by the detector in a highly coherent way.

The problem of wrong layer assignment could be identified after rigorously fitting a Spin Echo group function to the data with the fixed known layer distances. The signals from each layer have to correspond to the same waveform in phase, frequency and polarization. The procedure and the result is shown in Fig. 76. It turned out, that a comprehensive description was possible, if small additional contributions from sine functions with phase and polarization corresponding to the other layers, were allowed. Several reasons for this misidentification were found. The event filter algorithm was not adapted to the actual data structure as displayed in sec. 9.3.4, its design was based on generic assumptions on possible hit patterns, which especially did not take into account the long signal lengths on the GEM channels. Due to an insufficient electrical decoupling signals from one GEM could also be measured on the adjacent layers. As far as usually the topmost GEM is taken as the origin, this created false assignments upwards in the stack, i.e. towards the drift cathode. In order to correctly identify the conversion layer, the gas gain of the GEM has to be sufficiently high to create a signal above threshold on the respective channel, however, the effective gas gain within the stack is not identical and an amplification larger than 1 leads to a charge cloud being sensed at a later stage than its origin. The conversion ion spectrum in the gas continuously extends towards zero and shows especially for thick layers a pileup at low energies, see sec. 11.1. With the thick boron layers on the drift cathodes this effect is likely to create a misidentification on the lower lying GEMs. Tab. 15 summarizes the diagnosis and provides an outlook on the solutions.

Table 15: Key aspects of the detector optimization with the identified problems and the proposed solution. The outcome is evaluated as solved (checkmark) and partially solved (circle).

Classification	Problem	Solution	Goal
physics	neutron scattering	background by scattering off the detector material modeled by simulation	✓
electronics	weak signal	increase gas gain	⊙
	crosstalk	improve decoupling	✓
		adapt data reconstruction algorithm	⊙
firmware	ad-hoc event identification	implemented a pipeline algorithm based on raw data topology	✓

10.2 | ELECTRICAL DESIGN: SPICE SIMULATION

The significant crosstalk between the GEM channels was reduced by optimizing the capacitor network on the high voltage distributor board. The necessary decoupling quality is a function of the actual components on the board and the additional capacities of the GEMs within the stack. The latter were measured in a table top setup[b]. The results were:

- GEM top to bottom copper layer: C_{tb} = (23±0.5) nF,
- GEM stainless steel framing to grid framing with PTFE spacer C_{f} = (233±30) pF,
- GEM copper layer to grid area without stainless steel frame C_{a} = (100±10) pF.

Based on earlier works using the toolkit MultiSim [371] of [322] and U. Schmidt an electronic signal simulation was set up. As a charge sensitive amplifier a SPICE [372]

[b] The parasitic capacities, which are stray fields from one potential to every other potential, can only be approximated. Within the GEM stack the possible setup, which can be measured, leads inevitably to an underdefined equation system. Taking a piecewise standalone definition can only take into account the adjacent surfaces.

model of the VV50[c] was used, which in parallel was available to validate the results. The simulation allows to carry out a multivariate optimization of the network to minimize the crosstalk.

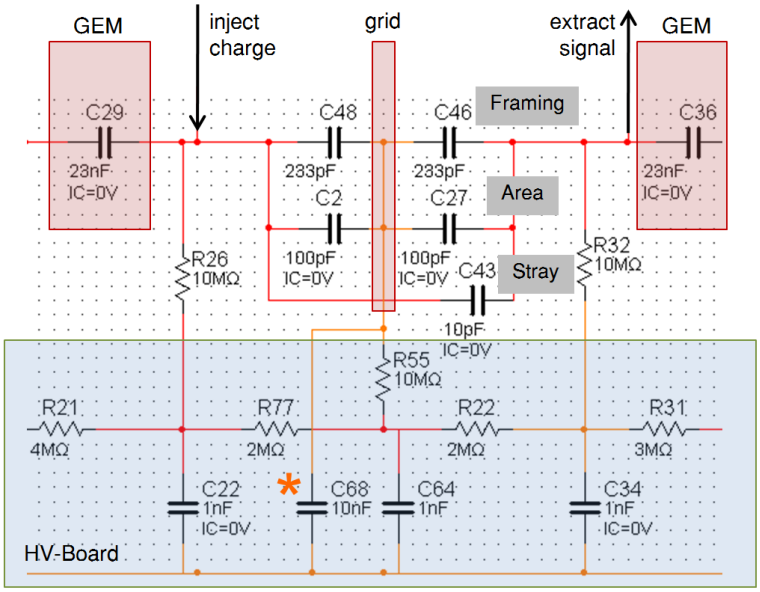

Figure 77: Cutout of one cell of the Multisim SPICE simulation of the cross talk between GEMs. Resistors and capacitors in the lower part correspond to components of the high voltage board, see sec. 9.2.3, and capacities in the GEM stack were measured. The orange star * shows the decoupling capacity of the grid, which is one of the parameters of the analysis.

The simulation model covered one half space and targeted the signal quality of the GEMs which are not directly attached to the readout. Fig. 77 shows a cutout of the relevant network around one grid with both adjacent GEMs. With this model different configurations of capacitors and resistors were tested by injecting a charge of 1 fC onto the potential corresponding to the top face of a GEM and then measuring the signal amplitudes at different positions within the network. It turned out, that a capacitor to ground connected to the grid is the most effective method to decrease the crosstalk. In Fig. 77 this component is marked by an orange *.

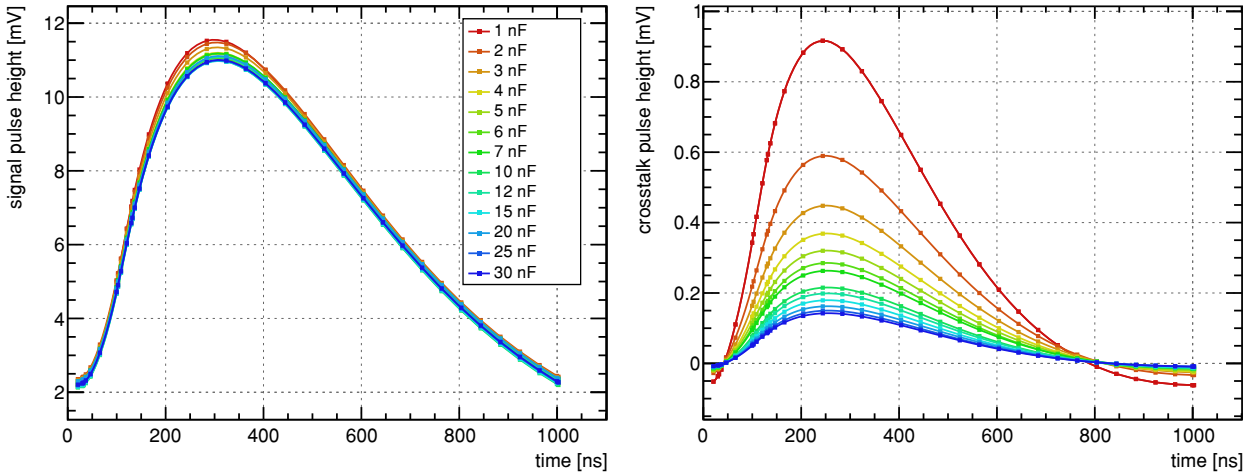

Figure 78: Pulse height for signal (left) and crosstalk (right) from the SPICE simulation. A simulated charge is injected into the resistor and capacitor network of Fig. 77 at one GEM and measured in parallel at another GEM. The series investigates the pulse heights measured by a VV50 (not baseline corrected) as a function of the decoupling capacity of the grid in between.

The response at the injection and extraction points[d], shown in Fig. 77 by arrows, is displayed in Fig. 78. The crosstalk is effectively reduced by increasing the grid

[c] The VV models are a series of low-noise amplifiers developed by the electronics workshop Heidelberg and were applied and described in an earlier works, e.g. [342].

[d] The significantly larger capacity of the GEM C_{tb} makes it nearly transparent for the charge signals.

decoupling capacity, which is also shown in Fig 79. However, also the signal amplitude is damped by (5-6) %, which is acceptable. Finally, C_{grid} = 10 nF was chosen due to availability reasons of this type of component, i.e. high voltage capacitors. The analysis shows, that by appropriate choice of capacitors in the network, the crosstalk can effectively be reduced to a few percent. However, the absolute values as shown in Fig. 78 have a systematic uncertainty originating from the uncertainties on the parasitic capacities.

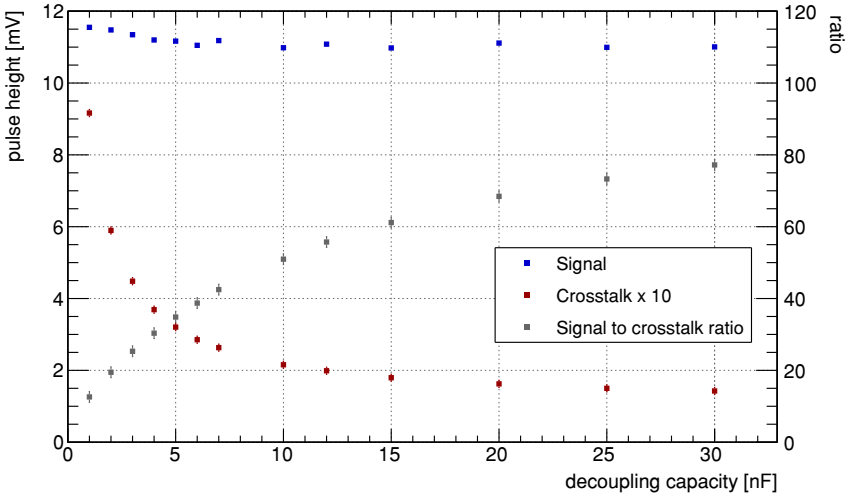

Figure 79: Evaluated pulse height, e.g. amplitude, for the charge responses presented in the SPICE simulation of Fig. 77 and Fig. 78. The crosstalk (red) is effectively reduced, whereas the signal (blue) pulse height is only marginally influenced by increasing decoupling capacities.

10.3 | Data analysis methods

10.3.1 | Event reconstruction

The previous firmware algorithm had the drawback that it was closing the event after the correlated X/Y channels stopped. Then, the topmost firing GEM was assigned to the event. However, as the T-GEM signals are much longer than those from the crossed stripes, event information inevitably collided with following neutron IDs. Taking the example from sec. 9.3.3, the cut would be set like indicated by the horizontal line in tab. 16 and the event would be assigned to the GEM in the top half space:

X stripes	Y stripes	top→	←bottom
□□■■■	□□□■■■■	□■■	□□□
□□□■■	□□□■■■■	□■■	□□□
□□□□□	□□■□□□□	□■■	□■■
■■■■■	■■■□□□□	□■■	■■■
■■■■■	□■□□□□□	□□■	■■■

Table 16: RAW data example with event separation according to the old firmware which would cut the event at the horizontal line.

Furthermore, it suppressed events which would cover too many stripes like the 5 X channels from the example would be too large. Although this topology is rare, it is not unusual. It also did not anticipate events being recognized on either X or Y one time slice earlier. For an even number of hit readout channels the center of gravity was set to the strip with the lower channel number.

For RAW data-based event reconstruction a C++ algorithm with a `CEvent` class was developed, which stores the full topology and has the following characteristics:

- X and Y coordinates can be evaluated according to a center-of-gravity algorithm or a leftmost/rightmost decision or a center-of-gravity method, which in case of an even number of stripes randomly selects the channel above or below,

- one time slice difference between X and Y information is allowed and one time slice without X and Y information is required for subsequent event,
- diagonal channel hits in the X/Y-t plane are not interrelated, e.g. the dark gray events in tab. 16 would not be correlated with the light gray hits,
- the closest T-GEM to the drift cathode is taken as origin,
- in case of events running into each other a GEM separation algorithm tries to select the actual GEM of the event with new X/Y information. In case of different half spaces firing the adjacent space is taken. In case there are channels of a GEM firing, which lies more close to the drift cathode in ±1 time slice, this ID is taken. For the high-rate reconstruction mode in case there is new X/Y information and only the lowest GEM at the readout is firing this ID is also assigned to the new event. This is the most probable choice for the conversion layer, however, there are ~10 % of the events without T-GEM information, which corresponds consequently to the approximate error of this method,
- a ratio analysis for the T-GEM signal length is carried out in order to suppress crosstalk, see sec. 10.3.3,
- the following flags can be assigned:
  - `Full`: information from X/Y and T is available.
  - `noGEM`: only data from the crossed stripes readout channels.
  - `OnlyGEM`: only signals from a T-GEM channel without X/Y information.
  - `NoXorY`: either X or Y information is missing.
  - `Broken`: no pure T-GEM channel information available if the event had been passed to the event separation algorithm and could be reconstructed, but T-GEM channel data of two different events overlapped[e]
  - `Ambiguous`: if the event had been passed to the event separation algorithm and could not be definitely reconstructed.
  - `MultiHit`: if a discontinued hit topology in X or Y is appearing, e.g. several channels firing apart from each other with no possibility for correlating the data.

10.3.2 | Voltage scan performance analysis

In order to evaluate the detector performance and the event reconstruction capability voltage scans were performed. The data presented in the following were taken at the HEiDi hot neutron diffractometer [84] at the FRM II. For hot neutrons the conversion probability and therefore the beam attenuation within the detector is much lower. This comes along with the benefit of a more uniform distribution of events within the stack compared to a thermal or cold spectrum. As will be seen in sec. 11.4.2, the detector is illuminated by a spot-sized beam, which simplifies the background suppression. Here and in the following, the system is described in terms of total voltage applied to the voltage divider, which has been described in sec. 9.2.3. The range for operation typically lies between 2600 V and 2800 V. As seen in the upcoming analysis, the effective gas gain factors are different in each layer, which prevents from the usual direct conversion of the GEM potential difference to a gas gain. Contrary to the helium counter a boron-lined detector does not exhibit a distinct plateau when increasing the gas gain. As

[e] In the firmware prior to this work a 'broken' flag was assigned to events with one or more GEMs along the projection not showing any signal. But as we will see later, for low gas gains this is not uncommon and does not invalidate the assignment of the conversion origin.

the conversion ion energy deposition in the gas continuously extends to zero, see sec. 11.1.3, the increase in gas gain at a given threshold leads to a strict monotonously rising detection rate. This feature can be seen in Fig. 80, which depicts the result from such a voltage scan for different event identification criteria.

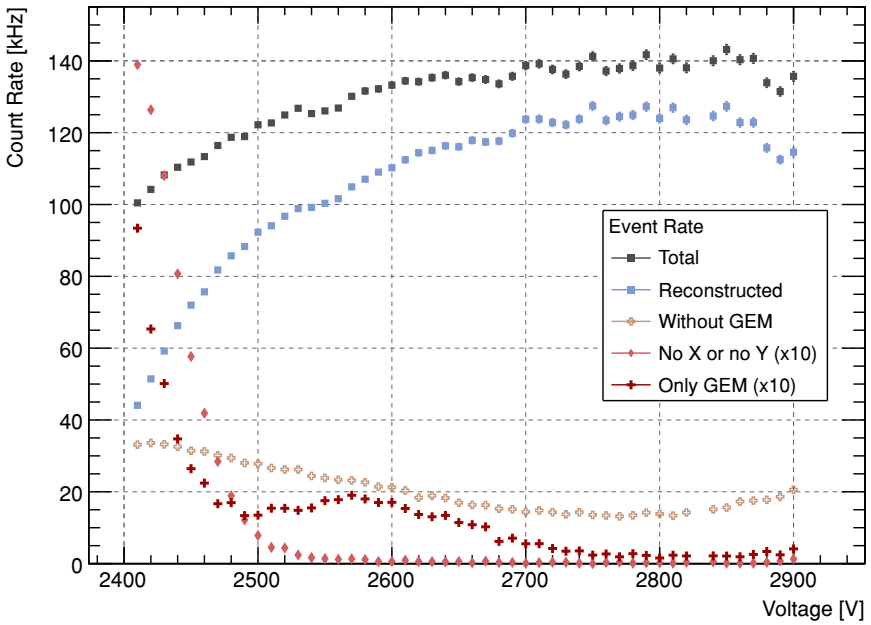

Figure 80: CASCADE performance scan with software reconstruction in units of voltage divider total potential difference. The total event rate is determined by the sum of all signal topologies. The maximum rate reaches a plateau at around 2750 V. Approx. 10 % of the events cannot be fully reconstructed, e.g. a correlation of X, Y and Z with mostly T-GEM information missing. The measured maximum rate of 140 kHz also provides an approximated limit for full 3D reconstruction. Errors according to counting statistics.

The total rate is the number of individual signal events in the detector per second from the raw data reconstruction without taking into account the data transfer dead time. Those events do not necessarily have to originate from a neutron conversion, yet, the majority of them are. Even in the best case at around 2800 V, nearly 10 % of the events are lacking a layer identification channel and only appear on the crossed-stripes readout[f] as the signals from the GEMs are much weaker than those from the 2D readout. For a full „reconstruction“ all channels need to deliver unambiguous information. The low T-GEM signal strength, or more specifically the different sensitivity of the X+Y and the T channels, is the main reason for an incomplete reconstruction. Another type of undesired signals are GEMs firing without a spatial information. Such are appearing up to 2700 V for typically only one time slice, but the number of such events is negligible for higher voltages. The third group of events, which appears below 2500 V, is a topology with lacking X- or Y-coordinate. For low gas gains the charge cloud is not large enough to raise many strip channels above their threshold. With a spacing of 1.56 mm and the nested double sided routing, depending on angle and center position of the charge cloud projection, there is probability of mainly hitting one channel for low energy tracklets, see also the readout structure presented in Fig. 40. Yet, this probability effectively becomes zero for gas gains within the typical range of operation. Therefore, the readout granularity is well adapted to the charge density and track length distribution in the detector.

Above 2850 V the reconstructed count rate drops. The reason for this effect is, that with increasing gas gain the charge signals measured on on the GEMs are so large, i.e. long, that the rate acceptance is limited by the signal duration. This topic will be discussed in sec. 10.3.3, yet, it is for large gas gains not unusual to get events which have the T-GEM channel firing for 15 time slices of 100 ns and more. Therefore, the rate acceptance with full reconstruction efficiency is limited to approximately 150 kHz on the total detector. However, as the signals on the crossed stripes readout typically

[f] In measurements with a distinct beam topology (not shown) those events lacking a T-GEM channel show the same spatial distribution as the fully reconstructed events, see also appendix B.1.6. Therefore, such events can be classified as neutron conversions as well.

stay above threshold for not longer than four clock cycles, in the 2D mode without layer identification much higher rates like the 2.7 MHz measured in [323] can be achieved.

The reconstruction efficiency, however, is different for the individual GEMs within the stack. Fig. 81 shows the data of the same voltage scan as presented in Fig. 80 for each T-GEM channel separately. Whereas both half spaces show a nearly identical qualitative reconstruction performance, the scaling of the layers with respect to each other is different. This especially can be seen in the right panel of Fig. 81, which shows the fractions of the respective intensity contributions. As explained above, if the T-GEM channel event length becomes too long compared to the neutron conversion rate, the dead time increases. Especially the reconstructed rate from the outermost layers drops as those events get amplified most and therefore appear to limit the rate acceptance. As shown later in sec. 10.3.3 the signal time over threshold from those layers measured on the layers adjacent to the readout, e.g. events from GEM 1 seen on GEM 3, becomes very long. As far as no new signals from the innermost GEMs can be identified correctly if they are still in the uptime from another event, the rate from those GEMs drops as well. The reason why the conversion rates from GEM 2 and 5 continue to rise are hence: The signals from conversions originating from those layers are for effective gas gains larger than 1 less long than those from the outermost GEMs. Additionally they do not get blocked by pass-by charges as long as the GEMs below. Thirdly, the capacitive coupling of GEM 2 and 5 is slightly worse than layer 1, 3, 4 and 6, which leads to those signals being commonly slightly weaker.

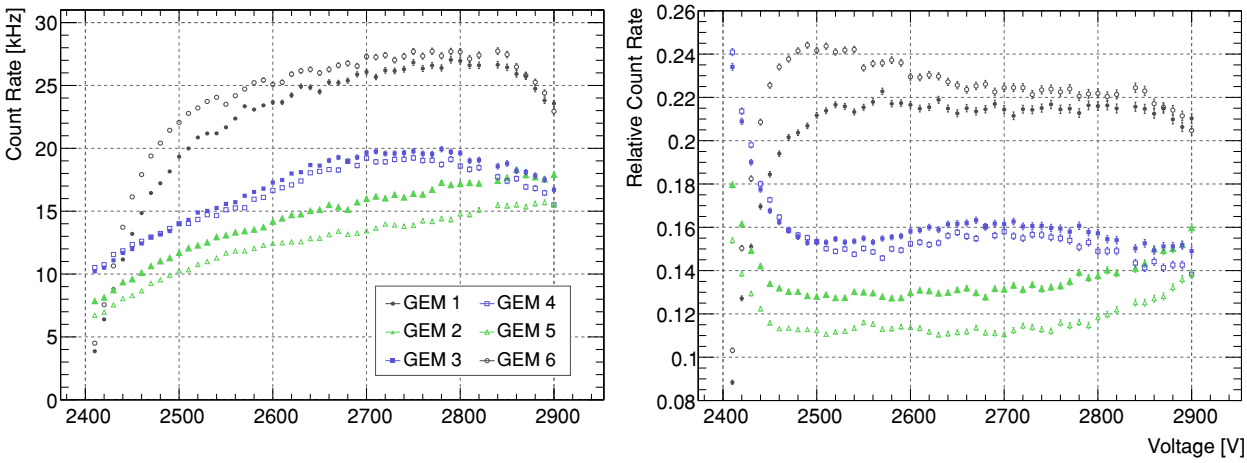

Figure 81: CASCADE performance scan with software reconstruction and individual GEM information in units of voltage divider total potential difference. The left panel shows the absolute count rates of the fully reconstructed events from Fig. 80 and the right panel shows the relative contributions. Due to an increasing T-GEM event length the rate acceptance drops for large gas gains. Errors according to counting statistics.

10.3.3 | Event length distribution

The individual GEM layer readout provides a pseudo energy measurement by the time-over-threshold of a signal passing by different T-GEM layers. Contrary to the crossed-stripes readout, for which it takes at the longest a few 100 ns to acquire an event, the GEM channels need much longer readout times. In the previous section the total count rate has been broken down to each layer. Here, the particular attention is set to review the signal shapes between the individual layers. Each half space can be split into six T-GEM categories: Signals S_3 originating from GEM 3, S_2 originating from GEM 2, $S_{2\to3}$ originating from GEM 2 and measured on GEM 3, S_1 originating from GEM 1, $S_{1\to2}$ originating from GEM 1 and measured on GEM 2, $S_{1\to3}$ originating from GEM 1 and measured on GEM 3. Fig. 82 shows those distributions exemplarily for one voltage and

one half space. The analysis shows, that events can be amplified significantly while traversing the stack from 1→3 (left panel).

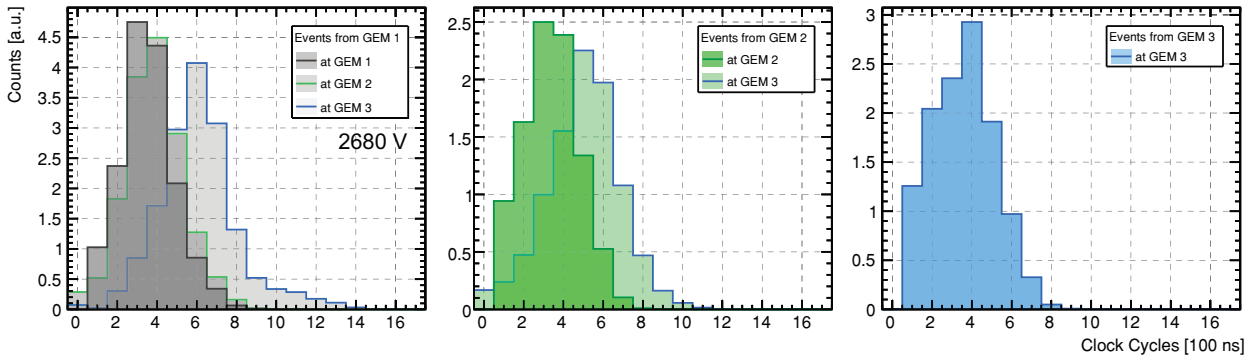

Figure 82: Event length distributions in clock cycles of 100 ns (CLK) for the top half space of the detector. In the left panel the CLK distribution is shown for events originating from GEM 1 (blue). Their duration measured on GEM 1 (dark outline) is approx. 4 cycles. On GEM 2 (green outline) the length is slightly increased, whereas on GEM 3 (blue outline) the distribution is much longer. A similar pattern can be seen for events from GEM 2 (green) in the middle panel. However, the distribution of conversions from GEM 2 at GEM 2 has a lower mean value. Events from GEM 3 have a similar length as those from GEM 1, except for the relative surplus for 1 and 2 clock cycles, which are most probably not identified at GEMs above.

Already at the presented data at a total voltage of 2680 V an event length of 1 µs on GEM 3 is not rare if the mean original uptime at GEM 1 is around three to four clock cycles. It has to be noted, that while for larger gas gains the distributions as shown keep their symmetry, the events in the category $i \rightarrow j$ with $(i \neq j) \in 1, 2, 3$ do not.

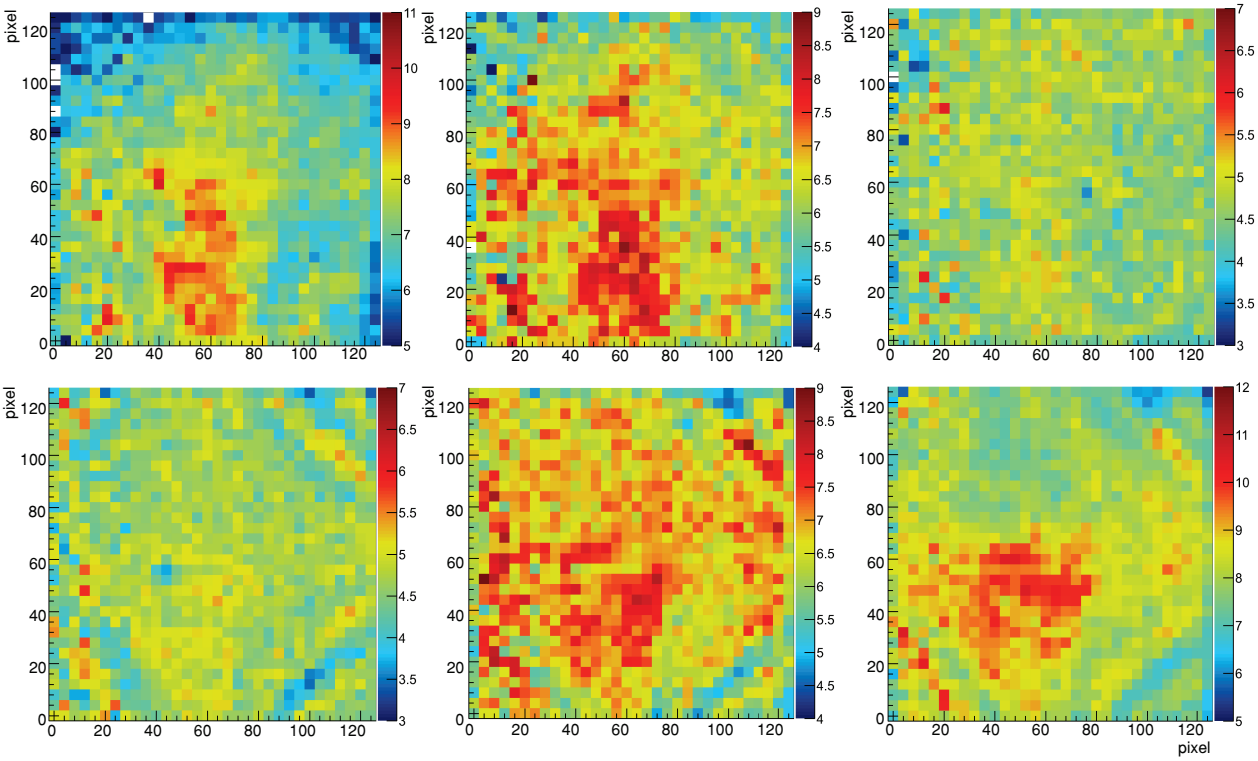

Figure 83: Spatial distribution of the mean total length of events in clock cycles originating from GEM 1 (top left) to GEM 6 (lower right). It shows that the gain is not uniform and also the geometry of the GEMs is visible like the diagonal stress lines from the GEM stretching. The deformations, which are only located on GEM 4, can also be seen in the plots of the GEMs 5 and 6 as the last gas amplification stage controls the charge transport from layers above. These plots are mainly for a qualitative evaluation, therefore no statistical errors are shown.

The long uptime tail seen in 1→3 extends until 2 µs and the distribution forms one peak below 1 µs and another peak above. One reason for this effect is, that the event length distribution is not spatially homogeneous. As the CASCADE detector is able to measure X,Y and identify the conversion layer, one can spatially map the gas gain on the GEMs itself. Fig. 83 shows such an evaluation with GEM 1 showing S_1 and GEM 2 showing S_2 and $S_{1\to2}$. GEM 4 has some drapes due to the stretching and framing, which has a significant effect on the gas gain. As all charges from layers above has to pass this GEM, the pattern get imprinted onto the others in this plot as well. The reason for the drapes in explained in appendix B.1.4.
The distributions also can already give an estimation for a misidentification rate. If a charge cloud is not large enough to be detected in one layer, it can be registered in the consecutive for effective gas gains larger than 1. S_1 for example seems to be shifted far enough to longer event lengths, that from an extrapolation to bin 0 CLK one would only expect a small fraction of undetected events. However, S_2 and S_3 show a significant accumulation above expectation, if taking S_1 as a reference, in bins 1 CLK and 2 CLK. Those events suggest, that a certain amount of events remain undetected at layers above and after a gas amplification larger than 1 are wrongly assigned to lower lying GEMs.

10.3.4 | Effective gas gain

The clock cycle distribution can also be used to express an effective gas gain for charges traversing the stack. Fig. 84 shows the result of the voltage scan for the identification categories presented in the previous section and shown in Fig. 82. In order to avoid contributions from extreme amplifications, like the tail seen in $S_{1\to3}$, and the misidentification contribution in the lower time bins, a Gaussian function with a linear offset has been fitted in the range

$$\left[\|S_i\|_{\max}[\mathrm{CLK}] - \left(0.6 * \sqrt{\mathrm{Var}\,(S_i)} \cdot \left(0.2 + \frac{n}{30}\right)\right), \|S_i\|_{\max}[\mathrm{CLK}] + \sqrt{\mathrm{Var}\,(S_i)} \cdot \left(3.2 - \frac{n}{20}\right)\right],$$

with n denoting the measurement number starting at a voltage of 2400 V and increasing in steps of 10 V.

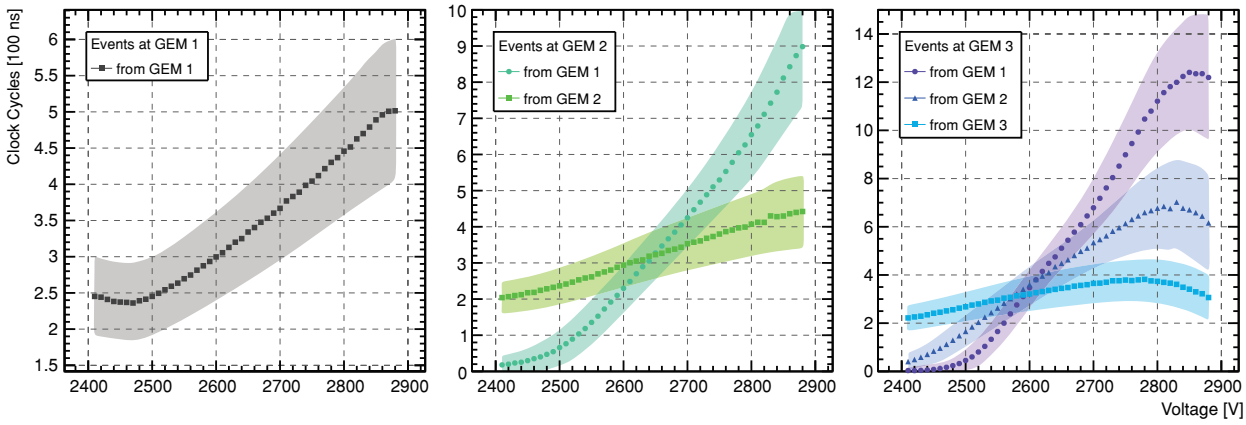

Figure 84: Voltage scan for the event length distributions in clock cycles in the top half space of the detector. In the left panel their distribution is shown for events originating from GEM 1. In the middle panel the length distributions for events at GEM 2 from GEM 2 (lime squares) and from GEM 1 (green circles) are displayed. The right panel shows the distributions for events at GEM 3 from GEM 3 (cyan squares), from GEM 2 (blue triangles) and from GEM 1 (purple circles). Especially events from GEM 1/6 can be detected on GEM 3/4 easily for 1 µs and longer. Error bands indicate the Gaussian standard deviation of the respective distribution.

The result from this analysis shows, that the individual layers scale differently in the event length distribution and therefore in the effective gas gain. The primary ionization gets amplified in one GEM layer, which exponentially depends on the voltage difference, is extracted from the GEM holes, which depends on the ratio of the field strength inside the whole and in the drift space and partially absorbed by the grid. This system does evidently not show a linear response for changes of the the total voltage, however, the points of equal effective gain are also different for each layer. Whereas for GEM 2 the crossing point of $S_{1\to2}$ and S_2 events can be located at (2640±5) V, for GEM 3 the crossing point of equal T-GEM length of $S_{1\to3}$, $S_{2\to3}$ and S_3 lies at (2590±10) V. The different scaling can especially be seen in the ratios of the clock cycles shown in Fig. 85. This ratio will be used to identify unwanted crosstalk.

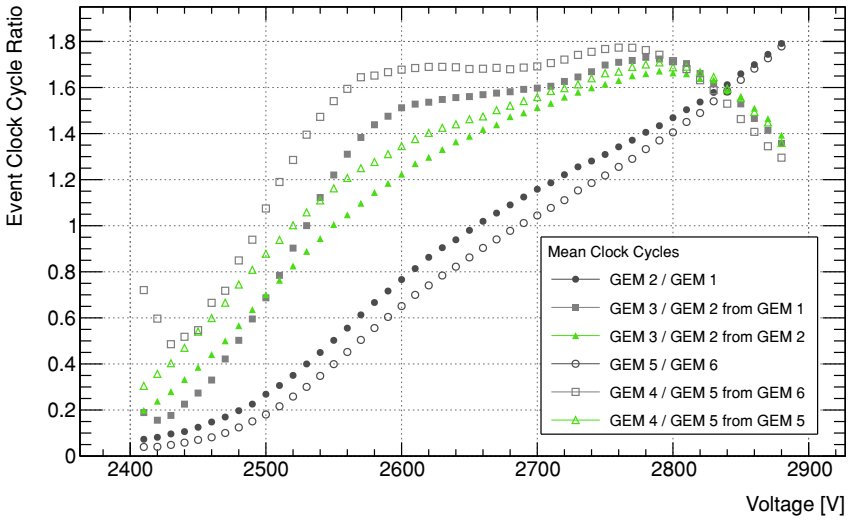

Figure 85: Voltage scan showing the ratio of the mean event length distributions from Fig. 84. The relative gain from each layer to the next is significantly different depending on at which GEM the event appeared first. There are also significant differences between both half spaces. Error bars are not shown here for reasons of comprehensibility.

10.3.5 | Crosstalk correction

In sec. 10.1 two layer identification problems have been introduced, one of them, the crosstalk, which remained after the new high voltage board had been introduced, is targeted here. The analysis of sec. 10.3.4 showed the dependency of the effective gas gain on the total voltage of the detector. The topology for most events yields a clock cycle ratio distribution centered around a mean value. However, apart from the expected gain behavior, one finds significant deviations when plotting the clock cycle distribution ratios. This is exemplarily shown in Fig. 86.

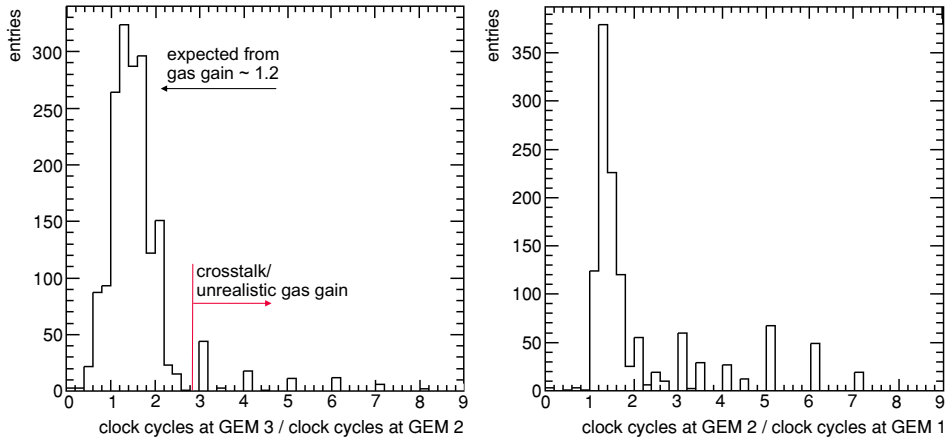

Figure 86: Examples of distributions for the ratio of the mean event length for the GEMs 3 and 2 (left) and GEM 2 and 1 (right). Due to the gas gain a distribution centered around its mean value is expected. Extreme deviations are possible according to the Polya distribution, but unlikely. Therefore such are flagged as crosstalk.

The events, which show large multiplicators can be identified as crosstalk according to sec. 10.2. It is unlikely, that an event appears to have increased from for example 1 to

5 clock cycles from one layer to the following. It is on the contrary most likely that an event with an already large energy deposition created a signal, which slightly raised the adjacent channel over threshold. For the typical range of operation, 2600 V to 2800 V, Fig. 84 shows, that the mean clock cycle ratio between GEMs can be approximated for a voltage divider potential difference of U as follows:

- layer 1/6 to layer 2/5: $0.7+0.4 \cdot (U\text{-}2600\,\text{V})/(100\,\text{V})$,
- layer 2/5 to layer 3/4: $1.3+0.2 \cdot (U\text{-}2600\,\text{V})/(100\,\text{V})$.

The algorithm to identify the crosstalk then calculates the clock cycle ratios between the GEM layers and if an event deviates more than a factor of 2 from the above mentioned ratio[g], it is not assigned the topmost active GEM, but the following. The efficiency of the algorithm is exemplarily presented in Fig. 87. For the two categories $S_{1\to3}$ and $S_{2\to3}$ an S_i, S_j correlation plot shows the signal discrimination and redistribution without (left) and with (right) crosstalk suppression. As an example in the top left panel there is a significant amount of events, which appears to have started with a few clock cycles at GEM 1 and ended up with a long uptime of T-GEM channel 3. With the main distribution unaffected, those events are filtered (top right panel) and assigned to GEM 2 (bottom right). In this case, both, the overall signal length distribution as well as the individual T-GEM channel distributions are improved.

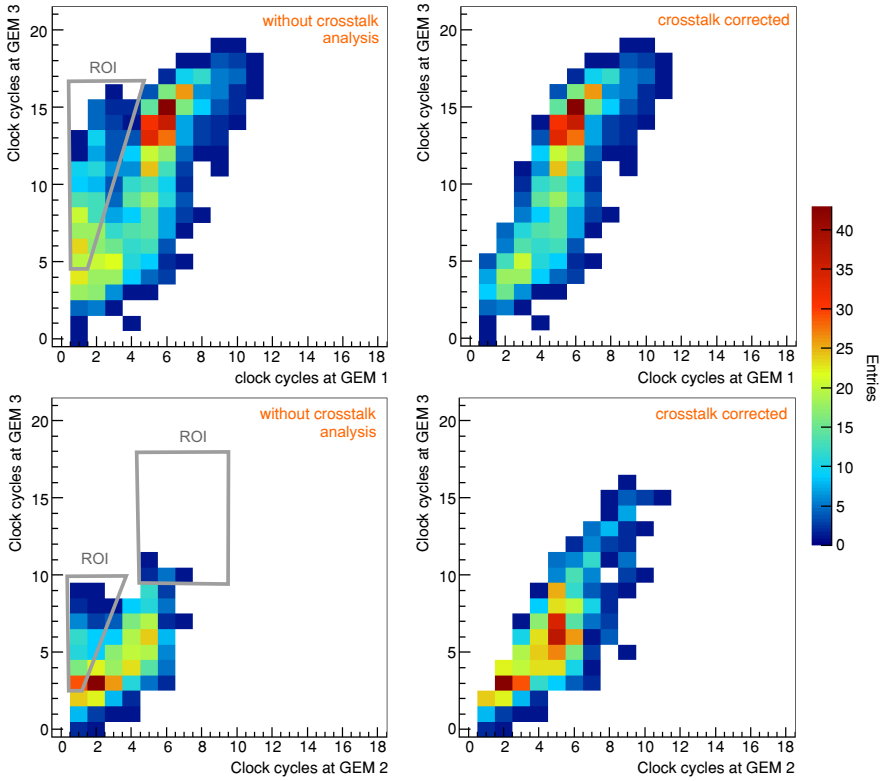

Figure 87: Examples of the effect of the crosstalk analysis in a correlation plot of clock cycles before applying the filter (left panels) and after applying the filter (right panels). In the top panels the events traversing the whole detector are shown (GEM 1 to GEM 3) and in the bottom panels, those flagged as originating from GEM 2. By applying the crosstalk filter the distributions are well centered around their means and events, which got a false assignment of the origin, are now appearing at their most probable layer.

[g] with the exception for events with small energy depositions. The combination of 1 to 3 clock cycles is allowed as due to statistical fluctuations this ratio appears to be common.

After the layer misidentification has been analyzed, an experimental quantification of this effect has been carried out. By tilting the detector with the maximum inclination possible a pencil shaped beam like shown in Fig. 88 probes unambiguously every single layer. It intersects the stack at distinct points creating a chain of displaced spots as seen in the top panel of Fig. 89.

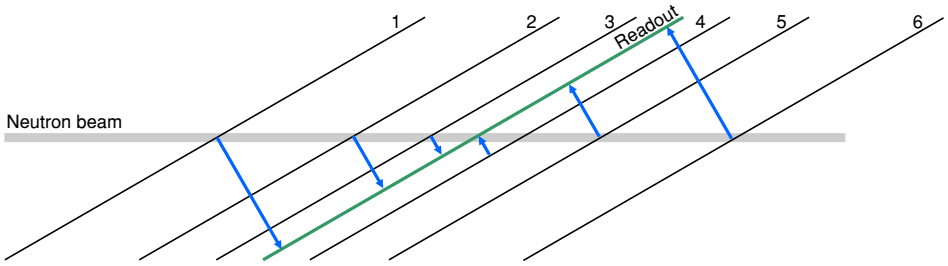

Figure 88: Sketch of the measurement principle to identify misidentification by a circular beam (gray) intersecting the layers of the CASCADE detector. Due to the inclination angle the points where the beam passes through the layer appear in the projection onto the readout, indicated by the arrows, in different locations along a line.

Any additional offset spot appearing as an artifact can be qualified as crosstalk, wrongly assigned upwards in the stack, or as a misidentification, a wrong downwards assignment. In the experiment the neutron beam was shaped using a pinhole aperture. However, due to an internal reflection and incomplete absorption in the V-cavity upfront the beamline, a divergent second beam hit the detector. The leftmost spot in Fig. 89 originates from this leakage of the polarizer. It is far enough out of the region of interest in order to not expect a significant influence. One can clearly identify in the log-scale plot of Fig. 89 the shadow beam images especially from GEM 1 on GEM 2 and GEM 3. In order to quantify this effect a projected cutout of 10 pixels width was fitted by a triple Gaussian distribution with the individual abscissa offsets fixed to the known geometry of the detector. The procedure to evaluate the voltage dependent contamination matrix is exemplarily shown in Fig. 90 and the result for the intensity contributions can be found in appendix B.1.8. The absolute distribution of events, however, depends on the relative conversion probability and therefore on the wavelength, in this case 5.4 Å. Therefore, the relative quantities have to be derived.

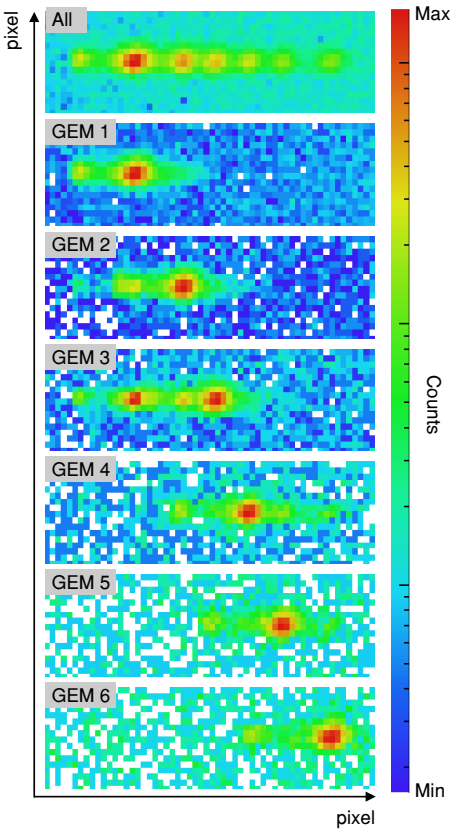

Figure 89: Cutout of the needle beam passing through the layers of the GEM detector (top to bottom). In the total projection (topmost panel) the first spot is due to an unwanted reflection from the V-cavity.

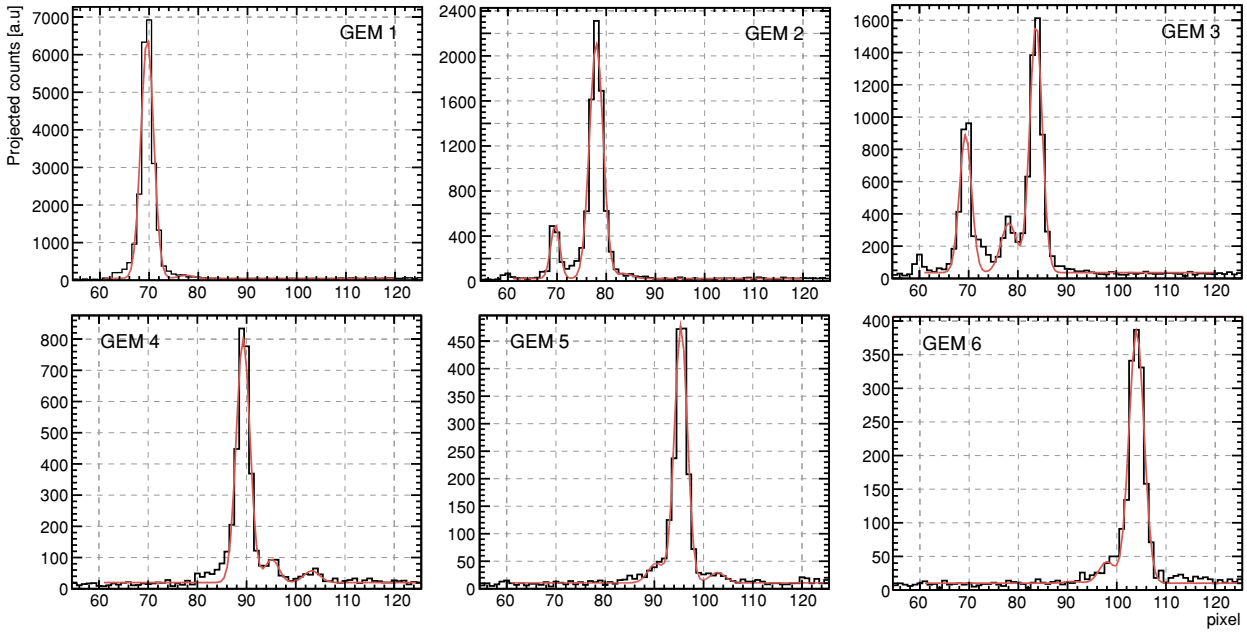

Figure 90: Projected measured spatial distribution of the needle beam experiment from GEM 1 (top left) to GEM 6 (lower right). In order to model the intensity of the spots at their known positions, Gaussian functions (red) were fitted to the projections. The small leftmost peak is due to a residual reflection of the V-cavity. This evaluation exemplarily shows the procedure for evaluating the relative misidentification contributions, see also Fig. 91.

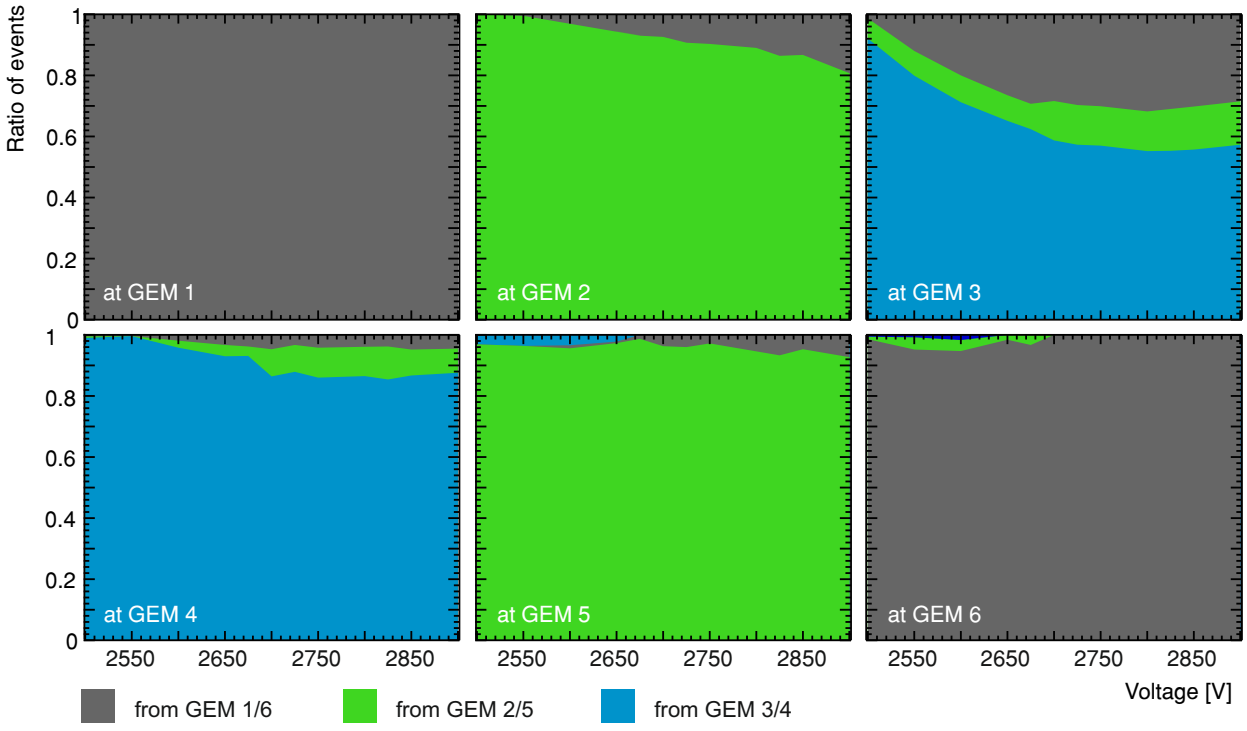

Figure 91: Experimental result of the signal purity of the T-GEM layer identification for the GEM stack (top left to bottom right) as a function of detector voltage. Events can either be assigned to the wrong GEM below towards the readout if not detected at the original conversion layer or signal crosstalk leads to a wrong assignment to the GEM above. The signal purity describes the relative contamination of each layer by events not originating from it. GEM 1 and GEM 6 appear to have a correct identification of nearly all events, however, a significant amount of their intensity is wrongly assigned to lower lying GEMs.

In order to evaluate the relative contributions the following procedure has been applied:
The intensity of each spot was determined by the integral of the Gauss function without

taking into account the offset. The result are two 3×3 correlation matrices G_{ij} for the GEM G_i to GEM G_j contributions plus the 1×6 vector $\overline{G}$ for the events without GEM information. The total sum of events $\sum_j G_{ij}$ originating from G_i is calculated by adding the extrapolated amount of „no GEM“ events. For those the relative fraction of the spot intensity corresponding to $\overline{G_i}$ is compared to sum of spot intensities $\sum_i \overline{G_i}$. This sum is scaled to the total amount of undetected events by taking the fraction of the total events without GEM information from the sum of all events $\sum_{i,j} G_{ij}$ as a reference. Finally, the maximum count rate of each layer is set to the maximum measured rate, which is derived from the mean count rates of the evaluations of the scan points at 2825 V and 2850 V.
The results of Fig. 91 show, that in effect the crosstalk is suppressed, however, there is a significant signal contamination. These are events, which are not identified on the topmost but on the lower lying GEMS, e.g. those adjacent to the readout structure. The direct identification of crosstalk in this measurement leads to similar results as the contamination estimation by Spin Echo group fits in the beginning of this chapter, see Fig. 76. One of the reasons for the comparably poor suppression in the top half space is, that the front drift cathode has a boron layer of 1.5 µm, whereas the backside is equipped with only a 1 µm coating. In sec. 11.1 it will be explained, how the layer thickness crucially affects the identification performance. As a matter of fact, there is also a remarkable similarity between the results from the Spin Echo fit estimation for the signal contamination of Fig. 76 and the experimental results from the pinhole evaluation. For the other GEM layers except the innermost an operating voltage of (2680-2700) V provides a reasonably good signal quality.

10.4 | Design modifications

Besides the redesign of the high voltage distributor board regarding the signal decoupling, based on the analysis of the detector performance, several improvements could be proposed and realized.

10.4.1 | Active detection volume modifications

Signal crosstalk between different channels for the layer identification within the stack is a result of capacitive coupling or insufficient capacitive decoupling of the system. The simulation in sec. 10.2 showed, that finally parasitic capacities limit the possible signal-to-noise ratio. However, in order to further reduce direct contributions, the GEM and grid frames have been replaced by a sandwich design of stainless steel and FR-4, a glass-reinforced epoxy laminate. This reduces the capacitive coupling by the framing.

The drift cathodes, which are the outermost conversion layers, are easier to coat by ^{10}B than the GEMs, therefore it seemed in the first place reasonable to increase the layer thickness for those in order to improve the detection efficiency. Yet, in thick layers the energy loss of the conversion ions inside the layers is already high, which leads to a significant amount of very low energetic tracks inside the gas. With the critically low sensitivity of the GEM channels this pileup increases the amount of events, which are probably not identified at the layer they converted in. Therefore, the bottom drift cathode, which originally had a 2 µm boron coating has been replaced by a 1 µm layer. As the contribution from the front drift cathode is still significant it can be targeted replacing it as well.

There are several options to further improve the performance of the detector. The effective gas gain is not properly adjusted to the scope of the detector. In order to improve the GEM layer identification the GEMs have to be operated at a higher gain. However, the total amount of charge traversing the stack has to be reduced in order to balance out the additional charge carrier production. The linear correction options are using meshes with a higher opacity and reducing the extraction or collection efficiency of the GEMs. The grids in between the GEM layers even allow to control both separately.

Segmented GEMs with a much lower capacity would significantly increase the signal quality and reduce the crosstalk. It would also allow for a higher rate acceptance. An n-fold segmentation would increase the number of high voltage and signal channels by a factor of n. In the current configuration $n = 4$ would not exceed the data handling and routing capabilities.

10.4.2 | Firmware and event reconstruction

The firmware has been redesigned in the filter and event builder unit. As contrary to the raw data analysis the data unit can only access the current state of the data stream, an event pipeline has been implemented, which mimics the algorithms developed in this work. Instead of a direct decision after the X/Y readout finished providing signals, the event topology is analyzed in a multi-stage architecture. It allows for a variable interpretation of the topology instead of an ad-hoc decision. For example a shift between X, Y and T-GEM channels of one time slice of 100 ns is accepted as a correlated event. The T-GEM channel analysis masks the bitstream and counts the number of mask operations per GEM. By masking the actually active channels, further events in the pipeline cannot receive the same GEM-ID as the currently signaling one, which requires at least one GEM with a higher number to provide a signal. Otherwise it gets flagged as without T-GEM channel information. The counted mask operations are then used after the event is finished or leaves the pipeline to evaluate the crosstalk correction with a static acceptance ratio, which has to be configured for the GEM channels via the SlowControl.

11

RESULTS

11.1 | CHARACTERISTICS OF BORON CONVERTERS

Part of the results about neutron conversion spectra presented in this chapter have been published in [K2016] and [K2016b].

Especially for detectors with solid state converters it is required to understand and characterize the precise neutron conversion ion tracks in terms of spatial extent and energy deposition. Contrary to gaseous converters or doped scintillators, the detection signatures are more complex as the ions already lose part of their energy within the converter itself. Therefore, various geometric factors have an influence on the final track topology in the gas, which is for the CASCADE detector crucial for its event reconstruction algorithm. In order to specifically understand the signal generation and optimization, simulations of the conversion particles were carried out by URANOS, which the combines neutron physics, track generation and energy loss in its computational model, which is presented in sec. 6.5.2.

11.1.1 | ABSORPTION EFFICIENCY

The general characteristics of solid boron and boron carbide as a converter has been studied by analytical models for gaseous detectors in various publications [373], [326], [374], [375] and theses [318], [376], [377]. The assumptions made are the following:

- the boron layer is either frontside or backside irradiated, for the latter being the case where the readout is in beam direction located after the coated substrate.
- thermal neutron capture inside a boron layer leads to the nucleus being split into a helium ion and the core remainder, which is referred to as a lithium ion.
- both either receive the full kinetic energy of 2.8 MeV with a probability of 6.4 % or an additional photon of 0.48 MeV is produced reducing the phase space accordingly. As both, the neutron and the converter atom, have only kinetic energies in the order of meV (k_BT), their initial momentum can be neglected.
- the fragments are emitted back-to-back.
- the trajectory is deterministic, that means neither straggling nor variations of the energy loss is taken into account.

These assumptions are good approximations, even ion straggling, which lies in the order of 5 %, has a negligible effect on the pulse height spectrum [376]. However, there are notable deviations in values reported from other authors. For 1.8 Å with a single layer of $^{10}B_4C$ [378] states 4 %, [376] reports a detection efficiency of 4.1 % and [379] as well as [375] 4.5 %. [380] calculated 4.1 % with GEANT4 and 4.5 % for FLUKA, [275] even approximately 8.8 %. For 1.8 Å with a single layer of ^{10}B [318] derived a maximum detection efficiency of 5.5 %, which was later corrected in [321] to 6.0 %. These deviations can be attributed to various reasons like different assumptions on cross sections, including enrichment, or material densities, which especially for sputter depositions strongly depends on the target temperature [381]. Furthermore,

the ionization model of SRIM [159] had been updated since the 2010 version leading to slightly higher maximum ranges for ions in boron. Simulations of URANOS yield a maximum detection efficiency for backside irradiation of approximately 6.5 %. This value is slightly higher than the one from analytic models.
However, there are notable deviations in values reported from other authors. For 1.8 Å with a single layer of $^{10}B_4C$ [378] states 4 %, [376] reports a detection efficiency of 4.1 % and [379] as well as [375] 4.5 %. [380] calculated 4.1 % with GEANT4 and 4.5 % for FLUKA, [275] even approximately 8.8 %. For 1.8 Å with a single layer of ^{10}B [318] derived a maximum detection efficiency of 5.5 %, which was later corrected in [321] to 6.0 %. These deviations can be attributed to various reasons like different assumptions on cross sections, including enrichment, or material densities, which especially for sputter depositions strongly depends on the target temperature [381]. Furthermore, the ionization model of SRIM [159] had been updated since the 2010 version leading to slightly higher maximum ranges for ions in boron. Simulations of URANOS yield a maximum detection efficiency for backside irradiation of approximately 6.5 %. This value is slightly higher than the one from analytic models.

The total absorption of a layer linearly increases with its thickness, see Fig. 92. As soon as the probability of lithium ions for being stuck inside the coating due to their limited range becomes significantly large, the detection efficiency starts to deviate from the absorption efficiency. Only for thin layers well below 1 µm the probability for both ions to escape into the gas approaches 1. For 1.2 µm already approximately 10 % of the ions are stuck inside the boron film. The maximum range of both particles limits the total efficiency then to ≈ 6.5 %, whereas beyond 2.5 µm layer thickness no significant increase of the detection probability can be achieved.

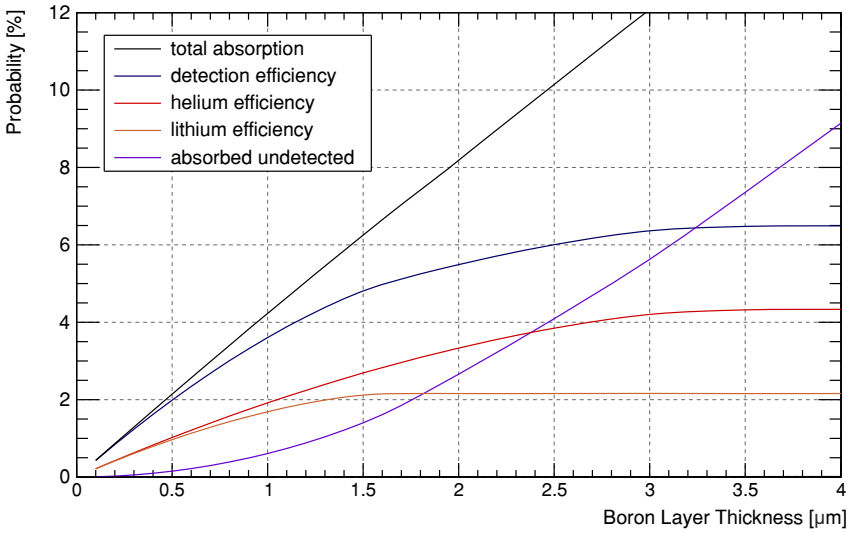

Figure 92: Thermal neutron conversion efficiency for backside irradiated ^{10}B. With increasing film thickness the probability of leaving the layer decreases due to their limited maximum range, which is much smaller for lithium ions than for helium ions.

11.1.2 | Track topology

Whereas the helium ion can be detected easily, lithium ions not only has less kinetic energy due to its higher mass but also its energy loss in the medium is higher. Therefore, the range of these ions inside the boron layer is less than half of their counterparts, see also Fig. 37. Typical maximum ranges R_{max} according to calculations by SRIM [159] are listed in the following tab. 17.
One can also derive, that the active conversion volume for each particle does not extend up to R_{max} due to the fact, that the possible escape angles ϑ get restricted to the surface normals, however, their occurrence scales by $\sin(\vartheta)$. If the minimum distance to the

E_{He} [MeV]	R_{max} [µm]	E_{Li} [MeV]	R_{max} [µm]
1.47	3.27	0.84	1.69
1.78	4.05	1.0	1.9

Table 17: Ranges of neutron conversion ions in ^{10}B according to SRIM [159].

interface is short, nearly all ions enter the gas volume, for longer distances the escape probability cone of angles narrows down quickly. This implies, that from thin layers the emission angles are equidistributed in $[0,\pi/2)$, for thick layers the distribution follows $\cos(\vartheta)$-law, which is the typical topology for example for alpha sources [382]. The mean emission angle then changes from

$$\langle\Theta\rangle_{d\ll 1\,\mu m} = \int_0^{\pi/2} 1\,d\vartheta = \pi/2 \quad \rightarrow \quad \langle\Theta\rangle_{d\gg 1\,\mu m} = \int_0^{\pi/2} \cos(\vartheta)\,d\vartheta \approx 0.57.$$

The method of centroiding [383], which means weighting the signal channels according the known energy deposition of a conversion track in a position-resolved system, has up to now only been used in gaseous detectors, e.g. [384]. This principle does not work for boron lined detectors with only one of both ions being emitted into the gas with a wide range of possible energies. Here, the conversion origin lies not in the midway on, but on either end of the track. The solution is distinguishing both tails of the tracklet by means of time-of-flight-based methods. However, only recent developments could achieve a time resolution high enough with strips [302] or pixels [K2018] to make use of this principle. In case the conversion tracks are not geometrically constrained, the total length can extend nearly up to 10 mm, see Fig. 37. Taking into account the ion angular distribution and considering a flat position-sensitive readout, the projected length of the tracks can without considering transversal diffusion still extend beyond 7 mm, see Fig. 93. The average orthogonal spread of the tracks depends on the ion type, with helium stretching out approximately twice as far as lithium, and the converter layer thickness. While the mean projected track lengths for 0.1 µm ^{10}B are 4.6 mm (He) and 2.4 mm (Li) it narrows down to 2.8 mm (He) and 1.7 mm (Li) for 3.0 µm of ^{10}B.

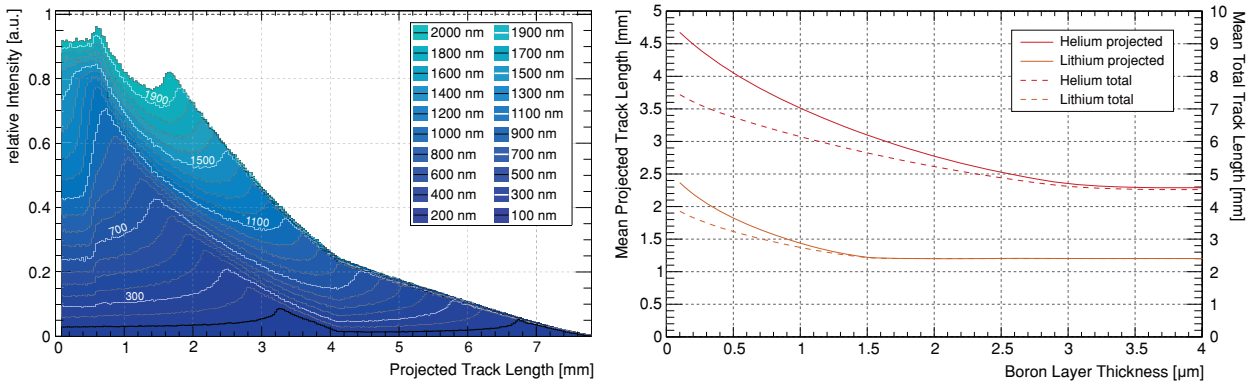

Figure 93: Spatial projection of the length of tracks released by boron layers as seen by a readout parallel to the coating (left). The two distinct peaks originate from the different topology of each ion species. As for thicker layers deeper conversion origins come with a limitation to the angular acceptance for detection, the mean projected track length narrows down with increasing layer thickness (right).

For detection systems with drift gaps of more than 10 mm, diffusion significantly broadens the tracks. However, when entering the gas volume, ions typically are already on the tail of the Bragg peak of the Bethe-Bloch equation (41), so the energy deposition

is very asymmetric, compare Fig. 38. This is the reason for the phenomenon, that for boron layers of usual thickness the origin appears to be more prominent than the actual end of the track, see also the bottom row of Fig. 39. Therefore, using a center-of-gravity approach [385] for the detected charge can even in the case of a boron-lined system lead to an improvement in the spatial resolution.

Both boron conversion products have different kinetic energy and energy loss inside the layer. Upon entering the gas volume their ionization spectra are significantly different. For a layer thickness below approximately 1 µm two distinct peaks can be identified with the maximum energy derived from the fractions of the q-value of the absorption process. Both spectra show tails towards lower energies from tracklets with slant angles. As stated before lithium does not show any further contribution beyond a conversion depth of 1.5 µm, which leads to a low energy pileup in the energy spectrum. Fig. 94 shows results from URANOS simulations for various ^{10}B layer thicknesses with both contributions separated. Additionally, Fig. 94 also shows an exemplary Gaussian convolution of the spectra in order to mimic a limited experimental resolution. For experimental practice it is important to note, that the lithium peak is lower and wider than the helium peak. When being convoluted with different energy resolution functions the helium peak smears out more than its counterpart. Therefore, their relative height is not a feature, which can be taken into account easily.

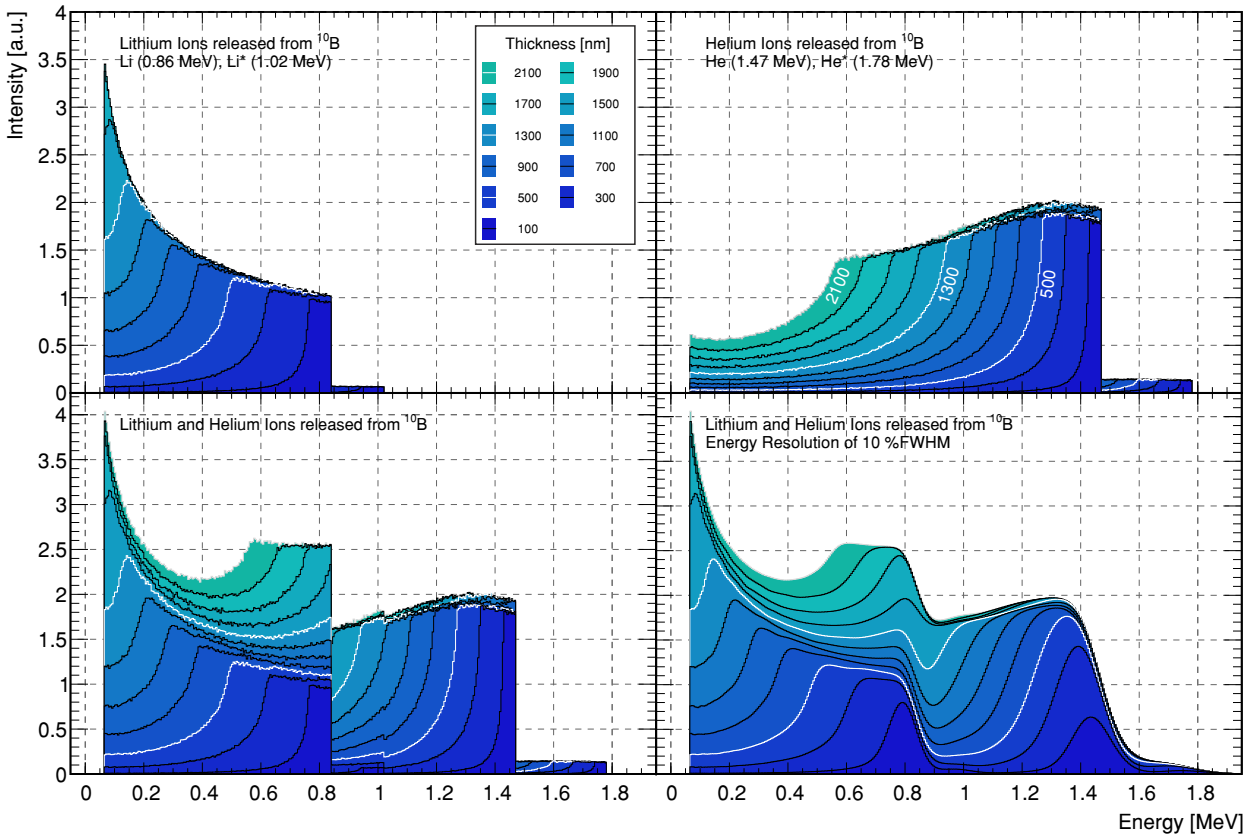

Figure 94: Simulation of the energy spectra of conversion products leaving ^{10}B layers of (100-2100) nm in a group spacing of 200 nm. (top) Spectra by particle type: lithium (left) and helium (right). (bottom left) Combined spectra and (bottom right) combined spectra exemplarily convoluted by an energy resolution of 10 % FWHM. [K2016b]

Compared to gaseous converters the shape of the spectrum is a drawback of boron-lined detectors. Helium-3 tubes can be operated with a distinct lower threshold as the spectrum does not extend significantly below 190 keV, see also Fig. 60, which lies well above the gamma background. With a continuous spectrum an inevitable low-energy cut does not only reduce the detection efficiency, but also fluctuating gains or drifting thresholds can lead to an unpredictable influence on the counting rate.

The simulated energy spectra have been compared to various test scenarios. In the CASCADE detector individual layers are too closely packed to provide a basis for evaluating the energy deposition as shown before in sec. 11.1.3. In an experimental series a single non-spatially resolved detector has been equipped with a very thin coated GEM in order to study signal gain for different hole spacings. Fig. 95 shows as an example the pulse height spectra for three different gas gains and in comparison the simulated spectra of Fig. 94, which have been convoluted by a Gaussian resolution function of the obtained peak full width half maximum. The gas ionization energy deposition here is slightly shifted downwards as the tracks emerging from the GEM are partly tallied by projection onto their surface instead of into a hole. For the usual 140 µm spacing already some field lines end on the surface potential of the GEM, therefore, not all electrons enter the gas amplification stage inside the holes. Yet, the simulation can well reproduce the measured spectra of the thin layer.

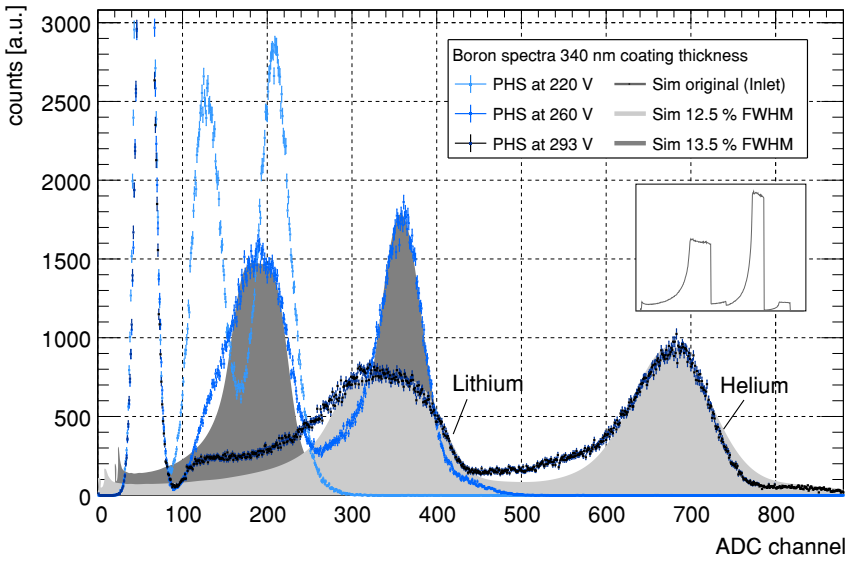

Figure 95: Pulse height spectra (PHS) of a test detector [386] composed of a single coated GEM and the readout, at three different gas amplifications given in the potential difference between both GEM faces. The data is compared to results from the simulation of the system with the energy deposition spectrum (inlay) being convoluted by a Gaussian energy resolution function. [K2016b]

In order to benchmark the simulation with thicker coatings, the data from [387] can be used a comparison as the detector features a good energy resolution while using the same Ar:CO_2 gas mixture as the CASCADE detector. In their test MWPC different B_4C layer thicknesses were studied. Data and simulation compare well to each other. The relative peak heights, which for thicker layers translate to plateau heights, agree with the results from the simulation. It is also interesting to note, that the 6 % conversion branch with the full q-value energy deposition appears to be clearly distinguishable and relates properly in intensity and position to the URANOS spectra.

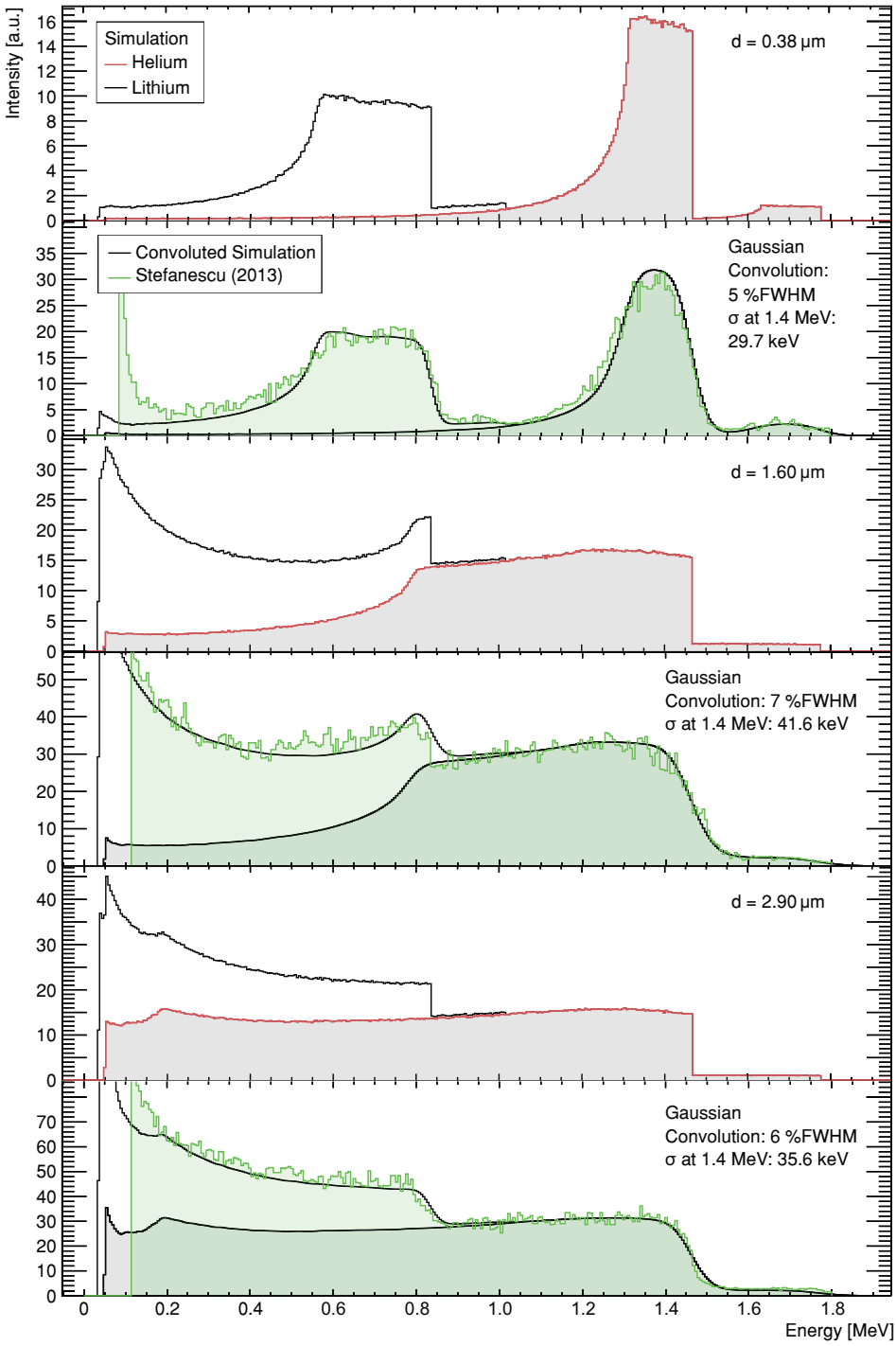

Figure 96: Pulse height spectra of flat cathode MWPC B_4C-based detector from [387] in comparison to simulations from URANOS for three different coatings. The respective top panels show simulated energy spectra for the determined layer thickness d with the individual helium and lithium ion contribution. The lower panels show the experimental data with the corresponding simulation convoluted by the best fitting energy resolution.

11.2 | Spin Echo measurements at RESEDA

Part of the results about Neutron Spin Echo measurements presented in this chapter have been published in [K2016b].

Spin Echo measurements, especially MIEZE techniques, require a high spatial and a very high time resolution. The oscillating interference pattern challenges detector technologies, as the Spin Echo group, which is exemplarily depicted in Fig. 98, can have an extension in space in the order of only millimeters and has to be sampled in the time domain in the order of MHz. Measurements were mainly conducted at the RESEDA cold neutron spectrometer [82, 388] at the FRM II. Spin Echo is based on analyzing the polarization loss of a spin polarized neutron interference pattern. It can be either static like in the case of classical (Neutron Resonance) Spin Echo, which is the first measurement presented here, or dynamic, in the case of MIEZE, which follows in the second part.

11.2.1 | In-beam Spin Echo wavelength calibration

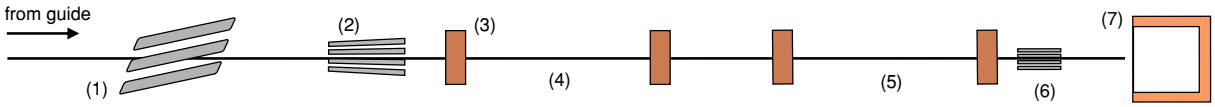

Figure 97: Setup for the wavelength calibration at RESEDA: Neutrons from guide NL5 pass the velocity selector (1) and the polarizer (2). The NRSE setup consists of two spin flipper coils (3) in each primary (4) and secondary (5) arm. The analyzer (6) projects one spin direction onto the CASCADE detector (7). Mu-metal shieldings and the neutron guide are not shown.

One of the advantages of the Spin Echo technique are, that precise energy measurements are possible although using a broad energy spectrum. A symmetric increase in the bandwidth of the beam only reduces the spatial extension of the interference pattern. However, the mean value of the spectrum has to be known precisely. The average wavelength is tuned by the velocity selector upfront the instrument[a]. It consists of a turbine with helical blades, which are coated by a neutron absorber, and allows only those neutrons to pass, which have velocities corresponding to a free trajectory in the rotating frame. As the velocity $v \sim \sqrt{E}$ and the wavelength $\lambda \sim \sqrt{E}^{-1}$ there is an inverse proportionality between both. From a precise determination of the Spin Echo interference pattern one can derive the kinetic energy of the neutrons by the spatial oscillation frequency and the wavelength spread by the envelope function. The Spin Echo group takes the following form

$$I_{\mathrm{SE}}(\nu) = \langle I_{\mathrm{SE}} \rangle \left(1 + P \cos\left(2\, k_0\, L\, \lambda_0\, (\nu - \nu_0)\right) \cdot \left(\frac{\sin\left(k_0\, L\, \lambda_0\, \Delta\lambda\, (\nu - \nu_1)\right)}{k_0\, L\, \lambda_0\, \Delta\lambda\, (\nu - \nu_1)} \right)^2 \right), \tag{153}$$

where $\langle I_{\mathrm{SE}} \rangle$ is the average intensity, P the beam polarization, $k_0 = 2\pi/3956$ the oscillation factor, L the distance between the two RF flipper coils in m, λ_0 the central wavelength in Å and $\Delta\lambda$ the wavelength distribution full width at half maximum. ν_0 and ν_1 are arbitrary phase terms in Hz, which are not necessarily equal, see also [201]. In order to calibrate the instrument the Spin Echo group is moved through the detector by scanning the RF field frequency $\Delta\nu = 3959/(\lambda L)$ mÅ/s, corresponding to a phase of 2π and assuming that the distance between both coils in the first arm is (1.925±0.002) m. This procedure is less error prone than shifting the actual detector due to the frequency

[a] The buildup is very similar to [389], further information is also provided in [206].

uncertainty being in the order of 10^{-7}. Exemplarily one data set of the measurements[b] is depicted in Fig. 98 for λ = (8.852±0.004) Å. The neutron interference pattern can be very well described by the expected curve, which along the stable operation of the instrument as a whole demonstrates the precision of the Spin Echo technique.

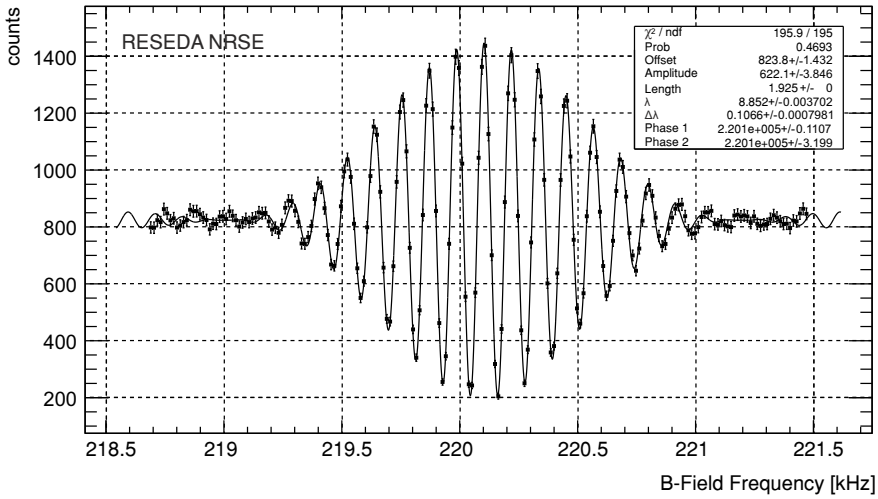

Figure 98: Example of a Neutron Resonance Spin Echo (NRSE) group measured by the CASCADE detector at RESEDA. By changing the frequency the interference pattern is moved spatially. At 8.85 Å and $\Delta\lambda/\lambda \approx 11\,\%$ the polarization reaches 75 %. The data is fitted by (153) [K2016b]

This Spin Echo group function was fitted to a series of 18 different rotation speeds of the velocity selector. The data itself is presented in appendix B.1.9, the corresponding fit results are shown in Fig. 99. As velocity and wavelength are inversely proportional an increasing rotation speed allows more highly energetic neutrons to pass, yet, even lowest possible wavelength lies below the peak of the flux density of the cold source, see also Fig. 20 in sec. 4.3. Therefore, the mean intensity increases towards higher rotation speeds. The loss of polarization, however, is due to fact, that the impedance matching for the RF coils is worse for the short wavelengths, where RESEDA typically is not operated. The velocity selector also shows roughly a constant $\Delta\lambda/\lambda$ slightly below 11 % with error bars increasing towards both extrema because of the loss of polarization at higher and loss of intensity at lower energies.

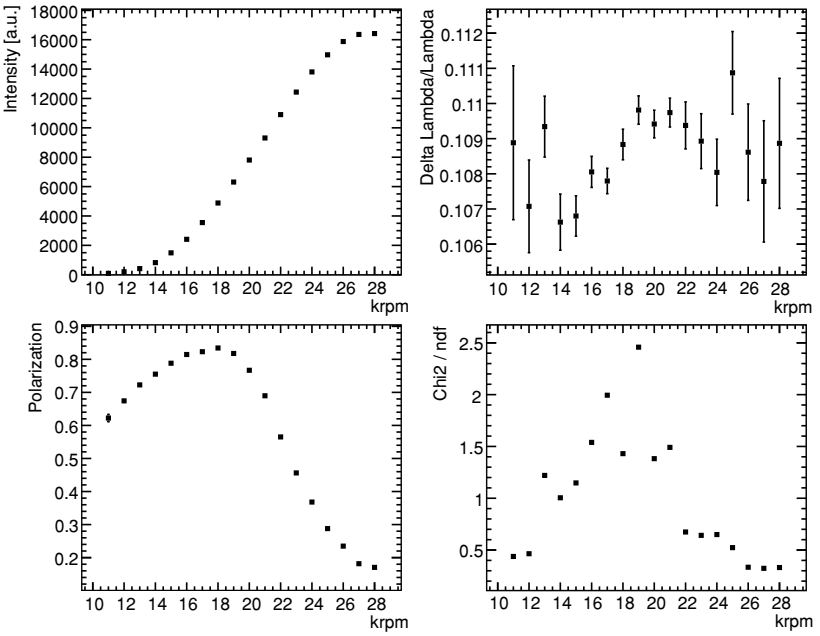

Figure 99: Results for the fit of theoretical spin echo curves (153) to the wavelength calibration data, see also Fig. 168 in appendix B.1.9, in the velocity selector rotation speed range (11,000-28,000) rpm. It covers the cold spectrum from approximately (4.5-11) Å with high frequencies selecting lower wavelengths and therefore (top left) a more intense part of the spectrum, see also Fig. 20. Additionally the velocity spread $\Delta\lambda/\lambda$ (top right), the polarization (lower left) and the fit quality (lower right) are plotted.

[b] In wavelength calibration runs the intensity has only been recorded in the center of GEM 1.

The fit results for the mean wavelength can be described by the calibration hyperbola of the following form:

$$\lambda_{\mathrm{Sel}} = a + \frac{b}{\nu_{\mathrm{Sel}}}. \tag{154}$$

The fit, see Fig. 100, yields a = (0.3441±0.003) Å and b = (119.10±0.06) krpm Å with both parameters being highly anticorrelated, e.g. $\rho(a, b) \approx$ -1.

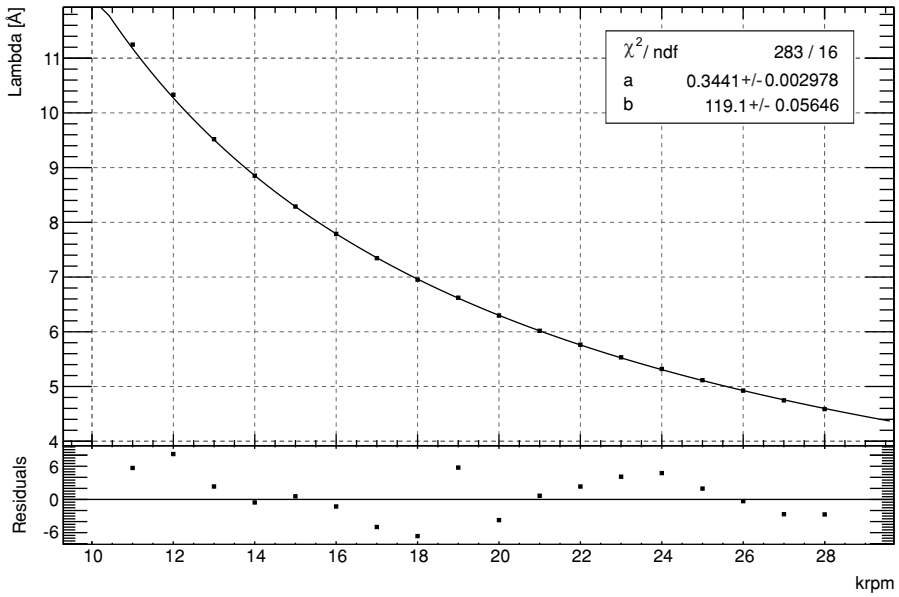

Figure 100: Results for the fit of theoretical spin echo curves (153) to the velocity selector calibration data, see also appendixappendix B.1.9, for the wavelength parameter λ as a function of rotation speed. (154) describes well the correlation between both parameters. Deviations are mainly attributed to varying rotation speeds.

The presented calibration is the basis for a precise wavelength-specific analysis with the CASCADE detector.

11.2.2 | MIEZE

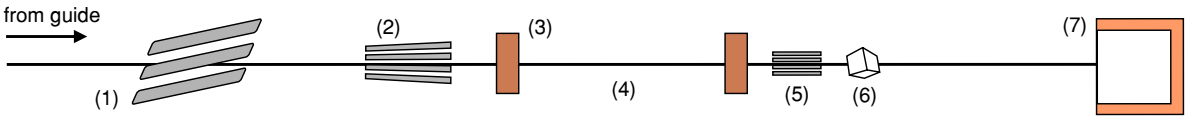

Figure 101: MIEZE setup at RESEDA: Neutrons from guide NL5 pass the velocity selector (1) and the polarizer (2). The NRSE setup consists of two spin flipper coils (3) in the primary (4) arm. The analyzer (5) is placed before the sample (6). The CASCADE detector (7) has to be positioned with its active detection volume inside the spin echo group. Mu-metal shieldings and the neutron guide are not shown.

A neutron interference measurement is an excellent benchmark of the detector to characterize its functionality, especially the multi-layer GEM identification. In a MIEZE measurement the intensity distribution oscillates in space and time as the neutron phase propagates through the detector. Further information can be obtained from [208], [209] or [199]. Whereas the data from Fig. 98 was taken in a standard NRSE setup, the following measurements were conducted in the MIEZE configuration. A thin graphite resolution sample [205] was placed in front of the detector creating a homogenous illumination. The intensity distribution integrated over the duration of the measurement is shown in Fig. 102 for each layer separately. The relative contribution of each channel depends on the boron thickness and the wavelength of the beam. As cold neutrons were used, most of the beam is converted in the first layer. The data of GEM 1 one also reveals the effect of an asymmetry in even and odd strip numbers due to different capacitive couplings, as each unit cell of the crossed-stripes readout is composed of a

2×2 interwoven matrix, see also Fig. 40 in sec. 6.5.2. GEM 3 shows in the corners a strain pattern which originates from stress undulations of the GEM which locally change the field strengths and therefore the GEM performance. GEM 3 also had lost part of its boron coating, which is depicted in the lower left corner of the third panel in Fig. 102.

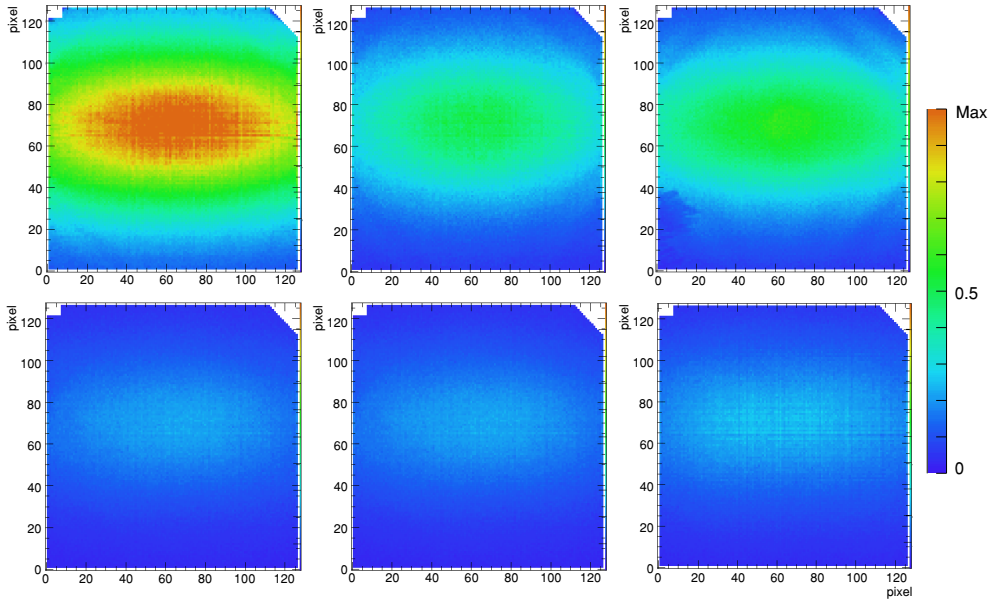

Figure 102: Intensity distribution separated by GEM channel (GEM 1 to 6 from top left to bottom right). This MIEZE measurement at RESEDA was carried out at a frequency of 53.5 kHz and a wavelength of 8.05 Å. The color scale is normalized to the maximum intensity and the data is reconstructed by the online FPGA algorithm. The upper corners are excluded from the data analysis due to sparks. [K2016b]

In the setup presented here the polarization frequency of 53.5 kHz is fed into the PLL and oversampled 16 times, which results in the detector following phase locked to the instrument at a readout frequency of 856 kHz. In every pixel on every layer of Fig. 102 the oscillating interference pattern of 9.2 mm wavelength can be measured. As an example Fig. 103 zooms into one small region and shows the time channel of each layer.

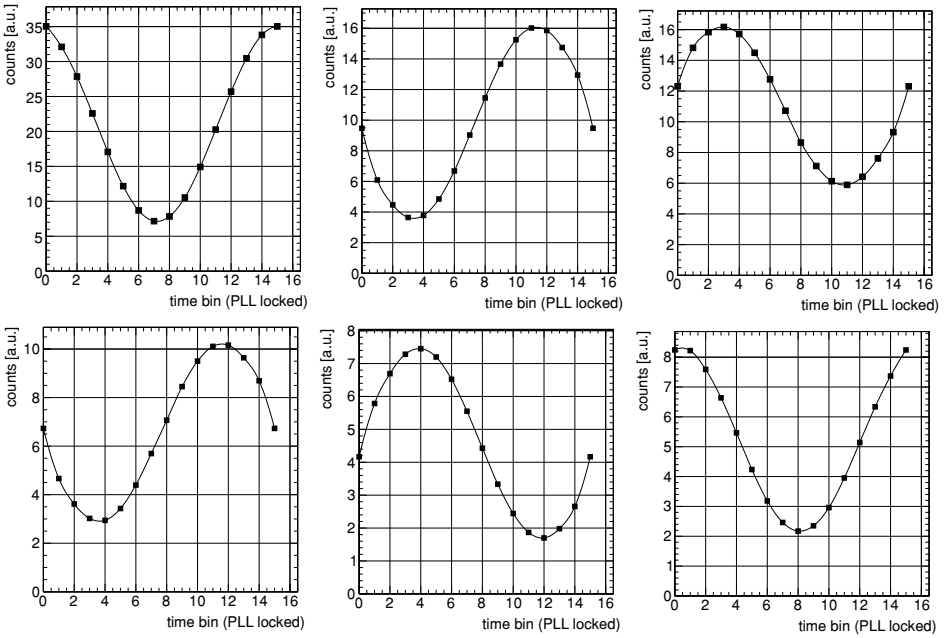

Figure 103: Measurement of the intensity distribution for each GEM channel summed over a central region of 9 pixels of the data set presented in Fig. 102. In the top row from left to right GEM 1 to 3 and in the bottom row GEM 4 to 6. The MIEZE period length of 18.7 µs is oversampled by a PLL. The full cycle is divided into 16 subchannels. While the single point error is far below 1 %, the sine fit describes the data very well giving a reduced χ^2 of approximately 1. [K2016b]

The resulting temporal sine function of the interference pattern is measured precisely. The following Fig. 104 shows the phase distribution across the detector at one specific point of time. The oscillation period can be followed through the layers in every pixel. This evidently shows that high spatial and time resolution is necessary to conduct this type of experiments.

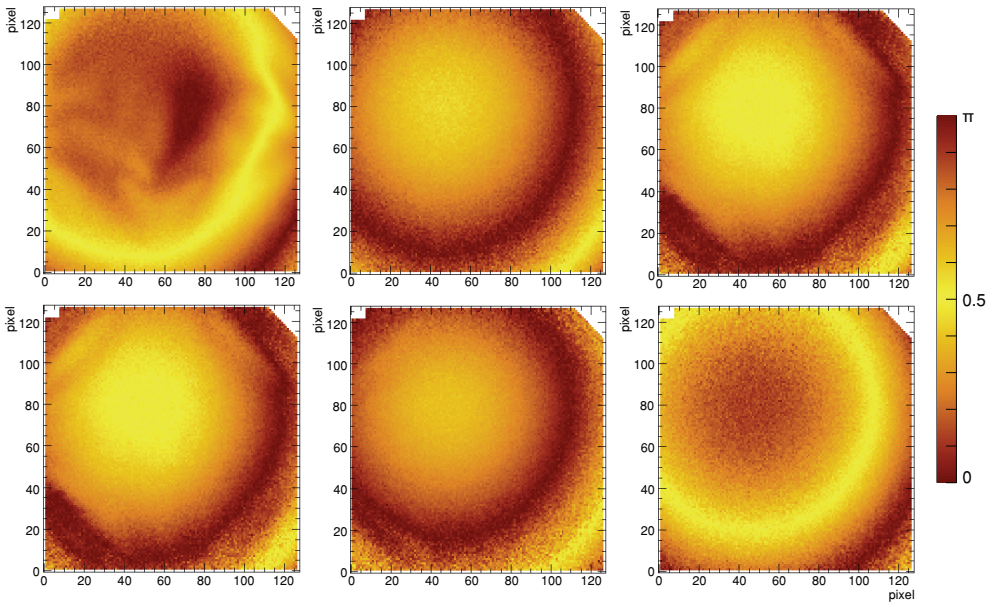

Figure 104: Phases of the neutron beam separated by GEM channel (GEM 1-6 from top left to bottom right). This MIEZE measurement at RESEDA was conducted at a frequency of 53.5 kHz and a wavelength of 8.05 Å and is also depicted in Fig. 102. The color code scales half a period from 0 to π, which equals 9.34 µs or 4.6 mm, and the data is reconstructed by the online FPGA-algorithm. The distances between the inner GEM layers are approximately half a period. [K2016b]

The first GEM in beam direction incidentally had received a bump on its front. One can exemplarily demonstrate the Spin Echo capabilities of the detector using this layer dislocation. As the neutron speed and oscillation period are well known by the instrument setup, the phase is used to spatially characterize the layers of the detection system with respect to the beam axis and towards each other. As an example the front-to-back distance of the first and the last conversion layer is depicted in Fig. 105. As the bottom drift cathode is planar and therefore acts as a reference, the displacement map accounts to the top layer. One can determine a bump depth of 1.7 mm with a in-beam-axis resolution of 0.1 mm per pixel. For a shorter oscillation period length than what is available for this accidental measurement the analysis can easily be improved by a factor of 10. Using this time-of-flight principle it is possible to physically characterize and align the detector itself by the precision of the neutron interference pattern.

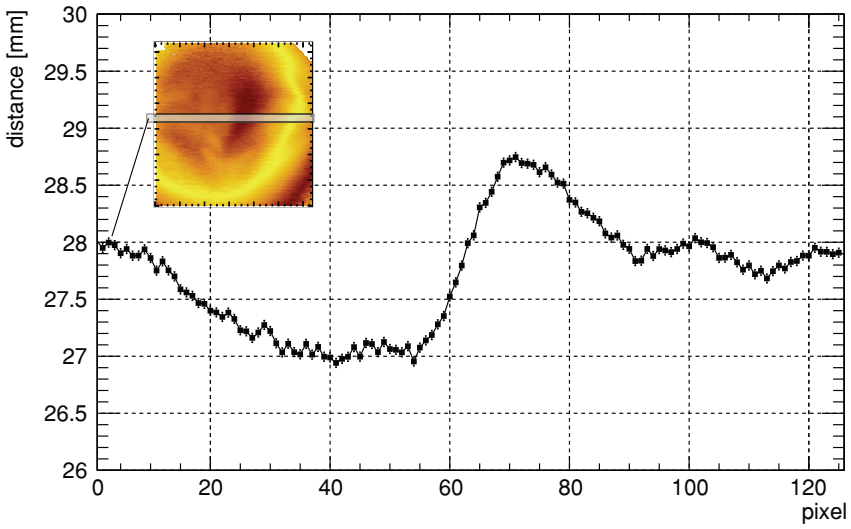

Figure 105: Profile view of the top to bottom displacement measurement by the neutron phase front, i.e. the length-converted phase difference of of GEM 1 and GEM 6 in Fig. 104. The cut view through the middle part of the phase difference map depicts the bump on the drift cathode. The total displacement of 1.7 mm can be determined down to a precision of 0.1 mm. [K2016b]

Part of the results about the spatial resolution of the CASCADE detector presented in this chapter have been published in [K2016].

The spatial resolution was determined at the RESEDA cold neutron spectrometer [82] at the FRM II, where the detector was placed at the end of the guide after a Dornier velocity selector providing neutrons of 5.4 Å (11 % FWHM). The instrument equipped with the CASCADE detector is designed for the purposes of neutron Spin Echo spectroscopy, especially the MIEZE technique, which requires a high spatial resolution.

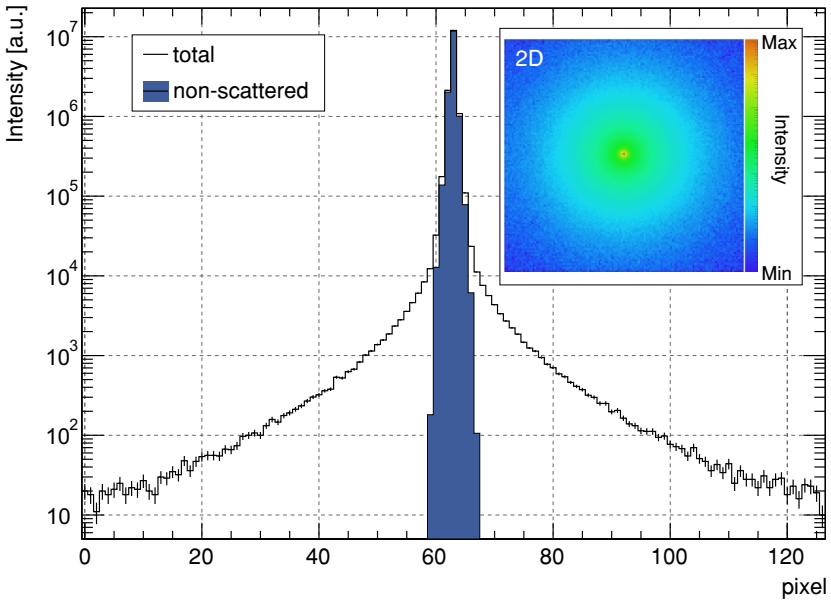

Figure 106: Point spread function of the detector visualized by a profile cut of the simulation of a pencil shaped beam. Those neutrons which did not undergo scattering in the detector itself (blue) are separated from the total counts. The inlay shows the full active area in 2D. [K2016]

Two approaches were carried out, (1) the edge multisampling method and (2) the Siemens star characterization, and both are compared to results from the detector simulation. The spatial resolution for this type of detector is nontrivial by itself, as is shown in Fig. 106 and analyzed later. The usual characterization in terms of statistical variance, i.e. Gaussian errors, does not strictly apply. The main reasons are:

- a significant contribution to the resolution function comes from the fact, that in the projection of the track onto the readout head and tail cannot be separated. This is rather an ambiguity of extremal possible values than a deviation from a mean.
- neutrons, which are scattered inside the detector create a broad plateau-type of background. As far as a point-like irradiation is considered, this contribution stays orders of magnitudes below the intensity in the signal region. However, in case the full active area of the detector is illuminated, the stochastic scattering integrates over the whole face leading to a background in the order of a few percent.

Therefore, two different methods are applied to account for the non-Gaussian point spread function (PSF). For the characterization the 1-σ standard deviation is used for the spatial resolution description as the full width at half maximum underestimates the width of the PSF due to the very specific shape.
For the optical **Siemens star method** a gadolinium coated pseudo random chopper was directly placed in front of the detector. Its sequence with the smallest sections having 2.835 degrees is described in [390]. A graphite sample provides a homogenous illumination. This contrast measurement is shown in Fig. 107.

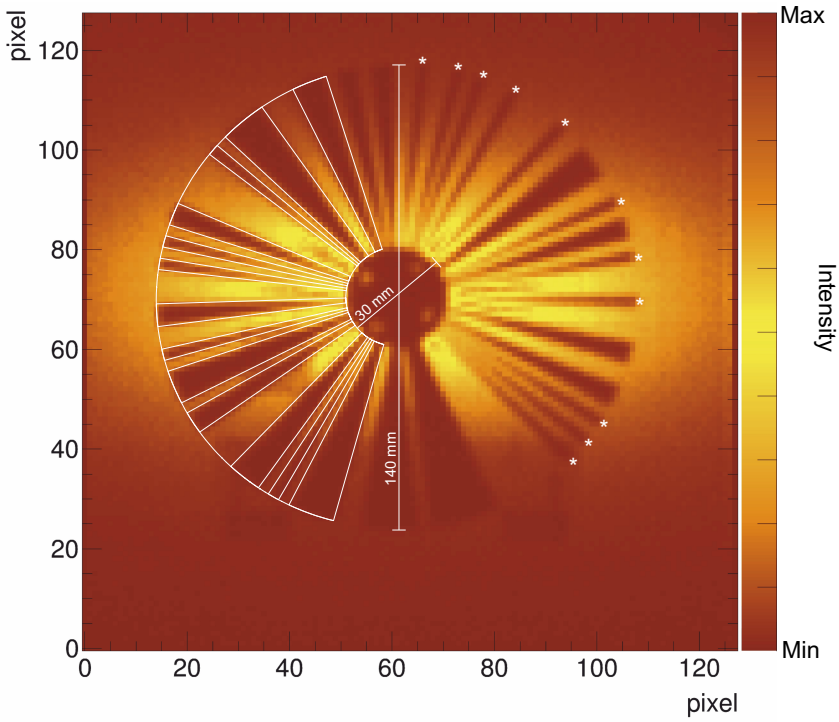

Figure 107: Image of a pseudo random chopper illuminated by a cold neutron beam scattering off a graphite characterization sample at RESEDA. The segments marked by * cover an opening angle of $\Delta\phi$ = 2.835 degrees. The linear twofold color code is applied to emphasize the contrast. [K2016]

The resolution σ_{opt} is calculated by determining the smallest possible spatial structure to be mapped by measuring the radius r at which the contrast is lost. For a result of r =(56±2) mm one finds

$$\sigma_{\text{opt}} = \pi r \Delta\phi / 360^\circ \;\rightarrow\; \sigma_{\text{opt}} = (1.39 \pm 0.05)\,\text{mm}. \tag{155}$$

For the **edge multisampling method** a straight cut cadmium absorber was placed in front of the detector at various distances oriented in a flat inclination angle with respect to the readout structure, see Fig. 108. By subtracting a bare illuminated shot without absorber, the edge spread function f_{es} is determined. It is a convolution of the Heaviside step function $\Theta(l(x,y))$ along a straight line $l(x,y)$ and a Gaussian point spread function $f(x,y,\sigma)$:

$$f_{\text{es}} = \int_{-\infty}^{\infty} \Theta(l(x,y) - r) f(r,\sigma) \mathrm{d}r, \tag{156}$$

whereas the standard deviation σ for an intrinsic detector resolution σ_0 and a beam with divergence angle α in a distance d is calculated by:

$$\sigma = \sqrt{\sigma_0^2 + \tan(\alpha)^2 d^2}. \tag{157}$$

This method involves three elements: (1) The detector resolution can be determined with high statistics over the whole active surface, (2) pixel size effects do not have an influence as the readout is sampled randomly by the aperture at different fractions of the individual pixel area and (3) the beam divergence spread will be removed from the measured resolution by extrapolating to a zero distance from the detector to the edge. The result from the fit for the intrinsic detector resolution is σ_0 = (1.454±0.007) mm, see also Fig. 109. This includes three effects. Firstly, the resolution of the readout can be denoted as $\sigma_r = 1.56\,\text{mm}/\sqrt{12} = 0.45\,\text{mm}$. Secondly, the ionization track lengths of the conversion ions in the gas make up the largest part of the error budget. And thirdly, there is a broadening of the resolution function by the elastic scattering of the neutrons

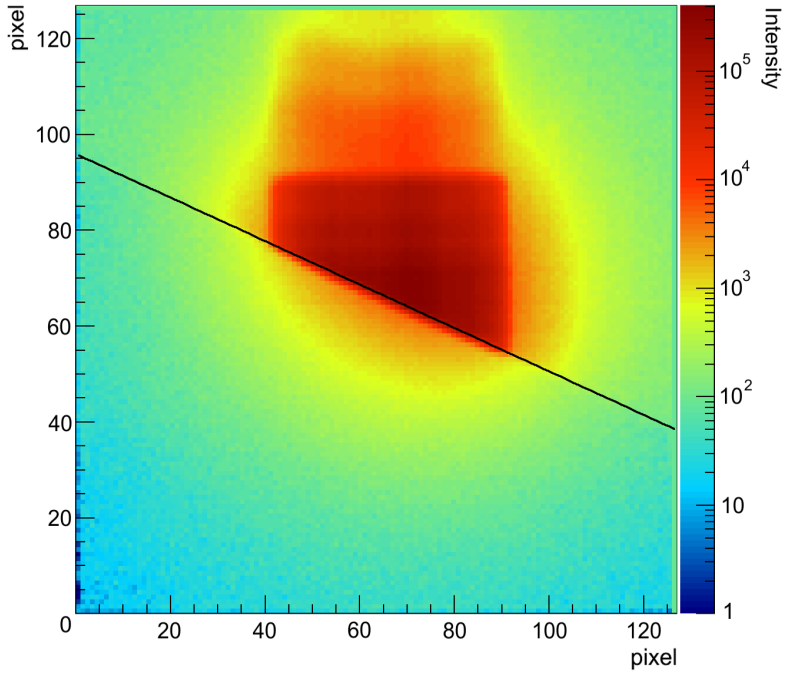

Figure 108: Image of a cold neutron beam at RESEDA in logarithmic scaling with a 1 mm thick cadmium aperture directly in front of the detector for determining the spatial resolution. The black line indicates the fit result of the edge spread function f_{es}. [K2016]

by hydrogen atoms in the detector material, which can be observed in Fig. 108 as a corona-like effect below the cadmium absorber.

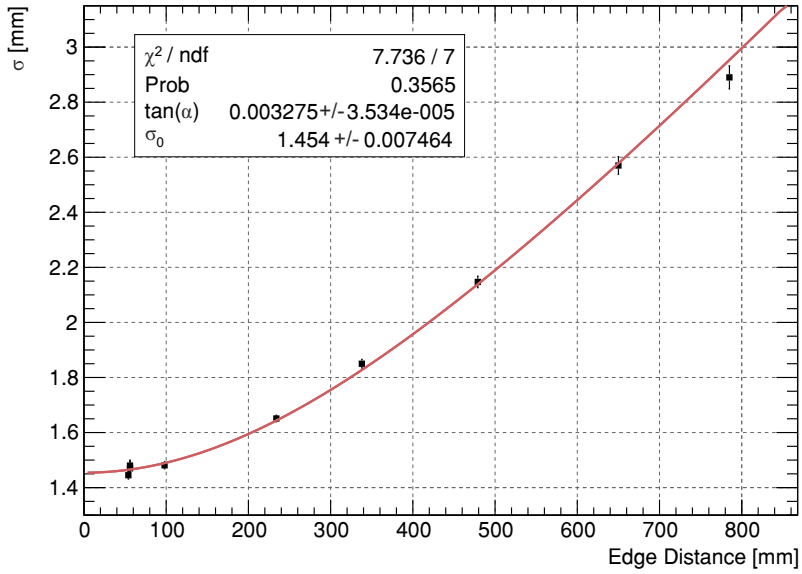

Figure 109: Determination of the spatial resolution. Fit results for the edge spread function (157) for increasing distances between detector and cadmium aperture, see also Fig. 108. [K2016]

Both aspects are addressed by URANOS simulations. Beginning and end of an ionization track cannot be separated in the detector due to the high electron drift velocities of approximately 3 cm per µs at 1 kV per cm [391]. Therefore, the spatial resolution ($1\,\sigma$) corresponds to one half of the projected track length. The mean free path varies by the size of the gap between the layers and also depends on the type of conversion product as the lithium ions escape the boron with lower energies compared to helium, see also sec. 11.1.2. Fig. 110 shows the track length distributions. The result for the total standard deviation is $1\,\sigma = 1.817\,\text{mm}/2 = 0.908\,\text{mm}$. Separated into conversion product types the results are $\sigma_{\text{He}} = 2.24\,\text{mm}$ for helium and $\sigma_{\text{Li}} = 1.31\,\text{mm}$ for lithium ions. The active detection volume of the detector contains hydrogen-based materials. The main contributors to the scattering cross section are the GEMs (50 µm thickness), the readout structure (100 µm) and the thermoplastic grids (44 µm). Instead of a gamma-dominated background this effect produces a homogenous low level

illumination by delocalized neutrons. As the scaling of scattering and absorption cross sections by wavelength is different the influence of this contribution also changes with the neutron energy. Albeit, most of the scattered neutrons are absorbed very closely to their origin. Typically, the amount of neutrons with a dislocation larger than one track length standard deviation stays well below 0.5 %, although at 5.4 Å for example 19 % of the detected neutrons have undergone at least one scattering process. The total point spread function of a simulated pencil shaped neutron beam at 5.4 Å is shown in Fig. 106.

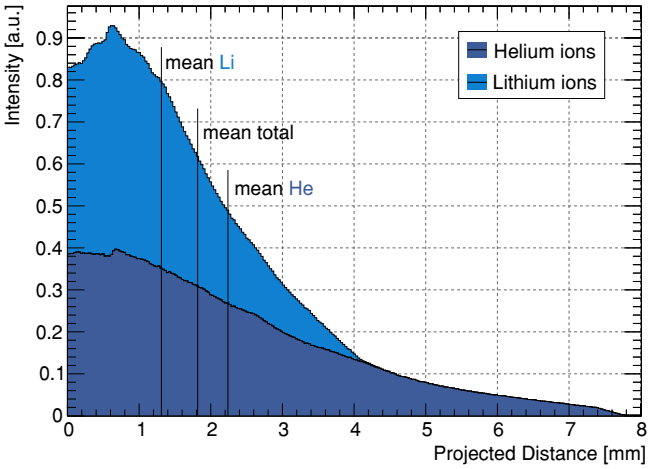

Figure 110: Simulation of the track length distribution of helium (dark blue) and lithium (light blue) conversion ions in the detector for the actual stack configuration. The vertical lines, denoted as „mean“, correspond to a width of 2 σ. [K2016]

The self scattering background plateau stays at least 4 orders of magnitude below the signal. In the simulation the total error defined by the 68.3 % quantile is found to be 1.56 mm. The error for self scattering effects then is calculated by subtracting the known errors from the total budget.
This error budget for the spatial resolution is denoted in tab. 18.

resolution	result [mm]	contribution
pixel size	0.45	10 %
ion smearing	0.908	39 %
self scattering	1.04	51 %
total	1.454±0.007	
Siemens star	1.39±0.05	

Table 18: Spatial resolution error budget for the 1 σ standard deviation. The total error is determined by measurement, the pixel effect by geometry, the ion smearing and the self scattering are determined by simulation. The contribution ratios refer to the total variance.

The specific shape of the point spread function with its non-Gaussian form and long tails can be targeted in different ways. In the optical measurement the aperture function sits on a background of constant illumination. Here, mainly the short range distribution contributes as the contrast loss of two approaching edges is determined and therefore it leads to the smallest result for the spatial resolution. By fitting an edge spread function to the projection of the aperture the effect of self scattering becomes more important, which is visible by the corona feature in the logarithmic intensity display of Fig. 108. Whereas in the measurements presented one cannot strictly distinguish between environmental and self scattered background, in the simulation one can track each neutron individually, which enables to include the specific plateau description of the point spread function. This leads to the result, that the homogeneously spread outliers contribute to an increase of the standard deviation.

11.4 | Detection efficiency

11.4.1 | The efficiency of a helium-3 tube

Depending on application or neutron source the detection efficiency is defined incongruently [392] and the reference literature is scarce for the 'gold standard': the helium-3 proportional counter.
Typically, in order to calculate the detection efficiency, the detector count rate N is determined from a shielded and moderated ^{252}Cf source with known fluence rate Φ. The detector response R, that measures the number of detector events per incident neutron fluence rate, is then given by $R = N/\Phi$. The applied industry standard requires to place the detector at a height of approximately 1 m in a distance of 2 m from the source, which follows the ISO recommendations [393]. The response of the instrument is then given in the unit [cps/ng], count rate per ng ^{252}Cf. As the source flux recorded by the detector consists of a direct component and a scattered component, additional corrections like to use of a shadow cone of borated polyethylene are necessary. Simulations of the response also rely on the emission spectrum of californium described in the same standard [149]. In reality, this measurement procedure is highly error-prone due to experimental limitations, like the arrangement of the calibration room, and environmental unknowns, like the exact material composition of the floor or air humidity. That complicates the commensurability of literature values, which mostly rely on this procedure. Therefore, it is necessary to calculate the efficiency of the helium-3 proportional counter to orthogonally incident neutrons of specifically relevant energies.

11.4.1.1 Analytic characterization

For materials with large capture cross sections and low scattering probabilities, $\sigma_\mathrm{a} \gg \sigma_\mathrm{s}$, one can use a simple attenuation law to describe the absorption efficiency of a counter tube or radius r_0:

$$\epsilon = \frac{1}{r_0}\int_0^{r_0} 1 - \exp\left(-2\mu(E,p)\sqrt{r_0^2 - x^2}\right)\mathrm{d}x \quad \text{with} \quad \mu(E,p) = p\frac{\rho N_a}{A}\,\sigma(E) \tag{158}$$

for materials of density ρ, pressure p, atomic weight a, Avogadro's number N_A and a cross section σ, in particular $\sigma_\mathrm{a}^{^3\mathrm{He}}(0.0253\,\mathrm{eV}) = 5330\,\mathrm{b}$ [98].

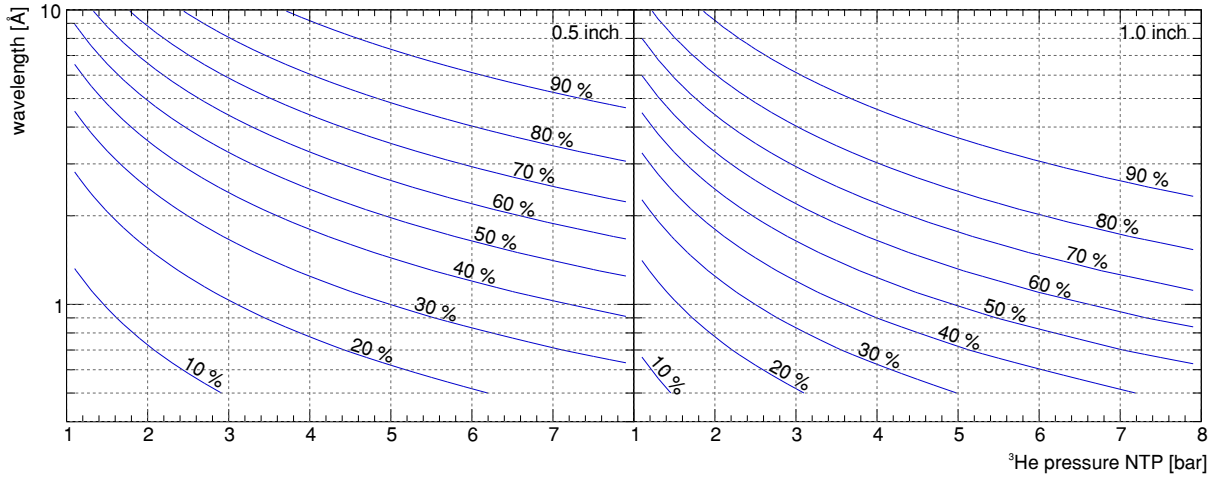

Figure 111: Absorption efficiency of helium-3 proportional counter tubes of two different diameters as a function of helium pressure and wavelength of monodirectional and monoenergetic neutrons. At usual pressures of 4 bar an efficiency of 40 % to 60 % can be reached for thermal energies (1.8 Å).

Due to both conversion ions being emitted back-to-back, see also sec. 8.2.1, the fraction of converted but undetected neutrons lies in the order of (1-2) %. This, however, only accounts for the mantle region. As commercial tubes of proportional counters are made of one piece of usually stainless steel without insulated endcaps, the deformation of the electric field leads to a significant dead region in the order of one tube diameter. The 'active length' is result of subtracting the latter from the total length of the counter tube.

The energy-dependent absorption efficiency in the center region of a tube is depicted in Fig. 111 for two different tube diameters and in Fig. 112 for the entire range of available diameters. Typical values for absorption efficiencies lie within (30-80) % with (50-60) % being a reasonable estimator for the commonly used 0.5 inch and 1 inch tubes.

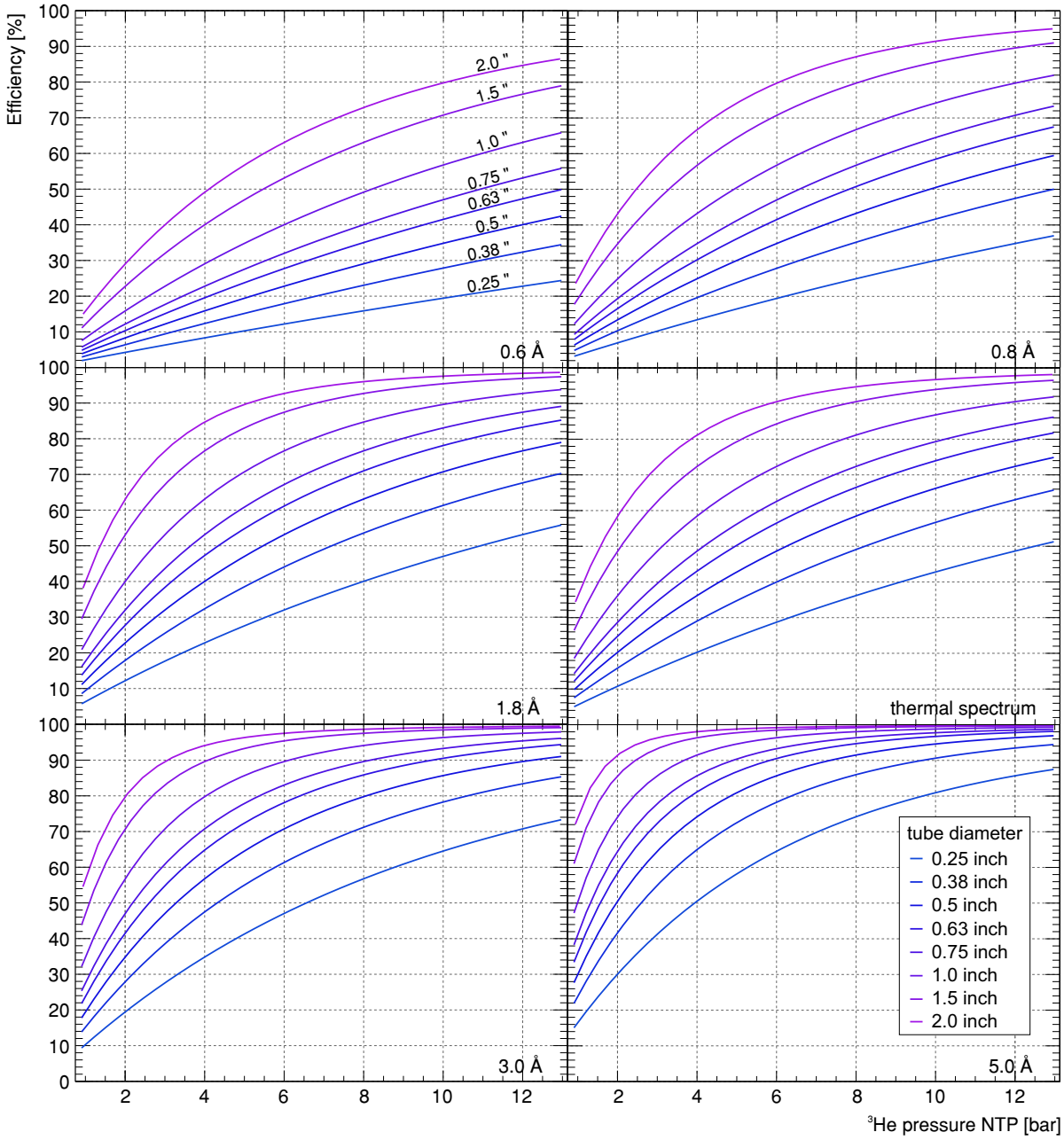

Figure 112: Absorption efficiency of helium-3 proportional counter tubes for relevant diameters as a function of helium pressure of monodirectional neutrons. The panels each represent a different incident wavelength with the middle row showing the difference between 1.8 Å and the integral over a thermal spectrum at 300 K ≈ 1.8 Å, e.g. (99).

The analytic efficiency models have been tested at the Heidelberg neutron source. The setup is shown in Fig. 113. The test sample, here a 2 inch GE Reuter Stokes 1.5 bar ^{3}He tube, is placed vertically in front of the reference counter „Manitu“, which is comprised of a 1 inch ^{3}He proportional counter shielded to all sides by boronated polyethylene except for an aperture of 2 cm width. The beamport A of the neutron source is much larger than the counter tubes with a width of 10 cm and a height of 5 cm. In order to avoid multiple scattering background the setup has to be placed as close as possible in front of the port. The source can additionally be shielded by a cadmium sheet of 1 mm width, which absorbs 99 % of the thermal neutrons[c]. In the measurement procedure the following count rates N are determined:

1. N_{bckg}: background measurement with all beamports closed,
2. N_{t}: source total flux measurement without the sample[d],
3. N_{Cd}: source epithermal flux measurement without the sample and with Cd sheet in front of the beamport,
4. $N_{\mathrm{Cd}}^{(\mathrm{S})}$: sample epithermal absorption measurement with Cd sheet in front of the beamport,
5. $N_{\mathrm{t}}^{(\mathrm{S})}$: sample total absorption measurement.

In case the total spectrum is know, steps 3 and 4 can be omitted, especially in case of a well-known absorber like helium-3. However, it can be used to verify or measure the thermal-to-epithermal fraction of the source spectrum.

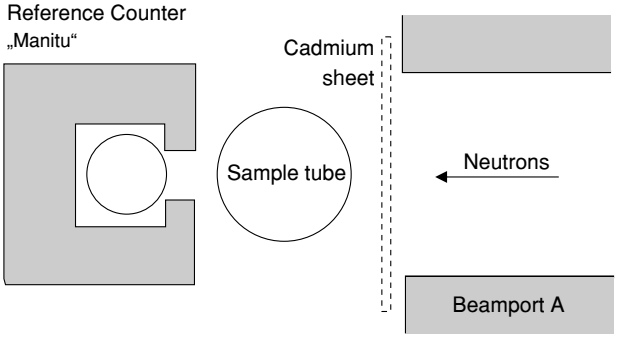

Figure 113: Setup for determining the neutron detector efficiency using the cadmium difference method, which separates thermal and epithermal flux. The reference counter, shielded by borated polyethylene (gray) measures the absorption efficiency of a sample placed in front.

The result for background-corrected absorbed flux by the sample tube was (58.5±1.5) %. In order to obtain the macroscopic cross section, i.e. the conversion gas pressure, this result has to be compared to the theoretical absorption efficiency. The source port emission spectrum Φ_S, which has been provided by U. Schmidt based on earlier Monte Carlo calculations from [394] is shown in Fig. 113. Φ_S has been fitted by a modified Westcott[e] function [395]

$$\Phi_S = \underbrace{I_1 \frac{E^2}{E_T^2} \exp\left(-\frac{E}{E_T}\right)}_{\text{thermal}} + \underbrace{I_2 \frac{E_T}{\left(1+\left(\frac{s_1}{E}\right)^7\right)\left(1-\frac{s_2}{1+\left(\frac{E}{s_3}\right)^5}\right)}}_{\text{joining term}} + \underbrace{f_1 E \sinh\left(\sqrt{2\frac{E-f_2}{\mathrm{MeV}}}\right)\exp\left(-\frac{E-f_2}{\mathrm{MeV}}\right)}_{\text{fission}},$$

[c] Due to its low-lying resonance ^{113}Cd absorbs nearly all neutrons exclusively below approximately 0.4 eV, see also Fig. 56.
[d] The total radiation environment of the source rooom is also depicted in Fig. 172 in appendix B.2.6.
[e] Carl Henry WESTCOTT, *1912-†1977, England.

with neutron energy E in eV and source energy $E_T = k_B T$ at a spectral temperature T. The remaining parameters have been evaluated from the fit: intensities of thermal and beyond-epithermal flux I_1 and I_2 as well the scaling variables s_1 to s_3 as the fission scaling parameters f_1 and f_2.

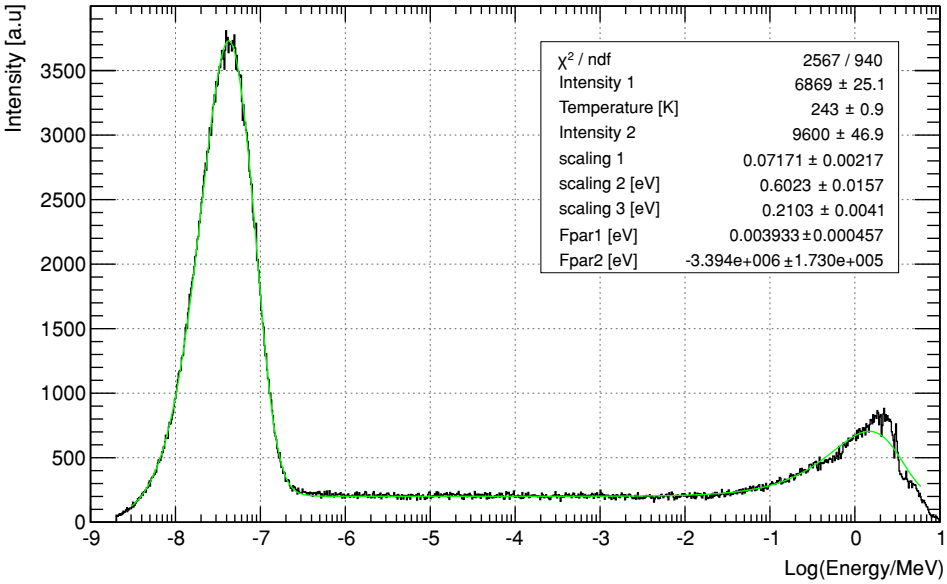

Figure 114: Spectrum of the Heidelberg neutron source from U. Schmidt based on the Monte Carlo model of [394], fitted by a modified Westcott function (159) (green).

Integrating the macroscopic cross section over the aperture using (158) yields for the measured[f] absorption efficiency of (58.5±1.5) % a partial pressure of (1.49±0.06) bar, see also Fig. 115. This is in close agreement for the value of 1.5 bar stated by the manufacturer.

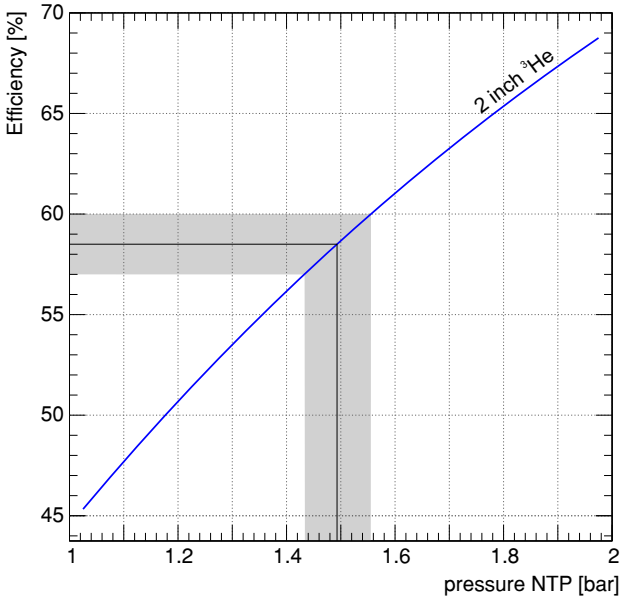

Figure 115: The calculated efficiency function (159) (blue), derived from earlier Monte Carlo simulations of the neutron source, yields for the measured absorption efficiency of the tube a partial ^{3}He pressure of (1.49±0.06) bar. The reference value is 1.5 bar.

[f] The reference tube used a Philips amplifier and has been read out by a LeCroy 3001 qVt Multi Channel Analyzer, which was connected to a Lattice MachXO2-based module designed by the PI electronics workshop, acting as a serial readout interface. However, as far as upper and lower thresholds are kept, the technical details of the readout electronics do not play a role for measurement of relative counting statistics.

11.4.2 | Efficiency determination at the hot neutron diffractometer

Part of the results about the efficiency determination of the CASCADE detector presented in this chapter have been published in [K2016].

The wavelength-dependent detection efficiency was measured at the HEiDi single crystal diffractometer [84] at the FRM II, which provides monochromatic hot neutrons, see also sec. 4.3.

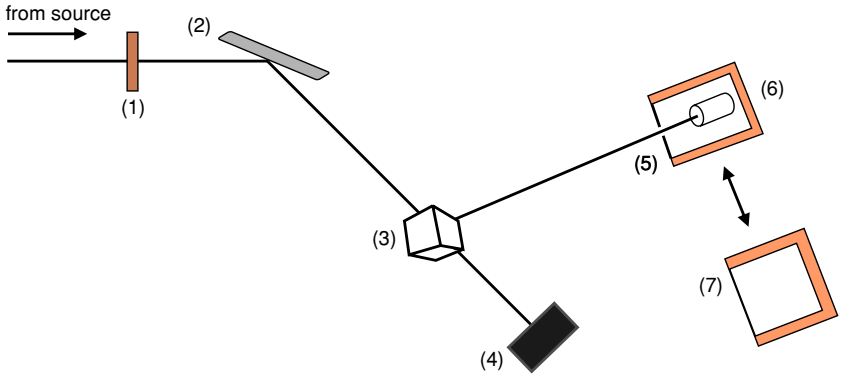

Figure 116: Setup for the efficiency determination at HEiDi: Neutrons pass an erbium filter (1) and a monochromator (2). In order to reduce divergence and contamination a silicon sample (3) on an Euler cradle reflects the beam towards the detector, which is either the reference helium tube (6) with its aperture (5) and borated polyethylene shielding (orange), or the CASCADE detector (7). A beam dump (4) absorbs the non-utilizable neutrons. The biological shield extends beyond the monochromator. Primary (fixed) and secondary collimator (optional) are not shown.

The experimental setup, see also Fig. 116 is the following: Neutrons coming from the 2300 K graphite source inside the reactor are wavelength selected by a germanium monochromator [396]. A 0.5 mm erbium foil removes a band in the hot spectrum below 0.5 Å [397]. Furthermore, the contamination is reduced by diffracting the beam by a cubic single crystal of silicon (125 mm^3) in Bragg condition at the sample position. Fig. 117 shows the spectrum at the hot source at the beginning of the guide to the HEiDi instrument.
As the flux density of high energetic neutrons below the measurement range is reasonably high, a beam contamination by integer fractions n of λ can occur. Small wavelength contributions are absent due to the product of spectral density and reflectivity of the sample. For Ge(311) the second reflex (622) is forbidden, which as well holds for Ge(533). The second reflex of Ge(422) and the third of Ge(311) are filtered by the erbium foil. The according domains are also depicted in Fig. 117. In total, the contribution of fractions of the selected wavelength stay below 0.5 %. In addition, a 15' collimator is used to reduce the horizontal divergence. Tab. 19 gives an overview about the configuration.

λ	Monochromator	Si (hkl)	2ϑ
0.593 Å	Ge(533)	(404)	36.0°
0.794 Å	Ge(422)	(404)	48.84°
1.17 Å	Ge(311)	(202)	35.52°

Table 19: Configurations for the wavelength selection at the HEiDi monochromator.

The standard HEiDi detector is an Eurisys 73NH17/5X ^{3}He counter tube with a pressure of 5 bar, a 4 mm alumina entrance window and an active length of 170 mm at a diameter

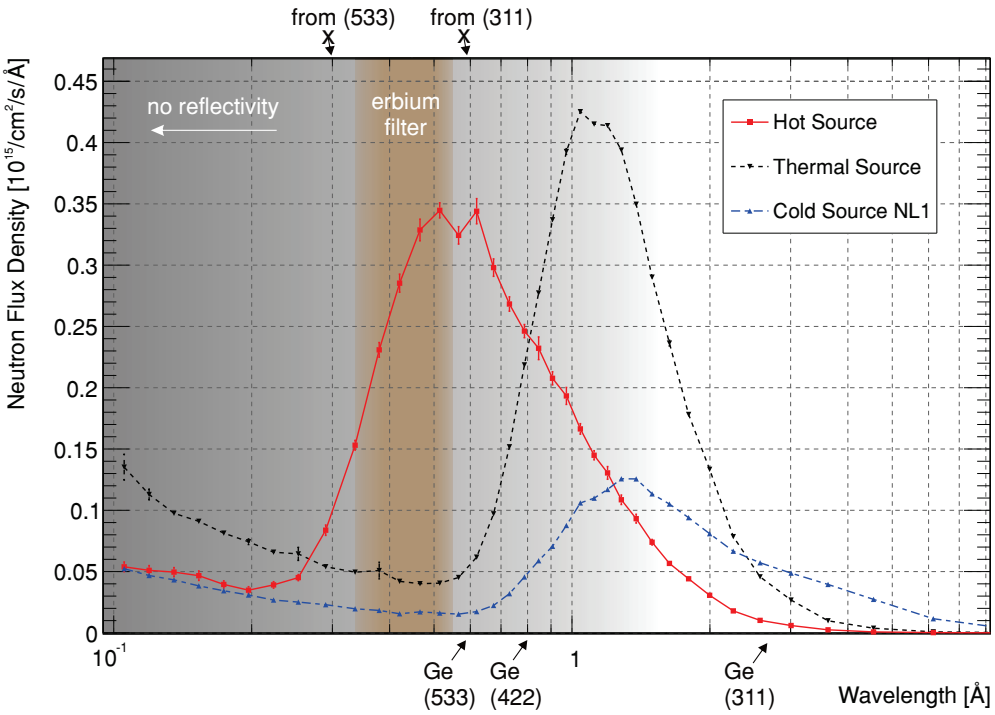

Figure 117: Neutron flux density as a function of wavelength at the FRM II for different beamlines. The HEiDi instrument is operated at the hot source (red). It uses a germanium monochromator to select specific wavelengths, indicated by the hkl reflexes. A high-energy cutoff by an erbium filter (brown) reduces higher order contributions, e.g. $\lambda/2$ and $\lambda/3$. Simulations published by the FRM and refined in 2010 by A. Röhrmoser. [K2016]

of 50 mm. The absorption of the entrance window is specified as 2 % for thermal neutrons, which translates to 1.3 % for the used wavelength of 1.17 Å. The tube can theoretically absorb more than 99.9 % of the remainder, see sec. 11.4.1. However, since no measurements exist for verification, the range provided by the manufacturer is used. In front of the detector at a distance of 200 mm a shielded aperture of 22 mm × 28 mm is mounted to limit the viewing angle towards the sample. Tab. 20 summarizes the reference measurements.

λ	efficiency	Bragg rate	background
0.593 Å	95.5 %	(512±2) 1/s	(3.76±0.18) 1/s
0.794 Å	97.0 %	(2618±2) 1/s	(20.0±0.8) 1/s
1.17 Å	98.5 %	(8015±8) 1/s	(38.3±0.6) 1/s

Table 20: Results for the reference measurements of the HEiDi ^{3}He counter for the specified wavelengths.

All measurement runs were conducted as a function of the inclination angle to investigate at the same time the characteristics of the signal distribution in each conversion layer as the comparably high energy of the neutrons leads to a more equal signal distribution throughout the layers. The efficiency measurements were carried out by placing the CASCADE detector at the position of the reference counter with the full active area oriented towards the sample. Therefore, the shielding around the detector housing covered only the backward facing 2π. In the Jalousie campaign [321] it was already found, that the instrument background is higher than expected.
The measurements suggested, that there is a considerable amount of neutrons leaking out of the beam access opening of the biological shield, which is furthermore scattered off the surrounding concrete walls. The contamination of the signal is strongly suppressed for the reference counter by its aperture and geometrical arrangement, compare also the left panel of Fig. 118. The CASCADE detector, however, is only shielded to five out of six sides, which in that case lowers the signal-to-noise ratio. The step in the background plateau seen in the middle panel of Fig. 118 shows for example the case, where at a higher inclination angle the sensitive area detector is already partly covered by the edges of the polyethylene shielding box.

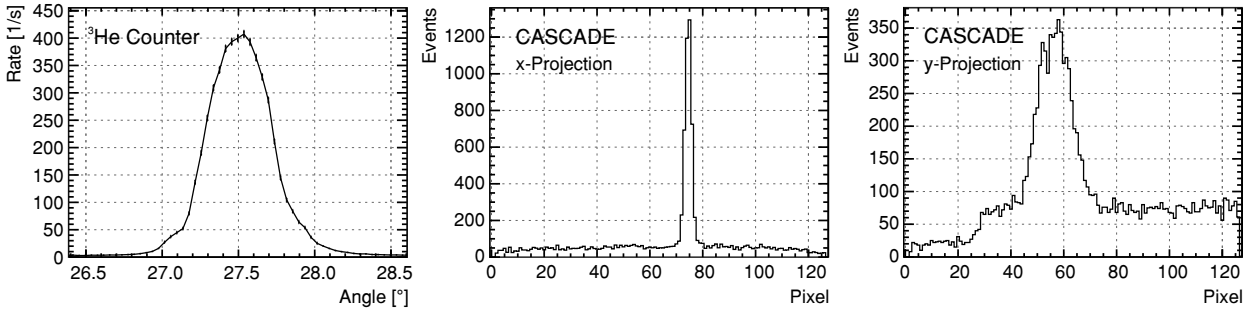

Figure 118: Beam spot measurements by the ^{3}He counter as a function of angle (left) and for the CASCADE detector in horizontal (x) and vertical (y) projection (middle and right). Due to the aperture limiting the field of view, the reference counter, unlike the CASCADE detector, is not susceptible to the divergence of the instrument background.

In the analysis it was found that by omitting to insert the vertical collimator before the sample, the beam broadened to a large extent, which would have complicated the evaluation in terms of precise aperture function calculations. In a comparative overview the spots for each wavelength as measured by the CASCADE detector are shown in Fig. 119.

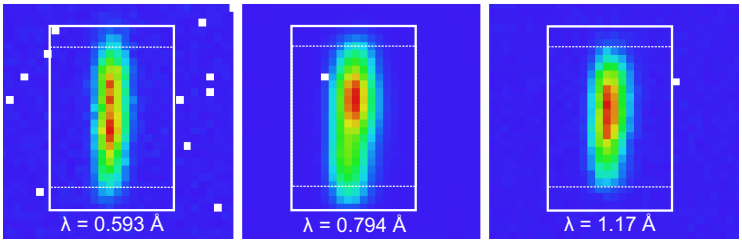

Figure 119: Spatial representation of the diffracted spots for each wavelength in a linear scaling relative to the maximum value present in the frame. The white boxes show the HEiDi ^{3}He counter aperture: in solid lines adapted to the beam divergence at the position of the CASCADE detector and dashed as scaled to the actual extent. [K2016]

Additionally, the beam at 1.17 Å showed an angular deviation of (0.91±0.15)° against both other wavelength runs, which can be a consequence of a slightly different focusing at each monochromator orientation. At a distance of 480 mm at the position of the aperture this translates to approximately 1 mm. This leads to a small fraction of the beam being absorbed and undetected by the reference counter. Therefore, the efficiency calculation is slightly overestimated as the ^{3}He count rate is compared to the results from the CASCADE detector, which does not have an artificial limitation on the viewing angle. Tab. 21 summarizes quantitatively the results of the efficiency measurements in comparison to the values obtained from the detector simulation.

	efficiency [%]		
λ	measured	simulation spot	simulation all
0.593 Å	7.82±0.04	7.95	8.33
0.794 Å	11.47±0.04	10.50	11.0
1.17 Å	16.21±0.04	14.95	15.62

Table 21: Results of the efficiency measurements of the 6-layer CASCADE detector in the imaging mode for the specified wavelengths compared to the simulated expectation values.

Fig. 120 shows the full angular data. For the efficiency analysis a circle cutout of 35 mm centered around beam spot has been chosen to accurately extrapolate the inhomogeneous background from the complementary pixel set. Therefore, in the simulation two values are given: one corresponding to the full detection efficiency and one for the expected count rate in the selection region. This distinction is attributed to the special shape of the spatial resolution function, see sec. 11.3. It has to be noted, that in

a generalized linear model, independent of the geometry, a scaling of the detection efficiency by λ is expected. The simulation can follow such an approximation for small wavelengths, however, the data points themselves are not strictly consistent with such a hypothesis.

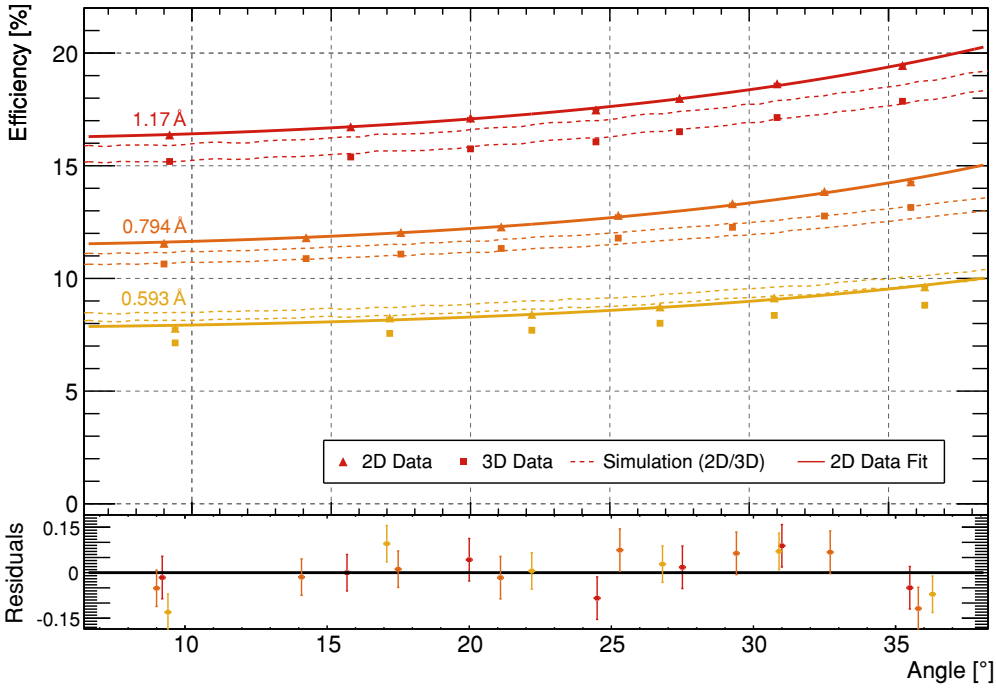

Figure 120: Efficiency of the CASCADE detector for three different wavelengths as a function of the inclination angle for the imaging and TOF mode. The residuals of the fit of an exponential to the data points are plotted in the lower panel. In comparison the simulation results are shown for the whole active detector area (upper curve) and the spot corresponding to the reference tube aperture (lower curve). [K2016]

For the reasons discussed before, which lead to deviations of the absolute count rate determination, in this measurement campaign the count rate uncertainty is conservatively set to 7 %. A deviation of similar magnitude was also found in the Jalousie campaign [321], which is as well technically different as the efficiency estimation was carried out by an analytical model.

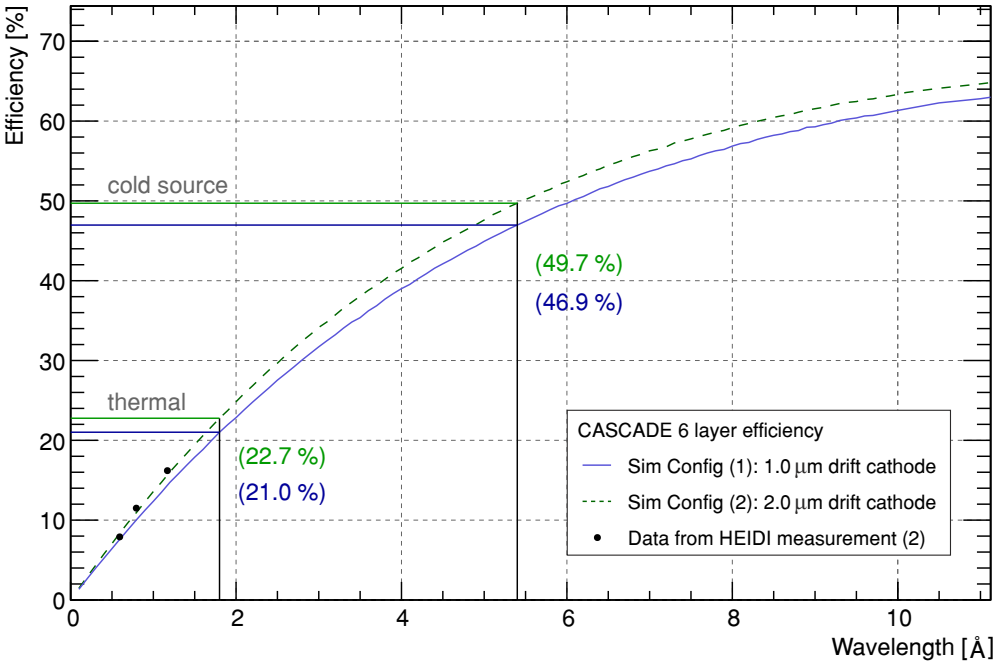

Figure 121: Efficiency of the CASCADE detector in both drift electrode configurations for the imaging mode at various wavelengths. The HEiDi measurements extrapolate to lower neutron temperatures. [K2016]

In conclusion one obtains for the efficiency at the selected wavelengths in the imaging mode: (7.8±0.5) % at 0.593 Å, (11.5±0.8) % at 0.794 Å and (16.2±1.1) % at 1.17 Å. The overall efficiency on the whole range of wavelengths is analyzed by the detector

simulation model, which is shown in Fig. 121. One obtains an efficiency for thermal neutrons (1.8 Å) of (22.7±1.6) % and (50.0±3.5) % for the 5.4 Å of the cold source at RESEDA. The updated detector with the 1 µm boron coating on the backside drift electrode has approximately 93 % of the count rate compared to the values determined in the measurements presented here.

Part V

COSMIC-RAY NEUTRON SENSING

12

INTRODUCTION

Throughout the history of Cosmic Ray discoveries 'range' was one of key observables. It started as early as 1900 when Villard[a] found a new type of radiation [398], which was later named γ and found to be produced by artificial sources as well as to be omnipresent in the environment. In order to disentangle ground from atmospheric effects numerous experiments were conducted, but it was not until balloon flights of Wulf[b] [399], Gockel[c] [400] and finally Hess[d] [401] from 1910-1914 studying the discharge of electrometers revealed the atmospheric contributions as the intensity did not decrease as expected by height. Although the invention of the Geiger counter and later the cloud chamber facilitated measurements by displaying and quantifying interactions of particles, the nature, intensity and composition of this cosmic radiation was subject to unsuccessful speculations. In 1933 Compton[e] concluded that the origin of this radiation are extraterrestrial high energetic particles [402], whereas Johnson's[f] experiments indicated that these would be largely positively charged [403]. During the 1930s different effects could be decomposed, so it could be understood by works of Bhabba[g] and Heitler[h] that the radiation is partly due to air showers [404] and a flux of galactic particles which alters by latitude and solar activity [405]. These highly energetic were as early as 1934 supposed to originate from supernovae [406].
The presence of neutrons in such air showers [407] was first investigated by Coccioni[i] by ground-based and airborne experiments, whereas Simpson[j] could identify nuclear disintegration as the main contributor [408] to the neutron production. As from the 1950s, based on established technologies, networks of neutron and myon monitors were set up in order to systematically study and characterize the cosmic radiation and its effects [409].

12.1 | SOIL MOISTURE SENSING TECHNIQUES

To date the measurement possibilities for determining the water content of the environment are either bound to local instrumentation or large-scale satellite-based technologies, both not meeting the typical correlation lengths for water resources, which has always been an issue for the interpretation of the available data [410]. This is called the intermediate scale gap [411]. Most of the local techniques are using in-situ probes which have to be installed and operated inside the soil. Although determining the water content by the electrical conductivity of the ground [412] is in general possible, this quantity depends on many other variables like salinity, temperature and nutrient content. Therefore, it is not possible to interpret such measurements without profound knowledge of the soil type. This holds true as well for similar methods, which make use of the dielectric properties of soil [413] for frequencies up to 1 GHz as the dipole moment of water is much higher than the one of other typical elements. The electri-

[a] Paul Ulrich VILLARD, *1860-†1934, France.
[b] Theodor WULF, *1868-†1946, German Empire.
[c] Albert GOCKEL, *1860-†1927, German Empire.
[d] Viktor Franz HESS, *1883-†1964, Austria-Hungary.
[e] Arthur Holly COMPTON, *1892-†1962, United States of America.
[f] Thomas Hope JOHNSON, *1899-†1998, United States of America.
[g] Homi Jehangir BHABHA, *1909-†1966, British India.
[h] Walter Heinrich HEITLER, *1904-†1981, German Empire.
[i] Vanna COCCONI-TONGIORGI, *1917-†1997, Kingdom of Italy.
[j] John Alexander SIMPSON, *1916-†2000, United States of America.

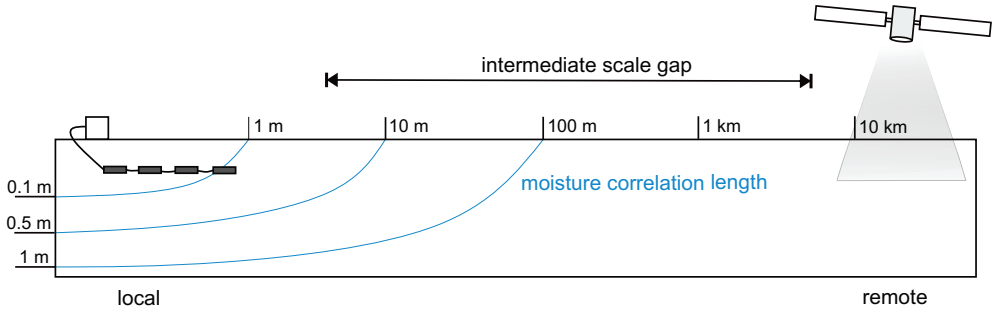

Figure 122: Ranges for different soil moisture sensing technologies with relevant scales for water distribution in the support volume.

cal properties of the soil also play the important role for **t**ime **d**omain **t**ransmission (TDT) and **t**ime **d**omain **r**eflectometry [414], which make use of the change of velocity for electromagnetic signals. This property is also used for **g**round **p**enetrating **r**adar (GPR) [415], which uses the transmission and reflection of electromagnetic waves in the subsurface and **e**lectro**m**agnetic **i**nduction (EMI) [416] based methods featuring mobile or stationary devices equipped with antennas or coils, respectively. In order to extend the scope any stationary technology can be distributed on an larger area in the form of sensor networks [417].

Among the non-invasive methods, which are typically referred to as remote sensing, there is the measurement of the blackbody emissivity of the soil in the microwave region either from ground-based stations [418], but meanwhile this technique is applied mostly from extremely high altitudes by dedicated satellites [419], most notable the recent ESA Copernicus program [420] with its Sentinel missions [421, 422]. As hydrogen also possesses the strongest nuclear magnetic moment the amount of water in the ground can also be determined by NMR devices [423]. A more sophisticated and experimental approach is the gravimetric determination of the surrounding subsurface-water by absolute microgravimeters [424]. Furthermore, the possibility to measure the water content by the reflection of GPS signals [425] is still in evaluation.

The methods mentioned mostly rely on electromagnetic properties of the soil, especially of water. Another exceptional property of hydrogen is the efficient slowing down of neutrons. Therefore, devices had been proposed which measure the thermalization of fission neutrons [426]. The absence of slow neutrons in a distance from an active source indicates the absence of water and/or the presence of a absorbers, and therefore this method suffers from the fact that already traces of isotopes like ^{10}B lead to a false interpretation without chemical analysis of the soil [427]. Nevertheless, this technique is still used in oil-well logging for downhole tools which have to be operated from the inside of a drilling tube [428].

12.2 | Cosmic-Ray neutron sensing: the technique

12.2.1 | The COSMOS sensor

Cosmic-ray neutron sensors of type CRS[k] are commercially available in several configurations, see Fig. 123. The CRS1000 and CRS1000/B are mainly in stationary use to monitor environmental neutron fluxes, and the Rover system [429] is typically used in vehicles for spatially resolved mobile surveys, for example in applications of agricultural land use [430]. A description of the main components can be found in [431]. The sensors comprise one or two moderated detector tubes sensitive to epithermal/fast neutrons, a high voltage generator, a pulse height analyzer, and a data logger with integrated telemetry. The detector can be regarded as a Bonner Sphere, see sec. 8.2.3, its energy sensitivity will be discussed in sec. 13.3. As a neutron moderator, high-

[k] Hydroinnova LLC, USA

density polyethylene of 1 inch thickness is used to encase the proportional counter. The CRS1000 uses helium-3, while the CRS1000/B uses boron trifluoride, which requires larger detectors in order to achieve the same count rate due to its lower cross section (3837 b vs. 5330 b at 25.3 meV) [98] and pressure (0.5 bar vs. 1.5 bar) and therefore lower macroscopic cross section. The Rover is technically equivalent, but consists of significantly larger detectors than the stationary sensors and two tubes in one moderated module to increase the event rate and therefore the time resolutions [432].

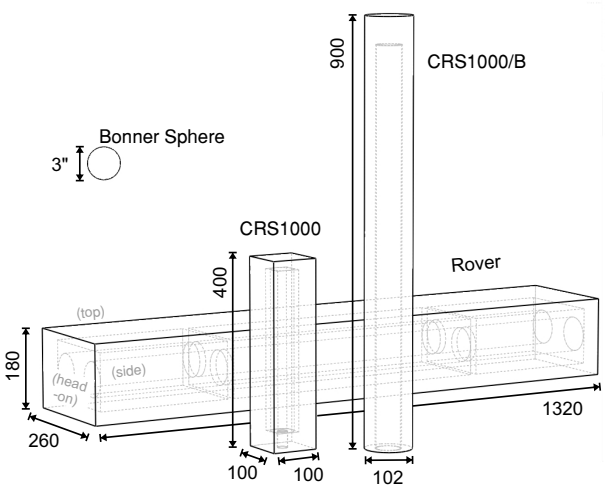

Figure 123: Variants of the cosmic-ray neutron detectors modeled in this study. Dimensions are in units of millimeters. To scale a Bonner Sphere is illustrated in comparison. [KS2018]

12.2.2 | SIGNAL CORRECTIONS

The cosmic-ray neutron spectrum is result of highly complex interplay of relativistic and non-relativistic particles, of leptons and baryons that create showers in the atmosphere like in a large calorimeter. Neutrons themselves as a by-product of these particle cascades make up a large part of the remaining radiation at ground level and are sensitive to the number of nucleons as long as being highly energetic and to hydrogen when being moderated. The neutron density N_n at the soil interface is influenced by various factors, which turn out to exhibit a non-linear scaling, including correlations to other relevant environmental variables. Nonetheless, in order to derive a soil moisture value θ, there is a set of linear off-the-shelf corrections, which are used for example in time series, but have mostly been gained empirically. The fully corrected neutron count rate of a sensor N_{corr} is calculated by

$$N_{\text{corr}} = N_n \cdot C_I \cdot C_p \cdot C_h, \tag{160}$$

where C_I denotes the incoming radiation correction, C_p the atmospheric pressure correction and C_h the air humidity correction - see also [433].
As discussed in section 3.1, the cosmic radiation, which penetrates the upper atmosphere creating secondary neutrons, is not constant in its flux. Its intensity depends on the solar cycle and the vertical cutoff rigidity and other temporal variations. These fluctuations can hardly be predicted and therefore are measured by neutron monitors[l] distributed in various locations around the world. Although these detectors primarily measure the highly-energetic proton component of the incoming radiation, there is a similar dynamic assumed for neutrons [431] for regions of the same cutoff rigidity. The **N**eutron **M**onitor **D**ata **B**ase (NMDB)[m] provides real-time data about the incoming radiation I, which can be retrieved automatically. The established correction method

[l] see sec. 8.2.2 and the time series in Fig. 9.
[m] accessible via http://www01.nmdb.eu/

uses then a standardized count rate for the respective detector I_{ref} for the **incoming radiation correction**

$$C_I = 1 + \gamma \left(\frac{I_{\text{ref}}}{I} - 1 \right) \tag{161}$$

using $\gamma = 1$. More sophisticated correction approaches are analyzed in [434].

The incoming radiation including the secondary particles are attenuated by the atmosphere. The reference pressure p at the sensor location provides a good estimator for the mass of the air column. The **barometric pressure correction** therefore can be written using the atmospheric depth at reference pressure $X_{\text{ref}} \approx 1000\,\text{g/cm}^{2\,[n]}$

$$C_p = \exp\left(\frac{X - X_{\text{ref}}}{\lambda_{\text{atm}}} \right) \tag{162}$$

and the atmospheric attenuation length λ_{atm}. In [435] $\lambda_{\text{atm}} = 132\,\text{g/cm}^2$ is assumed. Yet, this parameter itself depends on energy range, altitude and cutoff rigidity as it represents an average of interaction lengths of different primary and secondary air shower particles, e.g. seen in Fig. 12. Literature values of measurements range from (130-165) g/cm^2, overviews can be found in [435–438] and [439].

Atmospheric water vapor can account for three effects on the measured neutron signal. Firstly, it increases the area density and secondly especially the hydrogen abundance pre-moderates the spectrum. Albedo neutrons are then furthermore also scattered off these water molecules near the surface. [440] assumes, that the latter has a negligible effect[o] and proposes the following correction function:

$$C_h = 1 + \alpha_{\text{hum}} \left(h_{\text{abs}} - h_{\text{abs}}^{\text{ref}} \right) \tag{163}$$

with $\alpha_{\text{hum}} = 0.0054\,\text{m}^3/\text{g}$, absolute humidity h_{abs} and a reference value of $h_{\text{abs}}^{\text{ref}} = 12\,\text{g/m}^3$, which corresponds to 50 % relative humidity at 25 °C. Relative and absolute humidity h at a given temperature T (in K) can be approximated by

$$h(h_{\text{rel}}, T) = 1323.48 \frac{\text{g}}{\text{m}^3}\, h_{\text{rel}}\, 10^{\frac{aT}{b+T}} \quad \text{with} \quad (a,b) = \begin{cases} (7.5, 237.3\,\text{K}), & \text{if } T > 273.15\,\text{K}, \\ (7.6, 240.7\,\text{K}), & \text{otherwise.} \end{cases} \tag{164}$$

12.2.3 | Soil moisture determination

The above-ground neutron spectrum contains two parts. The pure incoming radiation Φ_{inc} never had any contact with soil. The albedo component φ_{alb} is then defined as those neutrons which passed the interface at least once:

$$\Phi_{\text{tot}} = \Phi_{\text{inc}} + \Phi_{\text{alb}} \rightarrow N = k_{\text{inc}} N_0 + k_{\text{alb}}(\theta) N_0. \tag{165}$$

Soil moisture θ is then inferred from the intensity change of the reflected component. As any hydrogen in the environment contributes to the signal, all water pools have to be added up, including biomass θ_{org} and chemically bound lattice water θ_{lw}, which is typically in the order of (1-2) % volumetric soil moisture:

$$\theta = \theta_{\text{mob}} + \theta_{\text{org}} + \theta_{\text{lw}}. \tag{166}$$

[n] standard conditions assume at sea level $p_{\text{NTP}} = 1013\,\text{hPa}$ and $X = \int_0^{h_{\max}} \rho_{\text{air}}(h)\text{d}h = p/g$.
[o] we will later see, that this is not the case.

Although the typical definitions of soil moisture account only for the available water θ_{mob}, this work for reasons of simplicity implicitly assumes the extension of this term by including hydrogen contributions, which can be converted to effective soil moisture values according to $\theta = \Sigma_i \theta_i$.
In [429] the count rate of the sensor N is assumed to be derived from a reference parameter N_0, which is supposed to be the instrument count rate over entirely dry soil[p]. The neutron flux as a function of gravimetric or volumetric soil moisture θ then follows a simple hyperbola

$$\theta(N) = \frac{a_0}{\frac{N}{N_0} - a_1} - a_2, \tag{167}$$

with the parameters $a_0 = 0.0808$, $a_1 = 0.372$ and $a_2 = 0.115$ derived from an empirical analysis in [429]. a_1 equals the incoming radiation fraction k_{inc}, a_0 and a_2 have the units of m^3/m^3 or kg/kg. Although the approach to use only the sensor-specific calibration parameter N_0 leads in many cases to satisfying results, individual site conditions, however, have led authors to use slightly different sets of a_i parameters [441–443]. The reasons for these ambiguous results will be discussed later and address the understanding of neutron transport and individual contributions to the signal, yet, relation (167) can be used to estimate the error σ_θ

$$\sigma_\theta = \left| \frac{\delta\theta}{\delta N} \sigma_N \right| = \frac{a_0 \frac{1}{N_0}}{\left(\frac{N}{N_0} - a_1\right)^2} \sigma_N = \ldots = (\theta + a_2)^2 \, \frac{\sigma_N}{a_0 N_0}, \tag{168}$$

for which due to counting statistics $\sigma_N = \sqrt{N}$ can be assumed. Hence, the relative error can be calculated as

$$\frac{\sigma_\theta}{\theta} = \left(1 + 2a_1 a_2 + a_1 \theta + \frac{1}{\theta}\left(a_2 + a_1 a_2^2\right)\right) \frac{1}{\sqrt{N}}. \tag{169}$$

As N and θ are related to each other by $N(\theta) = N_0 \cdot (\frac{a_0}{\theta + a_2} + a_1)$, using (167) one can replace the acquired counts by multiples of acquisition intervals of the parameter N_0.

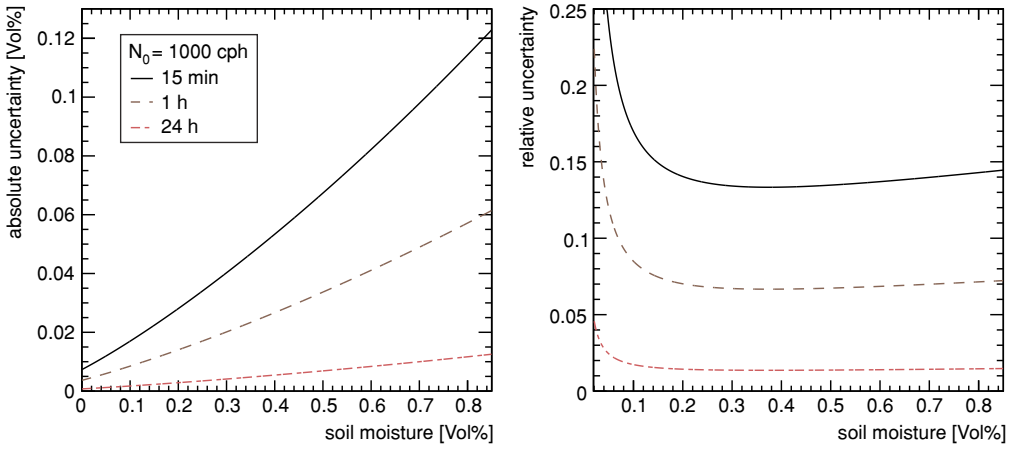

Figure 124: Absolute (left) and relative (right) errors for soil moisture determination using (167) for CRNS sensors.

[p] we will see later, that this definition has some drawbacks.

13

UNDERSTANDING THE COSMIC-RAY NEUTRON DETECTOR

Part of the results about the CRNS probe presented in this chapter have been published in [KS2018].

In order to reduce the enormous computational effort, which inevitably goes along with the large scale differences of a ~ 1 m^3 detector in a ~ 1 km^3 environment, effective response models have to be applied rather than using the geometrical detector itself in the simulation. The solution to increase the recorded flux is to adequately scale up the volume of the detector entity. However, if the recorded flux is supposed to be increased by use of such a detector with its actual enlarged geometry (e.g. moderator and converter tube), this significantly alters its characteristics. A virtual sensor entity with an effective model allows for the upscaling of the counting volume of a detector, while still retaining the same features as the unscaled type. It also allows to set the maximum detection probability within the operation range to 100 %. However, such neutron detection models are sensitive to the specific response function of the detector [444–446]. Previous studies, where the results of this work can be related to, were based especially on the modeling of Bonner Spheres [163–167], and showed [168] that the detector response function can be approximated by the product of an energy-dependent efficiency term and an angular term. Monte Carlo models which rely on the implementation of such functions, e.g. [447], are a subclass of global variance reduction methods [448], which aim on increasing the computational efficiency, especially in undersampled regions.

13.1 | THE DETECTOR MODEL

The detector models, which are actually used for Cosmic-Ray Neutron Sensing have been introduced in sec. 12.2.1. In URANOS the device is modeled by a voxel geometry. The central cutout of the rover configuration is shown exemplarily in Fig. 125, the other detectors are presented in appendix B.2.5. The sensor geometry has been derived from actual devices and from supporting information provided by the manufacturer [449], see also Fig. 123. Details of the mechanical parts have been reduced to features that

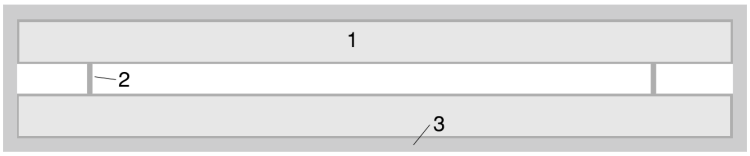

Figure 125: Cross section of the Rover detector simulation model with a length of 132 cm and a width of 26 cm. It features two gas filled proportional counter tubes in a stainless steel casing (1), aluminum mounting brackets (2) and a HDPE moderator (3). [KS2018]

have a significant influence on the neutron response, and only materials with significant macroscopic neutron cross sections have been considered. The size of the voxels has been set to 1 mm × 1 mm × h mm, whereas h denotes the layer height to which the voxel is extruded and varies from 1 mm, the generic cubic configuration, to 850 mm for the length of the CRS1000/B tube. The materials used are: high-density polyethylene

(CH_2), aluminum oxide (Al_2O_3), steel (Fe with 20 % Cr, 20 % Ni) at 8.03 g/cm^3, boron trifluoride (^{10}B enriched BF_3 gas), ^{3}He enriched noble gas, and air (78 % N_2, 21 % O_2, 1 % Ar). The partial gas pressure has been set to 1.5 bar for helium and to 0.5 bar for boron trifluoride. See also appendix B.2.3.
The stationary systems (CRS1000 and CRS1000/B) are oriented upright, while the mobile system „rover“ is oriented horizontally. Consequently, the „top“ facing neutron flux runs from the surface upwards through the short cuboid face of the stationary sensor, and through the long cuboid face of the mobile detector. The „side“ facing fluxes run parallel to the surface through the long faces of the stationary detector and through two short and two long faces of the mobile detector.

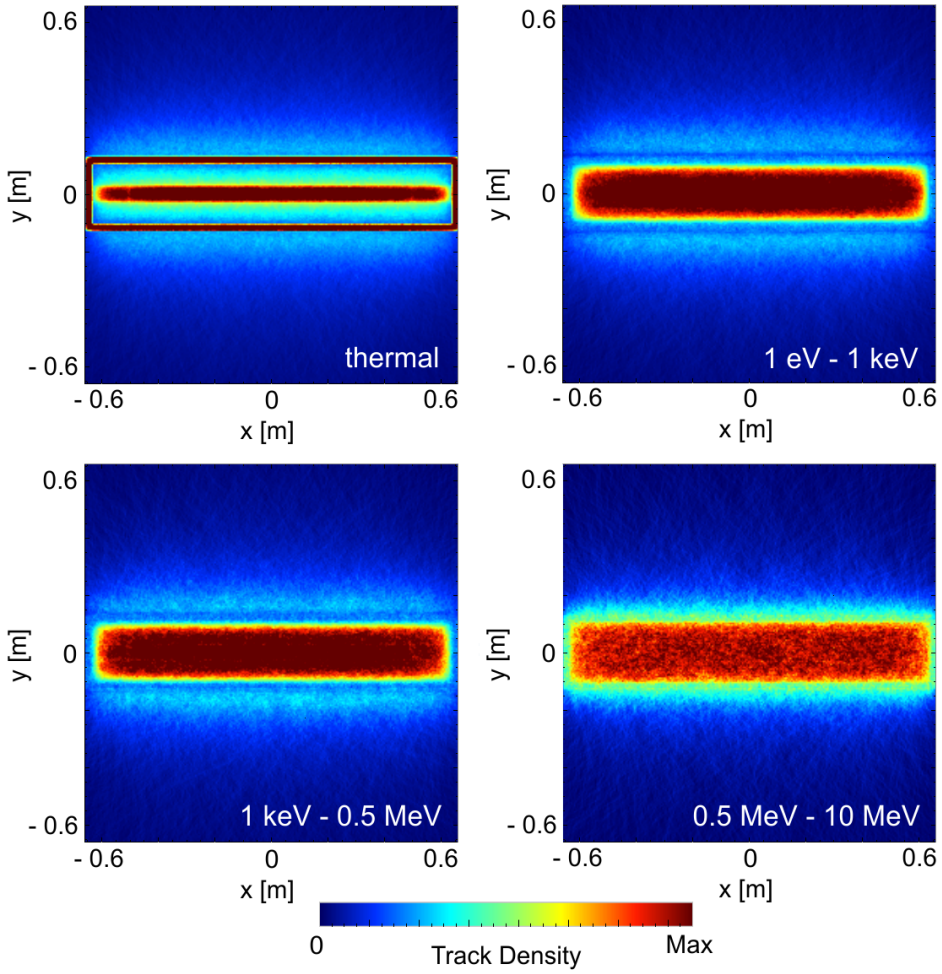

Figure 126: Track density within the $^{10}BF_3$ rover detector model using a randomly distributed flux from a plane source, illustrated for four energy regimes from thermal to MeV. The outer casing of the detector (see also Fig. 123) consists of polyethylene, which becomes visible by the outward directed flux. Neutrons of high energies (lower right panel) do not undergo enough interactions to stay contained in the casing. Thermalized neutrons (upper left panel) are scattered within the moderator and are efficiently absorbed by one of the two tubes, with a probability of ≈ 0.5 to be captured in either of them. [KS2018]

In order to simulate incoming cosmic-ray flux from the atmosphere, monoenergetic neutrons were released randomly from a virtual plane of the same extension as the model dimensions. The number of neutrons absorbed in the converter gas divided by the total number of neutrons released is defined as the efficiency $R(E, \vartheta)$ of the setup, which intrinsically normalizes the efficiency to the detector area. As for the CRS1000/B with its cylindrical housing also the identical plane source definitions are used, this geometry leads to an ambiguity in the efficiency definition, which has to be considered for interpreting the results, see also [392]. That means, due to the surface

normals being different for the cubic CRS1000 and the cylinder of the /B version, the directionality of an orthogonally incident flux cannot be defined consistently for both[a]. To study the behavior of neutrons inside a detector system, the simulated neutron track density is shown exemplarily for a $^{10}BF_3$ rover detector in Fig. 126. The tracks represent $4 \cdot 10^7$ histories of incident neutrons with kinetic energies spanning 10 orders of magnitude. From the perspective of MeV neutrons, the path length through the polyethylene casing is in the order of the scattering length. This leads to an almost geometrically homogeneous distribution, where reflected neutrons have a negligible probability of reentry. Neutrons with $E \geq 1\,\text{keV}$ exhibit shorter scattering lengths while the energy lost by moderation allows for more neutrons in the boundary region to escape the device (seen by the 'glow' at the perimeter). For smaller energies, $E \leq 1\,\text{keV}$, the leakage out of the device is minimized while the number of interactions within the moderator is maximized. In a cross section through the model (not shown) this equals the flux outside the polyethylene being lower compared to higher energy domains. As soon as neutrons are thermalized, their absorption in the converter gas gets most effective.

13.2 | The energy response function

The energy response of a detector system, $R(E, \vartheta)$, quantifies this sensitivity as a function of neutron energy E and incident angle ϑ:

$$R(E, \vartheta) = \epsilon(E) \cdot g(\vartheta)\,, \tag{170}$$

where an angle of $\vartheta = 0$ would correspond to an orthogonal neutron incidence. Averaged over the whole surface of the detector, the incoming flux can independently characterized as a function of these quantities. The analysis of the energy dependence is presented in the following. The results from the simulations of the angular sensitivity can be found in appendix B.2.5.2.

13.3 | Energy dependence

The energy-dependent component of the neutron response, $\epsilon(E)$, has been calculated by URANOS simulations of different detector configurations. The results presented in Fig. 127[b] show that all detector models exhibit qualitatively similar energy response in the range from 0.1 eV to 1 MeV with a maximum between 1 eV and 10 eV. The main differences in the resulting curves can be attributed to the absolute detection efficiency, which is a function of the detector model, the converter gas and casing area. The latter is influenced by the geometry and orientation of the detector, as the surface neutron flux is averaged over the exposed area. Minor qualitative deviations of the response functions are noticeable for different aspect ratios of moderator and counter tube, compare CRS1000 (top) and rover (side) in Fig. 127. The highest efficiency is achieved for neutrons in the energy range between 1 eV and 100 eV, while between 0.1 eV and 0.1 MeV average efficiencies can be found. The latter range corresponds to the 'water-sensitive domain' for the CRNS technique. The manufacturer has stated that the working energy range for the detectors is within 100 eV to 10 keV (unpublished data). This energy window appears to be too narrow compared to the results presented

[a] Nota bene: this definition is not phase space conserving under angular variation - considering a neutron beam incident onto the sensor from a specific direction, the effective projected area of the corresponding cuboid face has to be taken into account.

[b] The cosmic-ray neutron flux density is represented per logarithmic unit of energy, see (33) in sec. 1.4.1, given in units of $\mathrm{d}\Phi/\mathrm{d}(\log(E)) = E\,\mathrm{d}\Phi/\mathrm{d}E$.

here, indicating a hitherto underestimation of near-thermal neutrons. A significant contribution of eV-neutrons was also suggested by other authors using empirical [450] and modeling analysis [451]. The energy efficiency shows also remarkable similarity to reference curves of Bonner Spheres with equal moderator thickness, see Fig. 47. As an example, the rover detector system with the standard 1 inch moderator thickness approximately corresponds to a 3 inch moderator type with a 3.2 cm spherical counter [169], or to detectors equipped with a 4 mm ^{6}LiI crystal and a 2 inch moderator [165]. This example illustrates that the main influence on the energy-dependent response can be attributed to the thickness of the moderator. Similar results also have been presented for portal monitor type detectors [120]. For the actual integration of such a response into an environmental neutron transport model a probe-specific function derived from a cubic spline interpolation of this data or in good approximation Bonner Sphere calculations can be utilized.

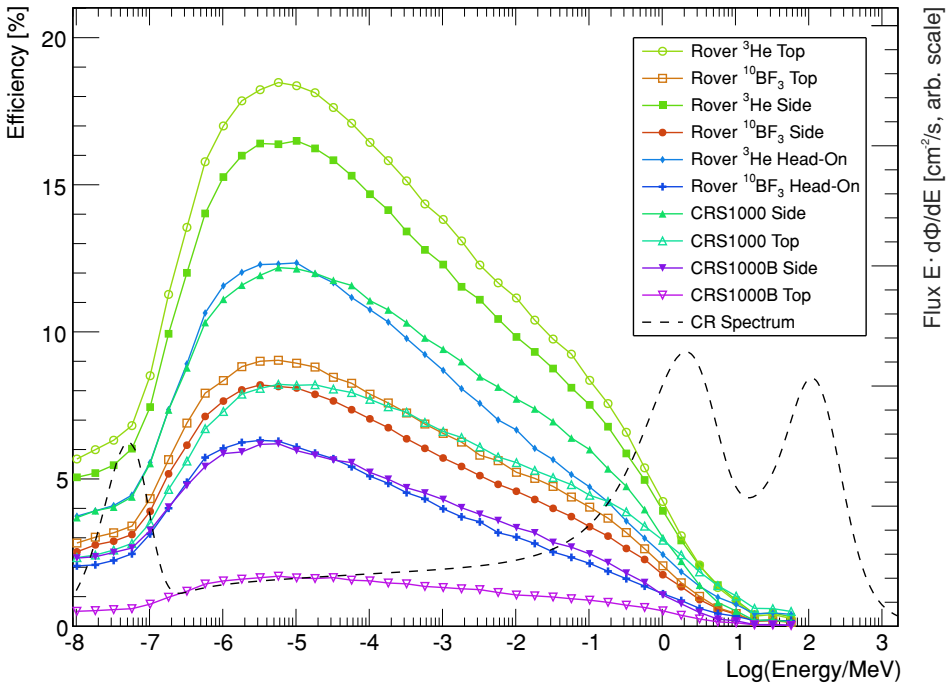

Figure 127: Absolute counting efficiency for various actual cosmic-ray neutron sensing devices. The results for perpendicular irradiation are averaged over the entire surface for each setup. For 'CRS1000 Side' exemplarily the effect of production-related density variations between 0.92 g/cm^3 (low) and 0.98 g/cm^3 (high) are plotted. The cosmic-ray neutron spectrum from [66] illustrates the relative abundance of neutrons above the surface. [KS2018]

13.4 | Detection probability within the case

The results above have addressed the detector efficiency averaged over the entire detector surface. However, the detector case itself cannot be considered as a homogeneously responsive device. A neutron hitting the detector centrally has a much higher absorption probability than a neutron entering at the very edge of a moderator. The spatial distribution of the detector efficiency can be illustrated by an efficiency map. As an example, Fig. 128 shows the boron trifluoride rover system with its two proportional counter tubes for 10 eV neutrons from the side- and top-facing perspective. The color scale represents the detection probability for a normally incident neutron, showing that detection is more probable in a narrower area for sideways incident neutrons compared to neutrons incident from the top. Although for the epithermal/fast regime Fig. 125 showed a homogeneous distribution of the tracks inside the casing, the absolute efficiency varies significantly depending on the individual original impact location.

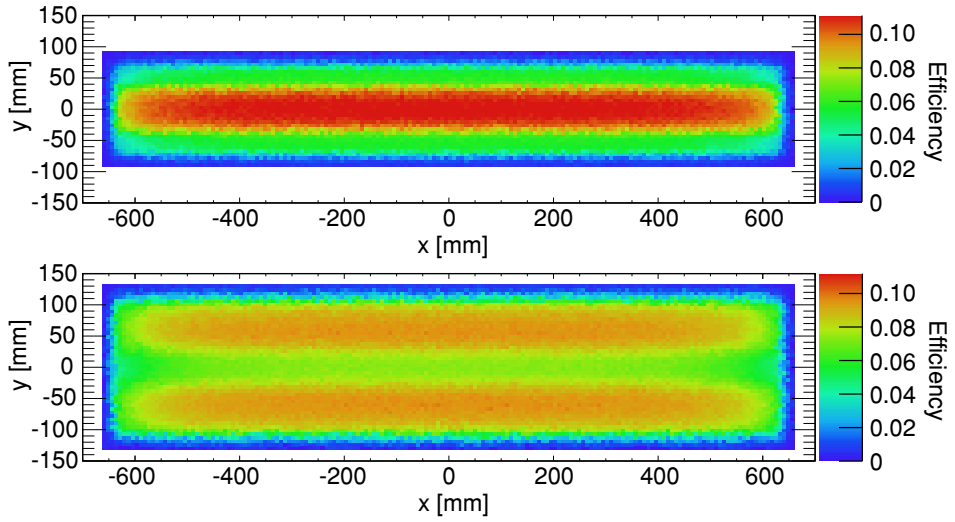

Figure 128: Efficiency map for the $^{10}BF_3$ rover system for orthogonally incident neutrons from the side (top panel) and the top direction (bottom panel), depicting the probability of being absorbed in the converter dependent on the x, y coordinate entering the detector. [KS2018]

13.5 | Uncertainty analysis

Simulations performed in this study were conducted with 10^6 released neutrons, which corresponds to a relative statistical error of the detector response R of $s_R = 10^{-2}/\sqrt{R}$, where $R = R(E, \theta)$ is given in units of percent and usually stays below 1 %. The good agreement with reference calculations from literature confirmed the reasonability of this approach, see also sec. 6.6.2. Systematic errors of potential relevance mainly involve the assumptions on material composition and geometry. For polyethylene the scattering kernel was emulated by water. Due to the higher mobility of water molecules, it could have biased the resulting efficiency by up to 10 %, particularly in the thermal regime. The fabrication related variations of polyethylene density could further alter the macroscopic cross sections of the real detector in the order of (1-2) %, thereby shifting the actual response function towards thicker or thinner moderators. Moreover, the abstraction level used for the modeled detector geometry has been high, as only moderator, absorber, and the metal parts have been taken into account. Nonetheless, the calculations showed that even drastic changes of the arrangement had only marginal effects on the response function.

13.6 | Implications of the sensitivity analysis

Although the internal assembly of the detector is clearly distinguishable in the impact location map of Fig. 128, the device is small compared to the diffusion length of environmental neutron fluxes, see also Fig. 30. Therefore, higher accuracy of the presented computational results would not lead to relevant information for environmental research.

Therefore, one can conclude that for the general analysis of neutron transport, a domain specified from 100 eV to 10 keV is suitable, slightly underestimating the contribution from both ends of the spectrum - fast and thermal neutrons. The implications of working with the simple model of a lower and upper threshold for the sensitive range are probably moderate. The entire spectrum from 1 eV to 0.1 MeV is dominated by elastic scattering and the cosmic-ray induced density of albedo neutrons. It is related to the environmental water content and scales uniformly in this regime [66]. Hence, the asymmetric shape of $\epsilon(E)$ has a minor influence on the sensitivity of the device in terms of soil moisture sensing. According to additional simulations (not shown), the change of the sensor's footprint radius, which will be investigated later, is negligible. The similarity to the response of Bonner Spheres, however, explains the reported influence of

thermal neutrons on CRNS detectors [450, 451].
Given the effective detection area of the cuboid sensor and its angular response, both conformations do exhibit a different sensitivity to the neutron flux directly below the sensor. In other words, near-field effects as seen later, can be attributed to the relatively high sensitivity to the downward direction and the flux distribution around the detector. In situations of small-scale changes of the topology below the sensor as for example in the monitoring of snow cover [452] with height and snow pack variations or dense and time-varying biomass estimations [433] there is a direct influence of the external flux field to the probe response.

14

FOOTPRINT INVESTIGATION

14.1 | FOOTPRINT PRELUDIUM

Part of the results about the footprint investigation presented in this chapter have been published in [KS2015] with complementary information in the follow-up publication [SK2017].

The aim of this work is to investigate the specific features of neutron transport at an air-ground interface. Specifically, the system can be regarded as an exponentially decreasing volume source from a low-density to a high-density region, whereas the latter slows down neutrons much faster due to the higher abundance of water. As hydrogen interactions also have a different scattering angle distribution the system behaves asymmetrically regarding the domain particle density parity. The goal of this study is to find and describe the ensemble dynamics in a highly non-linear system.

14.1.1 | THE COSMIC-RAY NEUTRON SPECTRUM ASSEMBLY

Continuing from the description in sec. 3.2 the focus is set on parameters for maximal atmospheric depths (low altitude) $d_0 = 1020\,\mathrm{g/cm^2}$, solar maximum conditions $s = 1700\,\mathrm{MV}$ and an exemplary cutoff rigidity of $r_c = 10\,\mathrm{GV}$. This procedure might introduce small differences for different places on Earth. However, measurements [65] show that geomagnetic latitude has only very small effects on the shape of the spectrum. It depends slightly on atmospheric depth, as at d_0 the detectable particle flux can be regarded as the tails of the high energetic cascades, see sec. 3.1. A lower cutoff rigidity means a higher contribution of low energetic particles to the primary spectrum and a higher altitude means a different ratio of proton and neutron fluxes, which each have different interaction lengths [32][a].

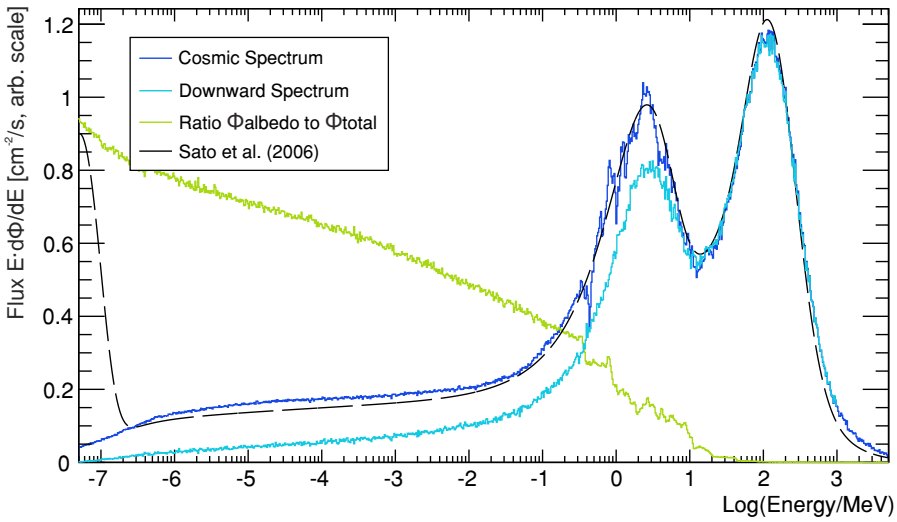

Figure 129: Cosmic-ray neutron spectra starting from the analytical angular integrated spectrum [66] (black) generating the downward flux only spectrum (cyan) by subtracting the albedo from the total spectrum (blue). The ratio (green) can be calculated independently over any, in this case water, body. Neutron flux given in units of lethargy (98).

[a] At sea level the hadronic flux can be estimated to be composed of 94 % neutrons, 4 % pions and 2 % protons. Therefore, the overall-nucleon flux is dominated by neutrons. Their attenuation length ranges from $140\,\mathrm{g/cm^2}$ at evaporation energies to $160\,\mathrm{g/cm^2}$ in the GeV range. The high-energy proton attenuation length, however, is much lower with $110\,\mathrm{g/cm^2}$ due to electromagnetic interactions in addition to the hadronic channels. Myons, as mainly electromagnetically interacting minimum ionizing particles, in comparison are much more penetrating with $520\,\mathrm{g/cm^2}$. This leads to a dynamic composition of the residual particles of atmospheric cascades and especially in regard to the above-ground neutron flux.

As the MeV-and-below-neutron spectra Φ generally consist of an incoming Φ_{inc} as well as a backscattered component Φ_{a}, an incident spectrum is obtained by two steps:

1. for the given spectrum a response spectrum is calculated over pure water,
2. the resulting backscattered spectrum is subtracted from the original spectrum.

$$I_{\text{inc}} = \Phi - \Phi_{\text{a}} = \Phi\,(1 - r) \tag{171}$$

with the ratio being defined as $r = \Phi_{\text{a}}/\Phi$. This recalculated spectrum then contains only incident neutrons and can be used as the source of incoming radiation for any surface condition. Fig. 129 shows the result of this calculation. From the response of a pure water body a factor for each energy bin is obtained which is used to generate the downward-facing part from the analytical spectrum of [66]. This energy distribution can be used to arrive again at the full spectrum in a simulation model. For epithermal and fast neutrons the flux is considered distributed in 2π. An exception to this otherwise isotropic distribution are emission angles of high-energy neutrons above 10 MeV, which are highly collimated along the downward facing direction (nadir angle θ). According to observations and simulations by Nesterenok [453] the non-uniformity of the angular spectrum $J(\theta)$ is given by[b]:

$$J(\theta) = e^{-2.5\,(1-\cos\theta)}. \tag{172}$$

This strategy combines a universal and validated source spectrum for cosmic neutrons with a high computational efficiency. As the location of the source is commonly traded against computational effort, whereas the initial energy spectrum is bonded to a variety of uncertainties, the modeling presented here can entirely focus on the description of the air-ground interface. A popular approach is to emit secondary cosmic-ray neutrons at approximately 8 km altitude and to perform a cascaded propagation through the atmosphere [437, 440, 455]. This strategy and related simplifications come with several drawbacks:

- Cross-sections of high-energy neutrons exhibit uncertainties of up to 50 % depending on element and type of reaction, though there has been progress in the last two decades. As a consequence, inconsistencies are apparent throughout different codes for galactic and atmospheric cosmic-ray transport [456–458].
- Measurements of cosmic-ray energy spectra are additionally accompanied by observational uncertainties. Comparative studies of Monte Carlo codes show differences of up to 20 % for calculating sensitivities of the neutron response to experimental devices [245, 459, 460] and as well for the spectrum unfolding technique [246].
- The exclusive neutron source at the top of the modeled atmosphere inadvertently neglects neutron generation throughout the atmosphere by other secondary particles like protons, pions and muons.
- Atmospheric water vapor is often ignored, although hydrogen is the main moderator for neutrons[c].
- The large difference in scale of the domain requires high computational effort to reach sufficient statistics.

[b] The factor of 2.4 for (172) originally published in [453] for atmospheric depths of 1000 g/cm^2 has been corrected to 2.5 according to [454]. As a comparison: the angular distribution over all energies in[158] scales by a factor of 1.9.

[c] However, the analytical spectrum by Sato [61, 66, 461] used in this work also has this shortcoming.

Models which rely on particle propagation through the upper atmosphere incorporate a high complexity and vulnerability to such uncertainties.
In the attempt to reduce computational effort, other studies identified the high-energy component of the cosmic-ray neutron spectrum as the precursor for the generation of fast neutrons in the soil [462, 463]. Since the attenuation process of high-energy neutrons in the ground is known, it seems likely that an artificial source in the soil is sufficient to mimic the production of evaporation neutrons. However, some drawbacks of this method are important to note:

- Attenuation of high-energy neutrons in the soil follows an exponential decrease that is dependent on soil type and location on Earth.
- There is no verified energy spectrum for neutrons in the soil.
- Evaporation neutrons are a significant part, but do not make up the spectrum as a whole, see Fig. 129. The incoming energy spectrum from the atmosphere exhibits low-energy components and particularly neutrons which already evaporated in the air.

Considering only evaporation neutrons in the soil can be an approach, especially for dry conditions, which tends to overestimate average neutron energies, as incident low-energy neutrons from the top are neglected, and thus also overestimates the footprint size. Moreover, the deduced footprint appears to be insensitive to soil moisture, because its influence on neutron moderation is underestimated. Here, a different approach is applied, which aims to combine the advantages as well as avoid the drawbacks of both strategies mentioned above. To minimize the uncertainties of the propagated energy spectrum, this study focuses on the domain close to the surface by using validated results from independent atmospheric simulations as model input.

14.1.2 | Experimental verification

Since the footprint definition is based on a radial symmetry, direct empirical evidence is difficult to achieve with natural structures. However, approaching water surfaces and transiting the coast line has been a common procedure to determine the range of detected neutrons. For example, [464] moved the detector over a lake and interprets that the signal strength is hardly sensitive to neutrons from the land side at distances greater than 200 m. In the last years, many experiments with CRNS detectors have been performed across a water-land boundary. Data from Oceanside Pier (California, US) indicate that the sensitive distance is on the order of (100-200) m at sea level. With URANOS attempts have been made to reproduce these transect experiments by moving a 4 m square-shaped detector over pure water and land with exemplary soil moistures from 1 % to 30 % and fixed air humidity $h = 10\,\mathrm{g/m^3}$. Figure 130 illustrates the simulations and the two experiments mentioned above. The simulated signal strengths clearly correspond to the measurements and give an indication of the soil water content which was unknown at the time of the experiments.
The signal gradient is asymmetric over water (Fig. 130 left) and land (Fig. 130 right), which agrees with results from [455], who investigated the influence of large wet structures on the signal strength. However, direct observables for neutron transport cannot be identified in the experiment as transect experiments do not give a direct measure of the footprint radius under conditions where the instrument is usually applied. These effects can be explained by (1) the overestimation of dry over wet regions in the signal, as a consequence of the non-linear relation: $\theta \mapsto N$, (2) the effective removal of traveling neutrons due to the presence of a water body on their way to the detector, and (3) the non-radial geometry of the experiment. However, the presented data provide

evidence for the valid performance of the URANOS model.

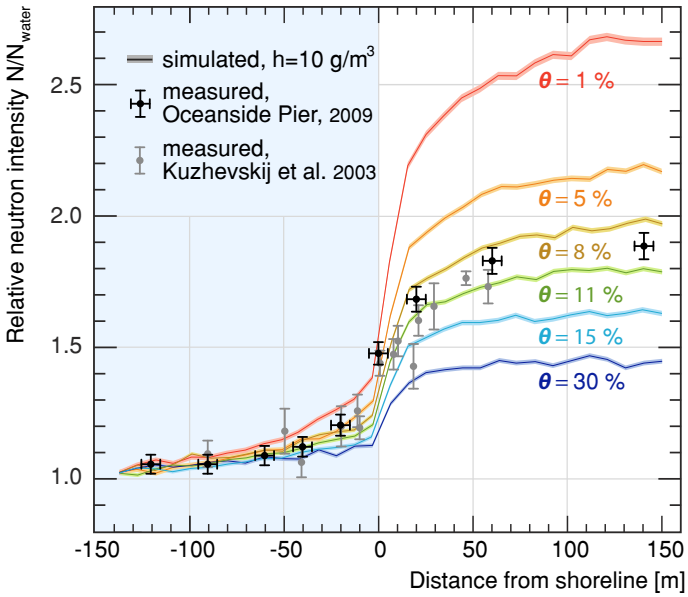

Figure 130: Coastal transect experiments simulated with a 4 m square-shaped detector every ±10 m from the coast line. Relative neutron counts show good agreement with measurements across a water-land boundary at the Oceanside Pier (US) as well as tests at Lake Seliger (RU) [464]. Air humidity h and soil moisture θ of the experiments were unknown. [KS2015]

In order to study the small-scale effects, which, as seen later, are predicted by URANOS, experiments have been carried out by M. Zreda with a detector over a pool. In a series

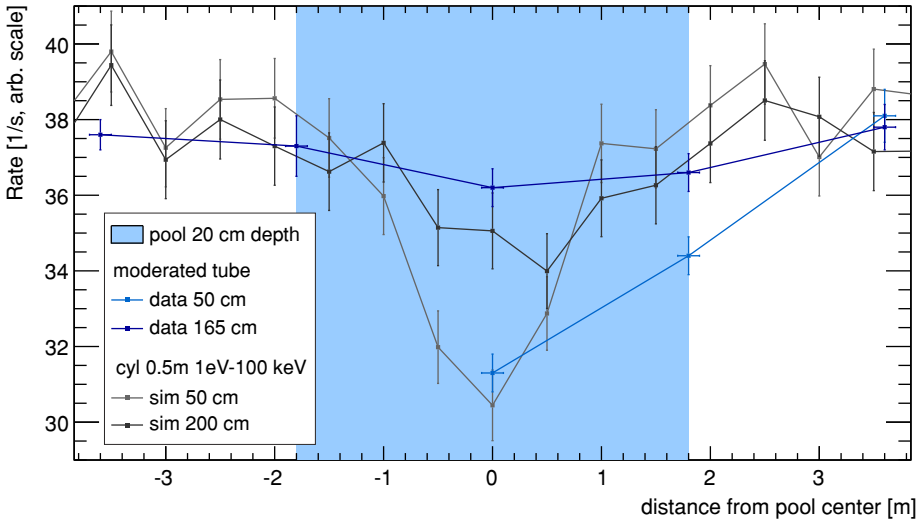

Figure 131: Swimming pool transect experiments by M. Zreda and accordingly simulated setup with virtual cylindrical detectors of 0.25 m radius. Furthermore, baseline measurements were taken in order to normalize simulation and experimental data outside the range shown in the plot.

of two transects at heights of 50 cm and 165 cm over a pool of 0.9 m radius filled with 20 cm of water. The experiment was carried out in a dry region of Arizona (US), where, using TDR probes, in the vicinity of the experiment θ =7 % was found and 9 % soil moisture was found in 20 m distance around a building structure. A rover-type of CRNS detector was used, see sec. 12.2.1, which has a significant spatial extension of 1.3 m length compared to the pool itself. For the simulations the soil moisture was set to 7 %, 6.5 g/m^3 air humidity and 920 mBar air pressure. The simulated detector entities were cylinders of radius 0.25 m and 0.5 m height, superimposed to the air layer, 100 % efficiency[d] and an energy range of 1 eV to 100 keV at heights of 0.5 m to 1 m and 2 m to 2.5 m. Experiment and simulation agree remarkably well in this case where the signal domain is tiny compared to the overall footprint with an areal contribution of 10^{-5} to 10^{-6}. The slightly stronger signal in the simulations can be attributed to

[d] yet non-absorbing, otherwise the simulated detectors would influence each other.

the slightly larger water body and to possible contributions of lattice water and soil moisture gradients in the order of 2 $\%_{Vol}$.

14.1.3 | A CLOSER LOOK AT THE AIR-GROUND INTERFACE

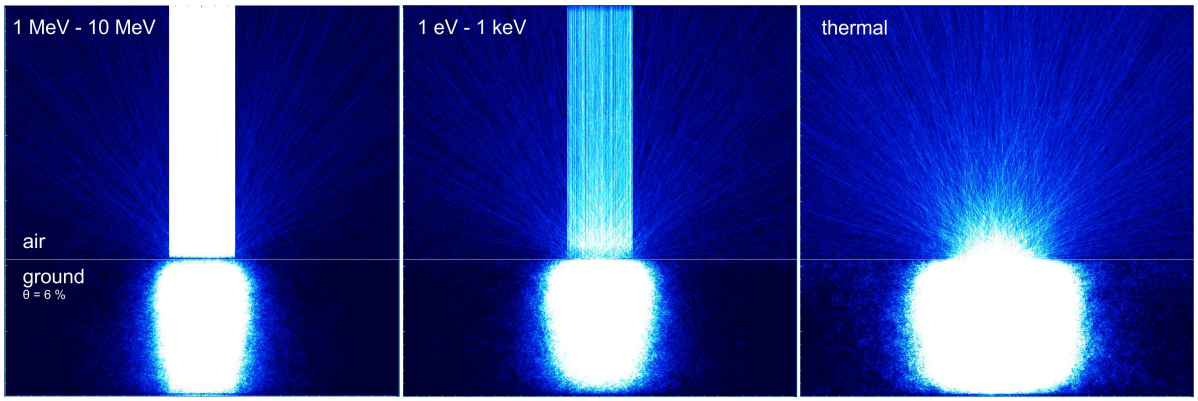

Figure 132: Flux calculation of an air-ground interface in which neutrons are artificially released centered straight down but with a CR spectrum according to Fig. 129 based on (67). The simulated neutron tracks from evaporation (MeV) to absorption (thermal) of $80{\cdot}10^4$ histories are displayed in a domain of 3 m × 3 m × 3 m.

In air the mean free path for neutrons is approximately 1000 times larger than in the soil, see also Fig. 30. In an artificial scenario aiming to visualize the transport at the interface, a flux column is released onto the ground. A rather dry condition is chosen in order to show a more spatially extended distribution. Fig. 132 shows the tracks of all neutrons in the domain in three different energy regimes. Most high-energy neutrons entering the soil are scattered in forward direction, therefore, the possibility of leaving the ground is considerably low - except originating from evaporation processes, that emit secondary particles nearly isotropically. However, only neutrons within the top few dozen centimeters below the interface border exhibit a significant probability for leaving. In general, this also leads to slant soil emission angles being suppressed. Epithermal neutrons below 1 MeV behave rather diffusively until they are moderated to thermal energies. As a first order approach, one can indeed expect neutrons to behave as a diffusive gas, as it was formulated by [465], and applied to a footprint estimate by [463] besides the modeling. But since every collision results in an energy loss for the neutrons, their mean free path between collisions changes and pure diffusion theory loses validity. The Fermi age theory, e.g. applied in [466], accounts for these energy losses in a diffusive system, but analytical solutions exist only for mono-energetic particles and are not feasible for the cosmic-ray neutron spectrum exposed to a wide range of environmental conditions with different cross sections.
The cosmic-ray spectrum is partly also made up of neutrons slowed down in air, which have a higher probability of being emitted back into the air[e]. For thermalized neutrons the soil can be regarded as a source. It can be explained by the fact that the moderation due to the presence of hydrogen is effective and no isotope having a large capture cross section is present, contrary to the case of air, in which argon and especially nitrogen are comparably strong absorbers.

[e] In this scenario the emitted flux is partially suppressed as all particles are released straightly downwards, which means that by collisions with hydrogen at least two scatterings are required to change the direction along the z-axis. In a more realistic simulation with rather slant impact angles onto the ground a scattering reaction in forward direction can already lead to leaving the soil.

14.1.4 | Model setup

14.1.4.1 Neutron source and detector

Neutrons are released from a volume source with randomly distributed origins from 2 m to 42 m above the surface. The amount of initial particles per run was chosen according to statistical errors - 10^7 histories are a reasonable trade-off between computational effort and precision for typical calculations presented here[f]. The simulations for the footprint analysis, which will be presented in the following, do not make use of the later implemented high energy cascade transport model.

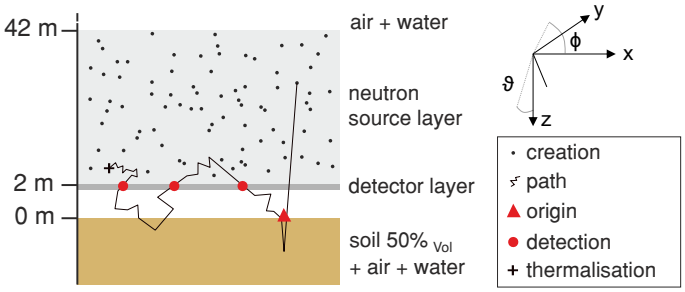

Figure 133: Setup of the simulation containing a 40 m thick neutron source layer in the atmosphere and a thin detector layer at 2 m above ground. A particle is counted as an albedo neutron if it had preceding contact with the soil. [KS2015]

Neutrons are recorded individually in an horizontally infinite detector layer, see also sec. 6.5.1. Any neutron that experienced interaction with the soil is counted as it passes the layer. The infinite plane detector overlays the atmosphere by means of a 25 cm high sheet at a vertical position of (175-200) cm, a usual height for mounting cosmic-ray probes. The detector layer is crossed by the neutrons and thus maps spatially the neutron density[g]. For the effective energy range to which the detector is sensitive, practical considerations by [463] and theoretical by for example [467], the detection energy is set to a window from 10 eV to 10^4 eV.The detection efficiency of moderated helium-3 detectors is nearly constant in that energy regime [468], which is why signal weighting for different energies is not necessary. However, common cosmic-ray neutron detectors, see sec. 12.2.1, are contaminated by approximately (10-20) % thermal neutrons [450]. It is not intended to account for this issue here, as this study aims to investigate characteristics for a detector ideally tailored to the needs of environmental water sensing.

14.1.4.2 Air, soil and water

The modeled pure air medium consists of 78 $\%_{Vol}$ nitrogen, 21 $\%_{Vol}$ oxygen and 1 $\%_{Vol}$ argon usually at a pressure of 1020 mbar. The soil extends to a depth of 3 m and the air to 1000 m. Both, soil and air are represented by planes of infinite extension, which can have subdomains, either to create a density profile in depth or to add specific entities like water or a detector. The soil consists of 50 $\%_{Vol}$ solids and a scalable amount of H_2O. The solid domain is comprised of 75 $\%_{Vol}$ SiO_2 and 25 $\%_{Vol}$ Al_2O_3 at a compound

[f] At the time of investigating the footprint such a calculation, depending on the soil moisture, took around 4 h. Due to further performance improvements URANOS meanwhile runs in such a setup approximately 250 neutrons per core per GHz per second, which means 10^7 histories can be tracked in around 40 min.

[g] Multiple counts of a single neutron in the detector layer account for the measured density equivalent for a single count per volume detector. This relation holds if (1) the dimension of the absorbing detector medium stays below typical scale lengths of neutron interactions (10 m-100 m), and (2) particles do not scatter multiple times in that volume. That is very unlikely for non-thermal neutrons and furthermore does not factorize in the count statistics.
Caveat: Typically Monte Carlo simulations like MCNP score particle flux as track length per volume. In the case presented here with no preferred detector orientation and infinite layer geometries this definition is at least unhandy.

density of 2.86 g/cm^3. Thus, the total densities vary from 1.43 g/cm^3 to 1.93 g/cm^3 for 0 %$_{Vol}$ and 50 %$_{Vol}$ soil moisture, respectively. Further chemical constituents regarding rock types are not significant[h] for the characteristics in the epithermal regime [431, 469]. Further material properties can be found in appendix B.2.3, however, the amount of chemically bound water in rocks lies in the order of a few percent, therefore 0 % soil moisture is a case mainly of theoretical interest.

14.1.5 | Soil moisture and above-ground neutron density

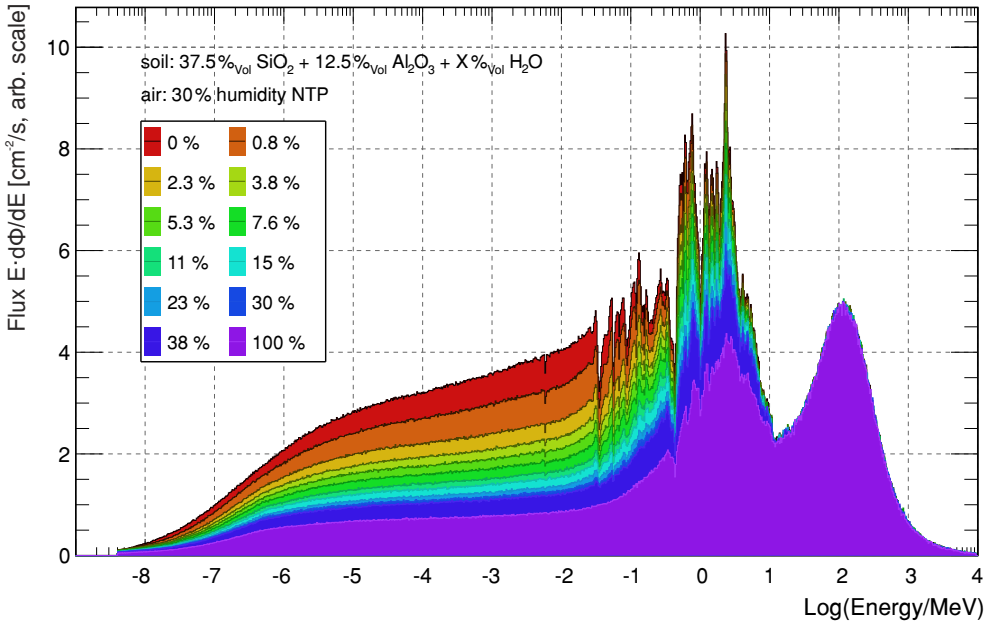

Figure 134: Neutron spectrum without thermal transport in a height of 2 m above the ground for different volumetric soil moisture conditions and a water body.

The response of the ground to the incoming flux of cosmic-ray neutrons lead to several interesting features in the resulting energy spectrum. Fig. 134 shows the efficient reduction of neutron intensity by soil moisture in the relevant energy range of the CRNS method. In general, the neutron density appears to be very sensitive to small amounts of hydrogen in the soil (and air).

The domain below 1 MeV is governed by elastic scattering, the relative density in this regime depends on how effectively neutrons are slowed down. Tab. 22 lists the stopping power, see also sec. 1.4.1, of some elements. It summarizes that isotopes heavier than hydrogen require an order of magnitude higher amount of collisions to reach thermal energies. For the effective moderating ratio the macroscopic cross section also has to be taken into account. Fig. 134 shows, that the relative neutron density difference between 0 % and 1 % soil moisture is large compared to any subsequent addition of further hydrogen. The change in above-ground flux from 0 % to 5 % is comparable to the change from 5 % to 50 % soil moisture. One can also observe that in the MeV-regime the spectrum above a water body reflects mainly the features of the cross section of oxygen, whereas for dry cases the silicon and nitrogen components become dominant. Yet, the details of the structure of the evaporation peak have a negligible influence for the method of soil moisture sensing.

This behavior can partly be related to the higher amount of neutrons being emitted into the air and partly to the transport within the system itself. Fig. 135 shows the flux spectrum emitted from the soil, e.g. neutrons which are either generated within the ground or reflected from it. One can observe a similar relation regarding soil moisture

[h] In rare cases larger amounts of heavier elements like iron can be present in rocks, which can slightly increase the amount of evaporation neutrons.

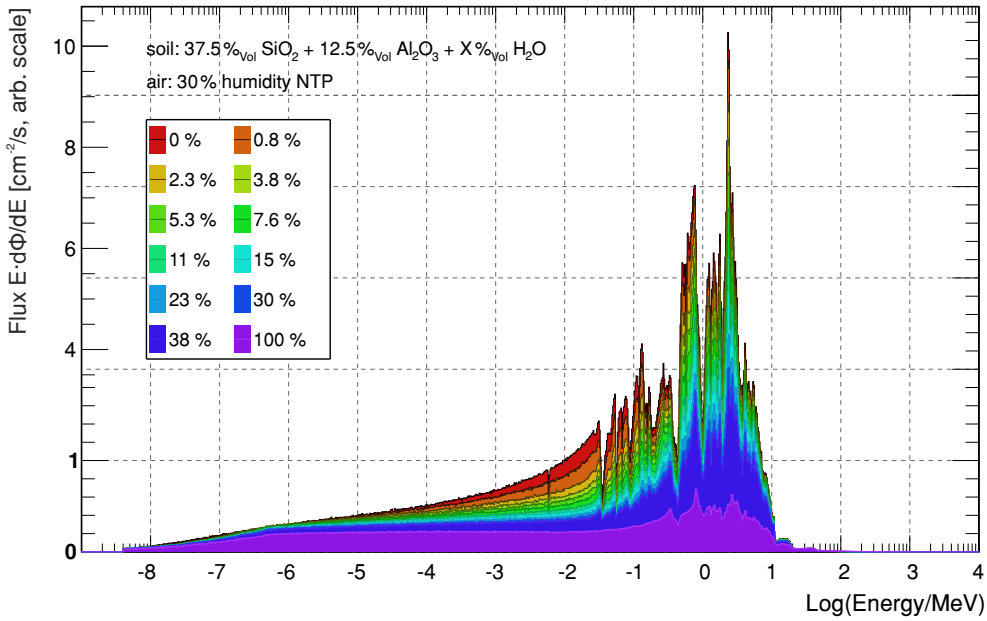

Figure 135: Neutron spectrum emitted from the soil without thermal transport in a height of 2 m above the ground for different soil moisture conditions and a water body.

Element	Mass [u]	log. energy decrement ξ	avg. no. collisions n_{col} to thermal	to 100 eV
H	1	1	18	10
H_2O	-	0.92	20	11
N	14	0.136	135	73
O	16	0.12	153	82
Al	27	0.0723	255	137
Si	28	0.0698	264	142
Fe	56	0.0353	522	280

Table 22: Slowing down of neutrons by interaction with different isotopes from 2 MeV to thermal and to an exemplary energy relevant for CRNS. Calculations according to (31) and (32).

changes as for the total spectrum, Fig. 134, which extends the trend to lower energies. In case of the total absence of hydrogen the system behaves nearly like a resonator with a small damping constant - neutrons are scattering within a domain which rather acts as a reflector. Therefore, the presence of a small amount of hydrogen already leads to a smooth scaling of the system.

Exemplarily also the effect of air humidity is presented in Fig. 136 for the scaling of the above-ground neutron flux for rather dry conditions. In temperate zones typically humidities around 10 g/m^3 can be expected and 33 g/m^3 would correspond to a rain forest climate. For hydrogen in air the following observations can be made: The intensity scaling can be found in the sub-MeV region due to the fact, that contrary to soil moisture it does not significantly change the direct albedo flux[i]. The scaling of the total neutron flux as a function of water vapor shows a nearly linear behavior, yet slightly more sensitive for low air humidities. However, the relative change in intensity also depends on the soil moisture itself. In the example of 4 % soil moisture we find a 15 % change in the epithermal regime for the given setups. This scaling decreases with comparably larger amounts of water in the soil.

As seen from the discussion above and Fig. 134 the above-ground flux scales by a hyperbolic law, as also already indicated by (167) from [429]. This description is also underlined by the results from this work. Fig. 137 provides a comparison of

[i] As the spectrum is released in the vicinity of the ground interface effects of atmospheric water vapor, which lead to a premoderation of the spectrum and an additional attenuation due to the increased area density, are neglected here.

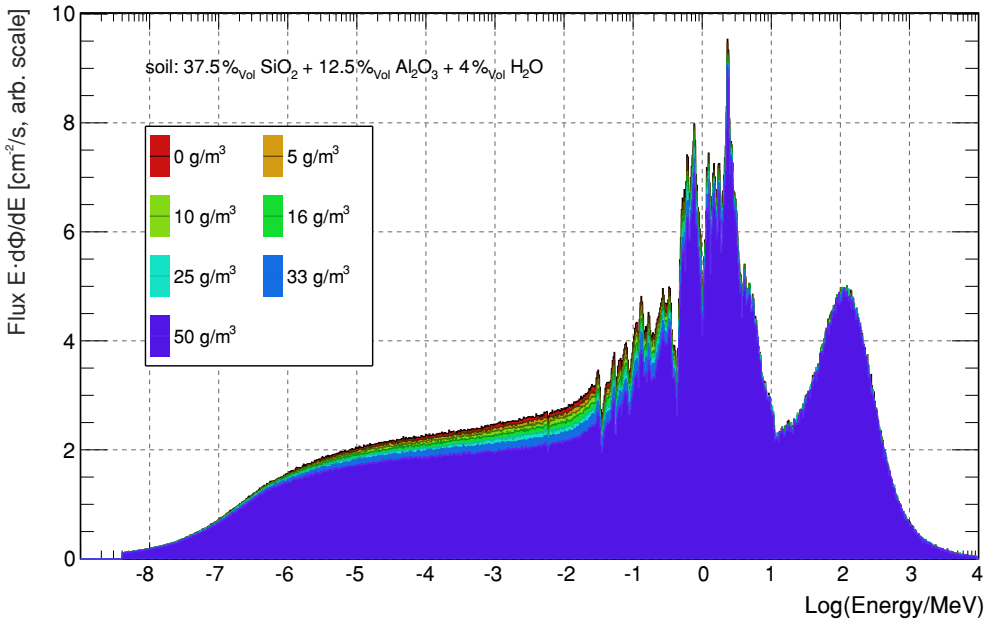

Figure 136: Neutron spectrum without thermal transport in a height of 2 m above the ground for different air humidity configurations.

neutron densities as a function of soil moisture normalized to (167). For URANOS settings with and without the high-energy transport model are presented, whereas the latter propagates the particles above 20 MeV with an interaction-balanced model yielding typical attenuation lengths for the high-energy regime. In case this model is not used, the flux into ground is lower on average, which leads to a smaller amount of evaporation neutrons being emitted into the air. However, there is no qualitative difference between both, which shows that the hyperbolic shape is entirely determined by the physics below 1 MeV. Results from MCNPX, see sec. 5.2.1, are presented in comparison, scaled to match the porosity. The slope appears to be slightly higher, yet both simulations agree remarkingly well given the complexity of the underlying system. However, the empirical results from [429] are not supported by any modeling. As seen from other experiments carried out afterwards and for example presented in sec. 14.1.2, simulation models can provide a consistent picture of measured above-ground densities.

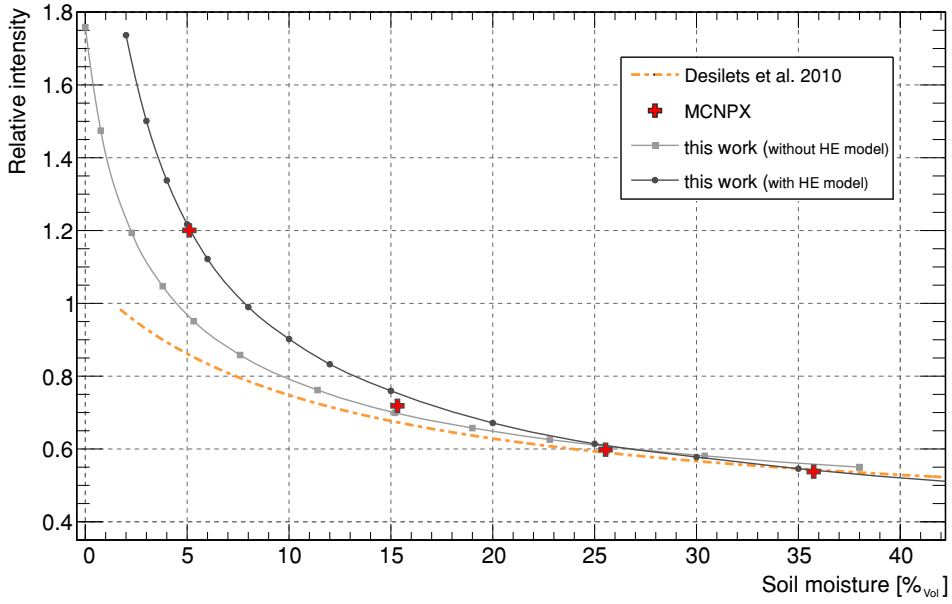

Figure 137: Above-ground neutron density as function of soil moisture, scored in the interval 1 eV-10 keV (with and without high energy particle transport) at $h = 3\,\mathrm{g/m^3}$ in comparison to MCNPX calculations ($h = 0\,\mathrm{g/m^3}$) and to the commonly used equation (167).

As already seen from the exemplary spectra of Fig. 136 the above-ground neutron intensity also depends on the water concentration in the air. The results from the

analysis of the intensity scaling, see Fig. 138, are the following: The general response at a fixed air humidity can be described by a hyperbolic expression. In first order humidity can be corrected linearly as proposed by [440], however, at least a cubic dependency correction has to be applied in addition. Furthermore, the sensitivity to water vapor also depends on the soil moisture itself.

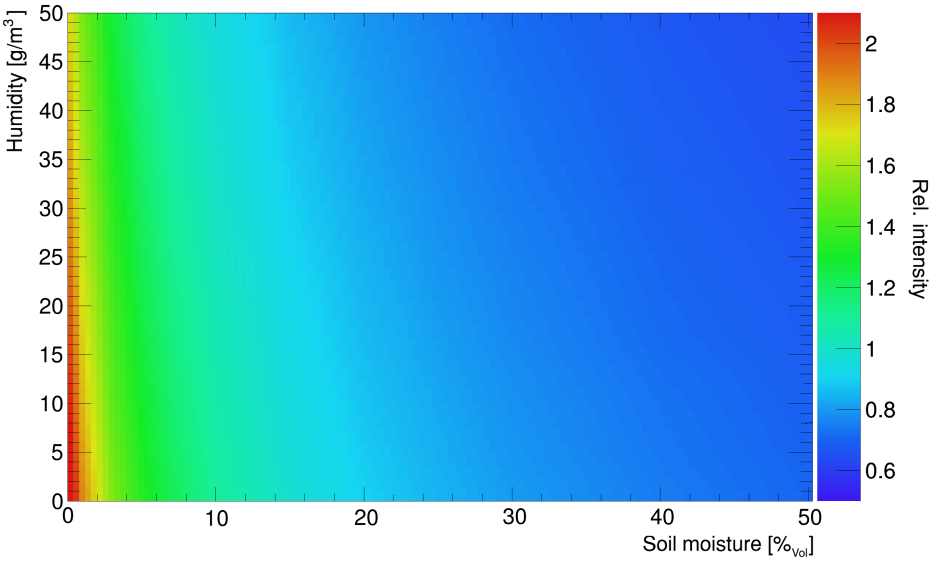

Figure 138: Dependency of the above-ground neutron density in the energy interval 100 eV-10 keV as a function of volumetric soil moisture and air humidity. The white grid lines show the fitted function (173).

A function, which has been found to describe the relative intensity $I(\theta, h)$ with the features mentioned above is the following:

$$I(\theta, h) = \left(k_0 \frac{1 - k_5 h}{\theta + k_2} + k_1 (1 + k_6) \exp(-k_3 \theta) + k_4 \right) \cdot (1 - k_7 h) \,. \tag{173}$$

The parameters k_i[j] are evaluated as summarized in tab. 23.

k_0	k_1	k_2	k_3	k_4	k_5	k_6	k_7
0.05774	0.217	0.03967	1.539	0.4964	0.0044	0.0026	0.00162

Table 23: Numerical values for the parameters of the intensity function (173).

14.1.6 | Tracking cosmic-ray neutrons in soil and air

The observed intensity scaling depending on different amounts of environmental water can be linked to the number of scatterings a neutron undertakes in such a system. Even for very dry conditions hydrogen contributes to at least 10 % of the interactions as can be seen in Fig. 139. Oxygen is as well present in air (O_2 molecules) as in water as in rocks. The contribution of nitrogen means significant transport via the atmosphere. Although in this chart ground and air are not scored independently, it can already be concluded from the relative share of aluminum and silicon atoms, that within the soil water is the main scattering partner, whereas in air nitrogen plays an important role. Therefore, soil tends to lose its reflection capability with increasing hydrogen content, whereas air, even in the case of 10 g/m³ humidity, acts as a transport medium.
In order to unfold the picture of Fig. 139 one can analyze the individual histories of the neutrons in the system. Fig. 140 shows for the conditions presented before the elastic and inelastic scattering distributions per neutron. Important for the interpretation is the peak for a large amount of scatterings. These neutrons have potentially a long

[j] With k_2 in [m³/m³], k_5 and k_7 in [m³/g].

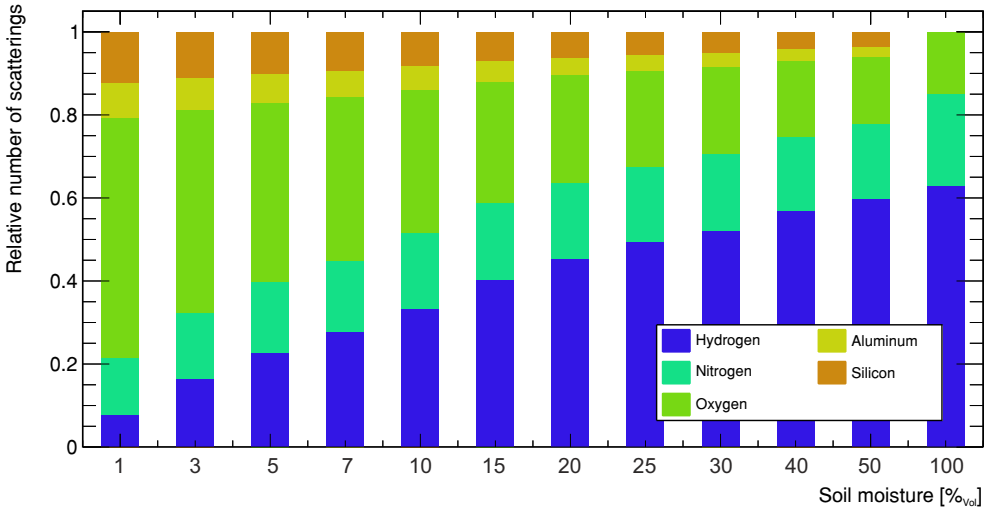

Figure 139: Relative distribution of scattering interactions for various volumetric soil moisture conditions and an air humidity of $h = 10\,\mathrm{g/m^3}$.

integrated travel distance and probed the soil many times and hence develop the characteristic of the system. At the lower end of the distribution histories of neutrons can be found, which directly leave the system, mainly downwards. For typical soil moisture conditions an antiproportional relation to the mean number of interactions can be observed. For extremely dry conditions the system changes towards an extremal behavior with neutrons, which never undergo any interaction with hydrogen as can be seen from the second peak of the 0 % distribution. Another interesting observation is the long tail in case of extremely wet conditions. It corresponds to neutrons which are transported mainly over the air when the reflection probability for interface crossings becomes considerably low.

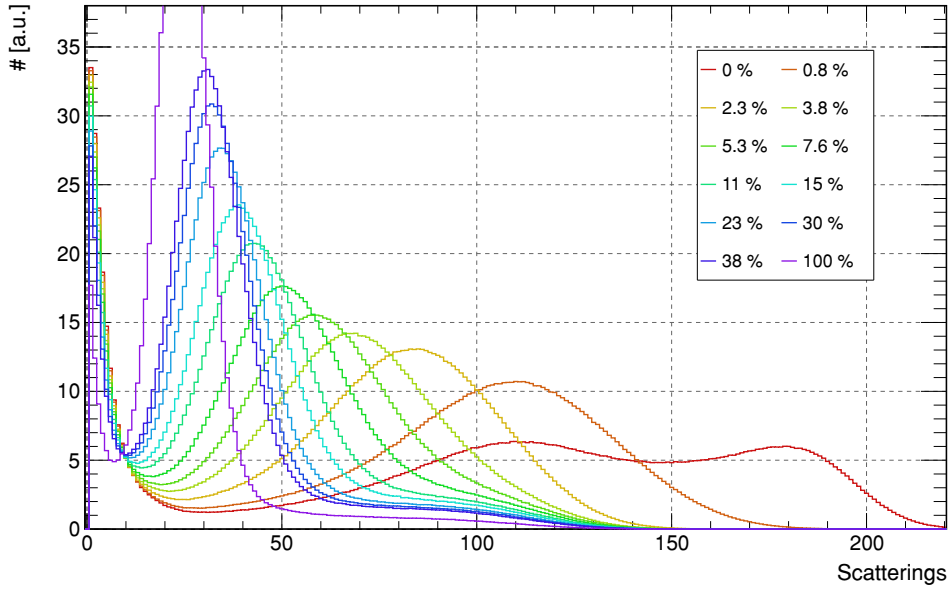

Figure 140: Average amount of scatterings per neutron for various soil moisture conditions.

For using the environmental neutron density as a proxy for soil moisture estimation the penetration depth is an important quantity for the probe depth. Yet, most neutrons are scattering within the soil without leaving it, see for example Fig. 132. In the further calculations of the characteristics of the air-ground interface the following definition is made:

- incoming radiation: no interaction with the soil,
- albedo neutrons: at least one interaction in the soil,

- direct albedo radiation: only one interface crossing. The majority of these neutrons are 'geometrically' transported to the sensor without further (diffusive) scattering in the air.

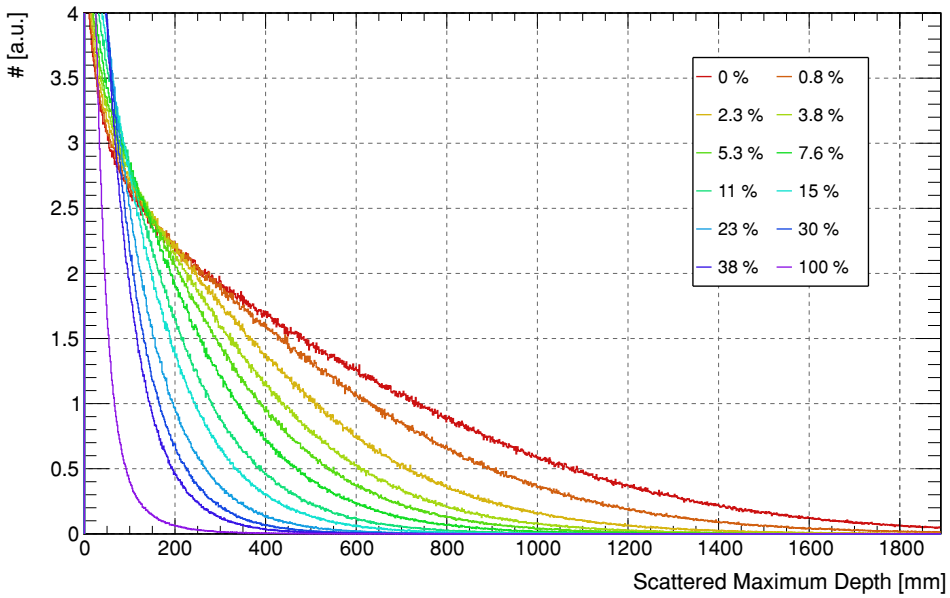

Figure 141: Maximum scattering depth of neutrons which reach the surface for various volumetric soil moisture conditions and $h = 10\,\mathrm{g/m^3}$.

It is important to note that probing the soil and its water content does not necessarily mean that a neutron had scattered off any hydrogen atom. Indeed, compared to the dry case any addition of soil moisture reduces the above-ground density, not only by slowing down neutrons faster, but also by reducing the escape probability once entered into the soil.
Fig. 141 shows the distribution of the maximum probe depth, e.g. the most deep scattering centers or evaporation origins. For dry conditions neutrons can probe the soil beyond depths of 1 m and for a pure water body information below 10 cm can hardly be obtained. To the distribution of the scattering locations a similar scaling with soil moisture like in the cases before can be attributes, however, the relation is not as strongly dependent on the water content here. It can be explained by the fact that this observable quantifies the extreme values of the ensemble.

14.2 | Cosmic-Ray Neutron Transport Analysis

14.2.1 | Theoretical Description by Neutron Transport Equations

Considering a point source in an infinite medium the integral version of the transport equation (9) reduces to

$$\Phi(r) = \underbrace{Q\frac{e^{-\Sigma_t r}}{4\pi r^2}}_{\text{transient}:=\Phi_{\text{tr}}} + \underbrace{\int \Sigma_s \Phi(r')\frac{e^{-\Sigma_t |r-r'|}}{4\pi(r-r')^2}\,\mathrm{d}V'}_{\text{diffusive transport}:=\Phi_{\text{dt}}}, \tag{174}$$

with as before Σ_t being the total cross section and Σ_s the scattering cross section for changes from $E \rightarrow E'$. The first term describes the direct/'geometric' transport without any collision from a source of strength Q to a surface proportional to r^2. At larger distances the integration of the second term leads to the asymptotic solution[k] of

$$\Phi_{\text{dt}}(r) \approx \frac{e^{-\kappa r}}{r}, \tag{175}$$

[k] The derivation can be found in [465].

with κ being a function of the ratio of the cross sections. It can be approximated in systems of weak absorption ($\Sigma_a \ll \Sigma_s$, in other words $\Sigma_s \approx \Sigma_t$) by[l]

$$\kappa^2 = 3\Sigma_a\Sigma_t. \tag{176}$$

In general we are facing terms that have to fulfill the diffusion equation, which can be described by a transport equation for the neutron balance in a specific volume as

$$\operatorname{div}\Phi + \Sigma_a\Phi = S. \tag{177}$$

Hence, in order to describe a plane or a volume source, Φ has to be described by terms for which the integration over the total volume in spherical coordinates $\mathrm{d}V = r^2 \sin\vartheta\,\mathrm{d}\vartheta\,\mathrm{d}\phi\,\mathrm{d}r$ does converge. Therefore, terms in Φ involving $\exp(-r)/r^n$ fulfill the norm $\|\cdot\|_{\mathcal{L}^1}$ for $n \leq 2$. In the case of (174) with $\Phi \propto \exp(-r)/r^2$ and $\Phi \propto \exp(-r)/r$ this is satisfied.
In general also solutions in the form of

$$\Phi(r) = \sum_i S_i \frac{e^{-r/L_1^{(i)}}}{r^{1+e^{-r/a_2^{(i)}}}} \tag{178}$$

can be allowed with individual parameters describing a diffusion length $L_1^{(i)}$ and absorption-to-scattering ratios $a_1^{(i)}$ and overall source contributions S_i (for example for different energies).

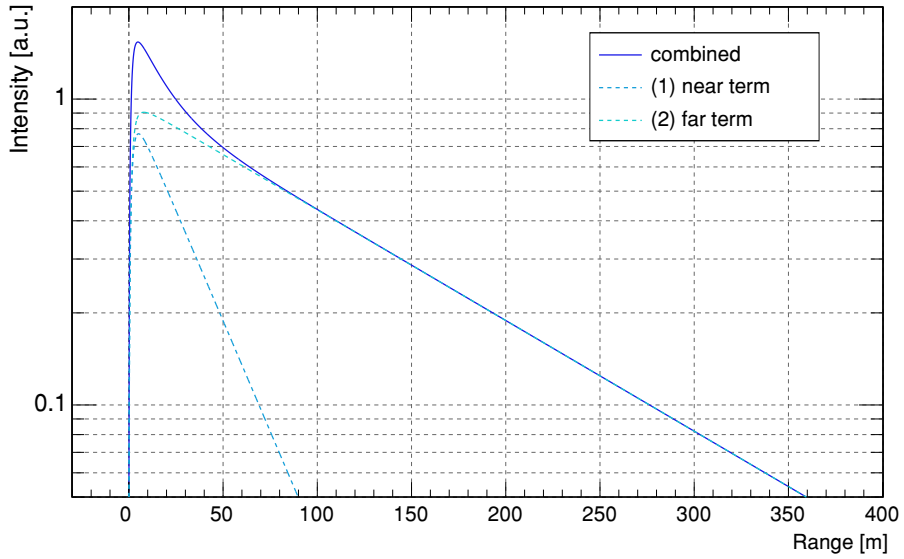

Figure 142: Theoretical neutron flux distribution for a diffusive point source with two energies according to (178). Term (1) with $L_1 = 15\,\mathrm{m}$ models a short range low energy distribution and term (2) with $L_2 = 120\,\mathrm{m}$ dominates the far field.

In general for a simple diffusion approach the resulting transport equation can characterize Φ by a sum of exponential functions. Such is exemplarily plotted in Fig. 142 with two terms, one describing a long-range transport from high energy neutrons and a second describing the transient near-field contributions. For a more complex configuration with a two-medium-interface, a spectral range for the source emission energies and for the detector acceptance energy, and an exponentially described volume source there is no simple general solution using Fermi-Age transport theory, nevertheless the exponential range dependence of the footprint can be motivated by the ansatz presented here.

[l] The derivation can be found in [23].

The footprint of a geophysical instrument generally covers the area in which the medium of interest is probed and the carrier of such information is detected. The scenario of a centrally located sensor which detects neutrons isotropically exhibits a lateral symmetry and thus leads to the assumption of a circular footprint area, $A = \pi r^2$. Here, the travel distance r is defined as the Euclidian[m] distance between the point of detection and the point of the neutron's first contact with the ground or its generation. Since the observable is a result of multiple interactions, r depends on the neutron's initial energy and number of collisions and it can cover values between 0 m and 10^3 m. Thus, a quantile definition is needed to find a distance R within which most of the detected neutrons have probed the ground. In a simple diffusion model of a point source one can assume an exponential drop of intensity with travel distance, therefore [462] and [463] legitimate the use of two e-folding lengths, i.e. the 86 % quantile Q_{86}, in order to define the footprint radius.

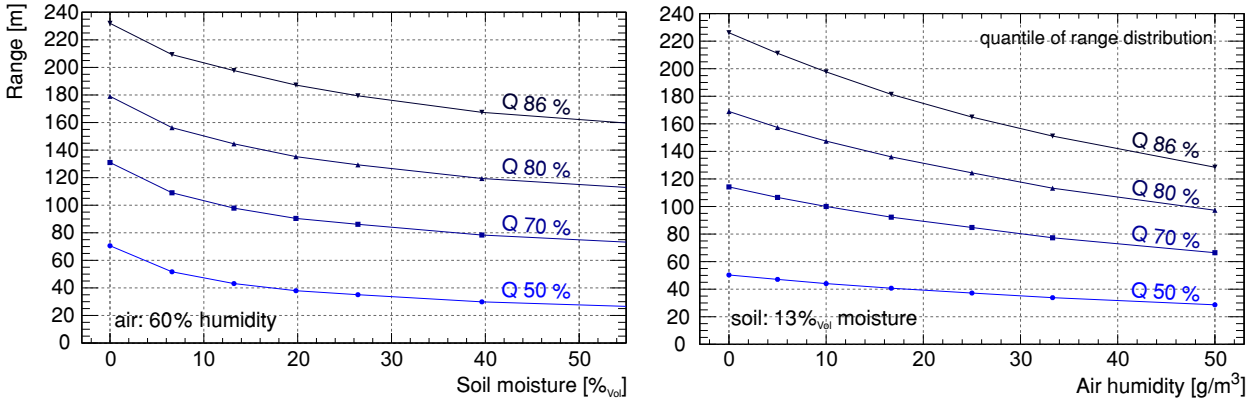

Figure 143: Travel distance of neutrons, exemplarily shown for four different quantiles Q, in the case of varying soil moisture (left) and varying air humidity (right).

Although the calculated response does not exhibit a simple exponential shape, any other quantile would be an arbitrary choice as well. A careful interpretation of this value is recommended, however, as a high quantile value will be biased towards long-range neutrons, see Fig. 143 and Fig. 144. Higher quantiles will also be biased towards the influence of air humidity, which plays an increasing role for large transport distances within the atmosphere. Nevertheless, going along with the 86 % quantile, the according footprint radius is denoted by R_{86} and the footprint area as $A = \pi R_{86}^2$.
The number of neutrons N_R that have originated within a distance R from the sensor is given by

$$N_R = \int_0^R W_r \, \mathrm{d}r. \tag{179}$$

In order to find the distance within which 86 % of the detected neutrons originate, the following equation is solved for R_{86} numerically:

$$\int_0^{R_{86}} W_r \, \mathrm{d}r = 0.86 \int_0^{\infty} W_r \, \mathrm{d}r. \tag{180}$$

[m] Eukleídēs, 300 BC, Ancient Greek.

In analogy the penetration depth D_{86} in the soil is defined as the integral of a depth weighting function W_d which is expected to also decrease with distance r to the sensor. This definition only indirectly takes into account how often a neutron has probed the soil, therefore, the applicability is restricted to cases of nearly homogeneous soil moisture conditions - inhomogeneous domains will be discussed later. However, it can already be concluded, that

- the footprint significantly depends on the environmental water content and
- compared to soil moisture, the influence of air humidity tends to be seen mainly in the higher quantiles, which represent the tails of the range distribution.

The latter can be seen especially in the comparison of both influence factors displayed in Fig. 144. Due to different transport paths around the interface soil water in the domain affects the travel distance distribution in a much more uniform way as air humidity. Long transport paths, where the macroscopic cross section of the water in the air plays an increasing role, manifest themselves in the higher quantiles of the range distribution.

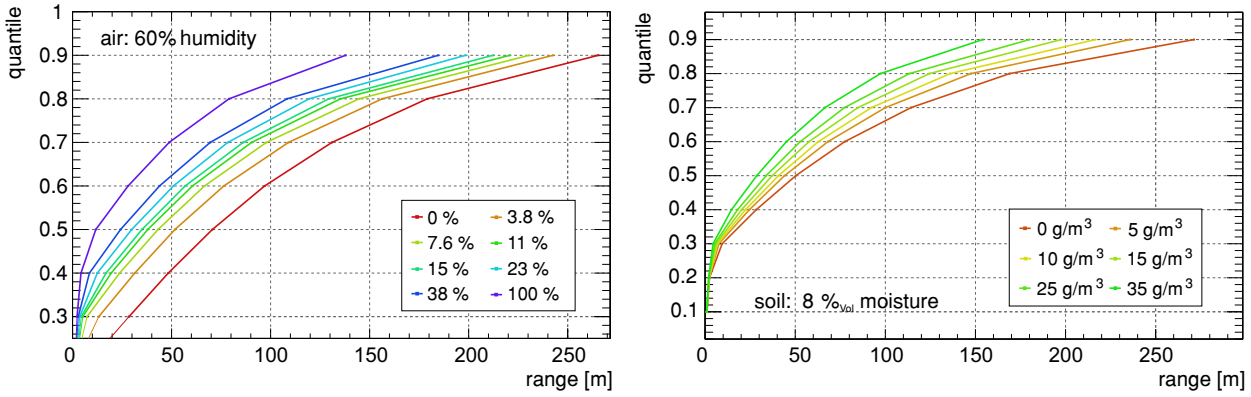

Figure 144: Travel distribution function of neutrons expressed by their quantiles in the case of varying soil moisture (left) and varying air humidity (right).

The decrease of travel distance by humidity shows a nearly linear effect on the quantiles, whereas for soil moisture a similar non-linear behavior, with 0 %$_{Vol}$ marking again a remarkable outlier, can be observed like before. The consequence in general is, that the range distribution is a function of different character in both variables. Another important finding, which is not shown here[n], is, that the influence of air humidity for example decreases for wet conditions and the scaling of soil moisture under dry conditions is larger for dry conditions than for humid air. Both variables are correlated in the range distribution. It also has been found that the effect of air pressure is nearly not correlated with both variables and that biomass, as far as it is located well below the instrument, can be budgeted with the soil water content. This means, that the range distribution is also nearly independent of small height changes of the sensor, except for purely geometrical effects.

14.2.3 | Analytical characterization of the footprint

The range distributions can be fitted very well in a frame of exponential functions by defining a near-field term below 50 m and a far-field term above. This approach is motivated by simple models of diffusion theory explained in sec. 14.2.1. The peak

[n] In total 13 different soil moisture conditions were simulated for 8 different humidity conditions, which are 104 range distributions for the base data set.

at $r < 10\,\mathrm{m}$ accounts for neutrons that directly emerge from the ground and have a high probability to be detected even though most of them come from the lower part of the neutron energy spectrum. The region up to $r < 50\,\mathrm{m}$ describes the average mean free path of most of the environmental neutrons in humid air. For distances between 50 m and 200 m neutrons interact with the soil multiple times until they are detected, which in turn means that with increasing r, average neutron energies quickly become insufficient in order to arrive at the detector before thermalization. From about 200 m on, detected neutrons are dominated by the higher energetic part of the spectrum, which appear to be higher in flux rates and are able to probe the soil very far from the detector.
The entire range distribution function is found to be

$$I_0(h,\theta)W_r(h,\theta) = I_0 \cdot \begin{cases} \left(F_1\, e^{-F_2\, r^*} + F_3\, e^{-F_4\, r^*}\right)\left(1 - e^{-F_0\, r^*}\right), & 0\,\mathrm{m} < r \leq 1\,\mathrm{m} \\ F_1\, e^{-F_2\, r^*} + F_3\, e^{-F_4\, r^*}, & 1\,\mathrm{m} < r \leq 50\,\mathrm{m} \\ F_5\, e^{-F_6\, r^*} + F_7\, e^{-F_8\, r^*}, & 50\,\mathrm{m} < r < 600\,\mathrm{m} \end{cases} \tag{181}$$

with I_0 representing the overall intensity and W_r denoting the radial weighting function. The parameters F_i represent either signal contributions or attenuation coefficients for a rescaled distance $r^*(r,p,\theta)$, which can be considered as an unmodified distance r for standard environmental conditions. Each above defined interval contains one function modeling the main functional contributor, i.e. the soil moisture dependency, and one reflecting the second order correction. In order to account for the effect of the detector layer being positioned at a height of 2 m, for ranges below 1 m a purely geometrical factor is added.

Finding a suitable analytic expression for the range distributions under typical environmental conditions is a question of multi-variate modeling. Therefore, all range distributions have been fitted by $I_0 \cdot W_r$ (181) and parametrized as functions of soil moisture and air humidity. At around 50 m the analytical description starts to deviate from the data. For this reason the value of 50 m has been chosen as a delimiter for both regimes. Although the above described functional dependency of W_r has mainly been motivated from the far-field transport theory, the agreement in the near-field with the model data is also very good. Therefore, one function with different sets of parameters can characterize the entire problem.

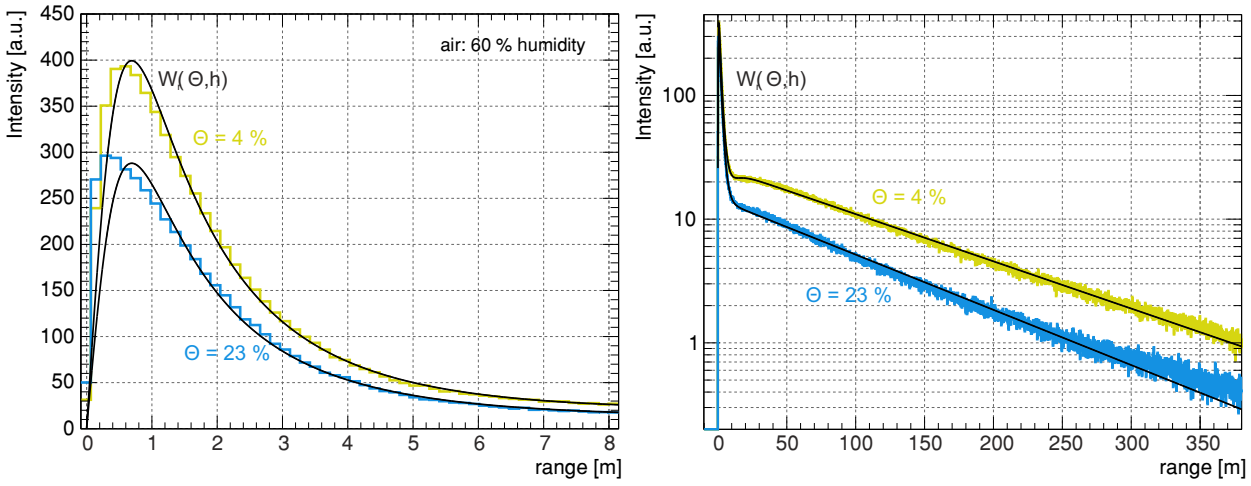

Figure 145: Test of the modeled function (194) with the parameter fits from tab. 28 in comparison to the simulated range distribution set in the near-field regime with focus on the first peak (left) and the far-field (right).

As shown in Fig. 145 for two exemplary cases, there is a very good agreement between the proposed model (194) and the simulated range distribution. The analytical description is able to represent the first steep rise as well as the nearly exponential curve in the far-field. Also the small plateau in the near-field regime for dry conditions at approximately 20 m can be reproduced. As mentioned before, the fit model offers the best approximation for average moisture conditions in the range (7-40) % for which the error from integrally evaluating Q_{86} stays well below 5 m. For more extreme conditions there are notable deviations, especially for very dry soils. For this reason the limit of this model is set to 2 $\%_{\mathrm{Vol}}$ soil moisture. Furthermore, the model has been evaluated for a sensor height of 2 m. As the sensor height has a significant influence on the range distribution for $r < 2$ m, where geometric transport dominates, deviations in that regime are anticipated and acceptable. Finally it should be noted, that the calculations only apply to cases of homogeneous environmental conditions. In domains with very inhomogeneous structures a significant deviation of the signal from the model can be observed. This will be discussed later, however, small inhomogeneities as can be found for natural soil moisture distribution patterns can still be covered.

14.2.4 | Analytical description of the penetration depth

The footprint covers an entire support volume, spatially extended into the ground. The comparably high thickness of the probed soil is an important advantage of the CRNS method compared to most remote-sensing products. Cosmic-ray neutrons can penetrate the first decimeters of the soil with nearly no interaction, whereas electromagnetic signals interact within the upper (0-5) cm. [469] showed that the effective representation of the penetration depth, $z^*(\theta)$, is a reciprocal function of soil moisture, but made no clear statement how it varies with the distance from the probe.
In URANOS the vertical positions, where neutrons probed the soil, were logged with their interaction coordinates. It has to be pointed out, that this procedure is different from scoring in air. In the atmosphere particle tracks at the (virtual) position of the detector have to be tracked. In the ground not the tracks itself, but the interactions, i.e. scattering centers, are relevant for the measurement process. Above $\theta \approx 10\,\%$, the penetration depth of neutrons appears to decrease exponentially. This behavior can be expected from a simple mono-energetic attenuation law approach, and has also been found by [462]. A simple analytical description of the vertical weighting function was found for $\theta \geq 10\,\%$:

$$W_d(r,\theta) \sim e^{-2d/D_{86}(r,\theta)}. \tag{182}$$

The relation can be used to obtain a properly averaged mean value of point measurements when compared to the cosmic-ray derived estimates. Of course, due to a much higher energy loss within the soil, the probe depth is lower for wet conditions. However, the penetration depth varies within the footprint of the sensor. Neutrons, which emerged from the soil in the direct vicinity of the instrument, can originate from or be scattered off locations more deep within the soil. The reason for this observation is simple, namely because neutrons leave the soil with a broad energy spectrum, see also Fig. 135.
Transport in the soil-air interface inevitably goes along with subsequent energy loss. Therefore, neutrons emitted from distant locations tend to have a higher emission energy as more collisions are necessary to reach the sensor. On the other this also requires less energy loss in the soil and therefore a rather shallow origin. With different soil moistures the balance of energies within the emission band changes as the transport

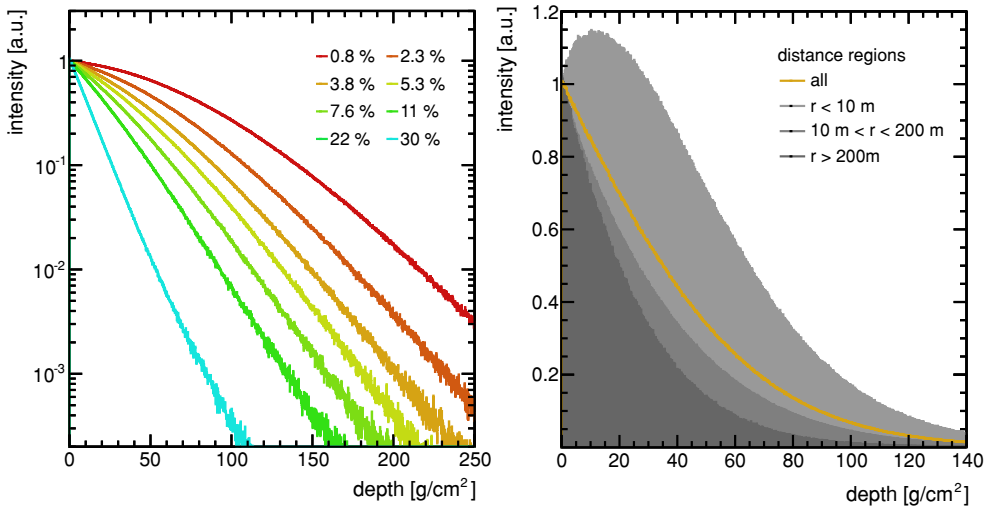

Figure 146: Penetration depth distribution characterization in the ground at a humidity of $h = 10\,\mathrm{g/m^3}$. Scattering center distribution (left) for different soil moistures and (right) mean scattering center distributions for different impact distance ranges to the sensor for $7\,\%_{\mathrm{Vol}}$ soil moisture.

efficiencies in the domain vary in parallel. This leads to fact that the mean depth distribution varies more for wet conditions in terms of percentage than for dry soils. The numerical determination of the penetration depth D_{86}, however, is certainly valid for any soil moisture condition:

$$D_{86} = \frac{\mathrm{g/cm^2}}{\varrho_{\mathrm{bulk}}} \left(p_0 + p_1 \left(p_2 + e^{-p_3\, r^*} \right) \frac{p_4 + \theta}{p_5 + \theta} \right), \quad \text{adapted distance } r^*. \tag{183}$$

The quantity denotes up to which depth 86 % of the detected neutrons had contact with constituents of the soil. Numerical parameters are provided in tab. 29 in appendix B.3.2.

14.2.5 | Pressure dependency

The footprint can also expand with decreasing air pressure, e.g. increasing altitude of the sensor location. The lower air density allows neutrons to cover longer distances between collisions. For example, the footprint can be 20 % larger at a $\approx 2000\,\mathrm{m}$ altitude ($\simeq 800\,\mathrm{mbar}$) compared to sea level. Although a reciprocal fit is a reasonable estimate [463], the results presented in Fig. 147 indicate an exponential dependence on p due to the presence of hydrogen:

$$f_p = \frac{0.5}{0.86 - \exp\left(-p/p_0\right)} \approx \frac{p_0}{p}. \tag{184}$$

However, differences between the two models appear to be insignificant. Yet, the footprint weighting function can be consistently scaled by the pressure correction function (184) in the far-field for typical soil moisture conditions and sensor altitudes.

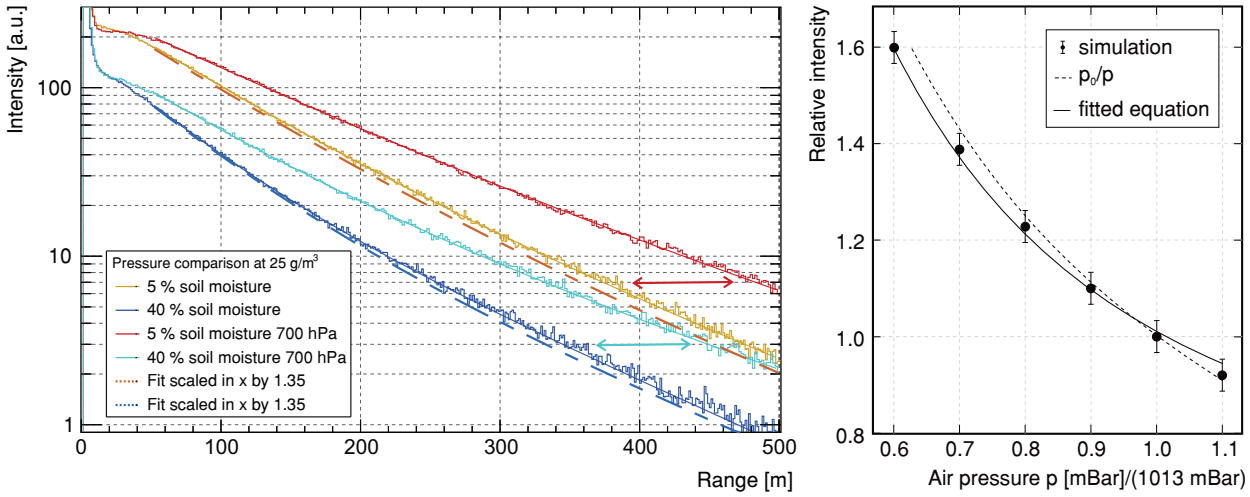

Figure 147: Pressure dependency of the range distribution for two exemplary soil moisture and air pressure conditions (left). The 1013 mb distributions are fitted by the far-field term of (181), if that function is then rescaled by a common factor, it matches the corresponding range distribution of the designated pressure. This model for the pressure dependency is depicted in the right panel.

14.2.6 | Height dependency

Stationary sensors are typically placed in heights of approximately 2 m as well as roving constrains the elevation by the use of vehicles. These requirements justify the emphasis of this study to that common setup distance to the ground. However, measurements of the environmental flux at larger heights have been carried out as early as 1966 [470] using an antenna tower or [65] performing airborne surveys. With large-scale soil moisture measurement campaigns on terrains, which cannot easily be accessed by roving, airborne measurements are discussed as a feasible solution. As discussed in the previous sec. 14.2.1 the near-field is dominated by geometrical transport of neutrons from the direct vicinity of the instrument.

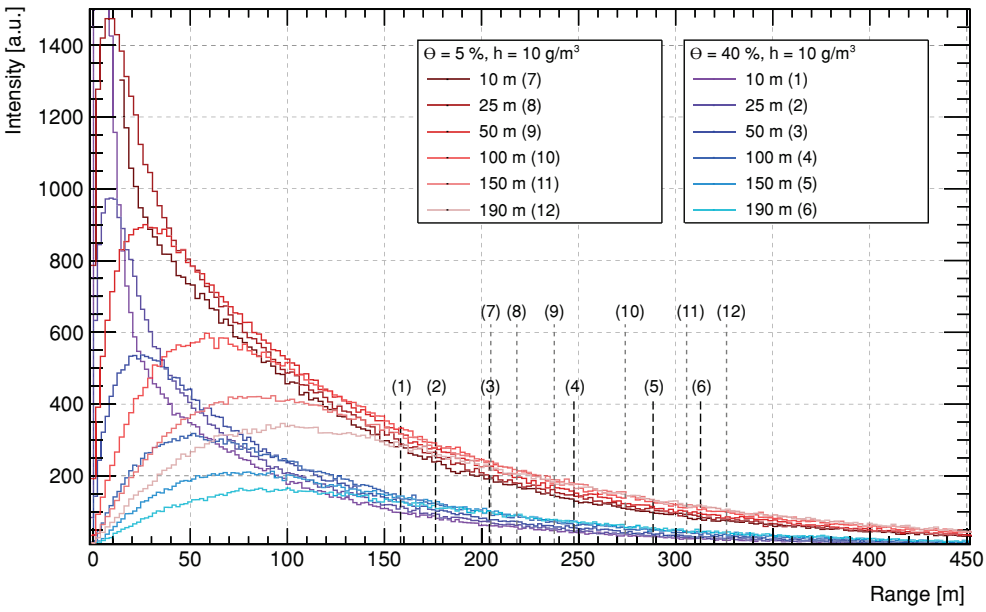

Figure 148: Height dependency of the range distribution for two soil moisture settings and elevations up to 200 m. It is clearly visible how the near-field is dominated by geometric transport, whereas the far-field consistently remains nearly unchanged. Lines and numbers indicate Q_{86} for each respective distribution, see also tab. 24.

Elevating the sensor by several tens of meters already increases the footprint substantially. Fig. 148 shows simulations, where the detector layer has been placed at heights up to 200 m. Two conclusions can be drawn from the depicted range distributions:

The dominant near-field peak, see also Fig. 173, smooths out and its peak drifts to higher range values, so that the overall footprint increases substantially. Furthermore, although the near-field entirely changes in the range distribution, the far-field is barely affected. As the latter is dominated by transport over the atmosphere, less than ground interaction, that result can be expected.
The following tab. 24 provides a characterization of the height dependent footprint increase.

Table 24: Elevated Footprint: Range quantiles Q_{86} depending on soil moisture and sensor height above ground. Conservatively, an error of 2 m can be assumed.

	Q_{86} [m] at elevation					
moisture [$\%_{Vol}$]	10 m	25 m	50 m	100 m	150 m	190 m
5	227	241	263	303	338	360
10	213	230	255	299	336	360
20	196	214	242	290	329	355
40	176	196	227	275	320	347

One can conclude, that the footprint can easily be expanded by a factor of 1.5 by elevating the sensor by 100 m and more.

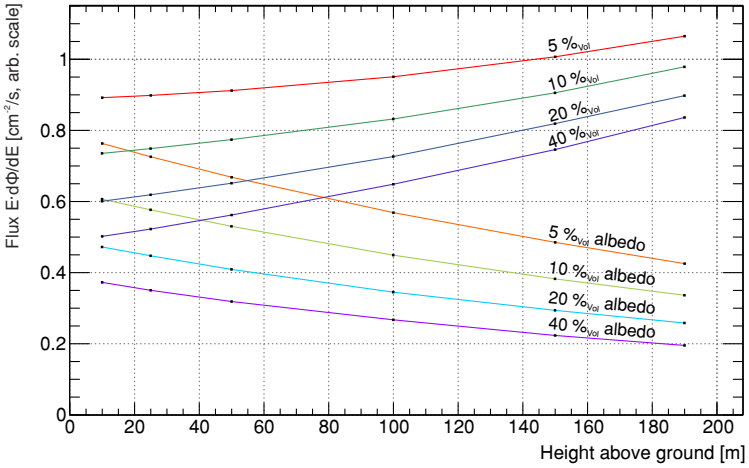

Figure 149: Height dependence of the measured neutron density. The total flux increases with increasing elevation. However, the fraction of the reflected component (albedo), which carries information about the soil moisture, decreases.

The flux of particles from atmospheric showers follows an exponential law as a function of altitude, e.g. Fig. 12 in sec. 3.1. Yet, with increasing distance to the ground, the albedo neutron component, which carries information about soil moisture, decreases. This can be seen in Fig. 149, which depicts the total flux and the fraction of albedo neutrons for different heights. These simulations also agree well with data from M. Zreda from a vertical profile measured using a helicopter (2009, unpublished). It can be concluded, that airborne measurements are feasible up to heights of 200 m above ground, but should be limited to approximately 100 m, where the signal fraction is in the order of 0.5, whereas approaching 0.25 at the largest altitude studied here.

14.3 | Results

The systematic analysis and modeling of the soil-air interface, see previous sec. 14.2.3, allows now to characterize the neutron transport problem for CRNS for any soil moisture and air humidity condition. In the following the consequent use of the footprint weighting function (181) provides various quantitative results, which have already significantly improved the interpretation of CRNS data from field campaigns.

14.3.1 | Intensity relation

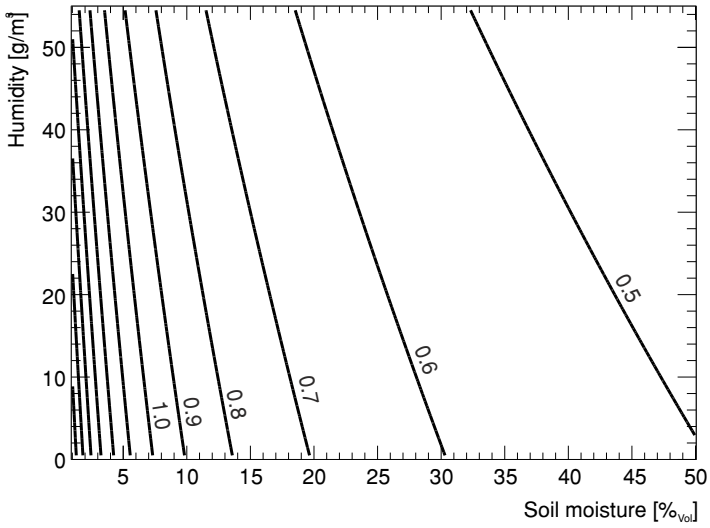

Figure 150: Dependency of the above-ground neutron density in the energy interval 100 eV-10 keV as a function of soil moisture and air humidity evaluated from (173).

The relative change of intensity generally follows a hyperbolic θ-dependency, yet, this relation is as well a function of the actual soil water content. One observes a 0.33 % change at 4 % soil moisture per 1 g/m^3 water vapor in the range h = 10 g/m^3 to h = 30 g/m^3 and a 0.16 % change at θ = 15 %. In cases of wet soils the fraction of hydrogen in the air at the same absolute humidity is lower. Therefore, slowing down predominantly takes place in the ground. Both values are lower than the static 0.54 % per 1 g/m^3 water vapor change from [440]. However, compared to the reference, this work utilizes a cosmic-ray neutron spectrum released directly from above the surface. This fact reduces the possible effect of premoderation by water vapor in the atmosphere as mainly the accumulated travel distance by neutron transport after soil contact can be considered here. Therefore, it is possible that the water column prior to the interface crossing can account for an additional reduction of the flux. However, the above-ground neutron density is a function of soil moisture and air humidity. Due to the pending analysis of the premoderation in air, the results of Fig. 150 can be considered as preliminary.

14.3.2 | Penetration depth scaling

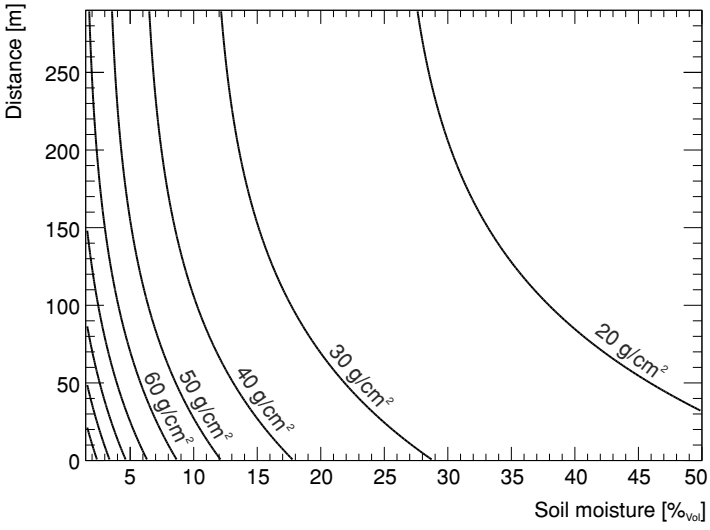

Figure 151: Dependency of the penetration depth D_{86} according to (183) on the radial impact distance r to the sensor for a range of soil water contents θ. Contour lines show D_{86} in intervals of 10 g/cm^2. An exemplary humidity h = 10 g/m^3 and soil composition according to sec. 14.1.4.2 is considered.

The average probe depth is typically a result of many interactions in the ground and nearly follows an exponential law with a soil moisture depending attenuation coefficient. However, this value also depends on the distance, where the neutron entered the soil in the first place. Fig. 151 shows the penetration depths $D_{86}(r, \theta)$ as a function of radial distance r from the sensor for exemplary soil moisture values θ. For dry soil $D_{86}(r, \theta \approx 1\,\%)$ ranges from 83 cm right below the sensor to 46 cm at $r = 300$ m distance. At most, the penetration depth varies between 15 cm and 83 cm below the sensor for wet and dry soil, respectively. This is in close agreement with depths of (12-76) cm given by [462]. The reported values are rather confirmed than contradicted by URANOS, because they stemmed from experiences and various studies in the research field of cosmogenic nuclide production and are thus independent of the mentioned model approach. On average over the first tens of meters distance, the functional dependency on θ, see (183), is relatively similar to the reciprocal model for the *effective sensor depth* $z^*(\theta)$ from [469]. Their model was constrained on the limits introduced by [462] and validated with measurements and hydrodynamic simulations. Further evidence for the correct performance of the URANOS model provides the comparison with measurement depths of (50-100) cm on the Moon or Mars missions, where cosmic-ray neutrons penetrate dry ground of similar chemical composition [471, 472].

14.3.3 | Footprint

The response to soil moisture variations is significant for humid climates between (15-50) $\%_{\mathrm{Vol}}$ as well as for very dry conditions $< 3\,\%_{\mathrm{Vol}}$. Previous studies underestimated the role of soil moisture for the footprint due to the choice of a modeled neutron source below the surface. This detail is the major cause for the discrepancy to findings from [463], who stated, that the footprint remains mainly unchanged for typical soil moisture conditions.

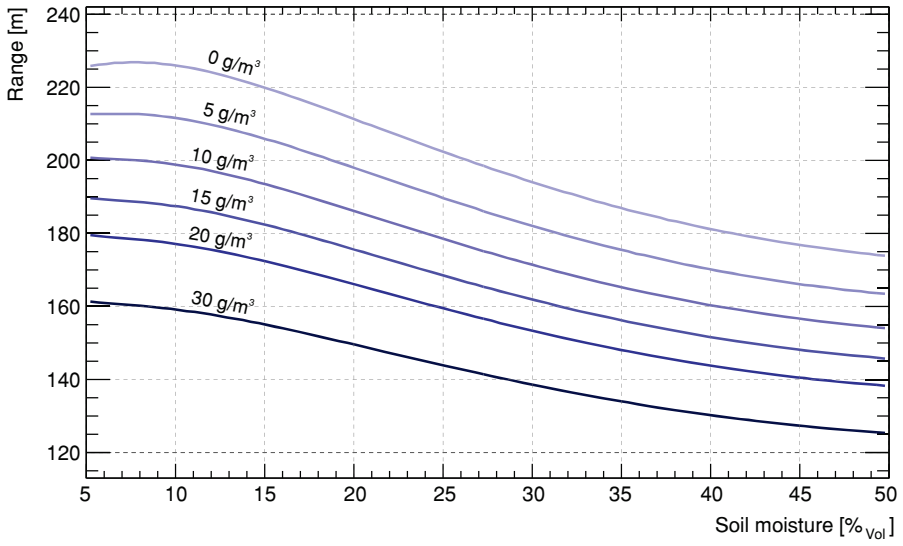

Figure 152: Dependency of the radial distance quantile Q_{86} according to (181) for a range of soil water contents θ. Contour lines show Q_{86} for different humidities.

The footprint itself is a function of soil moisture. This effect can be attributed to the different initial energies from the soil emission spectra and more importantly to the transport efficiency of the interface. Neutrons cross the air-ground boundary on average three times before they reach the sensor. With increasing soil moisture the probability of leaving after re-entry decreases. Hydrogen contributes to this behavior in two ways: The energy loss is much higher compared to any other element, which significantly decreases the average travel distance, and in elastic collisions backward-scattering is highly suppressed, which requires at least two collision with hydrogen for a neutron to

be emitted back into the air contrary to other elements that allow direct backscattering. For θ = 5 % to θ = 12 % the footprint radius is not significantly influenced. Beyond that a decrease of 10 m for every 5 % of soil moisture can be observed, see also Fig. 152.

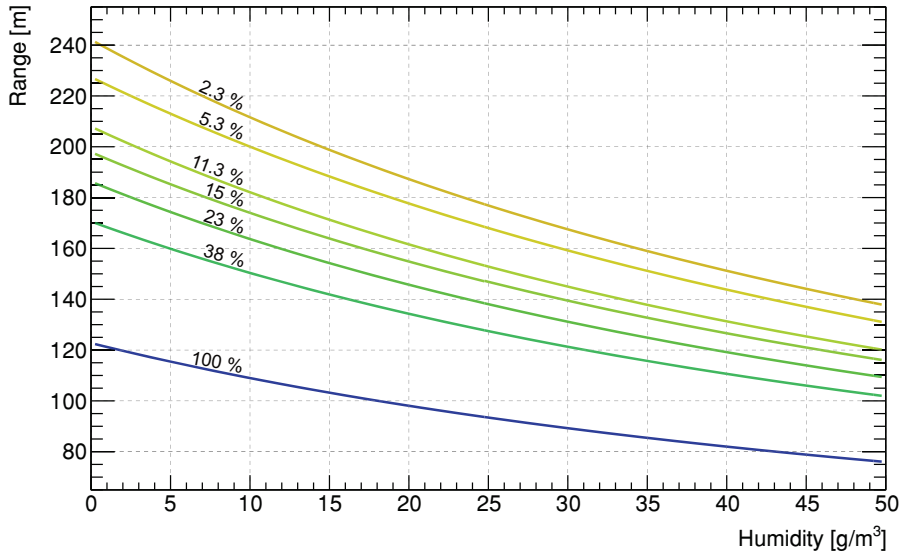

Figure 153: Dependency of the radial distance quantile Q_{86} according to (181) for a range of soil water contents θ. Contour lines show Q_{86} for different humidities.

Moreover, the response to variations of absolute humidity features a 10 m decrease of the footprint radius for every change of (4-6) g/m^3 water vapor, see Fig. 153. [431] refers to ≈ 10 % reduction of the footprint from dry to saturated air, which can easily span ≈ 25 g/m^3. This change corresponds to a 20 % change in footprint radius calculated with URANOS. However, [463] investigated the influence of humidity in further detail and found a 10 m decrease for every change of ≈ 6 g/m^3 humidity from MCNPX simulations with dry soil. This value is consistent with results from URANOS, whereas the slightly higher gradient is a consequence of the different energy spectra used in the models.

In summary, the contour plot Fig. 154 shows that the footprint radius ranges from 220 m to 130 m between arid and tropical climate, respectively.

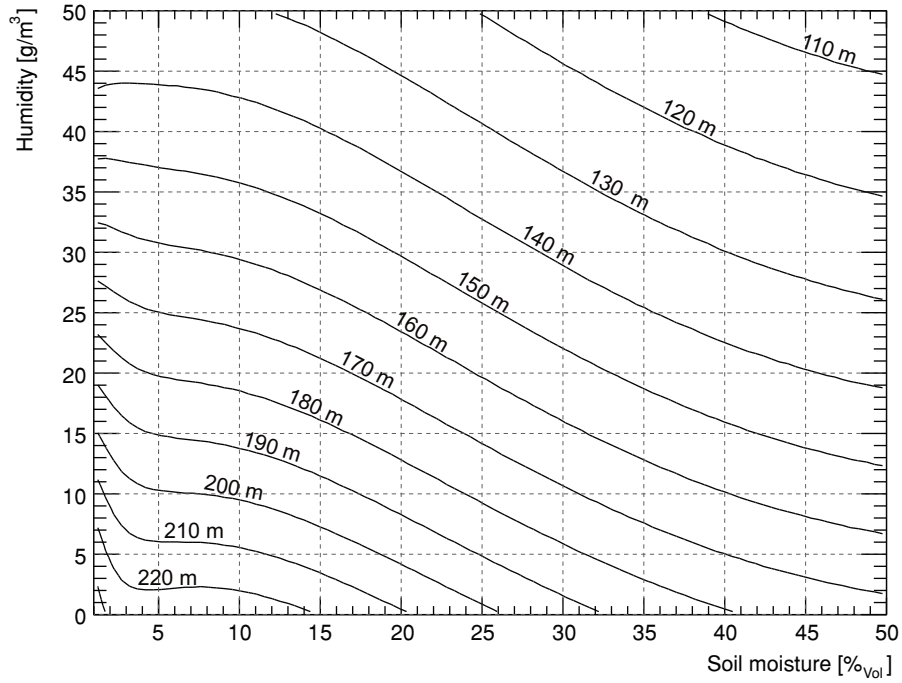

Figure 154: Dependency of the radial distance quantile Q_{86} according to (181) for a range of soil water contents θ. Contour lines show Q_{86} for different humidities.

The decrease of the footprint with increasing soil moisture does not necessarily imply that the area-average estimate is less representative. According to [473], the spatial

variability of soil moisture tends to be low for rather wet soils. In this context, the effective representativeness of the CRNS method appears to be almost unchanged. Conservatively, a total error of ΔR_{86} = (4-6) % can be assumed, which scales from wet to dry conditions. A detailed error budget is listed in appendix B.3.3.

14.3.4 | Where do neutrons come from?

CRNS sensors are sometimes placed close to roads, trees or rivers. Mobile rover surveys inevitably pass alongside forests, lakes or fields of different land use. In most of these cases an isotropic footprint cannot be expected, because large structures of different hydrogen content vary the transport paths towards the sensor.

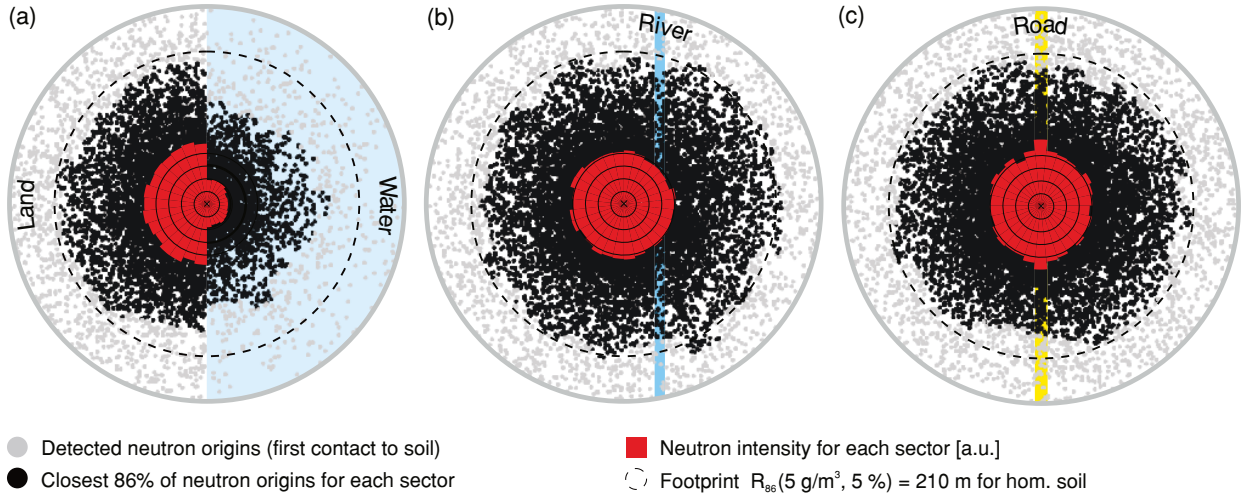

Figure 155: Anisotropy of detected neutron origins (black) and neutron intensity (red) determined for every 12° sectorof a circle around a centered detector. The displayed extent is 270 m in radius,whereas the dashed line represents the isotropic footprint. The three exemplary cases illustrate bare soil (white) with (a) a coast line to water (blue), (b) a 10 m river at 50 m distance and (c) a 10 m concrete road (yellow). [KS2015]

In order to quantify the anisotropy of detected neutrons, exemplary cases where such scenarios are extreme have been simulated. In Fig. 155 the vicinity of a centered detector is shown and the isotropic footprint $R_{86}(h = 5\,\mathrm{g/m^3}, \theta = 5\,\%) = 210\,\mathrm{m}$ is indicated (dashed line). Dots illustrate the origin of detected neutrons, where the closest 86 % of total neutrons are emphasized (black) in each direction. The area is discretized into 12° sectors in order to quantify range (black dots) and intensity (red). In a coast line setup, Fig. 155a, the density of the origins (dots) and neutron intensity (sectors) appear to be much smaller in the ponded area. The range of neutrons decreases by up to (30-40) % although neutrons still manage to travel long distances over water. Their contribution to the count rate sharply drops to about 40 % at the interface.

In Fig. 155b the detector is placed 50 m away from a 10 m wide river. This setup can especially found for irrigated land-use. The neutron origins clearly show that the river hardly contributes to the signal because most neutrons lose too much energy after probing water, see also point density and neutron intensity for water, Fig. 155a. This is also visible in the respective intensity which shows a slight asymmetry towards the dry side. However, the setup reveals a slightly wider footprint in the direction to the river, as a consequence of the intensity gap.

A detector carried on a dry, concrete road, see Fig. 155c, is the typical setup for rover applications. The sensor detects about (10-20) % more neutrons from the road than from other directions. However, the decrease of the footprint along the road due to

short-range dominated contribution is small. The effect of the road is especially studied in the following sec. 14.3.5.

14.3.5 | Inhomogeneous terrain: roads

Part of the results about mobile measurements on roads presented in this chapter have been published in [SK2018].

Cultivated fields, forests, mountainous terrain, and private land are often not accessible by vehicles. Hence, the CRNS rover is usually moved along existing roads, streets, and pathways in a site. This strategy is also practical when the rover is used to cover large areas at the regional scale in a short period of time. However, the neutron simulations presented here showed that the stationary CRNS detector is particularly sensitive to the first few meters around the sensor. This feature could be verified by moving stationary CRNS probes over highly inhomogeneous domains, see also for example Fig. 131 in sec. 14.1.2. The effect of dry structures in the footprint was introduced for the first time by [455] and was also observed by [432] and [SK2017b] on rover surveys through urban areas. [430] sensed soil moisture of agricultural fields by roving on paved and gravel roads, and speculated that the road material could have introduced a dry bias to their measurements. It is therefore critical to quantify such an effect, not only for the advancement of the CRNS roving method, but also for its application.
The radial sensitivity of a CRNS detector is strongly influenced by the first few meters around the sensor, see also Fig. 145. As a result of this local sensitivity, the CRNS measurement is biased significantly when the moisture conditions present in the road differ substantially from the actual field of interest. The footprint analysis as presented before, however, has been developed for homogeneous soil moisture conditions, especially the radial weighting function strictly only applies to domains of low variations in θ. One can already derive an estimation using the radial weighting function W_r (181) in order to calculate a road bias $N_b(x_c, w, \theta_{\text{field}})$

$$
\begin{aligned}
N_b = \Bigg(& \int_{-\infty}^{\infty} \int_{x_c - w/2}^{x_c + w/2} W_r\left(\sqrt{x^2 + y^2}, \theta_{\text{road}}\right) \mathrm{d}x \, \mathrm{d}y \\
& + \int_{-\infty}^{\infty} \int_{-\infty}^{x_c - w/2} W_r\left(\sqrt{x^2 + y^2}, \theta_{\text{field}}\right) \mathrm{d}x \, \mathrm{d}y + \int_{-\infty}^{\infty} \int_{x_c + w/2}^{\infty} W_r\left(\sqrt{x^2 + y^2}, \theta_{\text{field}}\right) \mathrm{d}x \, \mathrm{d}y \Bigg) \\
& \cdot \left(\int_{-\infty}^{\infty} \int_{-\infty}^{\infty} W_r\left(\sqrt{x^2 + y^2}, \theta_{\text{field}}\right) \mathrm{d}x \, \mathrm{d}y \right)^{-1},
\end{aligned}
\tag{185}
$$

with road width w and distance to the road center x_c. One observes already quite at some distance to the road that the intensity is enhanced compared to the field-only domain due to the significant geometric contribution. As soon as the sensor is located above or next to the road, depending on material and width a local enhancement in neutron density would create the impression of a false low water content. It can be expected that a potential 'road effect' is larger when differences between road moisture and surrounding field water content are larger. However, the integral approach cannot entirely take into account the inhomogeneous configuration as it disentangles both domains as there is no correction for the transport $\theta_i \rightarrow \theta_j$. (185) slightly overestimates the road contribution and leads a relative bias below a factor of 1, if $\theta_{\text{road}} < \theta_{\text{field}}$. The latter can be seen in the lowest curve of Fig. 156 with the integral values for the 7 m-asphalt road with an effective $\theta_{\text{road}} = 12\,\%$ within a a field of 10 % soil moisture.

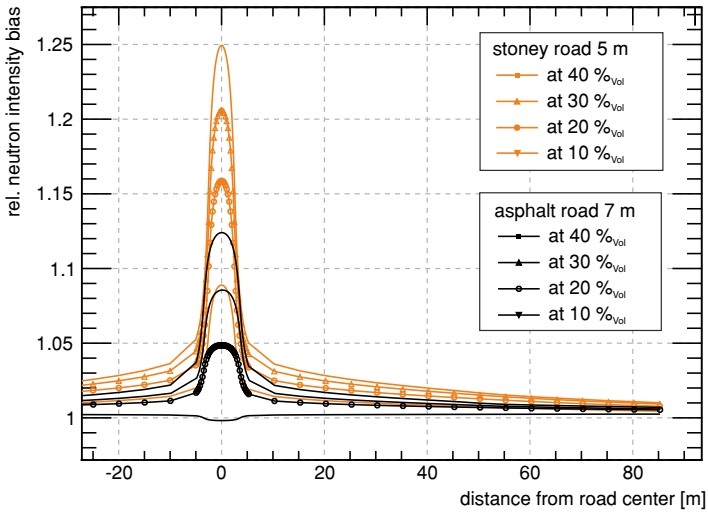

Figure 156: Road bias N_b evaluated by (185) using the readial weighting function (181). The sensor is located at a distance x_c from the road center, here two examples of stone and asphalt pavements. The influence of the road leads to a relative flux change compared to the one expected from a domain with θ_{field} alone.

The application of roving on roads has been taken as an example of inhomogeneous terrain, which is in the following further studied using URANOS. In order to The road is modeled as a 20 cm deep layer of either stone or asphalt, while the soil below was set to 5 % volumetric water content. Following the compendium of material composition data [146], asphalt pavement is modeled as a mixture of O, H, C, and Si, with an effective density of 2.58 g/cm^3, which corresponds to a soil water equivalent of $\theta_{\text{road}} \approx$ 12 %. Stone/gravel is a mixture of Si, O, and Al, plus 3 % volumetric water content at a total density of 1.4 g/cm^3. The wetness of the surrounding soil, θ_{field}, has been set homogeneously to 10 %, 20 %, 30 %, and 40 % volumetric water content. The neutron response to roads was simulated for road widths of 3 m, 5 m, and 7 m.

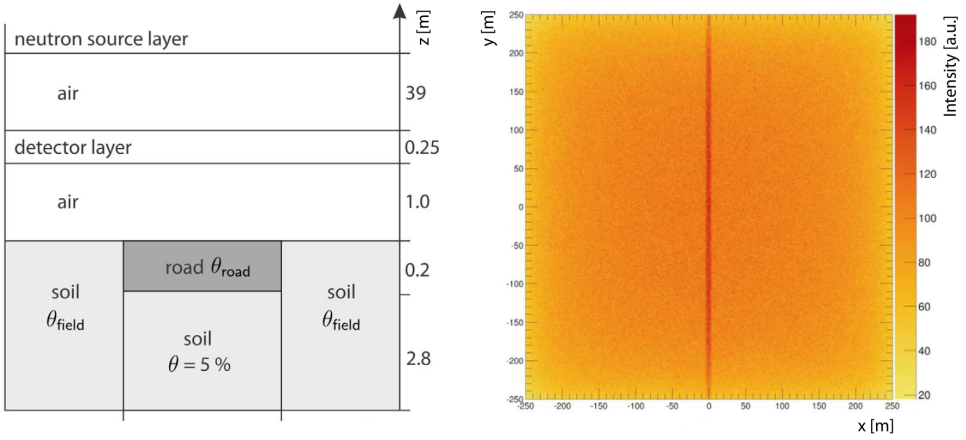

Figure 157: (left) Schematic of the model setup used by URANOS to simulate the response of cosmic-ray neutrons to ground materials. (right) Exemplary URANOS model output showing a birds-eye view of the neutron density in the horizontal detector layer for a 5 m stoney road and 50 % field soil moisture. [SK2018]

The result from the simulation confirms that the bias increases with increasing field soil moisture, increasing road width and decreasing road moisture. Fig. 158 plots the simulated road bias over distance from the road center, showing that the bias is a short-range effect that decreases a few meters away from the road, so that almost no measurable effect can be expected. Yet, there are two differences in the particle-tracking solution compared to the integral approach (185). The road bias is slightly emphasized for the asphalt road and a few percent lower for the stone road. Furthermore, the long-range enhancement tails at distances far from the road center appear slightly weaker. The quantitative differences between both approaches might not be relevant in practice compared to other sources of errors. It may be not feasible to estimate the hydrogen concentration of the road precisely, therefore, biases which correspond to effective soil moisture changes of the road in the order of 2 % can be expected. From this point of view the analytical approach can already provide a reasonably good estimation for the 'road effect'.

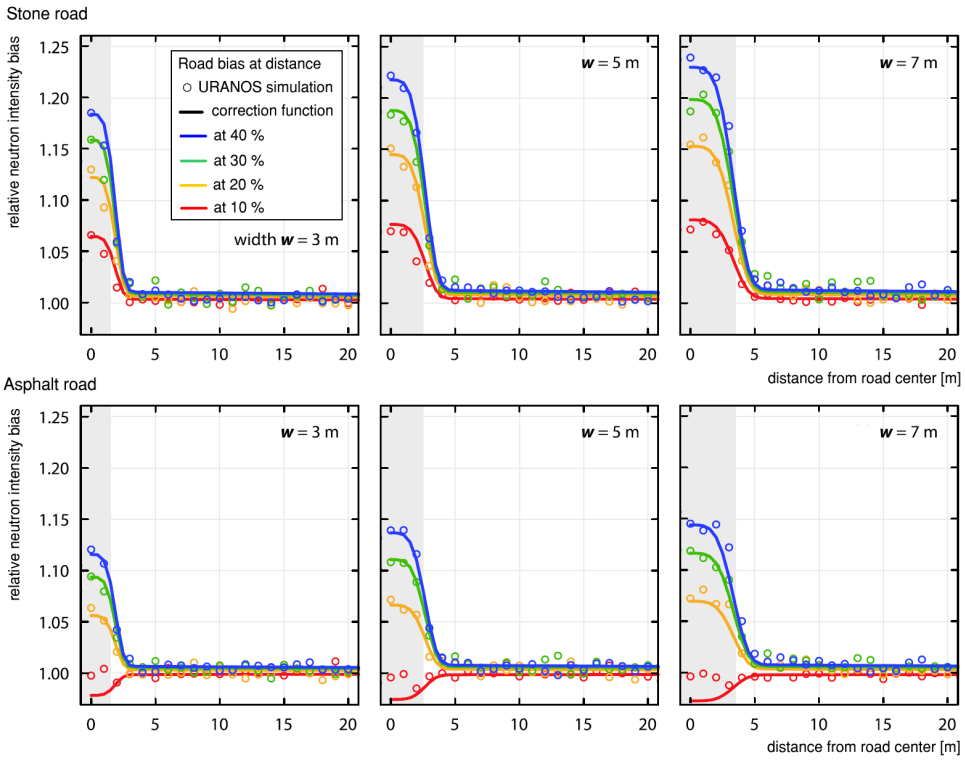

Figure 158: URANOS simulations (circles) and fitted correction functions representing the neutron bias at different distances x_c from the road center (x_c = 0 m) for various road widths w (geometry shaded), field soil moisture (color), and (top) stone road material with an effective water content of θ_{Vol} = 3 % and (bottom) asphalt road material with θ_{Vol} = 12 %. Field conditions that are dryer than the road moisture (lower panel, red curve) cannot be represented by the analytical approach. [SK2018]

Using the results from the simulations, a correction approach was developed with M. Schrön, which would allow to correct measurements of roving campaigns. The correction function C_{road}, which relates the measured neutron density N_{Corr} in the field to the flux bias from the road N_{road} as $N_{\mathrm{Corr}} = N_{\mathrm{road}}/C_{\mathrm{road}}$ should include an exponential dependency on the road width and road center distance due to the geometric contribution from the weighting function and a hyperbolic contribution from the domain water differences. In detail it is discussed in appendix B.3.4.

The function describes the simulation results, see Fig. 158, for different distances x_c from the road center and for different θ_{field}, θ_{road} and widths w. However, the validity of this analytical approach is limited to road widths below approximately 7 m, as for wider roads the neutron density saturates around the center at a peak value (not shown, but it can partly be already seen in the example of Fig. 158, lower right panel). Furthermore, this function is limited to effective values for θ_{road} between 1 % and 16 % and requires a prior knowledge about the field moisture conditions.

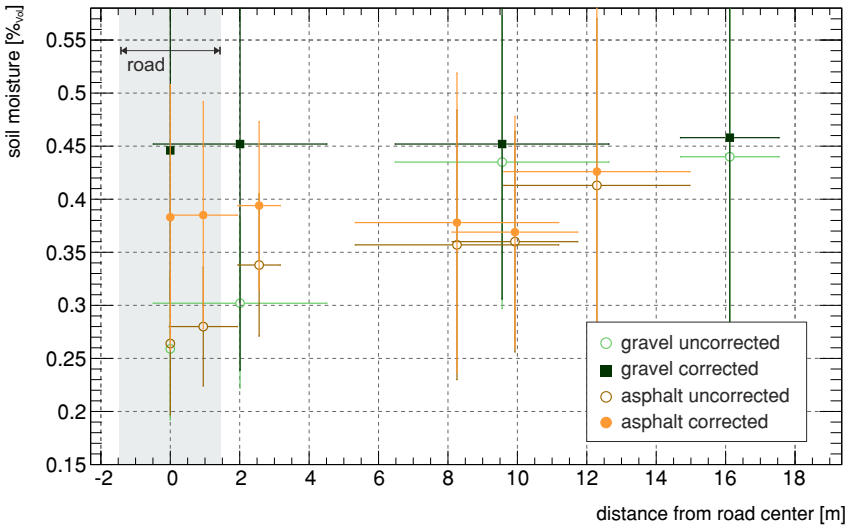

Figure 159: Roving measurements along an asphalt and a stone road. After application of the road correction function (195), measurements converge to similar values for all distances. Error bars are mainly due to the heterogeneity of the environmental water along the 400 m track length, i.e. account for the signal variance. [SK2018]

This function has extensively been applied in the study of [SK2018]. Here, exemplarily the correction of the data set of R. Rosolem and M. Schrön collected in the Lambourn catchment in South England (51°32'N, 1°29'W) is shown. The general objective of these experiments was to clarify whether the road correction function and the underlying simulations can be used to transfer the apparent soil moisture patterns seen from the road to values that were taken in the actual field. The loamy clay soil has an average bulk density of $\rho_{\mathrm{bd}} = 1.25\,\mathrm{g/cm^3}$ and a water equivalent of additional hydrogen pools has been determined to be $\theta_{\mathrm{Offset}} = 4\,\%$ with insignificant differences between the fields. The road network consists of a paved major road ($w = 3\,\mathrm{m}$) made of an asphalt/stone mixture with an estimated moisture equivalent of 11 %. The main side roads are made of a gravel/stone mixture with an estimated moisture equivalent of 7 %, mostly around 2.3 m wide, while the southern road is 4.5 m wide. Many non-sealed tracks ($w = 3\,\mathrm{m}$) follow the borders between fields which partly consist of sand, grass, and organic material, such that their average moisture equivalent was estimated to 12 %.

In the experiment a rover-type of cosmic-ray neutron detector, see sec. 12.2.1 and 13.1 was driven along a 400 m track in various distances from a gravel/stone road and an asphalt road. Upon application of the road correction function, see Fig. 159, measurements converge to similar values for all distances (right) and could also reveal different soil moisture conditions for the northern and southern fields (not shown). The overall result provides strong evidence that the analytical correction function properly represents the road bias at different distances and for different materials.

Part VI

SUMMARY AND CONCLUSION

CONCLUSION

This work is split into three parts which align in one development line. In order to precisely understand the physics of the CASCADE thermal neutron detector, the Ultra RApid Neutron-Only Simulation (URANOS) has been created. This tool turned out to be feasible to solve another problem of a novel method of soil moisture determination in environmental physics. It was able to correctly solve the neutron transport problem in the soil-air interface and laid the foundation to a detailed understanding of the measured response to different hydrogen pools.

THE URANOS NEUTRON MONTE CARLO TRANSPORT CODE

By a radical reset an entire neutron transport Monte Carlo has been built from scratch. It is the first of its kind natively written in C++ and based on a voxel engine. Neutrons interact with volumes rather than with surfaces, which makes compared to polygons the three-dimensional pixel to a geometry definition more close to the physical interaction. The computational framework could be slimmed down at decisive bottlenecks. The software mainly treats the propagation of neutrons as for example abandoning the complex gamma emissions, which come along with excited nuclei, are neither relevant for the CASCADE detector nor for the method of Cosmic-Ray Neutron Sensing. Further expenses could be avoided by not taking into account heat production, which for example changes the environment and the material cross sections, as from a neutron point of view the relevant systems here are entirely static.
The original motivation, however, which has been realized, was to merge all relevant parts from the initial beam to the signal generation into a detector simulation in order to study its performance in the highly demanding field of Spin Echo spectroscopy. Therefore it is necessary to simulate neutron interactions for the host instrument until being scattered or converted in the detector. The charged ion physics has to be incorporated, as well in the converter layer as in the detector gas. The ionization tracklet has to be projected through several stages of gas amplification while diffusing and drifting onto the nested readout structure of the detector, where multi-channel amplifiers with a specific threshold have to be triggered in order to generate a timestamp for a signal. Additionally, from the instrument upstream the neutron spin state has to be taken into account, as finally the detector response is analyzed in terms of the measured polarization.
Along with the language change, which makes it attractive as an open source project, an intuitive graphical user interface has been created, which has already attracted users without an extensive informatics background. Using URANOS allowed them to directly address their research question instead of training oneself for several weeks in the usage of sophisticated tools, which technically aim to calculate reactor criticality setups. Apart from the examples of the author presented in this work URANOS has successfully been employed in the study of the detector response of radiation portal monitors, in the development of novel neutron detectors for CRNS, in the calibration of an incoming cosmic radiation neutron detector and in the study of drip irrigation in agriculture. Most recently URANOS could impressively be used to study the feasibility of CRNS for measuring the integral snow water equivalent in the Alps. The data from a 3D laser scanner could directly be used to extrude the corresponding complex snow voxel landscape, allowing to calculate responses of the sensor during the different accumulation and melt-out phases.

THE CASCADE THERMAL NEUTRON DETECTOR

The CASCADE thermal neutron detector has become an established device for Spin Echo measurements. Besides the high precision requirements of a NRSE instrument the detector proposes a design for a helium-3 replacement system by adapting technology from developments of particle physics. The focus of this thesis is set to improve the performance of the 6-layer CASCADE setup used at RESEDA spectrometer at the FRM II in the technical realization, electronics and firmware. The use of Monte Carlo techniques to model the detector is necessary to understand the details of the underlying physics, especially the conversion ion energy and track length distribution.

In this work first the layer misidentification problem of the 6-layer detector had to be understood and characterized. Previous works could not find a stable point of operation with a reliable conversion layer assignment due to a variety of reasons, which had to consequently be disentangled and then addressed individually. By analog electronic circuit simulations of the GEM stack it was found, that grids inserted in between the GEMs could be used to electrically decouple the individual layers and further adaptations of the capacitor network led to improvements in the signal-to-noise ratio as well as the redesign of the GEM frames. The remaining unavoidable crosstalk could be identified by means of data analysis methods and an efficient algorithm on the FPGA could be implemented, which is able to suppress and reassign falsely identified events. Another degree of complexity linked to the use of solid ^{10}B coatings is the continuous energy spectrum of conversion ions deposited in the gas. Monte Carlo studies showed, that thick layers lead to a pileup at low energies, which inevitably lie either below the sensitivity or the gamma rejection threshold. With a necessary effective gas gain between the GEM layers slightly above 1, it occurs, that events are not identified at their original but at a subsequent layer. While the previous design had especially thick coatings on the drift cathodes, this effect could significantly be attenuated by reducing the outermost layer to 1 µm of ^{10}B.

The improved CASCADE detector has been characterized in terms of spatial resolution, detection efficiency and rate acceptance. The detector can be operated up to a rate capability of several MHz on its active surface of $20 \times 20\,\mathrm{cm}^2$, which, however, gets limited to approximately 150 kHz if the most efficient layer identification is required. The point spread function of the detector is not Gaussian due to scattering effects and the track topology of the conversion ions. Therefore, the spatial resolution has been determined by two methods. The optical contrast measurement leads to σ = (1.39±0.05) mm and the edge multisampling to σ = (1.454±0.007) mm. At the HEiDi diffractometer the detection efficiency has been measured by monochromatic beams at three different wavelengths. The results are extrapolated to any neutron energy by the detector Monte Carlo model. The obtained thermal neutron detection efficiency in the current configuration is (21.0±1.5) % and (46.9±3.3) % at 5.4 Å. In exemplary measurements presented in this work, the improved performance of the layer identification could be shown under experimental conditions for a Neutron Resonance Spin Echo and MIEZE setup by the successful spatial and time resolved tracking of the Spin Echo group interference pattern.

The CASCADE design offers further upscaling only by substantial adaptations of the active detection volume. However, with a well-balanced charge transfer through the stack, the multi-layered assembly allows to increase the effective amount of converter material in the beam to achieve a higher efficiency at a high spatial resolution. Future (MIEZE) Spin Echo systems extending to longer wavelengths and higher frequencies would strictly limit the effective detector depth as the Spin Echo group can be as short as a few millimeters. For this case ^{10}B systems like the CASCADE design are cost efficient to modularly instrument larger areas.

This work presents the most extensive study of neutron transport in the soil-air interface with specifically focusing on the dependency on hydrogen pools. To precisely understand the system this work heavily relies on Monte Carlo simulations, which allow to analyze the relevant observables with their influence factors. The so obtained data sets were parametrized by analytical functions, which describe the system without the further necessity to repeat a series of case studies.
The spatial distribution of neutrons can often be simplified in terms of thermodynamic models, however, it is very sensitive to initial energies and even to small amounts of hydrogen. As a consequence, the complexity of environmental neutron transport seems to impede any attempt to simplify the problem. Therefore, the need arose for revisiting neutron transport models and for addressing some of the open questions regarding the radial sensitivity, humid climate or terrain structures. As this study shows, the description of the footprint and neutron intensity is nontrivial to an exceptional degree.
Initially, the response functions of cosmic-ray neutron sensors were analyzed in terms of energy-dependent detection efficiency and angular sensitivity. The investigated detectors, which are specific models for hydrological research, comprise vertical (CRS1000) and horizontal configurations (Rover), each moderated by one inch of polyethylene and equipped with either $^{10}BF_3$ or ^3He proportional counters. The results show, that the energy window of highest response ranges from 0.1 eV to 10^6 eV. Hence, the typically used range of (10^2 - 10^4) eV provides a reasonable basis for CRNS investigations, yet, a significant fraction of neutrons are contributing to the signal of the sensor below and above this range.
The important result from this study for CRNS is, that the response to soil moisture varies significantly for humid climates between (10-40) $\%_{Vol}$ as well as for very dry conditions <3 $\%_{Vol}$. Previous studies underestimated the role of soil moisture for the footprint due to the choice of a modeled neutron source below the surface. This detail is the major cause for the discrepancy to findings from [463]. The footprint is defined by the radius of the 86 % quantile of the range distribution function of neutrons probing a soil of homogeneous moisture content. It has been found to range from approximately 160 m over a water body to 210 m over dry soil with a total error of about (4-6) %. The circular shape of the footprint remains isotropic for most field applications, like hilly terrain, nearby rivers or heterogeneous land. However, large water bodies or forests nearby can reduce range and intensity of detected neutrons from that direction.
The response to variations of absolute humidity features a 10 m decrease of the footprint radius for every change of (4-6) g/m^3 water vapor, which can easily span $\approx$ 25 g/m^3. This change corresponds to a 20 % change in footprint radius calculated with URANOS. The penetration depth $D_{86}(r, \theta)$ of detected neutrons directly below the sensor ranges from 15 cm to 83 cm depending on soil moisture. An exponential decrease with depth is a good estimate for the sensor's vertical sensitivity, whereas the depth in turn shrinks significantly with radial distance to the sensor.
The function W_r lays the basis for a refinement of the commonly applied sampling strategy, which assigned weights according to a static exponential radial function. In contrast, the present work shows that (1) the first tens of meters provide a dominant contribution to the signal in a rather non-exponential relation, and (2) the shape of the weighting function changes temporally as it is affected by variable moisture conditions. Subsequently, data can be weighted with $W_r(h, \theta)$ in an iterative procedure.
The revised footprint function could fundamentally improve the reliability of the CRNS method. Many deviations from the expected soil water response, which had been found in previous studies, can now be explained. Therefore, results from this work have quickly been adopted by the community and are meanwhile the basis for inter-

preting CRNS measurements. The improved understanding also allows to correct for systematic biases as have been found for the so-called „road effect“. This specifically high near-field sensitivity plays an important role for mobile measurements. The variability of the road width and material significantly influences the measurements and can now be corrected for analytically.

Part VII

APPENDIX

A

LITERATURE AND REFERENCES

A.1 | JOURNAL PUBLICATIONS

M. KÖHLI, F. ALLMENDINGER, et al. "Efficiency and spatial resolution of the CASCADE thermal neutron detector." In: *Nuclear Instruments and Methods in Physics Research Section A: Accelerators, Spectrometers, Detectors and Associated Equipment* **828** (Aug. 2016), pp. 242–249.
DOI: 10.1016/j.nima.2016.05.014

M. KÖHLI, M. KLEIN, et al. "CASCADE - a multi-layer Boron-10 neutron detection system." In: *Journal of Physics: Conference Series* **746**(1) (Sept. 2016), p. 012003.
DOI: 10.1088/1742-6596/746/1/012003

M. KÖHLI, M. SCHRÖN, et al. "Footprint characteristics revised for field-scale soil moisture monitoring with cosmic-ray neutrons." In: *Water Resources Research* **51**(7) (July 2015), pp. 5772–5790.
DOI: 10.1002/2015WR017169

M. HENSKE, M. KLEIN, et al. "The ^{10}B based Jalousie neutron detector: An alternative for ^{3}He filled position sensitive counter tubes." In: *Nuclear Instruments and Methods in Physics Research Section A: Accelerators, Spectrometers, Detectors and Associated Equipment* **686** (Sept. 2012), pp. 151–155.
DOI: 10.1016/j.nima.2012.05.075

G. MODZEL, M. HENSKE, et al. "Absolute efficiency measurements with the ^{10}B based Jalousie detector." In: *Nuclear Instruments and Methods in Physics Research Section A: Accelerators, Spectrometers, Detectors and Associated Equipment* **743** (Apr. 2014), pp. 90–95.
DOI: 10.1016/j.nima.2014.01.007

M. SCHRÖN, S.ZACHARIAS, et al. "Monitoring Environmental Water with Ground Albedo Neutrons and Correction for Incoming Cosmic Rays with Neutron Monitor Data." In: *PoS Proceedings of Science* **231** (Aug. 2015). The 34$^{\text{th}}$ International Cosmic Ray Conference, pp. 101–104.
DOI: 10.1063/1.2825756

M. SCHRÖN, M. KÖHLI, et al. "Improving Calibration and Validation of Cosmic-Ray Neutron Sensors in the Light of Spatial Sensitivity." In: *Hydrology and Earth System Sciences* **21**(10) (Oct. 2017), pp. 5009–5030.
DOI: 10.5194/hess-21-5009-2017

M. SCHRÖN, S. ZACHARIAS, et al. "Intercomparison of Cosmic-Ray Neutron Sensors and Water Balance Monitoring in an Urban Environment." In: *Geoscientific Instrumentation, Methods and Data Systems Discussions* **2017** (2017), pp. 1–24.
DOI: 10.5194/gi-2017-34

M. SCHRÖN, R. ROSOLEM, et al. "Cosmic-ray Neutron Rover Surveys of Field Soil Moisture and the Influence of Roads." In: *Water Resources Research* **54**(9) (May 2018), pp. 6441–6459.
DOI: 10.1029/2017WR021719

M. KÖHLI, M. SCHRÖN, and U. SCHMIDT. "Response functions for detectors in cosmic ray neutron sensing." In: *Nuclear Instruments and Methods in Physics Research Section A: Accelerators, Spectrometers, Detectors and Associated Equipment* **902** (Sept. 2018), pp. 184–189.
DOI: 10.1016/j.nima.2018.06.052

A.2 | Conference contributions

M. Köhli. *Das CASCADE-Projekt: Neutronendetektion mittels Bor-10 als Alternative zu Helium-3*. 76th DPG Annual Conference. HK 42.2. Mainz, Germany, Mar. 2012

M. Köhli. *Probing soil moisture by cosmic-ray induced Neutron Showers*. 78th DPG Annual Conference. UP 7.3. Berlin, Germany, Mar. 2014

M. Köhli. *Monte-Carlo Simulations on the Detector Sensitivity to Cosmic-Ray induced Neutron Showers*. 4th COSMOS Workshop. Leipzig, Germany, May 2014

M. Köhli. *The CASCADE Project - a perspective for solid state detectors*. International Workshop on Position Sensitive Neutron Detectors. Jülich, Germany, June 2014

M. Köhli. *Probing nano and macro scales: solid state detectors and cosmic neutron soil moisture determination*. 9th Annual PNN and Well Logging Conference. Klingenbach, Austria, Sept. 2014

M. Köhli. *CASCADE - eine alternative Perspektive für Festkörper-Neutronendetektoren*. Deutsche Tagung für Forschung mit Synchrotronstrahlung, Neutronen und Ionenstrahlen an Großgeräten 2014. Bonn, Germany, Sept. 2014

M. Köhli. *Soil moisture sensing by cosmic-ray induced neutron showers*. 79th DPG Annual Conference. UP 16.2. Heidelberg, Germany, Mar. 2015

M. Köhli. *The CASCADE Dectector - high-resolution neutron detection by solid ^{10}B layers*. Design and Engineering of Neutron Instruments Meeting (DENIM). Budapest, Hungary, Sept. 2015

M. Köhli. *The CASCADE Project - a multi-layer ^{10}B neutron detection system*. European Conference on Neutron Scattering (ECNS). Zaragossa, Spain, Sept. 2015

M. Köhli. *On the Phase Front of Neutron Detection*. Neutronen in der Forschung und Industrie. München, Germany, Nov. 2015

M. Köhli. *The method of soil moisture sensing by cosmic-ray neutrons*. 80th DPG Annual Conference. UP 15.1. Regensburg, Germany, Mar. 2016

M. Köhli. *The CASCADE Project - On the Phase Front of Neutron Detection*. 80th DPG Annual Conference. HK 70.6. Darmstadt, Germany, Mar. 2016

M. Köhli. *Neutron Transport Modelling with URANOS and Footprint Sensitivity - Making Neutrons great again*. 5th International COSMOS Workshop. Copenhagen, Denmark, Aug. 2016

M. Köhli. *Soil moisture sensing by detection of cosmic-ray neutrons*. 2nd ATTRACT TWD Symposium in Detection and Imaging. Strasbourg, France, Nov. 2016

M. Köhli. *Soil Moisture Measurement at the hectometer scale with cosmic-ray neutrons*. 81th DPG Annual Conference. UP 4.2. Bremen, Germany, Mar. 2017

M. Köhli. *High Spatial Resolution in Thermal Neutron Detection: CASCADE*. 81th DPG Annual Conference. HK 7.2. Darmstadt, Germany, Mar. 2017

M. Köhli. *Soil moisture measurement at the hectometer scale using CRNS for mobile applications*. 82th DPG Annual Conference. UP 8.2. Erlangen, Germany, Mar. 2018

M. Köhli. *URANOS - The Cosmic Ray Monte Carlo tool*. EGU General Assembly. GI 2.7. Vienna, Austria, Apr. 2018

[1] M. TANABASHI et al. "Review of Particle Physics." In: *Physical Review D* **98** (Sept. 2018), p. 030001. DOI: 10.1103/PhysRevD.98.030001.

[2] M. BATTAGLIA et al. *The CKM matrix and the unitarity triangle*. Oct. 2003. arXiv: 0304132v2 [hep-ph]. URL: https://arxiv.org/abs/hep-ph/0304132v2.

[3] CKMFITTER GROUP (J. CHARLES ET AL.) "CP violation and the CKM matrix: assessing the impact of the asymmetric B factories." In: *The European Physical Journal C - Particles and Fields* **41** (May 2005). updated results and plots available at: http://ckmfitter.in2p3.fr, pp. 1–131. DOI: 10.1140/epjc/s2005-02169-1.

[4] B. MÄRKISCH. *Experimental Status of V_{ud} from Neutron Decay*. July 2011. arXiv: 1107.3422 [nucl-ex]. URL: https://arxiv.org/abs/1107.3422.

[5] J.C. HARDY and I.S. TOWNER. "Superallowed $0^+ \to 0^+$ nuclear β decays: 2014 critical survey, with precise results for V_{ud} and CKM unitarity." In: *Physical Review C* **91** (Feb. 2015), p. 025501. DOI: 10.1103/PhysRevC.91.025501.

[6] S. DAR. *The Neutron EDM in the SM: A Review*. Aug. 2000. arXiv: hep-ph/0008248 [hep-ph]. URL: https://arxiv.org/abs/hep-ph/0008248.

[7] J.D. JACKSON. "The Nature of Intrinsic Magnetic Dipole Moments." In: *CERN Lectures* **77** (Sept. 1977).

[8] S. PAUL. "The puzzle of neutron lifetime." In: *Nuclear Instruments and Methods in Physics Research Section A: Accelerators, Spectrometers, Detectors and Associated Equipment* **611**(2) (Dec. 2009). Particle Physics with Slow Neutrons, pp. 157–166. DOI: 10.1016/j.nima.2009.07.095.

[9] N. FEATHER. "A History of Neutrons and Nuclei. Part 1." In: *Contemporary Physics* **1**(3) (1960), pp. 191–203. DOI: 10.1080/00107516008202611.

[10] W. SUTHERLAND. "XX. Cathode, Lenard, and Röntgen rays." In: *Philosophical Magazine Series 5* **47**(286) (1899), pp. 269–284. DOI: 10.1080/14786449908621259.

[11] E. RUTHERFORD. "Scattering of α and β Particles by Matter." In: *Philosophical Magazine Series 6* **21**(286) (Apr. 1911), pp. 669–688. DOI: 10.1080/14786440508637080.

[12] E. RUTHERFORD. "Bakerian Lecture. Nuclear Constitution of Atoms." In: *Proceedings of the Royal Society of London A: Mathematical, Physical and Engineering Sciences* **97**(686) (July 1920), pp. 374–400. DOI: 10.1098/rspa.1920.0040.

[13] E. RUTHERFORD. *Radio-activity*. 1st Edition. Cambridge University Press, Feb. 1904. 399 pp. URL: https://link.springer.com/article/10.1007/BF01390908.

[14] W. BOTHE and H. BECKER. "Künstliche Erregung von Kern-γ-Strahlen." In: *Zeitschrift für Physik* **66**(5) (May 1930), pp. 289–306. DOI: 10.1007/BF01390908.

[15] I. CURIE and F. JOLIOT. "Émission de protons de grande vitesse par les substances hydrogénées sous l'influence des rayons gamma très pénétrants." In: *Comptes rendus hebdomadaires des séances de l'Académie des Sciences* **194** (Jan. 1932), pp. 273–275. URL: https://gallica.bnf.fr/ark:/12148/bpt6k31473/f273.image.r=.

[16] E. AMALDI. *Ettore Majorana, Man and Scientist: Commemoration Speech*. Academic Press, 1966.

[17] J. CHADWICK. "Possible Existence of a Neutron." In: *Nature* **129**(3252) (Feb. 1932), p. 312. DOI: 10.1038/129312a0.

[18] D.D. IWANENKO. "The Neutron Hypothesis." In: *Nature* **129**(3265) (May 1932), p. 798. DOI: 10.1038/129798d0.

[19] J. CHADWICK. "The Existence of a Neutron." In: *Proceedings of the Royal Society of London Series A* **136** (June 1932), pp. 692–708.
DOI: 10.1098/rspa.1932.0112.

[20] W. HEISENBERG. "Über den Bau der Atomkerne. I." In: *Zeitschrift für Physik* **77**(1) (Jan. 1932), pp. 1–11.
DOI: 10.1007/BF01342433.

[21] H. BECKER and W. BOTHE. "Die in Bor und Beryllium erregten γ-Strahlen." In: *Zeitschrift für Physik* **76**(7) (July 1932), pp. 421–438.
DOI: 10.1007/BF01336726.

[22] L.M. MOTT-SMITH and G.L. LOCHER. "A New Experiment Bearing on Cosmic-ray Phenomena." In: *Physical Review* **38** (Oct. 1931), pp. 1399–1408.
DOI: 10.1103/PhysRev.38.1399.

[23] K.H. BECKURTS and K.W. WIRTZ. *Neutron Physics*. Berlin, Heidelberg: Springer Berlin Heidelberg, 1964. 439 pp. ISBN: 978-3-642-87616-5.
DOI: 10.1007/978-3-642-87614-1.

[24] E. AMALDI. "The Production and Slowing Down of Neutrons." In: *Neutrons and Related Gamma Ray Problems / Neutronen und Verwandte Gammastrahlprobleme*. 1st Edition. Berlin, Heidelberg: Springer Berlin Heidelberg, Jan. 1959, pp. 1–659. ISBN: 978-3-642-45922-1.
DOI: 10.1007/978-3-642-45920-7.

[25] M. BERGER, J.S. COURSEY, M.A. ZUCKER, and J. CHANG. *NIST XCOM: Stopping-Power and Range Tables for Electrons, Protons, and Helium Ions*. Website. https://www.nist.gov/pml/stopping-power-range-tables-electrons-protons-and-helium-ions; (01.03.2019). 2017.
DOI: 10.18434/T4NC7P.

[26] C. GRUPEN and B.A. SCHWARZ. *Particle Detectors*. 2nd ed. Cambridge University Press, Mar. 2008. 676 pp. ISBN: 978-0-521-84006-4.
URL: www.cambridge.org/9780521840064.

[27] F. SAULI. "Principles of operation of multiwire proportional and drift chambers." In: *CERN Academic Training Lecture*. CERN, Geneva, 1975 - 1976. CERN. Geneva: CERN, Sept. 1977.
DOI: 10.5170/CERN-1977-009.

[28] W.R. LEO. *Techniques for Nuclear and Particle Physics Experiments*. 2nd ed. Berlin Heidelberg: Springer, 1994. 377 pp. ISBN: 978-3-540-57280-0.
DOI: 10.1007/978-3-642-57920-2.

[29] T. DOKE, N. ISHIDA, and M. KASE. "Fano factors in rare gases and their mixtures." In: *Nuclear Instruments and Methods in Physics Research Section B: Beam Interactions with Materials and Atoms* **63**(4) (Mar. 1992), pp. 373–376.
DOI: 10.1016/0168-583X(92)95207-8.

[30] M. HAUSCHILD. *MediPix Simulations, gas properties and GEMs*. Website. http://hausch.home.cern.ch/hausch/MediPix.html; (01.03.2019). 2006.

[31] F. GAUTHIER-LAFAYE. "2 billion year old natural analogs for nuclear waste disposal: the natural nuclear fission reactors in Gabon (Africa)." In: *Comptes Rendus Physique* **3**(7) (Sept. 2002), pp. 839–849.
DOI: 10.1016/S1631-0705(02)01351-8.

[32] J.F. ZIEGLER. "Terrestrial cosmic rays." In: *IBM Journal of Research and Development* **40**(1) (Jan. 1996), pp. 19–39.
DOI: 10.1147/rd.401.0019.

[33] B.C. LACKI, T.A. THOMPSON, and E. QUATAERT. "The Physics of the Far-infrared-Radio Correlation. I. Calorimetry, Conspiracy, and Implications." In: *The Astrophysical Journal* **717**(1) (June 2010), p. 1.
DOI: 10.1088/0004-637X/717/1/1.

[34] C. CAPRINI and P.G. FERREIRA. "Constraints on the electrical charge asymmetry of the universe." In: *Journal of Cosmology and Astroparticle Physics* **2005**(02) (Feb. 2005), pp. 006–006.
DOI: 10.1088/1475-7516/2005/02/006.

[35] C.L. SARAZIN and R. LIEU. "Extreme-Ultraviolet Emission from Clusters of Galaxies: Inverse Compton Radiation from a Relic Population of Cosmic-Ray Electrons?" In: *The Astrophysical Journal Letters* **494**(2) (Feb. 1998), p. L177.
DOI: 10.1086/311196.

[36] R.M. BALTRUSAITIS, R. CADY, et al. "The Utah Fly's Eye detector." In: *Nuclear Instruments and Methods in Physics Research Section A: Accelerators, Spectrometers, Detectors and Associated Equipment* **240**(2) (Oct. 1985), pp. 410–428.
DOI: 10.1016/0168-9002(85)90658-8.

[37] T.K. GAISSER. "The Cosmic-ray Spectrum: from the knee to the ankle." In: *Journal of Physics: Conference Series* **47**(1) (Mar. 2006), pp. 15–20.
DOI: 10.1088/1742-6596/47/1/002.

[38] B.W. CARROLL and D.A. OSTLIE. *An Introduction to Modern Astrophysics*. Ed. by San Francisco ADDISON-WESLEY. 2nd. Pearson Education, July 2006. 1400 pp. ISBN: 978-0805304022.
DOI: 10.1017/9781108380980.

[39] A.M. BYKOV, D.C. ELLISON, A. MARCOWITH, and S.M. OSIPOV. "Cosmic Ray Production in Supernovae." In: *Space Science Reviews* **214**(1) (Jan. 2018), p. 41.
DOI: 10.1007/s11214-018-0479-4.

[40] L. MERTEN, C. BUSTARD, E.G. ZWEIBEL, and J.B. TJUS. "The Propagation of Cosmic Rays from the Galactic Wind Termination Shock: Back to the Galaxy?" In: *The Astrophysical Journal* **859**(1) (May 2018), p. 63.
DOI: 10.3847/1538-4357/aabfdd.

[41] V.N. ZIRAKASHVILI and H.J. VÖLK. "Cosmic ray reacceleration on the galactic wind termination shock." In: *Advances in Space Research* **37**(10) (Aug. 2006). Astrophysics, pp. 1923–1927.
DOI: 10.1016/j.asr.2005.06.013.

[42] F.C. MICHEL. "Cosmic-ray acceleration by pulsars." In: *Advances in Space Research* **4**(2) (1984), pp. 387–391.
DOI: 10.1016/0273-1177(84)90336-3.

[43] R. BLANDFORD, P. SIMEON, and Y. YUAN. "Cosmic Ray Origins: An Introduction." In: *Nuclear Physics B - Proceedings Supplements* **256-257** (Dec. 2014). Cosmic Ray Origin - Beyond the Standard Models, pp. 9–22.
DOI: 10.1016/j.nuclphysbps.2014.10.002.

[44] J. BEER, S.M. TOBIAS, and N.O. WEISS. "On long-term modulation of the Sun's magnetic cycle." In: *Monthly Notices of the Royal Astronomical Society* **473**(2) (Jan. 2018), pp. 1596–1602.
DOI: 10.1093/mnras/stx2337.

[45] K. KUDELA, H. MAVROMICHALAKI, A. PAPAIOANNOU, and M. GERONTIDOU. "On Mid-Term Periodicities in Cosmic Rays." In: *Solar Physics* **266**(1) (Sept. 2010), pp. 173–180.
DOI: 10.1007/s11207-010-9598-0.

[46] K.G. MCCRACKEN, H. MORAAL, and M.A. SHEA. "The high-energy impulsive ground-level enhancement." In: *The Astrophysical Journal* **761**(2) (Nov. 2012), p. 101.
DOI: 10.1088/0004-637X/761/2/101.

[47] H.V. CANE. "Coronal Mass Ejections and Forbush Decreases." In: *Space Science Reviews* **93**(1) (July 2000), pp. 55–77.
DOI: 10.1023/A:1026532125747.

[48] S.R. THOMAS, M.J. OWENS, and M. LOCKWOOD. "The 22-Year Hale Cycle in Cosmic Ray Flux - Evidence for Direct Heliospheric Modulation." In: *Solar Physics* **289**(1) (Jan. 2014), pp. 407–421.
DOI: 10.1007/s11207-013-0341-5.

[49] M.A. SHEA and D.F. SMART. "Geomagnetic cutoff rigidities and geomagnetic coordinates appropriate for the Carrington flare Epoch." In: *Advances in Space Research* **38**(2) (Sept. 2006). The Great Historical Geomagnetic Storm of 1859: A Modern Look, pp. 209–214.
DOI: 10.1016/j.asr.2005.03.156.

[50] M. ANDREASEN, K.H. JENSEN, D. DESILETS, T.E. FRANZ, M. ZREDA, H.R. BOGENA, and M.C. LOOMS. "Status and Perspectives on the Cosmic-Ray Neutron Method for Soil Moisture Estimation and Other Environmental Science Applications." In: *Vadose Zone Journal* **16**(8) (Aug. 2017), pp. 1–11. DOI: 10.2136/vzj2017.04.0086.

[51] L.I. DORMAN, S.G. FEDCHENKO, L.V. GRANITSKY, and G.A. RISHE. "Coupling and barometer coefficients for measurements of cosmic ray variations at altitudes of 260-400 mb." In: *Acta Physica* **2** (Jan. 1970). Supplement to Volume 29, pp. 233–236. URL: http://adsabs.harvard.edu/full/1970ICRC....2..233D.

[52] C.W. FABJAN and F. GIANOTTI. "Calorimetry for particle physics." In: *Reviews of Modern Physics* **75** (Oct. 2003), pp. 1243–1286. DOI: 10.1103/RevModPhys.75.1243.

[53] C. LEROY and R.-G. RANCOITA. "Physics of cascading shower generation and propagation in matter: principles of high-energy, ultrahigh-energy and compensating calorimetry." In: *Reports on Progress in Physics* **63**(4) (Apr. 2000), pp. 505–606. DOI: 10.1088/0034-4885/63/4/202.

[54] B.B. ROSSI. *High-energy Particles*. Prentice-Hall physics series. New York, 1952. 569 pp. ISBN: 978-0133873245.

[55] R. ULRICH, R. ENGEL, and M. UNGER. "Hadronic multiparticle production at ultrahigh energies and extensive air showers." In: *Physical Review D* **83** (Mar. 2011), p. 054026. DOI: 10.1103/PhysRevD.83.054026.

[56] A. CAPELLA, U. SUKHATME, C.-I. TAN, and J. TRAN THANH VAN. "Dual parton model." In: *Physics Reports* **236**(4) (Jan. 1994), pp. 225–329. DOI: 10.1016/0370-1573(94)90064-7.

[57] S.D. ELLIS and M.B. KISLINGER. "Implications of parton-model concepts for large-transverse-momentum production of hadrons." In: *Physical Review D* **9** (Apr. 1974), pp. 2027–2051. DOI: 10.1103/PhysRevD.9.2027.

[58] S. MOLLERACH and E. ROULET. "Progress in high-energy cosmic ray physics." In: *Progress in Particle and Nuclear Physics* **98** (Jan. 2018), pp. 85–118. DOI: 10.1016/j.ppnp.2017.10.002.

[59] D. HECK, J. KNAPP, J.N. CAPDEVIELLE, G. SCHATZ, and T. THOUW. *CORSIKA: A Monte Carlo code to simulate extensive air showers*. Tech. rep. FZKA 6019. Forschungszentrum Karlsruhe, 1998. 98 pp. URL: http://digbib.ubka.uni-karlsruhe.de/volltexte/fzk/6019/6019.pdf.

[60] G. PFOTZER. "Dreifachkoinzidenzen der Ultrastrahlung aus vertikaler Richtung in der Stratosphäre." In: *Zeitschrift für Physik* **102**(1–2) (Jan. 1936), pp. 41–58. DOI: 10.1007/BF01336830.

[61] T. SATO. "Analytical Model for Estimating Terrestrial Cosmic Ray Fluxes Nearly Anytime and Anywhere in the World: Extension of PARMA/EXPACS." In: *PLOS ONE* **10**(12) (Dec. 2015), pp. 1–33. DOI: 10.1371/journal.pone.0144679.

[62] K.K. GUDIMA, S.G. MASHNIK, and V.D. TONEEV. "Cascade-exciton model of nuclear reactions." In: *Nuclear Physics A* **401**(2) (June 1983), pp. 329–361. DOI: 10.1016/0375-9474(83)90532-8.

[63] E.T. JURNEY, J.W. STARNER, J.E. LYNN, and S. RAMAN. "Thermal-neutron capture by ^{14}N." In: *Physical Review C* **56** (July 1997), pp. 118–134. DOI: 10.1103/PhysRevC.56.118.

[64] R.E. TAYLOR. "Radiocarbon dating: The continuing revolution." In: *Evolutionary Anthropology: Issues, News, and Reviews* **4**(5) (June 1995), pp. 169–181. DOI: 10.1002/evan.1360040507.

[65] P. GOLDHAGEN, J.M. CLEM, and J.W. WILSON. "The energy spectrum of cosmic-ray induced neutrons measured on an airplane over a wide range of altitude and latitude." In: *Radiation Protection Dosimetry* **110**(1–4) (Aug. 2004), pp. 387–392. DOI: 10.1093/rpd/nch216.

[66] T. SATO and K. NIITA. "Analytical Functions to Predict Cosmic-Ray Neutron Spectra in the Atmosphere." In: *Radiation Research* **166**(3) (Sept. 2006), pp. 544–555.
DOI: 10.1667/RR0610.1.

[67] T. SATO, H. YASUDA, K. NIITA, A. ENDO, and L. SIHVER. "Development of PARMA: PHITS-based Analytical Radiation Model in the Atmosphere." In: *Radiation Research* **170**(2) (Aug. 2008), pp. 244–259.
DOI: 10.1667/RR1094.1.

[68] H. IWASE, K. NIITA, and T. NAKAMURA. "Development of General-Purpose Particle and Heavy Ion Transport Monte Carlo Code." In: *Journal of Nuclear Science and Technology* **39**(11) (Aug. 2002), pp. 1142–1151.
DOI: 10.1080/18811248.2002.9715305.

[69] M.S. GORDON, P. GOLDHAGEN, K.P. RODBELL, T.H. ZABEL, H.H.K. TANG, J.M. CLEM, and P. BAILEY. "Measurement of the flux and energy spectrum of cosmic-ray induced neutrons on the ground." In: *IEEE Transactions on Nuclear Science* **51**(6) (Dec. 2004), pp. 3427–3434.
DOI: 10.1109/TNS.2004.839134.

[70] R.M. BRUGGER. "We need more intense thermal-neutron beams." In: *Physics Today* **21**(12) (Dec. 1968), pp. 23–30.
DOI: 10.1063/1.3034644.

[71] J.M. CARPENTER and W.B. YELON. "2. Neutron Sources." In: *Neutron Scattering*. Ed. by K. SKÖLD and D.L. PRICE. Vol. 23. Methods in Experimental Physics. Academic Press, 1986, pp. 99–196.
DOI: 10.1016/S0076-695X(08)60555-4.

[72] K.H. ANDERSEN and C.J. CARLILE. "A Proposal for a Next Generation European Neutron Source." In: *Journal of Physics: Conference Series* **746**(1) (Oct. 2016), p. 012030.
DOI: 10.1088/1742-6596/746/1/012030.

[73] G.E. MOORE. "Cramming more components onto integrated circuits." In: *Electronics* **38**(8) (Apr. 1965). URL for IEEE reprint 2006, pp. 114–118.
URL: https://ieeexplore.ieee.org/document/4785860/.

[74] M.S. LIVINGSTON. *High-energy accelerators*. Interscience tracts on physics and astronomy. New York, U.S.A.: Interscience Publishers, May 1954. 157 pp.

[75] M. TIGNER. "Does Accelerator-Based Particle Physics Have a Future?" In: *Physics Today* **54**(1) (Jan. 2001), pp. 36–40.
DOI: 10.1063/1.1349610.

[76] THE EUROPEAN NEUTRON SCATTERING ASSOCIATION (ENSA). (accessed 26.08.2016). 2016. URL: http://www.neutrons-ensa.eu.

[77] M. ARAI and K. CRAWFORD. "Neutron Imaging and Applications: A Reference for the Imaging Community." In: *Neutron Scattering Applications and Techniques*. Ed. by I.S. ANDERSON, R.L. MCGREEVY, and H.Z. BILHEUX. Springer USA, 2009. Chap. Neutron Sources and Facilities, pp. 13–30.
ISBN: 9780387786933.
DOI: 10.1007/978-0-387-78693-3.

[78] INTERNATIONAL ATOMIC ENERGY AGENCY. *Research Reactors*. (accessed 10.03.2019). June 2016.
URL: https://nucleus.iaea.org/RRDB/RR/ReactorSearch.aspx.

[79] A. RÖHRMOSER. "Core model of new German neutron source FRM II." In: *Nuclear Engineering and Design* **240**(6) (2010), pp. 1417–1432.
DOI: 10.1016/j.nucengdes.2010.02.011.

[80] K. BÖNING, W. GLÄSER, and A. RÖHRMOSER. "Physics of the Munich compact core design." In: *Proceedings of the 1988 International Meeting on Reduced Enrichment for Research and Test Reactors*. Vol. 25. 17. ANL/RERTR/TM–13. July 1993, pp. 393–403.
DOI: 10.1109/NSSMIC.2007.4436548.

[81] T. BÜCHERL and S. SÖLLRADL. "NECTAR: Radiography and tomography station using fission neutrons." In: *Journal of large-scale Research Facilities* **1**(A19) (June 2015).
DOI: 10.17815/jlsrf-1-45.

[82] C. FRANZ and T. SCHRÖDER. "RESEDA: Resonance spin echo spectrometer." In: *Journal of large-scale Research Facilities* **1**(A14) (June 2015).
DOI: 10.17815/jlsrf-1-37.

[83] R. GEORGII and K. SEEMANN. "MIRA: Dual wavelength band instrument." In: *Journal of large-scale Research Facilities* **1**(A3) (June 2015).
DOI: 10.17815/jlsrf-1-21.

[84] M. MEVEN and A. SAZONOV. "HEiDi: Single crystal diffractometer at hot source." In: *Journal of large-scale Research Facilities* **1**(A7) (June 2015).
DOI: 10.17815/jlsrf-1-20.

[85] F. GRÜNAUER. "Design, optimization, and implementation of the new neutron radiography facility at FRM-II." PhD thesis. Institut E21, Technische Universität München, Sept. 2005. 199 pp.
URL: https://www.physi.uni-heidelberg.de//Publications/phd_haeusler.pdf.

[86] S. Ulam N. METROPOLIS. "The Monte Carlo Method." In: *Journal of the American Statistical Association* **44**(247) (Sept. 1949), pp. 335–341.
DOI: 10.2307/2280232.

[87] F. COCCETTI. "The Fermiac or Fermi's Trolley." In: *Il Nuovo Cimento C* **39**(2) (Sept. 2016).
DOI: 10.1393/ncc/i2016-16296-7.

[88] N. METROPOLIS. "The Beginning of the Monte Carlo Method." In: *Los Alamos Science* **15** (1987). Special Issue, Stanislaw Ulam 1909-1984, pp. 125–130.
URL: https://permalink.lanl.gov/object/tr?what=info:lanl-repo/lareport/LA-UR-88-9067.

[89] A. BURKS, H.D. HUSKEY, C. CHU, J.A. CUMMINGS, J.H. DAVIS, T.K. SHARPLESS, and R.F. SHAW. *Report on the ENIAC (Electronic Numerical Integrator and Computer)*. Technical Report. Moore School of Electrical Engineering. The University of Pennsylvania, June 1946. 786 pp.
URL: https://www.dtic.mil/get-tr-doc/pdf?AD=ADA622372.

[90] T. HAIGH, M. PRIESTLEY, and C. ROPE. "Los Alamos Bets on ENIAC: Nuclear Monte Carlo Simulations, 1947-1948." In: *IEEE Annals of the History of Computing* **36**(3) (July 2014), pp. 42–63.
DOI: 10.1109/MAHC.2014.40.

[91] M. MATSUMOTO and T. NISHIMURA. "Mersenne Twister: A 623-dimensionally Equidistributed Uniform Pseudo-random Number Generator." In: *ACM Transactions on Modeling and Computer Simulation* **8**(1) (Jan. 1998), pp. 3–30.
DOI: 10.1145/272991.272995.

[92] D.E. KNUTH. *The Art of Computer Programming, Volume 2 (3rd Ed.): Seminumerical Algorithms*. Boston, MA, USA: Addison-Wesley Longman Publishing Co., Inc., Nov. 1997. 106 pp. ISBN: 0-201-89684-2.

[93] E.M. GELBARD. *Epithermal scattering in VIM*. Tech. rep. FRA–TM–123. Argonne National Laboratory, 1979.

[94] P.K. ROMANO and B. FORGET. "The OpenMC Monte Carlo particle transport code." In: *Annals of Nuclear Energy* **51** (Jan. 2013), pp. 274–281.
DOI: 10.1016/j.anucene.2012.06.040.

[95] J.A. WALSH, B. FORGET, and K.S. SMITH. "Accelerated sampling of the free gas resonance elastic scattering kernel." In: *Annals of Nuclear Energy* **69** (July 2014), pp. 116–124.
DOI: 10.1016/j.anucene.2014.01.017.

[96] N. OTUKA, E. DUPONT, et al. "Towards a More Complete and Accurate Experimental Nuclear Reaction Data Library (EXFOR): International Collaboration Between Nuclear Reaction Data Centres (NRDC)." In: *Nuclear Data Sheets* **120** (June 2014), pp. 272–276.
DOI: 10.1016/j.nds.2014.07.065.

[97] M.B. CHADWICK, M. HERMAN, et al. "ENDF/B-VII.1 Nuclear Data for Science and Technology: Cross Sections, Covariances, Fission Product Yields and Decay Data." In: *Nuclear Data Sheets* **112**(12) (Dec. 2011). Special Issue on ENDF/B-VII.1 Library, pp. 2887–2996.
DOI: 10.1016/j.nds.2011.11.002.

[98] K. SHIBATA, O. IWAMOTO, et al. “JENDL-4.0: A New Library for Nuclear Science and Engineering.” In: *Journal of Nuclear Science and Technology* **48**(1) (Sept. 2011), pp. 1–30. DOI: 10.1080/18811248.2011.9711675.

[99] A. TRKOV, M. HERMAN, and D.A. BROWN. *ENDF-6 Formats Manual*. Report. Data Formats and Procedures for the Evaluated Nuclear Data Files ENDF/B-VI and ENDF/B-VII. National Nuclear Data Center. Brookhaven National Laboratory, Oct. 2012. 396 pp. URL: https://www-nds.iaea.org/public/endf/endf-manual.pdf.

[100] R. SEDGEWICK. *Algorithms in C*. Boston, USA: Addison-Wesley Longman Publishing Co., Inc., Dec. 1990. 672 pp. ISBN: 0-201-51425-7.

[101] J.F. BRIESMEISTER et al. “MCNP-A general Monte Carlo N-particle transport code.” In: *Version 4C, LA-13709-M* (Dec. 2000). URL: https://permalink.lanl.gov/object/tr?what=info:lanl-repo/lareport/LA-13709-M.

[102] SUN PROGRAMMERS GROUP. *Fortran 77 Reference Manual*. Tech. rep. Version 1.0. Mar. 1995. 513 pp. URL: http://wwwcdf.pd.infn.it/localdoc/f77_sun.pdf.

[103] X-5 MONTE CARLO TEAM. “MCNP-A general Monte Carlo N-particle transport code, Version 5.” In: *LA-UR-03-1987* (Apr. 2003). Volume I: Overview and Theory. URL: https://laws.lanl.gov/vhosts/mcnp.lanl.gov/pdf_files/la-ur-03-1987.pdf.

[104] L.S. WATERS, G.W. MCKINNEY, J.W. DURKEE, M.L. FENSIN, J.S. HENDRICKS, M.R. JAMES, R.C. JOHNS, and D.B. PELOWITZ. “The MCNPX Monte Carlo Radiation Transport Code.” In: *AIP Conference Proceedings* **896**(1) (Mar. 2007), pp. 81–90. DOI: 10.1063/1.2720459.

[105] SUN PROGRAMMERS GROUP. *Fortran 90 User’s Guide*. Tech. rep. Version 1.0. Mar. 1995. URL: http://smdc.sinp.msu.ru/doc/Fortran90UsersGuide.pdf.

[106] R.E. PRAEL and H. LICHTENSTEIN. “User Guide to LCS: The LAHET Code System.” In: *LA-UR-89-3014* (Sept. 1989). URL: https://permalink.lanl.gov/object/tr?what=info:lanl-repo/lareport/LA-UR-89-3014.

[107] K.K. GUDIMA, S.G. MASHNIK, and A.J. SIERK. “User Manual for the Code LAQGSM.” In: *LA-UR-01-6804* (Dec. 2001). URL: https://permalink.lanl.gov/object/tr?what=info:lanl-repo/lareport/LA-UR-01-6804.

[108] T. GOORLEY, M. JAMES, et al. “Initial MCNP6 Release Overview.” In: *Nuclear Technology* **180**(3) (Aug. 2012), pp. 298–315. DOI: 10.13182/NT11-135.

[109] G.W. MCKINNEY, H. ARMSTRONG, M.R. JAMES, J. CLEM, and P. GOLDHAGEN. “MCNP6 Cosmic-Source Option.” In: *LA-UR-12-22318* (June 2012). URL: https://permalink.lanl.gov/object/tr?what=info:lanl-repo/lareport/LA-UR-12-22318.

[110] G.W. MCKINNEY. “MCNP6 Cosmic and Terrestrial Background Particle Fluxes.” In: *LA-UR-13-24293* (June 2013). Release 3. URL: https://mcnp.lanl.gov/pdf_files/la-ur-13-24293.pdf.

[111] K. NIITA, H. TAKADA, S. MEIGO, and Y. IKEDA. “High-energy particle transport code NMTC/JAM.” In: *Nuclear Instruments and Methods in Physics Research Section B: Beam Interactions with Materials and Atoms* **184**(3) (Nov. 2001), pp. 406–420. DOI: 10.1016/S0168-583X(01)00784-4.

[112] A.T. NELMS. *Energy loss and range of electrons and positrons*. National Bureau of Standards Circular 577 and Suppl. July 1956, pp. 1–30. URL: https://catalog.hathitrust.org/Record/007291096.

[113] K. NIITA. “QMD and JAM Calculations for High Energy Nucleon-Nucleus Collisions.” In: *Journal of Nuclear Science and Technology* **39** (Aug. 2002). sup2, pp. 714–719. DOI: 10.1080/00223131.2002.10875198.

[114] O. IWAMOTO, N. IWAMOTO, S. KUNIEDA, F. MINATO, and K. SHIBATA. "The CCONE Code System and its Application to Nuclear Data Evaluation for Fission and Other Reactions." In: *Nuclear Data Sheets* **131** (Jan. 2016). Special Issue on Nuclear Reaction Data, pp. 259–288.
DOI: 10.1016/j.nds.2015.12.004.

[115] A. BOUDARD, J. CUGNON, J.-C. DAVID, S. LERAY, and D. MANCUSI. "New potentialities of the Liège intranuclear cascade model for reactions induced by nucleons and light charged particles." In: *Physical Review C* **87** (Jan. 2013), p. 014606.
DOI: 10.1103/PhysRevC.87.014606.

[116] G. BATTISTONI, T. BOEHLEN, et al. "Overview of the FLUKA code." In: *Annals of Nuclear Energy* **82** (Aug. 2015). Joint International Conference on Supercomputing in Nuclear Applications and Monte Carlo 2013, pp. 10–18.
DOI: 10.1016/j.anucene.2014.11.007.

[117] M.B. EMMETT. "The MORSE Monte Carlo Transport Code System." In: *ORNL-4972/R2* (Feb. 1975).
URL: https://inis.iaea.org/collection/NCLCollectionStore/_Public/16/029/16029296.pdf.

[118] S. AGOSTINELLI, ET AL. "GEANT4 - a simulation toolkit." In: *Nuclear Instruments and Methods in Physics Research Section A: Accelerators, Spectrometers, Detectors and Associated Equipment* **506**(3) (July 2003), pp. 250–303.
DOI: 10.1016/S0168-9002(03)01368-8.

[119] A.N. SOLOVYEV, V.V. FEDOROV, V.I. KHARLOV, and U.A. STEPANOVA. "Comparative analysis of MCNPX and GEANT4 codes for fast-neutron radiation treatment planning." In: *Nuclear Energy and Technology* **1**(1) (Sept. 2015), pp. 14–19.
DOI: 10.1016/j.nucet.2015.11.004.

[120] B.M. VAN DER ENDE, J. ATANACKOVIC, A. ERLANDSON, and G. BENTOUMI. "Use of GEANT4 vs. MCNPX for the characterization of a boron-lined neutron detector." In: *Nuclear Instruments and Methods in Physics Research Section A: Accelerators, Spectrometers, Detectors and Associated Equipment* **820** (June 2016), pp. 40–47.
DOI: 10.1016/j.nima.2016.02.082.

[121] L.B. LEVITT and R.C. LEWIS. *VIM-1, A Non-multigroup Monte Carlo Code for Analysis of Fast Critical Assemblies*. AI-AEC-12951. Jan. 1970. 94 pp.
DOI: 10.2172/4615237.

[122] E. BRUN, F. DAMIAN, et al. "TRIPOLI-4, CEA, EDF and AREVA reference Monte Carlo code." In: *Annals of Nuclear Energy* **82** (Aug. 2015). Joint International Conference on Supercomputing in Nuclear Applications and Monte Carlo 2013, pp. 151–160.
DOI: 10.1016/j.anucene.2014.07.053.

[123] D.E. CULLEN. "TART 2005 A Coupled Neutron-Photon 3-D, Combinatorial Geometry Time Dependent Monte Carlo Transport Code." In: *UCRL-SM-218009* (Nov. 2005).
URL: https://e-reports-ext.llnl.gov/pdf/329012.pdf.

[124] R.J. PROCASSINI, D.E. CULLEN, G.M. GREENMAN, and C.A. HAGMANN. "Verification and Validation of MERCURY: A Modern, Monte Carlo Particle Transport Code." In: *Proceedings of the Monte Carlo 2005 Conference, Chattanooga*. UCRL-CONF-208667. Dec. 2004.
URL: https://e-reports-ext.llnl.gov/pdf/314728.pdf.

[125] Y.Z. KANDIEV, E.A. KASHAEVA, et al. "PRIZMA status." In: *Annals of Nuclear Energy* **82** (Aug. 2015). Joint International Conference on Supercomputing in Nuclear Applications and Monte Carlo 2013, pp. 116–120.
DOI: 10.1016/j.anucene.2014.09.006.

[126] T.M. PANDYA, S.R. JOHNSON, G.G. DAVIDSON, T.M. EVANS, and S.P. HAMILTON. "Shift: A massively parallel Monte Carlo radiation transport package." In: *Proceedings of the ANS MC2015 - Joint International Conference on Mathematics and Computation*. Apr. 2015, pp. 19–23.
URL: https://www.casl.gov/sites/default/files/docs/CASL-U-2015-0170-000.pdf.

[127] J. LEPPÄNEN, M. PUSA, T. VIITANEN, V. VALTAVIRTA, and T. KALTIAISENAHO. "The Serpent Monte Carlo code: Status, development and applications in 2013." In: *Annals of Nuclear Energy* **82** (Aug. 2015). Joint International Conference on Supercomputing in Nuclear Applications and Monte Carlo 2013, pp. 142–150.
DOI: 10.1016/j.anucene.2014.08.024.

[128] E. WOODCOCK, T. MURPHY, P.J. HEMMINGS, and T.C. LONGWORTH. "Techniques used in the GEM code for Monte Carlo neutronics calculations in reactors and other systems of complex geometry." In: *Proc. Conf. Applications of Computing Methods to Reactor Problems*. Vol. 557. May 1965, pp. 557–579.
URL: https://yiningkarlli.com/projects/specdecomptracking/references/Woodcock1965.pdf.

[129] K. WANG, Z. LI, D. SHE, J. LIANG, Q. XU, Y. QIU, J. YU, J. SUN, X. FAN, and G. YU. "RMC - A Monte Carlo code for reactor core analysis." In: *Annals of Nuclear Energy* **82** (Aug. 2015). Joint International Conference on Supercomputing in Nuclear Applications and Monte Carlo 2013, pp. 121–129.
DOI: 10.1016/j.anucene.2014.08.048.

[130] B. COCHET, A. JINAPHANH, L. HEULERS, and O. JACQUET. "Capabilities overview of the MORET 5 Monte Carlo code." In: *Annals of Nuclear Energy* **82** (Aug. 2015). Joint International Conference on Supercomputing in Nuclear Applications and Monte Carlo 2013, pp. 74–84.
DOI: 10.1016/j.anucene.2014.08.022.

[131] N. SMITH, T. SHUTTLEWORTH, M. GRIMSTONE, L. HUTTON, M. ARMISHAW, A. BIRD, N. FRANCE, and S. CONNOLLY. "The Current Status and Future Plans for the Monte Carlo Codes MONK and MCBEND." In: *Advanced Monte Carlo for Radiation Physics, Particle Transport Simulation and Applications: Proceedings of the Monte Carlo 2000 Conference, Lisbon*. Berlin, Heidelberg: Springer, 2001, pp. 637–642. ISBN: 978-3-642-18211-2.
DOI: 10.1007/978-3-642-18211-2_102.

[132] G. ARNECKE, H. BORGWALDT, V. BRANDL, and M. LALOVIC. "KAMCCO, ein reaktorphysikalischer Monte Carlo Neutronentransportcode." In: *KFK 2190* (June 1976). Joint International Conference on Supercomputing in Nuclear Applications and Monte Carlo 2013.
URL: https://publikationen.bibliothek.kit.edu/270009404/3811483.

[133] W. MARTH. *The history of the construction and operation of the KNK II German Fast Breeder Power Plant*. Tech. rep. KFK–5155. IAEA INIS, Sept. 1993. 181 pp.
URL: https://publikationen.bibliothek.kit.edu/270038327/3813557.

[134] G. VAN ROSSUM. *The Python Language Reference Manual*. Tech. rep. Version 3.5.4. Aug. 2017.
URL: https://docs.python.org/3/library/.

[135] JUPYTER TEAM. *Jupyter Documentation*. Tech. rep. Version 4.1.1. Sept. 2017.
URL: https://media.readthedocs.org/pdf/jupyter/latest/jupyter.pdf.

[136] *Programming Languages - C++*. Standard. Geneva, CH: International Organization for Standardization, May 2013. 1374 pp.
URL: http://www.open-std.org/jtc1/sc22/wg21/docs/papers/2013/n3690.pdf.

[137] R. BRUN and F. RADEMAKERS. "ROOT - An Object Oriented Data Analysis Framework." In: *Proceedings of AIHENP'96 Workshop, Lausanne*. Vol. 389. see also https://root.cern.ch/. May 1997, pp. 81–86.
DOI: 10.1016/S0168-9002(97)00048-X.

[138] THE QT COMPANY LTD. *The Qt Framework*. Jan. 2018. URL: https://www.qt.io/qt-for-application-development/.

[139] M. GALASSI et al. *GNU Scientific Library: reference manual for GSL version 2.3*. Free Software Foundation, Dec. 2016.
URL: https://www.gnu.org/software/gsl/manual/gsl-ref.pdf.

[140] A. HÉBERT. "Multigroup Neutron Transport and Diffusion Computations." In: *Handbook of Nuclear Engineering*. Ed. by D.G. CACUCI. Boston: Springer US, Aug. 2010, pp. 751–911. ISBN: 978-0-387-98149-9.
DOI: 10.1007/978-0-387-98149-9_8.

[141] T. KITTELMANN and M. BOIN. "Polycrystalline neutron scattering for Geant4: NXSG4." In: *Computer Physics Communications* **189** (Apr. 2015), pp. 114–118.
DOI: 10.1016/j.cpc.2014.11.009.

[142] S.D. ROTH. "Ray casting for modeling solids." In: *Computer Graphics and Image Processing* **18**(2) (Feb. 1982), pp. 109–144.
DOI: 10.1016/0146-664X(82)90169-1.

[143] E. MAIRE and P.J. WITHERS. "Quantitative X-ray tomography." In: *International Materials Reviews* **59**(1) (Dec. 2013), pp. 1–43.
DOI: 10.1179/1743280413Y.0000000023.

[144] V. CNUDDE and M.N. BOONE. "High-resolution X-ray computed tomography in geosciences: A review of the current technology and applications." In: *Earth-Science Reviews* **123** (Aug. 2013), pp. 1–17.
DOI: 10.1016/j.earscirev.2013.04.003.

[145] L.W. GOLDMAN. "Principles of CT and CT Technology." In: *Journal of Nuclear Medicine Technology* **35**(3) (Sept. 2007), pp. 115–128.
DOI: 10.2967/jnmt.107.042978.

[146] R.J. MCCONN JR, C.J. GESH, R.T. PAGH, R.A. RUCKER, and R.G. WILLIAMS III. *Compendium of Material Composition Data for Radiation Transport Modeling*. Tech. rep. PNNL-15870 Rev. 1. Richland, Washington 99352: Pacific Northwest National Laboratory, Mar. 2011. 375 pp.
URL: https://www.pnnl.gov/main/publications/external/technical_reports/pnnl-15870rev1.pdf.

[147] *Information technology - ISO 7-bit coded character set for information interchange*. Standard. Geneva, CH: International Organization for Standardization, Dec. 1991. 15 pp.
URL: https://www.iso.org/standard/4777.html.

[148] *Information technology - Computer graphics and image processing – Portable Network Graphics (PNG)*. Standard. Geneva, CH: International Organization for Standardization, Mar. 2004. 80 pp.
URL: https://www.iso.org/standard/29581.html.

[149] *Reference neutron radiations - Part 1*. Standard. Geneva, CH: International Organization for Standardization, Feb. 2001. 24 pp.
URL: https://www.iso.org/standard/25666.html.

[150] V. WEISSKOPF. "Statistics and Nuclear Reactions." In: *Physical Review* **52** (Aug. 1937), pp. 295–303.
DOI: 10.1103/PhysRev.52.295.

[151] J. TERRELL. "Fission Neutron Spectra and Nuclear Temperatures." In: *Physical Review* **113** (Jan. 1959), pp. 527–541.
DOI: 10.1103/PhysRev.113.527.

[152] M.R. IYER and A.K. GANGULY. "Neutron Evaporation and Energy Distribution in Individual Fission Fragments." In: *Physical Review C* **5** (Apr. 1972), pp. 1410–1421.
DOI: 10.1103/PhysRevC.5.1410.

[153] B.E. WATT. "Energy Spectrum of Neutrons from Thermal Fission of ^{235}U." In: *Physical Review* **87** (Sept. 1952), pp. 1037–1041.
DOI: 10.1103/PhysRev.87.1037.

[154] A.B. SMITH, P.R. FIELDS, and J.H. ROBERTS. "Spontaneous Fission Neutron Spectrum of ^{252}Cf." In: *Physical Review* **108** (Oct. 1957), pp. 411–413.
DOI: 10.1103/PhysRev.108.411.

[155] J. CUGNON, C. VOLANT, and S. VUILLIER. "Nucleon and deuteron induced spallation reactions." In: *Nuclear Physics A* **625**(4) (Nov. 1997), pp. 729–757.
DOI: 10.1016/S0375-9474(97)00602-7.

[156] T. KAWANO, P. TALOU, I. STETCU, and M.B. CHADWICK. "Statistical and evaporation models for the neutron emission energy spectrum in the center-of-mass system from fission fragments." In: *Nuclear Physics A* **913**(Supplement C) (Sept. 2013), pp. 51–70.
DOI: 10.1016/j.nuclphysa.2013.05.020.

[157] R.L. BRAMBLETT and T.W. BONNER. "Neutron evaporation spectra from (p, n) reactions." In: *Nuclear Physics* **20**(Supplement C) (Nov. 1960), pp. 395–407.
DOI: 10.1016/0029-5582(60)90182-6.

[158] T. SATO. "Analytical Model for Estimating the Zenith Angle Dependence of Terrestrial Cosmic Ray Fluxes." In: *PLoS ONE* **11**(8) (Aug. 2016), pp. 1–22.
DOI: 10.1371/journal.pone.0160390.

[K2016] M. KÖHLI, F. ALLMENDINGER, W. HÄUSSLER, T. SCHRÖDER, M. KLEIN, M. MEVEN, and U. SCHMIDT. "Efficiency and spatial resolution of the CASCADE thermal neutron detector." In: *Nuclear Instruments and Methods in Physics Research Section A: Accelerators, Spectrometers, Detectors and Associated Equipment* **828** (Aug. 2016), pp. 242–249.
DOI: 10.1016/j.nima.2016.05.014.

[159] J.F. ZIEGLER, M.D. ZIEGLER, and J.P. BIERSACK. "SRIM - The stopping and range of ions in matter (2010)." In: *Nuclear Instruments and Methods in Physics Research Section B: Beam Interactions with Materials and Atoms* **268**(11-12) (June 2010). 19th International Conference on Ion Beam Analysis, pp. 1818–1823.
DOI: 10.1016/j.nimb.2010.02.091.

[160] K. NIKOLOPOULOS, P. BHATTACHARYA, V. CHERNYATIN, and R. VEENHOF. "Electron transparency of a Micromegas mesh." In: *Journal of Instrumentation* **6**(06) (June 2011), P06011.
DOI: 10.1088/1748-0221/6/06/P06011.

[161] X. LLOPART, R. BALLABRIGA, M. CAMPBELL, L. TLUSTOS, and W. WONG. "Timepix, a 65k programmable pixel readout chip for arrival time, energy and/or photon counting measurements." In: *Nuclear Instruments and Methods in Physics Research Section A: Accelerators, Spectrometers, Detectors and Associated Equipment* **581**(1–2) (Oct. 2007). VCI 2007, Proceedings of the 11th International Vienna Conference on Instrumentation, pp. 485–494.
DOI: 10.1016/j.nima.2007.08.079.

[162] R.S. CASWELL, R.F. GABBARD, D.W. PADGETT, and W.P. DOERING. "Attenuation of 14.1-Mev Neutrons in Water." In: *Nuclear Science and Engineering* **2**(2) (Apr. 1957), pp. 143–159.
DOI: 10.13182/NSE57-A25383.

[163] N.E. HERTEL and J.W. DAVIDSON. "The response of Bonner Spheres to neutrons from thermal energies to 17.3 MeV." In: *Nuclear Instruments and Methods in Physics Research Section A: Accelerators, Spectrometers, Detectors and Associated Equipment* **238**(2) (Aug. 1985), pp. 509–516.
DOI: 10.1016/0168-9002(85)90494-2.

[164] V. VYLET and A. KUMAR. "Energy response of Bonner Spheres to neutrons in parallel beam and point source geometries." In: *Nuclear Instruments and Methods in Physics Research Section A: Accelerators, Spectrometers, Detectors and Associated Equipment* **271**(3) (Sept. 1988), pp. 607–610.
DOI: 10.1016/0168-9002(88)90329-4.

[165] V. MARES and H. SCHRAUBE. "Evaluation of the response matrix of a Bonner Sphere Spectrometer with LiI detector from thermal energy to 100 MeV." In: *Nuclear Instruments and Methods in Physics Research Section A: Accelerators, Spectrometers, Detectors and Associated Equipment* **337**(2) (Jan. 1994), pp. 461–473.
DOI: 10.1016/0168-9002(94)91116-9.

[166] S. GARNY, V. MARES, and W. RÜHM. "Response functions of a Bonner Sphere Spectrometer calculated with GEANT4." In: *Nuclear Instruments and Methods in Physics Research Section A: Accelerators, Spectrometers, Detectors and Associated Equipment* **604**(3) (June 2009), pp. 612–617.
DOI: 10.1016/j.nima.2009.02.044.

[167] A.W. DECKER, S.R. MCHALE, M.P. SHANNON, J.A. CLINTON, and J.W. MCCLORY. "Novel Bonner Sphere Spectrometer Response Functions Using MCNP6." In: *IEEE Transactions on Nuclear Science* **62**(4) (Aug. 2015), pp. 1689–1694.
DOI: 10.1109/TNS.2015.2416652.

[168] E.A. BURGETT, N.E. HERTEL, and R.M. HOWELL. "Energy Response and Angular Dependence of a Bonner Sphere Extension." In: *IEEE Transactions on Nuclear Science* **56**(3) (June 2009), pp. 1325–1328.
DOI: 10.1109/TNS.2009.2019272.

[169] V. MARES, G. SCHRAUBE, and H. SCHRAUBE. "Calculated neutron response of a Bonner Sphere Spectrometer with ^{3}He counter." In: *Nuclear Instruments and Methods in Physics Research Section A: Accelerators, Spectrometers, Detectors and Associated Equipment* **307**(2) (Oct. 1991), pp. 398–412. DOI: 10.1016/0168-9002(91)90210-H.

[170] M. YAMASHITA, L.D. STEPHENS, and H.W. PATTERSON. "Cosmic-ray-produced neutrons at ground level: Neutron production rate and flux distribution." In: *Journal of Geophysical Research* **71**(16) (Aug. 1966), pp. 3817–3834. DOI: 10.1029/JZ071i016p03817.

[171] J. SWEEZY, N. HERTEL, and K. VEINOT. "BUMS - Bonner Sphere Unfolding Made Simple: an HTML based multisphere neutron spectrometer unfolding package." In: *Nuclear Instruments and Methods in Physics Research Section A: Accelerators, Spectrometers, Detectors and Associated Equipment* **476**(1) (Jan. 2002). International Workshop on Neutron Field Spectrometry in Science, Technology and Radiation Protection, pp. 263–269. DOI: 10.1016/S0168-9002(01)01466-8.

[172] D.J. THOMAS and A.V. ALEVRA. "Bonner Sphere Spectrometers - a critical review." In: *Nuclear Instruments and Methods in Physics Research Section A: Accelerators, Spectrometers, Detectors and Associated Equipment* **476**(1) (Jan. 2002). International Workshop on Neutron Field Spectrometry in Science, Technology and Radiation Protection, pp. 12–20. DOI: 10.1016/S0168-9002(01)01379-1.

[173] H. SCHRAUBE, J. JAKES, A. SANNIKOV, E. WEITZENEGGER, S ROESLER, and W. HEINRICH. "The Cosmic Ray Induced Neutron Spectrum at the Summit of the Zugspitze (2963 m)." In: *Radiation Protection Dosimetry* **70**(1-4) (Apr. 1997), pp. 405–408. DOI: 10.1093/oxfordjournals.rpd.a031986.

[174] W. RÜHM, V. MARES, C. PIOCH, G. SIMMER, and E. WEITZENEGGER. "Continuous measurement of secondary neutrons from cosmic radiation at mountain altitudes and close to the north pole - a discussion in terms of H*(10)." In: *Radiation Protection Dosimetry* **136**(4) (Aug. 2009), pp. 256–261. DOI: 10.1093/rpd/ncp161.

[175] H.W. BERTINI. "Low-Energy Intranuclear Cascade Calculation." In: *Physical Review* **131** (Aug. 1963), pp. 1801–1821. DOI: 10.1103/PhysRev.131.1801.

[176] A. HEIKKINEN, N. STEPANOV, and J.P. WELLISCH. "Bertini intranuclear cascade implementation in GEANT4." In: *eConf* **C0303241** (June 2003). Proceedings, 13$^{\text{th}}$ International Conference on Computing in High-Energy and Nuclear Physics (CHEP 2003): La Jolla, California, March 24-28, 2003, MOMT008. URL: http://www.slac.stanford.edu/econf/C0303241/proc/papers/MOMT008.PDF.

[177] G. FOLGER, V.N. IVANCHENKO, and J.P. WELLISCH. "The Binary Cascade." In: *The European Physical Journal A - Hadrons and Nuclei* **21**(3) (Aug. 2004), pp. 407–417. DOI: 10.1140/epja/i2003-10219-7.

[178] G. HUBERT, C.A. FEDERICO, M.T. PAZIANOTTO, and O.L. GONÇALES. "Long and short-term atmospheric radiation analyses based on coupled measurements at high altitude remote stations and extensive air shower modeling." In: *Astroparticle Physics* **74** (Feb. 2016), pp. 27–36. DOI: 10.1016/j.astropartphys.2015.09.005.

[179] M.T. PAZIANOTTO, M.A. CORTÉS-GIRALDO, C.A. FEDERICO, G. HUBERT, O.L. GONÇALEZ, J.M. QUESADA, and B.V. CARLSON. "Extensive air shower Monte Carlo modeling at the ground and aircraft flight altitude in the South Atlantic Magnetic Anomaly and comparison with neutron measurements." In: *Astroparticle Physics* **88** (Feb. 2017), pp. 17–29. DOI: 10.1016/j.astropartphys.2016.12.004.

[180] P. GOLDHAGEN, M. REGINATTO, T. KNISS, J.W. WILSON, R.C. SINGLETERRY, I.W. JONES, and W. VAN STEVENINCK. "Measurement of the energy spectrum of cosmic-ray induced neutrons aboard an ER-2 high-altitude airplane." In: *Nuclear Instruments and Methods in Physics Research Section A: Accelerators, Spectrometers, Detectors and Associated Equipment* **476**(1–2) (Jan. 2002), pp. 42–51. DOI: 10.1016/S0168-9002(01)01386-9.

[181] C.A. FEDERICO, O.L. GONÇALEZ, E.S. FONSECA, I.M. MARTIN, and L.V.E. CALDAS. "Neutron spectra measurements in the south Atlantic anomaly region." In: *Radiation Measurements* **45**(10) (Dec. 2010). Proceedings of the 11th Symposium on neutron and ion dosimetrty, pp. 1526–1528. DOI: 10.1016/j.radmeas.2010.06.038.

[182] M.T. PAZIANOTTO, M.A. CORTÉS-GIRALDO, C.A. FEDERICO, O.L. GONÇALEZ, J.M. QUESADA, and B.V. CARLSON. "Determination of the cosmic-ray-induced neutron flux and ambient dose equivalent at flight altitude." In: *Journal of Physics: Conference Series* **630**(1) (Apr. 2015), p. 012022. DOI: 10.1088/1742-6596/630/1/012022.

[SK2017b] M. SCHRÖN, S. ZACHARIAS, et al. "Intercomparison of Cosmic-Ray Neutron Sensors and Water Balance Monitoring in an Urban Environment." In: *Geoscientific Instrumentation, Methods and Data Systems Discussions* **2017** (2017), pp. 1–24. DOI: 10.5194/gi-2017-34.

[183] P. KOCHER, D. GENKIN, D. GRUSS, W. HAAS, M. HAMBURG, M. LIPP, S. MANGARD, T. PRESCHER, M. SCHWARZ, and Y. YAROM. *Spectre Attacks: Exploiting Speculative Execution*. Aug. 2018. arXiv: 1801.01203 [cs]. URL: https://arxiv.org/abs/1801.01203.

[184] E.L. HAHN. "Spin Echoes." In: *Physical Review* **80** (Nov. 1950), pp. 580–594. DOI: 10.1103/PhysRev.80.580.

[185] H.Y. CARR and E.M. PURCELL. "Effects of Diffusion on Free Precession in Nuclear Magnetic Resonance Experiments." In: *Physical Review* **94** (May 1954), pp. 630–638. DOI: 10.1103/PhysRev.94.630.

[186] P.T. CALLAGHAN. *Principles of Nuclear Magnetic Resonance Microscopy*. Oxford science publications. Clarendon Press, 1993. 492 pp. ISBN: 9780198539971.

[187] F. MEZEI. "Neutron Spin Echo: A new concept in polarized thermal neutron techniques." English. In: *Zeitschrift für Physik* **255**(2) (Apr. 1972), pp. 146–160. DOI: 10.1007/BF01394523.

[188] F. MEZEI. "The principles of Neutron Spin Echo." English. In: *Neutron Spin Echo*. Ed. by F. MEZEI. Vol. 128. Lecture Notes in Physics. Springer Berlin Heidelberg, Aug. 1980, pp. 1–26. ISBN: 978-3-540-10004-1. DOI: 10.1007/3-540-10004-0_16.

[189] M.M. CASTELLANOS, A. MCAULEY, and J.E. CURTIS. "Investigating Structure and Dynamics of Proteins in Amorphous Phases Using Neutron Scattering." In: *Computational and Structural Biotechnology Journal* **15** (2017), pp. 117–130. DOI: 10.1016/j.csbj.2016.12.004.

[190] P.G. de GENNES. "Reptation of a Polymer Chain in the Presence of Fixed Obstacles." In: *The Journal of Chemical Physics* **55**(2) (July 1971), pp. 572–579. DOI: 10.1063/1.1675789.

[191] V. GARCÍA SAKAI and A. ARBE. "Quasielastic neutron scattering in soft matter." In: *Current Opinion in Colloid & Interface Science* **14**(6) (Dec. 2009), pp. 381–390. DOI: 10.1016/j.cocis.2009.04.002.

[192] R. GOLUB and R. GÄHLER. "A neutron Resonance Spin Echo spectrometer for quasi-elastic and inelastic scattering." In: *Physics Letters A* **123**(1) (July 1987), pp. 43–48. DOI: 10.1016/0375-9601(87)90760-2.

[193] D. DUBBERS, P. EL-MUZEINI, M. KESSLER, and J. LAST. "Prototype of a zero-field Neutron Spin-Echo spectrometer." In: *Nuclear Instruments and Methods in Physics Research Section A: Accelerators, Spectrometers, Detectors and Associated Equipment* **275** (Feb. 1989), pp. 294–300. DOI: 10.1016/0168-9002(89)90700-6.

[194] R. GÄHLER, R. GOLUB, and T. KELLER. "Neutron Resonance Spin Echo - a new tool for high resolution spectroscopy." In: *Physica B: Condensed Matter* **180** (June 1992), pp. 899–902. DOI: 10.1016/0921-4526(92)90503-K.

[195] P. HANK, W. BESENBÖCK, R. GÄHLER, and M. KÖPPE. "Zero-field Neutron Spin Echo techniques for incoherent scattering." In: *Physica B: Condensed Matter* **234-236** (June 1997). Proceedings of the First European Conference on Neutron Scattering, pp. 1130–1132. DOI: 10.1016/S0921-4526(97)89269-1.

[196] C. PFLEIDERER, T. ADAMS, et al. “Skyrmion lattices in metallic and semiconducting B20 transition metal compounds.” In: *Journal of Physics: Condensed Matter* **22**(16) (Mar. 2010), p. 164207. DOI: 10.1088/0953-8984/22/16/164207.

[197] W HÄUSSLER, G. EHLERS, and U. SCHMIDT. “Field integral correction in neutron resonance spin echo.” In: *Physica B: Condensed Matter* **350**(1) (July 2004). Proceedings of the Third European Conference on Neutron Scattering, E807–E810. DOI: 10.1016/j.physb.2004.03.210.

[198] B. BÖHM. “Test und Weiterentwicklung eines longitudinalen Neutronenresonanzspinechos.” Dipl. Thesis. Physikalisches Institut, Heidelberg University, 2003. 103 pp. URL: https://www.physi.uni-heidelberg.de//Publications/dipl_boehm.pdf.

[199] N. MARTIN. “On the resolution of a MIEZE spectrometer.” In: *Nuclear Instruments and Methods in Physics Research Section A: Accelerators, Spectrometers, Detectors and Associated Equipment* **882** (Feb. 2018), pp. 11–16. DOI: 10.1016/j.nima.2017.11.021.

[200] N. AREND, R. GÄHLER, T. KELLER, R. GEORGII, T. HILS, and P. BÖNI. “Classical and quantum-mechanical picture of NRSE - measuring the longitudinal Stern-Gerlach effect by means of TOF methods.” In: *Physics Letters A* **327**(1) (June 2004), pp. 21–27. DOI: 10.1016/j.physleta.2004.04.062.

[201] T. KELLER, R. GOLUB, and R. GÄHLER. “Chapter 2.8.6 - Neutron Spin Echo - A Technique for High-Resolution Neutron Scattering.” In: *Scattering - Fundamentals*. Ed. by R. PIKE and P. SABATIER. London: Academic Press, 2002, pp. 1264–1286. ISBN: 978-0-12-613760-6. DOI: 10.1016/B978-012613760-6/50068-1.

[202] S. PEGGS et al. *European Spallation Source Technical Design Report*. Technical Design Report ESS. ESS-2013-001. Lundt: ESS, Apr. 2013. 690 pp. URL: http://docdb01.esss.lu.se/DocDB/0002/000274/006/TDR_final_130423_print_ch1.pdf.

[203] G. BRANDL. “First measurements of the linewidth in magnetic phases of MnSi using MIEZE.” Dipl. Thesis. Institut E21, Technische Universität München, 2010.

[204] R. GOLUB, R. GÄHLER, and T. KELLER. “A plane wave approach to particle beam magnetic resonance.” In: *American Journal of Physics* **62**(9) (June 1994), pp. 779–788. DOI: 10.1119/1.17459.

[205] G. BRANDL, R. GEORGII, W. HÄUSSLER, S. MÜHLBAUER, and P. BÖNI. “Large scales - long times: Adding high energy resolution to SANS.” In: *Nuclear Instruments and Methods in Physics Research Section A: Accelerators, Spectrometers, Detectors and Associated Equipment* **654**(1) (Oct. 2011), pp. 394–398. DOI: 10.1016/j.nima.2011.07.003.

[206] U. SCHMIDT. “Experimente mit polarisierten Neutronen zu Fragen höchstauflösenden Spektrometrie und Quantenoptik.” PhD thesis. Institut E21, Technische Universität München, Dec. 2012. 128 pp. URL: https://www.physi.uni-heidelberg.de//Publications/phd_uschmidt.pdf.

[207] W. HÄUSSLER. “Weiterentwicklung, Aufbau und Test eines Resonanzspinecho-Spektrometers zum Einsatz eines Multidetektors.” PhD thesis. Institut E21, Technische Universität München, Apr. 1998. 108 pp. URL: https://www.physi.uni-heidelberg.de//Publications/phd_haeusler.pdf.

[208] T. WEBER. “MIEZE in Theory, Simulation and Experiment.” Dipl. Thesis. Institut E21, Technische Universität München, Dec. 2012. 116 pp.

[209] N. ARENDT. “New Aspects of the MIEZE Technique and Verification of the Multi-level MIEZE Principle.” PhD thesis. Institut E21, Technische Universität München, Apr. 2007. 135 pp. URL: https://mediatum.ub.tum.de/download/618189/618189.pdf.

[210] F. GROITL. “High Resolution Spectroscopy with the Neutron Resonance Spin Echo Method.” PhD thesis. Fakultät II, Technische Universität Berlin, Dec. 2012. 154 pp. DOI: 10.14279/depositonce-3481.

[211] M. BLEUEL. "Aufbau des Neutronen-Resonanz-Spinecho-Spektrometers RESEDA am FRM-II." PhD thesis. Institut E21, Technische Universität München, Feb. 2003. 109 pp.
URL: https://mediatum.ub.tum.de/download/602955/602955.pdf.

[212] J. KINDERVATER. "Fluctuation-induced magnetic phase transitions in Fe and MnSi studied by neutron scattering." PhD thesis. Institut E21, Technische Universität München, June 2015. 163 pp.
URL: http://mediatum.ub.tum.de/doc/1256001/document.pdf.

[213] W. HÄUSSLER, D. STREIBL, and P. BÖNI. "RESEDA: double and multi-detector arms for neutron resonance spin echo spectrometers." In: *Measurement Science and Technology* **19**(3) (Jan. 2008), p. 034015.
DOI: 10.1088/0957-0233/19/3/034015.

[214] J. REPPER, W. HÄUSSLER, A. OSTERMANN, L. KREDLER, A. CHACÓN, and P. BÖNI. "The new polarizer devices at RESEDA." In: *Journal of Physics: Conference Series* **340** (Feb. 2012), p. 012036.
DOI: 10.1088/1742-6596/340/1/012036.

[215] KINDERVATER, J., MARTIN, N., HÄUSSLER, W., KRAUTLOHER, M., FUCHS, C., MÜHLBAUER, S., LIM, J.A., BLACKBURN, E., BÖNI, P., and PFLEIDERER, C. "Neutron Spin Echo spectroscopy under 17 T magnetic field at RESEDA." In: *EPJ Web of Conferences* **83** (Jan. 2015), p. 03008.
DOI: 10.1051/epjconf/20158303008.

[216] W. HÄUSSLER, U. SCHMIDT, G. EHLERS, and F. MEZEI. "Neutron resonance spin echo using spin echo correction coils." In: *Chemical Physics* **292**(2) (Aug. 2003). Quasielastic Neutron Scattering of Structural Dynamics in Condensed Matter, pp. 501–510.
DOI: 10.1016/S0301-0104(03)00119-8.

[217] H. ASCHAUER, A. FLEISCHMANN, C. SCHANZER, and E. STEICHELE. "Neutron guides at the FRM-II." In: *Physica B: Condensed Matter* **283**(4) (June 2000), pp. 323–329.
DOI: 10.1016/S0921-4526(00)00324-0.

[218] K. ZEITELHACK, C. SCHANZER, et al. "Measurement of neutron flux and beam divergence at the cold neutron guide system of the new Munich research reactor FRM-II." In: *Nuclear Instruments and Methods in Physics Research Section A: Accelerators, Spectrometers, Detectors and Associated Equipment* **560**(2) (May 2006), pp. 444 –453.
DOI: 10.1016/j.nima.2005.12.215.

[219] G.F. KNOLL. *Radiation detection and measurement; 4^{th} ed.* New York, NY, USA: Wiley, 2010. 864 pp. ISBN: 0-471-49545X.

[220] W.M. STACEY. *Nuclear Reactor Physics*. 2^{nd}, Completely Revised and Enlarged Edition. Wiley-VCH Verlag GmbH, May 2007. 735 pp. ISBN: 0-471-39127-1.
DOI: 110.1002/9783527611041.

[221] F.C. YOUNG. "Neutron Diagnostics for Pulsed Plasma Sources." In: *IEEE Transactions on Nuclear Science* **22**(1) (Feb. 1975), pp. 718–723.
DOI: 10.1109/TNS.1975.4327734.

[222] K. LODDERS. "Solar System Abundances of the Elements." In: *Principles and Perspectives in Cosmochemistry*. Ed. by A. GOSWAMI and B.E. REDDY. Berlin, Heidelberg: Springer Berlin Heidelberg, Mar. 2010, pp. 379–417. ISBN: 978-3-642-10352-0.
DOI: 10.1007/978-3-642-10352-0_8.

[223] G.D.O. GANN. "Everything under the Sun: A review of solar neutrinos." In: *AIP Conference Proceedings* **1666**(1) (July 2015), p. 090003.
DOI: 10.1063/1.4915568.

[224] M. WANG, G. AUDI, A.H. WAPSTRA, F.G. KONDEV, M. MACCORMICK, X. XU, and B. PFEIFFER. "The Ame2012 atomic mass evaluation." In: *Chinese Physics C* **36**(12) (Dec. 2012), pp. 1603–2014.
DOI: 10.1088/1674-1137/36/12/003.

[225] J. MEIJA, T. COPLEN, et al. "Isotopic compositions of the elements 2013 (IUPAC Technical Report)." In: *Pure and Applied Chemistry* **88**(3) (Feb. 2016), pp. 293–306.
DOI: 10.1515/pac-2015-0503.

[226] CURRAN, S.C. and CRAGGS, J.D. *Counting Tubes: Theory And Applications*. New York: Academic Press, Dec. 1949. 238 pp.

[227] E. RUTHERFORD and H. GEIGER. "An Electrical Method of Counting the Number of α-Particles from Radio-Active Substances." In: *Proceedings of the Royal Society of London A: Mathematical, Physical and Engineering Sciences* **81**(546) (Aug. 1908), pp. 141–161.
DOI: 10.1098/rspa.1908.0065.

[228] E. KOWALSKI. *Nuclear Electronics*. 1st Edition. Berlin, Heidelberg: Springer Berlin Heidelberg, Jan. 1970. 410 pp. ISBN: 978-3-642-87664-6.
DOI: 10.1007/978-3-642-87663-9.

[229] THE LINDE GROUP. *Helium-3 Material Safety Data Sheet*. 0 (Initial Release). München, July 2011.

[230] S.S. DESAI and A.M. SHAIKH. "On studies of ^{3}He and isobutane mixture as neutron proportional counter gas." In: *Nuclear Instruments and Methods in Physics Research Section A: Accelerators, Spectrometers, Detectors and Associated Equipment* **557**(2) (Feb. 2006), pp. 607–614.
DOI: 10.1016/j.nima.2005.11.182.

[231] D. MAZED, S. MAMERI, and R. CIOLINI. "Design parameters and technology optimization of ^{3}He-filled proportional counters for thermal neutron detection and spectrometry applications." In: *Radiation Measurements* **47**(8) (June 2012), pp. 577–587.
DOI: 10.1016/j.radmeas.2012.06.002.

[232] Z. DĘBICKI, K. JĘDRZEJCZAK, J. KARCZMARCZYK, M. KASZTELAN, R. LEWANDOWSKI, J. ORZECHOWSKI, B. SZABELSKA, J. SZABELSKI, P. TOKARSKI, and T. WIBIG. "Helium counters for low neutron flux measurements." In: *Astrophysics and Space Sciences Transactions* **7**(4) (Nov. 2011), pp. 511–514.
DOI: 10.5194/astra-7-511-2011.

[233] T.J. LANGFORD, C.D. BASS, E.J. BEISE, H. BREUER, D.K. ERWIN, C.R. HEIMBACH, and J.S. NICO. "Event identification in ^{3}He proportional counters using risetime discrimination." In: *Nuclear Instruments and Methods in Physics Research Section A: Accelerators, Spectrometers, Detectors and Associated Equipment* **717** (July 2013), pp. 51–57.
DOI: 10.1016/j.nima.2013.03.062.

[234] C.J. HATTON and H. CARIMICHAEL. "Experimental Investigation of the NM-64 Neutron Monitor." In: *Canadian Journal of Physics* **42** (Dec. 1964), pp. 2443–2472.
DOI: 10.1139/p64-222.

[235] A. ENDO, E. KIM, Y. YAMAGUCHI, T. SATO, M. YOSHIZAWA, S. TANAKA, T. NAKAMURA, and A.H.D. RASOLONJATOVO. "Development of Neutron-Monitor Detectors Applicable to Energies from Thermal to 100 MeV." In: *Journal of Nuclear Science and Technology* **41**(sup4) (Mar. 2004), pp. 510–513.
DOI: 10.1080/00223131.2004.10875759.

[236] J.A. SIMPSON, W. FONGER, and S.B. TREIMAN. "Cosmic Radiation Intensity-Time Variations and Their Origin. I. Neutron Intensity Variation Method and Meteorological Factors." In: *Physical Review* **90** (June 1953), pp. 934–950.
DOI: 10.1103/PhysRev.90.934.

[237] R.A. NOBLES, R.A. ALBER, L.L. NEWKIRK, M. WALT, and C.J. WOLFSON. "White mountain cosmic ray neutron multiplicity monitor." In: *Nuclear Instruments and Methods* **70**(1) (Apr. 1969), pp. 45–51.
DOI: 10.1016/0029-554X(69)90178-5.

[238] P. PASCHALIS, H. MAVROMICHALAKI, and L.I. DORMAN. "A quantitative study of the 6NM-64 neutron monitor by using Geant4: 1. Detection efficiency for different particles." In: *Nuclear Instruments and Methods in Physics Research Section A: Accelerators, Spectrometers, Detectors and Associated Equipment* **729** (Nov. 2013), pp. 877–887.
DOI: 10.1016/j.nima.2013.08.057.

[239] D. MAURIN, A. CHEMINET, L. DEROME, A. GHELFI, and G. HUBERT. "Neutron monitors and muon detectors for solar modulation studies: Interstellar flux, yield function, and assessment of critical parameters in count rate calculations." In: *Advances in Space Research* **55**(1) (Jan. 2015), pp. 363–389.
DOI: 10.1016/j.asr.2014.06.021.

[240] R.L. BRAMBLETT, R.I. EWING, and T.W. BONNER. "A new type of neutron spectrometer." In: *Nuclear Instruments and Methods* **9**(1) (Oct. 1960), pp. 1–12.
DOI: 10.1016/0029-554X(60)90043-4.

[241] W.W. ENGE JR. *A user's manual for ANISN: a one-dimensional discrete ordinate transport code with anisotropic scattering*. Report. K-1693. Oak Ridge Gaseous Diffusion Plant, Union Carbide Corp. Oak Ridge, USA, Mar. 1967. 93 pp.
URL: https://www.osti.gov/scitech/servlets/purl/4448708.

[242] E. AZA, N. DINAR, G.P. MANESSI, and M. SILARI. "A Bonner Sphere Spectrometer for pulsed fields." In: *Radiation Protection Dosimetry* **168**(2) (Feb. 2016), pp. 149–153.
DOI: 10.1093/rpd/ncv180.

[243] M.C. CHU, K.Y. FUNG, T. KWOK, J.K.C. LEUNG, Y.C. LIN, H. LIU, K.B. LUK, H.Y. NGAI, C.S.J. PUN, and H.L.H. WONG. "Development of a Bonner Sphere neutron spectrometer from a commercial neutron dosimeter." In: *Journal of Instrumentation* **11**(11) (Nov. 2016), P11005.
DOI: 10.1088/1748-0221/11/11/P11005.

[244] M. MATZKE. "Propagation of uncertainties in unfolding procedures." In: *Nuclear Instruments and Methods in Physics Research Section A: Accelerators, Spectrometers, Detectors and Associated Equipment* **476**(1) (Jan. 2002). International Workshop on Neutron Field Spectrometry in Science, Technology and Radiation Protection, pp. 230–241.
DOI: 10.1016/S0168-9002(01)01438-3.

[245] S. BARROS, V. MARES, R. BEDOGNI, M. REGINATTO, A. ESPOSITO, I. F. GONÇALVES, P. VAZ, and W. RÜHM. "Comparison of unfolding codes for neutron spectrometry with Bonner Spheres." In: *Radiation Protection Dosimetry* **161**(1-4) (Jan. 2014), pp. 46–52.
DOI: 10.1093/rpd/nct353.

[246] W. RÜHM, V. MARES, C. PIOCH, S. AGOSTEO, A. ENDO, M. FERRARINI, I. RAKHNO, S. ROLLET, D. SATOH, and H. VINCKE. "Comparison of Bonner Sphere responses calculated by different Monte Carlo codes at energies between 1 MeV and 1 GeV - Potential impact on neutron dosimetry at energies higher than 20 MeV." In: *Radiation Measurements* **67**(0) (May 2014), pp. 24–34.
DOI: 10.1016/j.radmeas.2014.05.006.

[247] D.A. SHEA and D. MORGAN. "The Helium-3 Shortage: Supply, Demand, and Options for Congress." In: *CRS Report for Congress* (Dec. 2010). R41419.
URL: https://www.fas.org/sgp/crs/misc/R41419.pdf.

[248] C. TYLER. "Running Low." In: *1663 - Los Alamos Science and Technology Magazine* (Aug. 2014), pp. 9–13.
URL: https://www.lanl.gov/discover/publications/1663/2014-august/_assets/docs/1663_22_HE3.pdf.

[249] L.T. ALDRICH and A.O. NIER. "The Occurrence of ^{3}He in Natural Sources of Helium." In: *Physical Review* **74** (Dec. 1948), pp. 1590–1594.
DOI: 10.1103/PhysRev.74.1590.

[250] NATIONAL COMMISSION ON TERRORIST ATTACKS UPON THE UNITED STATES. *The 9/11 Commission Report: Final Report of the National Commission on Terrorist Attacks Upon the United States*. Ed. by T.H. KEAN and L. HAMILTON. Washington, DC: W.W. Norton and Company, July 2004. 567 pp.
ISBN: 9780393326710.
URL: https://9-11commission.gov/report/.

[251] B.D. GEELHOOD, J.H. ELY, R.R. HANSEN, R.T. KOUZES, J.E. SCHWEPPE, and R.A. WARNER. "Overview of portal monitoring at border crossings." In: *Nuclear Science Symposium Conference Record, 2003 IEEE*. Vol. 1. Oct. 2003, pp. 513–517.
DOI: 10.1109/NSSMIC.2003.1352095.

[252] G. ALOISE and T.M. PERSONS. "Neutron Detectors - Alternatives to using helium-3." In: *GAO - Report to Congressional Requesters* (Sept. 2011). GAO11-753.
URL: https://www.gao.gov/assets/590/585514.pdf.

[253] G. ALOISE and T.M. PERSONS. "Managing Critical Isotopes - Weaknesses in DOE's Management of Helium-3 Delayed the Federal Response to a Critical Supply Shortage." In: *GAO - Report to Congressional Requesters* (May 2011). GAO11-472.
URL: https://www.gao.gov/assets/320/318377.pdf.

[254] S. ADEE. "Physics Projects Deflate for Lack of Helium-3 - U.S. radiation detectors suck up the existing supply." In: *IEEE Spectrum* (Aug. 2010).
URL: http://spectrum.ieee.org/biomedical/diagnostics/physics-projects-deflate-for-lack-of-helium3.

[255] A. CHO. "Helium-3 Shortage Could Put Freeze On Low-Temperature Research." In: *Science* **326**(5954) (Nov. 2009), pp. 778–779.
DOI: 10.1126/science.326_778.

[256] O. KIRSTEIN, R. HALL-WILTON, et al. *Neutron Position Sensitive Detectors for the ESS*. Nov. 2014. arXiv: 1411.6194 [physics.ins-det]. URL: https://arxiv.org/abs/1411.6194.

[257] R.T. KOUZES, A.T. LINTEREUR, and E.R. SICILIANO. "Progress in alternative neutron detection to address the helium-3 shortage." In: *Nuclear Instruments and Methods in Physics Research Section A: Accelerators, Spectrometers, Detectors and Associated Equipment* **784** (June 2015). Symposium on Radiation Measurements and Applications 2014 (SORMA XV), pp. 172–175.
DOI: 10.1016/j.nima.2014.10.046.

[258] L. ROPELEWSKI, M. TITOV, J.-M. LE GOFF, and P.M. JIMENEZ. *12th RD51 Collaboration Meeting and Workshop on Neutron Detection with MPGDs*. https://indico.cern.ch/event/267513/. Oct. 2013.

[259] L. ROPELEWSKI, M. TITOV, J.-M. LE GOFF, and P.M. JIMENEZ. *2nd Academy-Industry Matching Event on Neutron Detection and 15th RD51 Collaboration Meeting*. https://indico.cern.ch/event/365380/. Mar. 2015.

[260] K. ZEITELHACK. "Search for alternative techniques to helium-3 based detectors for neutron scattering applications." In: *Neutron News* **23**(4) (Dec. 2012), pp. 10–13.
DOI: 10.1080/10448632.2012.725325.

[261] D.P. MITCHELL, J.R. DUNNING, E. SEGRÈ, and G.B. PEGRAM. "Absorption and Detection of Slow Neutrons." In: *Physical Review* **48** (Nov. 1935), pp. 774–775.
DOI: 10.1103/PhysRev.48.774.

[262] The European COMMISSION. *The European Framework Programme for Research and Technological Development for 2002-2006*. (accessed 10.03.2019). Jan. 2016. URL: https://ec.europa.eu/research/fp6/index_en.cfm.

[263] The European COMMISSION. *European Research and Innovation funding programme for 2007-2013*. (accessed 10.03.2019). Jan. 2016. URL: https://ec.europa.eu/research/fp7/index_en.cfm.

[264] The European COMMISSION. *The European Framework Programme for Research and Innovation for 2014-2020*. (accessed 10.03.2019). Jan. 2016. URL: https://ec.europa.eu/programmes/horizon2020/.

[265] S.S. ALIMOV, A. BORGA, et al. "Development of very high rate and resolution neutron detectors with novel readout and DAQ hard- and software in DETNI." In: *Nuclear Science Symposium Conference Record, NSS IEEE*. Oct. 2008, pp. 1887–1900.
DOI: 10.1109/NSSMIC.2008.4774759.

[266] B. GEBAUER, C. SCHULZ, and T. WILPERT. "Novel large-area thermal neutron imaging detectors comprising ^{157}GdCsI-convertors and micro-strip gas detectors with low-pressure, two-stage amplification and delay line readout." In: *Nuclear Instruments and Methods in Physics Research Section A: Accelerators, Spectrometers, Detectors and Associated Equipment* **392**(1–3) (June 1997). Position-Sensitive Detectors Conference 1996, pp. 68–72.
DOI: 10.1016/S0168-9002(97)00245-3.

[267] A.S. BROGNA, S. BUZZETTI, et al. "MSGCROC - an ASIC for high count rate readout of position sensitive Microstrip Gas Chambers for thermal neutrons." In: *Nuclear Science Symposium Conference Record, 2008. NSS '08. IEEE*. Oct. 2008, pp. 1482–1488.
DOI: 10.1109/NSSMIC.2008.4774695.

[268] A.S. BROGNA, S. BUZZETTI, W. DABROWSKI, T. FIUTOWSKI, B. GEBAUER, M. KLEIN, C.J. SCHMIDT, H.K. SOLTVEIT, R. SZCZYGIEL, and U. TRUNK. "N-XYTER, a CMOS read-out ASIC for high resolution time and amplitude measurements on high rate multi-channel counting mode neutron detectors." In: *Nuclear Instruments and Methods in Physics Research Section A: Accelerators, Spectrometers, Detectors and Associated Equipment* **568**(1) (Nov. 2006). New Developments in Radiation Detectors. Proceedings of the 10th European Symposium on Semiconductor Detectors, pp. 301–308. DOI: 10.1016/j.nima.2006.06.001.

[269] B. GUÉRARD. *The MILAND detector*. (accessed 10.03.2019). Jan. 2016. URL: https://www.ill.eu/science-technology/neutron-technology-at-ill/detectors/miland/.

[270] M. JOHNSON and H. SCHOBER. *Integrated Infrastructure Initiative for Neutron Scattering and Muon Spectroscopy*. (accessed 10.03.2019). Jan. 2016. URL: https://nmi3.eu.

[271] G. MANZIN, B. GUÉRARD, F.A.F. FRAGA, and L.M.S. MARGATO. "A gas proportional scintillator counter for thermal neutrons instrumentation." In: *Nuclear Instruments and Methods in Physics Research Section A: Accelerators, Spectrometers, Detectors and Associated Equipment* **535**(1-2) (Dec. 2004). Proceedings of the 10th International Vienna Conference on Instrumentation, pp. 102–107. DOI: 10.1016/j.nima.2004.07.140.

[272] N.J. RHODES. *NMI3-II, Second periodic report (August 2013 – January 2015), Work Package 21: Detectors*. Tech. rep. Oxford: ISIS STFC, Feb. 2015. URL: http://ftp.nd.rl.ac.uk/NJR/Microsoft%20Word%20-%20WP21%20PR2%202015%20v13.pdf.

[273] A. STOYKOV, J.-B. MOSSET, U. GREUTER, M. HILDEBRANDT, and N. SCHLUMPF. "A SiPM-based ZnS:^{6}LiF scintillation neutron detector." In: *Nuclear Instruments and Methods in Physics Research Section A: Accelerators, Spectrometers, Detectors and Associated Equipment* **787** (July 2015). New Developments in Photodetection NDIP14, pp. 361–366. DOI: 10.1016/j.nima.2015.01.076.

[274] S. ANDRIAMONJE, D. CANO-OTT, et al. "Experimental studies of a Micromegas neutron detector." In: *Nuclear Instruments and Methods in Physics Research Section A: Accelerators, Spectrometers, Detectors and Associated Equipment* **481**(1–3) (Apr. 2002), pp. 120–129. DOI: 10.1016/S0168-9002(01)01246-3.

[275] I. STEFANESCU, Y. ABDULLAHI, J. BIRCH, I. DEFENDI, R. HALL-WILTON, C. HÖGLUND, L. HULTMAN, M. ZEE, and K. ZEITELHACK. "A ^{10}B-based neutron detector with stacked MultiWire Proportional Counters and macrostructured cathodes." In: *Journal of Instrumentation* **8**(12) (Dec. 2013), P12003. DOI: 10.1088/1748-0221/8/12/P12003.

[276] F. PISCITELLI, J.C. BUFFET, J.F. CLERGEAU, S. CUCCARO, B. GUÉRARD, A. KHAPLANOV, Q. LA MANNA, J.M. RIGAL, and P. VAN ESCH. "Study of a high spatial resolution ^{10}B-based thermal neutron detector for application in neutron reflectometry: the Multi-Blade prototype." In: *Journal of Instrumentation* **9**(03) (Mar. 2014), P03007. DOI: 10.1088/1748-0221/9/03/P03007.

[277] M. JOHNSON. *Science and Innovation with Neutrons in Europe in 2020*. (accessed 10.03.2019). Jan. 2016. URL: https://sine2020.eu.

[278] R. ARNALDI, E. CHIAVASSA, et al. "RPC for thermal neutron detection." In: *Journal of Physics: Conference Series* **41**(1) (Jan. 2006), pp. 384–390. DOI: 10.1088/1742-6596/41/1/042.

[279] *Journal Citation Reports*. (accessed 26.08.2016). 2016. URL: https://jcr.incites.thomsonreuters.com.

[280] A.J. PEURRUNG. "Recent developments in neutron detection." In: *Nuclear Instruments and Methods in Physics Research Section A: Accelerators, Spectrometers, Detectors and Associated Equipment* **443**(2–3) (Mar. 2000), pp. 400–415. DOI: 10.1016/S0168-9002(99)01165-1.

[281] E. SEGRÈ and C. WIEGAND. "Boron Trifluoride Neutron Detector for Low Neutron Intensities." In: *Review of Scientific Instruments* **18**(2) (Aug. 1947), pp. 86–89. DOI: 10.1063/1.1740909.

[282] K. TSORBATZOGLOU and R.D. MCKEAG. "Novel and efficient ^{10}B lined tubelet detector as a replacement for ^{3}He neutron proportional counters." In: *Nuclear Instruments and Methods in Physics Research Section A: Accelerators, Spectrometers, Detectors and Associated Equipment* **652**(1) (Oct. 2011). Symposium on Radiation Measurements and Applications (SORMA) XII 2010, pp. 381–383.
DOI: 10.1016/j.nima.2010.08.102.

[283] J.L. LACY, A. ATHANASIADES, C.S. MARTIN, L. SUN, and G.L. VAZQUEZ-FLORES. "The Evolution of Neutron Straw Detector Applications in Homeland Security." In: *Nuclear Science, IEEE Transactions on* **60**(2) (Apr. 2013), pp. 1140–1146.
DOI: 10.1109/TNS.2013.2248166.

[284] K. ANDERSEN, T. BIGAULT, J. BIRCH, J.-C. BUFFET, J. CORREA, P. VAN ESCH, B. GUÉRARD, R. HALL-WILTON, L. HULTMAN, and C. HÖGLUND. *Multi-Grid Boron-10 detector for large area applications in neutron scattering science*. Jan. 2012. arXiv: 1209.0566 [physics.ins-det]. URL: https://arxiv.org/pdf/1209.0566v1.pdf.

[285] G. CHARPAK, J. DERRÉ, Y. GIOMATARIS, and P. REBOURGEARD. "Micromegas, a multipurpose gaseous detector." In: *Nuclear Instruments and Methods in Physics Research Section A: Accelerators, Spectrometers, Detectors and Associated Equipment* **478**(1–2) (Feb. 2002). Proceedings of the 9th International Conference on Instrumentation, pp. 26–36.
DOI: 10.1016/S0168-9002(01)01713-2.

[286] D.R. NYGREN. "The Time Projection Chamber: A New 4pi Detector for Charged Particles." In: *1974 PEP summer study*. Vol. C740805. Dec. 1974, pp. 58–78.
URL: http://lss.fnal.gov/conf/C740805/p58.pdf.

[287] D. PFEIFFER, F. RESNATI, et al. "The muTPC method: improving the position resolution of neutron detectors based on MPGDs." In: *Journal of Instrumentation* **10**(04) (Apr. 2015), P04004.
DOI: 10.1088/1748-0221/10/04/P04004.

[288] R. SANTONICO and R. CARDARELLI. "Development of resistive plate counters." In: *Nuclear Instruments and Methods in Physics Research* **187**(2) (Aug. 1981), pp. 377–380.
DOI: 10.1016/0029-554X(81)90363-3.

[289] D.S. MCGREGOR, S.L. BELLINGER, and J.K. SHULTIS. "Present status of microstructured semiconductor neutron detectors." In: *Journal of Crystal Growth* **379** (Sept. 2013). Compound Semiconductors and Scintillators for Radiation Detection Applications: A Special Tribute to the Research of Michael Schieber, pp. 99–110.
DOI: 10.1016/j.jcrysgro.2012.10.061.

[290] J. UHER, C. FRÖJDH, J. JAKŮBEK, C. KENNEY, Z. KOHOUT, V. LINHART, S. PARKER, S. PETERSSON, S. POSPIŠIL, and G. THUNGSTRÖM. "Characterization of 3D thermal neutron semiconductor detectors." In: *Nuclear Instruments and Methods in Physics Research Section A: Accelerators, Spectrometers, Detectors and Associated Equipment* **576**(1) (June 2007). Proceedings of the 8th International Workshop on Radiation Imaging Detectors, pp. 32–37.
DOI: 10.1016/j.nima.2007.01.115.

[291] R.G. FRONK, S.L. BELLINGER, et al. "Development of the dual-sided microstructured semiconductor neutron detector." In: *2014 IEEE Nuclear Science Symposium and Medical Imaging Conference (NSS/MIC)*. Nov. 2014, pp. 1–4.
DOI: 10.1109/NSSMIC.2014.7431247.

[292] C.B. HOSHOR, T.M. OAKES, et al. "A portable and wide energy range semiconductor-based neutron spectrometer." In: *Nuclear Instruments and Methods in Physics Research Section A: Accelerators, Spectrometers, Detectors and Associated Equipment* **803** (Dec. 2015), pp. 68–81.
DOI: 10.1016/j.nima.2015.08.077.

[293] R. TURCHETTA, J.D. BERST, et al. "A monolithic active pixel sensor for charged particle tracking and imaging using standard VLSI CMOS technology." In: *Nuclear Instruments and Methods in Physics Research Section A: Accelerators, Spectrometers, Detectors and Associated Equipment* **458**(3) (Feb. 2001), pp. 677–689.
DOI: 10.1016/S0168-9002(00)00893-7.

[294] M. HAVRÁNEK, T. HEMPEREK, H. KRÜGER, Y. FU, L. GERMIC, T. KISHISHITA, C. MARINAS, T. OBERMANN, and N. WERMES. "DMAPS: a fully depleted monolithic active pixel sensor - analog performance characterization." In: *Journal of Instrumentation* **10**(02) (Feb. 2015), P02013.
DOI: 10.1088/1748-0221/10/02/P02013.

[295] D. MANEUSKI. "Pixellated Radiation Detectors for Scientific Applications." PhD thesis. Department of Physics and Astronomy, University of Glasgow, June 2009.
URL: https://core.ac.uk/download/pdf/9654425.pdf.

[296] S.R. AMENDOLIA, E. BERTOLUCCI, et al. "Medipix: a VLSI chip for a GaAs pixel detector for digital radiology." In: *Nuclear Instruments and Methods in Physics Research Section A: Accelerators, Spectrometers, Detectors and Associated Equipment* **422**(1–3) (Feb. 1999), pp. 201–205.
DOI: 10.1016/S0168-9002(98)01094-8.

[297] J. JAKŮBEK, S. POSPIŠIL, J. UHER, J. VACIK, and D. VAVŘIK. "Single neutron pixel detector based on Medipix-1 device." In: *Nuclear Science Symposium Conference Record, 2003 IEEE*. Vol. 2. Oct. 2003, pp. 1444–1447.
DOI: 10.1109/NSSMIC.2003.1351966.

[298] J. JAKŮBEK, T. HOLÝ, E. LEHMANN, S. POSPIŠIL, J. UHER, J. VACIK, and D. VAVŘIK. "Neutron imaging with Medipix-2 chip and a coated sensor." In: *Nuclear Instruments and Methods in Physics Research Section A: Accelerators, Spectrometers, Detectors and Associated Equipment* **560**(1) (May 2006). Proceedings of the 13th International Workshop on Vertex Detectors - VERTEX 2004, pp. 143–147.
DOI: 10.1016/j.nima.2005.11.243.

[299] J. JAKŮBEK, P. SCHMIDT-WELLENBURG, P. GELTENBORT, M. PLATKEVIC, C. PLONKA-SPEHR, J. SOLC, and T. SOLDNER. "A coated pixel device TimePix with micron spatial resolution for UCN detection." In: *Nuclear Instruments and Methods in Physics Research Section A: Accelerators, Spectrometers, Detectors and Associated Equipment* **600**(3) (Mar. 2009), pp. 651–656.
DOI: 10.1016/j.nima.2008.12.078.

[300] P. KANDLAKUNTA and L. CAO. "Gamma-ray rejection, or detection, with gadolinium as a converter." In: *Radiation Protection Dosimetry* **151**(3) (Mar. 2012), pp. 586–590.
DOI: 10.1093/rpd/ncs031.

[301] F. ANGELINI, R. BELLAZZINI, A. BREZ, M.M. MASSAI, G. SPANDRE, M.R. TORQUATI, R. BOUCLIER, J. GAUDAEN, and F. SAULI. "The microstrip gas chamber." In: *Nuclear Physics B - Proceedings Supplements* **23**(1) (July 1991), pp. 254–260.
DOI: 10.1016/0920-5632(91)90056-K.

[302] D. PFEIFFER, F. RESNATI, et al. "First measurements with new high-resolution gadolinium-GEM neutron detectors." In: *Journal of Instrumentation* **11**(05) (May 2016), P05011.
DOI: 10.1088/1748-0221/11/05/P05011.

[303] M.A. REICHENBERGER, T.C. UNRUH, P.B. UGOROWSKI, T. ITO, J.A. ROBERTS, S.R. STEVENSON, D.M. NICHOLS, and D.S. MCGREGOR. "Micro-Pocket Fission Detectors (MPFDs) for in-core neutron detection." In: *Annals of Nuclear Energy* **87** (Jan. 2016). Part 2, pp. 318–323.
DOI: 10.1016/j.anucene.2015.08.022.

[304] F.D.U. AMARO, C.M.B. MONTEIRO, J.M.F. DOS SANTOS, and A. ANTOGNINI. "Novel concept for neutron detection: proportional counter filled with ^{10}B nanoparticle aerosol." In: *Scientific Reports* **7**(41699) (Feb. 2017).
DOI: 10.1038/srep41699.

[305] M. SCHIEBER, M. ROTH, A. ZUCK, O. KHAKHAN, J. UHER, V. LINHART, S. POSPIŠIL, and M. FIEDERLE. "Polycrystalline BN and LiF Based Semiconductor Alpha Particle and Neutron Detectors." In: *2006 IEEE Nuclear Science Symposium Conference Record*. Vol. 6. Oct. 2006, pp. 3728–3731.
DOI: 10.1109/NSSMIC.2006.353804.

[306] K.A. NELSON, J.L. NEIHART, T.A. RIEDEL, A.J. SCHMIDT, and D.S. MCGREGOR. "A novel method for detecting neutrons using low density high porosity aerogel and saturated foam." In: *Nuclear Instruments and Methods in Physics Research Section A: Accelerators, Spectrometers, Detectors and Associated Equipment* **686** (Sept. 2012), pp. 100–105.
DOI: 10.1016/j.nima.2012.04.084.

[307] D. VARTSKY, M.B. GOLDBERG, A. BRESKIN, R. CHECHIK, B. GUÉRARD, and J.F. CLERGEAU. "Large-area imaging detector for neutron scattering based on boron-rich liquid scintillator." In: *Nuclear Instruments and Methods in Physics Research Section A: Accelerators, Spectrometers, Detectors and Associated Equipment* **504**(1–3) (May 2003). Proceedings of the 3rd International Conference on New Developments in Photodetection, pp. 369–373.
DOI: 10.1016/S0168-9002(03)00817-9.

[308] A.S. TREMSIN, J.B. MCPHATE, J.V. VALLERGA, O.H.W. SIEGMUND, J.S. HULL, W.B. FELLER, and E. LEHMANN. "High-resolution neutron radiography with microchannel plates: Proof-of-principle experiments at PSI." In: *Nuclear Instruments and Methods in Physics Research Section A: Accelerators, Spectrometers, Detectors and Associated Equipment* **605**(1-2) (June 2009). ITMNR Proceedings of the 6th Topical Meeting on Neutron Radiography, pp. 103–106.
DOI: 10.1016/j.nima.2009.01.137.

[309] J.L. WIZA. "Microchannel plate detectors." In: *Nuclear Instruments and Methods* **162**(1) (June 1979), pp. 587–601.
DOI: 10.1016/0029-554X(79)90734-1.

[310] E.H. LEHMANN, P. VONTOBEL, G. FREI, and C. BRÖNNIMANN. "Neutron imaging - detector options and practical results." In: *Nuclear Instruments and Methods in Physics Research Section A: Accelerators, Spectrometers, Detectors and Associated Equipment* **531**(1-2) (June 2004). Proceedings of the 5th International Workshop on Radiation Imaging Detectors, pp. 228–237.
DOI: 10.1016/j.nima.2004.06.010.

[311] P. TRTIK, J. HOVIND, C. GRÜNZWEIG, A. BOLLHALDER, V. THOMINET, C. DAVID, A. KAESTNER, and E.H. LEHMANN. "Improving the Spatial Resolution of Neutron Imaging at Paul Scherrer Institut - The Neutron Microscope Project." In: *Physics Procedia* **69** (Sept. 2015). Proceedings of the 10th World Conference on Neutron Radiography (WCNR-10) 2014, pp. 169–176.
DOI: 10.1016/j.phpro.2015.07.024.

[312] B. KHAYKOVICH, M.V. GUBAREV, Y. BAGDASAROVA, B.D. RAMSEY, and D.E. MONCTON. "From x-ray telescopes to neutron scattering: Using axisymmetric mirrors to focus a neutron beam." In: *Nuclear Instruments and Methods in Physics Research Section A: Accelerators, Spectrometers, Detectors and Associated Equipment* **631**(1) (Mar. 2011), pp. 98–104.
DOI: 10.1016/j.nima.2010.11.110.

[313] T. FUJIWARA, U. BAUTISTA, Y. MITSUYA, H. TAKAHASHI, N.L. YAMADA, Y. OTAKE, A. TAKETANI, M. UESAKA, and H. TOYOKAWA. "Microstructured boron foil scintillating G-GEM detector for neutron imaging." In: *Nuclear Instruments and Methods in Physics Research Section A: Accelerators, Spectrometers, Detectors and Associated Equipment* **838** (Sept. 2016), pp. 124–128.
DOI: 10.1016/j.nima.2016.09.005.

[314] V.N. MARIN, R.A. SADYKOV, D.N. TRUNOV, V.S. LITVIN, S.N. AKSENOV, and A.A. STOLYAROV. "A new type of thermal-neutron detector based on ZnS(Ag)/LiF scintillator and avalanche photodiodes." In: *Technical Physics Letters* **41**(9) (Sept. 2015), pp. 912–914.
DOI: 10.1134/S1063785015090242.

[315] Z. WANG, M.A. HOFFBAUER, et al. "A multilayer surface detector for ultracold neutrons." In: *Nuclear Instruments and Methods in Physics Research Section A: Accelerators, Spectrometers, Detectors and Associated Equipment* **798** (Oct. 2015), pp. 30–35.
DOI: 10.1016/j.nima.2015.07.010.

[316] F. SAULI. "GEM: A new concept for electron amplification in gas detectors." In: *Nuclear Instruments and Methods in Physics Research Section A: Accelerators, Spectrometers, Detectors and Associated Equipment* **386**(2-3) (Feb. 1997), pp. 531–534.
DOI: 10.1016/S0168-9002(96)01172-2.

[317] D. FIOLKA. "Entwicklung eines neuen Detektors für Neutronen." Dipl. Thesis. Physikalisches Institut, Heidelberg University, 1999. 109 pp.

[318] M. KLEIN. "Experimente zur Quantenmechanik mit ultrakalten Neutronen und Entwicklung eines neuen Detektors zum ortsaufgelösten Nachweis von thermischen Neutronen auf großen Flächen." PhD thesis. Physikalisches Institut, Heidelberg University, July 2000. 137 pp.
URL: https://www.physi.uni-heidelberg.de//Publications/phd_klein.pdf.

[319] A. OED. "Position-sensitive detector with microstrip anode for electron multiplication with gases." In: *Nuclear Instruments and Methods in Physics Research Section A: Accelerators, Spectrometers, Detectors and Associated Equipment* **263**(2–3) (Jan. 1988), pp. 351–359.
DOI: 10.1016/0168-9002(88)90970-9.

[320] N. VELLETTAZ. "Optimisation d'un detecteur gazeux a micro-pistes destine a la localisation a deux dimensions des neutrons thermiques." PhD thesis. Institut Laue-Langevin, Grenoble, 1997. 125 pp.

[321] G. MODZEL, M. HENSKE, A. HOUBEN, M. KLEIN, M. KÖHLI, P. LENNERT, M. MEVEN, C.J. SCHMIDT, U. SCHMIDT, and W. SCHWEIKA. "Absolute efficiency measurements with the ^{10}B based Jalousie detector." In: *Nuclear Instruments and Methods in Physics Research Section A: Accelerators, Spectrometers, Detectors and Associated Equipment* **743** (Apr. 2014), pp. 90–95.
DOI: 10.1016/j.nima.2014.01.007.

[322] G. MODZEL. "Entwicklung einer Ersatztechnologie für den Standard ^{3}He Detektor zum Nachweis thermischer Neutronen auf großen Flächen." PhD thesis. Physikalisches Institut, Heidelberg University, July 2014. 92 pp.
URL: https://archiv.ub.uni-heidelberg.de/volltextserver/17217/1/Doktorarbeit_gedruckt_07.06.2014.pdf.

[323] M. KLEIN and C.J. SCHMIDT. "CASCADE, neutron detectors for highest count rates in combination with ASIC/FPGA based readout electronics." In: *Nuclear Instruments and Methods in Physics Research Section A: Accelerators, Spectrometers, Detectors and Associated Equipment* **628**(1) (Feb. 2011). VCI 2010 Proceedings of the 12$^{\text{th}}$ International Vienna Conference on Instrumentation, pp. 9–18.
DOI: 10.1016/j.nima.2010.06.278.

[324] D.S. MCGREGOR, J.T. LINDSAY, C.C. BRANNON, and R.W. OLSEN. "Semi-insulating bulk GaAs thermal neutron imaging arrays." In: *Nuclear Science, IEEE Transactions on* **43**(3) (June 1996), pp. 1357–1364.
DOI: 10.1109/23.507065.

[325] D.S. MCGREGOR, S.M. VERNON, H.K. GERSCH, S.M. MARKHAM, S.J. WOJTCZUK, and D.K. WEHE. "Self-biased boron-10 coated high-purity epitaxial GaAs thermal neutron detectors." In: *Nuclear Science, IEEE Transactions on* **47**(4) (Aug. 2000), pp. 1364–1370.
DOI: 10.1109/23.872979.

[326] F. PISCITELLI and P. VAN ESCH. "Analytical modeling of thin film neutron converters and its application to thermal neutron gas detectors." In: *Journal of Instrumentation* **8**(04) (Apr. 2013), P04020.
DOI: 10.1088/1748-0221/8/04/P04020.

[327] H. BRUHNS. "Bau eines CASCADE - Neutronendetektors." Dipl. Thesis. Physikalisches Institut, Heidelberg University, 2002. 91 pp.
URL: https://www.physi.uni-heidelberg.de//Publications/dipl_bruhns.pdf.

[328] K. SCHINDLER. "Bau und Entwicklung der Ausleseelektronik des CASCADE - Neutronendetektors." Staatsexamen. Physikalisches Institut, Heidelberg University, 2002. 66 pp.

[329] B. MÄRKISCH. "Studies on CASCADE Detector Prototypes and Development of its Infrastructure." Dipl. Thesis. Physikalisches Institut, Heidelberg University, 2002. 78 pp.
URL: https://www.physi.uni-heidelberg.de//Publications/dipl_maerkisch.pdf.

[330] W.E. FISCHER. "SINQ - The spallation neutron source, a new research facility at PSI." In: *Physica B: Condensed Matter* **234–236** (May 1997). Proceedings of the First European Conference on Neutron Scattering, pp. 1202–1208.
DOI: 10.1016/S0921-4526(97)00260-3.

[331] S. BACKFISCH. "Weiterentwicklung und Charakterisierung des CASCADE - Detektors und Tests am VCN-Strahl des ILL." Dipl. Thesis. Physikalisches Institut, Heidelberg University, 2007.

[332] W. HINDERER. "Der 2D-CASCADE Neutronendetektor und seine Auslese." PhD thesis. Physikalisches Institut, Heidelberg University, Dec. 2005. 174 pp.
URL: https://www.physi.uni-heidelberg.de//Publications/phd_hinderer.pdf.

[333] J. BETZ. "Entwicklung einer FPGA-basierten Speicherschnittstelle für den CASCADE - Detektor." Dipl. Thesis. Physikalisches Institut, Heidelberg University, 2007.

[334] B. BÖHM. “Erste Untersuchungen zum CASCADE - Röntgendetektor und Messung zur Neutron-Spiegelneutron-Oszillation.” PhD thesis. Physikalisches Institut, Heidelberg University, Feb. 2007. 132 pp.
URL: https://www.physi.uni-heidelberg.de//Publications/phd_boehm.pdf.

[335] A.P. SEREBROV, E.B. ALEKSANDROV, et al. “Experimental search for neutron - mirror neutron oscillations using storage of ultracold neutrons.” In: *Physics Letters B* **663**(3) (May 2008), pp. 181–185.
DOI: 10.1016/j.physletb.2008.04.014.

[336] H. FRIEDRICH. “Charakterisierung und Weiterentwicklung des CASCADE - Detektors.” Dipl. Thesis. Physikalisches Institut, Heidelberg University, 2007. 85 pp.

[337] G. MODZEL. “Weiterentwicklung und Optimierung der hochintegrierten Ausleseelektronik des CASCADE - Detektors und erstmalige Inbetriebnahme des neuentwickelten nXYTER Auslesechips.” Dipl. Thesis. Physikalisches Institut, Heidelberg University, 2007. 92 pp.

[338] I. SOROKIN, T. BALOG, V. KRYLOV, and C.J. SCHMIDT. “Transconductance calibration of n-XYTER 1.0 readout ASIC.” In: *Nuclear Instruments and Methods in Physics Research Section A: Accelerators, Spectrometers, Detectors and Associated Equipment* **714** (June 2013), pp. 136–140.
DOI: 10.1016/j.nima.2013.02.013.

[339] M. KÄSTNER. “Entwicklung und Design eines Beammonitors für das PERC Experiment und Entwicklung einer VHDL-Firmware zur Inbetriebnahme des n-XYTER Auslesechips.” Dipl. Thesis. Physikalisches Institut, Heidelberg University, 2013. 82 pp.

[340] F. GARCÍA, R. TURPEINEN, et al. “Super-FRS GEM-TPC prototype development based on n-Xyter ASIC for the FAIR facility.” In: *2012 IEEE Nuclear Science Symposium and Medical Imaging Conference Record (NSS/MIC)*. Oct. 2012, pp. 1119–1123.
DOI: 10.1109/NSSMIC.2012.6551281.

[341] M. LIEBIG. “Weiterentwicklung eines CASCADE - Detektors für MIEZE - Anwendungen.” Dipl. Thesis. Physikalisches Institut, Heidelberg University, June 2014. 114 pp.

[342] F. GROITL. “MIEZE mit dem CASCADE-Detektor.” Dipl. Thesis. Physikalisches Institut, Heidelberg University, May 2009. 89 pp.

[343] F. ALLMENDINGER. “Weiterentwicklung des CASCADE - MIEZE - Detektors und dessen Integration in RESEDA.” Dipl. Thesis. Physikalisches Institut, Heidelberg University, Nov. 2011. 77 pp.
URL: https://www.physi.uni-heidelberg.de/Forschung/ANP/XenonEDM/Documents/DiplomarbeitFabianAllmendinger.pdf.

[K2016b] M. KÖHLI, M. KLEIN, F. ALLMENDINGER, A.-K. PERREVOORT, T. SCHRÖDER, N. MARTIN, C.J. SCHMIDT, and U. SCHMIDT. “CASCADE - a multi-layer Boron-10 neutron detection system.” In: *Journal of Physics: Conference Series* **746**(1) (Sept. 2016), p. 012003.
DOI: 10.1088/1742-6596/746/1/012003.

[344] H. BÖRNER, P. JALOCHA, et al. *Development of high resolution Si strip detectors for experiments at high luminosity at the LHC*. Tech. rep. CERN-DRDC-91-10. DRDC-P-26. Geneva: CERN, 1991.
URL: https://cds.cern.ch/record/291225.

[345] L. EVANS and P. BRYANT. “LHC Machine.” In: *Journal of Instrumentation* **3**(08) (Aug. 2008), S08001.
DOI: 10.1088/1748-0221/3/08/S08001.

[346] R. BRENNER, H. VON DER LIPPE, J. MICHEL, E. NYGÅRD, T. ØDEGAARD, N.A. SMITH, P. WEILHAMMER, and K. YOSHIOKA. “Design and performance of an analog delay and buffer chip for use with silicon strip detectors at LHC.” In: *Nuclear Instruments and Methods in Physics Research Section A: Accelerators, Spectrometers, Detectors and Associated Equipment* **339**(3) (Feb. 1994), pp. 564–569.
DOI: 10.1016/0168-9002(94)90194-5.

[347] R. BRENNER, J. KAPLON, H. von der LIPPE, E. NYGÅRD, S. ROE, P. WEILHAMMER, and K. YOSHIOKA. “Performance of a LHC front-end running at 67 MHz.” In: *Nuclear Instruments and Methods in Physics Research Section A: Accelerators, Spectrometers, Detectors and Associated Equipment* **339**(3) (Feb. 1994), pp. 477–484.
DOI: 10.1016/0168-9002(94)90184-8.

[348] E.P. HARTOUNI et al. “HERA-B: An experiment to study CP violation in the B system using an internal target at the HERA proton ring. Design report.” In: *DESY-PRC Report* (DESY-PRC-95-01) (Jan. 1995).
URL: https://cds.cern.ch/record/1478622.

[349] DESY. “HERA - A Proposal for a Large Electron Proton Colliding Beam Facility at DESY.” In: *DESY-HERA Report* (DESY-HERA-81-10) (Oct. 1981).
URL: https://cds.cern.ch/record/1480597.

[350] E. SEXAUER. “Charakterisierung des HELIX 128 Auslesechips für HERA-B.” Dipl. Thesis. ASIC Labor, Heidelberg University, May 1997. 66 pp.
URL: https://archiv.ub.uni-heidelberg.de/volltextserver/26/1/26_1.pdf.

[351] W. FALLOT-BURGHARDT et al. “HELIX: A readout chip for the HERA-B microstrip detectors.” In: *Electronics for LHC experiments. Proceedings, 2nd Workshop, Balatonfüred, Hungary, 1996*. Sept. 1996, pp. 503–505.
URL: http://inspirehep.net/record/432494.

[352] W. FALLOT-BURGHARDT. “A CMOS Mixed-Signal Readout Chip for the Microstrip Detectors of HERA-B.” PhD thesis. Physikalisches Institut, Heidelberg University, June 1998. 254 pp.
URL: https://archiv.ub.uni-heidelberg.de/volltextserver/469/.

[353] C. BAUER, W. FALLOT-BURGHARDT, et al. “Performance and Radiation Tolerance of the HELIX128-2.2 and 3.0 Readout Chips for the HERA-B Microstrip Detectors.” In: *5th Conference on Electronics for LHC Experiments, Snowmass, USA*. OPEN-2000-111. Sept. 1999, pp. 508–512.
DOI: 10.5170/CERN-1999-009.508.

[354] HERMES COLLABORATION. “HERMES technical design report.” In: *DESY-PRC Report* (DESY-PRC-93-06) (July 1993).
URL: https://cds.cern.ch/record/1478621.

[355] G. WOLF et al. “The ZEUS Detector: Technical Proposal.” In: *DESY Report* (DESY-HERA-ZEUS-1) (Mar. 1986).
URL: https://cds.cern.ch/record/1478623.

[356] N. VAN BAKEL, M. VAN BEUZEKOM, et al. “Performance of the Beetle readout chip for LHCb.” In: *8th Workshop on Electronics for LHC Experiments*. Sept. 2002, pp. 121–124.
DOI: 10.5170/CERN-2002-003.121.

[357] P.R. BARBOSA-MARINHO et al. *LHCb VELO (VErtex LOcator): Technical Design Report*. Technical Design Report LHCb. Geneva: CERN, Nov. 2001. ISBN: 929083179.
URL: https://cds.cern.ch/record/504321.

[358] S. LÖCHNER. “Charakterisierung und Entwicklung eines CIP-Auslese-ASIC für das H1-Upgrade-Projekt 2000.” Dipl. Thesis. Physikalisches Institut, Heidelberg University, Dec. 1998. 97 pp.
URL: https://www.physik.uzh.ch/groups/h1/text/DiplArb_SLoechner.ps.gz.

[359] D. BAUMEISTER. “Entwicklung und Charakterisierung eines ASICs zur Kathodenauslese von MW-PCs für das H1 Experiment bei HERA.” Dipl. Thesis. Physikalisches Institut, Heidelberg University, Mar. 1999. 113 pp.
URL: https://www.physik.uzh.ch/groups/h1/text/DiplArb_Baumeister.ps.gz.

[360] U. STANGE. “Charakterisierung und Weiterentwicklung des CIPix.” Dipl. Thesis. Physikalisches Institut, Heidelberg University, Mar. 2000. 60 pp.
URL: https://www.physik.uzh.ch/groups/h1/text/DiplArb_UStange.ps.gz.

[361] A. VOLLHARDT. “Entwurf und Bau einer Frontend-Steuerung für das CIP-Upgrade Projekt für H1 bei HERA.” Dipl. Thesis. Physikalisches Institut, Heidelberg University, Jan. 2001. 106 pp.
URL: https://www.physik.uzh.ch/groups/h1/text/DiplArbeit_Vollhardt.ps.gz.

[362] J. BECKER, K. BÖSIGER, et al. “A vertex trigger based on cylindrical multiwire proportional chambers.” In: *Nuclear Instruments and Methods in Physics Research Section A: Accelerators, Spectrometers, Detectors and Associated Equipment* **586**(2) (Feb. 2008), pp. 190–203.
DOI: 10.1016/j.nima.2007.11.024.

[363] H1 COLLABORATION. “Technical proposal for the H1 detector.” In: *DESY-PRC Report* (PRC-86-02) (1986).
URL: https://cds.cern.ch/record/108544.

[364] P. HOROWITZ and W. HILL. *The Art of Electronics*. 3rd ed. New York, NY, USA: Cambridge University Press, 2015. 1225 pp. ISBN: 978-0-521-80926-9.
URL: https://www.cambridge.org/9780521809269.

[365] C.J. SCHMIDT. *AS20 CIPix-Boards Reference Manual*. CDT Detector GmbH. Hans-Bunte-Str. 8-10, Heidelberg, July 2011. 35 pp.

[366] Philips SEMICONDUCTORS. *The I^2C Bus specification*. 2.1. document order number: 9398 393 40011. Jan. 2000. 46 pp.
URL: https://www.csd.uoc.gr/~hy428/reading/i2c_spec.pdf.

[367] XILINX, INC. *Virtex-II Platform FPGAs: Complete Data Sheet*. 4.0. DS031. San José, California, USA, Apr. 2014. 319 pp.
URL: https://www.xilinx.com/support/documentation/data_sheets/ds031.pdf.

[368] STRUCK INNOVATIVE SYSTEME GMBH. *SIS 1100-OPT Gigabit CMC*. Hamburg, Jan. 2001.
URL: https://www.struck.de/sis1100-opt.htm.

[369] A.S. BROGNA et al. *The n-XYTER Reference Manual*. 1.50 (Draft). GSI. Dec. 2009. 113 pp.
URL: https://cbm-wiki.gsi.de/foswiki/pub/Public/PublicNxyter/nXYTER.pdf.

[370] C.J. SCHMIDT and M. KLEIN. *CDT Detector Control Reference Manual*. CDT Detector GmbH. Hans-Bunte-Str. 8-10, Heidelberg, Oct. 2012. 46 pp.

[371] NATIONAL INSTRUMENTS. *NI MultiSim User Manual*. Austin, Texas, USA, Jan. 2009. 713 pp.
URL: http://www.ni.com/pdf/manuals/374483d.pdf.

[372] T. QUARLES, A.R. NEWTON, D.O. PEDERSON, and A. SANGIOVANNI-VINCENTELLI. *SPICE3 Version 3f3 User's Manual*. University of California. Berkeley, USA, May 1993. 146 pp.
URL: http://www.gianlucafiori.org/appunti/Spice_3f3_Users_Manual.pdf.

[373] D.S. MCGREGOR, M.D. HAMMIG, Y.-H. YANG, H.K. GERSCH, and R.T. KLANN. "Design considerations for thin film coated semiconductor thermal neutron detectors - I: basics regarding alpha particle emitting neutron reactive films." In: *Nuclear Instruments and Methods in Physics Research Section A: Accelerators, Spectrometers, Detectors and Associated Equipment* **500**(1–3) (Mar. 2003), pp. 272–308.
DOI: 10.1016/S0168-9002(02)02078-8.

[374] D.J. SALVAT, C.L. MORRIS, et al. "A boron-coated ionization chamber for ultra-cold neutron detection." In: *Nuclear Instruments and Methods in Physics Research Section A: Accelerators, Spectrometers, Detectors and Associated Equipment* **691** (Nov. 2012), pp. 109–112.
DOI: 10.1016/j.nima.2012.06.041.

[375] L.M.S. MARGATO and A. MOROZOV. "Boron-10 lined RPCs for sub-millimeter resolution thermal neutron detectors: conceptual design and performance considerations." In: *Journal of Instrumentation* **13**(08) (Aug. 2018), P08007.
DOI: 10.1088/1748-0221/13/08/p08007.

[376] F. PISCITELLI. "Boron-10 layers, Neutron Reflectometry and Thermal Neutron Gaseous Detectors." PhD thesis. Università degli Studi di Perugia, May 2013. 186 pp.
URL: https://arxiv.org/pdf/1406.3133.pdf.

[377] J. WEIMAR. "Entwicklung und Charakterisierung eines ^{10}B-basierten Neutronendetektors im Rahmen der COSMOS-Methode zur Bestimmung von Bodenfeuchte auf der Hektarskala." Master Thesis. Physikalisches Institut, Heidelberg University, Aug. 2017. 97 pp.
URL: https://www.physi.uni-heidelberg.de/Forschung/ANP/Cascade/Documents/MAJannis.pdf.

[378] T. KITTELMANN, K. KANAKI, E. KLINKBY, X.X. CAI, C.P. COOPER-JENSEN, and R. HALL-WILTON. "Using Backscattering to Enhance Efficiency in Neutron Detectors." In: *IEEE Transactions on Nuclear Science* **64**(6) (June 2017), pp. 1562–1573.
DOI: 10.1109/TNS.2017.2695404.

[379] Y.B. GALIM. "Comparison between Boron-Carbide based thermal neutron detectors and other detection technologies applicable to Homeland Security." Master Thesis. Department of nuclear engineering, Ben-Gurion University of the Negev, June 2014. 145 pp.

[380] G. TSILEDAKIS, A. DELBART, D. DESFORGE, I. GIOMATARIS, A. MENELLE, and T. PAPAEVANGELOU. "A large high-efficiency multi-layered Micromegas thermal neutron detector." In: *Journal of Instrumentation* **12**(09) (Aug. 2017), P09006.
DOI: 10.1088/1748-0221/12/09/p09006.

[381] C. HÖGLUND, J. BIRCH, et al. "B4C thin films for neutron detection." In: *Journal of Applied Physics* **111**(10) (May 2012), p. 104908.
DOI: 10.1063/1.4718573.

[382] D. YEATES, S. HARRIS, and C. DOUST. "A study of the angular distribution and energies of alpha particles emitted by ^{241}Am sources." In: *Nuclear Instruments and Methods* **80**(2) (Apr. 1970), pp. 320–324.
DOI: 10.1016/0029-554X(70)90781-0.

[383] R.K. CRAWFORD. "Position-sensitive detection of slow neutrons: survey of fundamental principles." In: *SPIE Conference Proceedings* **1737** (Feb. 1993), pp. 1–14.
DOI: 10.1117/12.138661.

[384] F.A.F. FRAGA, L.M.S. MARGATO, S.T.G. FETAL, M.M.F.R. FRAGA, R. FERREIRA-MARQUES, A.J.P.L. POLICARPO, B. GUÉRARD, A. OED, G. MANZINI, and T. van VUURE. "CCD readout of GEM-based neutron detectors." In: *Nuclear Instruments and Methods in Physics Research Section A: Accelerators, Spectrometers, Detectors and Associated Equipment* **478**(1) (Feb. 2002). Proceedings of the 9th International Conference on Instrumentation, pp. 357–361.
DOI: 10.1016/S0168-9002(01)01829-0.

[K2018] M. KÖHLI, K. DESCH, M. GRUBER, J. KAMINSKI, F.P. SCHMIDT, and T. WAGNER. "Novel neutron detectors based on the time projection method." In: *Physica B: Condensed Matter* **551** (Dec. 2018). The 11th International Conference on Neutron Scattering (ICNS 2017), pp. 517–522.
DOI: 10.1016/j.physb.2018.03.026.

[385] F. PISCITELLI, F. MESSI, et al. "The Multi-Blade Boron-10-based neutron detector for high intensity neutron reflectometry at ESS." In: *Journal of Instrumentation* **12**(03) (Mar. 2017), P03013.
DOI: 10.1088/1748-0221/12/03/p03013.

[386] A.-K. PERREVOORT. "Messung der Verstärkung an GEM-Folien in Abhängigkeit des GEM-Lochabstandes für borbeschichtete Driftelektroden." Bachelor Thesis. Physikalisches Institut, Heidelberg University, 2010. 55 pp.

[387] I. STEFANESCU, Y. ABDULLAHI, J. BIRCH, I. DEFENDI, R. HALL-WILTON, C. HÖGLUND, L. HULTMAN, D. SEILER, and K. ZEITELHACK. "Development of a novel macrostructured cathode for large-area neutron detectors based on the ^{10}B-containing solid converter." In: *Nuclear Instruments and Methods in Physics Research Section A: Accelerators, Spectrometers, Detectors and Associated Equipment* **727** (Nov. 2013), pp. 109–125.
DOI: 10.1016/j.nima.2013.06.003.

[388] W. HÄUSSLER, B. GOHLA-NEUDECKER, R. SCHWIKOWSKI, D. STREIBL, and P. BÖNI. "RESEDA - The new resonance spin echo spectrometer using cold neutrons at the FRM-II." In: *Physica B: Condensed Matter* **397**(1) (July 2007), pp. 112–114.
DOI: 10.1016/j.physb.2007.02.086.

[389] H. FRIEDRICH, V. WAGNER, and P. WILLE. "A high-performance neutron velocity selector." In: *Physica B: Condensed Matter* **156-157** (Jan. 1989), pp. 547–549.
DOI: 10.1016/0921-4526(89)90727-8.

[390] F.J. MACWILLIAMS and N.J.A. SLOANE. "Pseudo-random sequences and arrays." In: *Proceedings of the IEEE* **64**(12) (Dec. 1976), pp. 1715–1729.
DOI: 10.1109/PROC.1976.10411.

[391] C. BREZINA. "A GEM based Time Projection Chamber with pixel readout." PhD thesis. Physikalisches Institut, Universität Bonn, May 2013. 184 pp.
URL: https://hss.ulb.uni-bonn.de/2013/3316/3316.pdf.

[392] D.S. MCGREGOR and J.K. SHULTIS. "Reporting detection efficiency for semiconductor neutron detectors: A need for a standard." In: *Nuclear Instruments and Methods in Physics Research Section A: Accelerators, Spectrometers, Detectors and Associated Equipment* **632**(1) (Mar. 2011), pp. 167–174.
DOI: 10.1016/j.nima.2010.12.084.

[393] *Reference neutron radiations - Part 2*. Standard. Geneva, CH: International Organization for Standardization, Aug. 2000. 31 pp.
URL: https://www.iso.org/standard/25667.html.

[394] I. MAUCH. "Aufbau eines Praktikumsversuchs und neutronenphysikalische Experimente." Staatsexamen. Physikalisches Institut, Heidelberg University, 1998. 46 pp.

[395] C.H. WESTCOTT. *Effective cross section values for well-moderated thermal reactor spectra*. Tech. rep. 20. AECL–1101-REV, 3rd Ed. corrected. Atomic Energy of Canada, Nov. 1970. 42 pp.
URL: https://www.iaea.org/inis/collection/NCLCollectionStore/_Public/41/057/41057250.pdf?r=1.

[396] F.U. AHMED, S.M. YUNUS, I. KAMAL, S. BEGUM, A.A. KHAN, M.H. AHSAN, and A.A.Z. AHMAD. "Optimization of germanium monochromators for neutron diffractometers." In: *International Journal of Modern Physics E* **05**(01) (Mar. 1996), pp. 131–151.
DOI: 10.1142/S0218301396000062.

[397] D. LANÇON, R.A. EWINGS, J.R. STEWART, M. JIMÉNEZ-RUIZ, and H.M. RØNNOW. "The use of selected neutron absorption resonance filters to suppress spurious events on hot neutron spectrometers." In: *Nuclear Instruments and Methods in Physics Research Section A: Accelerators, Spectrometers, Detectors and Associated Equipment* **780** (Apr. 2015), pp. 9–14.
DOI: 10.1016/j.nima.2014.12.114.

[398] P.U. VILLARD. "Sur la réflexion et la réfraction des rayons cathodiques et des rayons déviables du radium." In: *Comptes rendus hebdomadaires des séances de l'Académie des Sciences* **130** (Jan. 1900), pp. 1010–1012.
URL: https://gallica.bnf.fr/ark:/12148/bpt6k3086n/f1010.image.r=.

[399] T. WULF. "Über die in der Atmosphäre vorhandene Strahlung von hoher Durchdringungsfähigkeit." In: *Physikalische Zeitschrift* **10**(5) (Mar. 1909), pp. 152–157.

[400] A. GOCKEL. "Messungen der durchdringenden Strahlung bei Ballonfahrten." In: *Physikalische Zeitschrift* **12**(14) (July 1911), pp. 595–597.

[401] V.F. HESS. "Über die Absorption der γ-Strahlung in der Atmosphäre." In: *Physikalische Zeitschrift* **12**(22) (Nov. 1911), pp. 998–1001.

[402] A.H. COMPTON. "A Geographic Study of Cosmic Rays." In: *Physical Review* **43** (Mar. 1933), pp. 387–403.
DOI: 10.1103/PhysRev.43.387.

[403] T.H. JOHNSON. "The Azimuthal Asymmetry of the Cosmic Radiation." In: *Physical Review* **43** (May 1933), pp. 834–835.
DOI: 10.1103/PhysRev.43.834.

[404] H.J. BHABHA and W. HEITLER. "The Passage of Fast Electrons and the Theory of Cosmic Showers." In: *Proceedings of the Royal Society of London A: Mathematical, Physical and Engineering Sciences* **159**(898) (Apr. 1937), pp. 432–458.
DOI: 10.1098/rspa.1937.0082.

[405] S.E. FORBUSH. "World-wide cosmic ray variations, 1937–1952." In: *Journal of Geophysical Research* **59**(4) (Dec. 1954), pp. 525–542.
DOI: 10.1029/JZ059i004p00525.

[406] W. BAADE and F. ZWICKY. "Remarks on Super-Novae and Cosmic Rays." In: *Physical Review* **46** (July 1934), pp. 76–77.
DOI: 10.1103/PhysRev.46.76.2.

[407] V. COCCONI-TONGIORGI. "Neutrons in the Extensive Air Showers of the Cosmic Radiation." In: *Physical Review* **75** (May 1949), pp. 1532–1540.
DOI: 10.1103/PhysRev.75.1532.

[408] J.A. SIMPSON and R.B. URETZ. "On the Latitude Dependence of Nuclear Disintegrations and Neutrons at 30,000 Feet." In: *Physical Review* **76** (Aug. 1949), pp. 569–570.
DOI: 10.1103/PhysRev.76.569.

[409] J.A. SIMPSON. "The Cosmic Ray Nucleonic Component: The Invention and Scientific Uses of the Neutron Monitor - (Keynote Lecture)." In: *Space Science Reviews* **93**(1) (July 2000), pp. 11–32.
DOI: 10.1023/A:1026567706183.

[410] H. VEREECKEN, J.A. HUISMAN, H. BOGENA, J. VANDERBORGHT, J.A. VRUGT, and J.W. HOPMANS. "On the value of soil moisture measurements in vadose zone hydrology: A review." In: *Water Resources Research* **44**(4) (Apr. 2008), W00D06.
DOI: 10.1029/2008WR006829.

[411] D.A. ROBINSON, C.S. CAMPBELL, J.W. HOPMANS, B.K. HORNBUCKLE, S.B. JONES, R. KNIGHT, F. OGDEN, J. SELKER, and O. WENDROTH. "Soil Moisture Measurement for Ecological and Hydrological Watershed-Scale Observatories: A Review." In: *Vadose Zone Journal* **7**(1) (Feb. 2008), pp. 358–389.
DOI: 10.2136/vzj2007.0143.

[412] J.D. RHOADES, P.A.C. RAATS, and R.J. PRATHER. "Effects of Liquid-phase Electrical Conductivity, Water Content, and Surface Conductivity on Bulk Soil Electrical Conductivity." In: *Soil Science Society of America Journal* **40**(5) (Apr. 1976), pp. 651–655.
DOI: 10.2136/sssaj1976.03615995004000050017x.

[413] T.J. DEAN, J.P. BELL, and A.J.B. BATY. "Soil moisture measurement by an improved capacitance technique, Part I. Sensor design and performance." In: *Journal of Hydrology* **93**(1) (Feb. 1987), pp. 67–78.
DOI: 10.1016/0022-1694(87)90194-6.

[414] G.C. TOPP, J.L. DAVIS, and A.P. ANNAN. "Electromagnetic determination of soil water content: Measurements in coaxial transmission lines." In: *Water Resources Research* **16**(3) (June 1980), pp. 574–582.
DOI: 10.1029/WR016i003p00574.

[415] R. KNIGHT. "Ground Penetrating Radar for Environmental Applications." In: *Annual Review of Earth and Planetary Sciences* **29**(1) (May 2001), pp. 229–255.
DOI: 10.1146/annurev.earth.29.1.229.

[416] E. DE JONG, A.K. BALLANTYNE, D.R. CAMERON, and D.W.L. READ. "Measurement of Apparent Electrical Conductivity of Soils by an Electromagnetic Induction Probe to Aid Salinity Surveys." In: *Soil Science Society of America Journal* **43**(4) (Mar. 1979), pp. 810–812.
DOI: 10.2136/sssaj1979.03615995004300040040x.

[417] B. MAJONE, F. VIANI, E. FILIPPI, A. BELLIN, A. MASSA, G. TOLLER, F. ROBOL, and M. SALUCCI. "Wireless Sensor Network Deployment for Monitoring Soil Moisture Dynamics at the Field Scale." In: *Procedia Environmental Sciences* **19** (July 2013). Four Decades of Progress in Monitoring and Modeling of Processes in the Soil-Plant-Atmosphere System: Applications and Challenges, pp. 426–435.
DOI: 10.1016/j.proenv.2013.06.049.

[418] C.A. LAYMON, W.L. CROSSON, T.J. JACKSON, A. MANU, and T.D. TSEGAYE. "Ground-based passive microwave remote sensing observations of soil moisture at S-band and L-band with insight into measurement accuracy." In: *IEEE Transactions on Geoscience and Remote Sensing* **39**(9) (Sept. 2001), pp. 1844–1858.
DOI: 10.1109/36.951075.

[419] J.R. EAGLEMAN and W.C. LIN. "Remote sensing of soil moisture by a 21-cm passive radiometer." In: *Journal of Geophysical Research* **81**(21) (July 1976), pp. 3660–3666.
DOI: 10.1029/JC081i021p03660.

[420] I. MANAKOS and S. LAVENDER. "Remote Sensing in Support of the Geo-information in Europe." In: *Land Use and Land Cover Mapping in Europe: Practices & Trends*. Ed. by I. MANAKOS and M. BRAUN. Dordrecht: Springer Netherlands, Jan. 2014, pp. 3–10. ISBN: 978-94-007-7969-3.
DOI: 10.1007/978-94-007-7969-3_1.

[421] D. GEUDTNER, R. TORRES, P. SNOEIJ, M. DAVIDSON, and B. ROMMEN. "Sentinel-1 System capabilities and applications." In: *2014 IEEE Geoscience and Remote Sensing Symposium*. July 2014, pp. 1457–1460.
DOI: 10.1109/IGARSS.2014.6946711.

[422] F.D. VAN DER MEER, H.M.A. VAN DER WERFF, and F.J.A. VAN RUITENBEEK. "Potential of ESA's Sentinel-2 for geological applications." In: *Remote Sensing of Environment* **148** (May 2014), pp. 124–133.
DOI: 10.1016/j.rse.2014.03.022.

[423] B. WOLTER and M. KRUS. "Moisture Measuring with Nuclear Magnetic Resonance (NMR)." In: *Electromagnetic Aquametry: Electromagnetic Wave Interaction with Water and Moist Substances*. Ed. by K. KUPFER. Berlin, Heidelberg: Springer Berlin Heidelberg, 2005, pp. 491–515. ISBN: 978-3-540-26491-0.
DOI: 10.1007/3-540-26491-4_21.

[424] D.R. POOL and J.H. EYCHANER. "Measurements of Aquifer-Storage Change and Specific Yield Using Gravity Surveys." In: *Ground Water* **33**(3) (Aug. 1995), pp. 425–432.
DOI: 10.1111/j.1745-6584.1995.tb00299.x.

[425] F. KOCH, F. SCHLENZ, M. PRASCH, F. APPEL, T. RUF, and W. MAUSER. "Soil Moisture Retrieval Based on GPS Signal Strength Attenuation." In: *Water* **8**(7) (July 2016), pp. 1–22.
DOI: 10.3390/w8070276.

[426] I.F. LONG and B.K. FRENCH. "Measurement of Soil Moisture in the Field by Neutron Moderation." In: *Journal of Soil Science* **18**(1) (Mar. 1967), pp. 149–166.
DOI: 10.1111/j.1365-2389.1967.tb01496.x.

[427] M. QUINTA-FERREIRA, J.F. DIAS, and S. ALIJA. "False low water content in road field compaction control using nuclear gauges: a case study." In: *Environmental Earth Sciences* **75**(14) (July 2016), p. 1114.
DOI: 10.1007/s12665-016-5901-1.

[428] D.V. ELLIS and J.M. SINGER. "Basic Neutron Physics for Logging Applications." In: *Well Logging for Earth Scientists*. Dordrecht: Springer Netherlands, 2007, pp. 325–349. ISBN: 978-1-4020-4602-5.
DOI: 10.1007/978-1-4020-4602-5_13.

[429] D. DESILETS, M. ZREDA, and T.P.A. FERRÉ. "Nature's neutron probe: Land surface hydrology at an elusive scale with cosmic rays." In: *Water Resources Research* **46**(11) (Nov. 2010), W11505.
DOI: 10.1029/2009WR008726.

[430] T.E. FRANZ, T. WANG, W. AVERY, C. FINKENBINER, and L. BROCCA. "Combined analysis of soil moisture measurements from roving and fixed cosmic ray neutron probes for multiscale real-time monitoring." In: *Geophysical Research Letters* **42**(9) (May 2015), pp. 3389–3396.
DOI: 10.1002/2015gl063963.

[431] M. ZREDA, W.J. SHUTTLEWORTH, X. ZENG, C. ZWECK, D. DESILETS, T.E. FRANZ, and R. ROSOLEM. "COSMOS: The COsmic-ray Soil Moisture Observing System." In: *Hydrology and Earth System Sciences* **16**(11) (Nov. 2012), pp. 4079–4099.
DOI: 10.5194/hess-16-4079-2012.

[432] B. CHRISMAN and M. ZREDA. "Quantifying mesoscale soil moisture with the cosmic-ray rover." In: *Hydrology and Earth System Sciences* **17**(12) (Dec. 2013), pp. 5097–5108.
DOI: 10.5194/hess-17-5097-2013.

[KS2018] M. KÖHLI, M. SCHRÖN, and U. SCHMIDT. "Response functions for detectors in cosmic ray neutron sensing." In: *Nuclear Instruments and Methods in Physics Research Section A: Accelerators, Spectrometers, Detectors and Associated Equipment* **902** (Sept. 2018), pp. 184–189.
DOI: 10.1016/j.nima.2018.06.052.

[433] H.R. BOGENA, J.A. HUISMAN, R. BAATZ, H.-J. HENDRICKS-FRANSSEN, and H. VEREECKEN. "Accuracy of the cosmic-ray soil water content probe in humid forest ecosystems: The worst case scenario." In: *Water Resources Research* **49**(9) (Sept. 2013), pp. 5778–5791.
DOI: 10.1002/wrcr.20463.

[434] M. SCHRÖN. "Cosmic-ray neutron sensing and its applications to soil and land surface hydrology." PhD thesis. University of Potsdam, June 2017. 226 pp. ISBN: 978-3-8439-3139-7.
URL: https://nbn-resolving.org/urn:nbn:de:kobv:517-opus4-395433.

[435] D. DESILETS, M. ZREDA, and T. PRABU. "Extended scaling factors for in situ cosmogenic nuclides: new measurements at low latitude." In: *Earth and Planetary Science Letters* **246**(3-4) (June 2006), pp. 265–276.
DOI: 10.1016/j.epsl.2006.03.051.

[436] D. DESILETS and M. ZREDA. "On scaling cosmogenic nuclide production rates for altitude and latitude using cosmic-ray measurements." In: *Earth and Planetary Science Letters* **193**(1–2) (Nov. 2001), pp. 213–225.
DOI: 10.1016/S0012-821X(01)00477-0.

[437] C. Zweck, M. Zreda, and D. Desilets. "Snow shielding factors for cosmogenic nuclide dating inferred from Monte Carlo neutron transport simulations." In: *Earth and Planetary Science Letters* **379** (Aug. 2013), pp. 64–71.
DOI: 10.1016/j.epsl.2013.07.023.

[438] N. Lifton, T. Sato, and T.J. Dunai. "Scaling in situ cosmogenic nuclide production rates using analytical approximations to atmospheric cosmic-ray fluxes." In: *Earth and Planetary Science Letters* **386**(0) (Jan. 2014), pp. 149–160.
DOI: 10.1016/j.epsl.2013.10.052.

[439] J.F. Ziegler. "Terrestrial cosmic ray intensities." In: *IBM Journal of Research and Development* **42**(1) (Jan. 1998), pp. 117–140.
DOI: 10.1147/rd.421.0117.

[440] R. Rosolem, W.J. Shuttleworth, M. Zreda, T.E. Franz, X. Zeng, and S.A. Kurc. "The Effect of Atmospheric Water Vapor on Neutron Count in the Cosmic-Ray Soil Moisture Observing System." In: *Journal of Hydrometeorology* **14**(5) (Oct. 2013), pp. 1659–1671.
DOI: 10.1175/JHM-D-12-0120.1.

[441] C.A. Rivera Villarreyes, G. Baroni, and S.E. Oswald. "Integral quantification of seasonal soil moisture changes in farmland by cosmic-ray neutrons." In: *Hydrology and Earth System Sciences* **15**(12) (Dec. 2011), pp. 3843–3859.
DOI: 10.5194/hess-15-3843-2011.

[442] L. Lv, T.E. Franz, D.A. Robinson, and S.B. Jones. "Measured and Modeled Soil Moisture Compared with Cosmic-Ray Neutron Probe Estimates in a Mixed Forest." In: *Vadose Zone Journal* **13**(12) (Dec. 2014).
DOI: 10.2136/vzj2014.06.0077.

[443] J. Iwema, R. Rosolem, R. Baatz, T. Wagener, and H.R. Bogena. "Investigating temporal field sampling strategies for site-specific calibration of three soil moisture–neutron intensity parameterisation methods." In: *Hydrology and Earth System Sciences* **19**(7) (July 2015), pp. 3203–3216.
DOI: 10.5194/hess-19-3203-2015.

[444] J.M. Clem and L.I. Dorman. "Neutron Monitor Response Functions." In: *Space Science Review* **93**(1) (July 2000), pp. 335–359.
DOI: 10.1023/A:1026508915269.

[445] H. Krüger, H. Moraal, J.W. Bieber, J.M. Clem, P.A. Evenson, K.R. Pyle, M.L. Duldig, and J.E. Humble. "A calibration neutron monitor: Energy response and instrumental temperature sensitivity." In: *Journal of Geophysical Research: Space Physics* **113**(A8) (Aug. 2008). A08101.
DOI: 10.1029/2008JA013229.

[446] C. Pioch, V. Mares, and W. Rühm. "Influence of Bonner Sphere response functions above 20 MeV on unfolded neutron spectra and doses." In: *Radiation Measurements* **45**(10) (May 2010), pp. 1263–1267.
DOI: 10.1016/j.radmeas.2010.05.007.

[447] J.C. Wagner, D.E. Peplow, and S.W. Mosher. "FW-CADIS Method for Global and Regional Variance Reduction of Monte Carlo Radiation Transport Calculations." In: *Nuclear Science and Engineering* **176**(1) (Jan. 2014), pp. 37–57.
DOI: 10.13182/NSE12-33.

[448] A. Haghighat and J.C. Wagner. "Monte Carlo variance reduction with deterministic importance functions." In: *Progress in Nuclear Energy* **42**(1) (Jan. 2003), pp. 25–53.
DOI: 10.1016/S0149-1970(02)00002-1.

[449] D. Desilets. *CRS1000 and CRS1000/B User's Guide*. Report. Cosmic-Ray Soil Moisture/Snow Sensing System. Hydroinnova. Albuquerque, USA, Apr. 2013. 48 pp.
URL: http://hydroinnova.com/_downloads/CRS-1000_complete.pdf.

[450] D. McJannet, T.E. Franz, A. Hawdon, D. Boadle, B. Baker, A. Almeida, R. Silberstein, T. Lambert, and D. Desilets. "Field testing of the universal calibration function for determination of soil moisture with cosmic-ray neutrons." In: *Water Resources Research* **50**(6) (June 2014), pp. 5235–5248.
DOI: 10.1002/2014WR015513.

[451] M. ANDREASEN, H. Karsten JENSEN, M. ZREDA, D. DESILETS, H. BOGENA, and C.M. LOOMS. "Modeling cosmic ray neutron field measurements." In: *Water Resources Research* **52**(8) (2016), pp. 6451–6471.
DOI: 10.1002/2015wr018236.

[452] P. SCHATTAN, G. BARONI, S.E. OSWALD, J. SCHÖBER, C. FEY, C. KORMANN, M. HUTTENLAU, and S. ACHLEITNER. "Continuous monitoring of snowpack dynamics in alpine terrain by aboveground neutron sensing." In: *Water Resources Research* **53**(5) (May 2017), pp. 3615–3634.
DOI: 10.1002/2016WR020234.

[KS2015] M. KÖHLI, M. SCHRÖN, M. ZREDA, U. SCHMIDT, P. DIETRICH, and S. ZACHARIAS. "Footprint characteristics revised for field-scale soil moisture monitoring with cosmic-ray neutrons." In: *Water Resources Research* **51**(7) (July 2015), pp. 5772–5790.
DOI: 10.1002/2015WR017169.

[SK2017] M. SCHRÖN, M. KÖHLI, et al. "Improving Calibration and Validation of Cosmic-Ray Neutron Sensors in the Light of Spatial Sensitivity." In: *Hydrology and Earth System Sciences* **21**(10) (Oct. 2017), pp. 5009–5030.
DOI: 10.5194/hess-21-5009-2017.

[453] A. NESTERENOK. "Numerical calculations of cosmic ray cascade in the Earth's atmosphere - Results for nucleon spectra." In: *Nuclear Instruments and Methods in Physics Research B* **295** (Jan. 2013), pp. 99–106.
DOI: 10.1016/j.nimb.2012.11.005.

[454] A. NESTERENOK. personal communication. 2013.

[455] T.E. FRANZ, M. ZREDA, T.P.A. FERRÉ, and R. ROSOLEM. "An assessment of the effect of horizontal soil moisture heterogeneity on the area-average measurement of cosmic-ray neutrons." In: *Water Resources Research* **49**(10) (Oct. 2013), pp. 6450–6458.
DOI: 10.1002/wrcr.20530.

[456] Z.W. LIN, J.H. ADAMS JR., A.F. BARGHOUTY, S.D. RANDENIYA, R.K. TRIPATHI, J.W. WATTS, and P.P. YEPES. "Comparisons of several transport models in their predictions in typical space radiation environments." In: *Advances in Space Research* **49**(4) (Feb. 2012), pp. 797–806.
DOI: 10.1016/j.asr.2011.11.025.

[457] F. LEI, A. HANDS, S. CLUCAS, C. DYER, and P. TRUSCOTT. "Improvements to and Validations of the QinetiQ Atmospheric Radiation Model (QARM)." In: *IEEE Transactions on Nuclear Science* **53**(4) (Aug. 2006), pp. 1851–1858.
DOI: 10.1109/TNS.2006.880567.

[458] R.J. SHEU and S.H. JIANG. "Cosmic-ray-induced neutron spectra and effective dose rates near air/ground and air/water interfaces in Taiwan." In: *Health Physics* **84**(1) (Jan. 2003), pp. 92–99.
DOI: 10.1097/00004032-200301000-00008.

[459] K.-W. LEE, M.-C. YUAN, S.-H. JIANG, and R.-J. SHEU. "Comparing standard Bonner Spheres and high-sensitivity Bonner cylinders." In: *Radiation Protection Dosimetry* **161**(1-4) (Dec. 2014), pp. 233–236.
DOI: 10.1093/rpd/nct333.

[460] D.J. THOMAS, N.P. HAWKES, L.N. JONES, P. KOLKOWSKI, and N.J. ROBERTS. "Characterization and utilization of a Bonner Sphere set based on gold activation foils." In: *Radiation Protection Dosimetry* **126**(1–4) (May 2007), pp. 229–233.
DOI: 10.1093/rpd/ncm047.

[461] T. SATO. "Analytical Model for Estimating the Zenith Angle Dependence of Terrestrial Cosmic Ray Fluxes." In: *PLOS ONE* **11**(8) (Aug. 2016), pp. 1–22.
DOI: 10.1371/journal.pone.0160390.

[462] M. ZREDA, D. DESILETS, T.P.A. FERRÉ, and R.L. SCOTT. "Measuring soil moisture content non-invasively at intermediate spatial scale using cosmic-ray neutrons." In: *Geophysical Research Letters* **35**(21) (Nov. 2008), p. L21402.
DOI: 10.1029/2008GL035655.

[463] D. DESILETS and M. ZREDA. "Footprint diameter for a cosmic-ray soil moisture probe: Theory and Monte Carlo simulations." In: *Water Resources Research* **49**(6) (June 2013), pp. 3566–3575.
DOI: 10.1002/wrcr.20187.

[464] B.M. KUZHEVSKIJ, O.Y. NECHAEV, E.A. SIGAEVA, and V.A. ZAKHAROV. "Neutron flux variations near the Earth's crust. A possible tectonic activity detection." In: *Natural Hazards and Earth System Science* **3**(6) (Jan. 2003), pp. 637–645.
DOI: 10.5194/nhess-3-637-2003.

[465] S. GLASSTONE and M.C. EDLUND. *The Elements of Nuclear Reactor Theory*. New Jersey and New York: D. Van Nostrand Company, Nov. 1952. 416 pp.
URL: https://babel.hathitrust.org/cgi/pt?id=mdp.39015026517386;view=1up;seq=1.

[466] L.M. BARKOV, V.K. MAKARIN, and K.N. MUKHIN. "Measurement of the slowing down of neutrons in the energy range 1.46–0.025 eV in water." In: *Journal of Nuclear Energy (1954)* **4**(1) (Oct. 1957), pp. 94–102.
DOI: 10.1016/0891-3919(57)90124-9.

[467] N.E. HERTEL and J.W. DAVIDSON. "The response of Bonner Spheres to neutrons from thermal energies to 17.3 MeV." In: *Nuclear Instruments and Methods in Physics Research A* **238** (Aug. 1985), pp. 509–516.
DOI: 10.1016/0168-9002(85)90494-2.

[468] R.T. KOUZES, E.R. SICILIANO, J.H. ELY, P.E. KELLER, and R.J. MCCONN. "Passive neutron detection for interdiction of nuclear material at borders." In: *Nuclear Instruments and Methods in Physics Research Section A: Accelerators, Spectrometers, Detectors and Associated Equipment* **584**(2–3) (Jan. 2008), pp. 383–400.
DOI: 10.1016/j.nima.2007.10.026.

[469] T.E. FRANZ, M. ZREDA, T.P.A. FERRÉ, R. ROSOLEM, C. ZWECK, S. STILLMAN, X. ZENG, and W.J. SHUTTLEWORTH. "Measurement depth of the cosmic ray soil moisture probe affected by hydrogen from various sources." In: *Water Resources Research* **48**(8) (Aug. 2012).
DOI: 10.1029/2012WR011871.

[470] L.D. HENDRICK and R.D. EDGE. "Cosmic-Ray Neutrons near the Earth." In: *Physical Review* **145** (May 1966), pp. 1023–1025.
DOI: 10.1103/PhysRev.145.1023.

[471] R.C. ELPHIC, P. CHU, S. HAHN, M.R. JAMES, D.J. LAWRENCE, T.H. PRETTYMAN, J.B. JOHNSON, and R.K. PODGORNEY. "Surface and downhole prospecting tools for planetary exploration: tests of neutron and gamma ray probes." In: *Astrobiology* **8**(3) (Aug. 2008), pp. 639–652.
DOI: 10.1089/ast.2007.0163.

[472] G.W. MCKINNEY, D.J. LAWRENCE, T.H. PRETTYMAN, R.C. ELPHIC, W.C. FELDMAN, and J.J. HAGERTY. "MCNPX benchmark for cosmic ray interactions with the Moon." In: *Journal of Geophysical Research: Planets* **111**(E6) (June 2006), E06004.
DOI: 10.1029/2005JE002551.

[473] W. KORRES, T.G. REICHENAU, et al. "Spatio-temporal soil moisture patterns - A meta-analysis using plot to catchment scale data." In: *Journal of Hydrology* **520**(0) (Jan. 2015), pp. 326–341.
DOI: 10.1016/j.jhydrol.2014.11.042.

[SK2018] M. SCHRÖN, R. ROSOLEM, et al. "Cosmic-ray Neutron Rover Surveys of Field Soil Moisture and the Influence of Roads." In: *Water Resources Research* **54**(9) (May 2018), pp. 6441–6459.
DOI: 10.1029/2017WR021719.

[474] M. HENSKE, M. KLEIN, M. KÖHLI, P. LENNERT, G. MODZEL, C.J. SCHMIDT, and U. SCHMIDT. "The ^{10}B based Jalousie neutron detector: An alternative for ^{3}He filled position sensitive counter tubes." In: *Nuclear Instruments and Methods in Physics Research Section A: Accelerators, Spectrometers, Detectors and Associated Equipment* **686** (Sept. 2012), pp. 151–155.
DOI: 10.1016/j.nima.2012.05.075.

[SK2015] M. SCHRÖN, S.ZACHARIAS, M. KÖHLI, J. WEIMAR, and P. DIETRICH. "Monitoring Environmental Water with Ground Albedo Neutrons and Correction for Incoming Cosmic Rays with Neutron Monitor Data." In: *PoS Proceedings of Science* **231** (Aug. 2015). The 34$^{\text{th}}$ International Cosmic Ray Conference, pp. 101–104.
DOI: 10.1063/1.2825756.

[493] F. JAMES. *MINUIT - Function Minimization and Error Analysis*. Manual. D506. CERN. Geneva, Switzerland, Mar. 1994. 56 pp.
URL: https://root.cern.ch/sites/d35c7d8c.web.cern.ch/files/minuit.pdf.

B

ADDENDUM

B.1 | THE CASCADE DETECTOR

B.1.1 | DETECTOR COMPONENTS

The active detection volume is composed of a stack of modules. Each of them consists of the GEM or Grid glued into a double sided frame. The modules themselves are placed in a stack with teflon spacers in between each other. The whole detector consists of two half spacings, which are separated by the double-sided crossed-stripes readout. The readout and the individual GEM channels are connected to the high voltage board, which hosts the voltage divider and connects to the multichannel amplifiers ASICs. Fig. 160 shows the actual setup of the active detection volume of the CASCADE detector with the old high voltage board and Fig. 161 presents the readout unit, which is connected to the GEM stack from below.

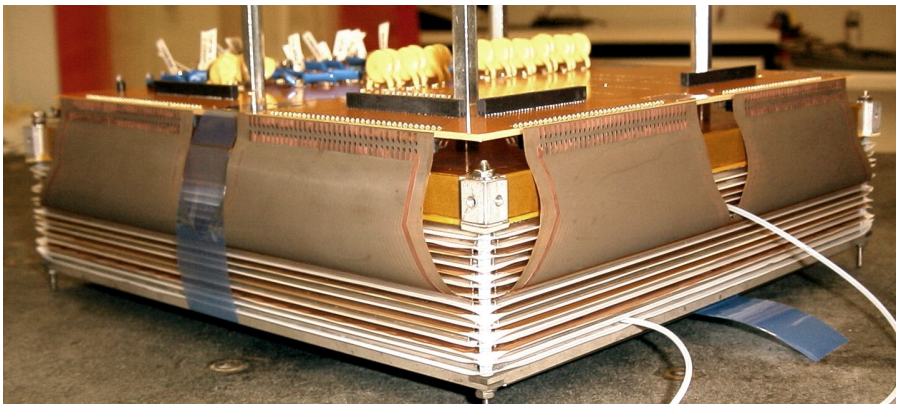

Figure 160: Photography by M. Henske of the active detection volume of the CASCADE detector with the old high voltage distributor board. Six GEMs are stacked in between both drift cathodes. The readout board sits in between both half-spaces and is connected to the high voltage board.

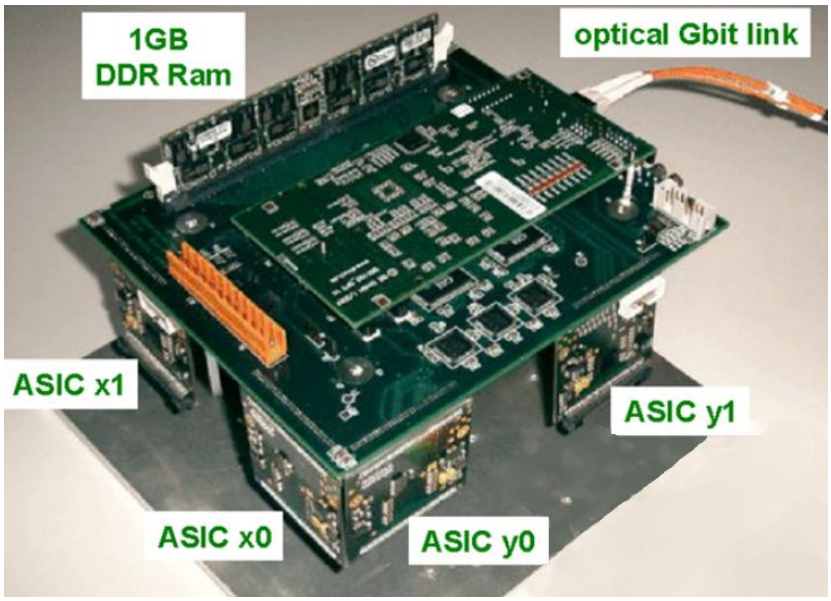

Figure 161: Photography of the readout unit [323], which consists of the main FPG board, additionally the ADC card and the data link. The four visible CIPix ASICS are connected to the readout structure of the active detection unit. The T-GEM channel CIPix is mounted opposite on the rear side.

The following tab. 25 presents the measured individual positions of the frames within the stack. For each assembled module the height has been measured at four positions (H 1 to H 4). As the modules due to mechanical stress are not entirely flat and only finally clamped together the total height of the stack has been measured after the assembly. The inter-module spaces have been determined by subtracting the sum of the average heights from the total stack height and then dividing by the number of teflon spacers. This yields a result of 0.27 mm. The important positions of then Boron layers finally are determined by the distance to the top drift cathode by adding up half a module and the corresponding spacer.

Table 25: Geometry of the active detection volume with the thickness of each module measured on all four corners (H 1 to H 4) and averaged. By including the teflon spacer the center position in the stack can be derived.

	Distances (mm)						
Element	H 1	H 2	H 3	H 4	H Mean	Position	Height
Drift Top	2.23	2.23	2.24	2.21	2.2275	1.11	2.23
						2.49	0.27
GEM 1	2.05	2.08	2.07	2.07	2.0675	3.53	2.07
						4.83	0.27
Grid	2.12	2.15	2.16	2.15	2.145	5.90	2.15
						7.24	0.27
GEM 2	2.16	2.14	2.19	2.24	2.1825	8.33	2.18
						9.69	0.27
Grid	2.13	2.14	2.14	2.13	2.135	10.76	2.14
						12.09	0.27
GEM 3	2.2	2.1	2.09	2.15	2.135	13.16	2.14
						14.49	0.27
Readout	1.95	1.9	2	1.88	1.9325	15.46	1.93
						16.69	0.27
GEM 4	2.12	2.1	2.13	2.1	2.1125	17.75	2.11
						19.07	0.27
Grid	2.19	2.2	2.21	2.21	2.2025	20.17	2.20
						21.54	0.27
GEM 5	2.17	2.14	2.13	2.13	2.1425	22.61	2.14
						23.95	0.27
Grid	2.2	2.2	2.2	2.19	2.1975	25.05	2.20
						26.41	0.27
GEM 6	2.15	2.14	2.14	2.13	2.14	27.48	2.14
						28.82	0.27
Drift Bottom	2.1	2.1	2.1	2.1	2.1	29.87	2.10
Sum	27.77	27.62	27.8	27.69	27.72		
Stack Total						31.5	

In the course of this work, the high voltage board had to be redesigned in order to improve the signal decoupling and avoid crosstalk between GEM channels. The corresponding analysis, which lead to an optimized electrical configuration, is presented in sec. 10.2. Fig. 162 shows the total board layout with all layers. GEMs are connected to the right side along the voltage divider and the signal decoupling to the T-GEM CIPix can be selected by a multiplexer. The design furthermore already foresees to supply a detector stack of up to ten layers.

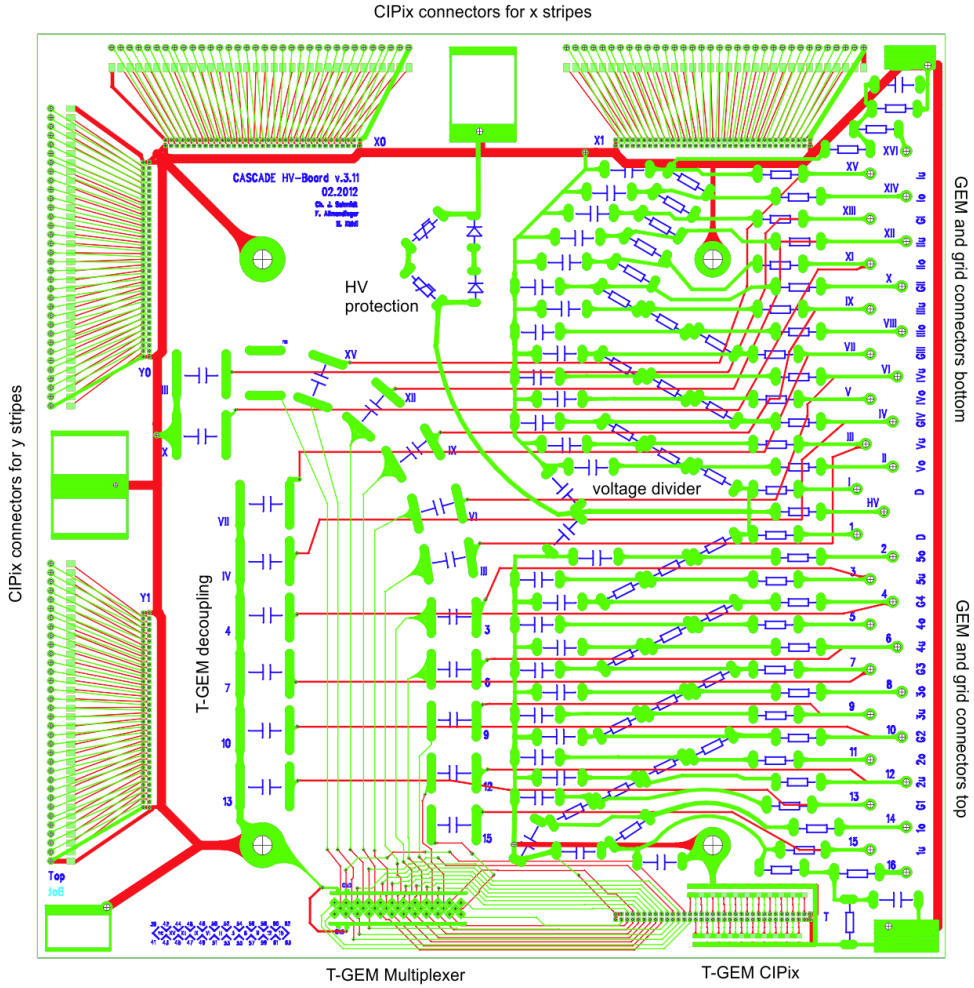

Figure 162: Redesigned high voltage distributor board v3.11. The voltage divider (right part, slanted resistors) with spark protection (right part, horizontal resistors) allows for up to five layers of GEMs and grids in two half-spaces. Each grid is decoupled by a ground capacity and each GEM is read read out via a capacitor which is connected to the T-GEM CIPix ASIC connector. The multiplexer (lower left) allows for choosing up to four CIPix pins in case of dead channels. The four CIPix connectors for x and y are fed through. Annotations in black are not part of the layout.

B.1.4 | GEM TENSION AND FRAMING

Since [336] the fiberglass frames for the GEMs have been replaced by stainless steel frames[a]. The idea was to replace the standard GEM fabrication procedure, which requires a stretching tool, by a self stretching frame. A slab of length L, fixed at both ends, to which a uniform force F is applied, follows the function

$$W(x) = -\frac{FL^4}{2Ehb^3}\left(\frac{x}{L} - 2\left(\frac{x}{L}\right)^3 + \left(\frac{x}{L}\right)^4\right), \tag{186}$$

with the Young[b] modulus E, width b and height h of the slab. If the slab is shaped with a curvature following this function and by application of force brought back to a rectangular form and glued onto a GEM, it will inversely create a uniform tension along the line. The use of this principle showed good results for the sides of the frame, however, as (186) requires a line element with fixed end points, the corners of the stainless steel frames are not experiencing any tension. Therefore, the diagonals of the GEMs are not stretched at all. This leads, as Fig. 163 shows, to drapes orthogonally to the diagonals.

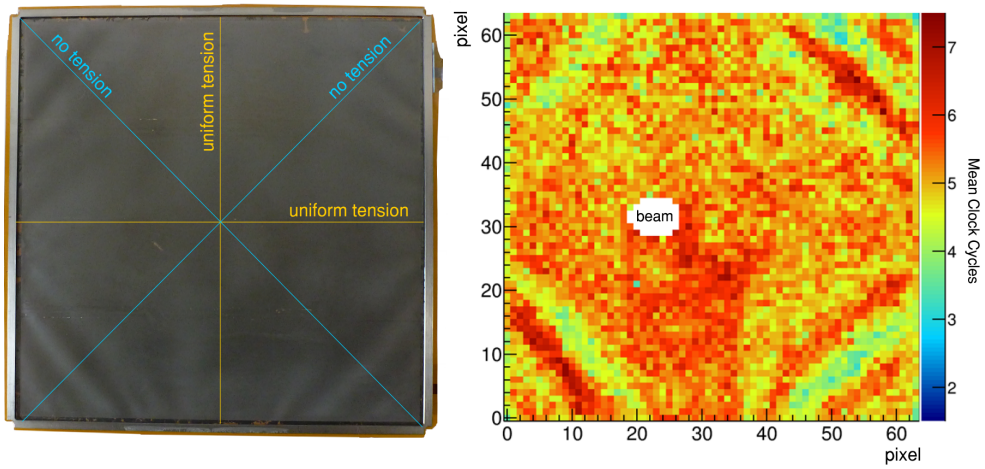

Figure 163: Example of tension wrinkles on a boron coated 10 cm × 10 cm GEM (left) [341] and its impact on the effective gas gain (right) depicted by the mean clock cycles per event measured on the respective T-GEM channel, see also sec. 10.3.3. The prestrained framing applies a uniform tension orthogonally to the frame borders. This, however, leads to the no tension force along the diagonals causing the folding of the material.

B.1.5 | SPICE SIMULATION

The SPICE simulation in sec. 10.2 was used to reduce the crosstalk between GEM layers by optimizing the RC network. By injecting a charge of 1 fC, the pulse heights at different points of the circuit were studied by measuring the response with a VV50, which was also modeled in SPICE and showed a comparable performance to the CIPix with respect to the relative signal amplitudes. The respective signal shapes are displayed in Fig. 164 exemplarily for a benchmark with different series input resistors.

[a] The same principle is also applied to the slabs, which are used to clamp the entire GEM stack.
[b] Thomas YOUNG, *1773-†1829, England.

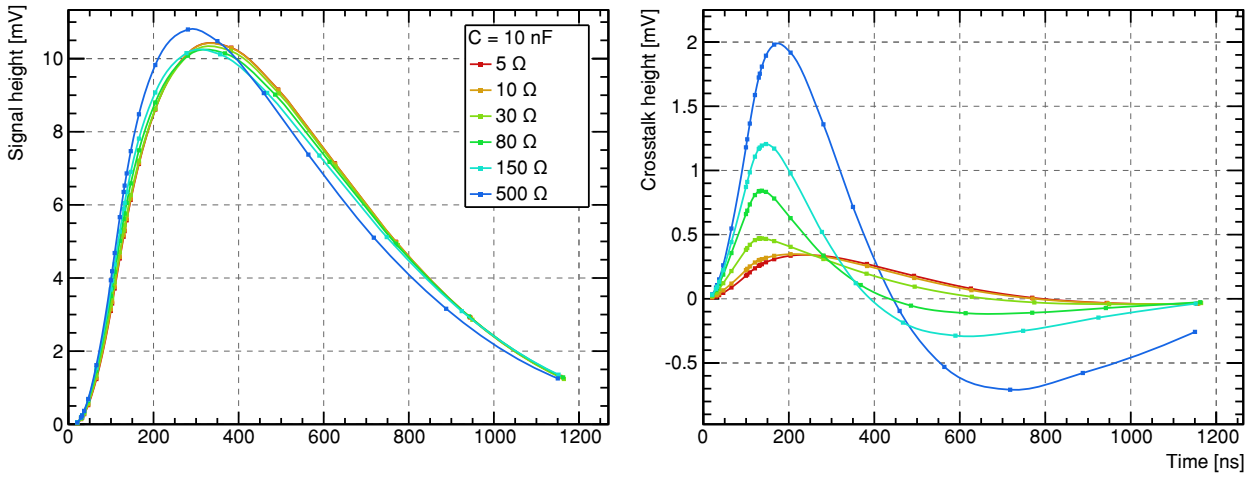

Figure 164: Pulse shapes for signal (left) and crosstalk (right) for the SPICE simulation presented in sec. 10.2. A simulated charge is injected into the resistor and capacitor network at one GEM and measured at the same time at another GEM with a decoupling grid connected to ground by capacity C. In both cases the signal is amplified by a model of a VV50, see [342], with an input resistor in series.

B.1.6 | Events with lacking T-GEM channels

The voltage scan, which is presented in sec. 10.3.2, revealed, that there is a low percentage of events, which are lacking the T-GEM channel information due to the much higher effective sensitivity of the crossed stripes readout. In order to analyze the reason for those not fully reconstructed events, the deposited energy in form of the geometric track size seen by the readout is studied. The unit of this footprint A_{2D} is

$$A_{2D} = \sum_{i} X_i \cdot T_{X_i}, \tag{187}$$

with the hit stripes X_i and the signal duration in active time slices T_{X_i}. Fig. 165 shows, that those events with lacking T-GEM channel are mainly originating from geometrically small projections. Such are very short tracks and therefore low energy deposition, see sec. 6.5.2 and sec. 11.1.3. This strongly indicates, that the main reason for the incomplete event information is the mismatch in sensitivity of the crossed-stripes and the GEM readout structure.

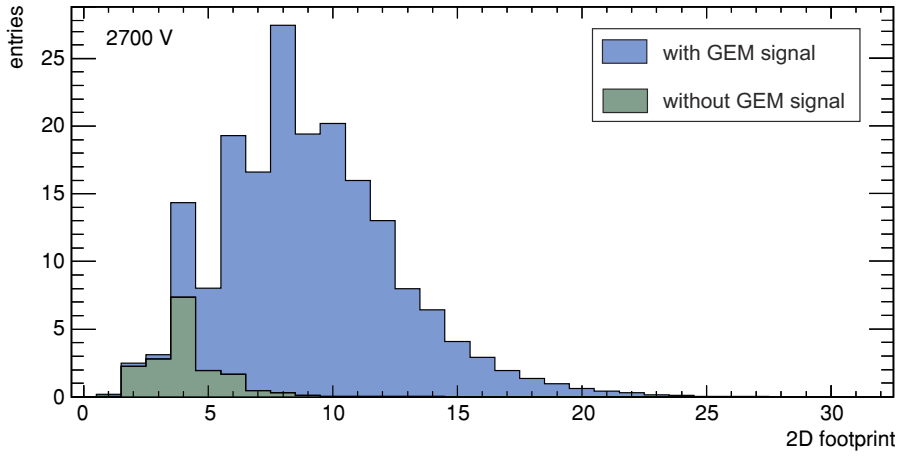

Figure 165: For an exemplary voltage with an average gas gain the footprint of events with GEM information (blue) is compared to those lacking the GEM signals (green). The footprint is in units of active channels times time slices above threshold.

In addition to the data presented in Fig. 82 in sec. 10.3.3, the event length distributions of two further voltages are shown here in Fig. 166. For very low gas amplifications, as seen in the top panels, a significant amount of events stays undetected with the T-GEM channel distributions being close to zero. For very large gas gains, as presented in the lower panels, especially long events can occur if the charge gets amplified more than once. The nature of this double peak structure is not fully understood. Those events also increase the dead time and limit the rate capability. The other half space, which is not shown here, does not exhibit a qualitative difference to the data of GEM 1 to 3.

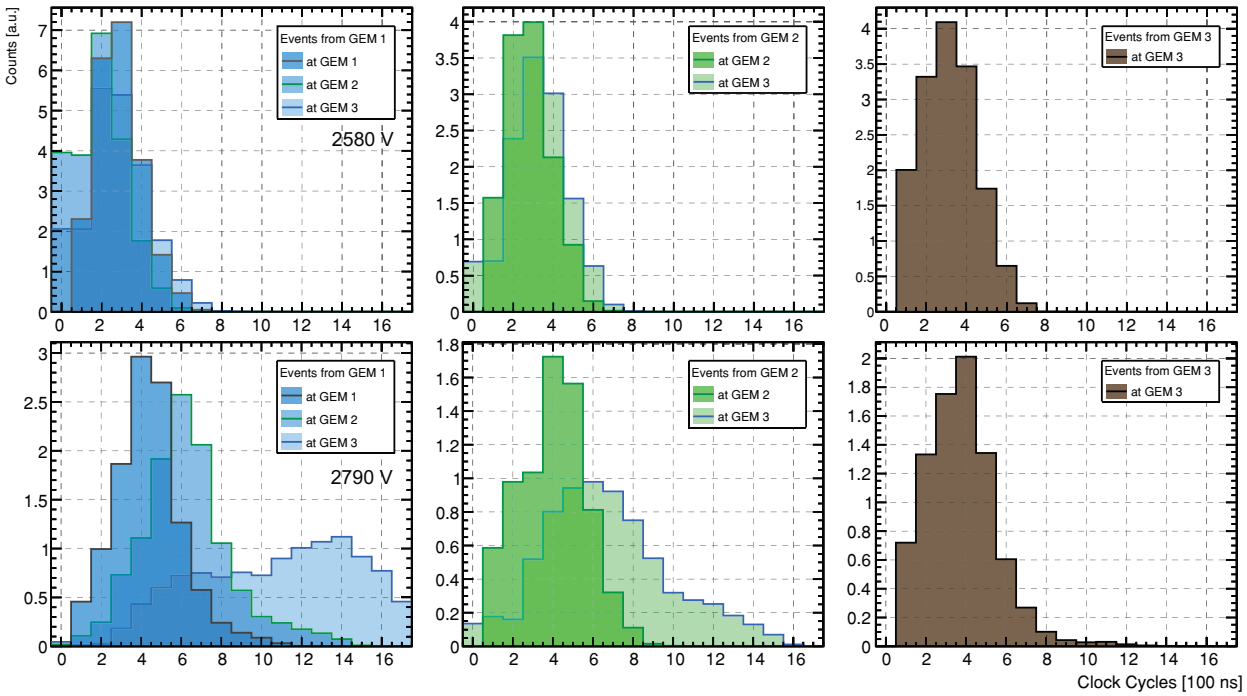

Figure 166: Event length distributions in clock cycles of 100 ns (CLK) for the top half space of the detector for two different voltages. In the left panel the CLK distribution is shown for events originating from GEM 1. Their duration measured on GEM 1 (dark outline) is approx. 4 cycles. On GEM 2 the length is slightly increased, whereas on GEM 3 the distribution is much longer. A similar pattern can be seen for events from GEM 2 in the middle panel. However, the distribution of conversions from GEM 2 at GEM 2 has a lower mean value.

The pinhole experiment of sec. 10.3.6 was used to quantify the misidentification rate as a function of gas gain. Fig. 91 summarized the relative contribution to each signal channel from different layers. Here, Fig. 167 shows the absolute distribution of events, which is the direct result of the fits as presented in Fig. 90. In addition to the assignment of wrong channel, in terms of absolute numbers the possibility of a signal to be not detected at all is to be taken into account additionally. These are classified as „no GEM“. The total count rate, to which the rate fractions presented here refer to, was evaluated by the maximum count rate and therefore also the maximum count rate of each layer. Approximately (5-20) % of the events are lacking a GEM information. Those events with 2D information only can be quantified by an additional fit from the data of the readout structure, but not directly assigned to a conversion layer. The „no GEM“ events were then distributed among the layers according to the relative intensity of the corresponding spots. This procedure can be considered as a first order correction. As the overall background in the region of interest does not necessarily have to be of the same wavelength as the beam spot, the signal-to-background distribution within the layers is slightly different. However, as the „no GEM“ events are a smaller subset of the measured total signals, a second order correction of their distribution according to the evaluation of sec. 10.3.6 would not significantly alter the result.

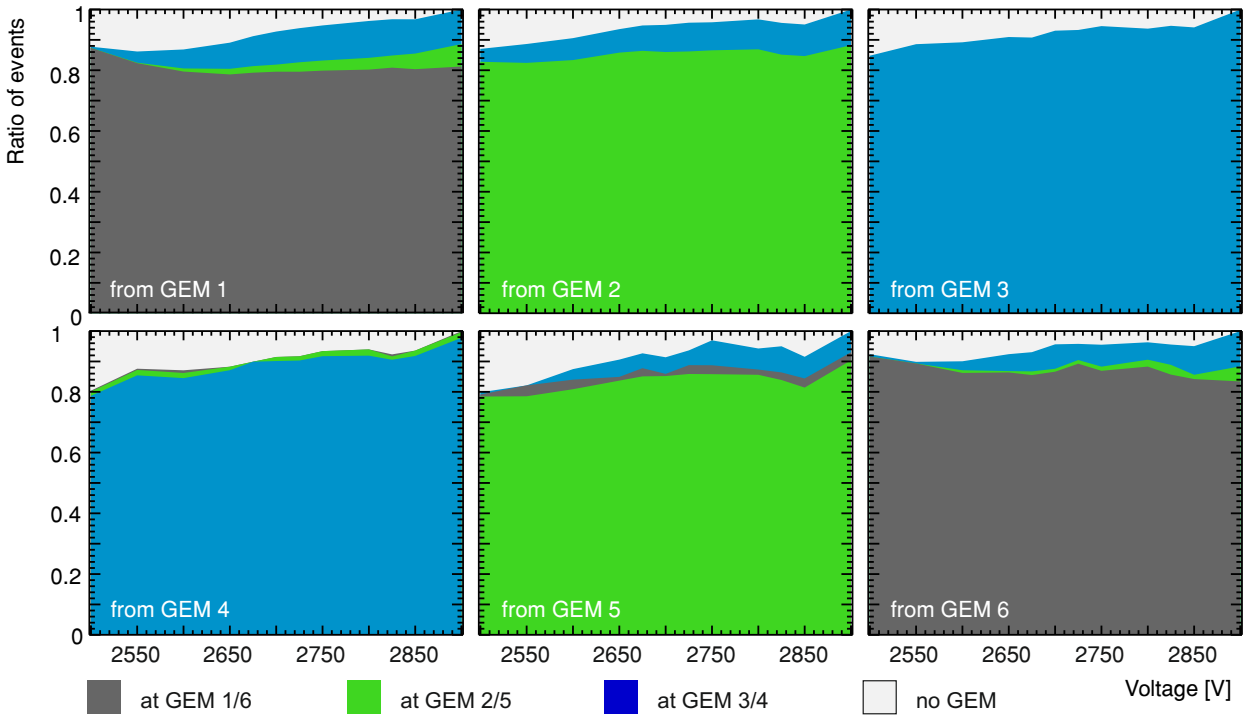

Figure 167: Experimental result of the signal distribution of the T-GEM layer identification for the pinhole measurement in sec. 10.3.6 as a function of detector voltage. Events can either be assigned to the wrong GEM below towards the readout if not detected at the original conversion layer or signal crosstalk leads to a wrong assignment to the GEM above. The signal distribution describes the absolute contamination of each layer by events originating not from it and depends on the absolute intensity distribution among the layers and therefore the selected wavelength, which was 5.4 Å in this experiment.

The full data set for the wavelength calibration, see sec. 11.2.1 is presented in Fig. 168.

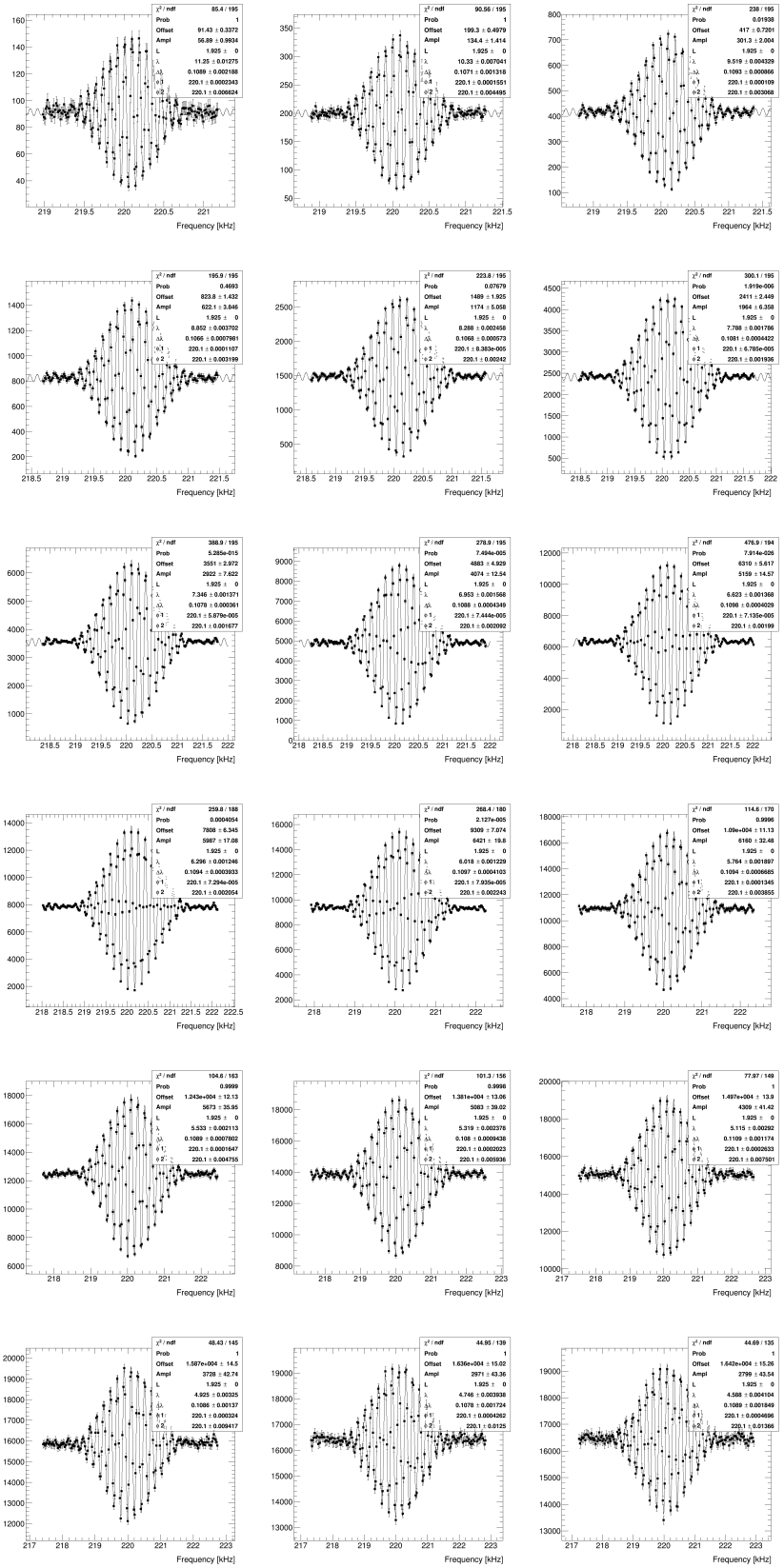

Figure 168: Augenstein-Plot of Spin Echo curves for the wavelength calibration of the velocity selector in the range (11,000-28,000) rpm and fit of (153).

B.2 | URANOS Monte Carlo simulation

B.2.1 | Geometrical calculations

The following calculations are based on the mixed geometry definition of cartesian support and spherical direction vectors

$$\vec{x} = \begin{pmatrix} x \\ y \\ z \end{pmatrix} \quad \text{and} \quad \vec{r} = \begin{pmatrix} r \\ \vartheta \\ \phi \end{pmatrix}.$$

B.2.1.1 Distance to a vertical line

Assuming a vertical line L through point $\vec{P} = (x_P, y_P, z_P)$ one can define regarding $\vec{x}$ the following quantities

$$\begin{aligned} n_x &= \sin(\vartheta)\sin(\phi), \\ n_y &= -\sin(\vartheta)\cos(\phi) \end{aligned} \tag{188}$$

and hence the distance to the line d_L is calculated by

$$d_L = \frac{\|(x - x_P)n_x + (y - y_P)n_y\|}{\sqrt{n_x^2 + n_y^2}}. \tag{189}$$

B.2.1.2 Distance to a point

Assuming the point $\vec{P}$ has the coordinates (x_P, y_P, z_P) one can define regarding $\vec{x}$ the following quantities

$$\begin{aligned} g_x &= \sin(\vartheta)\cos(\phi), \\ g_y &= \sin(\vartheta)\sin(\phi), \\ g_z &= \cos(\vartheta), \\ k_{rx} &= g_y(z - z_P) - g_z(y - y_P), \\ k_{ry} &= g_z(x - x_P) - g_x(z - z_P), \\ k_{rz} &= g_x(y - y_P) - g_y(x - x_P), \end{aligned} \tag{190}$$

and hence the distance to the point d_P is calculated by

$$d_P = \frac{\sqrt{k_{rx}^2 + k_{ry}^2 + k_{rz}}}{\sqrt{g_x^2 + g_y^2 + g_z^2}}. \tag{191}$$

The database of URANOS materials relies on a library of predefined elements. Such are described by ENDF cards, which are extracted from the existing sources mentioned in chapter 5.1.4 and stored individually. The following tab. 26 is a comprehensive list of isotopes, which have been selected and implemented.

Table 26: Available isotopes in URANOS and cross sections used, identifiers according to [99] and chapter 5.1.4.1.

Isotope	Elastic	Inelastic	Absorption and others
^{1}H	MT=2 (MF=3, 4)	n/A	MT=5, 102, 208-210
^{3}He	MT=2 (MF=3, 4)	n/A	MT=102, 103, 104
^{10}B	MT=2 (MF=3, 4)	MT=51-54	MT=107
^{11}B	MT=2 (MF=3, 4)	MT=51-54	MT=107
^{12}C	MT=2 (MF=3, 4)	MT=51-58	MT=5, 102, 103, 107
^{14}N	MT=2 (MF=3, 4)	MT=51-60	MT=5, 102-108, 208-210
^{16}O	MT=2 (MF=3, 4)	MT=51-70	MT=5, 102, 103, 105, 107, 208-210
^{19}F	MT=2 (MF=3, 4)	MT=51-54	MT=102, 103, 107
^{23}Na	MT=2 (MF=3, 4)	MT=51-56	MT=5, 102, 103, 107
^{27}Al	MT=2 (MF=3, 4)	MT=51-58	MT=5, 102, 103, 107, 208-210
^{28}Si	MT=2 (MF=3, 4)	MT=51-58	MT=5, 102, 103, 107, 208-210
^{32}S	MT=2 (MF=3, 4)	MT=51-55	MT=5, 102, 103, 107
^{35}Cl	MT=2 (MF=3, 4)	MT=51-56	MT=5, 102, 103, 107
^{40}Ar	MT=2 (MF=3, 4)	MT=51-55	MT=5, 102, 103, 107, 208-210
^{52}Cr	MT=2 (MF=3, 4)	MT=51-55	MT=5, 102, 103, 107
^{53}Cr	MT=2 (MF=3, 4)	MT=51-55	MT=5, 102, 103, 107
^{56}Fe	MT=2 (MF=3, 4)	MT=51-58	MT=5, 102, 103, 107, 208-210
^{58}Ni	MT=2 (MF=3, 4)	MT=51-54	MT=5, 102, 103, 107
^{63}Cu	MT=2 (MF=3, 4)	-	MT=102
^{65}Cu	MT=2 (MF=3, 4)	-	MT=102
^{155}Gd	MT=2 (MF=3, 4)	MT=51-54	MT=102
^{157}Gd	MT=2 (MF=3, 4)	MT=51-54	MT=102

URANOS provides a list of already predefined materials, which are combinations of elements described in section B.2.2. Tab. 27 summarizes all available compositions which are implemented as materials.

Table 27: List of preconfigured materials available in URANOS with their composition and density.

Material	Density	Description
Helium	0.125 kg/m^3	^{3}He enriched gas
Boron	2.34 g/cm^3	97 % ^{10}B enriched
Boron natural	2.46 g/cm^3	80.1 % ^{10}B, 19.9 % ^{11}B
Boron carbide	2.42 g/cm^3	^{10}B enriched B_4C
Boron carbide	2.51 g/cm^3	B_4C with natural boron
Boron trifluoride	2.76 kg/m^3	^{10}B enriched BF_3 gas
Methane	0.656 kg/m^3	CH_4 gas
Detector gas	1.8 kg/m^3	$ArCO_2$ gas (70:30, 80:20)
Aluminum	2.66 g/cm^3	
Aluminum oxide	3.94 g/cm^3	Al_2O_3
Iron	7.87 g/cm^3	
Steel (304L)	8.03 g/cm^3	with 72 % ^{56}Fe, 16.34 % ^{52}Cr, 2.66 % ^{53}Cr, 9 % ^{58}Ni
Copper	8.94 g/cm^3	
Salt	2.16 g/cm^3	
Gadolinium oxide	7.41 g/cm^3	Gd_2O_3 with 14.8 % ^{155}Gd, 15.65 % ^{157}Gd
Polyethylene	0.95 g/cm^3	HDPE, CH_2
PE boronated	0.95 g/cm^3	HDPE with 3 % natural boron
Polyimide	1.43 g/cm^3	$C_{22}H_{10}N_2O_5$
Quartz	2.5 g/cm^3	SiO_2
Stones	1.43 g/cm^3	75 % SiO_2, 25 % Al_2O_3
Water	1.0 g/cm^3	H_2O
Soil	>1.43 g/cm^3	50 % stones, (0-50) % water
Air	1.2 kg/m^3	78 % N_2, 21 % O_2, 1 % Ar
Concrete	2.0 g/cm^3	50 % stones, 10 % water
Cat litter	1.1 g/cm^3	44 % H, 44 % O, 12 % Si
Asphalt pavement	2.58 g/cm^3	14 % H, 50 % O, 11 % C, 25 % Si
Plants	>2.2 kg/m^3	14 % H, 72 % O, 14 % C, plus air
Wood	0.5 g/cm^3	like plants
Snow new	0.03 g/cm^3	like water
Snow old	0.3 g/cm^3	like water
Ice	0.85 g/cm^3	like water

The parameters for (68), (69) and (70) in sec. 3.2 published in [66] are the following:

$$
\begin{aligned}
a_1(r_c) &= 12.9 + \frac{15.7}{1+\exp\left(\frac{r_c-5.62}{1.79}\right)},\\
a_2(r_c) &= 0.00706 + \frac{0.00057}{1+\exp\left(\frac{r_c-5.99}{1.94}\right)},\\
a_3(r_c) &= 0.975 - \frac{0.210}{1+\exp\left(\frac{r_c-0.99}{2.24}\right)},\\
a_4(r_c) &= 0.0084 + \frac{0.00441}{1+\exp\left(\frac{r_c-2.24}{2.66}\right)},\\
a_5(r_c) &= -0.00701 + \frac{0.0258}{1+\exp\left(\frac{r_c-10.9}{2.38}\right)},\\
a_9(r_c) &= 642 + \frac{189}{1+\exp\left(\frac{r_c-2.32}{0.897}\right)},\\
a_{10}(r_c) &= 0.00112 + \frac{0.000181}{1+\exp\left(\frac{r_c-8.84}{0.587}\right)},\\
a_{11}(r_c) &= 1.26 + \frac{0.958}{1+\exp\left(\frac{r_c-3.18}{1.47}\right)},\\
c_4(d) &= a_5(r_c) + \frac{0.000171d}{1+0.53\exp\left(0.00136d\right)},\\
c_{12}(d) &= a_9(r_c)\exp\left(-a_{10}(r_c)d\right) + a_{11}(r_c)\exp\left(-0.0133d\right),\\
g_3(w) &= -25.2 + \frac{2.73}{w+0.0715},\\
g_5(w) &= 0.348 + 3.35w - 1.57w^2.
\end{aligned}
\tag{192}
$$

In the original publication [66] $g_3(w)$ has been denoted as a multiplication, but it is supposed to be a sum like presented above.

B.2.5.1 DETECTOR VOXEL MODELS

In sec. 13 the efficiency of commonly used detectors for CRNS has been calculated as well as their angular sensitivity. The evaluation was carried out for each face individually, see also Fig. 127. The rover model has been presented in the respective chapter, e.g. Fig. 125, therefore here the other two types are shown.
The CRS1000 consists of a 400 mm × 100 mm × 100 mm polyethylene casing with a wall thickness of 25 mm. It encloses a stainless steel proportional counter tube with a wall thickness of 2 mm filled with 1.5 bar of helium-3. For reasons of simplicity the tube has been modeled in rectangular shape and the gas pressure was scaled by $\pi/4$.
The CRS1000/B consists of a cylindrical polyethylene casing of 25 mm width at a diameter of 104 mm and a length of 900 mm. It encloses an 850 mm long stainless steel proportional counter tube with a wall thickness of 2 mm filled with 0.5 bar of BF_3. For the material definitions see appendix B.2.3.

Figure 169: Cross sections of the detector models for the CRS1000 (bottom) and 1000/B (top) detectors with their proportional counter tube (1) ion a stainless steel housing (2), surrounded by a polyethylene moderator. The grayscale pictures are the actual geometry input files.

B.2.5.2 ANGULAR DEPENDENCE

The angular sensitivity component of the response function (170) is shown in Fig. 170, averaged over all energies and the detector face area. The angle $\vartheta = 0$ is oriented perpendicular to the respective surface and efficiencies are normalized to $g(\vartheta = 0) = 1$.

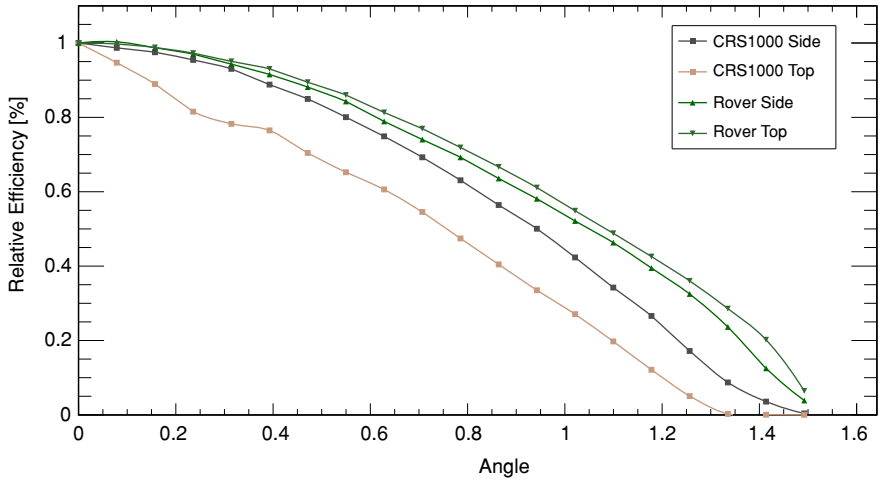

Figure 170: Relative counting efficiency for some selected detector models and faces as a function of inclination angle of the incoming flux representing the angular term of (170). [KS2018]

The detectors show lowest sensitivity to neutrons from directions parallel to the surface, as for slant angles ($\vartheta = \pi/2$ or 90°) the probability of detection drops to zero. Highest

sensitivity for all detectors is achieved for orthogonal incidence with $\vartheta = 0$. This result stresses the importance of accounting for neutron fluxes directly from atmospheric cosmic rays and directly from beneath the sensor. An analytical approximation for the angular distribution of the large faces can be given as:

$$g(\vartheta) = 1.24 - 0.254 \exp(1.087\,\vartheta)\,. \tag{193}$$

Yet, for the CRS1000 top face a linear model is sufficient. Like discussed above, the geometric arrangement of the moderator has a minor influence on the response function. For energies in the epithermal to fast regime the angular response does not change significantly.

B.2.6 | Simulation of the neutron source room

A simplified version of the radiation environment of the neutron source within its room has been simulated by URANOS. The room, which is sketched in Fig. 171, consists of the following elements, see also the material compendium in appendix B.2.3: air with 5 g/m^3 humidity, concrete floor, walls and ceiling, two aluminum tables with boronated rubber mats and vertical polyethylene absorbers covered by boronated rubber mats, one wooden table, a fused silica window, wooden and steal doors. The source itself consists of a large block of boronated and non-boronated polyethylene. Beamport A is open. At its inner center face, which is the moderator of the californium source, a moderated spectrum (159), based on simulations by U. Schmidt, is released in port direction into 2π. A more detailed description of the simulations and the source buildup can also be found in [394].

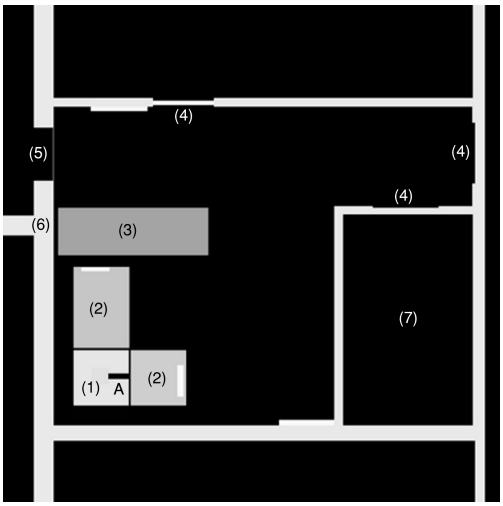

Figure 171: Setup for the source room simulation: (1) Moderated shielded source with spectrum (159) through beamport A, (2) aluminium tables with boron rubber mat covers and vertical absorbers, (3) wooden table, (4) doors, (5) window, (6) concrete wall and (7) isotope storage room.

The goal was to analyze whether an additional thermal shielding on the outside of the source buildup would reduce the background for measurements. The result of this simulation is, that covering the source by an additional absorber has no significant influence on the overall thermal neutron background. The reason can be easily identified in Fig. 172. The background, which can be measured for experimental setups on the tables (2), is not due to neutrons leaking out of the source, but rather originates from the fast neutron, which are scattered within the room and thermalize elsewhere. As the source partly consists of boronated polyethylene, there is no direct contribution from thermal neutrons coming from the source moderator, but instead from all other objects in the room. In that case, the best background suppression can be achieved by placing

the detector as far as possible from any large object. However, the example here is only for qualitative evaluation of the radiation background in the source room.

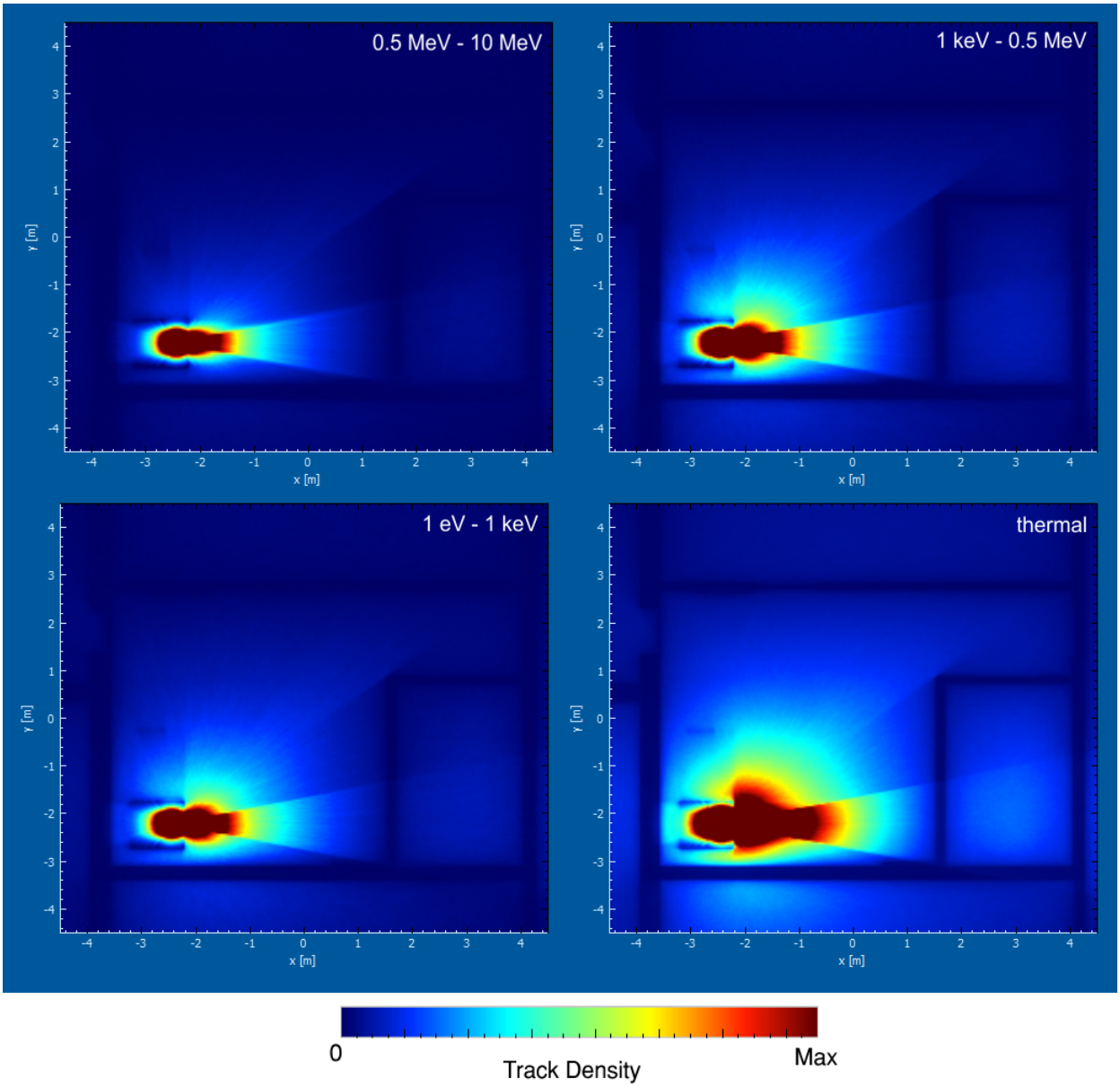

Figure 172: URANOS simulation of the radiation environment in the room of the neutron source with one beamport open for four different energy ranges (scaled relatively to the respective maximum). The source spectrum is modeled by a modified Westcott function (159). The track density is displayed only in air and integrated over the room height.

B.3.1 | Modeling the footprint

In sec. 14.2.3 the footprint weighting function has been introduced and characterized as a sum of exponential functions. This section describes more in detail the procedure to find the analytical relation (181) by the following steps: For all data sets the F_i coefficients of W_r and the intensity I_0 were plotted as a function of soil moisture. Then, for each F_i an individual function with a minimal set of parameters was constructed. One result is exemplarily shown in Fig. 174 for $h = 10\,\mathrm{g/m^3}$. Although some parameters have a physical meaning, in general it should be regarded as an empirical model to mathematically model the range distribution. Then the procedure was repeated for all air humidities and the functional dependency on that variable was studied. However, as previously mentioned, the scaling of the weighting function is not independent of the different water pools. Hence, only a multivariate fit in the θ, h-space can cope with the problem. Such a plot with the correlated soil moisture and air humidity representation is exemplarily shown for the far-field terms in Fig. 176 for I_0 and Fig. 177 for the parameters of the weighting function.

In order to validate the functional dependencies, all range distribution histograms were fitted by $I_0 \cdot W_r$ (181). The fitted exponential functions, shown exemplarily in Fig. 173, agree well with the data from the transport modeling. As mentioned above, at around 50 m the analytical description starts to deviate from the data (right panel), which is especially visible for the top curve, that describes the practically not relevant case of 0 % soil moisture. For this reason the value of 50 m has been chosen as a delimiter for both regimes. Although the above described functional dependency of W_r has mainly been motivated from the far-field transport theory, the agreement in the near-field with the model data is also very good.

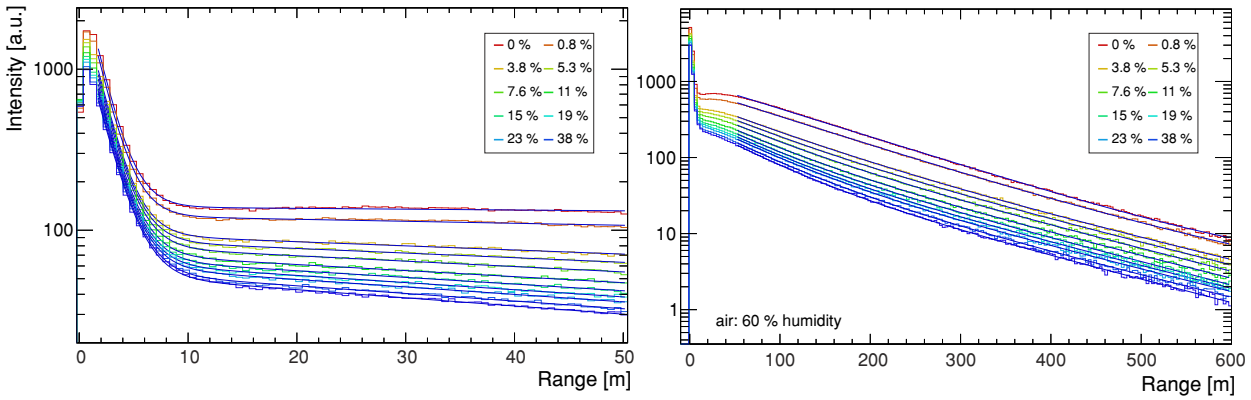

Figure 173: Range distribution histograms and fitted exponential functions according to (181) in the near-field (left) and the far-field regime (right).

For some dependencies a linear correlation between both observables can be assumed, but in most cases more complicated relations have to be used. In general, the goal was set to reduce the amount of free parameters as much as possible - although the fit could still be improved by adding polynomials of arbitrary order, the choice was to keep the congruency of the model and data integrals to yield an error not larger than 5 m on the quantile, especially Q_{86}.

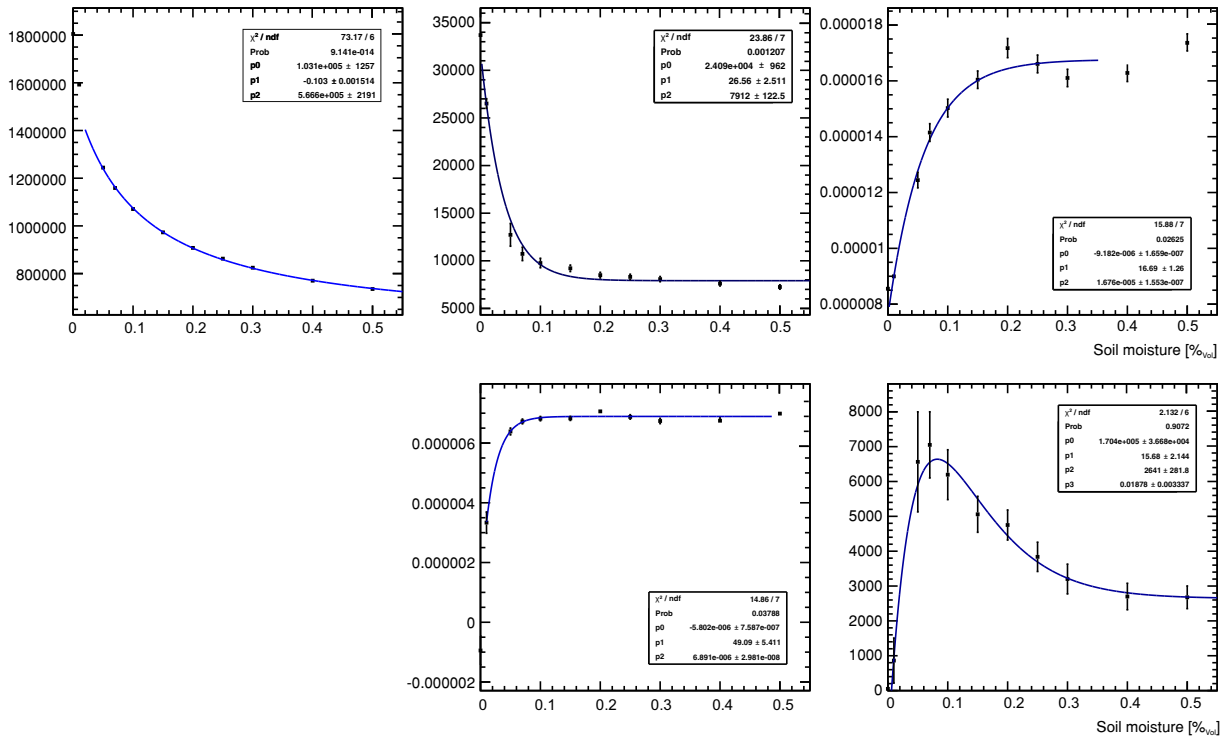

Figure 174: Parameters from the fits for the far-field term of (181) (black dots with statistical errors) for $h = 10\,\mathrm{g/m^3}$. From the top left to the lower right panel: I_0, F_5, F_6, F_7 and F_8. To each set, plotted here depending on soil moisture, the functions (194) are fitted.

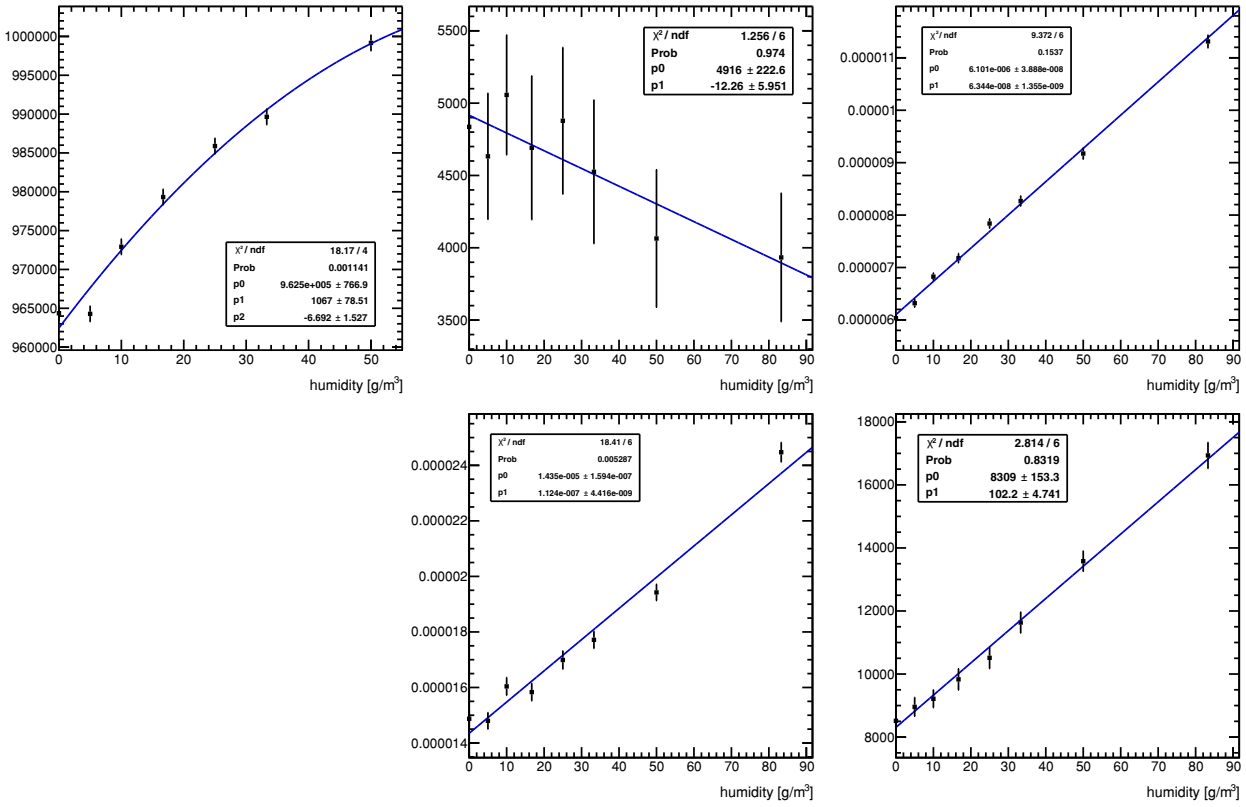

Figure 175: Parameters from the fits for the far-field term of (181) (black dots with statistical errors) for $\theta = 11\,\%$. From the top left to the lower right panel: I_0, F_5, F_6, F_7 and F_8. To each set, plotted here depending on air humidity, the functions (194) are fitted.

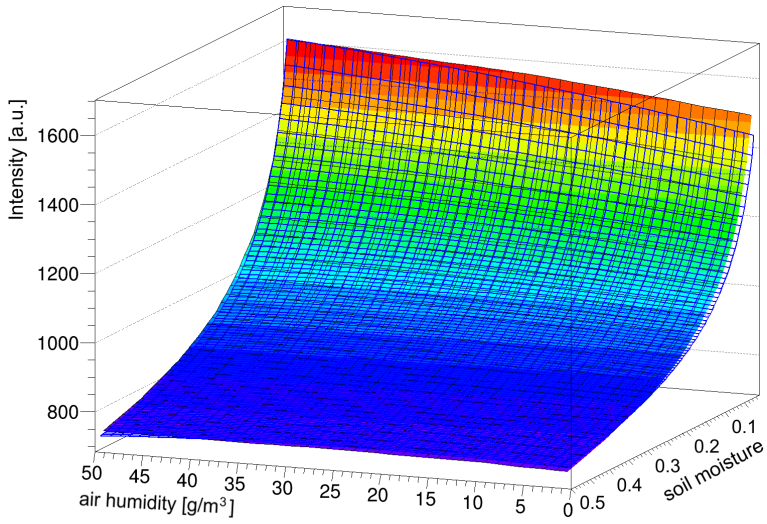

Figure 176: Fitting of the footprint parameters: Intensity I_0 in (181) as a function of volumetric soil moisture fractions and air humidity. The colored hypersurface represents the interpolation of the results from the parameter fits of the range distribution function like in Fig. 174, the grid (blue) represents the modeled function.

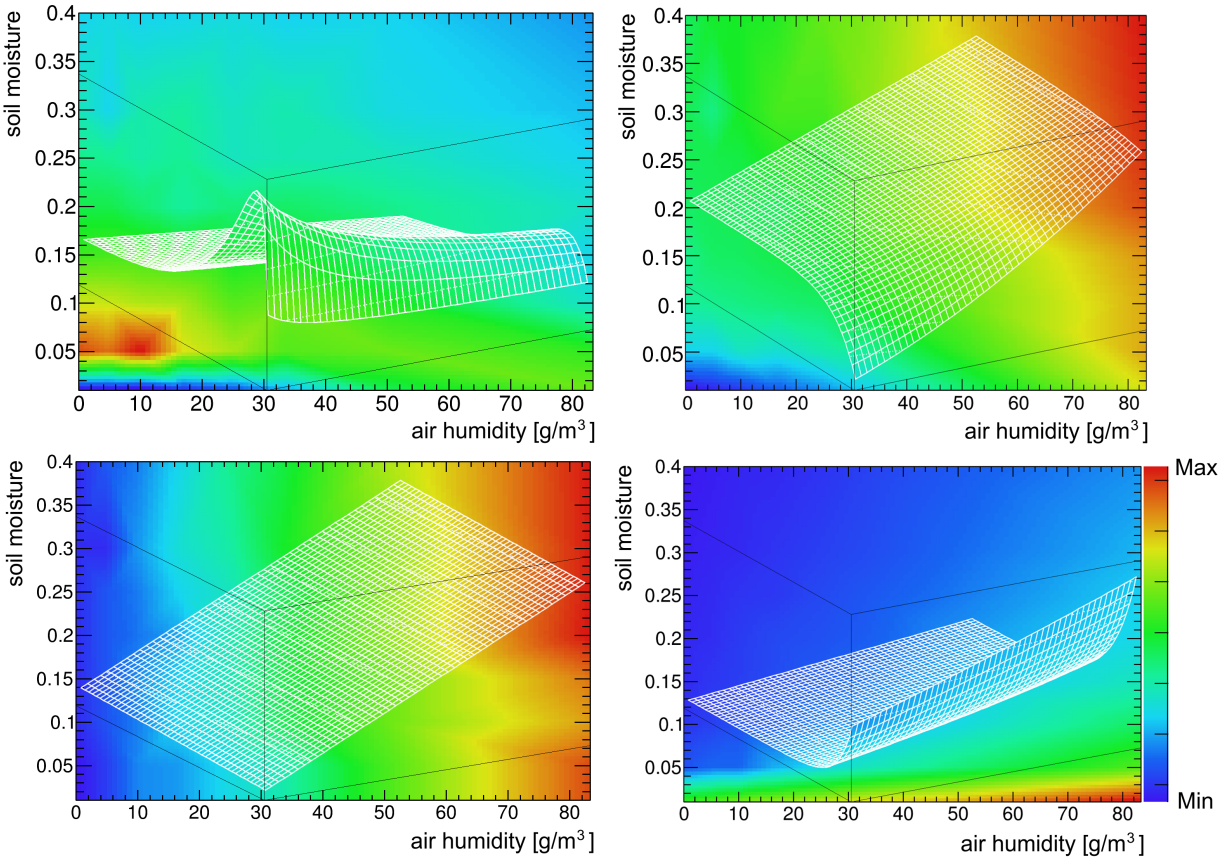

Figure 177: Fitting of the footprint parameters: from the top left to lower right panel as a function of volumetric soil moisture fractions and air humidity: F_5, F_6, F_7 and F_8. The plots show an interpolation of the results from the parameter fits from (181) like in the previous Fig. 176 shown as a hypersurface. The rainbow scaled color code shows the relative differences necessary for constructing the functional dependencies. The grid (white) represents the finally modeled function (194).

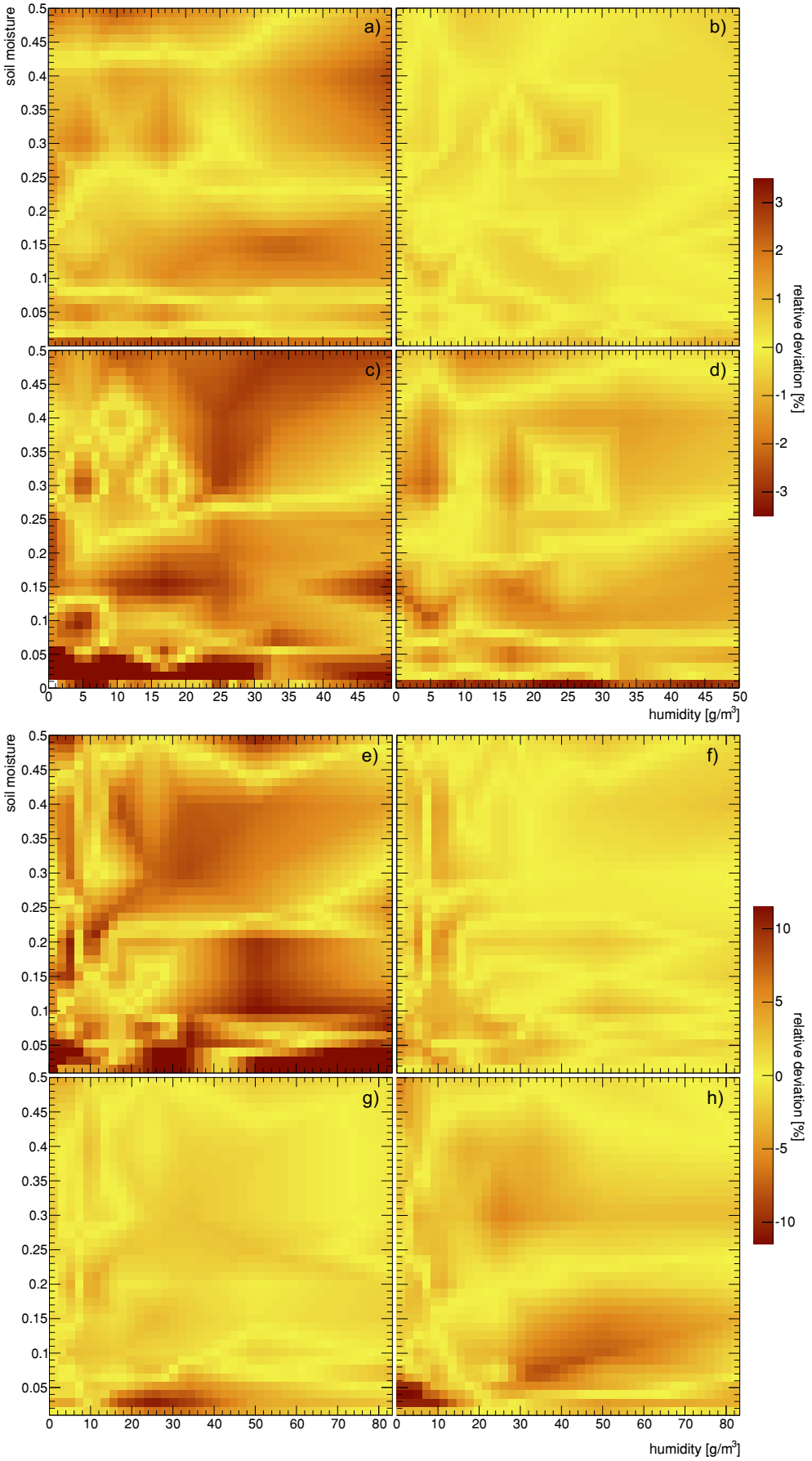

Figure 178: Fitting of the footprint parameters: Relative deviation of the fitted parameters of function (181) to the values evaluated from the simulation, e.g. the colored hypersurface of Fig. 177, as a function of volumetric soil moisture fractions and air humidity. The four top panels a) to d) present the residuals of parameters F_1 to F_4 in (181), which model the near-field terms. Panels e) to h) present the residuals of parameters F_5 to F_8 in (181), which model the far-field terms. Deviations are mostly due to statistical variations.

The following expressions have been found for modeling the radial weighting function:

$$
\begin{aligned}
F_0 &= p_0, \\
F_1 &= p_0\,(1+p_3 h)\,e^{-p_1\theta} + p_2\,(1+p_5 h) - p_4\theta, \\
F_2 &= \left((p_4 h - p_0)\,e^{-\frac{p_1\theta}{1+p_5\theta}} + p_2\right)(1+p_3 h)\,, \\
F_3 &= p_0\,(1+p_3 h)\,e^{-p_1\theta} + p_2 - p_4\,\theta\,, \\
F_4 &= p_0\,e^{-p_1\theta} + p_2 - p_3\,\theta + p_4\,h, \\
F_5 &= \left(p_0 - \frac{p_1}{p_2\,\theta + h - 0.13}\right)(p_3 - \theta)\,e^{-p_4\,\theta} - p_5\,h\,\theta + p_6\,, \\
F_6 &= p_0(h+p_1) + p_2\theta, \\
F_7 &= \left(p_0\,(1-p_6 h)\,e^{-p_1\theta(1-p_4 h)} + p_2 - p_5\theta\right)(2+p_3 h)\,, \\
F_8 &= \left((p_4 h - p_0)\,e^{\frac{-p_1\theta}{1+p_5 h+p_6\theta}} + p_2\right)(2+p_3 h)\,, \\
F_p &= p_0 / \left(p_1 - e^{-p/(1013\,\mathrm{mbar})}\right)\,.
\end{aligned}
\tag{194}
$$

with air pressure p, nondimensionalized air humidity h and volumetric soil moisture θ and with the parameters[c]:

Table 28: Numerical values for the parameters for the horizontal weighting function (194) in (181)

	p_0	p_1	p_2	p_3	p_4	p_5	p_6
F_0	3.7						
F_1	8735	22.689	11720	0.00978	9306	0.003632	
F_2	0.027925	6.6577	0.028544	0.002455	$6.851 \cdot 10^{-5}$	12.2755	
F_3	247970	23.289	374655	0.00191	258552		
F_4	0.054818	21.032	0.6373	0.0791	$5.425 \cdot 10^{-4}$		
F_5	39006	15002330	2009.24	0.01181	5.49	16.7417	3727
F_6	$6.03 \cdot 10^{-5}$	98.5	0.0013826				
F_7	11747	55.033	4521	0.01998	0.004572	3347.4	0.00475
F_8	0.01543	13.29	0.01807	0.0011	$8.81 \cdot 10^{-5}$	0.0405	26.74
F_p	0.4922	0.86					
D_{86}	8.321	0.14249	0.96655	0.01	20.0	0.0429	

This function allows to describe the neutron transport problem for the footprint investigation analytically.

B.3.2 | Modeling the depth distribution

In sec. 14.2.4 the depth penetration function has been introduced. In order to find a suitable parametrization, the procedure was similar to the footprint evaluation in sec. 14.2.3 and described in sec. B.3.1. For each setup the D_{86} quantiles were calculated additionally as a function of the impact distance to the sensor. Fig. 179 shows exemplarily such distributions additionally to Fig. 146. One can also see, that the maximum penetration depth (top left panel) is much different to the mean penetration. However, this value shall only be taken into account as a limit, not as a probe depth.

[c] It has to be noted, that a few constant numbers had to be inserted in the equations, like the 0.13 in F_5, in order to stabilize the multidimensional fit of `TMinuit` [493].

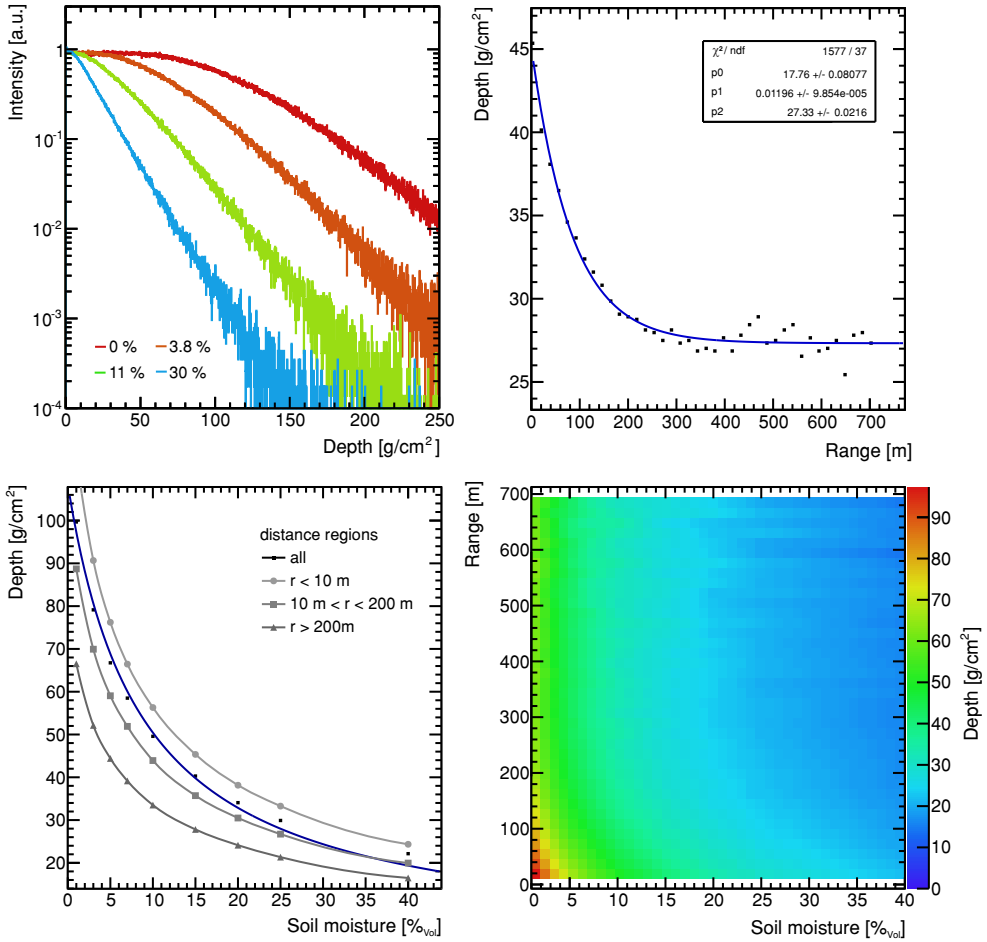

Figure 179: Penetration depth distribution characterization in the ground at a humidity of $h = 10\,\mathrm{g/m^3}$. Top row: Scattering center distribution with only the maximum penetration depth scored (left) for different soil moistures and (right) penetration depth quantile D_{86} for 15 $\%_{\mathrm{Vol}}$ as a function of impact distance with an exponential fit $p_0 \exp(-p_1 r) + p_2$ (right). Bottom row: Depth quantile as a function of soil moisture for different impact distance regions (left) and penetration depth quantile D_{86} as a function of impact distance and soil moisture (right). The D_{86} distribution is fitted by (183) with the parameters from tab. 29.

	p_0	p_1	p_2	p_3 [1/m]	p_4 [m^3/m^3]	p_5 [m^3/m^3]
D_{86}	8.321	0.14249	0.96655	0.01	20.0	0.0429

Table 29: Parameters for the depth weighting function (183) using the scheme of (181).

B.3.3 | Uncertainty analysis of the CRNS transport problem

In the simulated system containing soil, atmosphere, and a detector, uncertainties propagate non-linearly due to the variety of neutron interactions involved. As an indication of their total effect, uncertainties of the calculations were analyzed by means of the influence on the footprint radius R_{86}.

B.3.3.1 Errors on cross sections

	elastic		inel.	absorption		MT107
Element	$\Delta_{\sigma(\mathrm{th})}$	$\Delta_{\sigma(10\,\mathrm{MeV})}$	$\Delta_{\sigma(10\,\mathrm{MeV})}$	$\Delta_{\sigma(\mathrm{th})}$	$\Delta_{\sigma(10\,\mathrm{MeV})}$	$\Delta_{\sigma(\mathrm{MeV})}$
^{1}H	0.3	2.4	N/A	2.6	20	N/A
^{12}C	0.5	10	-	3	20	10
^{14}N	4	2	-	30	7.5	
^{16}O	2	4	-	10	-	10
^{27}Al	1.8	13	-	1.7	60	-
^{28}Si	1	8	30	20	40	25

Table 30: Relative uncertainties of cross sections in % according to ENDF/B-VII.1 at thermal energy and 10 MeV.

Here exemplary uncertainties are given representative for specific energy ranges. Typically, errors on cross sections listed in the ENDF data base do not vary significantly in the elastic scattering region. Therefore, uncertainties in the thermal and the MeV regime are chosen.

B.3.3.2 Error estimation on the footprint range

To estimate the influence of uncertainties in the cross sections, calculations have been carried out by modifying the cross section sets obtained from the data base. Here the results are presented for changes by one and two standard deviations.

	86 % quantile of range distribution [m]				
moisture [$\%_{Vol}$]	base	+1 Δ CS	−1 Δ CS	+2 Δ CS	−2 Δ CS
2.3	223.6(2)	216.4	233.6	208.9	241.3
7	202.7(3)	195.7	209.6	189.8	215.2
30	166.3(3)	162.7	170.3	157.5	176.6

Table 31: Error estimation for h = 10 g/m^3. Statistical errors on range quantiles are 0.3 % of the value for 4 % soil moisture and 0.7 % otherwise.

		rel. deviations to base range quantile [%]			
moisture [$\%_{Vol}$]	base [m]	+1 Δ CS	−1 Δ CS	+2 Δ CS	−2 Δ CS
2.3	223.6(2)	-3.2	4.5	-6.6	7.9
7	202.7(3)	-3.4	3.4	-6.3	6.2
30	166.3(3)	-2.1	2.4	-5.3	6.2

Table 32: Error estimation for h = 10 g/m^3. Relative deviations on range quantiles for varying cross section. Errors on deviations are 0.4 % for 4 % soil moisture and 0.7 % otherwise.

B.3.3.3 Uncertainties induced by the choice of the energy sensitivity

The evaluation of the footprint was carried out mainly using the canonical limits for the energy sensitivity of 100 eV to 10 keV, which represents the mean energy for neutrons slowing down from evaporation to thermal energies. As the prior analysis showed the travel distance of neutrons in the soil-air interface depends significantly on the amount of environmental water. However, the average relevant transport range barely depends on the choice of the sensitive energy range. Fig. 180 shows the lethargy-averaged mean range of neutrons recorded by a single detector entity exemplarily for three different soil moisture conditions.

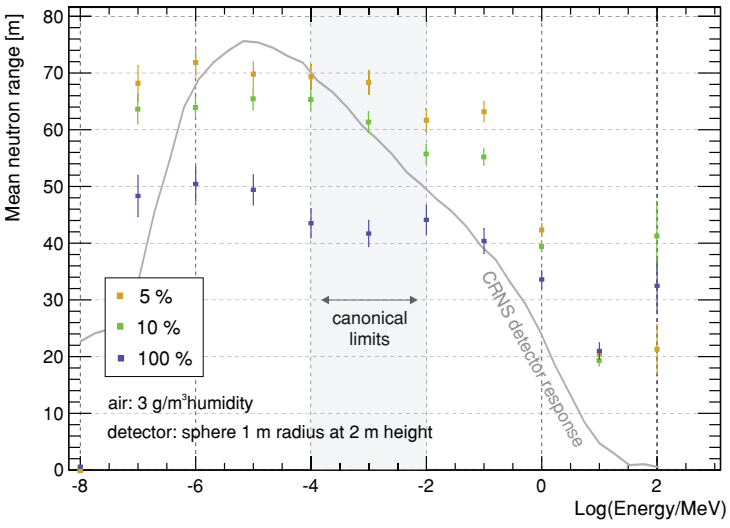

Figure 180: Range evaluation using a spherical detector with 1 m radius in a 600 m domain and $950 \cdot 10^6$ neutrons for three different soil moisture conditions. As a comparison the simulated detector response is plotted together with the energy threshold as chosen for the footprint evaluation.

Within the water-sensitive domain of 1 eV to 0.1 MeV the transport distance stays remarkably constant as a function of neutron energy. Within this regime one obtains a maximum change of 10 %, however, taking into account to the actual detector sensitivity, this variation averages out. Especially the chosen threshold energies center around the inflection point of this plateau. Therefore, considering a thermally shielded detector which does not record neutrons below 0.5 eV, one can assume an error of 2 % on the footprint attributed to the choice of the used detection thresholds.

B.3.3.4 Uncertainties induced by the choice of the input spectrum

In a test case of 13 % soil moisture the influence of errors of the input model on the footprint was investigated. Assuming high energetic neutrons to impinge perpendicular to the surface, instead of the sampling from the distribution given by Nesterenok, leads to a (2.3±0.2) % decrement of the Q_{86} radius. Assuming a perpendicular incidence for low energetic neutrons instead of an isotropic distribution leads to a (3.1±0.2) % decrement. Furthermore, modifications of the energy dependent function $Cf(E)$ generating the source from the Sato spectrum have been studied. Overcompensation, i.e. increasing $Cf(E)$, by 50 % leads to (7.1±0.2) % increase of the footprint radius, whereas underestimation by 50 % leads to a (5.0±0.2) % decrease. Taking the unmodified Sato pure water spectrum as a source reduces the footprint radius by (9.2±0.3) %.

	86 % quantile of range distribution			
input model	r_{Q86} [m]	$\Delta_{r(Q86)}$ [m]	rel. [%]	$\Delta_{rel.}$ [%]
Low energy: all 0°	196.4	0.4	-3.1	0.2
High energy: all 0°	198.0	0.4	-2.3	0.2
Corr x 0	184.1	0.4	-9.2	0.3
Corr x 0.5	192.6	0.4	-5.2	0.2
Corr x 0.8	198.3	0.4	-2.2	0.2
Corr x 1.5	217.1	0.4	7.1	0.2
Corr x 2.5	240.9	0.4	18.9	0.3

Table 33: Error estimation for h = 10 g/m³ and 10 % soil moisture. Relative deviations on range quantiles for varying input model. The following assumptions were evaluated: all low/high energetic neutrons are released with an angle of 0° instead of the distribution used and the correction function, which generates the incoming-only function from the total flux spectrum (67), was changed by larger factors.

B.3.3.5 Uncertainty analysis summarized

Variations of cross sections by their standard deviation, given in the ENDF data base, lead to changes of R_{86} by 4 %, 3 %, and 2 % for θ = 3 %, 10 % and 40 %, respectively. The effect of elastic scattering dominates the budget by approximately 70 %. The errors of the cross sections can be considered as systematic for neutron transport simulations in general. The impact of different source spectra as model input in a test case with 10 % soil moisture and 5 g/m³ air humidity was also analyzed. As explained in sec. 14.1.1 the incident spectrum was generated over water by subtracting the soil response from the original mixed spectrum. Variations of this soil response spectrum by 20 % alters R_{86} by 2.5 %. If the emission angles of source neutrons were not set according to their angular distributions, but chosen perpendicular to the surface, the change of the footprint radius would be 2.5 % applied to high energetic neutrons only and 3.0 % also including sub-MeV neutrons. Compared to the uncertainties involved in the calculations the impact of other source spectrum models can be much higher. The integration of the counted particles further leads to statistical uncertainties on R_{86} in the order of 0.2 % for 10^7 neutrons. For the final fit model Fig. 178 shows the residuals of the fit function (194) to the base data set. Except for extremely low environmental water conditions there are no significant or systematic deviations to the underlying data. Most of the variations in Fig. 178 are due to statistical errors. For example the overall

integral of the near-field terms of the weighting function (181) leads to an error in the order of 0.5 %.

B.3.4 | THE ROAD CORRECTION FUNCTION

The function, which has been developed with M. Schrön for correcting the road bias presented in sec. 14.3.5, is

$$\begin{aligned} C_{\mathrm{Corr}}\left(\theta_{\mathrm{field}}, \theta_{\mathrm{road}}, w, x_c\right) = 1 & \\ + c_0 \left(1 - c_1 \frac{w}{\mathrm{m}}\right) \left(\theta_{\mathrm{field}} - \theta_{\mathrm{road}}\right) \frac{c_2 - c_3 \theta_{\mathrm{road}}}{\theta_{\mathrm{field}} - c_4 \theta_{\mathrm{road}} + c_5} & \\ \cdot \left(c_6 \exp\left(-c_7 \left(\frac{w}{\mathrm{m}}\right)^{-c_8} \left(\frac{x_c}{\mathrm{m}}\right)^4 \right) + (1 - c_6) \exp\left(-c_9 \frac{x_c}{\mathrm{m}}\right) \right). & \end{aligned} \tag{195}$$

The data from the simulation were fitted by (195). The resulting parameters are summarized in tab. 34:

c_0	c_1	c_2 [$\mathrm{m^3/m^3}$]	c_3	c_4	c_5 [$\mathrm{m^3/m^3}$]	c_6	c_7	c_8	c_9
0.42	0.50	1.11	4.11	1.78	0.30	0.94	1.10	2.70	0.01

Table 34: Numerical values for the parameters of the road bias correction function (195).

The function describes roads of widths below approximately 7 m, as for wider roads the neutron density saturates around the center at a peak value. Furthermore, this function is limited to effective values for θ_{road} between 1 % and 16 % and requires a prior knowledge about the field moisture conditions. A more detailed analysis is presented in [SK2018].

In collaboration with the Helmholtz Centre for Environmental Research - UFZ, Leipzig, and especially M. Schrön, a graphical user interface (GUI) for URANOS has been developed, which specifically targets the needs of environmental sciences. URANOSGUI allows to run the Monte Carlo with the full feature list described in sec. 6 except for the readout simulation for gaseous detector. It enables researchers to carry out neutron transport simulations without the need of configuring the setup by text files[d], which is the usual modus operandi for the codes mentioned in sec. 5.2. It especially does not require profound knowledge of the internal software buildup, as the relevant features and settings are all accessible from the graphical frontend. Instead of drop-down menus or child windows it uses a tabbed document interface, which is functionally split into two parts horizontally partitioned by the golden ratio. The left side functionally controls the program, its general settings and problem-related configurations. The right side tabs provides a direct insight into the ongoing computation. It shows the actual neutron density and track distribution, interaction range and depth and detector scoring results. The top bar represents the dashboard for starting and stopping the simulation as well as exporting the results. It also shows the expected time to accomplish the actual job. A simulation, like presented in the following screenshots of the UFZ site Fig. 181 to Fig. 184, is carried out by creating a layer structure, setting vertical positions and defining a ground layer, a source layer and a detector layer for scoring. The GUI then automatically loads *n*.png or *n*.dat files, with *n* being the layer number, placed in the configured work directory. According to the pixel or ASCII matrix voxels are extruded based on the predefined material codes of sec. B.2.3.

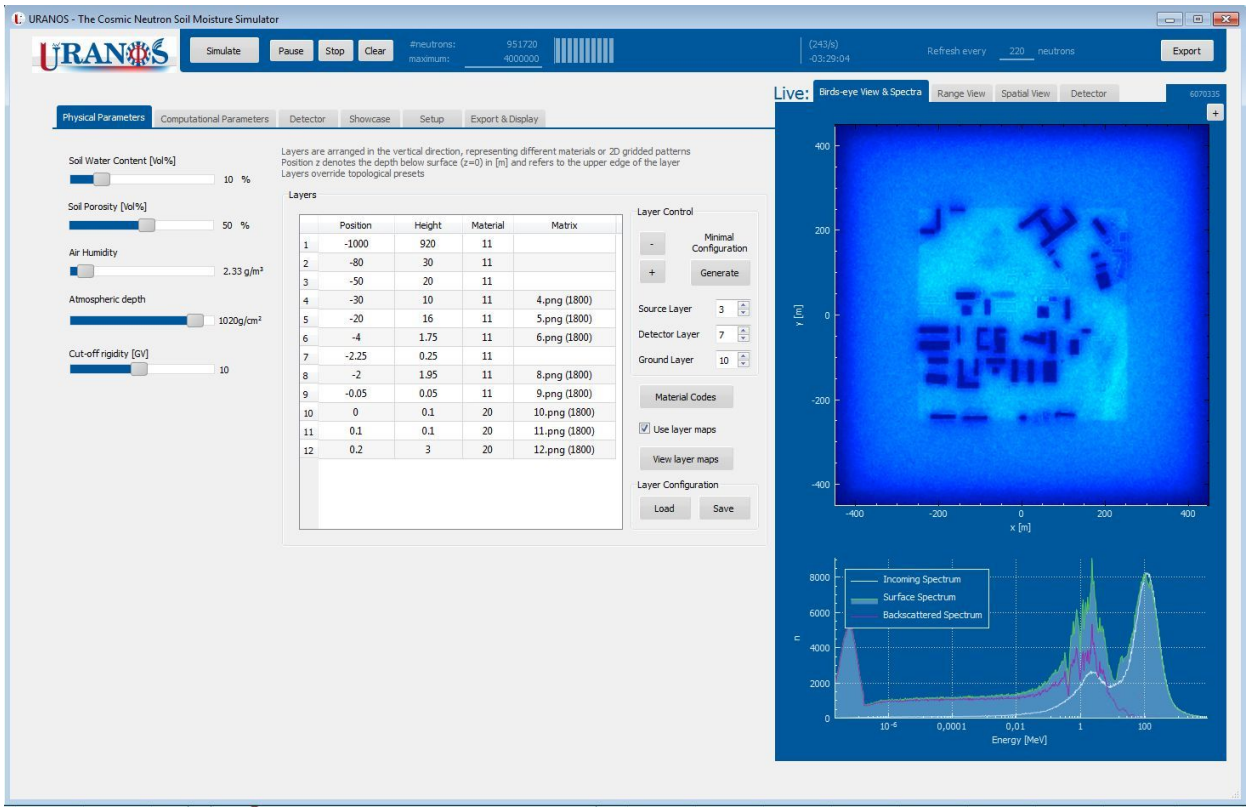

Figure 181: URANOS GUI main tabs: Setup for the layer arrangement for the vertical geometry and environmental parameters (left) and birds-eye view with the above-ground neutron spectrum (right).

[d] It also offers for advanced users a command line option to be configured and run by steering files, which also provide access to features not available in the GUI.

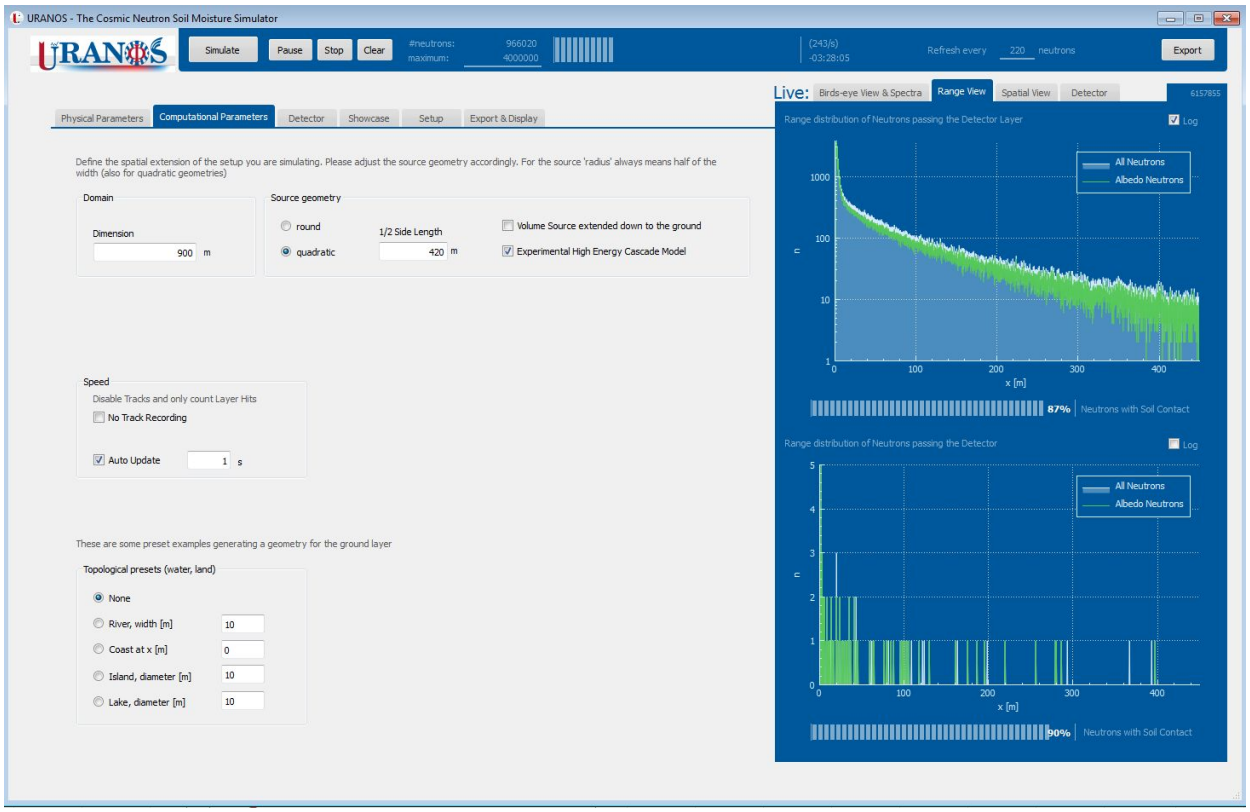

Figure 182: URANOS GUI main tabs: Setup for the general domain geometry and computation (left) and live view for the range distribution in the detector layer and the virtual detector (right).

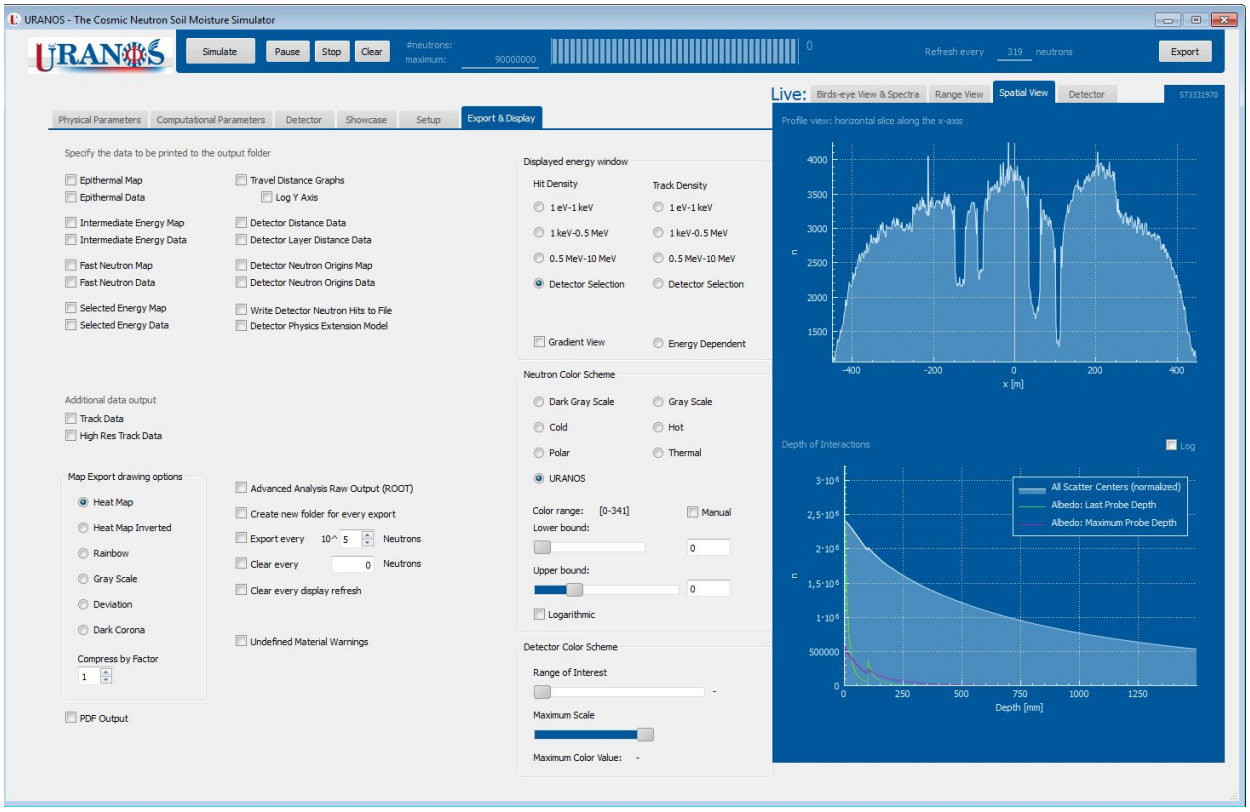

Figure 183: URANOS GUI main tabs: Export options and configurations of the live-view display (left) and spatial neutron distributions (right). The top panel shows the horizontal neutron density in the detector layer by cut view through the center of the domain and the bottom panel show the vertical interaction depth distribution in the ground.

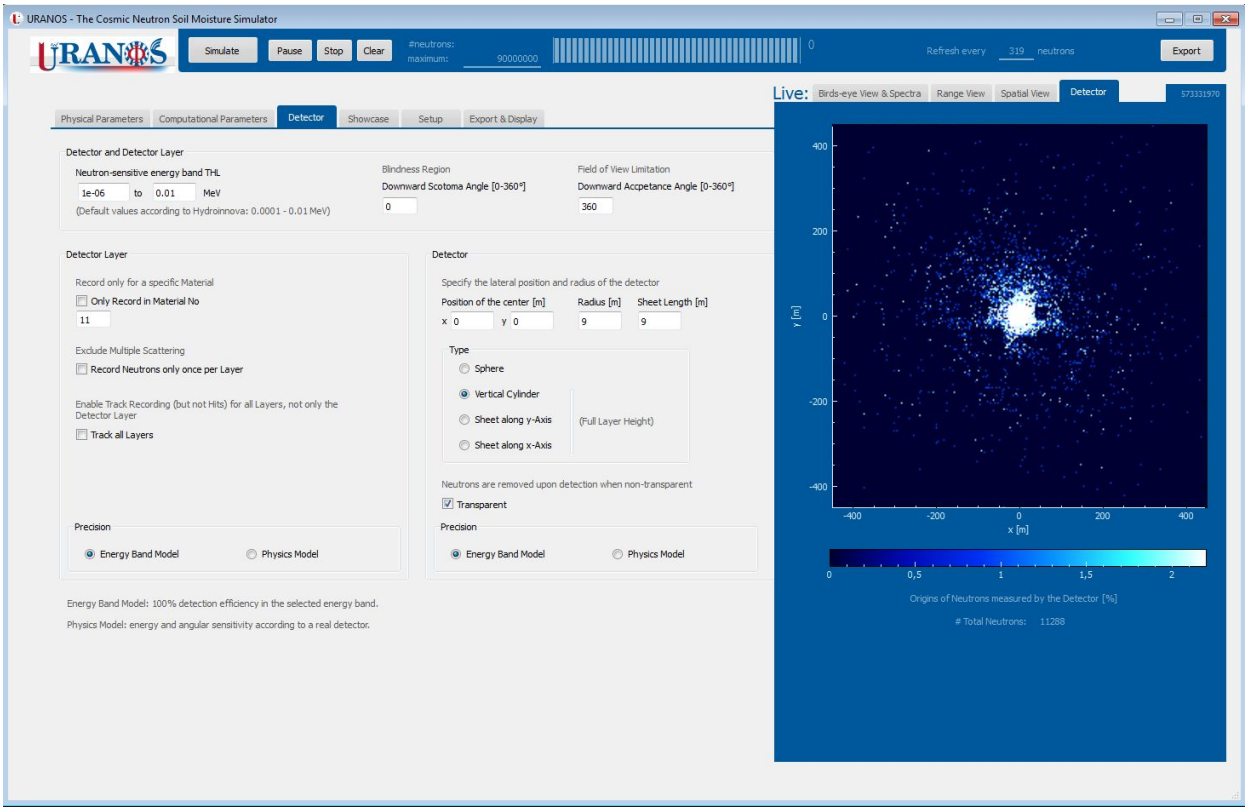

Figure 184: URANOS GUI main tabs: Setup for the scoring of the detector and detector layer (left) and distribution of neutron origins recorded by the virtual detector (right).

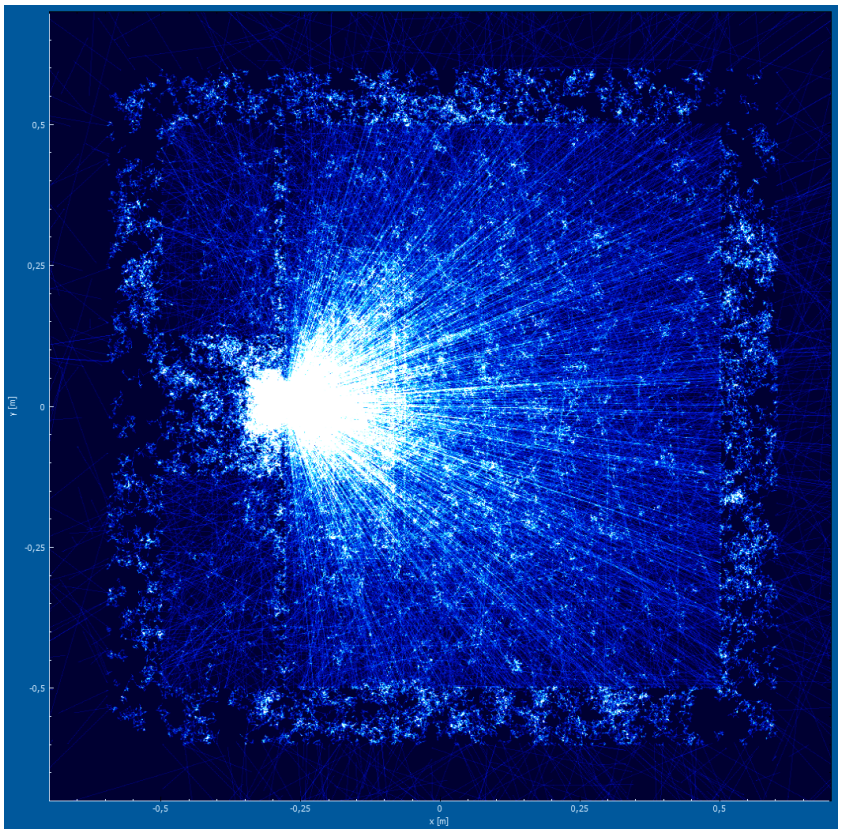

Figure 185: URANOS GUI high resolution track view with histories of thermal neutrons integrated over 1 s: Example of the simulation of a thermal neutron source inside a polyethylene detector test box.

C

ACKNOWLEDGEMENTS

This work could not have been realized without the financial support during many years of research and experiments. The largest part of the funding has been provided by the Bundesministerium für Bildung und Forschung (BMBF) in the frame of the project „Neutron Detectors for the MIEZE method“. Further contributions came from the Physikalisches Institut, Heidelberg University, from the Deutsche Forschungsgemeinschaft (DFG), from the Helmholtz Centre for Environmental Research-UFZ, Leipzig. Beam times at large-scale research facilities were additionally supported by the Technical University Munich and the Institute of Nuclear Chemistry of the Mainz University. Part of the measurements were performed at the single crystal diffractometer, which is jointly operated by the RWTH Aachen University Institute of Crystallography and the Jülich Centre for Neutron Science (JCNS) as well as the RESEDA Spin Echo spectrometer, operated by the Technical University Munich, both located at the Heinz Maier-Leibnitz Zentrum (MLZ) in Garching.

Furthermost I want to thank my collaborator Martin Schrön at the UFZ, Leipzig: six joint papers and more to come, numerous conferences and approximately 4700 mutual emails in total within approximately six years (which makes a remarkable 2.5 emails per day, including the non-stop weekends) speak by itself.
I am grateful for having nice, supportive and sometimes critical colleagues around me at the Physikalisches Institut: Fabian Allmendiger, Matthias Janke, Peter Augenstein, Jannis Weimar, Christoph Roick, Manuel Fohler, Peter Vivell, Lukas Raffelt, Dirk Wiedner, Gerd Modzel, Max Lamparth, Carmen Ziener, Christian Färber, Martin Klein and Maarten DeKieviet.
Among my students I especially want to acknowledge Michael Liebig, Boris Rivkin, Jan Hammerich and Fabian Schmidt for the good teamwork in the office and the laboratory.
Many thanks also go to the excellent team of the electronics and mechanics workshop of the Physikalisches Institut as well as for the technical support of Markus Henske.
At the UFZ my thanks go to Steffen Zacharias and Peter Dietrich.

Also I want to thank the meanwhile numerous scientists in team of the RESEDA and the MIRA instrument at the FRM II: Wolfgang Häußler, Christian Franz, Franz Haslbeck, Olaf Soltwedel, Steffen Säubert, Stefan Söllradl, Nicolas Martin, Thorsten Schröder, Tobias Weber and Robert Georgii along with Martin Meven, instrument scientist at HEiDi, and Malgorzata Makowska, instrument scientist at NECTAR.
Honorable mentions for my beam times at the TRIGA reactor: Christian Stieghorst.

This acknowledgment should not close without a special mention to my international collaboration partners in Cosmic-Ray Neutron Sensing: Marek Zreda, Darin Desilets, Paul Schattan and Tatsuhiko Sato.

Special thanks go to Ernst Peter Fischer, author and science historian, for his inspiring lectures and his contributions in my seminar „The most important mistakes in physics' history“.

Last, but not least, my supervisor Ulrich Schmidt, whom I would like to thank with the following poem:

Eternal

I am in the corridor of days enclosed
and burdened even by the skies.
I look into centuries, but live in minutes
waiting for the Saturday of Saturdays.

The end of troubles in my fate,
blind wanderings of the soul.
O day, come, deign me sight
with all bizarre to be known.

I will get another soul
with all the worries vault'd.
I will bless the golden road
to the Sun from the soiled.

And he, who walked by my paths
in thunder and meek silence,
who was cruel to my pleasures
and merciful to my flaws,

who taught to fight and to bear
and of all the ancient wisdom profound,
will lower the staff, turn around,
and simply say: We are here.

Nikolay S. GUMILËV

translation from Гумилёв, Вечное (1912),
with special thanks to Джетъ - Антология (2007).

Vente, gresle, gelle,

j’ay mon pain cuit.

François VILLON

Statement of authentication
I hereby declare that I have written the present thesis independently without the use of other resources than those indicated. All published work is cited completely and correctly.

Markus Köhli